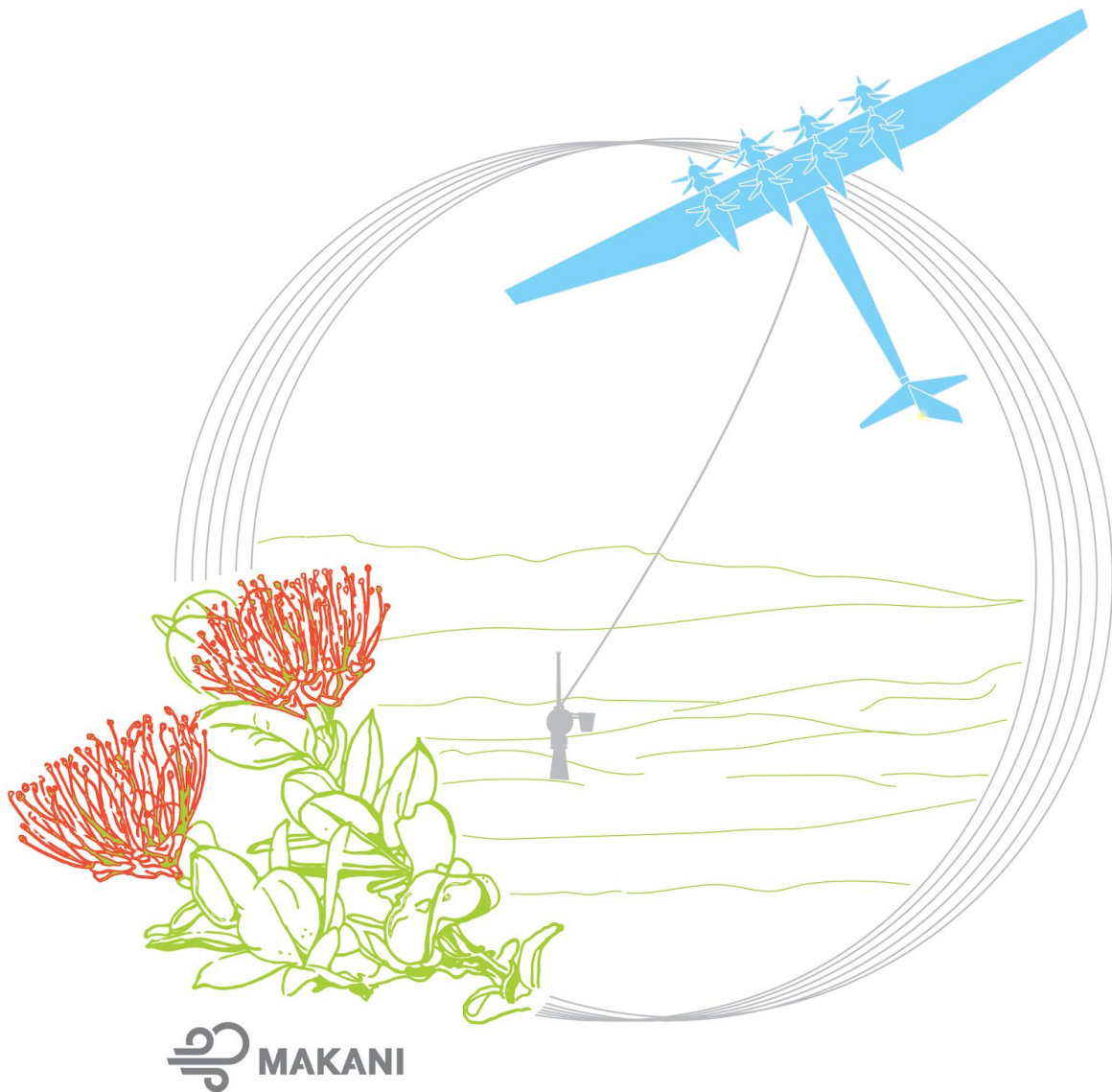


The Energy Kite

Selected Results from the Design, Development and Testing of
Makani's Airborne Wind Turbines

Part II, Technical Artifacts



Makani Team



The Energy Kite: Selected Results from the Design, Development, and Testing of Makani's Airborne Wind Turbines (Part II of III) / by Paula Echeverri, Tobin Fricke, Geo Homsy, Nicholas Tucker, on behalf of the Makani team.

Copyright © 2020 by Makani Technologies LLC

Distributed under the [Creative Commons CC BY 4.0 License](https://creativecommons.org/licenses/by/4.0/). You are free to copy and redistribute this material in any medium or format for any purpose, even commercially.



Intended for electronic publication and distribution. Copies of this volume may be found at <https://archive.org>

Additional information is at <https://x.company/projects/makani>

Corresponding author: Paula Echeverri, paulae@alum.mit.edu

Published September 2020

Photos: Andrea Dunlap and archive team

Front cover illustration: Kate Stirr

Editing and layout: Betsy Pfeiffer

Cover art: Hawaiian 'ōhi'a lehua flower and Makani's M600 energy kite flying crosswind on the big island of Hawai'i.

Contents

Makani Systems Overview	5
<i>Comprehensive overview (slide deck) of the M600 system, including market opportunity, system components, design methods, and validation approach.</i>	
A Low-Cost Fiber Optic Avionics Network for Energy Kites	97
<i>Kurt Hallamasek, Eric Chin, Paul Miller, Mike Mu, Michael Scarito, Eric Uhrhane Describes how Makani has achieved commercial-aviation-like network integrity and reliability, using low cost consumer-grade COTS components.</i>	
Base Station Team Final Documentation	117
<i>Simon Nolet, Dean Levy, Sean Chou Documentation of base station design considerations for the next generation system, as would have been developed for a commercial demonstration project beginning operations in 2023. Based on lessons learned operating the GS02 machine that was used in Hawaii and Norway flight testing.</i>	
Ozone Rev1 Design Document	147
<i>Andrew Goessling Explains the process for arriving at electrical specifications for the Makani motor controller, and notional electronic design that meets those specifications. Requires extensive Makani-specific context (motor out operation, etc) to understand 100%, but this will be useful in general for high-power-density aviation designs.</i>	
Control Telemetry Users Guide	179
<i>Description of the telemetry data produced by the simulator and flight tests. Essential to understanding and making use of the online archive of flight test data.</i>	
Effect of Design Parameters on the M600 Stability in Crosswind	199
<i>Jerome Sicard An introduction to the problems introduced into flight stability by the tether.</i>	
Kite Stability in Crosswind Flight	223
<i>Jerome Sicard, Geo Homsy, Michael Abraham Gives a ground-up derivation of tethered crosswind flight stability.</i>	

Tether Attachment and Bridle Knot Trim Considerations for Energy Kites	233
Geo Homsy, Trevor S. Orr, Nicholas Tucker <i>Makani's observations on placement of bridle attachment points for energy kites, to maximize controllability and power output.</i>	
Crosswind Kinematics	257
Michael Abraham <i>Calculations of the motion required to follow a flight trajectory while also tracking angle-of-attack, angle-of-sideslip, and airspeed commands.</i>	
The Spreadsheet Kite Structure Sizer	273
Florian Kapsenberg <i>Explains how we compute predicted airframe mass from performance requirements and input parameters.</i>	
Dimensionalizing and Sizing of Control Surfaces for Stability and Authority	291
Makani Oktoberkite Team <i>Gives best practices on how to size an empennage and associated control surfaces, for adequate stability and control authority. Includes an important observation specific to energy kites, in which the propulsion system extracts energy from the flow instead of adding. This has significant implications for surface sizing.</i>	
BigM600 Tail Sizing White Paper	297
TLG Aerospace Engineering (consultant) <i>A much more detailed approach to tail sizing than that used by Makani in the preliminary design.</i>	
Airfoil Design for the October Kite: Feasibility Studies	333
TLG Aerospace Engineering (consultant) <i>Gives a discussion of how to design from first principles a high-lift, two-element, actuated flap airfoil for energy kite use.</i>	

Note: These artifacts were produced as Makani internal work products and are presented here as they were written. They may contain references to other material that has not been released or that no longer exists.



System Overview

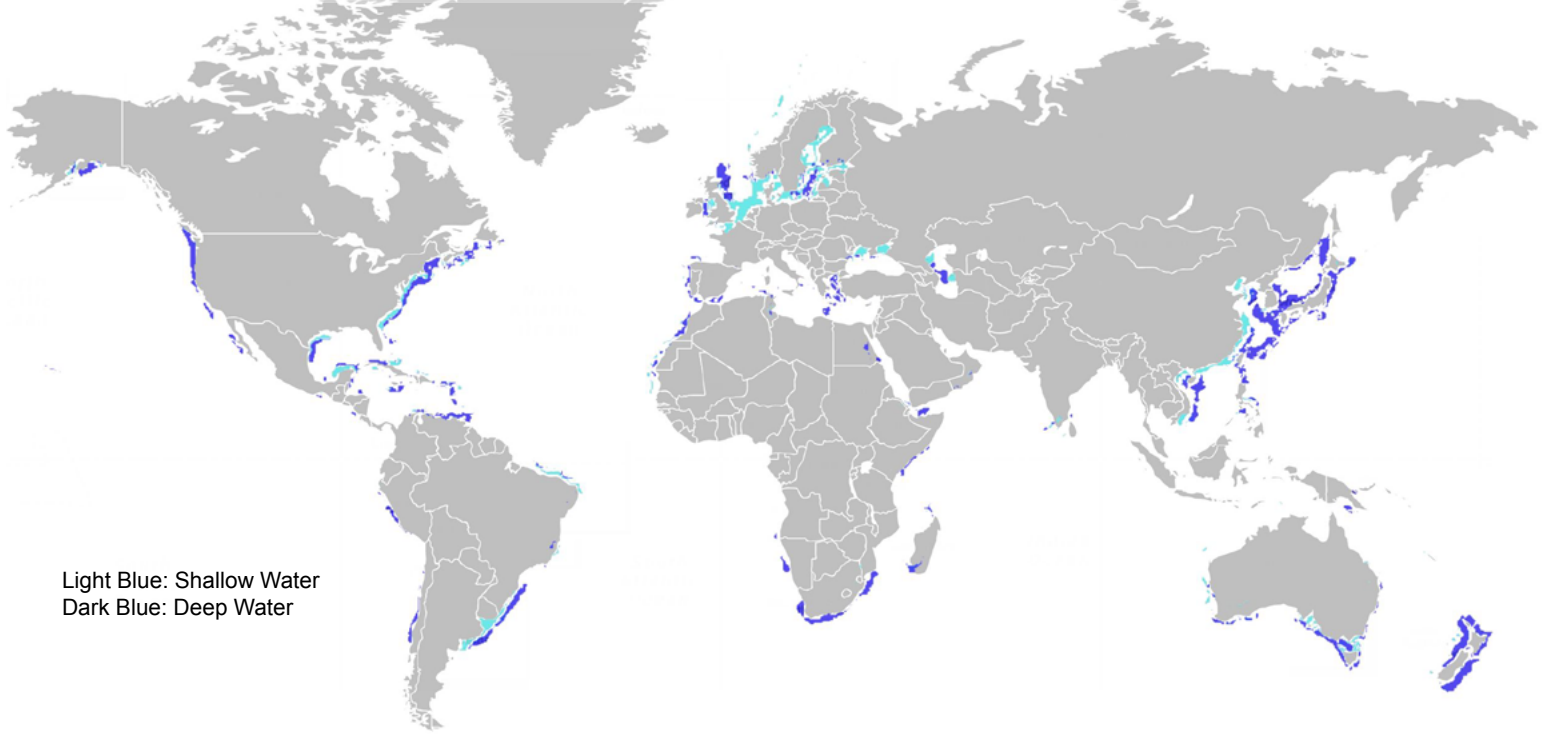
March 2019

Modified from the original for public release (2020)

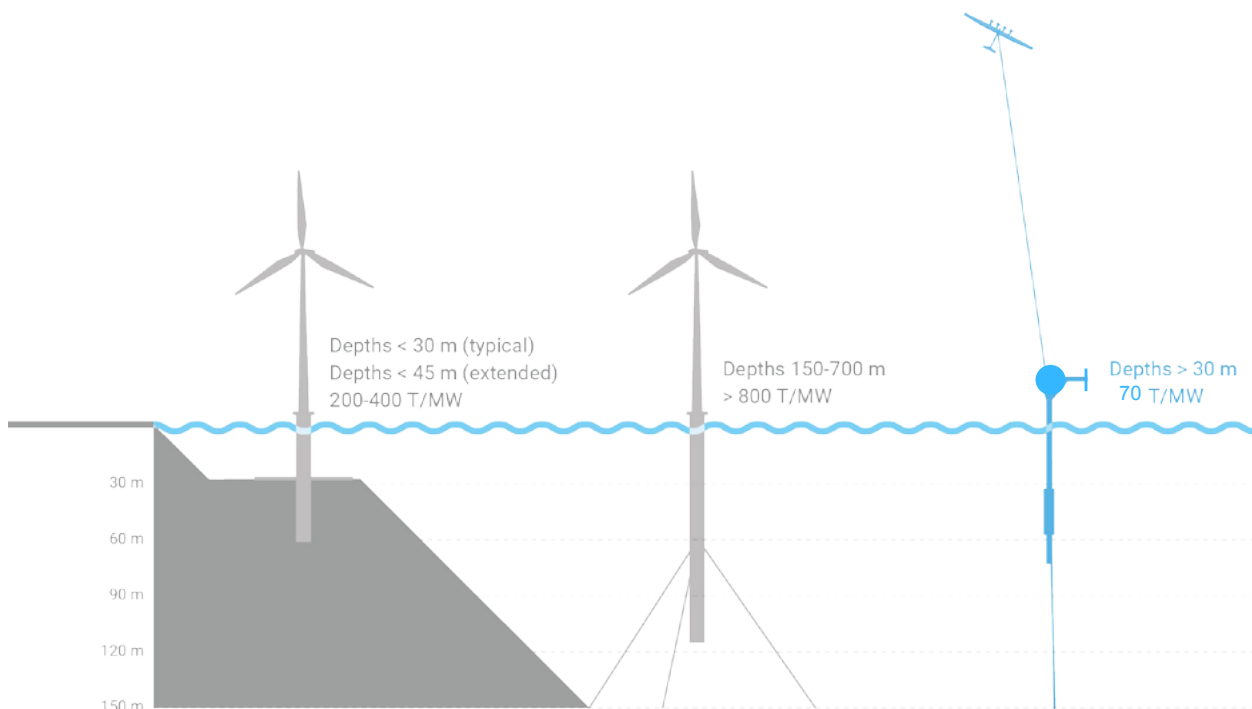


Opportunity

But Two-thirds of Windy, Populated Coastal Zones are Stranded in Deepwater

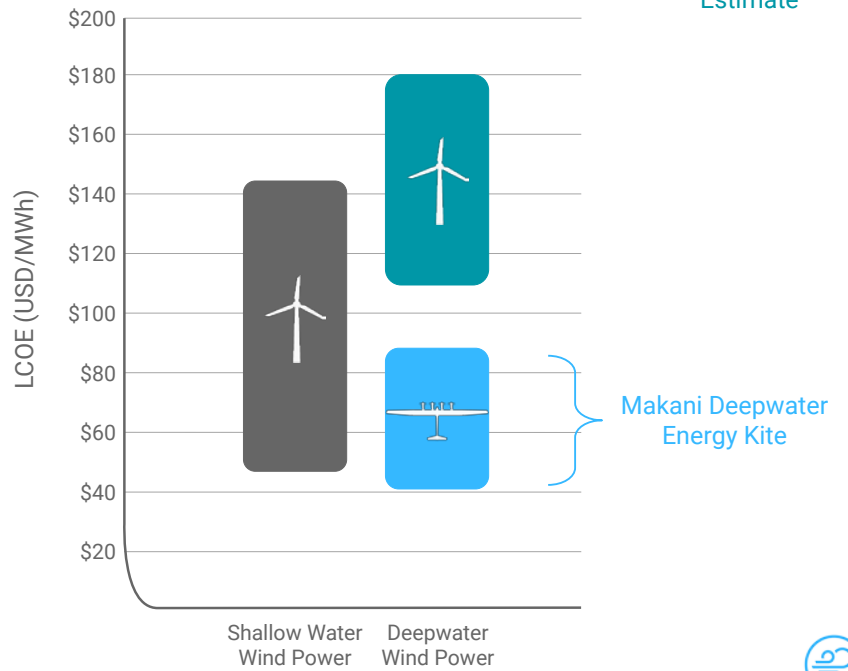


Accessing Deepwater Requires a Low-Cost Floating Technology



Lightweight Tech = Lower Costs in Deepwater

- Offshore wind levelized cost of energy by water depth estimated range within the next decade
- 1/10 mass results in large reduction in capex, construction and logistics cost
- Makani Energy Kites can create a brand new market for deep water offshore



Why Makani?

- Fully autonomous
- Much lower mass
- First airborne technology offshore
- Robust, worldwide IP portfolio
- Team experience at intersection of wind power & autonomous aircraft
- Have been flying at scale for years
- Detailed systems engineering and techno-economic analysis
- Validated simulation tools
- Well funded



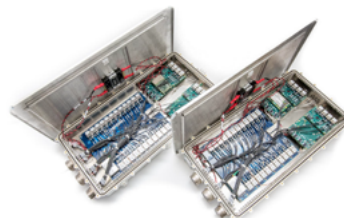


M600 Overview

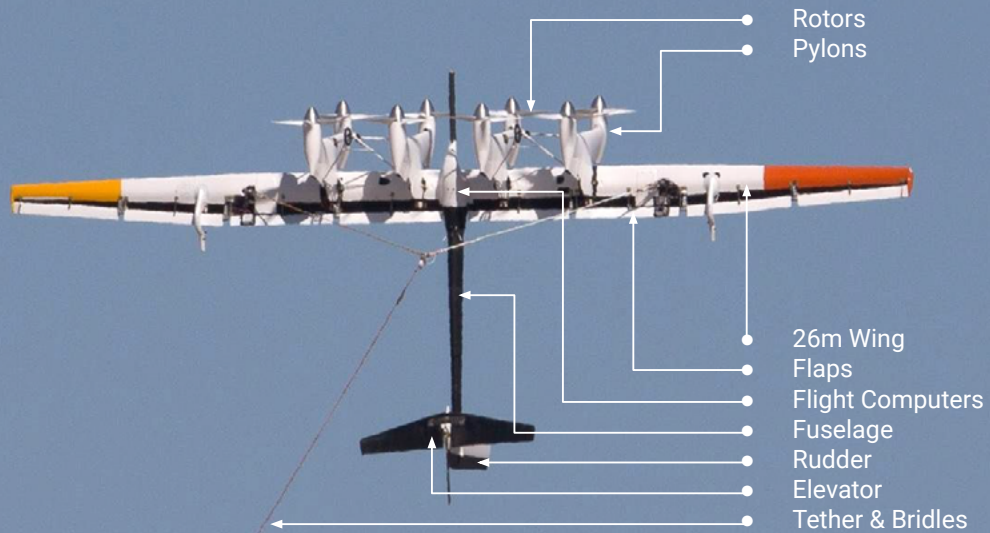


M600 Overview

- High-lift, lightweight carbon fiber composite airframe
- Permanent magnet direct-drive motor/generators
- Silicon carbide power inverters
- Triple-redundant flight control computers
- Fiber optic avionics communications network
- High performance tether with pultruded carbon fiber core
- Completely autonomous flight
- Growth to 1 MW
- Less than 3 tons per megawatt

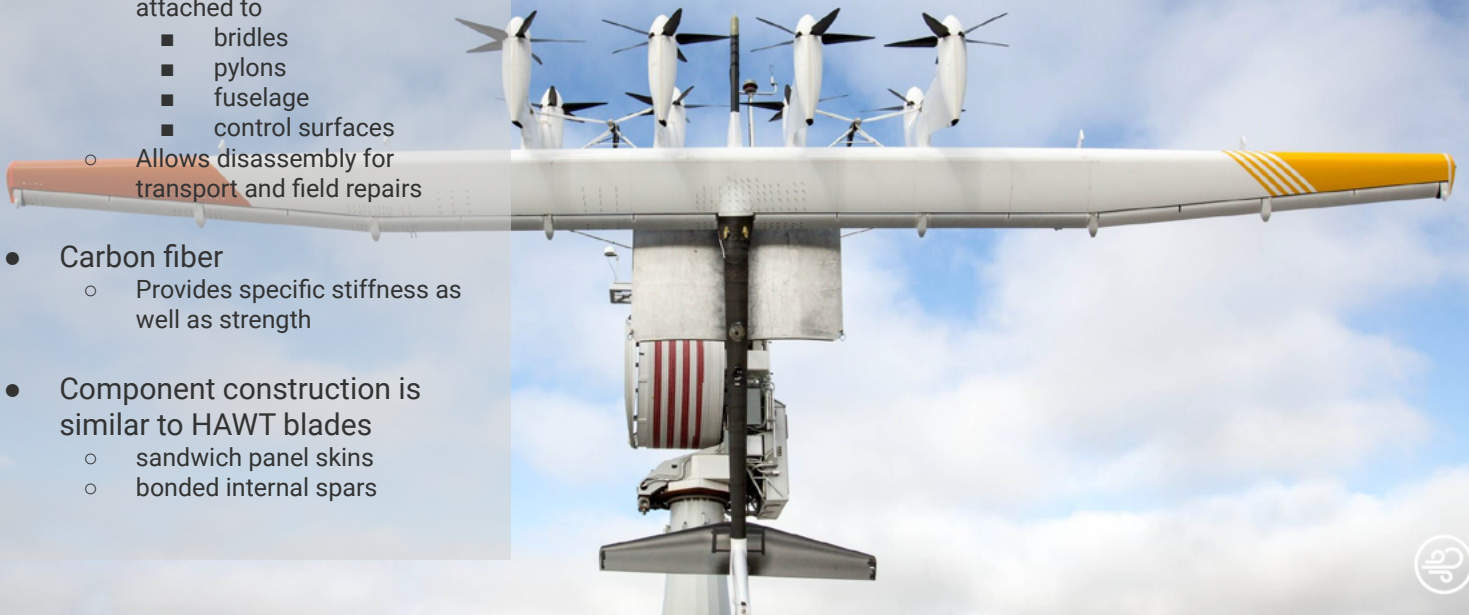


Kite Components



Technology: Airframe

- **Modular composite structure**
 - Single-piece wing backbone attached to
 - bridles
 - pylons
 - fuselage
 - control surfaces
 - Allows disassembly for transport and field repairs
- **Carbon fiber**
 - Provides specific stiffness as well as strength
- **Component construction is similar to HAWT blades**
 - sandwich panel skins
 - bonded internal spars



Technology: Rotors

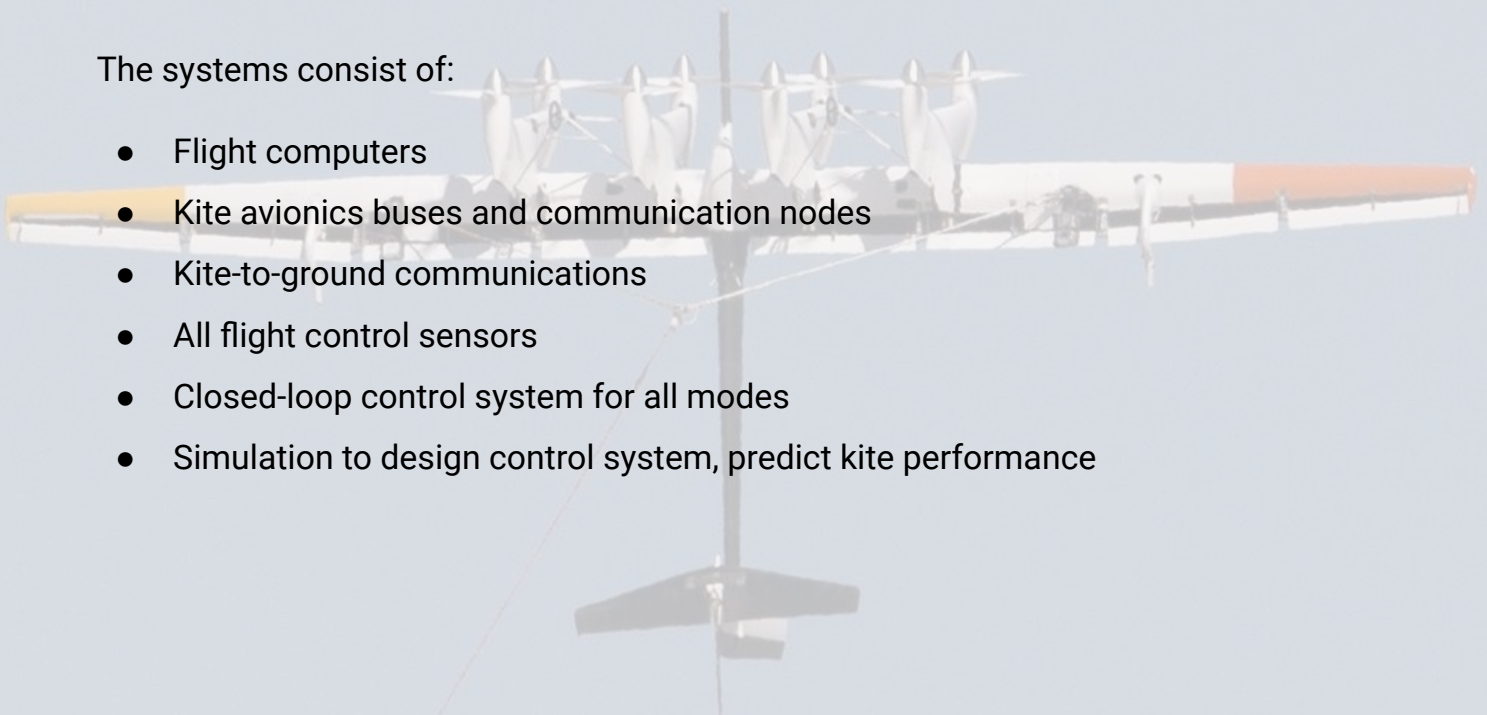
- Designed for:
 - Thrust and generation
 - Low noise signature
 - Low inertia to minimize gyroscopic loads
 - Structural simplicity for low manufacturing cost
 - Durability
- Carbon fiber construction for stiffness, low mass
- Leading edge erosion protection
- Fixed pitch for lower O&M costs



Avionics + Control System

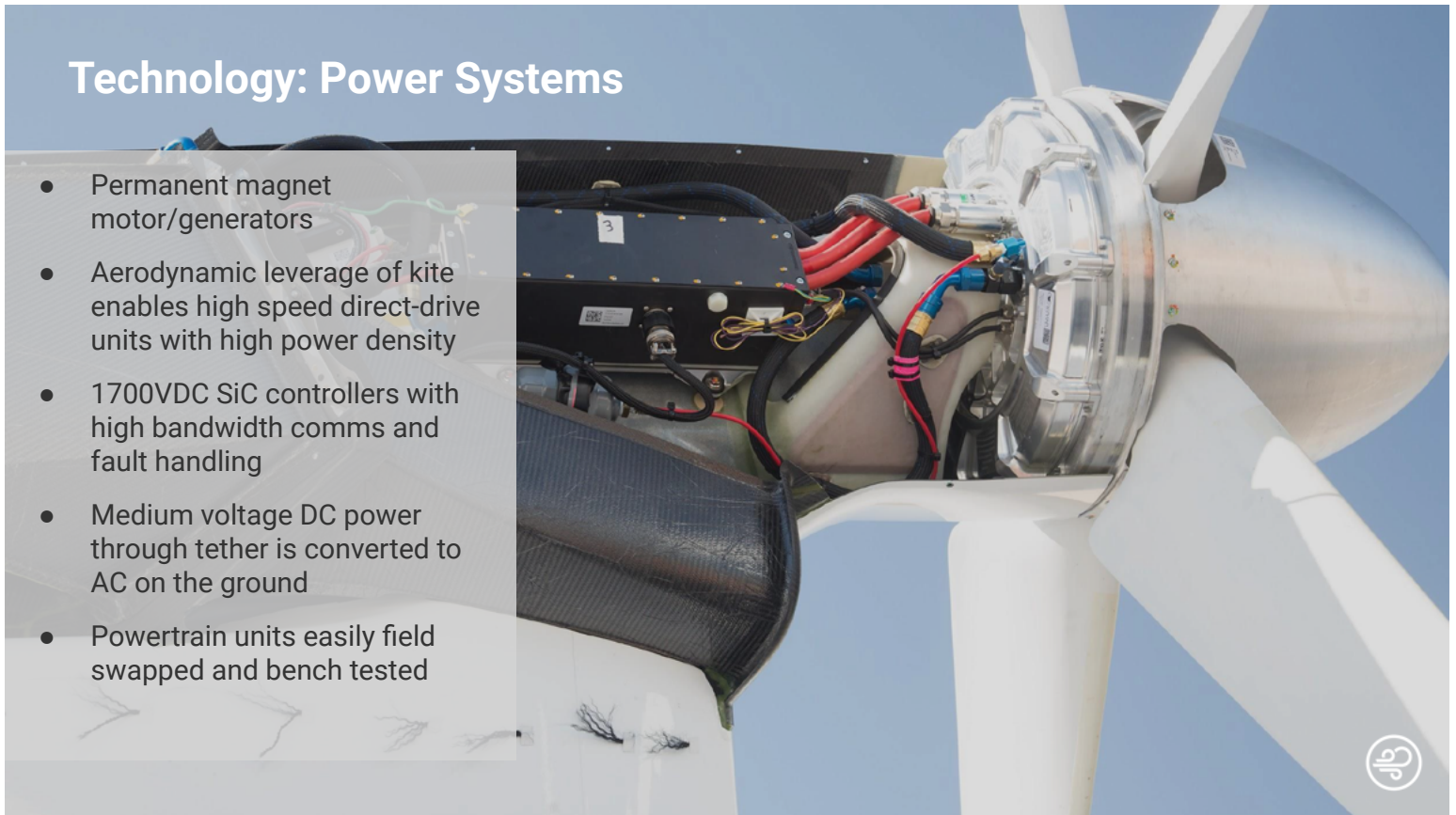
The systems consist of:

- Flight computers
- Kite avionics buses and communication nodes
- Kite-to-ground communications
- All flight control sensors
- Closed-loop control system for all modes
- Simulation to design control system, predict kite performance



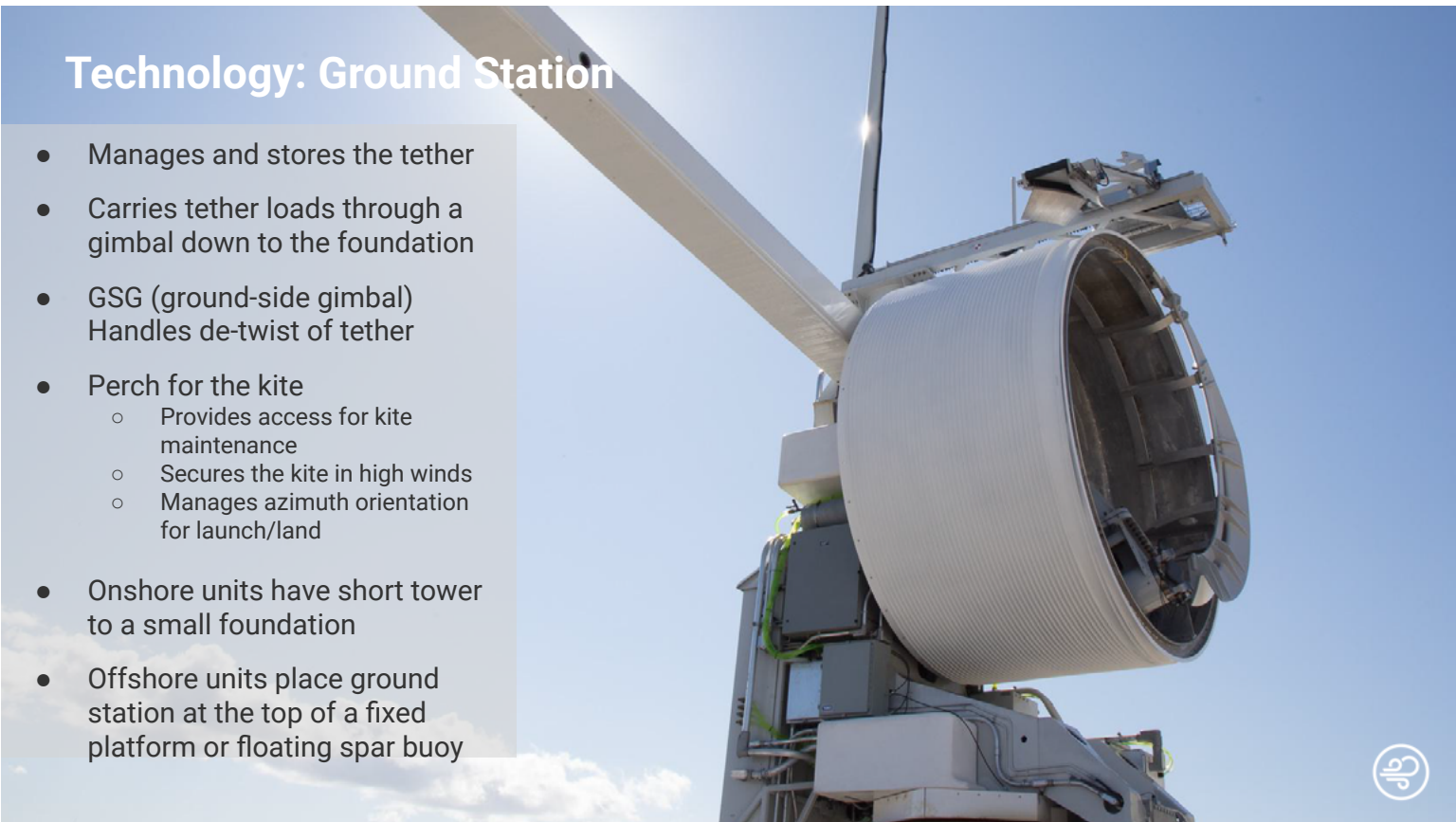
Technology: Power Systems

- Permanent magnet motor/generators
- Aerodynamic leverage of kite enables high speed direct-drive units with high power density
- 1700VDC SiC controllers with high bandwidth comms and fault handling
- Medium voltage DC power through tether is converted to AC on the ground
- Powertrain units easily field swapped and bench tested



Technology: Ground Station

- Manages and stores the tether
- Carries tether loads through a gimbal down to the foundation
- GSG (ground-side gimbal)
Handles de-twist of tether
- Perch for the kite
 - Provides access for kite maintenance
 - Secures the kite in high winds
 - Manages azimuth orientation for launch/land
- Onshore units have short tower to a small foundation
- Offshore units place ground station at the top of a fixed platform or floating spar buoy



Technology: Floating Platform

- 45m-50m Floating spar (slender buoy concept)
- Rolled steel, welded
- 80-100 metric tonnes
- 4-5m diameter
- Transition piece connects spar to Ground Station
- Single line, tension-leg mooring cable (proposed)
- Gravity anchor
- Size and construction similar to wind turbine tower





Makani System Information



Makani System Information

The goal of this section is to provide enough information about the Makani system for you to understand the scope of the task. It will not provide enough detail to develop detailed cost estimates.

Makani anticipates ramping up production to many gigawatts of systems. The next milestone on this path is to complete pilot design requirements, specifications, design, and fabrication of 1MW pre-production pilot systems that will begin operations in 2021.

Makani system components in scope:

- Kite
- Ground Station
- Buoy (optional)

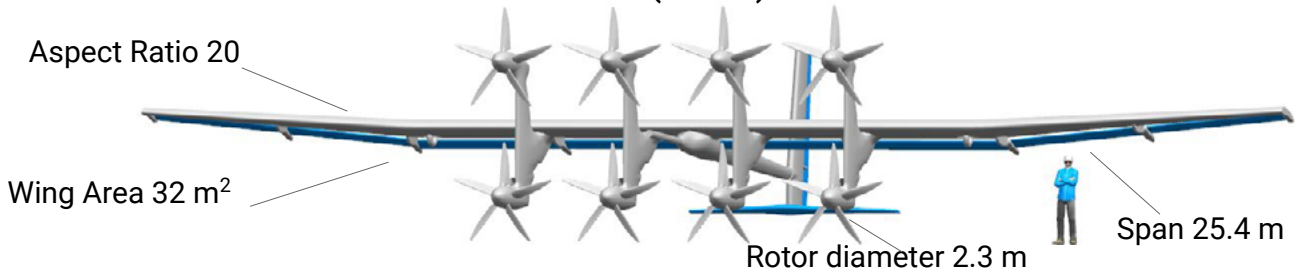
Additional system information (provided for context):

- Offshore Balance of Plant
- Offshore Operation and Maintenance
- System modeling, Simulation Tools and Validation
- Reliability, Safety, and Product Risk

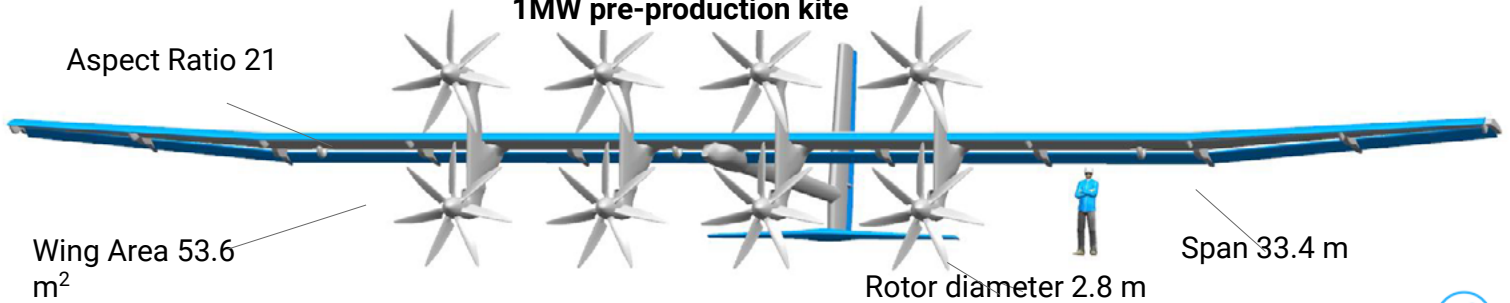


The Pre-production kite = M600 (600kW) evolved to a 1MW kite

M600 (600kW)



1MW pre-production kite



Pilot Requirements: L0 - Pre-production prototype

ID	Requirement	Description
1.0	Human Safety	<i>Risk</i> of human injury equal or better than conventional wind energy systems.
2.0	Perceived safety	Shall operate in a manner that customers and the public will perceive as safe .
3.0	Energy production	Will extract energy from the wind and convert to electrical power per Loyd (1980).
4.0	Low LCOE	Shall produce electricity at a target LCOE (\$300/kWh) specific to target market.
5.0	Standards-based design	Shall be compliant with applicable standards in all cases where relevant.
6.0	Bankable/ Certifiable	PPP will provide sufficient operating data such that Production design is bankable .



Pilot Requirements: L1 - System level (sample)

Electrical safety	Shall comply with UL 6141 Standard for Wind Turbines (insulation, tether)
Fault handling	Single-point faults handled in robust and safe manner
Motor failure	Failure of a motor or power converter shall not cause loss of flight vehicle
Emergency Shutdown	Shall be capable of remote shutdown (trans-out, reel in) And remote emergency shut-off (when perched)
Security hardening	Security system shall prevent kite from being harmed or from harming
Wind Class, IB	Average wind speed at "hub": $V_{ave} = 10$ m/s Reference turbulence intensity: $I_{ref} = 0.14$ @ $V = 15$ m/s
Survival WS @ perch	$V_{ref} = 35.8$ m/s (10-minute average) $V_{e50} = 50.1$ m/s (3-sec gust)
Density (operating)	1.10 to 1.35 kg/m ³
Health monitoring	Critical components (e.g., tether) shall have health monitoring systems

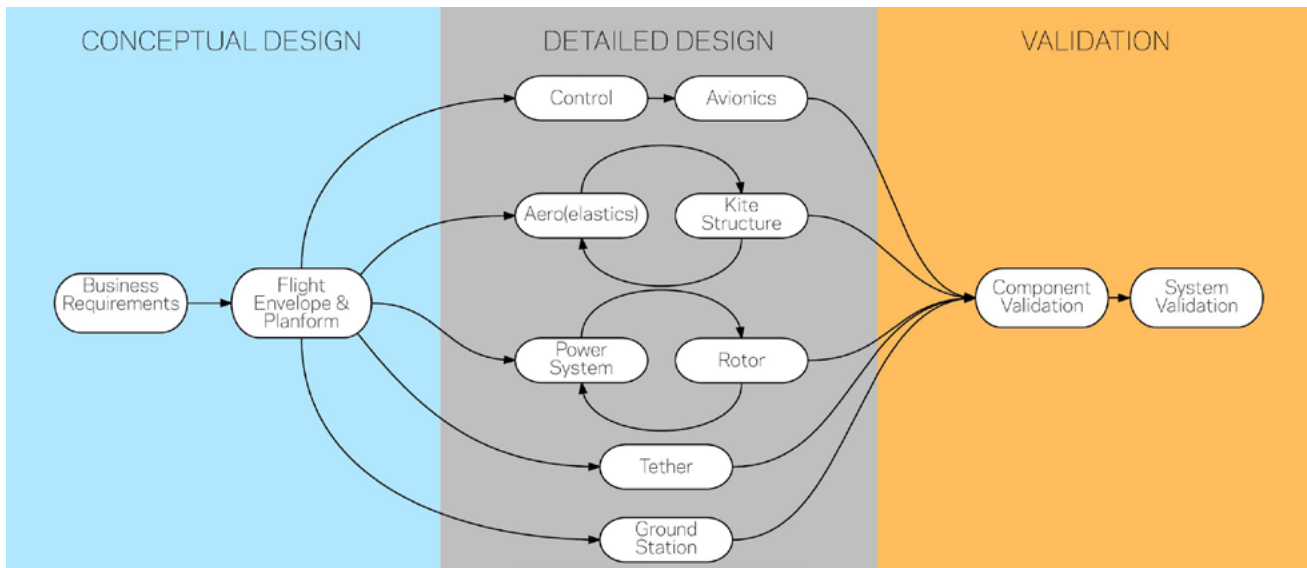


Understanding Makani's Design Process

- Establish system requirements for a certified "market ready" utility-scale energy kite
- Develop specifications for the pre-production energy kite, based on simulation, analysis, and M600 operating experience
- Iterate the design
- Refine specifications for the 1st commercial energy kite, based on simulation, analysis, and pre-production Pilot operating experience
- Design 1st commercial energy kite
- Seek to minimize changes between the M600 and the pre-production system, and again minimize changes between the pre-production and the commercial system.



DESIGN: PROCESS

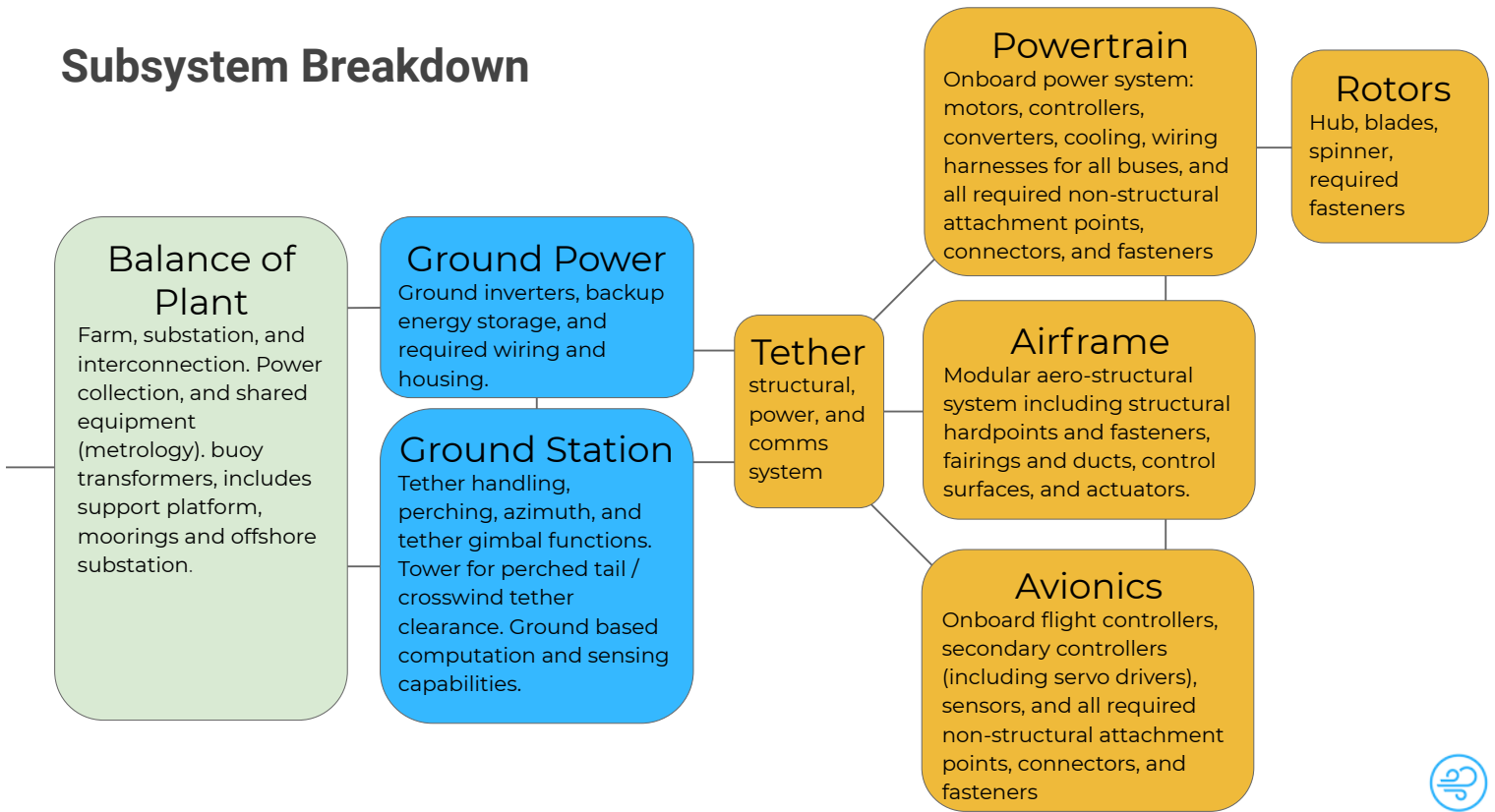


Go-to-Market Roadmap

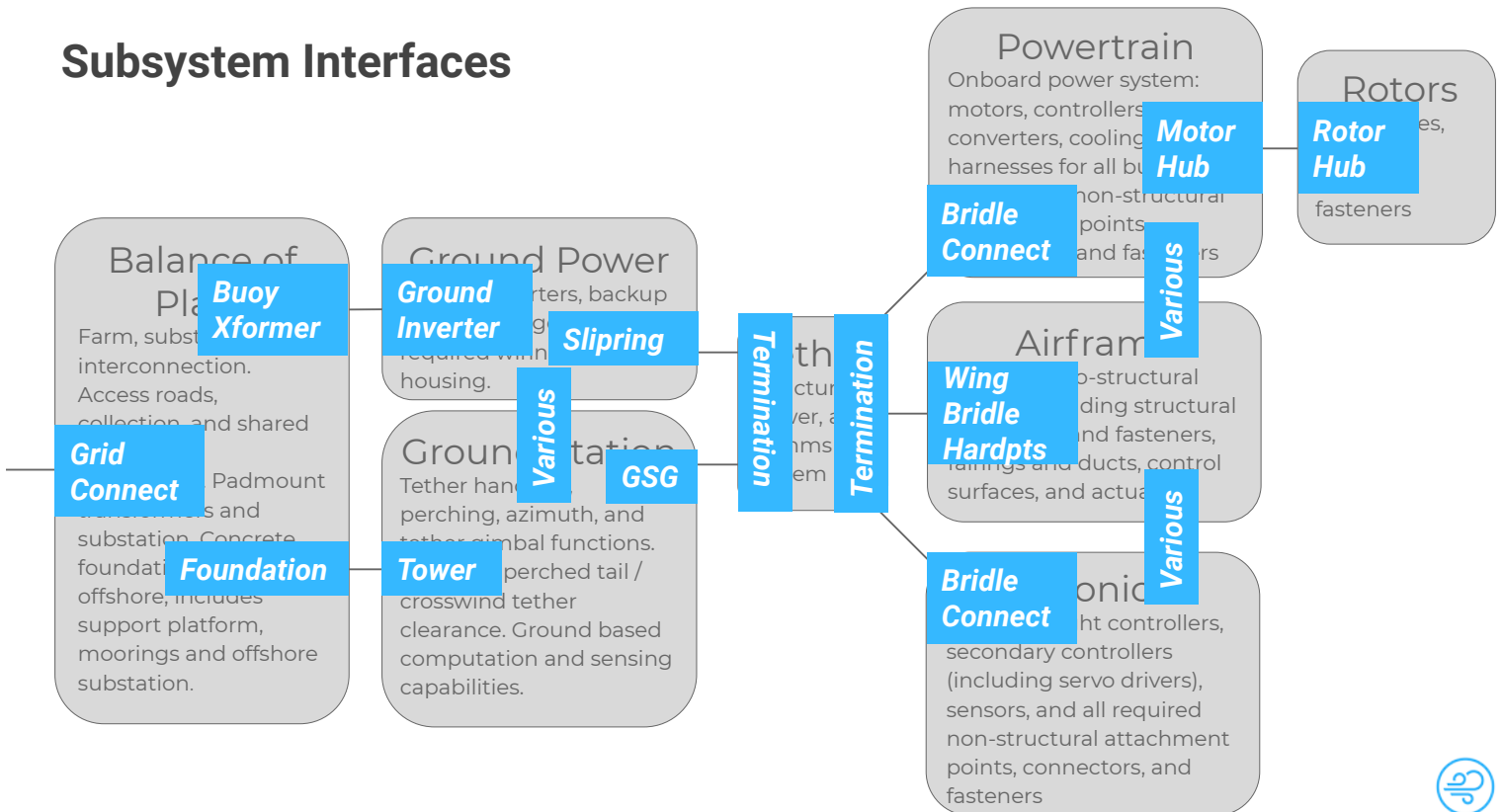
- Extensive techno-economic modeling revealed that a Makani **deepwater offshore product is much more cost competitive than an onshore product**
- **There is a series of incremental steps** from the kite we are flying today (M600) to a deepwater offshore pre-production kite and...
- We can get there with a **capable manufacturing partner**



Subsystem Breakdown



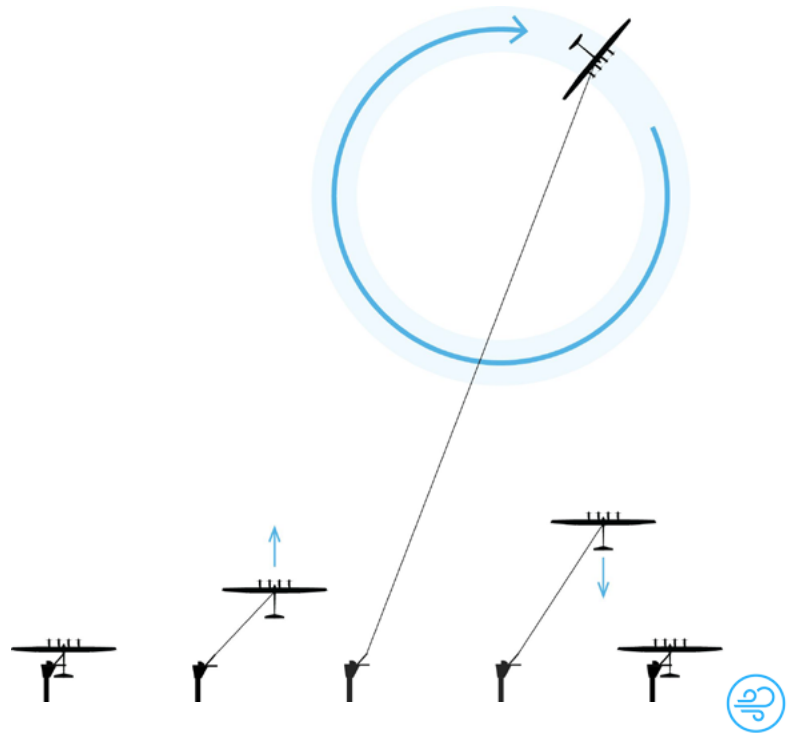
Subsystem Interfaces



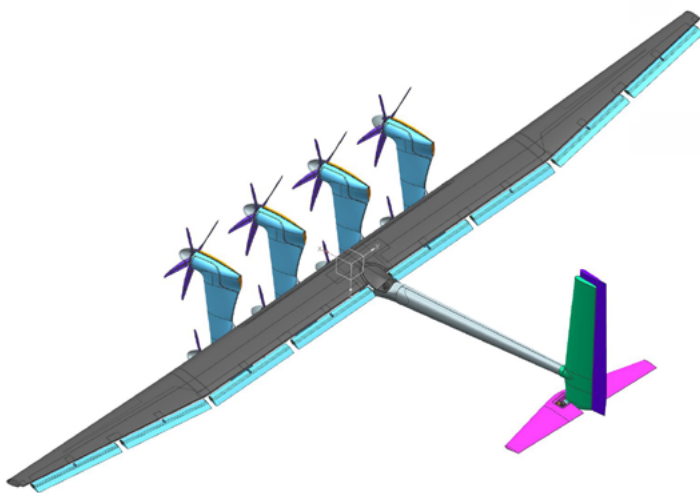
Normal Operation

Normal operational modes

- Launch/land via hover when winds are between V_{in} and V_{out}
- Transition between hover and crosswind flight
- In crosswind, adjust virtual hub height (inclination), azimuth (yaw) and cone angle (loop radius) and other parameters to optimize power production across operating range



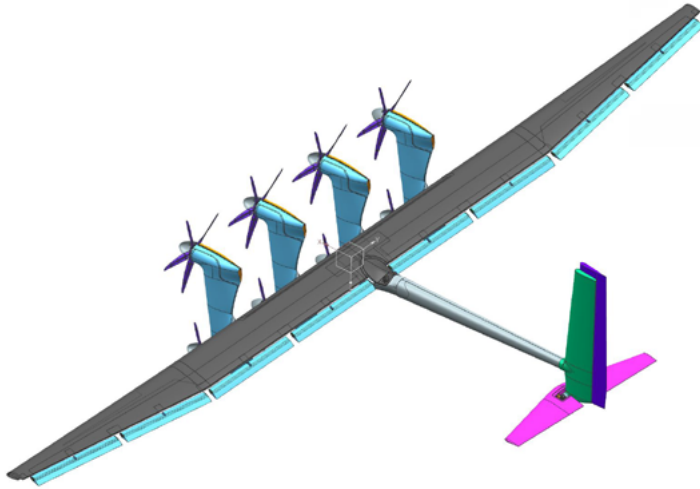
M600 AIRFRAME: Dimensions of Major Structural Components



- Wing Span: 25.4 m
- Wing Area: 32 sqm
- Rotor Diameter: 2.3 m
- Overall length: 10.2 m
- Overall height: 5.5 m
- Carbon fiber composite



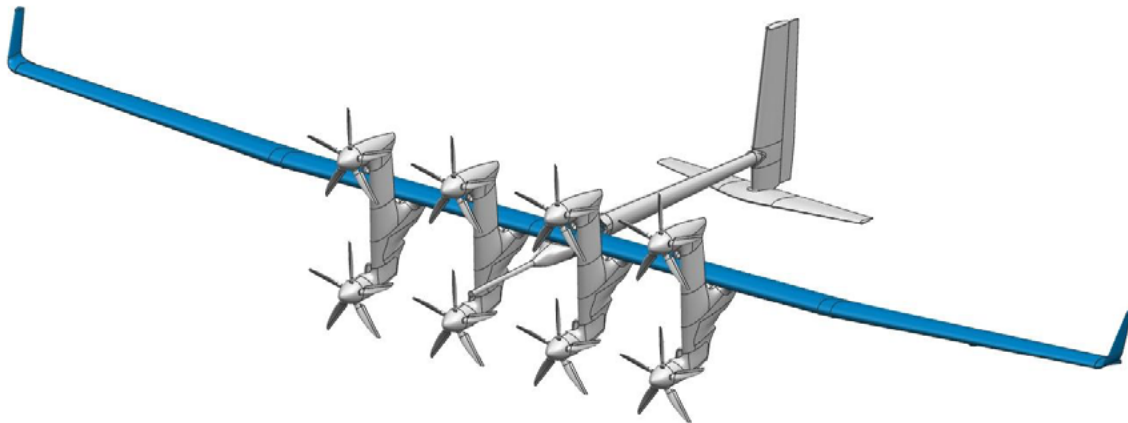
M600 AIRFRAME: Weights of Major Structural Components



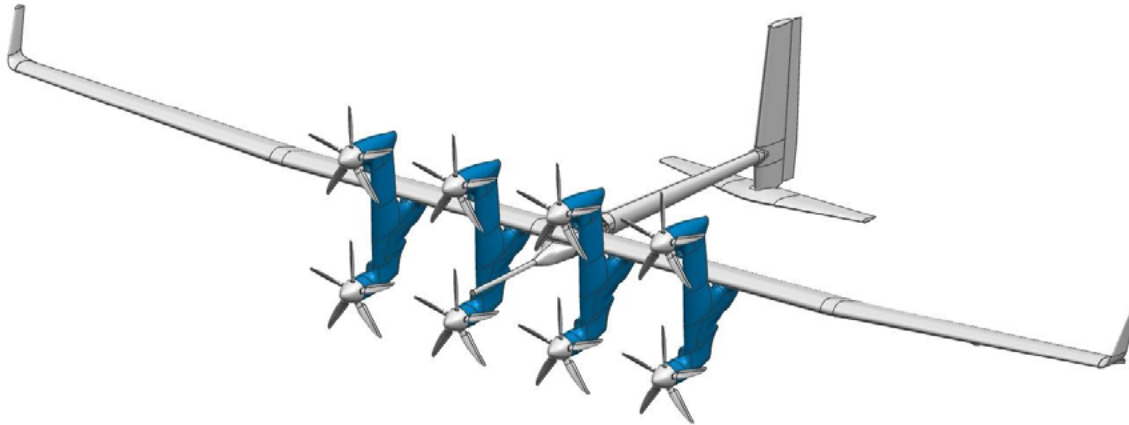
Component	Weight (per system)
Wing Assembly	450 kg
Pylons	175 kg
Fuselage	75 kg
Empennage	65 kg
Rotors/Spinners	65 kg
Covers/Fairings	15 kg



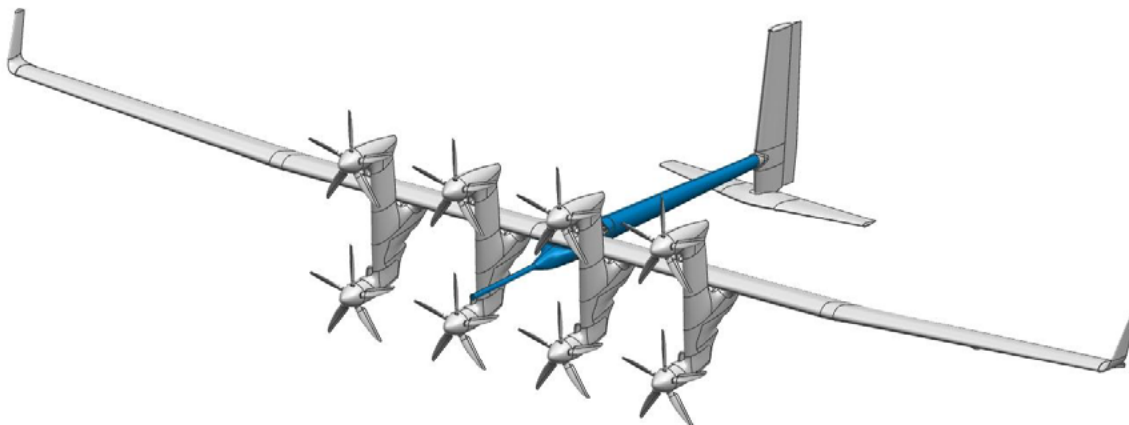
M600 AIRFRAME: Wing Assembly w/ Covers = 450 kg



M600 AIRFRAME: Pylons = 175 kg



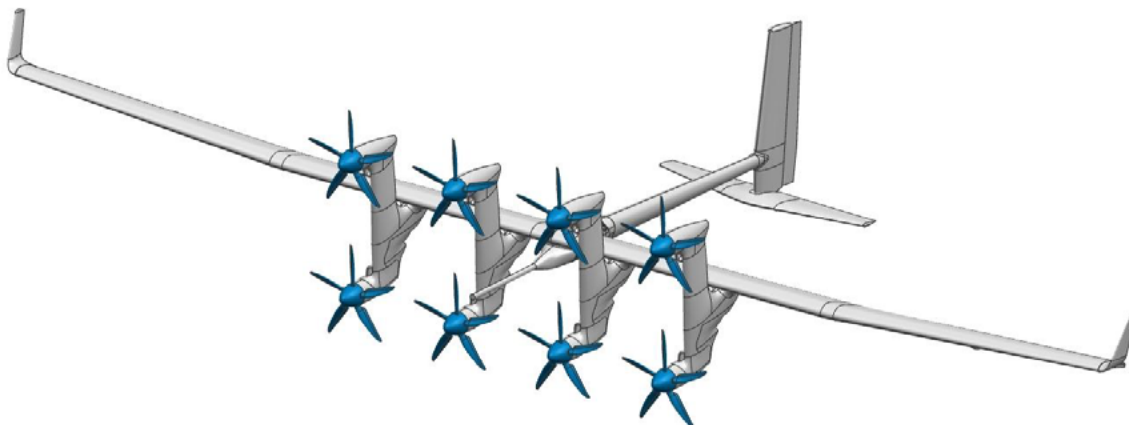
M600 AIRFRAME: Fuselage = 75 kg



M600 AIRFRAME: Empennage = 65 kg



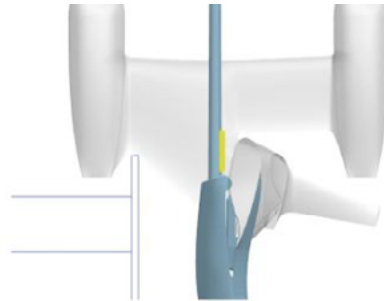
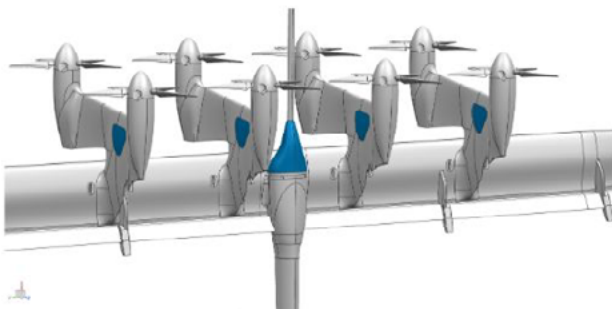
M600 AIRFRAME: Rotors and Spinners = 65 kg



M600 AIRFRAME: Covers and Fairings = 15 kg

Access to installed equipment

- Majority of wing internal structural space is not usable / open for access (driven by fatigue, mass)
- Harness runs are external in wiring channel
- Each pylon includes access to internal storage for avionics and power system components
- Fuselage fairing provides additional mounting and access

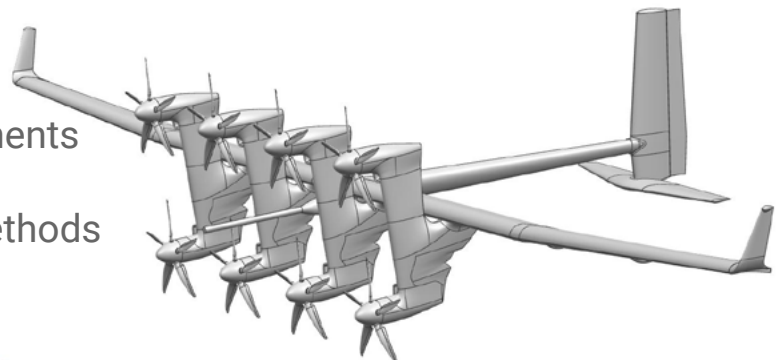


M600 AIRFRAME

The modular structure of the M600A Kite; its design approach, methodology, requirements and risks.

Presentation Outline

1. Requirements and Objectives
2. Topology + Approach
3. Architecture of Major Components
4. Structural Interfaces
5. Detailed Design + Analysis Methods
6. Validation
7. Overview of Risks



M600 AIRFRAME: REQUIREMENTS

Airframe Shall:

- Conform to OML.
- Have an as-built mass at or below budget.
- Maintain required residual strength + stiffness margins across operational envelope and lifetime.
- Provide interfaces for onboard components, tether, handling, and perching.
- Be transportable in field-replaceable units which fit under standard over-length regulations.
- Be manufacturable at small volumes (<50/yr); permit design changes as requirements evolve.



M600A AIRFRAME: REQUIREMENTS

Airframe Shall:

- Conform to OML.
- Have an as-built mass at or below budget.
- Maintain required residual strength + stiffness margins across operational envelope and lifetime.
- Provide interfaces for onboard components, tether, handling, and perching.
- Be transportable in field-replaceable units which fit under standard over-length regulations.
- Be manufacturable at small volumes (<50/yr); permit design changes as requirements evolve.



M600A AIRFRAME: REQUIREMENTS

Airframe Shall:

- Conform to OML.
- Have an as-built mass at or below budget.
- Maintain required residual strength + stiffness margins across operational envelope and lifetime.
- Provide interfaces for onboard components, tether, handling, and perching.
- Be transportable in field-replaceable units which fit under standard over-length regulations.
- Be manufacturable at small volumes (<50/yr); permit design changes as requirements evolve.



M600A AIRFRAME: REQUIREMENTS

Airframe Shall:

- Maintain required residual strength + stiffness margins across operational envelope and lifetime.

Incorporates the following design considerations:

- Fatigue: 60 million load cycles
- Flutter + stability: stiffness requirements
- Control surface effectiveness, slot gaps
- Durability: strength after impact for example
- Damage detection and repair strategies



M600A AIRFRAME: REQUIREMENTS

Airframe Shall:

- Conform to OML.
- Have an as-built mass at or below budget.
- Maintain required residual strength + stiffness margins across operational envelope and lifetime.
- Provide interfaces for onboard components, tether, handling, and perching.
- Be transportable in field-replaceable units which fit under standard over-length regulations.
- Be manufacturable at small volumes (<50/yr); permit design changes as requirements evolve.



M600A AIRFRAME: REQUIREMENTS

Airframe Shall:

- Conform to OML.
- Have an as-built mass at or below budget.
- Maintain required residual strength + stiffness margins across operational envelope and lifetime.
- Provide interfaces for onboard components, tether, handling, and perching.
- Be transportable in field-replaceable units which fit under standard over-length regulations.
- Be manufacturable at small volumes (<50/yr); permit design changes as requirements evolve.



M600A AIRFRAME: REQUIREMENTS

Airframe Shall:

- Conform to OML.
- Have an as-built mass at or below budget.
- Maintain required residual strength + stiffness margins across operational envelope and lifetime.
- Provide interfaces for onboard components, tether, handling, and perching.
- Be transportable in field-replaceable units which fit under standard over-length regulations.
- Be manufacturable to meet stated cost targets for pilot and permit design changes as requirements evolve.



M600A AIRFRAME: DESIGN DRIVERS

Major design drivers across airframe:

1. Mass
2. Conforming to aerodynamic OML
3. Modular interfaces
4. Secondary (bonded) joints
5. Buckling (panel and individual facesheet)
6. Lifetime (fatigue, durability)
7. Stiffness (flutter, control surface effectiveness)
8. Manufacturing
9. Scalable to rate production



PILOT AIRFRAME: ADDITIONAL DESIGN DRIVERS

Major changes/additions to PILOT design drivers across airframe will need to include:

1. **Cost Sensitivity**
2. **Certifiable Composite Material database** (schedule to certification and cost to certifiable product)
3. **Design for manufacturing** to reduce touch labor during fab and integration and improved speed of fab and integration
4. **Design considerations specific to offshore operations** (environmental protection, austere maintenance environment, cost to perform maintenance)



M600A AIRFRAME: STRUCTURAL APPROACH

CFRP - why?

- Specific strength
- Specific strain fatigue
- Complex/changing OML; optimization flexibility

Oven cured (OOA) - why?

- Lower capital expenditure
- Faster build times

Prepreg - why?

- More repeatable products
- Controlled material properties



M600A AIRFRAME: STRUCTURAL APPROACH

Continuously cored skins

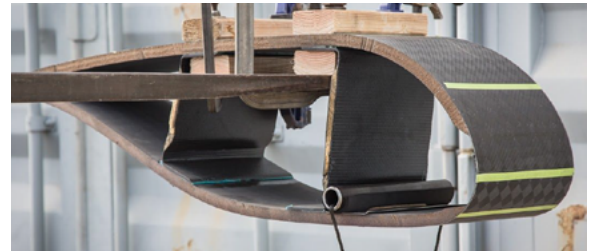
- Using core for shear + buckling
- Core does not drop at spars
- Rib/stringer 'free' (largely)

Trades / Risks associated

- Reduces part count
- Simplified skin fabrication, assembly
- Limits inspection
- Limits manufacturing processes
- Facesheet/core failure modes

Risk Mitigation

- Analysis
- Subcomponent testing



M600A AIRFRAME: STRUCTURAL APPROACH

Paste adhesive secondary assembly

- Structural paste bonds
- No fasteners at composite joints

Trades / Risks associated

- Handle variations in bond gap
- No stress risers at fastener locations
- Paste is sensitive to process/environment
- Lower repeatability
- Peel + crack propagation

Risk Mitigation

- Process controls
- Low stress bonds w/anti-peel geometry



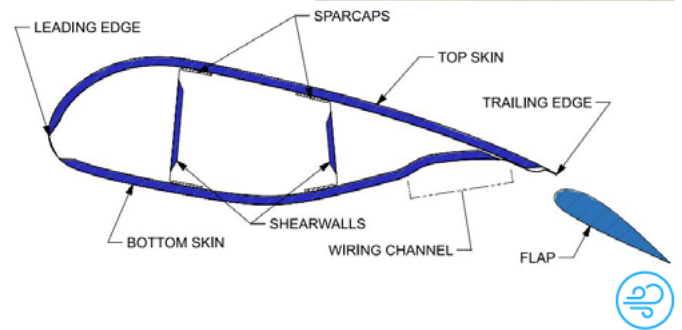
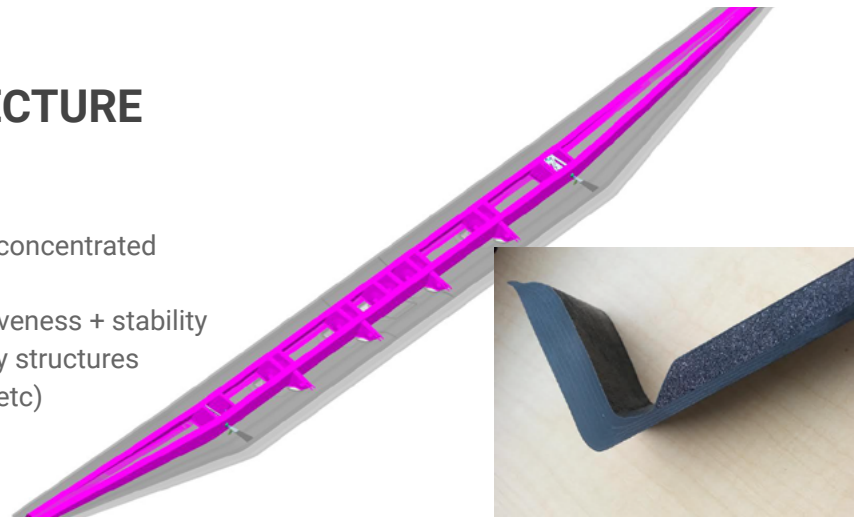
M600 AIRFRAME: ARCHITECTURE

WING STRUCTURAL REQUIREMENTS

- Carry distributed (aero, inertial) and concentrated (hardpoint) loads
- Maintain stiffness for control effectiveness + stability
- Provide attachment for other primary structures
- Mount secondary parts (harnesses, etc)

WING PRIMARY STRUCTURE

- Cored skins
- 2x full span C-channel spars
- Local hardpoint ribs for pylons, fuselage, bridle attach
- LE+TE lap joints
- External bonded on pads for flap attachment



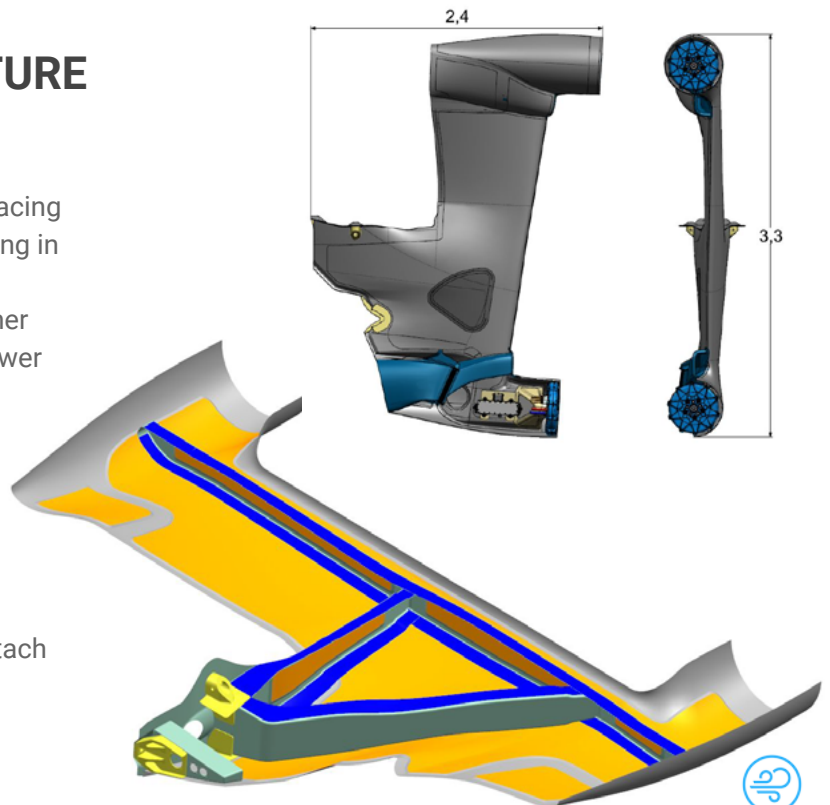
M600 AIRFRAME: ARCHITECTURE

PYLON STRUCTURAL REQUIREMENTS

- Mount powertrains/rotors at required spacing
- Develop aerodynamic side force for turning in crosswind
- Attach to wing in a simple + robust manner
- Secondary mounting for avionics and power systems components
- Perch interface for ground station

PYLON PRIMARY STRUCTURE

- 4 identical structures
- Cored skins
- C-channel internals
- Local hardpoints for motors and wing attach



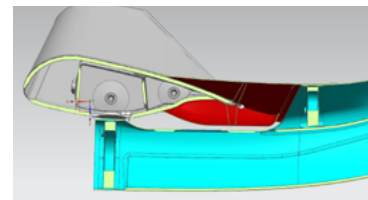
M600 AIRFRAME: ARCHITECTURE

FUSELAGE STRUCTURAL REQUIREMENTS

- Carry tail loads into wing with sufficient stiffness for stability + control effectiveness
- Attach to wing in a simple + robust manner
- Provide perch peg location
- Permit forward attachment of mass balance, avionics etc

FUSELAGE PRIMARY STRUCTURE

- Roll-wrapped/mandrel-wound main tube
- Forward “tub” structure for wing attach
- End cap for empennage attach
- Perch peg



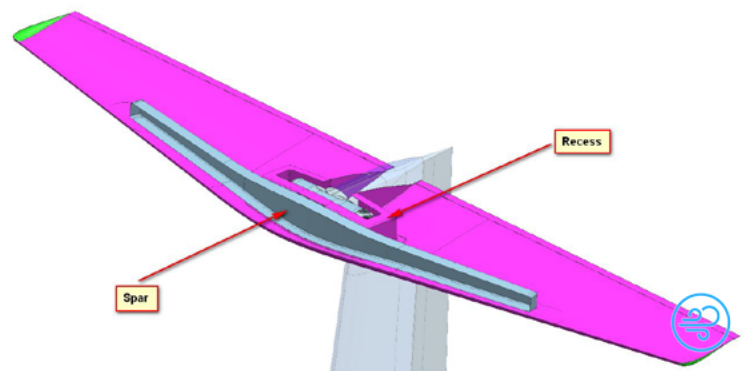
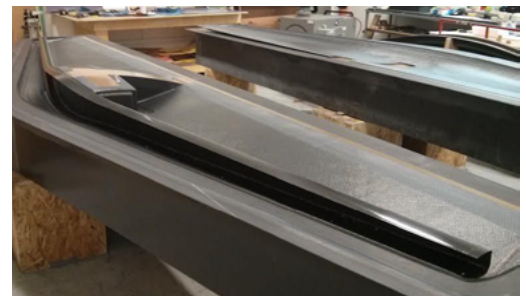
M600 AIRFRAME: ARCHITECTURE

TAIL STRUCTURAL REQUIREMENTS

- Carry aerodynamic and inertial loads to the fuselage attachment
- Maintain stiffness for stability and control effectiveness
- Enable actuation of the elevator and rudder control surfaces
- Package local avionics components

TAIL PRIMARY STRUCTURES

- Fully moving stabilator
- Aero- and mass-balanced rudder
- Similar 2-skin cored architecture as wing
- Single primary C-channel spars
- Attachments at fuselage and elevator detailed in later slide



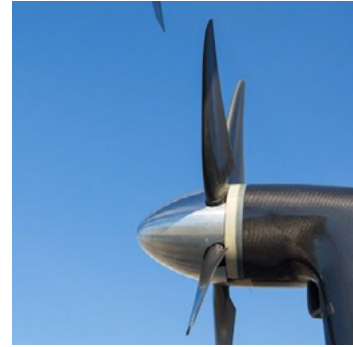
M600 AIRFRAME: ARCHITECTURE

ROTOR STRUCTURAL REQUIREMENTS

- Carry aero, inertial, gyroscopic loads to motor
- Mass balanced
- repeatable attachment
- Mount aerodynamic spinners
- Resistant to erosion

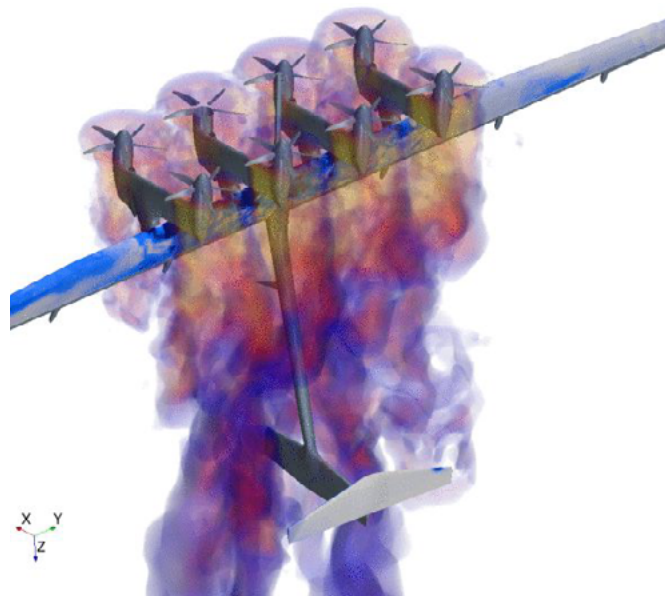
ROTOR PRIMARY STRUCTURE

- Solid foam core, carbon fiber skins, blades
- Circular flange w/ capture feature
- Ground-adjustable pitch
- Through bolts to thread inserts on motor
- Traditional spinner mounting
- LE protection



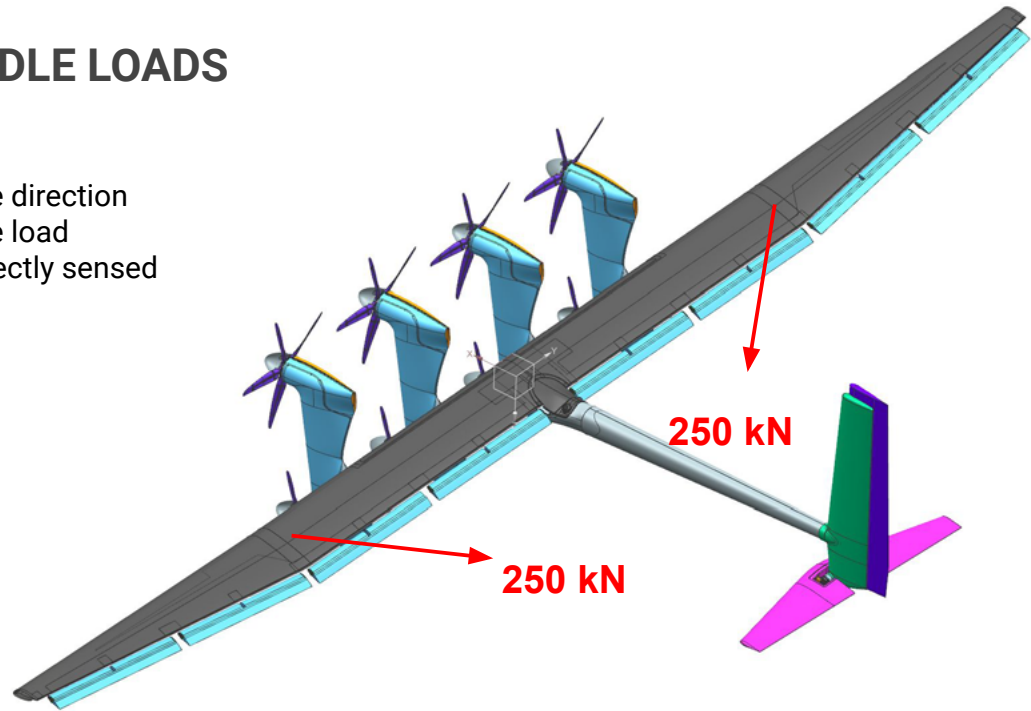
BRIEF SUMMARY OF LOADS

- Aerodynamic
- Inertial
- Tether



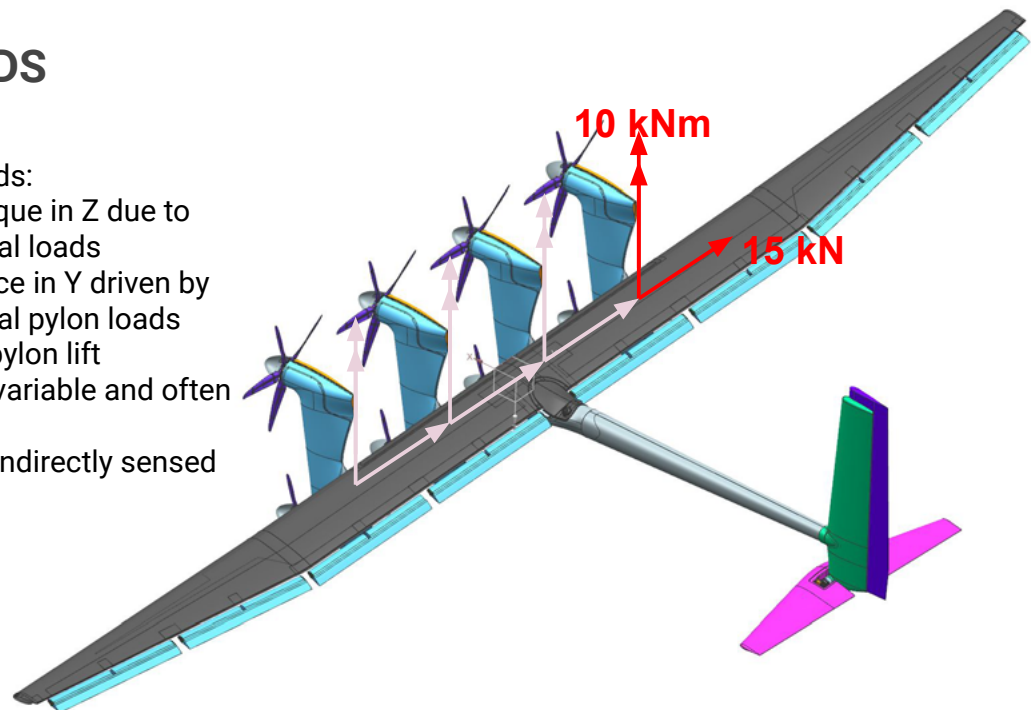
TETHER/BRIDLE LOADS

- Predictable direction
- Predictable load
- Load is directly sensed



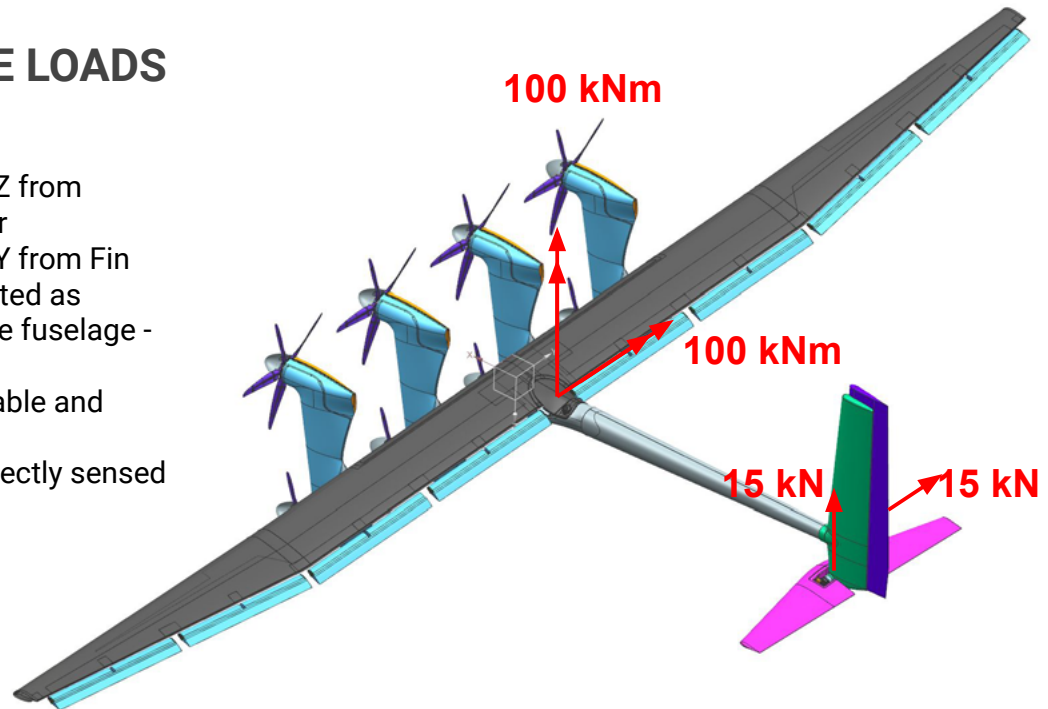
PYLON LOADS

- Driving loads:
 - A torque in Z due to inertial loads
 - A force in Y driven by inertial pylon loads and pylon lift
- Loads are variable and often reversing
- Loads are indirectly sensed



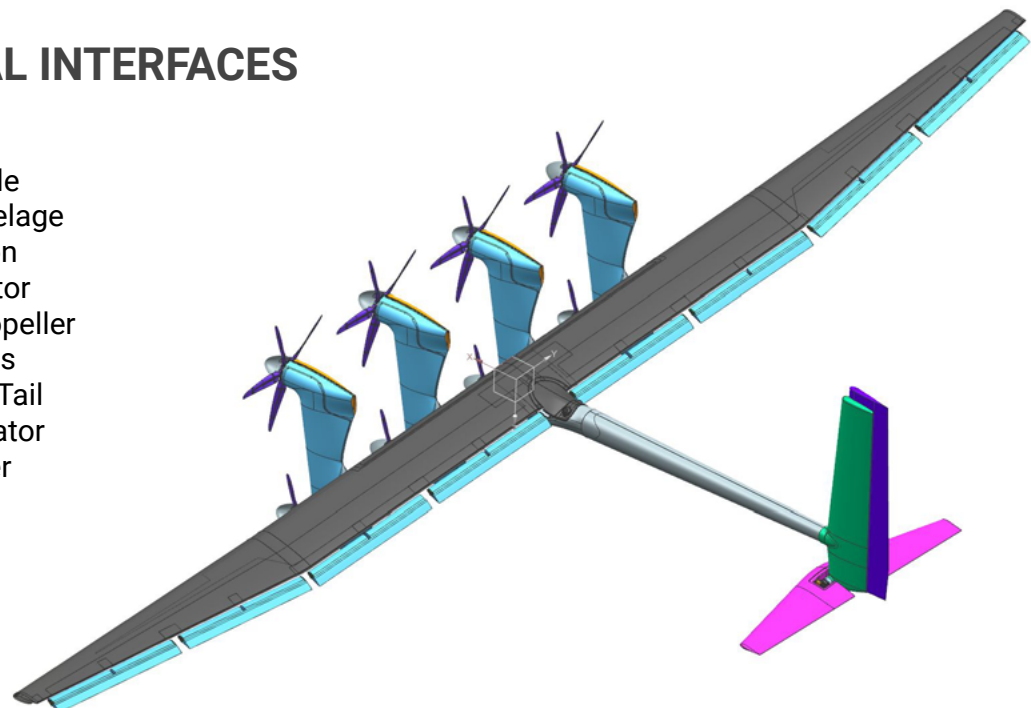
EMPENNAGE LOADS

- Driving loads
 - Force in Z from Stabilator
 - Force in Y from Fin
- These are reacted as moments at the fuselage - wing junction
- Loads are variable and reversing
- Loads are indirectly sensed



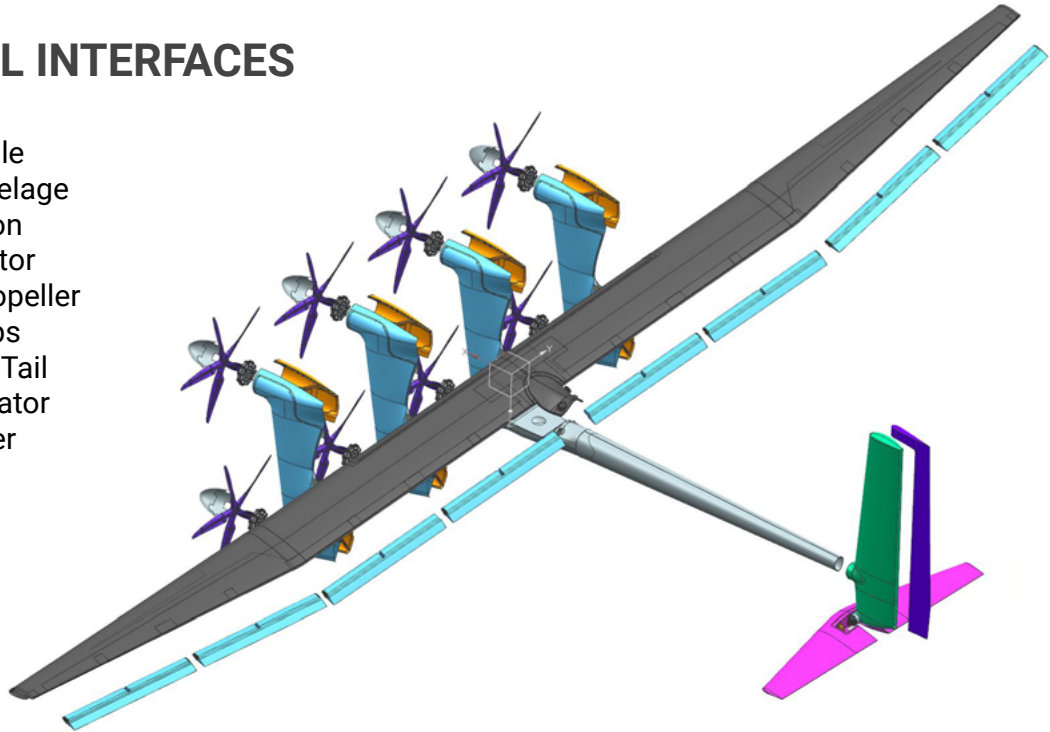
STRUCTURAL INTERFACES

- Wing to Bridle
- Wing to Fuselage
- Wing to Pylon
- Pylon to Motor
- Motor to Propeller
- Wing to Flaps
- Fuselage to Tail
- Fin to Stabilator
- Fin to Rudder



STRUCTURAL INTERFACES

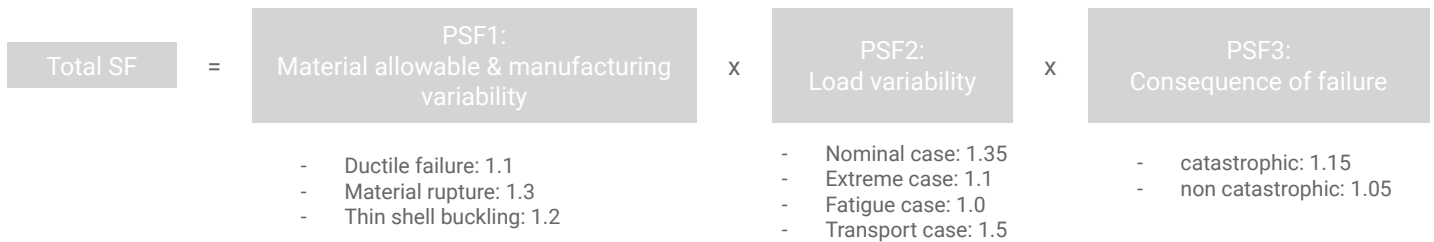
- Wing to Bridle
- Wing to Fuselage
- Wing to Pylon
- Pylon to Motor
- Motor to Propeller
- Wing to Flaps
- Fuselage to Tail
- Fin to Stabilator
- Fin to Rudder



SAFETY FACTORS

Partial safety factor approach

- Based on IEC 61400 and GL IV
- General methodology:



Typical total SF in analyses

- Composite structure under nominal loads: SF=2 on strength, 1.85 on stability (buckling)
- Composite structure under extreme loads: SF=1.64 on strength, 1.52 on stability (buckling)
- Metallic part under fatigue loads: SF=1.72



M600 AIRFRAME: VALIDATION

How do we validate an M600A structural design

- Coupon testing (materials, adhesives)
- Selected subcomponent testing
- Component level testing
 - GVT/stiffness testing
 - Proof
 - Ultimate
 - Fatigue
- Process controls
- Inspection



M600 AIRFRAME: VALIDATION

We expect manufacturing partners to

- Use material qualification databases such as AGATE and NCAMP
- Or use internal, traceable design data for processing and manufacture of composite materials

EASA CM No.: EASA CM - S - 004 Issue: 01

EASA	CERTIFICATION MEMORANDUM
	<p>EASA CM No.: EASA CM - S - 004 Issue: 01 Issue Date: 14th of January 2014 Issued by: Structures section Approved by: Head of Certification Experts Department Regulatory Requirement(s): CS 2X.603, CS 2X.605, CS 2X.613, CS-E 70 and CS-P 170</p>
<p><small>EASA Certification Memoranda clarify the European Aviation Safety Agency's general course of action on specific certification items. They are intended to provide guidance on a particular subject and, as non-binding material, may provide complementary information and guidance for compliance demonstration with current standards. Certification Memoranda are provided for information purposes only and must not be misconstrued as formally adopted Acceptable Means of Compliance (AMC) or as Guidance Material (GM). Certification Memoranda are not intended to introduce new certification requirements or to modify existing certification requirements and do not constitute any legal obligation.</small></p> <p><small>EASA Certification Memoranda are living documents into which either additional criteria or additional issues can be incorporated as soon as a need is identified by EASA.</small></p>	
<p>Subject</p> <p>Composite Materials – Shared Databases</p> <p>Acceptance of Composite Specifications and Design Values Developed using the NCAMP Process</p>	

Federal Aviation Administration

Memorandum

Date: SEP 20 2010

To: All Directorate Managers
All Aircraft Certification Office Managers

From: *For* David W. Hempe, Manager, Aircraft Engineering Division, *SJM Callen*
AIR-100

Prepared By: Mark Freisthler, Aerospace Engineer, Transport Airplane Directorate, (ANM-115)

Supported By: Robert Stegeman (ACE-111), Dale Hawkins (AIR-120) and Larry Ilcewicz (AIR-100).

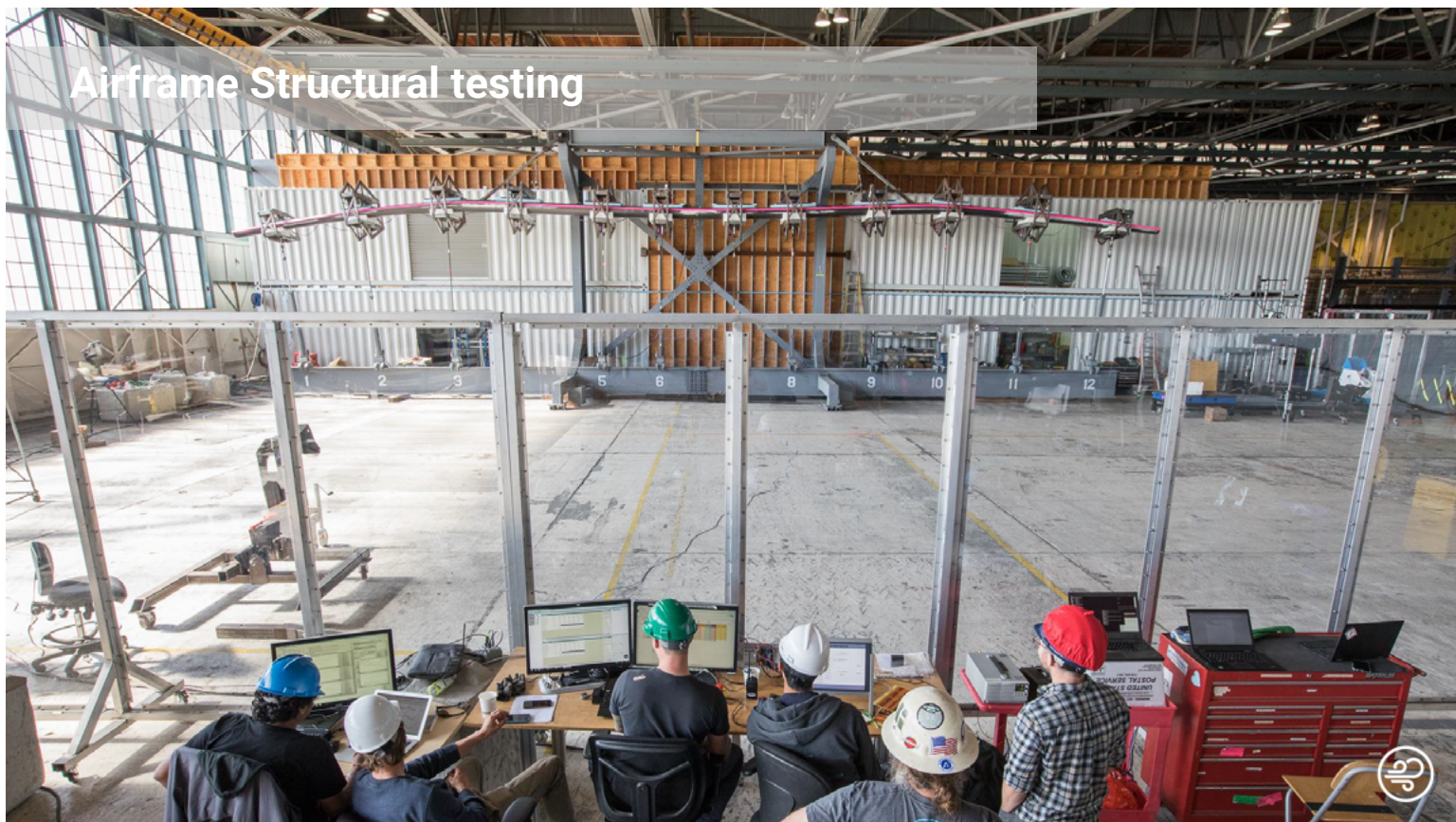
Subject: **INFORMATION:** Acceptance of Composite Specifications and Design Values Developed using the NCAMP Process

Memo No.: AIR100-2010-120-003

Regulatory Reference: §§23.603, 23.605 and 23.613
§§25.603, 25.605 and 25.613
§§27.603, 27.605 and 27.613
§§29.603, 29.605 and 29.613
§§33.15 & §33.17



Airframe Structural testing

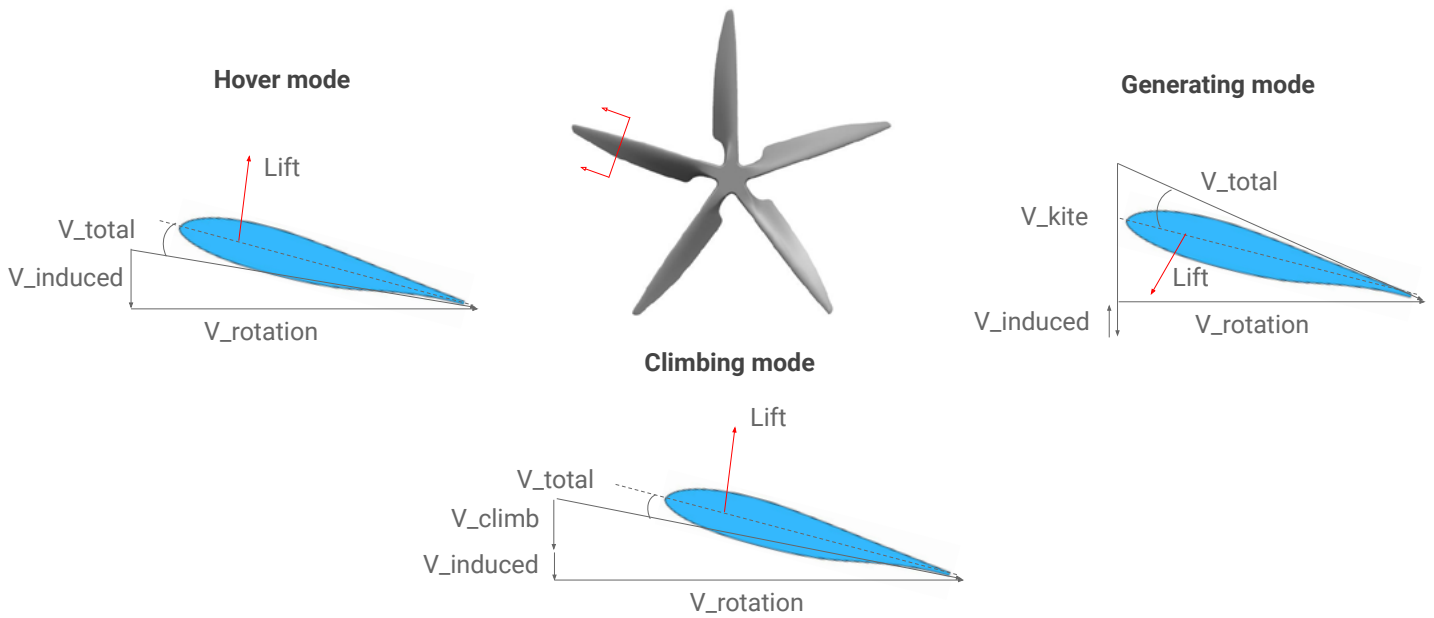


Rotors

- Designed for:
 - Lift and generation
 - Low noise signature
 - Low inertia to minimize gyroscopic loads
 - Structural simplicity for low manufacturing cost
 - Durability
- Carbon fiber construction for stiffness, low mass
- Leading edge erosion protection
- Fixed pitch for lower O&M costs and mass



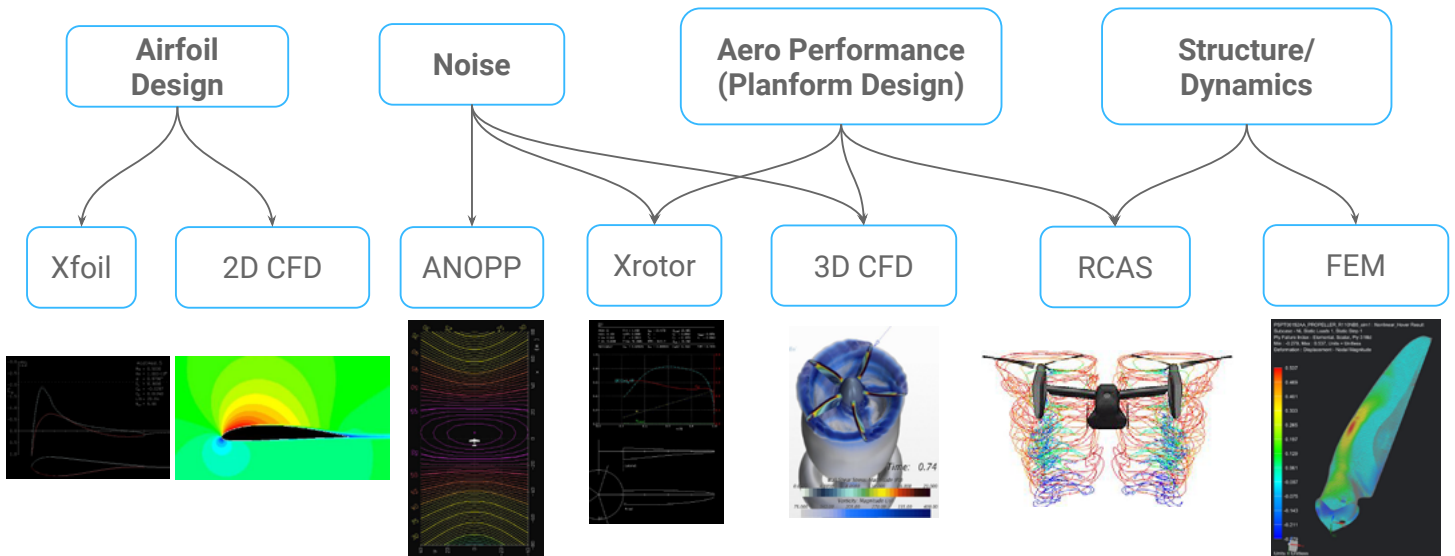
Rotor Operational Modes



Compromises required for **blade pitch** and **airfoil section**



Rotor Design Tool Suite



Complementary suite with varying fidelity



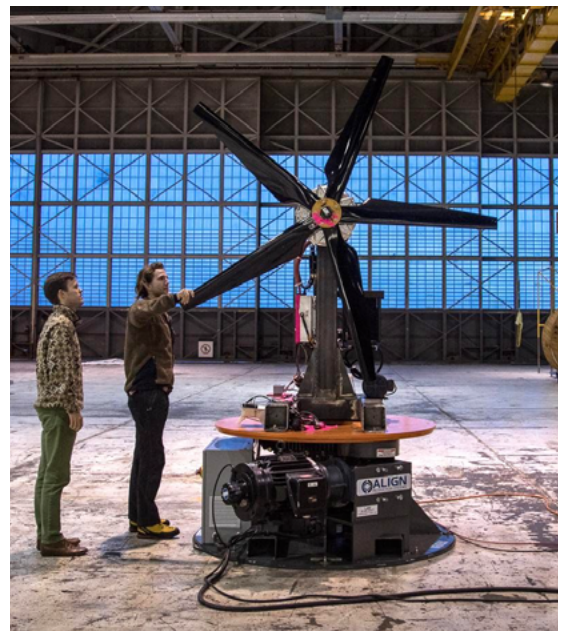
Rotors

- Ground adjustable pitch
- Aluminum hub
- Easy to replace single blades
- Interface with motor is 5 bosses
- Bolts are threaded into Motor



Rotor testing

- Qualification testing for prototype use
- Hover performance validation
- Gyroscopic moment proof testing
 - Combined Rotor load/Motor bearing load testing
- Noise studies






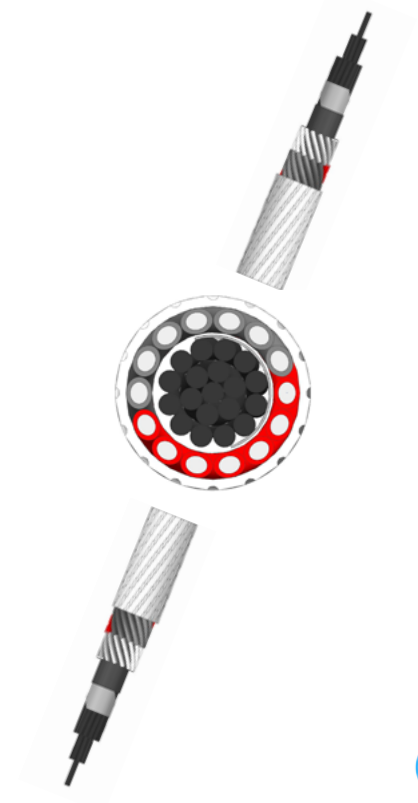
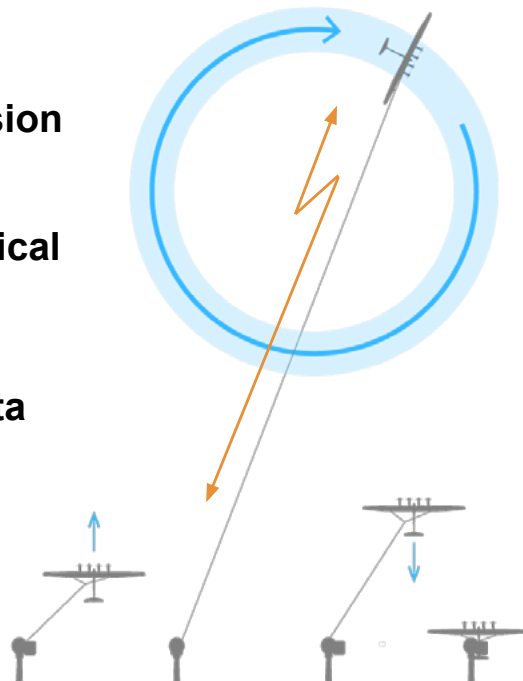
Tether System

- Structural, Electrical, and Data connection between the Kite and Ground Station.
- Bundled carbon fiber pultruded rods offer high strength and stiffness to weight.
- Helical wound aluminum conductors for best specific conductivity.
- Fluted jacket for reduced drag coefficient at minimal weight penalty.



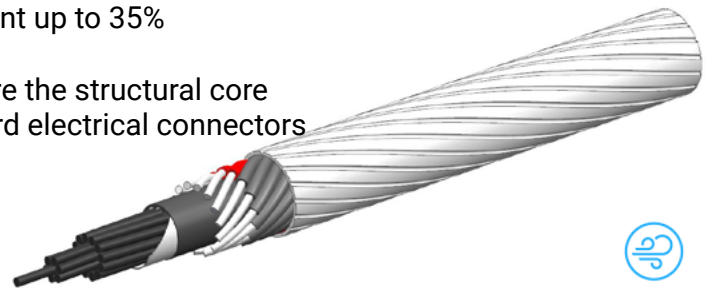
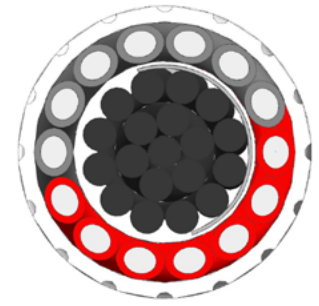
Tether Overview

-  **250 kN of Tension**
-  **1 MW of Electrical Power**
-  **30 Mbit/sec Data Transfer**

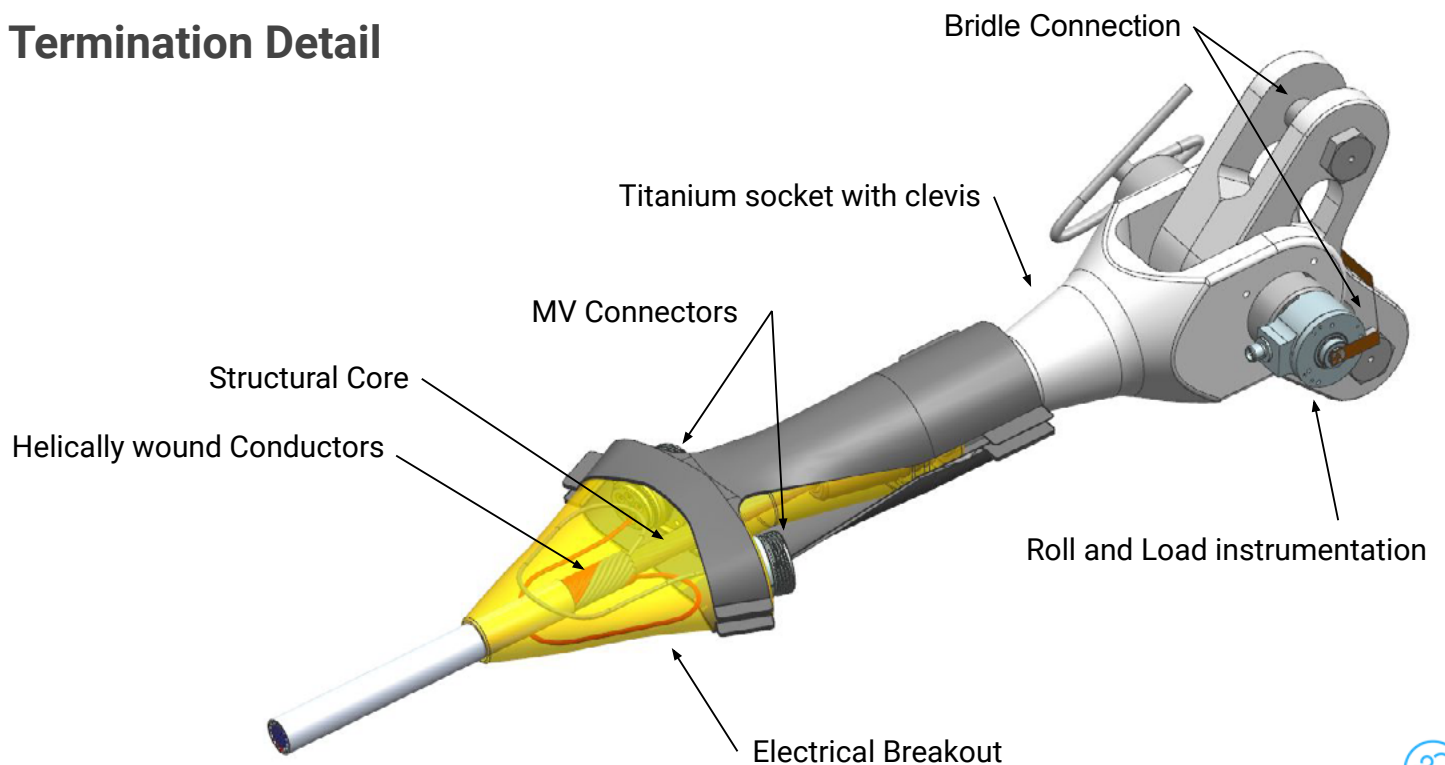


Tether Design

- Strength member
 - 1x19 wire rope construction of pultruded carbon fiber rods
 - Offers high fatigue tolerance, robustness, and redundancy
 - Thermoplastic sheath
- Electrical conductors
 - Solid Aluminum wires
 - Low friction, high temperature and abrasion resistant insulation
 - Helically wound around carbon core sheath
- Data Transfer
 - Copper coax
 - Helical wound with the insulated conductors
- Jacket
 - Proprietary 'flutes' reduce the drag coefficient up to 35%
- Termination
 - Titanium socket and epoxy casting to secure the structural core
 - Electrical conductors break out into standard electrical connectors



Termination Detail



Tether Testing and Validations - Requirements and Test Plan

Test Requirements

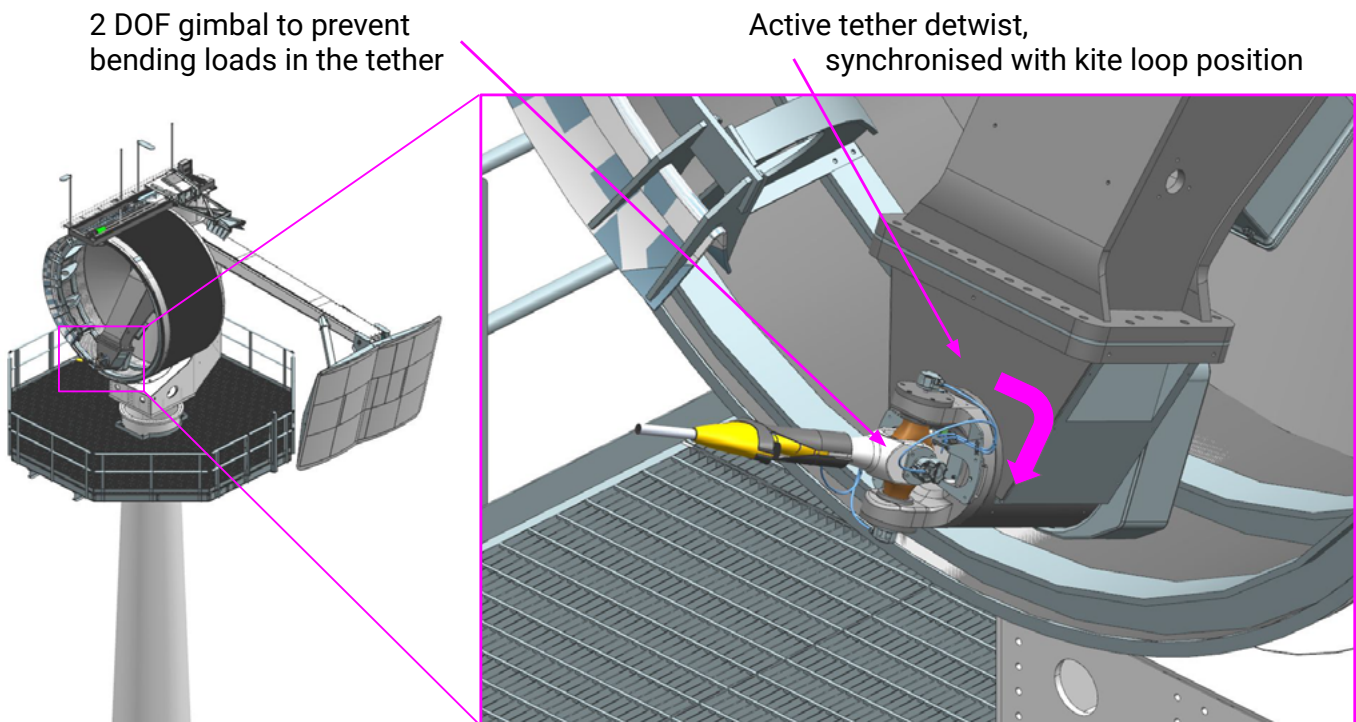
- Structural Carbon Rod Core
 - Mainly focused around tensile fatigue and bending.
 - 50-250 kN cyclic tension at 10^6 cycles - coincides with observed flight loads and reasonable life target for current stage of development.
 - Achieve strength and fatigue targets at 80°C continuous operating temperature.
- Insulated Aluminum Conductors
 - 200A sustained current at 5kV DC.
 - Insulation withstand voltage of 10kV.
 - Equivalent fatigue resistance to carbon core.

Test Approach

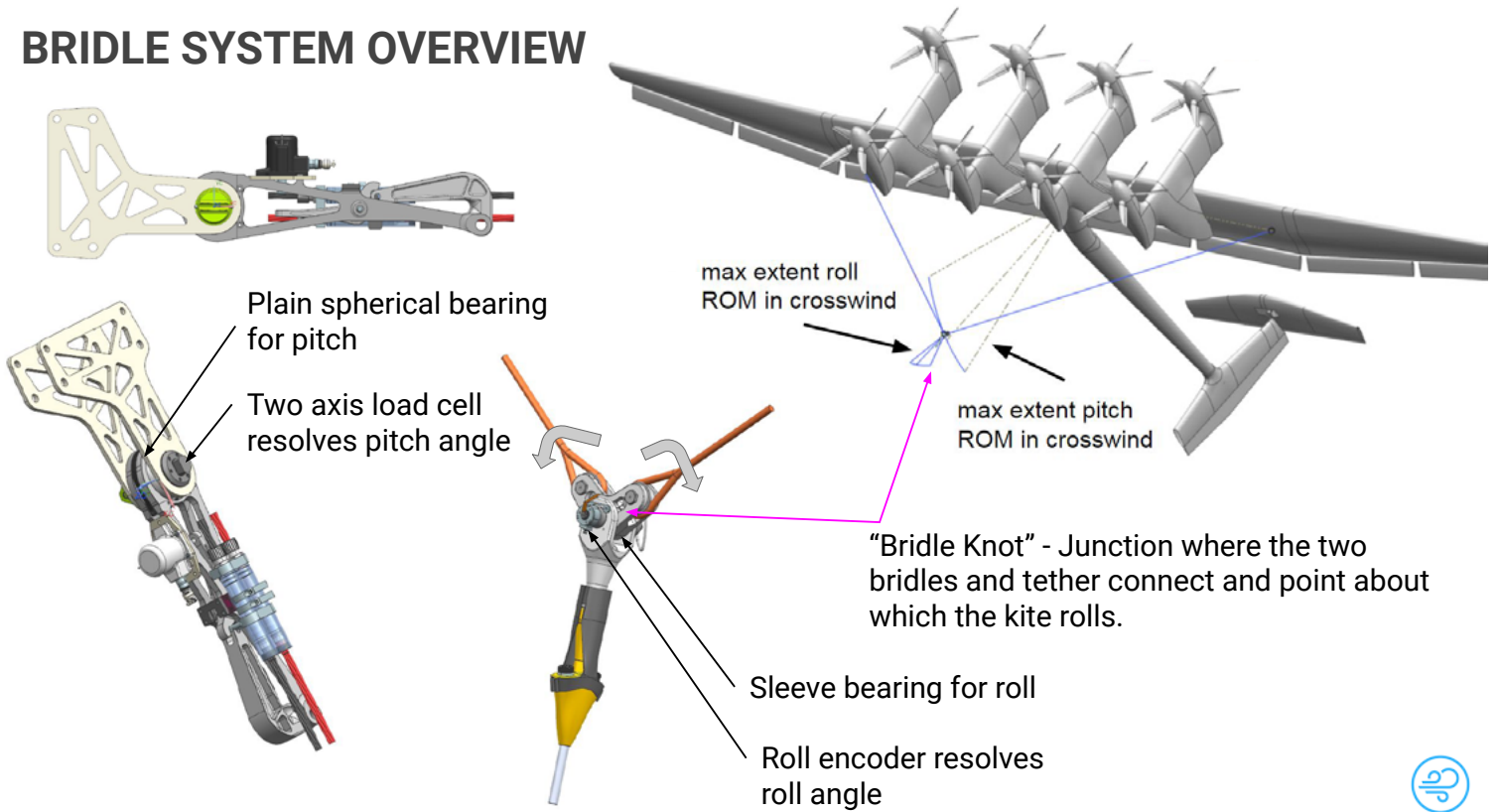
- Work up to a fully representative tether qualified to above requirements.
- Run cyclic tension fatigue with DC current through conductors to provide heating.
- Intermittent hipot testing of insulation.
- Continuous DCR measurement of conductors.



Tether termination at ground-side gimbal (GSG)



BRIDLE SYSTEM OVERVIEW



Power Systems

- Aerodynamic leverage of kite enables high speed direct-drive units with high power density
- Permanent magnet motor/generators (5kW/kg) and (22Nm/kg)
- 1700VDC SiC controllers with high bandwidth comms and fault handling
- Medium voltage DC power through tether is converted to AC on the ground
- Powertrain units easily field-swapped and bench-tested



SUBSYSTEM OVERVIEW

Kite-side

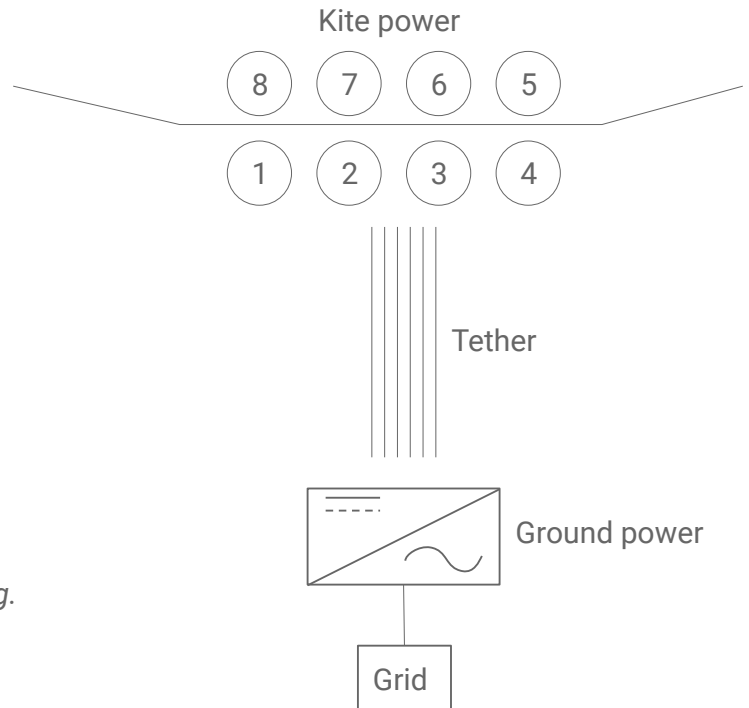
Eight two-quadrant motor/generators (M/G)
 Eight SiC motor controllers
 MV to LV converter

Tether

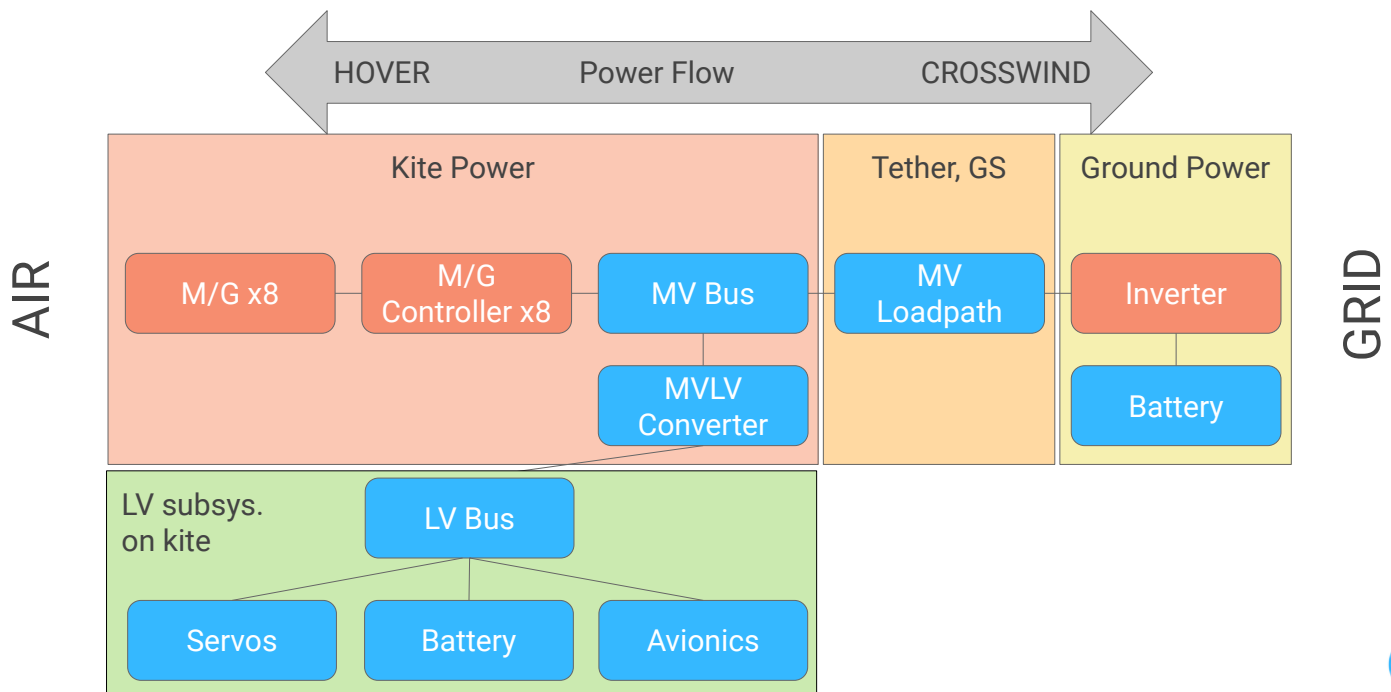
14 separately insulated conductors
 $V \sim 4000\text{ V}$
 $I \sim 200\text{ A}$
 DC

Grid-side

Standard service-level interconnect to grid (e.g. 480VAC 3ph 4w)



FUNCTIONAL BLOCKS, ENERGY FLOW



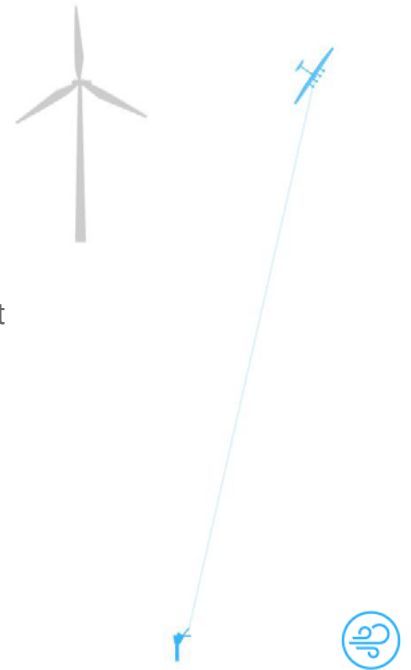
SYSTEM LEVEL REQUIREMENTS

Base requirements for single kite system

- Basic functionality: power transfer to grid (IEEE 1547, NEC)
- Performance
- Reliability

Challenges particular to airborne system

- Lightweight
- Fail-safe, robust against failures at *wing or ground* (major asset is at risk)
- Need backup power!
- Bidirectional for hover (technically “easy”, but unconventional)
- MVDC (tether optimization)



HOW TO DO MVDC? “STACKING”

Stacked M/G, inverters

- 4 series, 2 parallel

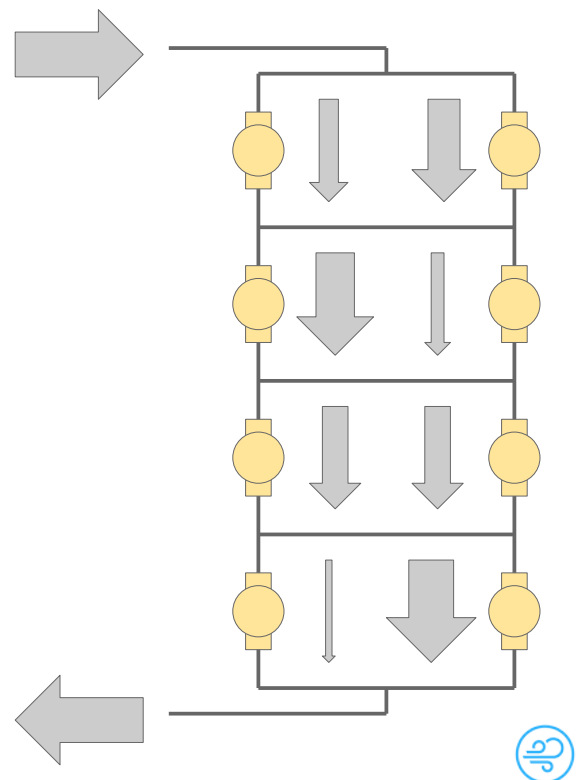
8 DOF, 3 restrictions

Leaves 5 effective DOF

- Enough for flight control

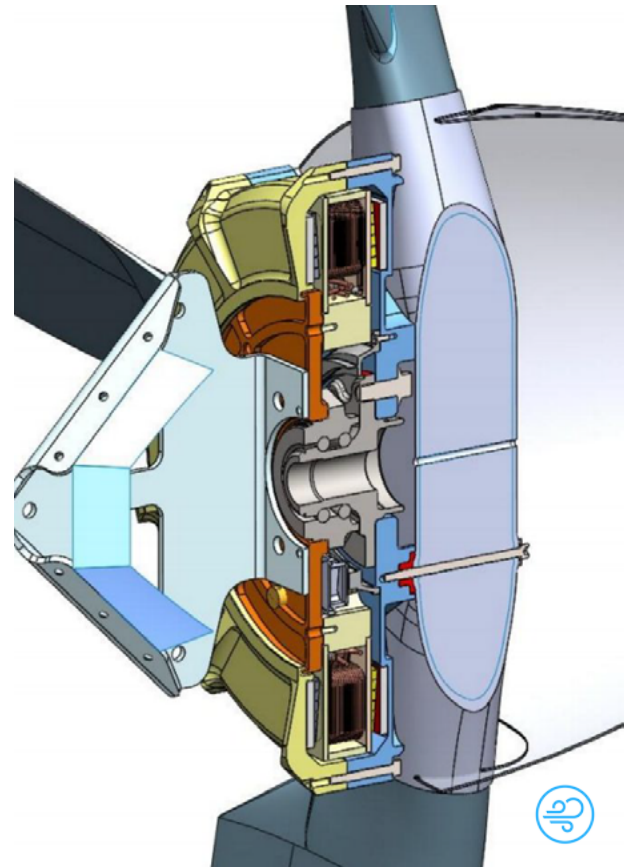
High bandwidth comms / balancing loop

Fusing, crosslink, failure management



STACKED M/G'S (CURRENT DESIGN)

- Axial flux, twin-rotor design
- "Outrunner" topology
- 36 teeth, 30 poles (12/10 structure)
- 150 kW, 36 kg



STACKED M/G'S - STATOR ASSEMBLY

- SMC teeth
- Edge-wound coils
- "Sandwich bonded" assembly
- "Wet stator" design with dielectric coolant
- Casing is laminated G-10



STACKED M/G'S - ROTOR ASSEMBLY

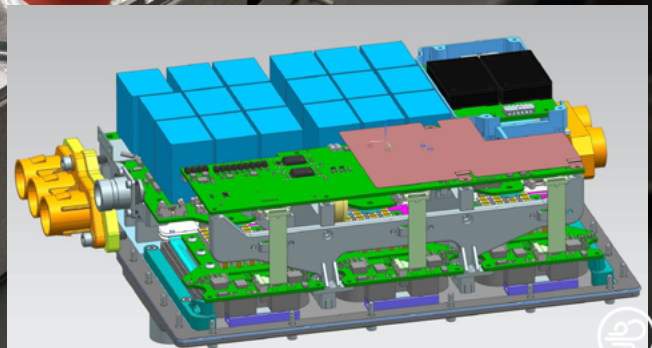
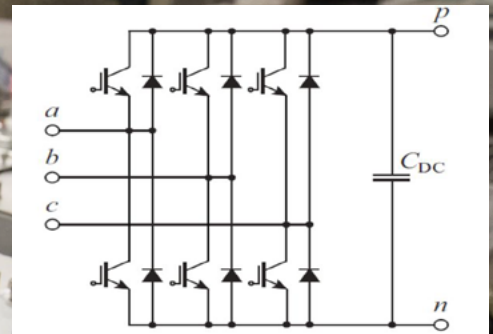
- Aluminum outer shell
- Coiled Silicon Steel back iron laminate
- Bonded NdFeB 45-SH magnets



STACKED MOTOR DRIVE

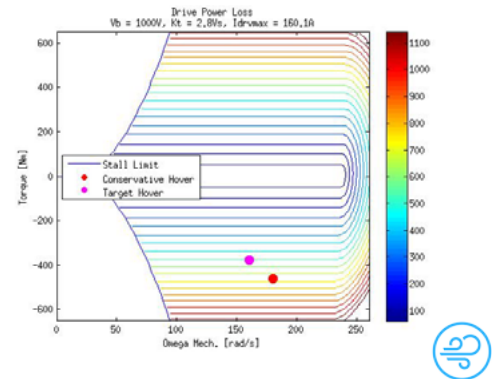
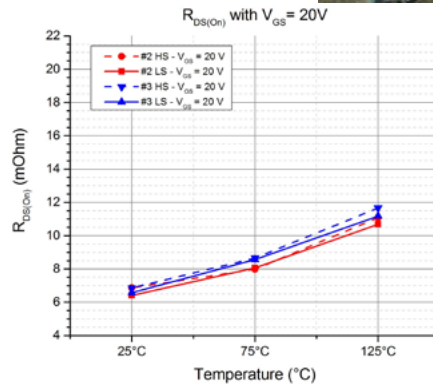
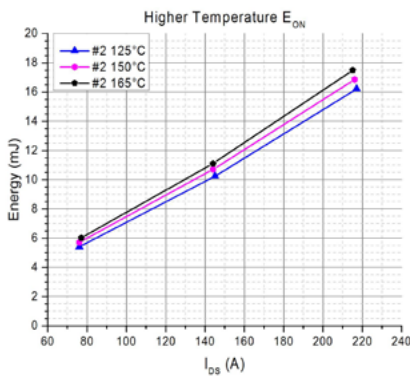
1700V SiC MOSFET design

- SVPWM @ $f_{sw} = 10$ kHz
- Liquid cooling plate
- 1 kHz comms loop to facilitate stacking stability
- Has passed significant rel and environmental testing
- 7 kg each



STACKED MOTOR DRIVE

- Extra margin to decouple wing and ground faults
- Internal floating ground architecture
- Accurately characterized switches
- Quadratic thermal model based on I_d



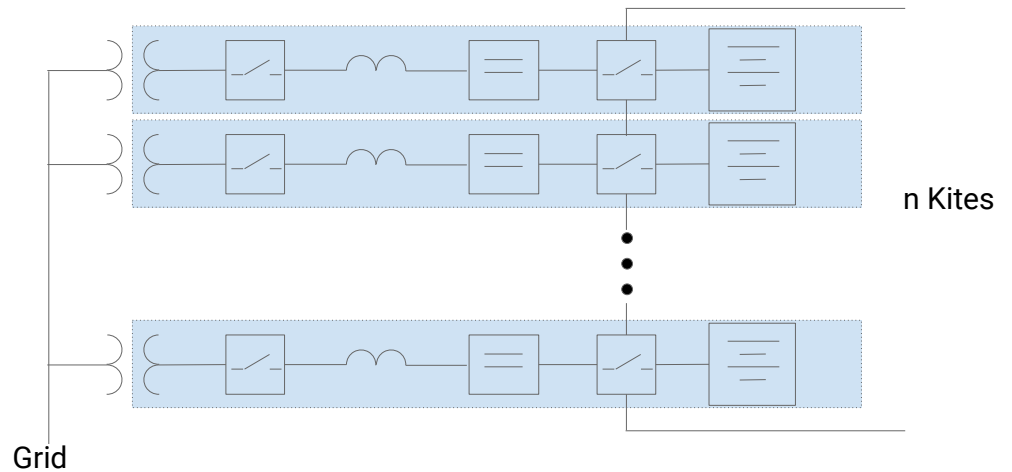
GROUND-SIDE INVERTER

- 6 x 250 kW commercial inverters
- DC series connected
- Inverter section is floated to develop 4000V DC
- Custom designed, high isolation transformer

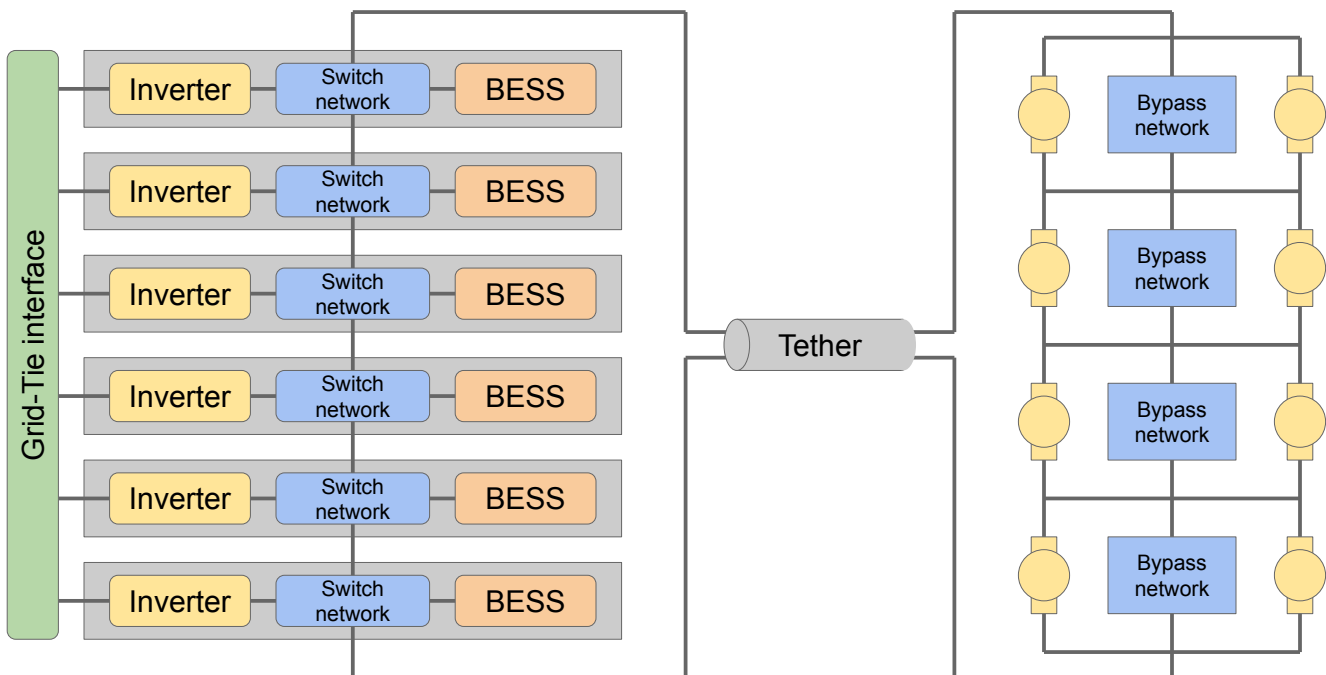


GROUND-SIDE ARCHITECTURE (cont.)

- Low cost
- 4-5 kV
- Fault tolerant
- Battery backup



Failure Mode Effects Management



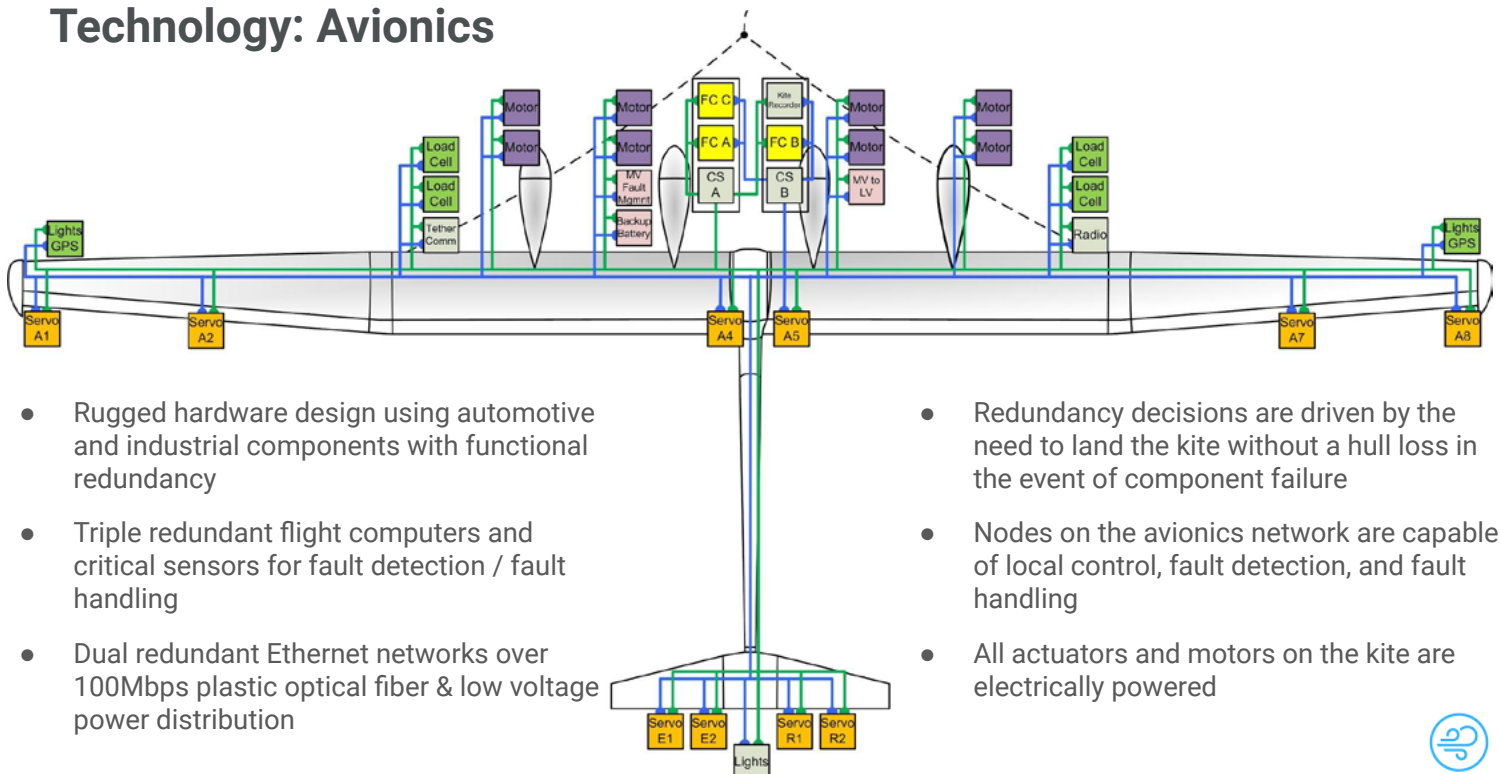
Technology: Avionics + Control System

The systems consist of:

- Flight computers
- Kite avionics buses and communication nodes
- Kite-to-ground communications
- All flight control sensors
- Closed-loop control system for all modes
- Simulation to design control system, predict kite performance



Technology: Avionics



- Rugged hardware design using automotive and industrial components with functional redundancy
- Triple redundant flight computers and critical sensors for fault detection / fault handling
- Dual redundant Ethernet networks over 100Mbps plastic optical fiber & low voltage power distribution

- Redundancy decisions are driven by the need to land the kite without a hull loss in the event of component failure
- Nodes on the avionics network are capable of local control, fault detection, and fault handling
- All actuators and motors on the kite are electrically powered



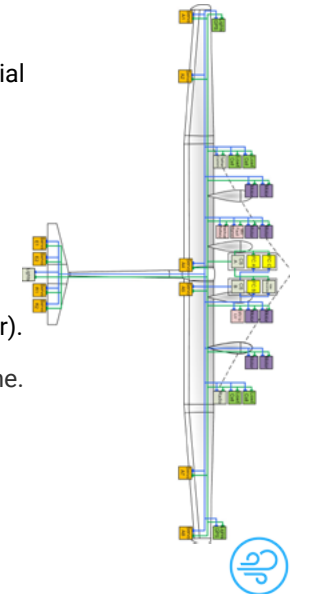
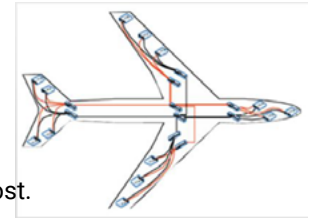
Avionics

The Requirement:

Achieve the reliability of military or commercial aircraft flight control systems, without their prohibitive cost.

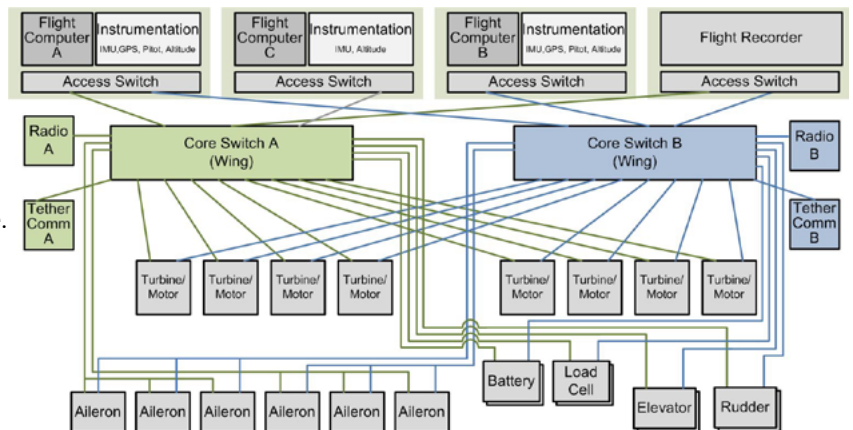
The Solution:

- A network-centric design that adapts technology from automotive/ industrial /telecom /commercial electronics to reduce cost.
- Dual-Redundant Ethernet with Makani Avionics Input/Output (AIO) protocol
 - uses vanilla Ethernet integrated circuits and protocols
 - uses micros certified for safety-critical automotive applications
 - our AIO protocol manages double/triple/n-level redundancy
 Big win over conventional avionics busses in terms of cost, weight, development time.
- A fiber-optic network using plastic fiber (cheaper/more rugged than glass fiber, lighter than copper).
- Low-cost triple-redundant flight computers with Cortex-A9 Arm processors over Ethernet backbone.



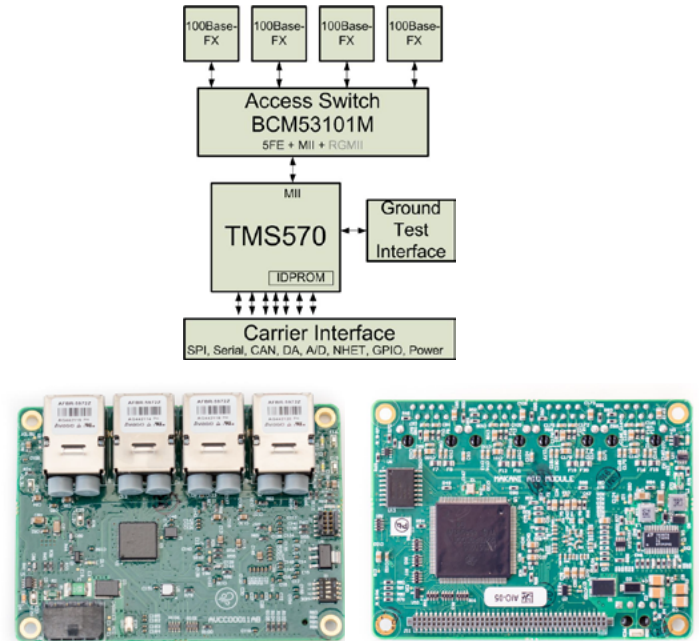
Avionics AIO Network

- Dual-redundant network with zero failover time
- Uses COTS L2 switches
 - **Access Switch** integrated into each AIO node.
 - **Core Switch** routes AIO Message to destination (multicast group).
- Network is statically configured at compile time.
- Multicast messages allows one sender to transmit to multiple destinations.



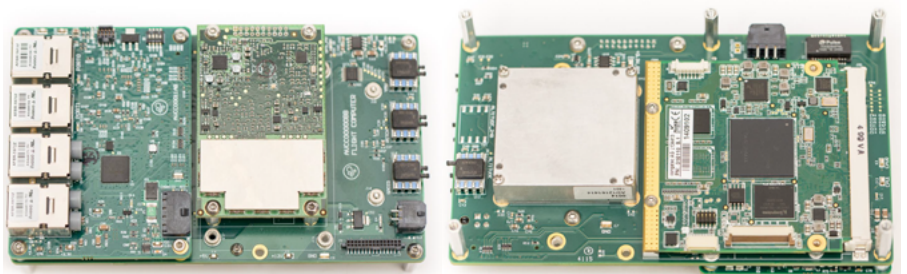
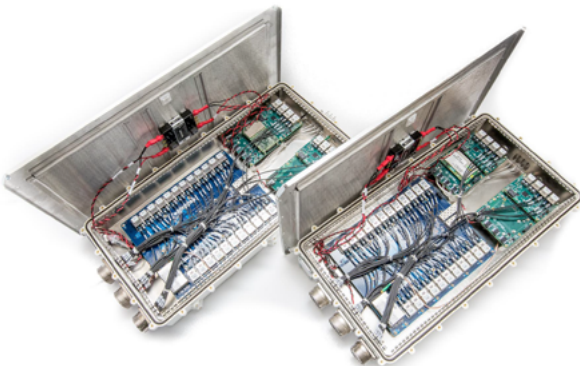
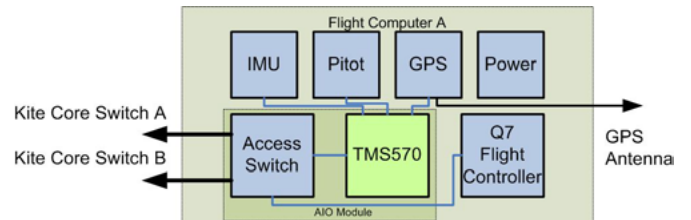
Avionics Building Block: Avionics I/O Module

- Built around TMS570 safety-critical processor (SIL-3)
- Common avionics component used throughout the kite includes a safety-critical microcontroller, an ethernet switch, and four POF ports
- Carrier boards implement node specific functionality: flight computers, sensor interfaces, servo control, etc
- Software framework for communication, status monitoring, drivers, and bootloading
- Allows for simpler configuration control and faster development

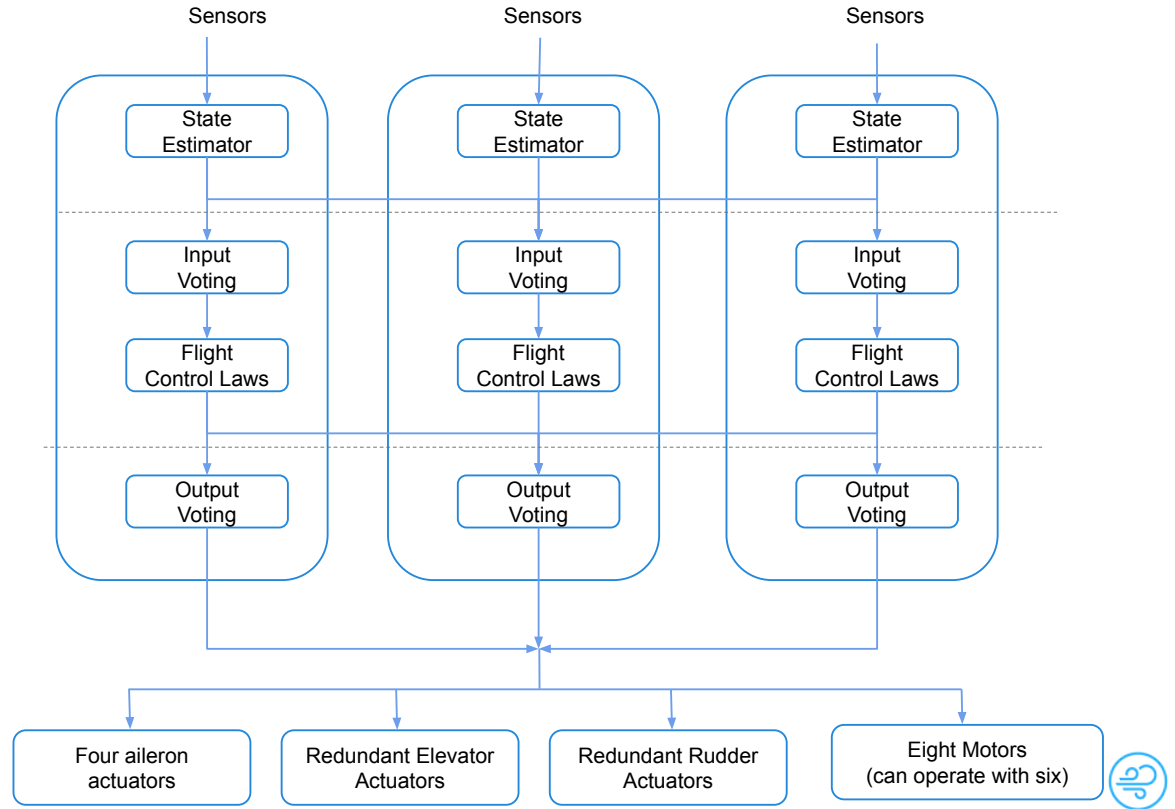


Avionics Flight Computers

- Q7 computer runs the estimation and control algorithms
 - Freescale Cortex-A9 processor
 - Embedded Linux
 - Multiple vendors and CPUs
- AIO Module connects to IMU, GPS, and Pitot sensors and provides the network interface



Redundancy



Avionics Network Physical Medium

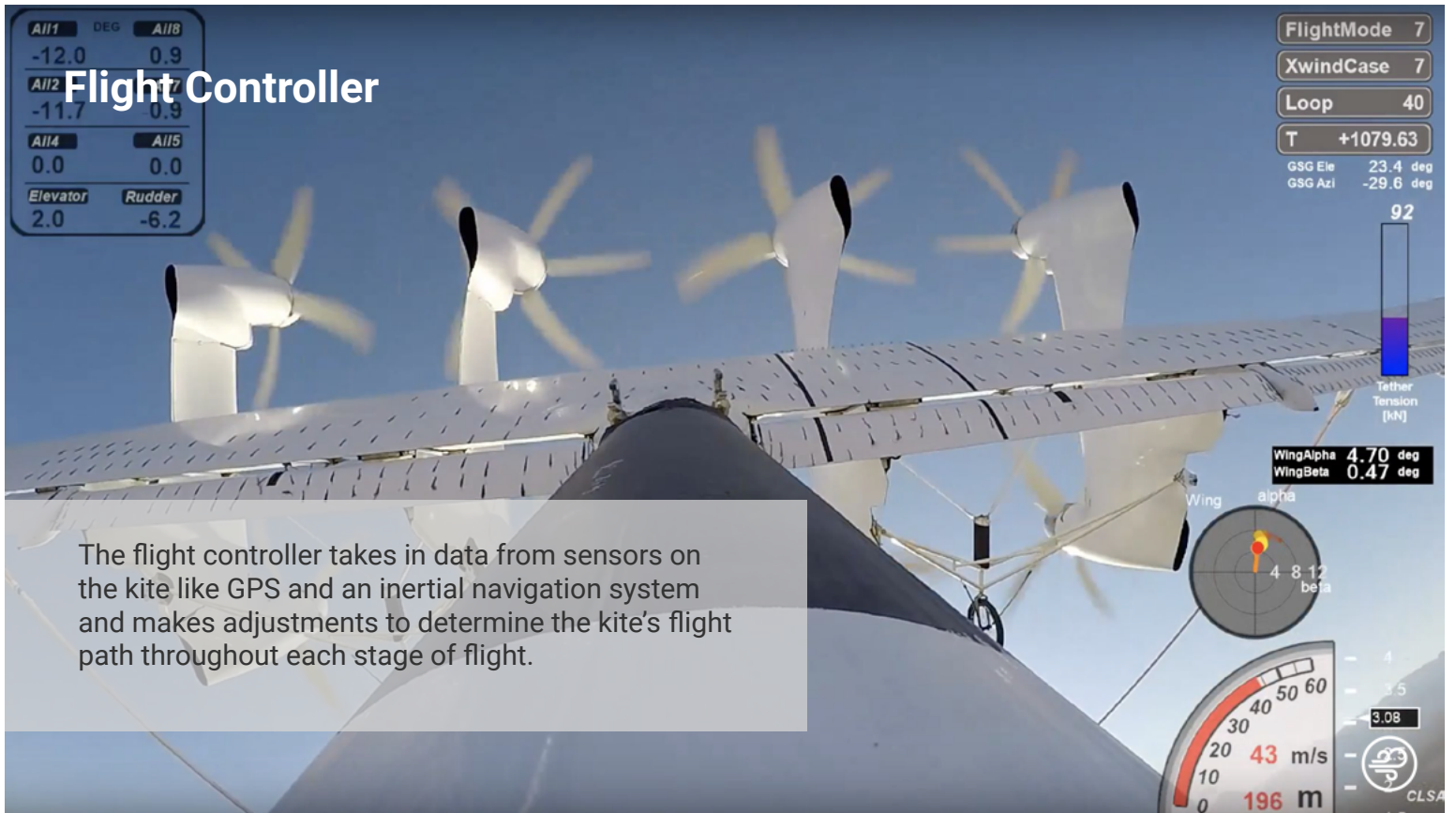
Polymer (Plastic) Optical Fiber (POF)

- Provides galvanic isolation for stacked motor operation
- No susceptibility to lightning, EMI
- 100 Mbits/sec, 50 meters
- Easily terminated in the field
- High-density MIL-STD-38999 -type connectors available
- Much higher tolerance to contaminants, scratches than glass fiber
 - Low-cost alternative to expanded beam connections

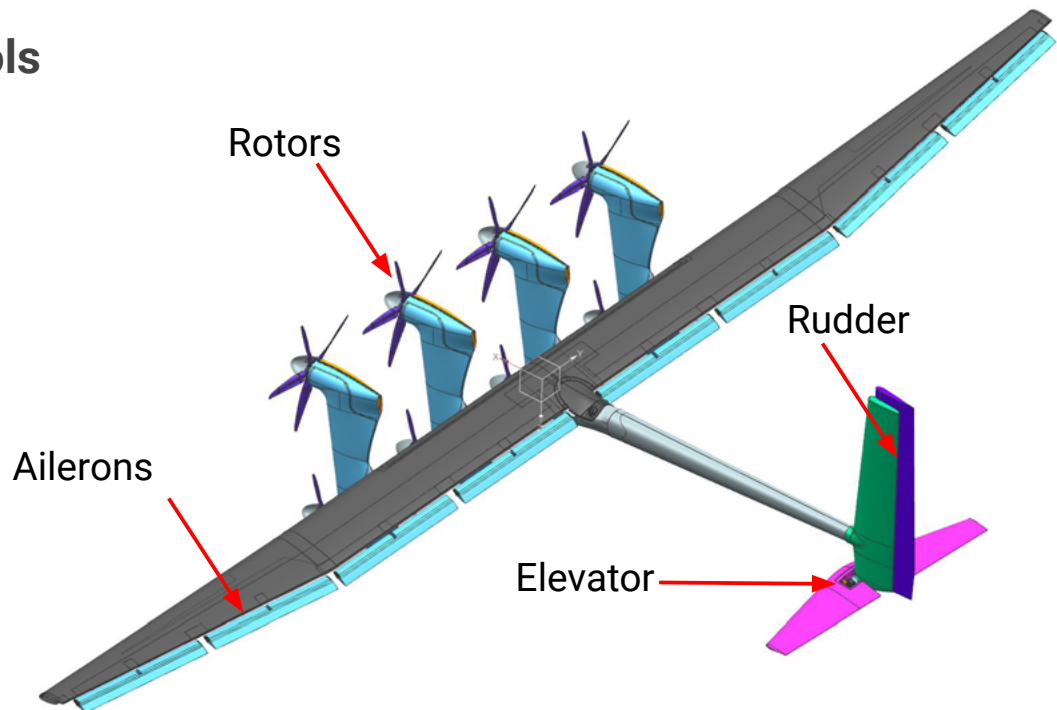
Multi Mode Glass Fiber
50 to 62.5 μm core
1000BASE-SX

Plastic Optical Fiber
1mm core
100BASE-FX

Single Mode Fiber
9 μm core
1000BASE-LX, EX, ZX, BX



Flight Controls

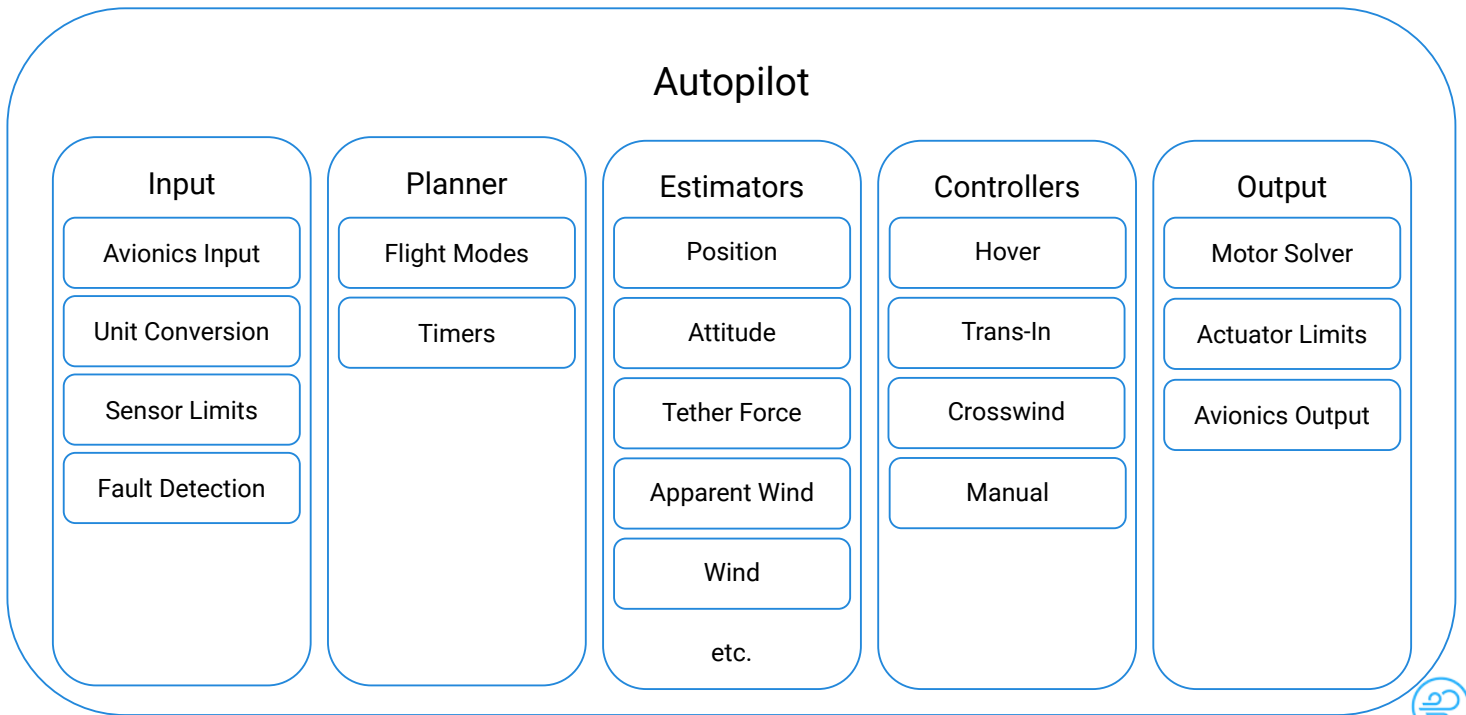


Control System Requirements

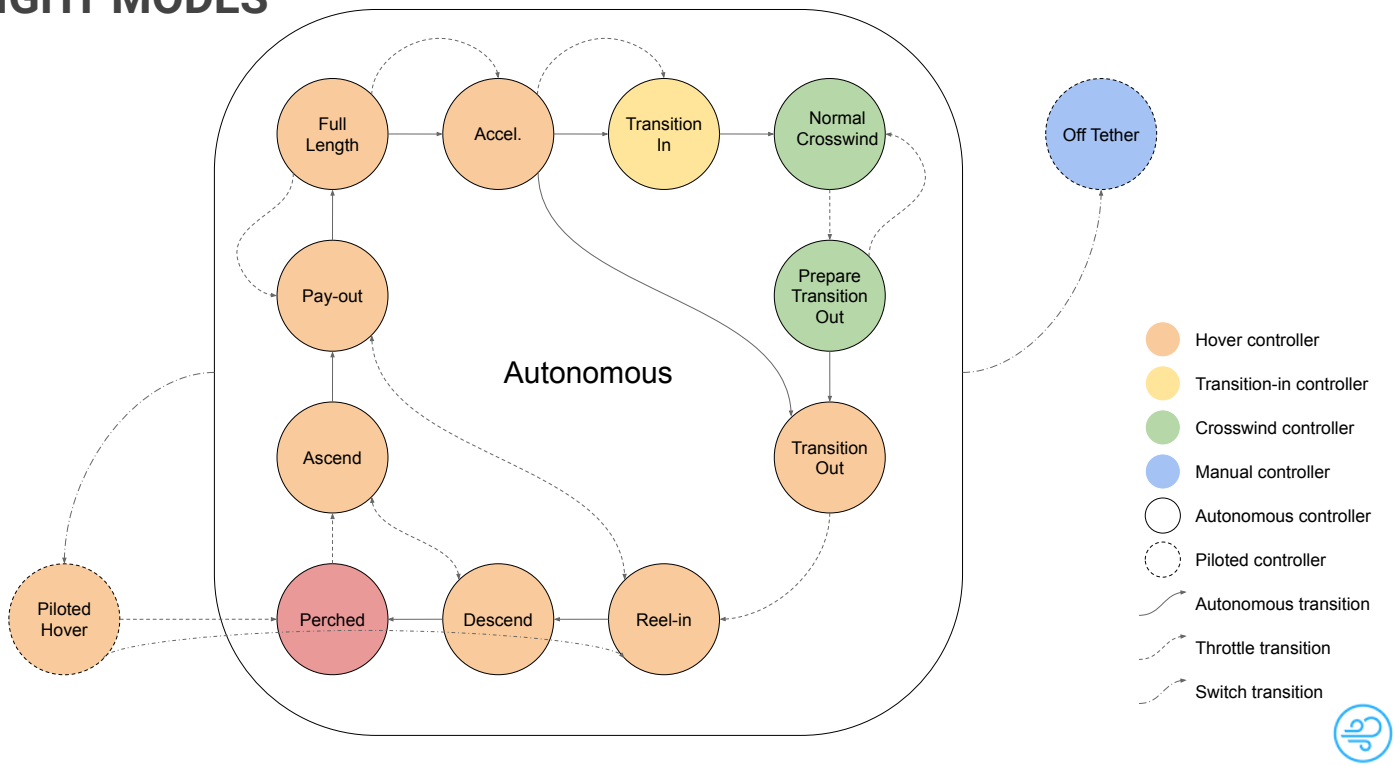
- Robust and safe autonomous control with fault handling
- Remote shutdown + emergency shut off capability
- Maintain minimum ground clearance
- Accurate / robust kite + ground station interactions
- Comply with IEC/ISO standards where applicable
- Reliable
- Lightweight



OVERVIEW



FLIGHT MODES



Level of autonomy and required human intervention

- Normal operation is fully autonomous
- Fault tolerant
- For commercial product,
 - there will be no required human intervention
 - If a malfunction occurs the kite will transition out of crosswind and into hover (automatically) and reel in per normal process
 - If the kite loses power or cannot otherwise be reeled in then it is designed to control its flight into the ground to minimize the flight path.



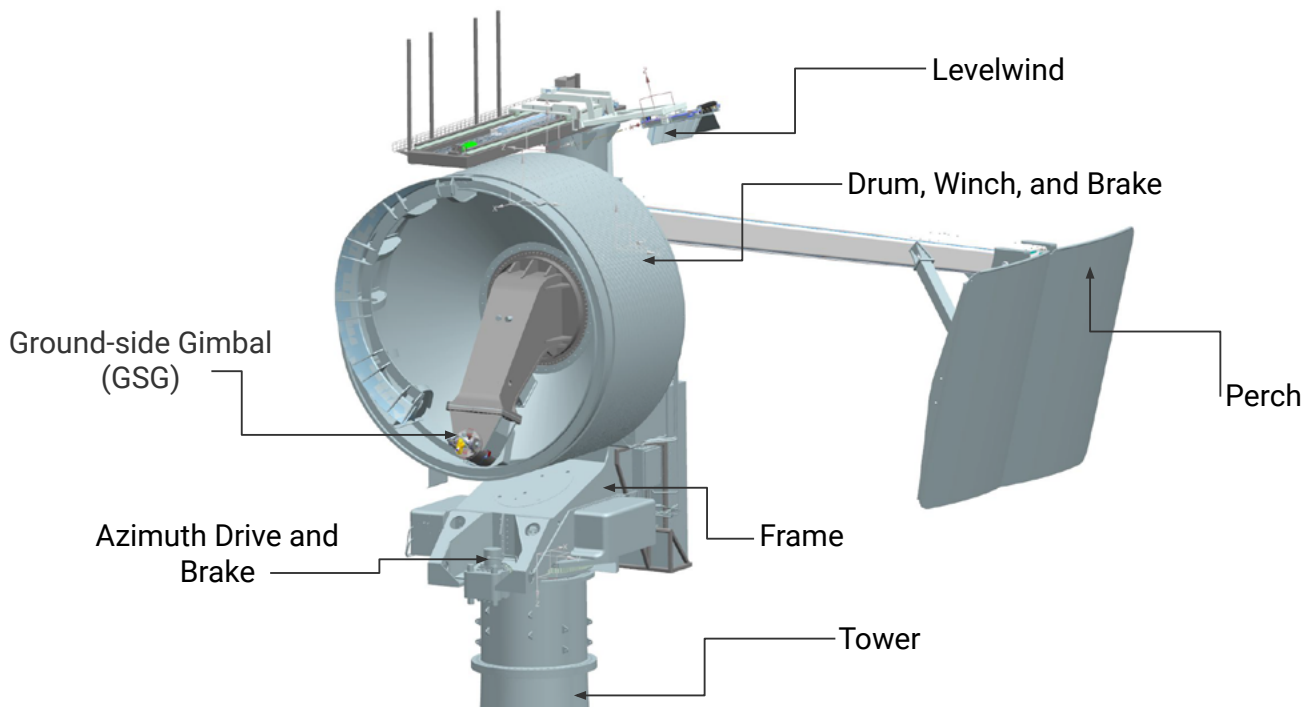
Ground Station



- Anchors and stores the tether
 - Electrical connection (+/- 1.5MW) and stores 435m of tether
- Carries tether loads through a gimbal down to the foundation
 - Up to 280 kN in operation
- Handles de-twist of tether in flight
- Perch for the kite
 - Provides access for kite maintenance
 - Manages azimuth orientation for launch/land
- Onshore units have short tower to a small foundation
- Offshore units place ground station at the top of a fixed platform or floating spar buoy



Ground Station Components - INTRO of Major Components



Ground Station: Major Component Weights and Dimensions

- GS total: 32,000 kg
- Production system needs significant weight reduction
- Production system needs significant cost reduction
- GS overall height: 17.5 m
- GS largest width: 12.8 m
- GS smallest width: 5.8 m

Weights of Major Components:

- Winch frame: 6,200 kg; (A572-G50 steel)
- Perch: 900 kg; (5083 Al (panel) / fiberglass (boom))
- Drum: 2,500 kg; (5083 aluminum)
- Tower: 9,000 kg; (A572-G50 steel)

Dimensions of Major Components:

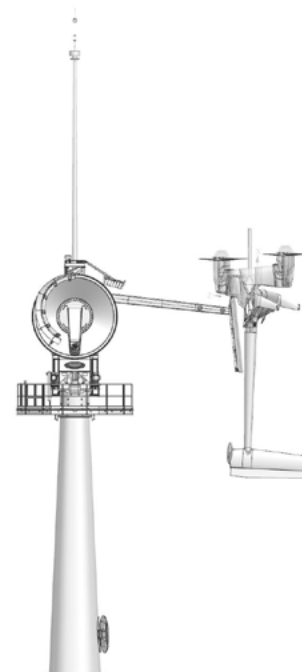
- Winch frame: 3.7m (h) x 2.3m (w) x 2.3m (l)
- Perch: 3.3m (h) x 3.8m (w) (panel) / 7.8m (L) (boom)
- Drum: 3.8m x 2.4m
- Tower: 11.5m x 1.5m/2.5m



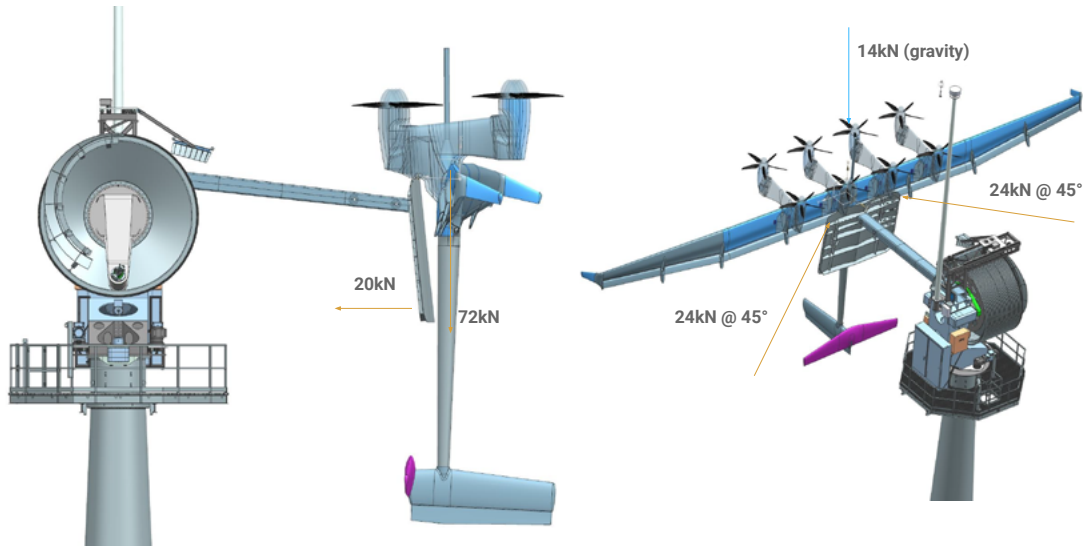
M600 GROUND STATION - OPERATING MODES

Perched

- Brakes applied, no motion
- Provides access for maintenance
- Monitoring wind speed and direction



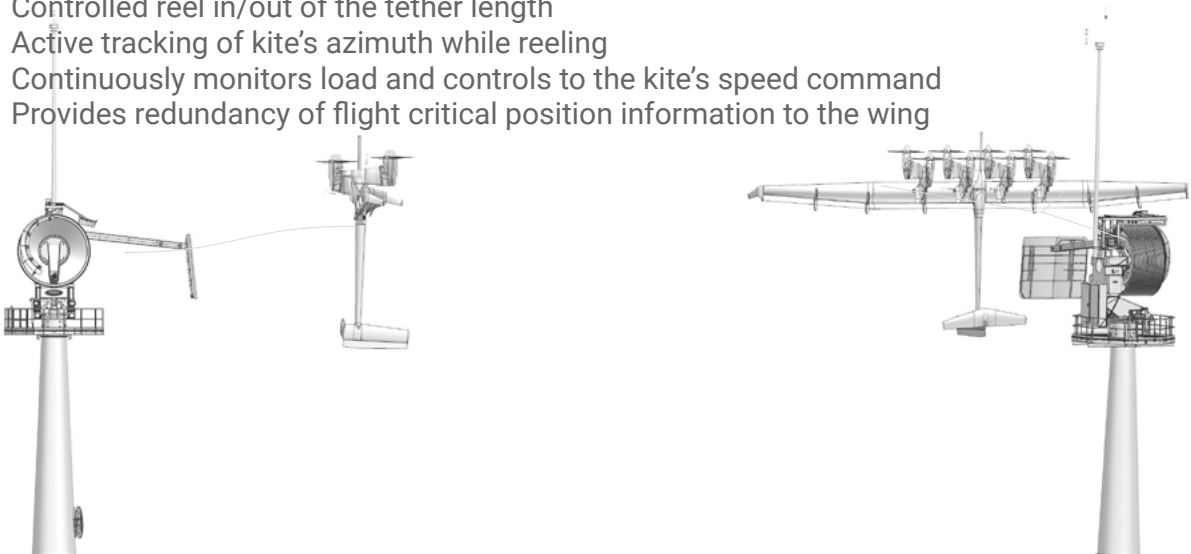
M600 GROUND STATION - Operating Loads while Perched



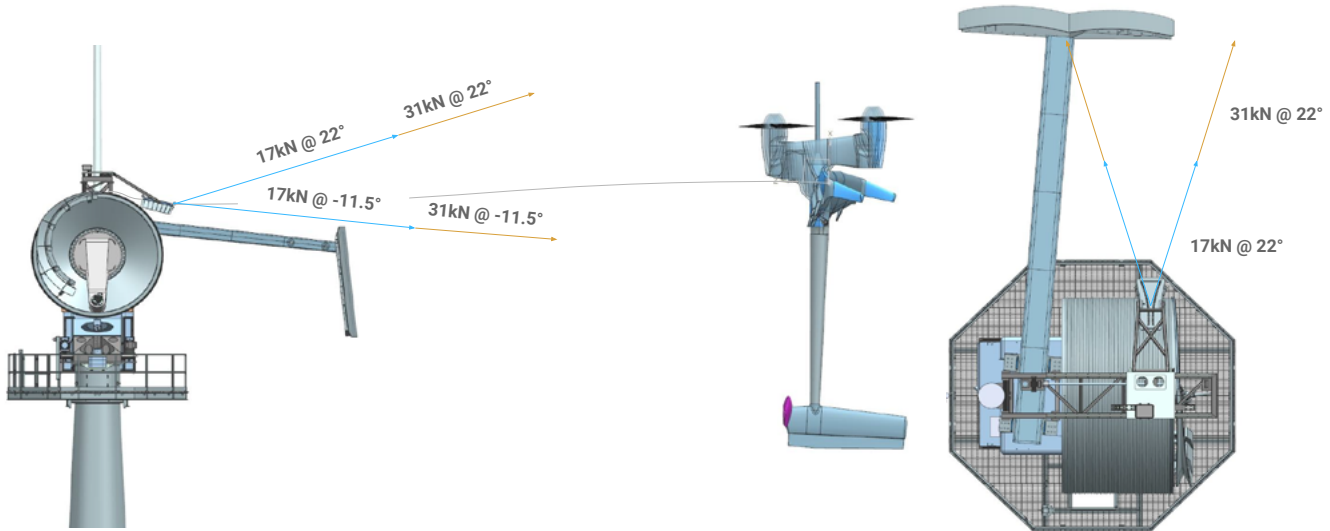
M600 GROUND STATION - OPERATING MODES

WINCHING

- Orients the kite downwind when on the perch
- Controlled reel in/out of the tether length
- Active tracking of kite's azimuth while reeling
- Continuously monitors load and controls to the kite's speed command
- Provides redundancy of flight critical position information to the wing



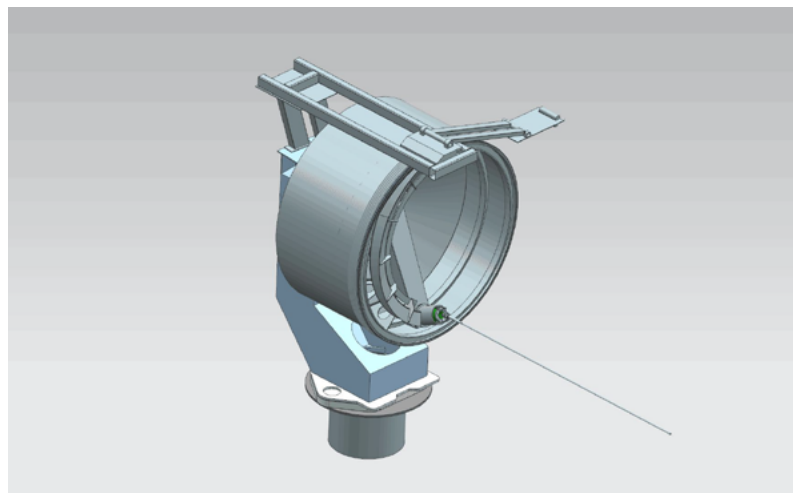
M600 GROUND STATION - Operating Loads Winching/Transform



M600 GROUND STATION - OPERATING MODES

TRANSFORM

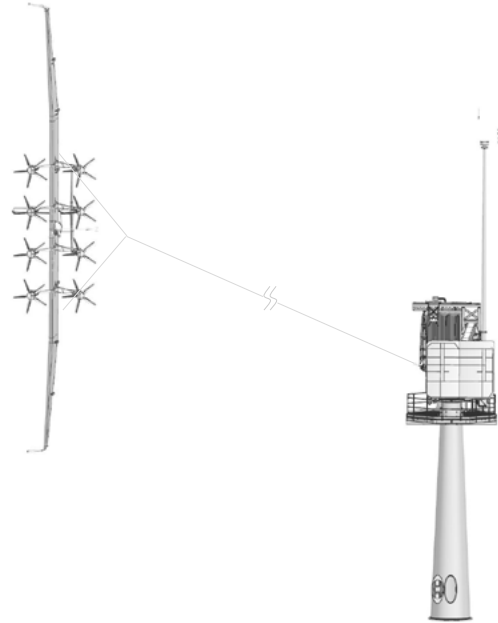
- Transition from winching to crosswind flight
- Tether unwinds from the drum and is constrained only by the Ground Side Gimbal (GSG)
- Motion requires coordination of multiple rotational axis - azimuth, winching, and detwist



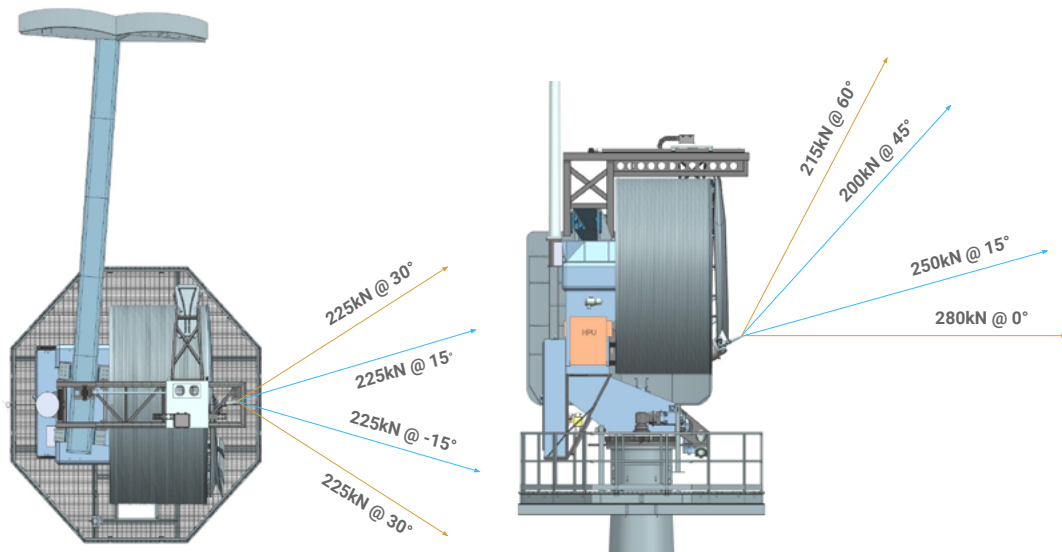
M600 GROUND STATION - OPERATING MODES

CROSSWIND FLIGHT

- Maintains azimuth position centered on the kite's flight cone
- Actively unwinds the tether to prevent twists from accumulating
- Provides redundancy of flight critical position information to the wing



M600 GROUND STATION - Operating Loads in Crosswind Flight



M600 GROUND STATION - REQUIREMENTS

M600 L0 Requirements

1. Safe, low cost and reliable operation

Ground Station L2 Requirements

1. Provide a platform to support kite
2. Prevent bending and abrasion failures of the tether while in operation and to store tether when reeled in
3. Transfer power to and from the kite
4. Support all applied loads in crosswind flight, hover and landing
5. Provide controls redundancy



PILOT GROUND STATION - ADDITIONAL REQUIREMENTS

PILOT L0 Requirements

1. Cost target
2. Reduced complexity

PILOT Ground Station L2 Requirements

1. Modularity to support marine operations and maintenance concepts
2. Needs to be able to support both, onshore and offshore concept of operations



M600 GROUND STATION - DESIGN OBJECTIVES

RELIABILITY FOCUSED

Design Failure Mode Effects and Analysis (DFMEA) approach focused on reducing severity and improving detectability
Extensive validation program for all high Risk Priority Number (RPN) flight critical components

LOW COST MANUFACTURING

Conventional, readily available materials
Limited use of expensive manufacturing techniques

HIGH DEGREE OF CONTROL

Reduced mass and inertia
Low inertia / high power density drivetrains
Active braking systems on both primary axis
Accurate sensing of all degrees of freedom

EASE OF MAINTENANCE

Access to all critical components which require inspection
Active monitoring of all systems
Automated maintenance reduces likelihood of error and downtime



M600 GROUND STATION - RELIABILITY & ROBUSTNESS

RISK REDUCTION

Tight timelines, extended life cycles and the need to operate autonomously requires de-risk

DFMEA work on previous architectures highlighted two significant issues

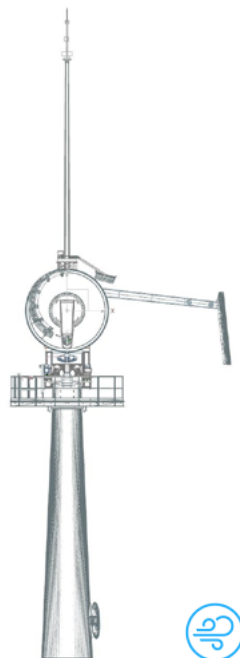
1. Severity of failures was often loss of vehicle
2. Detectability relied on very frequent inspection or huge amount of durability testing

Severity

- Reduce single point failures (redundancy)
- Change failures from loss of function to degradation of function (system derating, active monitoring)

Detectability

- Open loop sensing & monitoring, reducing labor intensive inspection
 - Facilitates reliability centered maintenance (RCM)
- Validation testing
 - Highly Accelerated Life Testing (HALT) through elevated load conditions
 - Bench / sample testing



M600 GROUND STATION - DESIGN OVERVIEW

WINCH FRAME

AZIMUTH DRIVETRAIN &
BRAKE ASSEMBLY

WINCH DRIVETRAIN & BRAKE
ASSEMBLY

PERCH

GSG & GSG MOUNT

DRUM

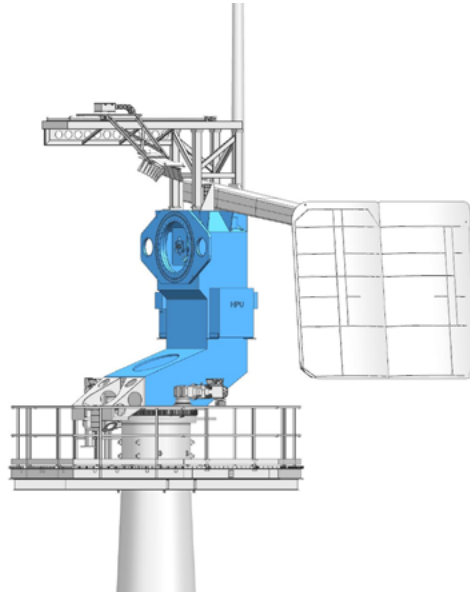
LEVELWIND

GROUND STATION
ELECTRONICS

HUMAN PLATFORM

WIND MAST

TOWER



M600 GROUND STATION - WINCH FRAME

FUNCTIONS & REQUIREMENTS

- Support all crosswind, hover and landing loads
- Provides mounting for all other major components
- Provide routing for all MV and LV components

SPECIFICATIONS

mass: 6200 kg

dimensions: 3.7m (h) x 2.3m (w) x 2.3m (l)

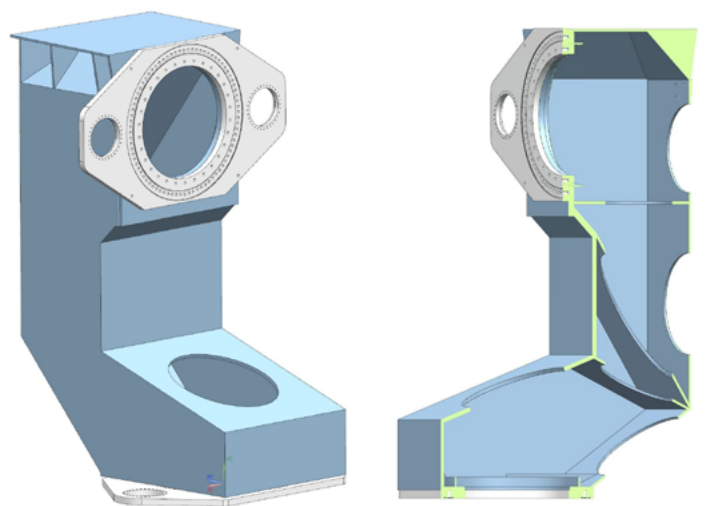
material: A572-G50 steel

construction: Welded plate w/ two precision machined bearing mounts

KEY ATTRIBUTES

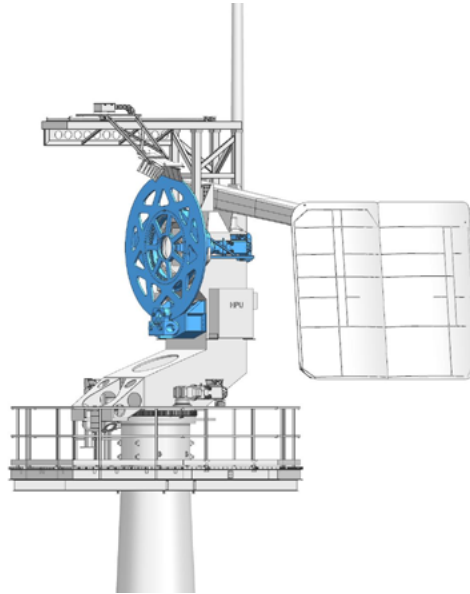
Large steel boxed weldment with internal trussing

- Only precision surfaces are made separable assemblies to reduce manufacturing cost
- Location of key datums with respect to each other not a critical characteristic



M600 GROUND STATION - DESIGN OVERVIEW

- WINCH FRAME
- AZIMUTH DRIVETRAIN & BRAKE ASSEMBLY
- WINCH DRIVETRAIN & BRAKE ASSEMBLY
- PERCH
- GSG & GSG MOUNT
- DRUM
- LEVELWIND
- GROUND STATION ELECTRONICS
- HUMAN PLATFORM
- WIND MAST
- TOWER



M600 GROUND STATION - DRIVETRAIN / ELECTRONICS

FUNCTIONS & REQUIREMENTS

Azimuth

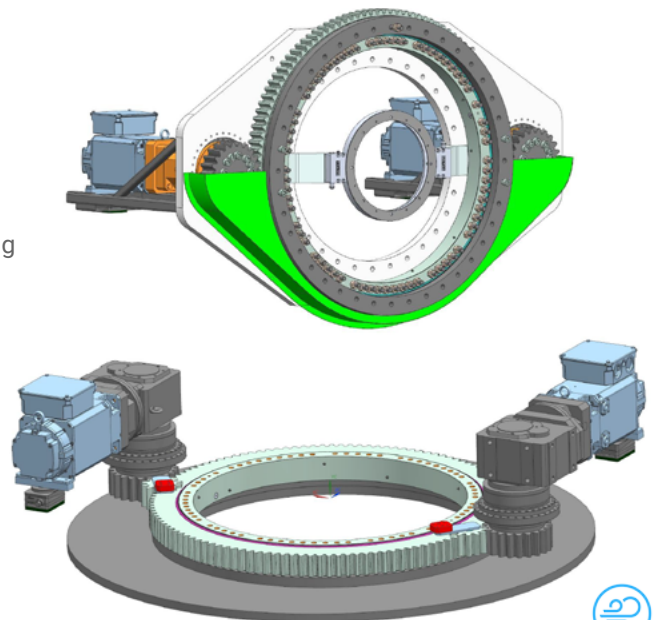
- Always position the kite downwind
- Prevent excessive torsional strain in tower cabling
- Control ground station motion in hover and transform
- Measure and communicate position

Winching

- Maintain commanded winching speed and control winching motion during hover and transform
- Support winching loads
- Measure and communicate position

KEY ATTRIBUTES

- Load sharing evenly distributes wear and thermal loading
- Redundancy in both drivetrains w/ fault detection and mitigation
- Automated lubrication allows for consistent and reliable maintenance



M600 GROUND STATION - DRIVETRAIN / ELECTRONICS

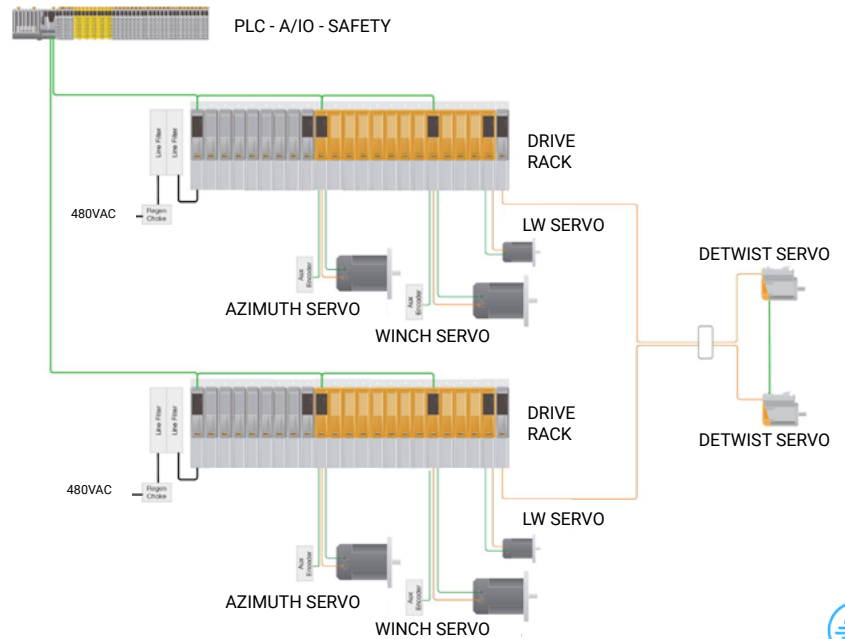
KEY ATTRIBUTES

Winching electronics architecture is robust to nearly all single point failures

- Two parallel drive backplanes
- Each responsible for one branch of the electronics architecture
- No single servo or drive failure will cascade other failures

Environmental protection

- NEMA 4x aluminum enclosure
 - lightweight and corrosion resistant
- Internal heater to prevent condensation
- Clean air exchange through a salt-air panel filter



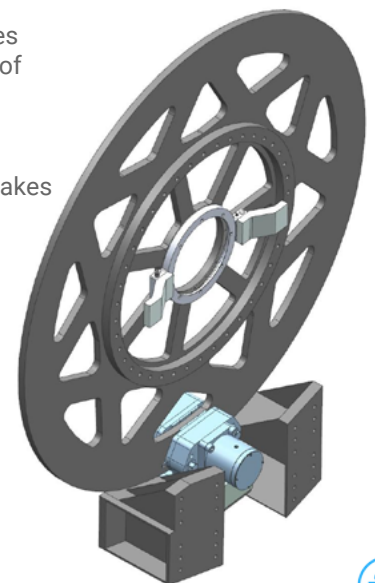
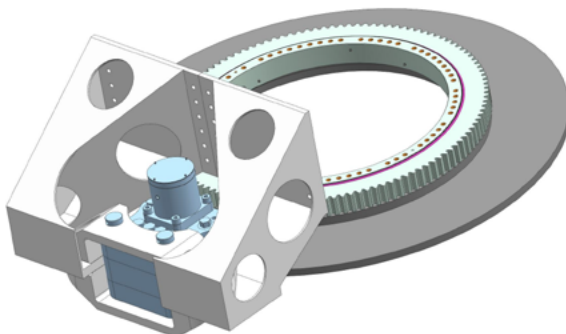
M600 GROUND STATION - HYDRAULIC BRAKING

FUNCTIONS & REQUIREMENTS

- Isolate drivetrains from crosswind flight loads
- Control reorientation of the ground station about that azimuth axis during crosswind
- Provide protection to the drivetrains during turbulent hover conditions

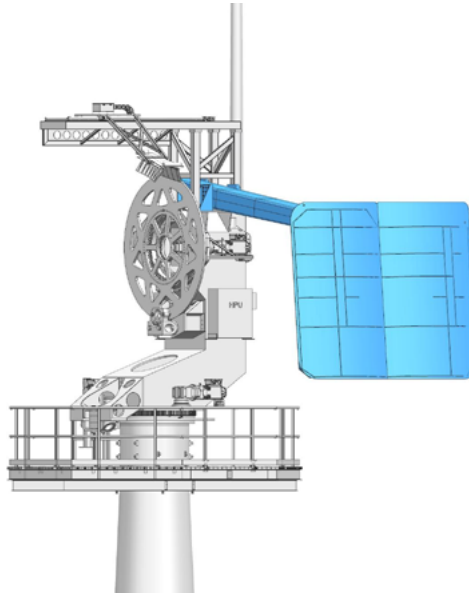
KEY ATTRIBUTES

- Proportional control of both brakes allows for close loop modulation of brake pressure
 - Environmental factors
 - Dynamic control
- Hydraulic pressure disengages brakes allowing for fail-safe condition



M600 GROUND STATION - DESIGN OVERVIEW

- WINCH FRAME
- AZIMUTH DRIVETRAIN & BRAKE ASSEMBLY
- WINCH DRIVETRAIN & BRAKE ASSEMBLY
- PERCH
- GSG & GSG MOUNT
- DRUM
- LEVELWIND
- GROUND STATION ELECTRONICS
- HUMAN PLATFORM
- WIND MAST
- TOWER



M600 GROUND STATION - PERCH

FUNCTIONS & REQUIREMENTS

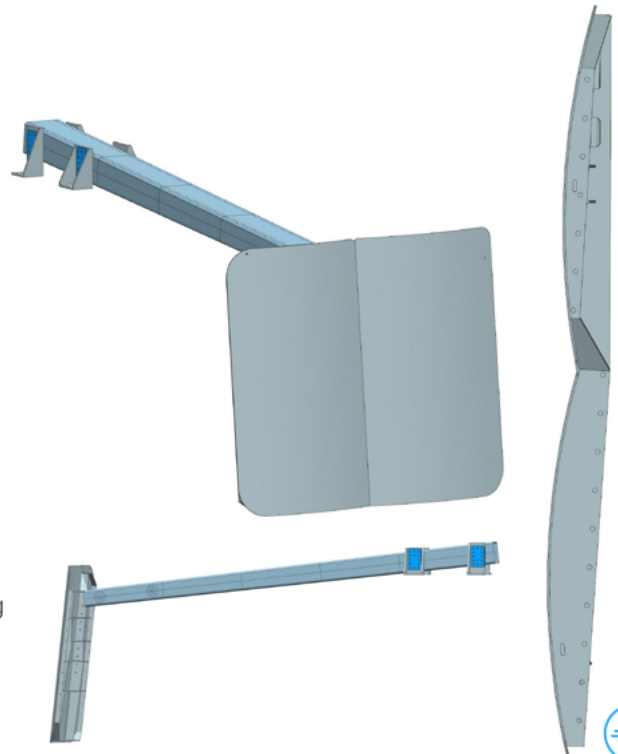
- Horizontally locate the wing for landing
- Support the wing
- Minimize wing impact loads

SPECIFICATIONS

mass: 500kg (panel) / 400kg (boom)
dimensions: 3.3m (h) x 3.8m (w) (panel) / 7.8m (L) (boom)
material: 5083 Al (panel) / fiberglass (boom)
construction: Welded Al plate (panel) / infusion molded e-glass (boom)

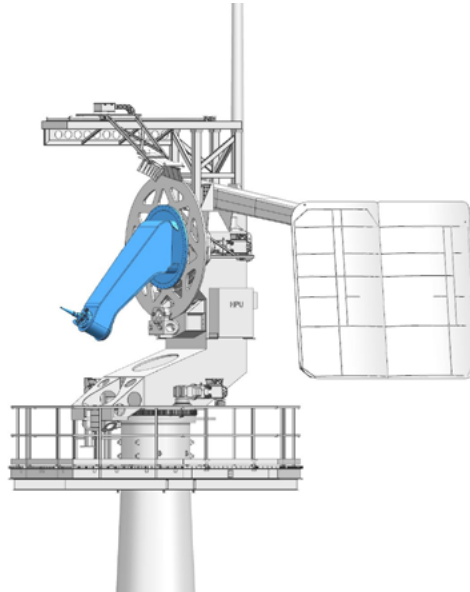
KEY ATTRIBUTES

- Removes landing gear loads from the kite
- Panel shape designed to center the wing for landing
- Al alloys chosen do not require heat treating after welding
- Simplistic & symmetric boom construction minimizes tooling and labor costs



M600 GROUND STATION - DESIGN OVERVIEW

- WINCH FRAME
- AZIMUTH DRIVETRAIN & BRAKE ASSEMBLY
- WINCH DRIVETRAIN & BRAKE ASSEMBLY
- PERCH
- GSG & GSG MOUNT
- DRUM
- LEVELWIND
- GROUND STATION ELECTRONICS
- HUMAN PLATFORM
- WIND MAST
- TOWER



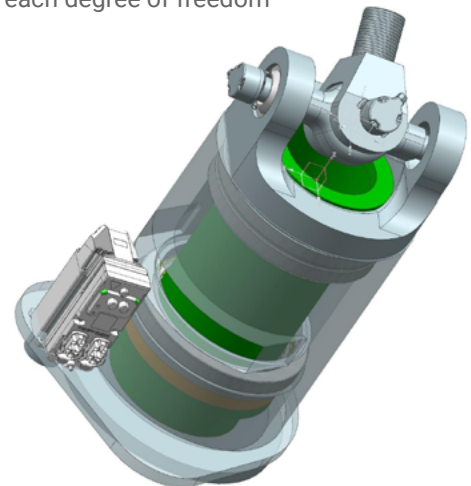
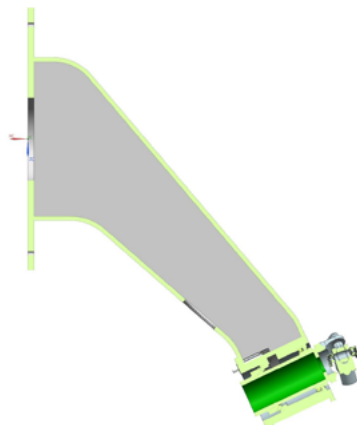
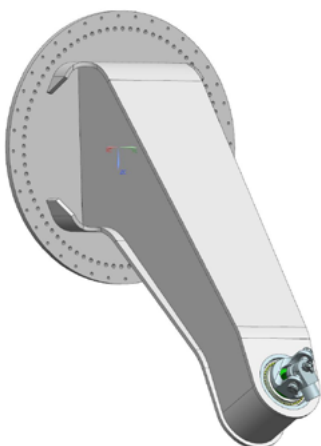
M600 GROUND STATION - GROUND SIDE GIMBAL

FUNCTIONS & REQUIREMENTS

- Support crosswind flight loads
- Prevents torsional stress in the tether during crosswind flight
- Provide redundant position measurement for the kite

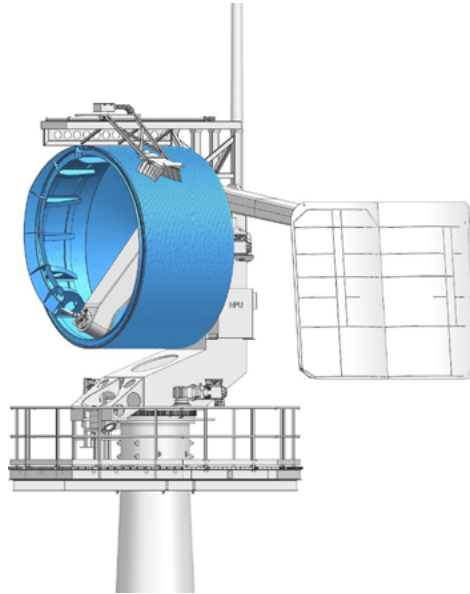
KEY ATTRIBUTES

- Dual servo drives provide redundancy
- Cassette design incorporates entire linkage and both LV and MV slip rings
- Dual encoders on each degree of freedom



M600 GROUND STATION - DESIGN OVERVIEW

- WINCH FRAME
- AZIMUTH DRIVETRAIN & BRAKE ASSEMBLY
- WINCH DRIVETRAIN & BRAKE ASSEMBLY
- PERCH
- GSG & GSG MOUNT
- DRUM**
- LEVELWIND
- GROUND STATION ELECTRONICS
- HUMAN PLATFORM
- WIND MAST
- TOWER



M600 GROUND STATION - DRUM

FUNCTIONS & REQUIREMENTS

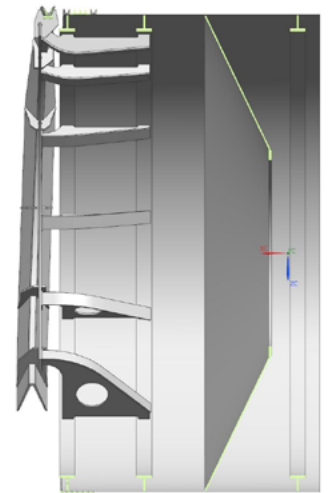
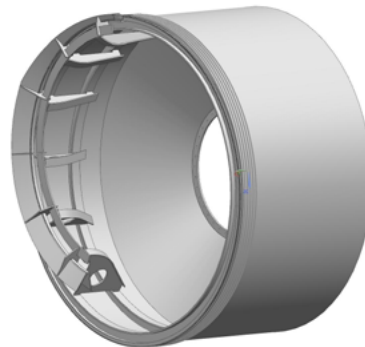
- Tether handling - min bend, contact stress, abrasion
- Supports tether compressive load

SPECIFICATIONS

mass: 2500kg
dimensions: 3.8m (dia) x 2.4m (w)
material: 5083 aluminum
construction: Rolled and welded aluminum plate, skin is extruded plastic

KEY ATTRIBUTES

- Rolled section with main internal conical mounting
- Requires minimal stiffening ribs, provides excellent structural efficiency
 - Single shear mounting vastly improved serviceability & maintenance
 - Similar in size and mass to the tether reels, potentially allowing for tethers to be installed on the drum at the manufacturer



PILOT GROUND STATION (offshore) - TRANSITION PIECE

FUNCTIONS & REQUIREMENTS

- Support all crosswind, hover and landing loads
- Provides mounting for winch frame
- Provide routing for all HV and LV components
- Provide transition from lightweight floating platform to ground station

KEY ATTRIBUTES

Minimal tower height results in numerous benefits

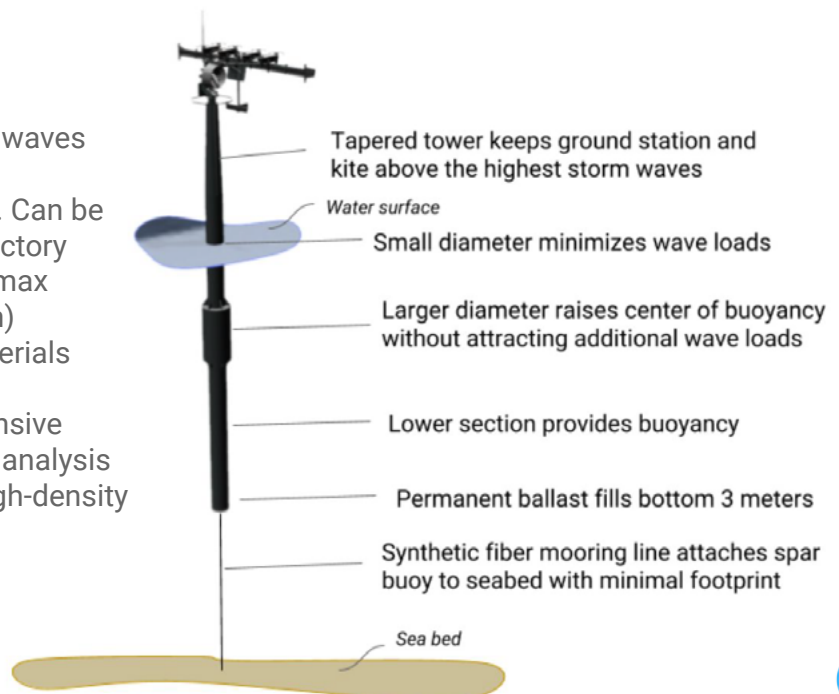
- **4.95 m instead of 11.5 m - Offshore tower morphs into a transition piece - much shorter, much lower mass, much lower cost**



Technology: Deep Water Offshore Buoy (response optional)

Tension-Leg Spar Buoy

- Support ground station above waves
- Transfer kite loads to seabed
- Simple rolled steel fabrication. Can be built in a wind turbine tower factory (max plate thickness 50 mm; max diameter 5 m, max length 50m)
- Off-the-shelf mooring line materials (Dyneema or similar)
- Gravity anchor precludes extensive geophysical and geotechnical analysis (approx 5m cube filled with high-density ballast material)



Thank You

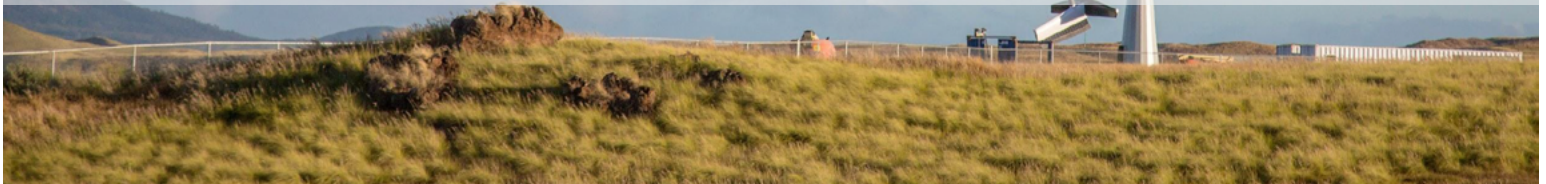


Additional Information



Additional Information Contents

- **System modeling**
- **Simulation Tools and Validation**
- **DWOS BOP: Mooring, anchoring, installation methodologies and other offshore structures related aspects**
- **Operations and Maintenance**
- **Reliability and Safety**
- **Product Risk**



System Modeling



System Design Tools

Analytical methods

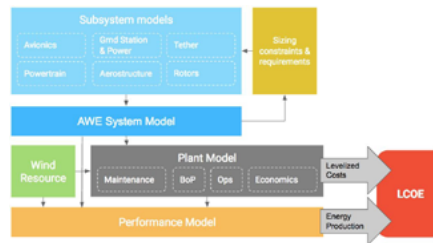
- Large base of knowledge, papers, and material

$$P(v_w) = \begin{cases} 0 & v_w \leq v_{w, \text{cut-in}} \\ P_0 \left(\frac{v_w}{v_{w, \text{cut-in}}} - 1 \right) & v_{w, \text{cut-in}} < v_w \leq \frac{3}{2} v_{w, \text{cut-in}} \\ \frac{1}{2} \rho v_w^3 A_k C_{\text{max}} & \frac{3}{2} v_{w, \text{cut-in}} < v_w \leq v_{w, T} \\ P_{\text{max}} & v_{w, T} < v_w \leq v_{w, P} \\ 0 & v_{w, P} < v_w \leq v_{w, \text{cut-out}} \\ & v_w > v_{w, \text{cut-out}} \end{cases}$$



System modeling tools

- System sizing and optimization
- System performance model
- LCOE estimation
- Sensitivity analysis



~11,000 line python model, contains all models to describe LCOE



System Design: Example

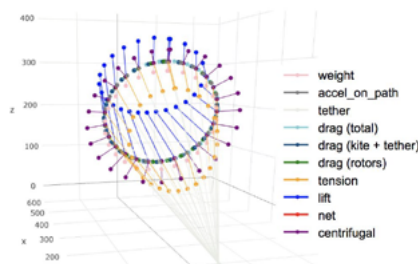
Inclination for best power (θ_{best}) is a function of wind shear (α) and is independent of:

- tether length
- system performance
- average wind speed
- ...and anything other than shear

$$\theta_{best} = \tan^{-1}(\sqrt{\alpha})$$

Can we verify this result with more detailed performance model?

- Use simple system performance model shown before



Makani team member and kiteboard racer Johnny Heineken (white kite) keeping it low during a race



System Design: Example

Using the simple performance model:

- Sweep shear and inclination
- Find best power

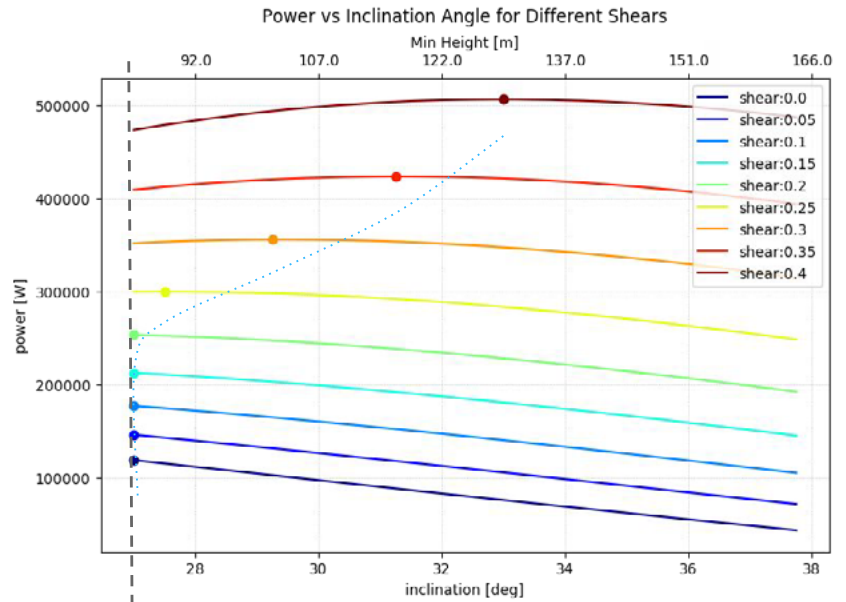
Results:

- More shear is very good for us!
- Best power is as low as you can go until shear ≥ 0.2
- High sensitivity to inclination at low shear due to cutoff of curve
 - A few degrees = 10s of kW and 10s of %

Notes:

Approx representative of M600 in RPX03-06 config at China Lake

120m radius loops with $v_{w_ref} = 10\text{m/s}$ and $h_{ref} = 80\text{m}$



Inclination of $\sim 27^\circ$ with $r_{loop} = 120\text{m}$ corresponds with $h_{min} = 80\text{m}$...that's approx as low as we'll want to go.



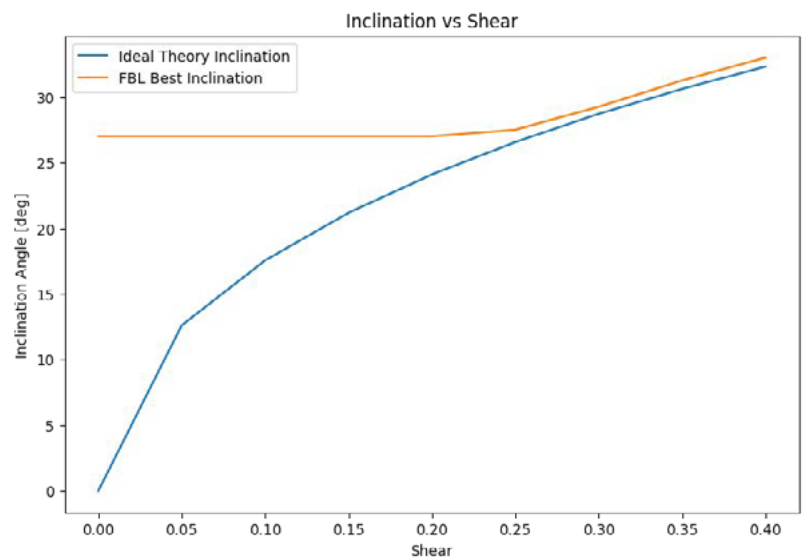
System Design: Example

How does this compare to the simple solution?

- Best inclination limited by the min possible inclination at low shears
- Simple theory with min height constraint is very good approximation for best inclination
- Vast majority of sites we will be as low as we can go
 - Which is still higher than HAWTs!
 - Benefit from shear more than HAWTs

Unable to capture all additional power from higher altitude winds

$$\theta_{best} = \tan^{-1}(\sqrt{\alpha})$$



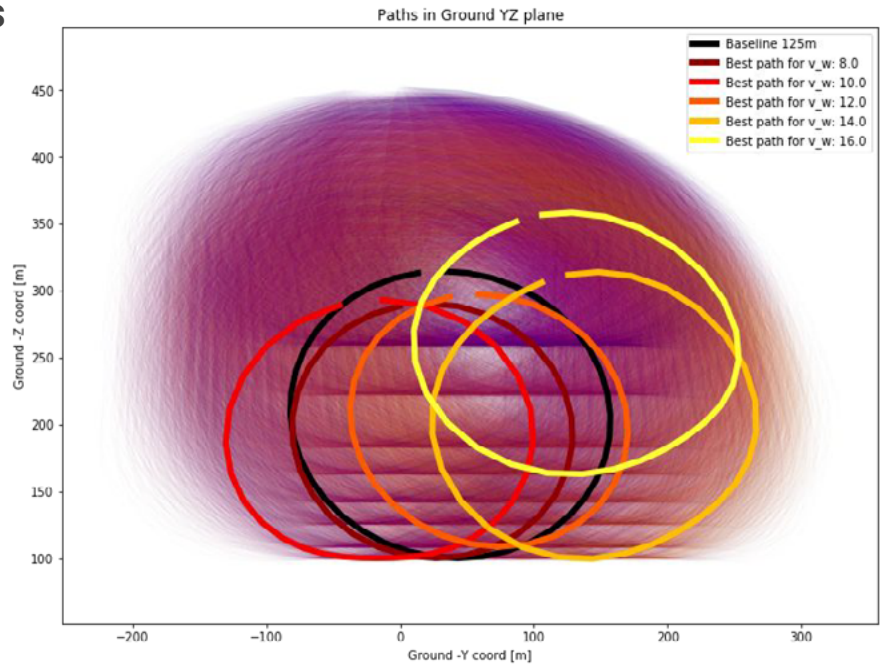
System Design: Flight Paths

FBL model used to evaluate different flight paths

- How sensitive are we to variations of our nominal circular flight path?

Makani has evaluated non-circular paths in the past

- Circular paths keep kite more directly downwind and make more power (vs figure 8)
 - But require detwist
- Figure 8 may still be used as part of rated power strategy



Composite of ~25,000 paths of different circular-ish shapes (ovals, eggs, beans, circles, etc), size, elevation, and azimuth, evaluated for each wind speed.



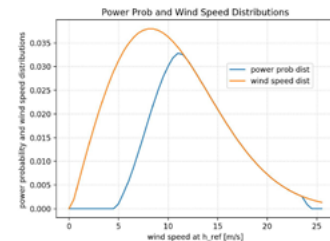
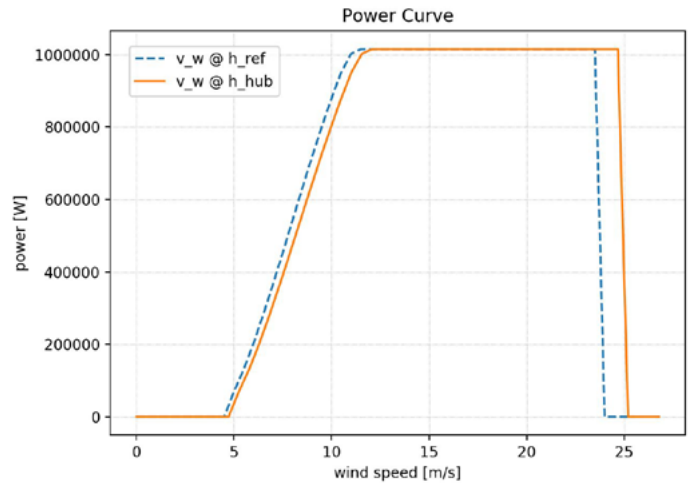
System Design: Power Curve and AEP

Power curves for LCOE estimates from FBL model for mature product

- Eventual power curves will come from sim and test

AEP from:

- wind distribution
 - normally use rayleigh distribution, but can be specified as anything
- availability from maintenance model
- typical collection grid, substation, and curtailment losses
- wake losses conservatively estimated to be ~1/2 that of HAWTs
 - kites interact with much larger volume of air



Data shown for mature product.

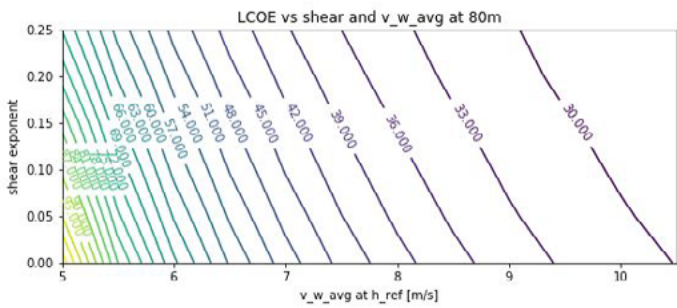


System Design: Environmental Factors

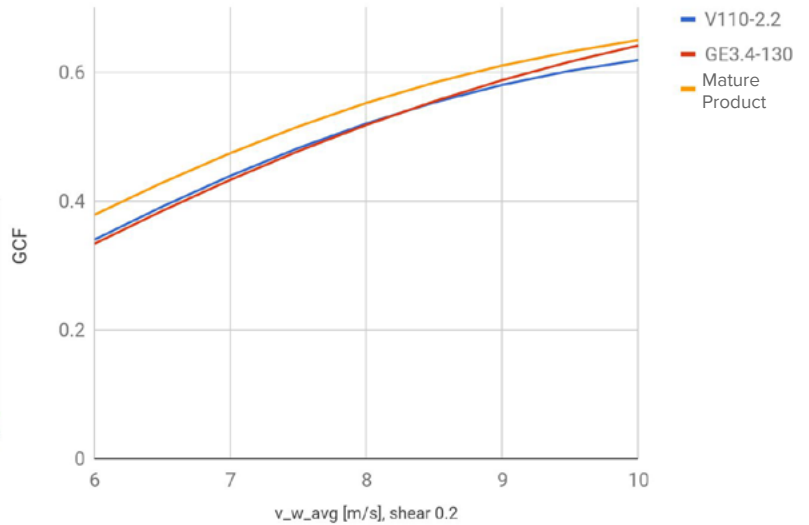
Kites are sensitive to shear

Mature product shown here optimized for high shear onshore site

- Gross Capacity Factor changes a lot with shear (GCP plot shows shear = 0.2)



Gross Capacity Factor vs Resource

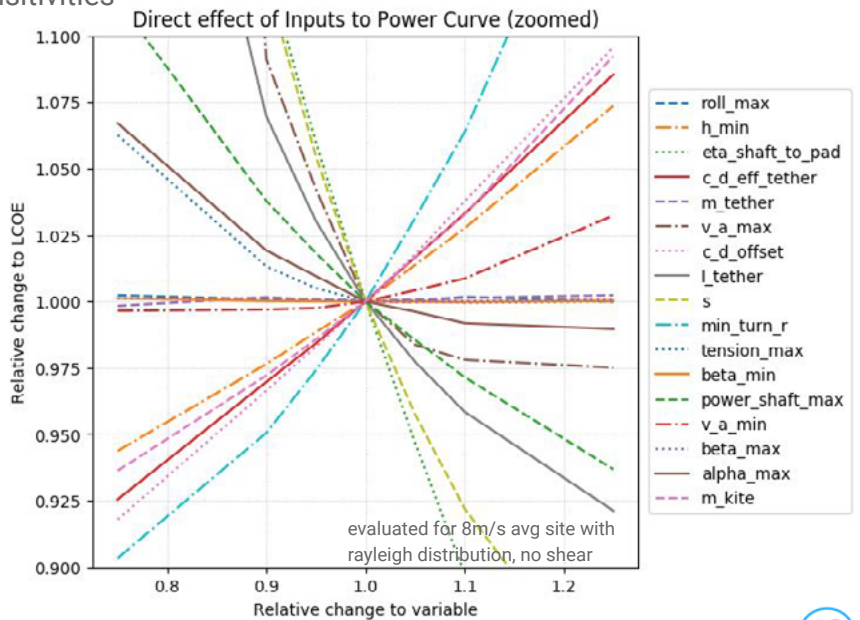
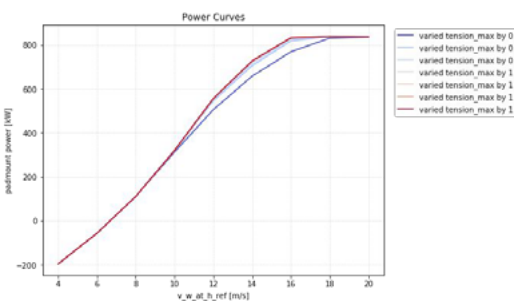
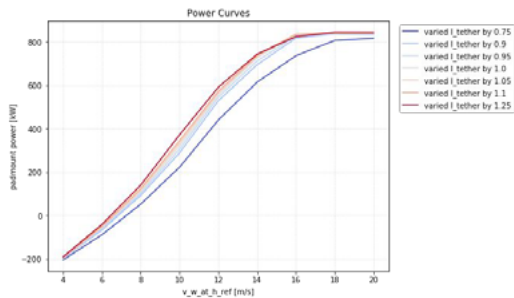


Data shown for mature product.



System Design: Sensitivities

FBL model used to explore power curve sensitivities



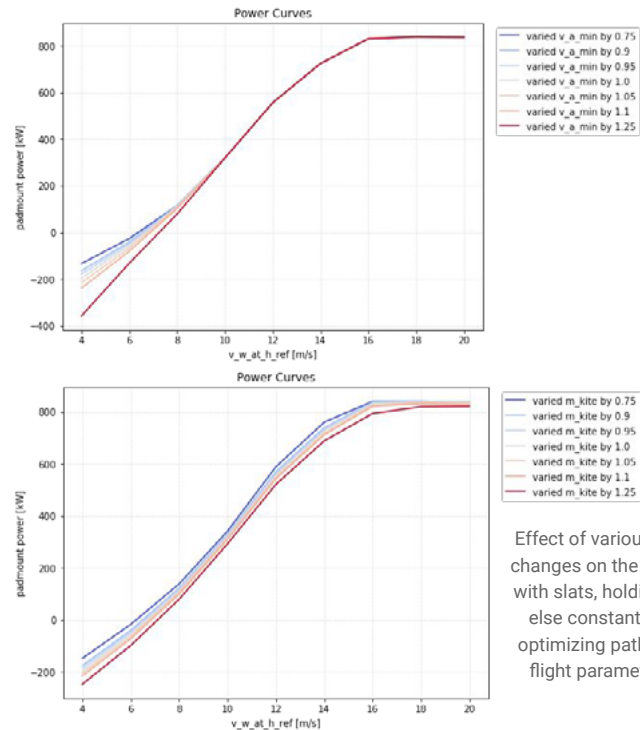
Effect of various kite changes on the M600 with slats, holding all else constant but optimizing path and flight parameters



System Design: Mass Sensitivity

Mass in crosswind has 3 major effects:

- Increased “loiter power”
 - Power needed to maintain flight
- Increased minimum airspeed
 - Moves you from the Loyd ideal at lower winds
- Increased gravity losses
 - Must balance round trip efficiency losses with non-ideal speed losses

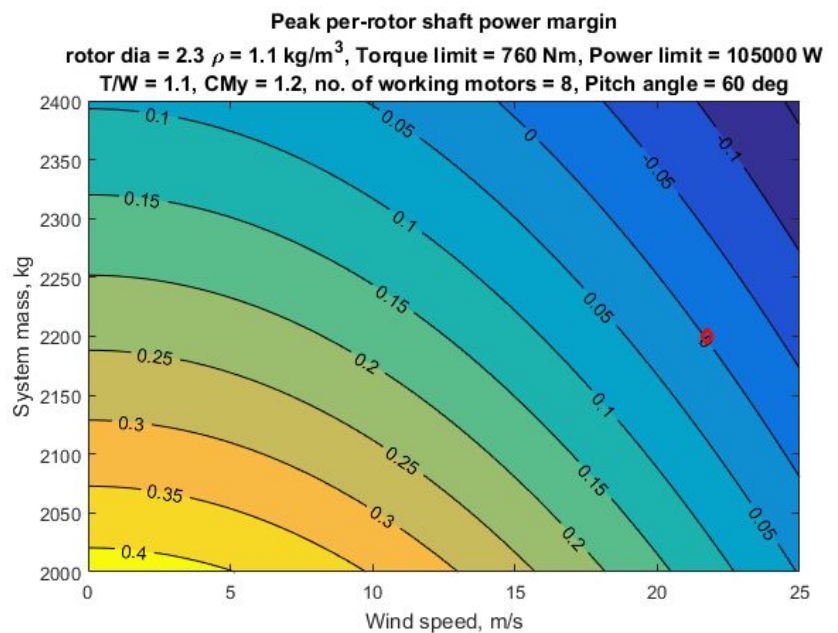


System Design: Mass Sensitivity

Mass in hover

- More weight = more thrust required
- High winds:
 - Increased tether tension due to drag, which has a downward component
 - Increased pitching moment, which reduces max thrust

Trades between hover mass, rotor size, efficiency, and motor torque and power limits included in system design and optimization tools



M600 hover margins. System mass includes full mass of tether.

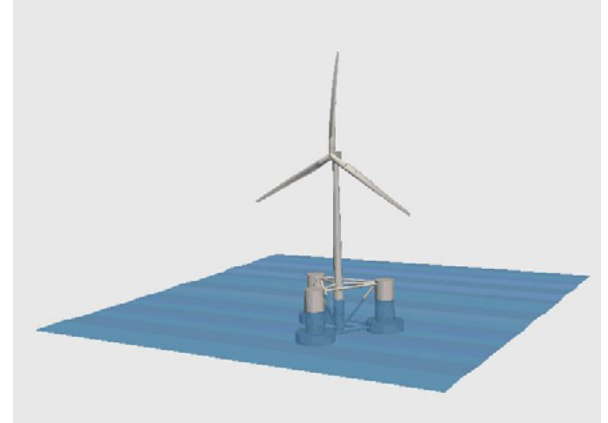
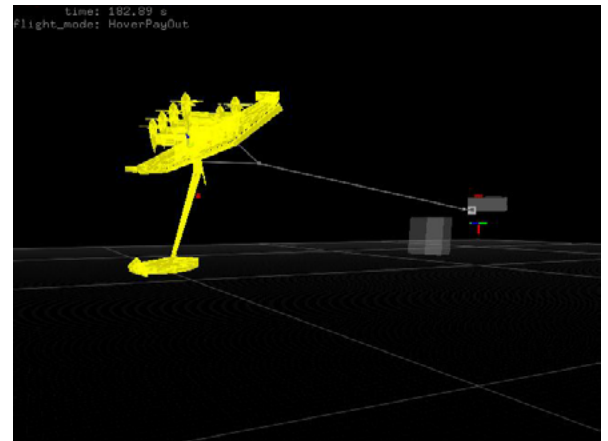
Sim Tools Overview

CSim

- In-house developed sim
- Flight controller and hardware in the loop capable
- Crosswind flight in turbulent wind environment
- Power generation prediction
- Sensor fault injection
- Batch and Monte Carlo simulations

KiteFAST

- Extension of NREL's coupled dynamics wind turbine model for use with kites
- Intended to supplement loads analysis and outside validation of sim
- Still a work in progress, but nearing completion



CSim Overview

Purpose

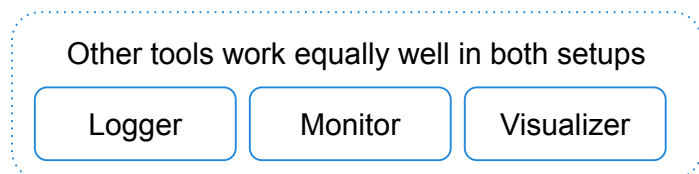
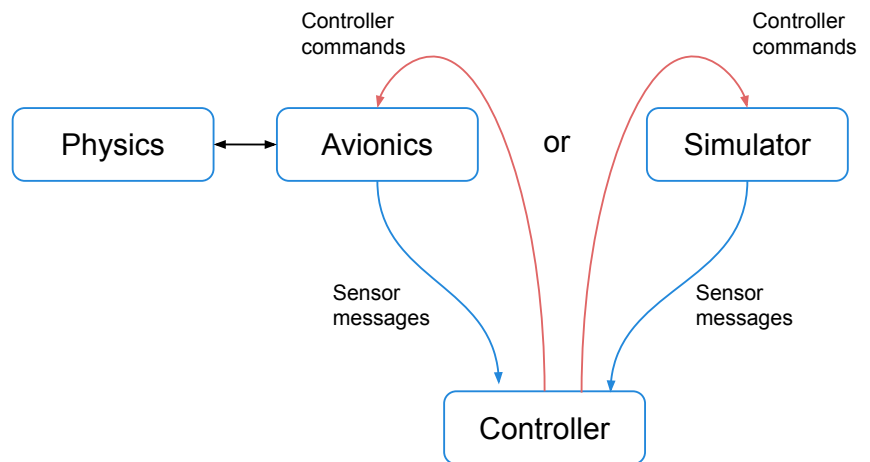
- Develop flight controller
- Estimate power performance
- Test new system configurations
- Provide tools for linearization
- Support HITL testing
- Pilot training

Goals

- Realistic physics
- Output indistinguishable from avionics during flight
- Support different levels of realism
- Plug-and-play modules

History

- Started as Simulink model
- Ported to C++ for speed, stability, and maintainability
- Validated through Plank, W4, W6, and W7 test programs



Sim Capabilities: Monte Carlo

Simulation and lots of cloud compute are powerful combo

- Heavy use of Monte Carlo analysis
- Extensive scoring functions for flight quality and limits
- Batch runs for fast and extensive A/B testing

Example:

- Sim showed problems on transout tether roll limits
 - Poor scoring on many sims
- Monte carlo A/B tests shows robustness of controls change to fix
 - ECR 306



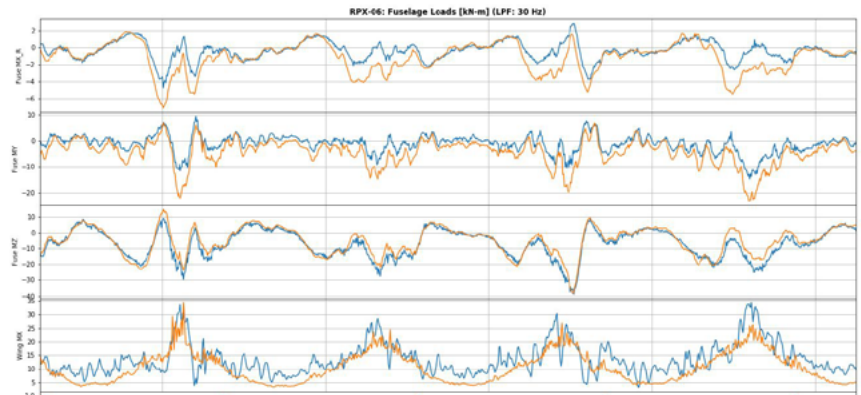
Small sample of batch sim results page - standard results are 1050 different cases



Sim Capabilities: Flight Quality Scoring

Extensive scoring functions enable quantifiable flight quality

- Cover wide range of areas
 - Crash
 - Exceeding load limits, airspeeds, etc
 - Quality
 - Power generated
 - Command following
 - Control saturations
 - Etc
- 87 in place now
 - many more in progress



Example of fuselage loads scoring function.

Flight test data from strain gages (blue) calibrated from proof test agree well with estimated loads (orange) derived from state information from estimator that is available during sim.



Sim Capabilities: Turbulence

Full simulation is only tool that can adequately capture effects of turbulence

Dryden gust model

- Current default gust model
- MIL-F-8785C

Turbsim model

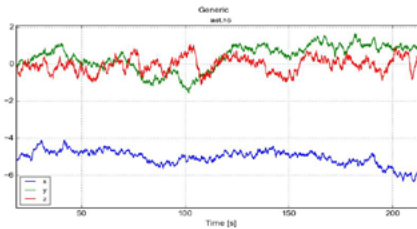
- Recommended by IEC-61400-1
- Implemented in sim
- Sweep through precomputed gust field at mean wind speed

Wind shear

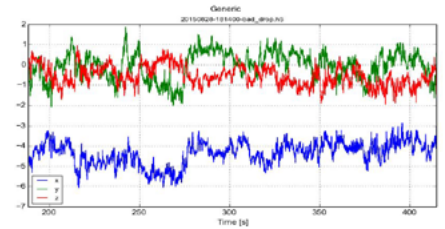
- Standard power law wind shear with adjustable exponent

$$v(h) = v_0 \left(\frac{h}{h_0} \right)^\alpha$$

Simulator



From test

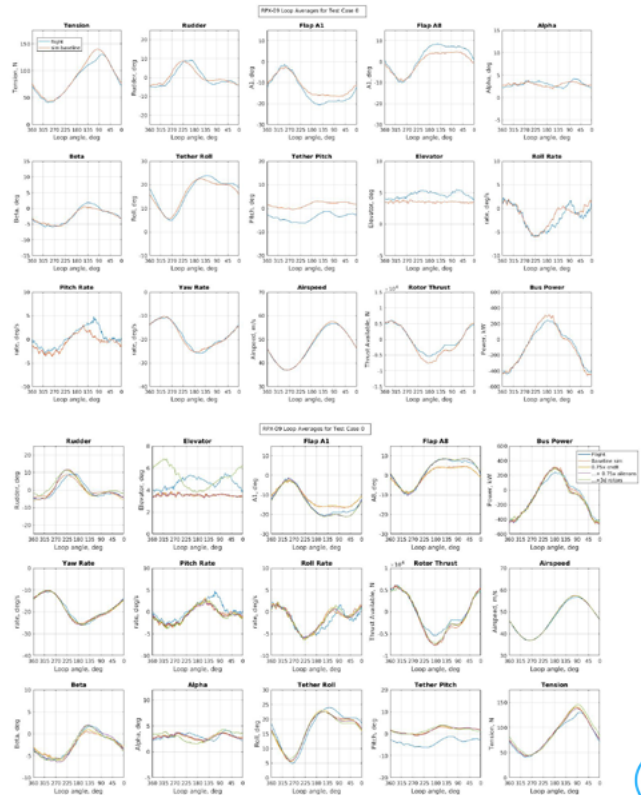
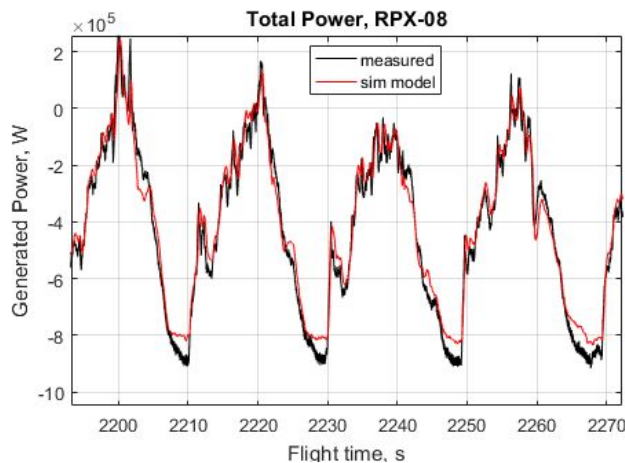


Controller is too much of a work in progress to give definitive answer on the impact of turbulence on kite power curves

Sim: Validating

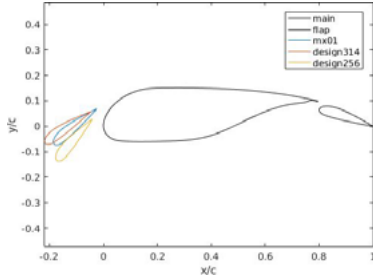
Each flight test provides validation opportunities

Much improved sim comparisons since first flight tests - still a work in progress

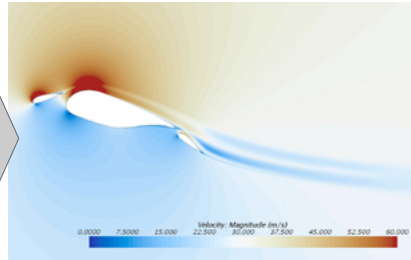


Sim: Aero Models

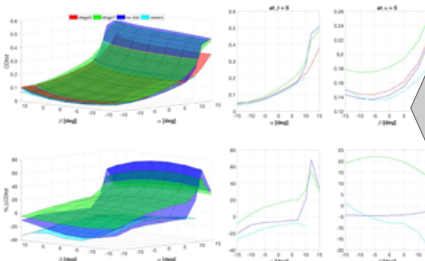
Begin with generated 2d geometries...



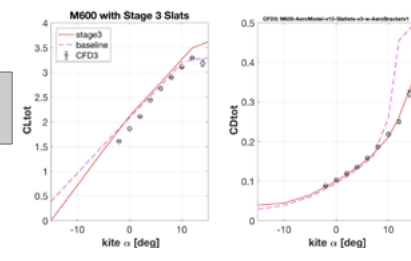
...evaluate with 2d CFD...



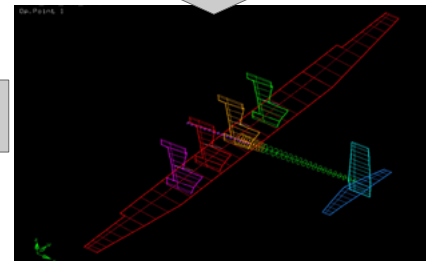
... check methodology with wind tunnel testing...



... and generate aero databases for sim.



... spot check with full 3D CFD models...



... feed 2d properties into ASWING model (vortex lattice model)...

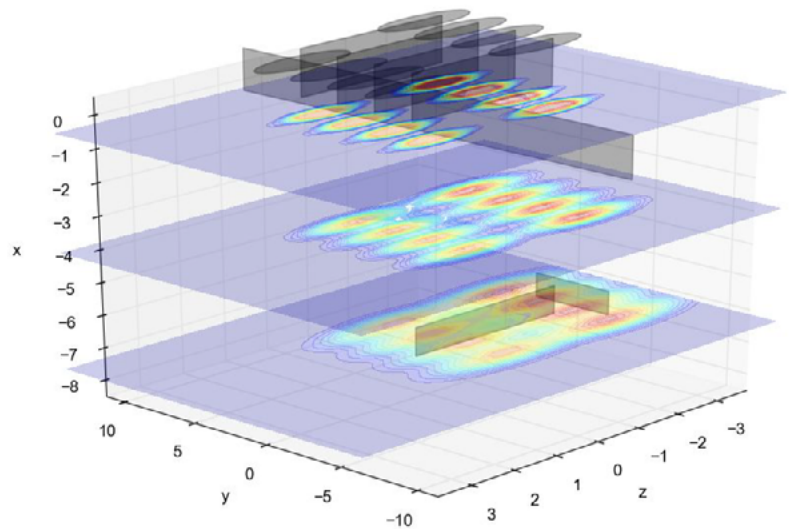


Sim: Aero Validation

Nearly every flight has resulted in improvements to our sim aero models

Examples:

- 3d rotor tables capturing edgewise flow
- Extension of rotor wake impingement effects to crosswind flight
 - Wake model already in place in hover models
- C_D offset to capture drag of small components not modeled in ASWING
 - Backed out from flight data
- Revision of high AoA model blend points (to capture stall effects)



Power Curve Verification

- Follow power curve testing procedures laid out in the IEC61400-12 standard as close as possible
 - Use an industry established lidar
 - Can measure up to 500 m
 - Data requirements and valid sectors can be done according to the standard
- Some exceptions to standard at Parker Ranch
 - No 200 m met tower to augment Lidar for complex terrain (likely 60-100m Met tower)
 - Can take measurements directly in front of kite operations for primary wind direction
 - Could eliminate the need for site calibration
 - Traditional distance between measurement and kite is 2.5 D
 - Not needed for Makani kites as kite is not an obstruction
 - Could also take wind measurements behind the kite



Offshore Balance of Plant



Offshore Balance of Plant (Pilot/Commercial)

Category	Scope of Supply	Dimensions
Foundation		
Primary structure (hull, internal stiffeners and bulkheads)	Materials, labor, paint (level II).	100 tons, 45-50m X 4.5-5m diameter
Secondary structure	External ladders/platforms, boat bumpers, mooring foundations; J-tubes	20 tons
Cathodic protection	aluminum cathodes, installed	1 ton
Mooring		
Anchor	Gravity anchor	5m cube with high density ballast
Mooring Lines	engineering of tendon and connector	300 ton MBL
Installation		
Assembly in harbor	crane mob and de-mob; in-harbor assembly	120 ton mobile crane
Offshore construction	engineering; fixtures/jigs; vessel mob/de-mob; tow-out, mooring hookup	Supply vessel with 50 ton crane
Electrical and Transmission		
Array cables and export cable	array cables, installed	
Offshore substation	foundation, electrical equipment, installation	



Steps to Prevent Corrosion

Prevention and Design

- Material swap to lower galvanic potential
- Add electric insulators between large galvanic pairings
- Passivation Anodize/Alodine/Chromate conversion
- Paint
- Dielectric protective barrier

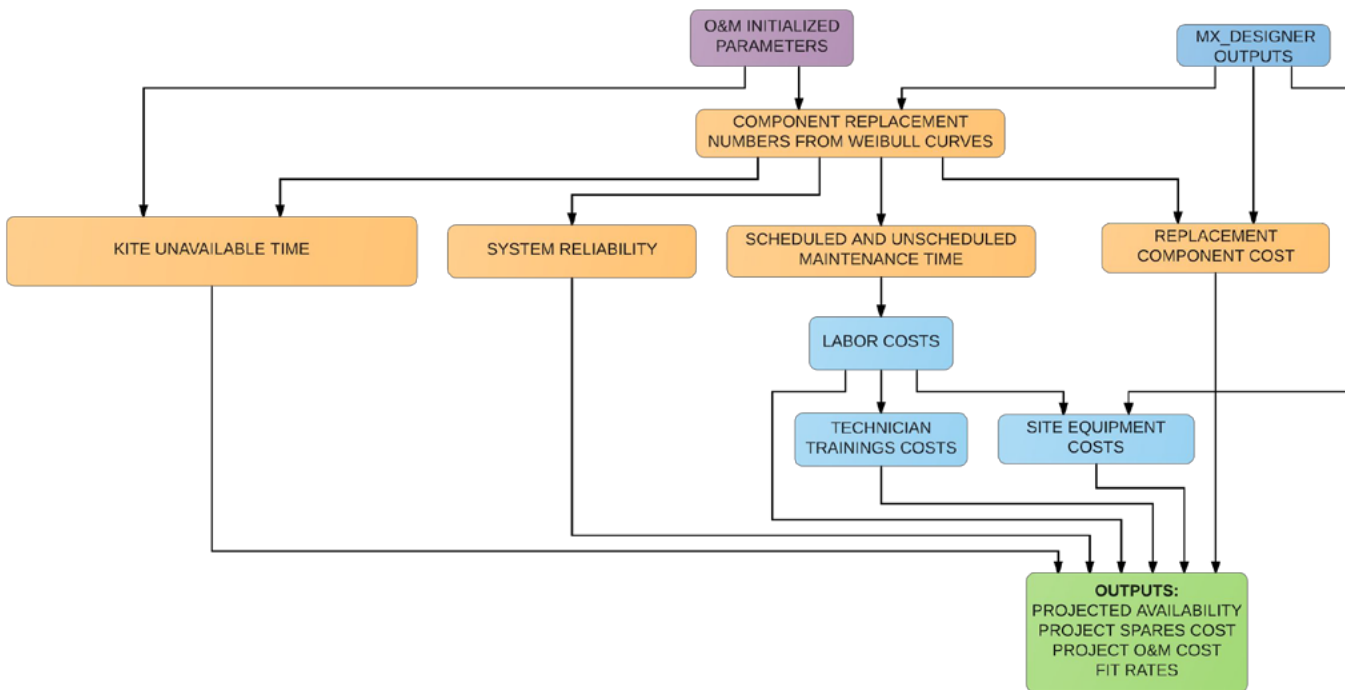
Operations

- Controlled environment (Tent w/AC, HEPA filters)
- Warm up/cool-down procedure
- Inspection
- Covers/cowlings
- Acid/rust inhibitor to locally passivate corrosion





O&M Model Structure



Onshore O&M Modeling Assumptions

A bottom-up model with numerous detailed assumptions

Component Specific Critical Assumptions:

- Infant mortality
- MTBF
- Weibull shape factor
- Time to replace
- Time to service
- Scheduled maintenance frequency

Example of O&M model output for 500 MW onshore project with 20 year life.

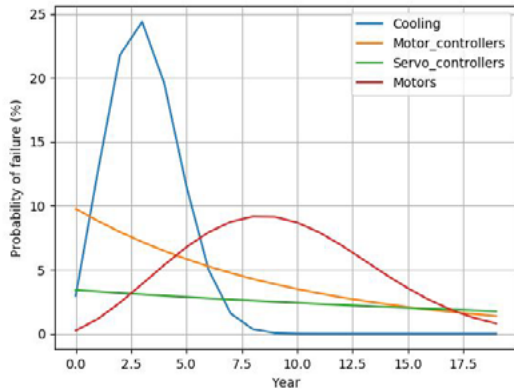
Project Level Assumptions	Value	Unit
Fault/troubleshooting time multiple of unscheduled time	100	%
Average kite wait time before a tech response	8	hr
Average travel time for a tech to get a kite	0.5	hr
Average time to get in a service position once at the kite	0.5	hr
General inspections each time accessing the kite	7.5	min
% effectiveness increase decrease in tech time year over year	1.0	%
Burden rate for handling spares	5	%
% of scheduled maintenance done below cut-in	20	%
# of carbon fiber repairs per kite per year	2.0	
Cost per kite per year of carbon fiber repairs	1500	\$
Average # of hr down for a carbon fiber repair	24	hr
% of time that techs are working but not fixing kites	15 -11	%



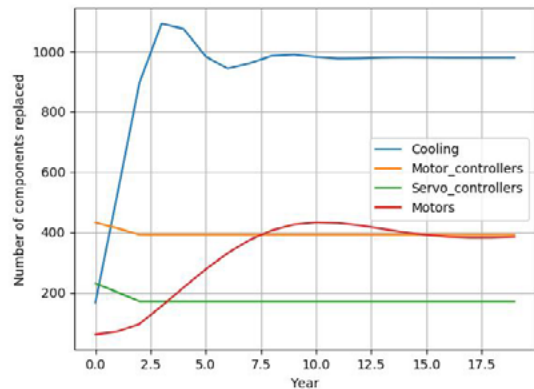
O&M Modeling Approach

Example of O&M model output for 500 MW onshore project with 20 year life.

Single Component Weibull Curves



Number of Components Replaced per year



Component	MTBF (hrs)	Shape	Scale (yrs)	# of components per kite	# of components per project
Motors	67500	2.5	11.6	8	3944
Motor controllers	67500	1	10.3	8	3944
Cooling	25000	2	1.7	8	3944
Servo Controllers	200000	1	28.8	10	4930



Top Sensitivities

Example of top sensitivities from O&M modeling of offshore project with 20 year life.

O&M:

- Motor controller replacements
- Motor replacements
- Rotor replacements and scheduled maintenance period
- Kite access times
- Fault multiplier
- Carbon fiber repairs
- Overhead assumptions (Admin staff/unproductive time - e.g., waiting for weather windows)

Reliability:

- Tether
- Bridle
- Kite MV wiring, Ground inverter, and GS MV path - if not redundant
- Other single point failures: Electrical Fires, Lightning



Top O&M Risks and Mitigations

Severity \times Likelihood = Criticality

Item At Risk (phrased constructively. Risk is "Inability or failure to ___")	Criticality	Mitigation
incorporate adequate lightning strike protection: power + tether	9.0	Develop lightning strike strategy and needed protection inclusion
reduce scheduled maintenance frequency to annually for offshore	6.0	Fly + Learn + revise design as needed. Rotor improvements.
develop tether system health monitoring	4.5	Run termination fatigue tests with electrical health monitoring
have carbon repairs no more frequently than estimated	4.0	Increase accuracy of modeling to include wind turbine bird/hail/debris estimates and run tests with structures
effectively estimate fault and troubleshooting time	4.0	Gather data from M600 and from industry partners
to have a rotor with the required reliability level with only quarterly inspections	4.0	Fatigue testing of representative structure. Impact investigations.
include ground inverter redundancy	4.0	Add in redundant inverters or a switching network
increase slip ring reliability to at least 50M cycles	3.0	Increased slip ring testing and development; Supplier development
add in MV wiring redundancy	3.0	Increased design effort and tolerance for increased cost and mass
prevent serial defects which could greatly increase OM costs	3.0	Add serial defects to model and follow existing standards to minimize the chance of serial defects



Reliability



DFMEA

- DFMEA's were completed in 2015 on all M600 subsystems
- Findings directed the test program for the M600
- Current risks are tracked on the Makani risk register and in numerous bug reports
- Iterating to our final product
 - No full design cycle before demo
 - Evaluate risks for each change using "Engineering Change Review" reports
 - On-going bugs include many software and hardware concerns that are being addressed
- RCCA analysis is utilized to address failures

DFMEA Focus Areas
Complete System - High Level Behavior
Avionics - Servos, Nodes, Buses, FCU
Airframe
Power Systems
Power Train System
Motor Controller
Fault Mitigation Module
Wing Wiring
Tether
Ground Station
Wing Wiring
Top Hat



M600 Reliability Testing

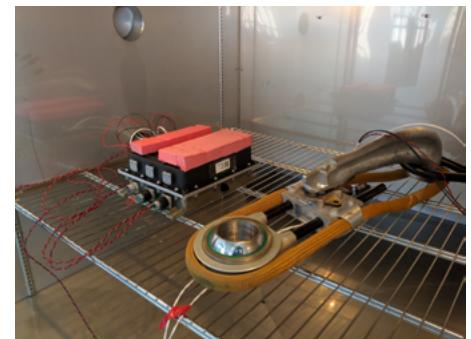
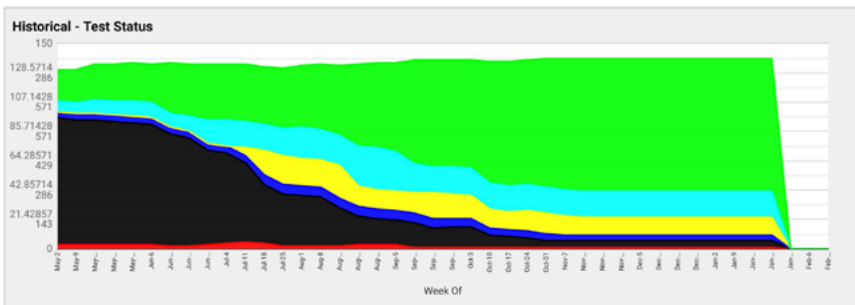
- Follow a standard procedures for determining test requirements
 - Determined system reliability requirement
 - Determined system reliability breakdown between sub systems
 - Broke reliability numbers to component level targets
 - Determined target test hours for each component to meet reliability targets for prototype testing
 - Completed required testing before first RPX flight finished up additional testing in the following month

Systems/Subsystem/component Units	Qty	Parent	Fault Allocation [% of parent]	Final Required Test Time [hrs]
M600	1		100.0%	16
Power System	1	M600	22.5%	73
EoP HV Junction Block	1	Power System	9.5%	768
Slip Ring (Meridian)	1	Power System	9.5%	768
Powertrain	8	Power System	66.7%	877
ALL Capacitor FRU/ Bulk Capacitor Bank (8)	1	Powertrain	14.3%	6140
ALL LV to 12 V Converter (8)	1	Powertrain	14.3%	6140
Motor (8)	1	Powertrain	14.3%	6140
Motor Controller (8)	1	Powertrain	42.9%	2047
Balance of Powertrain (cooling sys and hoses) (8)	1	Powertrain	14.3%	6140
LV Power System (Battery boxes)	1	Power System	14.3%	512
Avionics	1	M600	22.5%	73
Servo System	8	Avionics	28.6%	295
Servo Actuator	1	Servo System	50.0%	499
Servo Controller	1	Servo System	50.0%	499
FCU A	1	Avionics	14.3%	512
FCU B	1	Avionics	14.3%	512
EoP Filter	1	Avionics	14.3%	512
Release - ERM Electronics	1	Avionics	14.3%	68
Bridge Electronic Enclosure	2	Avionics	14.3%	1023
Tether System	1	M600	22.5%	10
Tether-only	1	Tether System	40.0%	24
Bridles	2	Tether System	40.0%	49
Conductors	1	Tether System	20.0%	365
Airframe	1	M600	22.5%	10
Empennage - Elevator	1	Airframe	11.1%	88
Empennage - Elevator Pedestal	1	Airframe	11.1%	88
Empennage - Rudder - Servo Frame	1	Airframe	11.1%	88
Empennage - Vertical Tail	1	Airframe	11.1%	88
Empennage - Vertical Tail- Fuselage Junction	1	Airframe	11.1%	88
Fuselage - Tub	1	Airframe	11.1%	88
Fuselage - Tube	1	Airframe	11.1%	88
Fuselage - Wingside Mount	1	Airframe	11.1%	88
Wing - Flap	2	Airframe	11.1%	175
Controls	1	M600	5.0%	329
Ground Structures	1	M600	5.0%	44
Remote Perch	1	Ground Structures	30.0%	146
Tower - top hat	1	Ground Structures	10.0%	439
GSG	1	Ground Structures	60.0%	73



Pre Flight-test Validations

- Tests were completed from 2016 to Jan 2017
- 139 different tests were run
- Tests included function, quality, ground, flight and reliability tests
- System, Subsystem, and component tests were completed



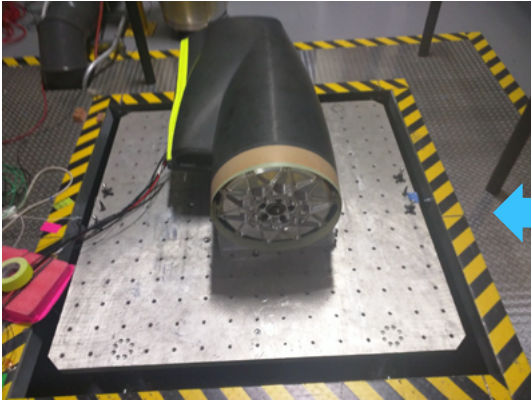
Component Level Testing

- To maximize value, requires proper design cycle: test, find bug, determine root cause, fix, rebuild, validate.
- Makani bugs identified through reliability testing: 60 (45 fixed / validated)

Complete
Partial Credit

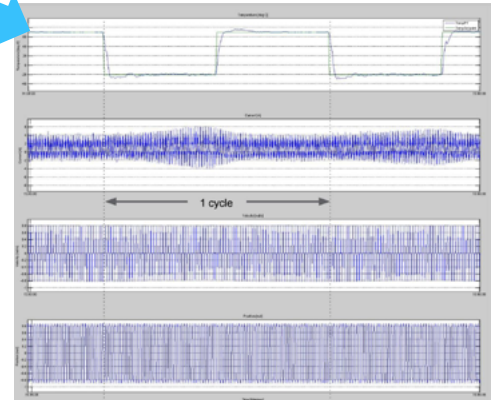
UNIT	EoP HV Junction Block	Slip Ring (Meridian)	Powertrain	Small Battery Box	Large Battery Box	Servo Actuator	Servo Controller	FCU A	FCU B	EoP Filter	Dridle Electronics Enclosure PORT	Dridle Electronics Enclosure PORT
Thermal Characterization												
GUT (PTCE + HTHOE)												
Random Vibration												

Powertrain Vibration Testing



Thermal Characterization = -20C to +70C Cycles
Grand Unified Test (GUT) = High Temperature and Humidity Operating Endurance (Zero Failures) + Powered Temperature Cycle Endurance (Zero Failures)
Random Vibration = Each Axis
 Low level Sine Sweep - .25g flat 15-2kHz
 Low Level Random 15-2kHz 2.4g
 Low Level Random 15-2kHz 5.2g
 Sine Sweep - .25g flat 15-2kHz

Servo Thermal Characterization



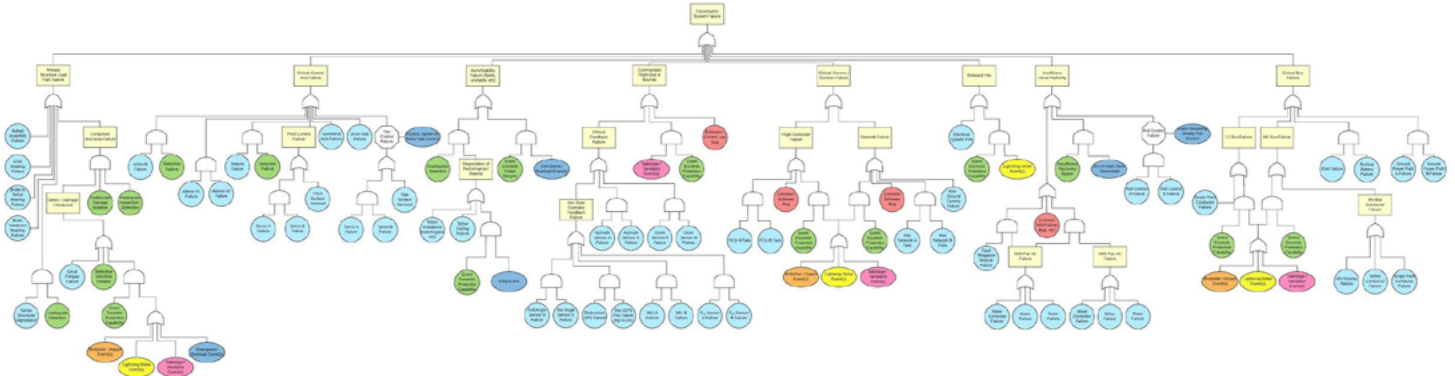
Pre Flight-test Validations

ID	Validation Name	Description & Pass Criteria	IPT	Result
V089	Dyno - Low Power HITL (No RPX Ground Power)	Dyno HITL with the stacked harness; Full power NOT required; RPX Ground Power NOT required.	Power Systems	Passed
V090	Dyno - High Power Endurance HITL (No RPX Ground Power)	Dyno HITL with the stacked harness; RPX Ground Power NOT required; Full power required. Parameters: - 10 hrs consecutive all-flight-modes HITL each with different representative simulator conditions. - Duration of at least 1 of those flights shall exceed the expected first flight time by a factor of 10 (or as permitted by the dyno hardware). - Generated power should exceed expected first flight power by a factor of > 1.3 (or as permitted by the dyno hardware).	Power Systems	Passed
V091	TransIn Power Stress Test	As part of V090, conduct at least 10 flights where: - TransIn duration should exceed expected trans-in times by a factor >1.0. - TransIn Power consumption should exceed expected by a factor >1.0.	Power Systems	Partial credit/ Not Required
V093	Dyno - Low Power HITL (with RPX Ground Power)	Dyno HITL with the stacked harness; RPX Ground Power required; Full power is NOT required.	Power Systems	Passed
V094	Dyno - High Power HITL (with RPX Ground Power)	Dyno HITL with the stacked harness; RPX Ground Power required; Full power required.	Power Systems	Passed



Fault Tree Analysis

[Qualitative fault tree](#) for failures that lead to a catastrophic system-level failure.

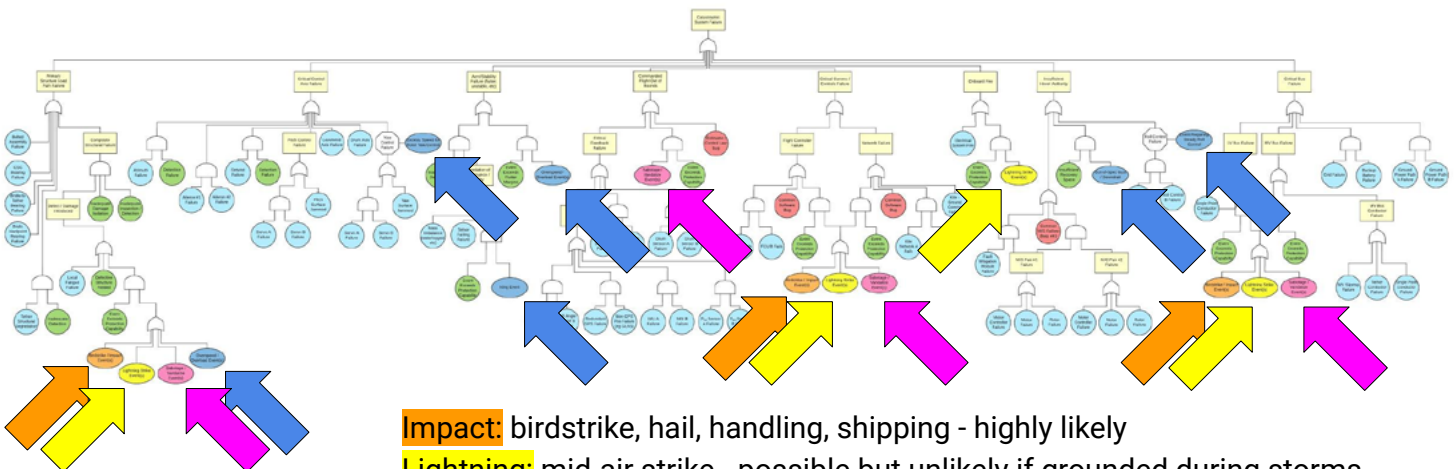


Purpose:

- Identify critical areas for redundancy and detection
- Highlight failure cases where detection or redundancy is impractical
- Illustrate common failure modes and (some) common mechanisms, eg. lightning
- Inform a probabilistic analysis



Fault Tree: Common Mechanisms



Impact: birdstrike, hail, handling, shipping - highly likely

Lightning: mid-air strike - possible but unlikely if grounded during storms

Vandalism: physical interference, hacking, jamming - likelihood unknown

Environment: icing, gusts, high winds - site dependent

All require protection / detection capabilities



Safety



Abnormal Operations



Fault handling

- There is no “failsafe” mode to easily enter in an uncertain event or fault condition
- Kite must successfully transition out and hover down to perch
- Drives for redundancy - but also good detection methods and health monitoring

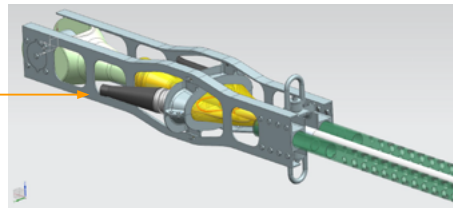
Challenges we face

- Not all single point failure modes can be eliminated (tether)
- Prediction of reliability critical components yet to be developed
- Common mechanisms can affect many subsystems at once

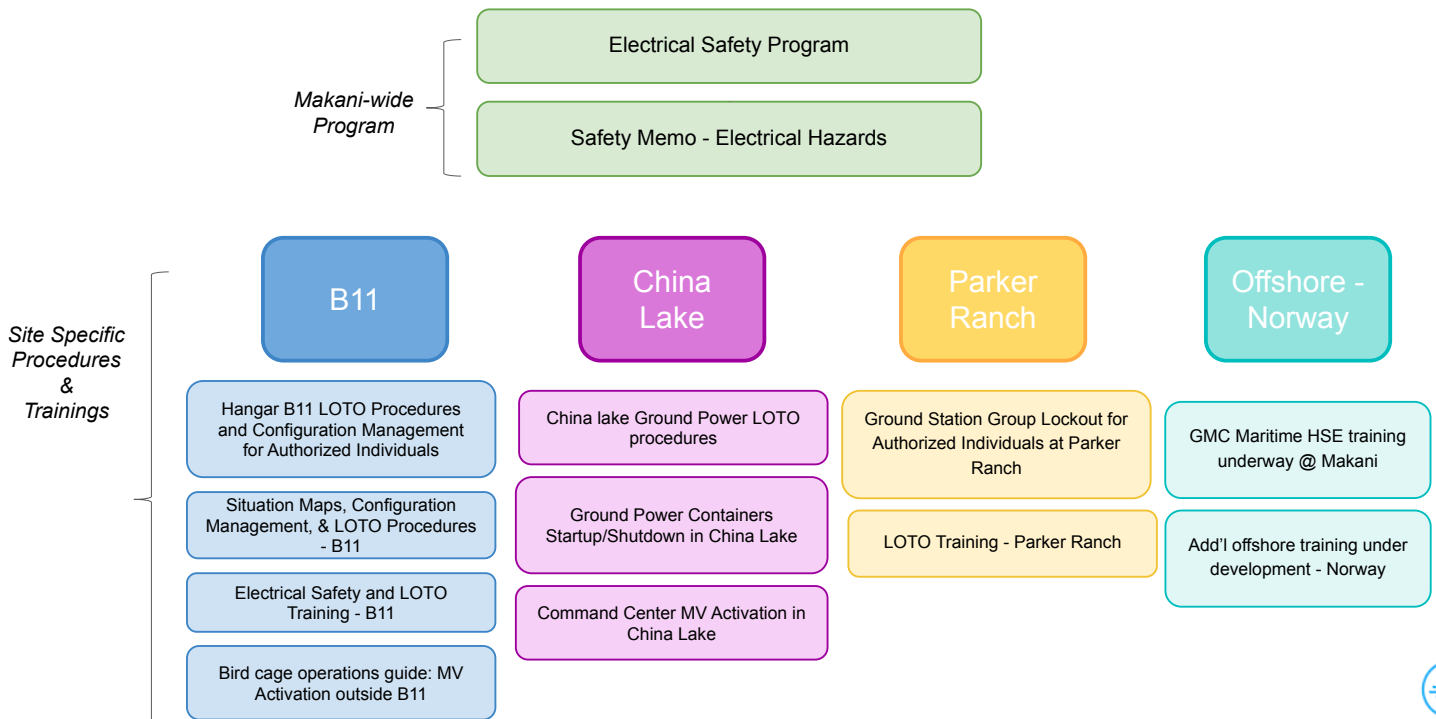


Tether Safety

- The tether is designed to be robust to expected operating conditions- tension, bending, handling, etc.
 - Early learnings pushed us to a more robust stranded core tether.
- Each tether is proof loaded using a remote controlled winch in a secure area before being put into service.
 - Additionally, Makani currently operates with a safety buffer around the kite to ensure no people are in the tether radius in case of break (this will continue for Offshore Demo and Pilot)
 - Offshore the 20 m minimum tether height will keep boats and other obstacles away from the tether
- Tether Failures (No near miss due to improper safeguards)
 - One tether broke during proof load due to manufacturing quality issues. UFIT prevented.
 - One solid core tether broke before RPX-01 due to bending.
 - Corrective actions
 - Use stranded core tether
 - Stiffer support for tether connection
 - Stiffer bending strain relief connector



Electrical Safety Programs & Procedures (example)



Hazard Analysis

- M600 Test Hazard Analysis completed
 - Risk mitigations put in place for each hazard
- Conclusion from THA
 - Category B risk assessment is assigned to this test program
 - Test activities present a slightly greater risk than normal operations, which is inherent to the test's scope
 - There will be no additional risk to personnel after all precautionary and mitigating actions are taken.
- Testing and safety procedures were approved by the US Navy for use on the China Lake test range
- Testing and safety procedures passed initial FAA approval at Parker Ranch (Hawaii) test site

Hazard	Residual Risk Category
1. Hull loss	B (III/C)
2. Tether snap-back	B (III/C)
3. Thrown blade	B (III/C)
4. Electric shock	A (I/D)

Residual Risk Category:

A - Equipment and procedures in place at test site pose no greater risk to personnel than normal operations.

B - slightly greater risk to equipment than normal operations; no additional risk to personnel



Risk Register Summary

Register tracks **major risk items**

Items included only if they need to be tracked in

- System budgets (mass, cost, reliability)
- Program budgets (yearly)
- Program timeline (yearly)

Primary items are **risks, not mitigations**

- risks are reduced through a series of mitigations
- mitigation strategies can change over time without re-defining the risk
- Mitigation approaches are tracked secondarily

Risks are categorized for clarity, but don't always cleanly fit into a single bin

Technical	Long term autonomy and fault handling Predictive tools
Techno-Economic	Low cost, high reliability components System protection Operations and maintenance Controls
Economic	Learning curves Cost modeling Supply chain
Market	Competitive dynamics Public perception Key stakeholders Certification Bankability
Regulatory	Aviation Environmental Interconnection Local communities
Execution	Team and partners Testing and safety Manufacturing Funding Strategy and narrative IP

Top Risks

Criticality of 6 and higher

Low costs at required reliability + performance

Certification and bankability of new tech

Compatibility with aviation

Sustaining expertise, vision, and backing

Category	Item At Risk (phrased constructively, Risk is "Inability or failure to ___")	Severity If unable to address risk	Likelihood risk will not be resolved	Criticality Severity x Likelihood
Technical	develop launch/land control for offshore system	3	2	6
	develop a low cost, light, durable faired tether	2	3	6
	develop low cost, lightweight durable rotors	3	2	6
Techno-Economic	Fatigue → find/develop fatigue resistant structures	3	2	6
	Lightning → incorporate adequate lightning strike protection: power + tether	3	3	9
	O&M → incorporate adequate lightning strike protection: avionics	3	2	6
	achieve lifetime at target rate	2	3	6
Economic	realize economically viable balance of plant costs	3	2	6
	develop and sustain market pull	3	2	6
Market	UFITs → operate below target threshold	3	2	6
	achieve acceptable IEC type certification status - system	3	2	6
	achieve acceptable IEC type certification status - tether	3	2	6
	achieve acceptable IEC type certification status - lightning protection	3	2	6
	achieve acceptable IEC type certification status - electrical	3	2	6
	achieve acceptable IEC type certification status - controls software	3	2	6
	achieve bankability qualifications (PPAs, proven technology (4000+ hrs))	3	2	6
Regulatory	Noise → develop acceptable sound profile for onshore permitting	3	3	9
	accurately predict and quantify wind resource	2	3	6
	develop acceptable lighting and marking framework	3	2	6
	achieve complementarity with local airport ops / VFR	3	2	6
Execution	acceptable off-tether scenarios	3	2	6
	achieve complementarity with US DOD airspace and ops	3	2	6
	Birds → develop acceptable non-US aviation regulation framework	3	2	6
	develop and sustain in house expertise and cohesive team	3	2	6
	develop and sustain partnership expertise	3	2	6
	execute in a manner that is consistently safe for all team members	3	2	6
	sustain X / ABC support for long term vision	2	3	6
	sustain rigorous, comprehensive plan to achieve moonshot	3	2	6
	sustain team alignment on vision and strategy	3	2	6

Top Risk Items Snapshot

Technical

- Accurate flight envelope / power curve modeling
- Launch / land control (offshore)

Techno-Economic

- Lightning strike protection (powertrain / tether)
- Hitting targeted O&M costs
- Low mass and high reliability/fatigue at low upfront cost

Economic

- Viable Balance of Plant costs
- Achieve expected cost reductions at scale on a range of items (composites, batteries, etc)

Market

- Acceptable onshore sound profile (rotor noise)
- Achieving a suite of certification and bankability statuses

Regulatory

- Compatibility with aviation
- Acceptable avian environmental profile

Execution

- Sustain + build expertise, alignment, plan, and safe execution



De-Risking Mechanisms

A variety of approaches for reducing risk are available:

- M600 flight testing
 - Controls, generation, interactions, sensing + state estimation, environment, noise, aeroelastics...
- Ground testing
 - Mat'l, components, and subsystems; performance, thermal, strength, fatigue, durability, reliability...
- Scale testing
 - Aerodynamics (wind tunnel), dynamics / controls, manufacturing...
- Design and Analysis
 - Robust, tolerant design approaches. Simulation, FEM, CFD. 3rd party expertise.
- Leveraging existing data, designs
 - Using off the shelf components with known quantities whenever possible (rarely, unfortunately)
- Working with relevant bodies, groups
 - Certification, regulatory, environmental, potential partners...

There are far more valid options to pursue than resources will permit. Robust prioritization - eg, through design reviews - is critical.



A Low-Cost Fiber Optic Avionics Network for Control of an Energy Kite

Kurt Hallamasek, Eric Chin, Paul Miller, Mike Mu, Michael Scarito, Eric Uhrhane

October 2017

Abstract

We describe low-cost and fault tolerant data communication on an energy kite with on-board flight control and power generation. The requirements on availability and safety of a modern wind turbine demand that the kite avionics system has failure rate and fault tolerance on par with equivalent systems on commercial aircraft. Yet, substantially lower cost targets for wind turbines do not allow the straight-forward adoption of solutions that have successfully addressed similar operational requirements in commercial and military aircraft. This paper describes the design and implementation of a low-cost avionics bus, used on a prototype energy kite, that retains safety critical traits of modern avionics buses.

The control system for flight and power generation is based on a modular and scalable architecture: motor controllers, control surface actuators and centralized computer modules each incorporate a microcontroller, purpose-designed for safety-critical applications. The microcontrollers, in addition to performing local control functions and issuing motor commands, collect sensor data over diverse short distance busses local to each node and collate this data into messages adhering to the avionics I/O protocol. These messages are routed between the over 20 nodes that are distributed on the energy kite, which has a wingspan of 25 meters, using dual-redundant Ethernet networks. Plastic Optical Fiber is used as the physical medium for low-cost, robust interconnections and immunity to electromagnetic interference (EMI). Zero-failover time, message routing with bounds on latency, and a rich set of diagnostic features are achieved, by leveraging features available in modern network switches. No new low-level hardware protocols were employed.



Fig. 1: The M600 energy kite has 8 turbines and a 25 m wingspan.

I. Background

The M600 energy kite is a prototype airborne wind turbine. The M600 energy kite converts wind energy to electricity with turbines on the kite, which it then transmits to the ground via conductors in the tether. The energy kite has two primary flight modes: hover and crosswind. In the hover mode, the kite hovers, much like a quadcopter, from its perch on the ground, downwind and to a high altitude, where higher wind speeds prevail. In this mode, the turbines on the kite function as motors to drive the rotors to provide the thrust to lift the kite while keeping the tether in tension. Once the tether is fully extended at altitude, the kite transitions into the crosswind mode. In crosswind mode, the kite is powered by the wind itself. The kite flies in a direction close to perpendicular to the wind, the kite speed increases to a multiple of the wind speed. The air pushing through the rotors powers the turbines which send electricity down the tether. To return to the perch, the kite transitions once again to hover mode, allowing the ground station to reel the tether back in. A good simplified analysis of crosswind power generation can be found in the seminal Loyd paper [1].

To control the kite in the primary flight modes and the transitions in between, the M600 energy kite is equipped with eight turbine/motors, eight actuated control surfaces, a suite of sensors, flight computers and communication electronics. There is enough functional redundancy that the kite remains controllable should one any one of these subsystems fail. All of the intelligence to regulate flight and power generation resides on the kite. The airborne operations are carried out autonomously, but human operators can intervene to take over control.

The block diagram below shows schematically the arrangement of the electronics on the kite. Triple-redundant flight computers (FC A, FC B, FC C) are installed in two separate enclosures in the

center of the kite. The flight computers include inertial measurement units, GPS receivers, magnetometers, pressure sensors for air data sensors and altimeters. The two independent networks linking all nodes route messages through to core switches (CS A, CS B). Elevators and Rudders have redundant actuators (E1, E2, R1, R2).

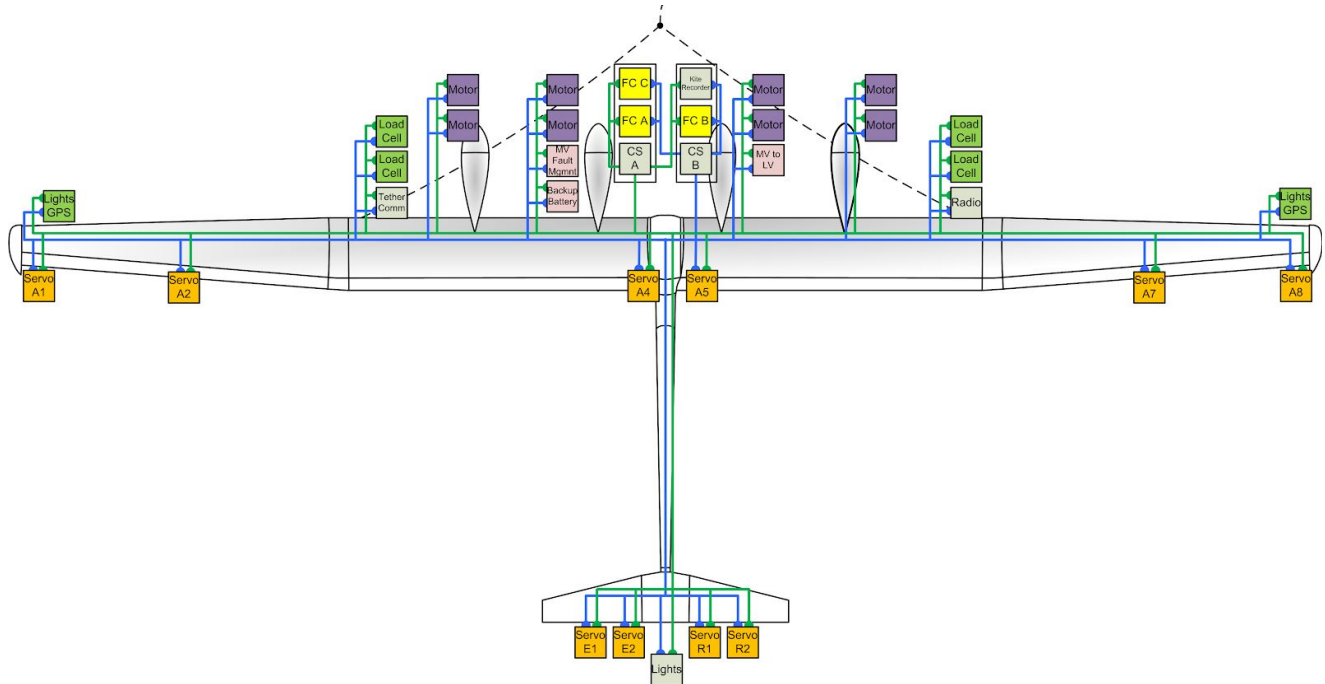


Fig. 2: The M600 kite network consists of two independent Ethernet networks, routed by two core switches (CS A, CS B). The networks link triple-redundant flight computers (FC A, FC B, FC C), motor controllers, control surface servo controllers, telemetry links, power converters, sensors and anti-collision lights on the kite.

II. High-level Requirements for the Kite Avionics Network

The application software on the kite autonomously regulates flight and power generation. The avionics network provides the means to exchange data between the flight computers executing the software and the “Line Replaceable Units” (LRUs) distributed on the kite. These LRUs house sensors, radios for communication, controllers for actuators and turbines.

The real-time feedback control of the system requires reliable low-latency communication between these subsystems: the control law for the turbine motors updates at a one kHz rate while the control loops for the kite run at 100 Hz. The technical requirements for the network on the energy kite—in terms of operational environment, real-time performance, scalability, safety, availability, maintainability—are similar to requirements on civilian or military aircraft. There, traditional

Avionics data busses have been successfully replaced in the last couple of decades with switched IEEE 802.3 Ethernet networks, specially adapted to aircraft requirements. [2], [3], [4]. The primary motivation is improved capabilities and lower implementation costs, resulting from leveraging both commercial-off-the-shelf (COTS) hardware and software.

To make Ethernet suitable for safety-critical real-time control systems, the “plug-and-play” features that make Ethernet attractive in home and office environments have to be curtailed. Deterministic performance is important for reliability and fault detection. Hence the network topology has to be fixed and closed; data flow has to be predictable and profiled. In an office environment, we can accept the occasional second-long gap in data transmission, due a momentary traffic increase, or due an automatic network reconfiguration. It is a price we are willing to pay for a network that virtually configures itself when we attach yet another device. However, a second-long dropout in a feedback control system could have dire consequences. To achieve the reliability targets in aircraft, Ethernet adaptations are implemented with dual-redundant networks, in which failures are quickly detected and no data is delayed or lost due to the failure of one of the networks.

On both the Airbus A380 and the Boeing 787 Dreamliner, specific Ethernet implementations known as “Avionics Full Duplex Switched Ethernet (AFDX)” have been successfully deployed [5]. AFDX has dual redundant networks and provides bounds on latency for real-time performance. The physical-layer hardware of AFDX – i.e. the transceivers for transmitting data on and recovering data from the physical copper or fiber connections – remain compliant with IEEE 802.3 specifications. However, AFDX modifies the Media Access (MAC) layer to manage redundancy and shape traffic flow, resulting in AFDX frames that look similar to Ethernet frames, but with some fields containing different parameters. This approach was probably taken to facilitate migration of avionics systems using the ARINC 429 bus to the new AFDX bus. As a result, the integrated circuits developed for the ubiquitous networking hardware found in offices and homes cannot be used to implement the data-link layer functions of the AFDX protocol. Typically, FPGAs are used to process the frames and manage the redundancy for AFDX. IP cores can be licensed for these tasks (e.g.[6]). In order to speed up development time and to eliminate the cost of FPGAs in each node, we instead rely on features natively supported by IEEE 803.2 compliant integrated circuit switches developed for SOHO applications. We use VLANs, static multicast routing and port throttling to route messages with predictable bounds on latency, without the requirement for custom hardware processing Ethernet frames.

How do the reliability requirements in aviation and energy kites compare? The NTSB gathers data on aviation accidents in the US. For 2015, accidents with fatalities in civil aviation occur at a rate of $\sim 10^{-6}$ per flight hour [7]. For economic reasons, energy kites target a rate of $\sim 10^{-7}$ loss of vehicle events per operating hour, or better. The failure rate of avionics systems, like a flight computer or a network switch, is typically in the range of 10^{-5} to 10^{-6} failures/hour [8]. Redundancy is therefore required to achieve the required level of reliability.

III. The Kite Avionics Network

A high-level goal of the kite electronics hardware design was to keep cost, size, weight and power consumption low. This resulted in choosing 100 Mbps Ethernet over Gigabit Ethernet, using microprocessors with ARM cores rather than x86 processors and FPGAs for link layer protocols. Most microprocessors only have one network interface. To avoid high speed interfaces like PCI or PCI Express that are used to expand network connectivity, it was important to devise a network that allows a microprocessor to connect to redundant networks with a single network interface.

A. Network Architecture and Topology

The kite avionics network, dubbed AIO network for Avionics I/O, consists of dual-redundant networks (an “A” network and a “B” network) operating in parallel. A representative network fragment is shown below. Every end system on the kite includes a TMS570 microcontroller, certified for safety-critical applications. This microcontroller accesses both networks through its single Ethernet Media Access Controller (EMAC) via the Access Switch. For the M600 kite network, this Access Switch is a five-port switch, the BCM53101M, with integrated PHYs that support 10/100Base-TX and 100Base-FX signalling, and a reduced media-independent interface (RMII) used as interface to the microcontroller. In our convention, the A-network connections are made to even-numbered ports, B-network connections are made to odd numbered ports.

Network switches are designed to quickly replicate Ethernet frames. They are thus capable of generating potentially network congesting amounts of traffic. For example, by default, switches flood frames with unknown destination addresses to all ports, other than to the port that received the frame from the sender. To avoid packet storms, it is important not to have loops in the network topology. However, a dual-redundant path that originates and terminates in a single node necessarily creates a loop. Therefore, a primary function of the Access Switch is to prohibit traffic between ports that connect to the A networks and ports that connect to the B networks. To this end, network facing ports are isolated from each other using port-based VLANs (Virtual Local Area Networks). VLANs were originally developed to allow small businesses to share networking hardware between different departments, while still providing separate networks for each department. A single switch can provide isolated local area networks for Payroll, Accounting and Engineering, while still allowing all departments to share a network printer.

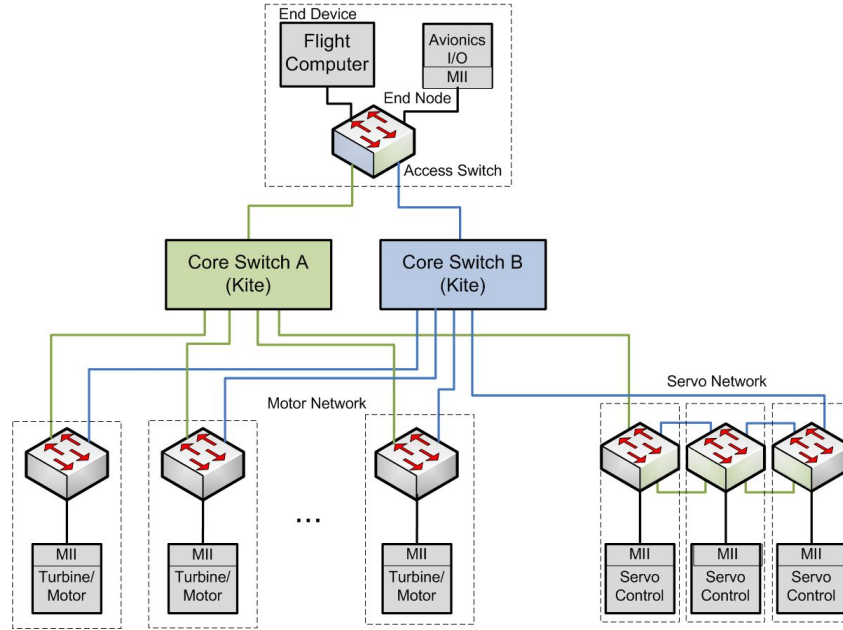


Fig. 3: An AIO network fragment with star and chain nets

The kite network supports daisy chain topologies, in addition to star topologies. The turbine motors which exchange data at a 1 kHz rate connect directly to the core switch for low-latency connections. The networks for the control surface servos are daisy-chained to reduce cabling and core switch port count.

The scheme can be extended to higher-order redundancy. There is also no strict requirement for the A and B networks to be identical.

B. Network Protocol and Redundancy Management

The principal network interconnect hardware is transparent multiport bridges [9], i.e. network switches that implement layer-two functions in the OSI framework. The switches route data frames based on MAC addresses. In this application, MAC addresses are locally administered to associate each individual node on the kite with a specific MAC address and a corresponding IP address. All network links are switched full-duplex links, thus avoiding collisions and eliminating the need of the collision avoiding protocol (CSMA/CD) developed for the original Ethernet.

We have developed a layer 5 protocol, called AIO protocol, in-house for exchanging flight critical messages. AIO uses the User Datagram Protocol (UDP), the simplest and fastest transport protocol in the TCP/IP protocol suite (layer 4 in the OSI framework), with multicast, as interface to the network stack. Unlike the commonly used TCP protocol, UDP does not check for successful delivery of packets to retransmit packets in case their receipt is not acknowledged; in UDP packets are simply pushed onto the IP layer (layer 3, the network layer) and sent. The UDP header simply provides for transport layer addressing and data integrity checks, it does not manage a connection. Rather than relying on TCP on the kite network, the AIO message protocol manages data

availability, in a manner suitable for real-time control: here it is more important to receive data with low-latency, rather than to guarantee that each packet is delivered. In a control system, there is no point in receiving a re-transmitted packet three seconds after it was first sent. UDP avoids the buffering, the cost of extra protocol states and extra traffic for acknowledgements and retransmission. The AIO protocol is implemented as a thin application in user space that provides the interface between the kite software applications and the conventional network stack (only using the UDP protocol).

UDP allows for multicast addressing, where datagrams can be sent from one sender to multiple destinations. In the AIO protocol, each message type is associated with a multicast address. Multicast makes for very efficient network utilization on the kite: for example, when motor controllers share state information with the other seven motors at a kilohertz rate, each motor controller sends a status message to a multicast group which has all motor controllers as members. The Access Switch on the originating motor controller duplicates the message and forwards it to each of the Core Switches. In the Core Switches, messages are replicated and forwarded based on statically programmed multicast routes to all the ports associated with the members of the multicast group (except for the ingress port). Network bandwidth is used efficiently, as messages are only routed to the destination ports. Each sender only sends the message once. Each message is received in duplicate at each of the destination nodes.

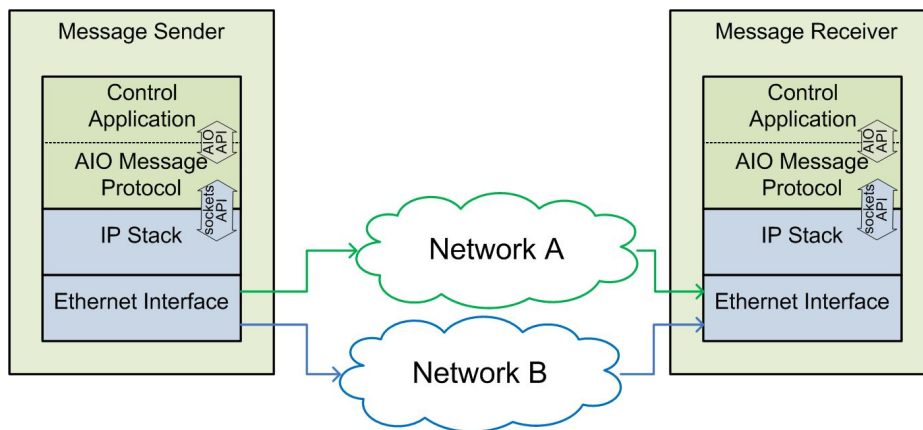


Fig. 4: The AIO protocol stack

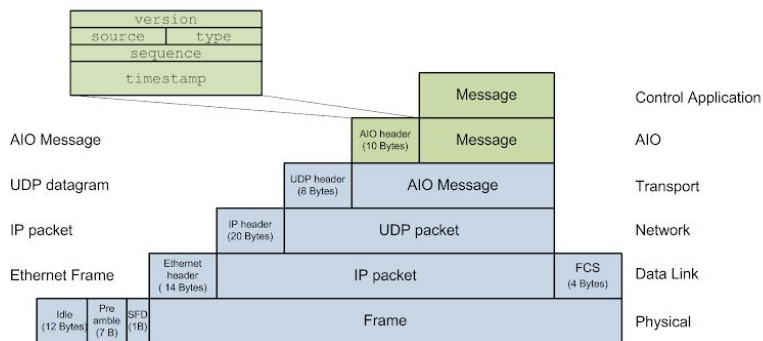


Fig. 5: AIO message frames and packets

Message deduplication at the destination node is handled in the Avionics I/O (AIO) protocol layer. This lightweight application layer on top of the transport layer uses a 10-byte AIO Message header for deduplication and consistency checks. This layer also provides services for diagnostic monitoring.

The message sequence number in the header is used to maintain a Current Value Table (CVT) at each node. This CVT is the interface for Control Application for data received via the kite network. For each message type, the CVT points to the most recent message received from each sender. An acceptance window for the 16-bit sequence number defines how many sequence numbers ahead of the entry to consider more recent (5K). An expiration time defines the maximum amount of time to consider the current message within the CVT as current (0.5 sec). When an entry becomes stale, all messages are accepted. Note that there is no requirement for a global clock to manage messaging on the network.

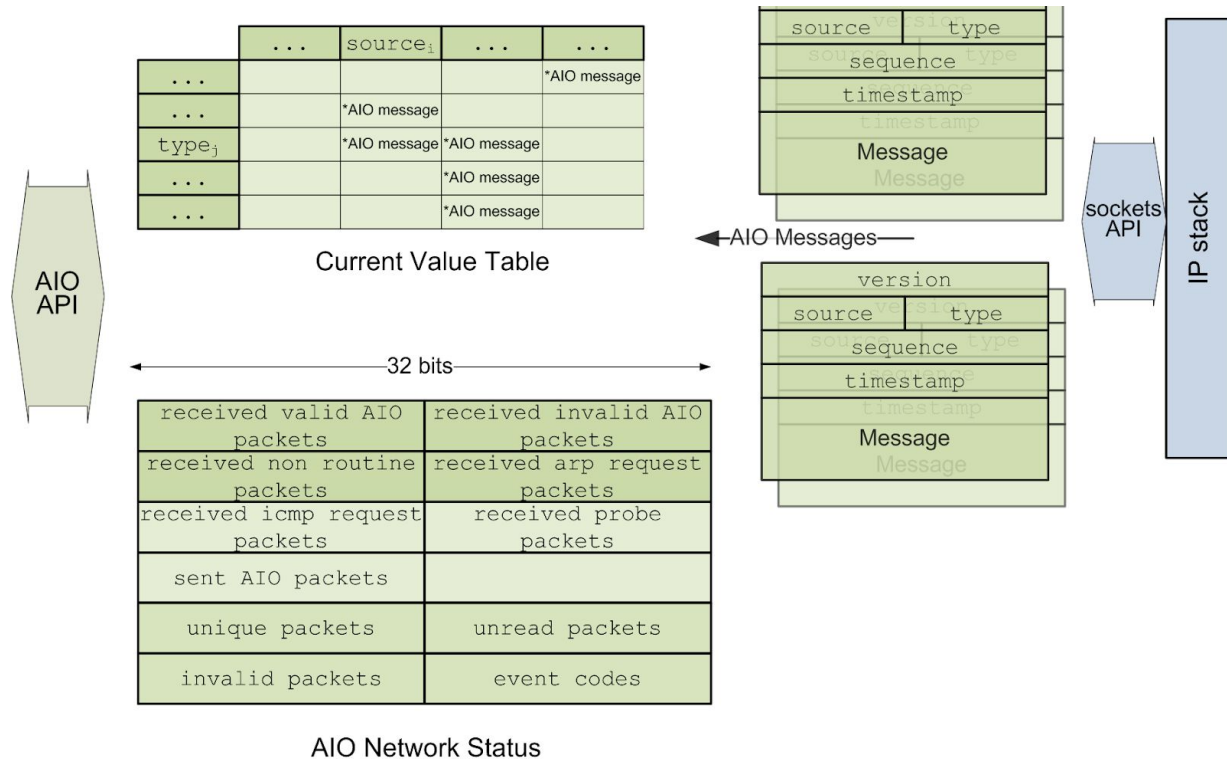


Fig. 6: The Current Value Table is the interface the kite application software uses to access data received on the network.

C. Data integrity

What are the odds that the content of the AIO message received differs from the content of the message sent? The previous section outlined how the kite network AIO protocol is layered on top of the UDP protocol which is implemented with a conventional IP stack (Fig. 4). We rely heavily on

the error detection features built into this stack where each layer has its own provision to detect corrupted data. Corruptions, detected on any layer, simply result in discarding the frame or packet. Even though error recovery is possible, in principle, from the CRC in the Ethernet frame, correcting errors is neither practical nor necessary in a real-time control system. Similarly, it is not appropriate to initiate retransmission of corrupt packets (like TCP does) for a network used for real-time feedback control. The types and rates of faults are, however, logged for diagnostic monitoring and maintenance. A brief review of the error checking mechanisms in the protocol stack follows in the next paragraphs.

On the Physical Layer, the interpacket gap (IPG), the preamble and the start-of-frame delimiter SFD are used to synchronize the bit clock, and determine byte and frame alignment to recover the Ethernet packet on the media. Only frames adhering to specified timing are detected and decoded. Runt frames are discarded before passing the Ethernet Frame to the Link Layer.

In the Link Layer, the Frame Check Sequence (FCS) at the end of the frame is a 32 bit cyclic redundancy check (CRC). This is the most powerful error check in the protocol stack and it is handled in hardware by the network switch. The FCS detects any 1 bit error, any two adjacent 1 bit errors, any odd number of 1 bit errors, and any burst of errors with a length of 32 or less. Per the functional requirements document of the IEEE Project 802 [10], the undetected byte errors are allowed to occur at a rate of 5×10^{-14} per byte of data. The cumulative kite network traffic is about 4×10^6 bytes/sec, allowing an error rate of 2×10^{-7} per second, corresponding to one byte error for every two month of continuous operation. In addition to CRC checks, the network switch will discard packets that don't adhere to the standard format. Even when erroneous frames pass the CRC and format checks, they will still have to pass IP parity checks and AIO version checks before they penetrate to the kite application software.

In the network layer (we use IPv4), a 16-bit one's complement checksum protects the header information of the IP packet, but not the payload data itself. The header includes, amongst other administrative fields, source and destination addresses and the packet length. Misrouted or mangled IP packets can then be discarded based on IP checksum errors. The checksum will catch any burst error of 16 bits or less. For uniformly distributed errors, the undetected error rate is $1/2^{16}$ or 1×10^{-5} . In the UDP layer, checksum calculation is optional in IPv4. If enabled, a 16-bit one's complement checksum is computed on the payload data, source and destination address.

In the AIO layer, the version number must be correct and the message type must be recognized for the message to be entered into the CVT.

IV. Bandwidth Control and Babbling Idiot Containment

By design, nodes on the network transmit messages at a constant rate. This can be expected in a real-time feedback control system: sensors are read and control actions are computed at fixed rates. On the kite, turbine motor controllers operate at 1000 Hz, control surfaces commands are updated at a 100 Hz rate. When the kite is operational, there are no event-driven messages on the kite network. The data rate of any link can then be readily computed. This is not only useful for profiling network usage, it can also be used for real-time diagnostics. Network switches aggregate

statistics on nominal traffic (and error events) for each port, so it is easy to detect deviations from the nominal rates.

Managed network switches provide port-level ingress control to guard against packet storms and to allow traffic shaping. This port throttling mechanism is used on the kite network to guard against babbling idiot failures. (A babbling idiot is a fault condition in which a node transmits more data than it should, most likely due to a hardware failure.)

A. Network Configuration

The kite network is automatically configured by the software by means of a configuration file. This human-readable (.yaml) file defines the network topology, i.e. all the connections for the nodes that exist on the network. It also defines the message type senders, the rates at which messages are sent, and recipients. This configuration is used to determine message routes at each access switch or core switch, where message routes are statically programmed at startup. The configuration file also allocates bandwidth. Our switches can be automatically configured to block unknown traffic and to handle non-operational (debugging or provisioning) traffic at a lower priority.

As the network topology is described in the configuration file, a mechanism exists to automatically monitor the network to validate the layout. Again we can use a VLAN mechanism: a VLAN domain is established for each physical link. VLAN tagged probe packets are periodically sent between adjacent nodes to determine that each node is connected to the correct neighbors. This can help detect a miswiring or a faulty connection even when the network redundancy might mask its effects.

Special network scenarios, such as the wing to ground links, are described and automatically configured. In the case of the redundant wing to ground links, we can replicate high priority traffic and limit lower priority debugging traffic to the high bandwidth links, allowing us to simultaneously preserve redundancy while remaining flexible to both low and high bandwidth connections.

B. Network Security

The best practices to secure a local area network also apply to the AIO network. We take basic initiatives, such as using FIPS compliant encryption on our wireless links, as those are potentially susceptible to RF injection. The POF used on our internal harnesses is highly resistant to any form of traffic injection. To limit the potential for a denial of service attack on our wing to ground links we plan to use ethernet-over-coax or glass fiber rather than wireless as a primary link medium.

Our core and access switches provide opportunities for defense in depth on the network. Switches can be configured to drop all non-operational traffic at every hop, meaning that at any potential point of attack undesired traffic will be filtered immediately. The core switches can additionally validate traffic, blocking all non-conforming traffic with invalid AIO versions, invalid sizes, or any unexpected traffic type. The fixed message routes ensure that arbitrary traffic cannot be injected at any point on the network, thus limiting the potential damage from any specific point of attack.

The connection between the ground station and the rest of the wind farm is the most exposed portion of the system. Here we will use a firewall to isolate the avionics network from the rest of the farm for all non-essential traffic. The firewall will limit the traffic that can pass onto the network to strictly high level commands (take off, land, etc.). Our core switches will further enforce this restriction by only permitting messages required for these necessary features with no additional functionality to be abused.

C. Maintenance and Diagnostic Monitoring

Network switches keep a rich set of statistics on network traffic. Per-port statistics track number of bytes received and transmitted, multicast and unicast packets received and transmitted, packets dropped for various types of errors, whether there was a route specified for the packet and if packets were dropped due to congestion. These statistics gauge the health and utilization of the network. They can be used to diagnose physical layer and link layer problems. The figure below shows the number of packets received and packets forwarded by each port on the kite's redundant core switches during one test flight. Plotted are the minimum, maximum and average multicast packets. Message rates are nominally constant, so ideally these values should be the same or close to each other for each port. Traffic is nominally the same on both A and B networks, so the corresponding ports on Core Switch A and Core Switch B should experience the same number of packets.

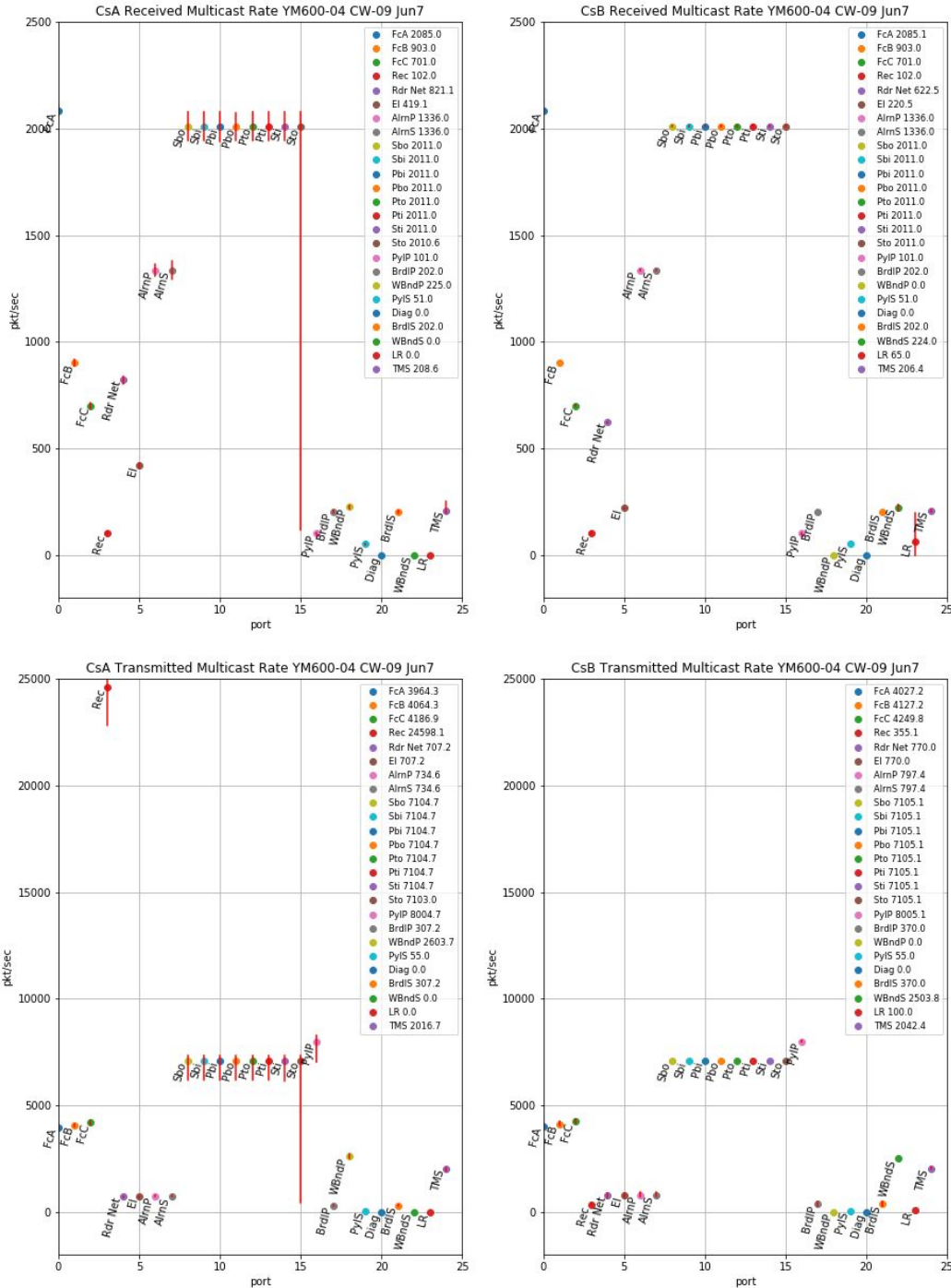


Fig. 7: Multicast packets received and transmitted on each port of the core switch during a test flight.

D. Plastic Optical Fiber as Physical Medium

The physical medium for Ethernet communication is plastic optical fiber (POF). POF is made of a super pure polymethylmethacrylate (PMMA) fiber core, which is cladded with a fluoropolymer jacket. The core of POF is about 1mm - considerably larger than the 10 μm, 50 μm or 62.5 μm

typical for glass optical fiber (GOF). The comparatively large diameter core of the POF reduces the mechanical precision required by connectors. It allows the use of low-cost connector systems that are suitable for use in industrial environments. The numerical aperture is large, allowing the use of low-cost LED sources as transmitters. POF is easy and economical to terminate: the fiber can be cut with a sharp razor blade and polished with 600 grit abrasive paper followed with 3 μ m lapping film.

The M600 harnesses use plastic versions of the MIL-STD38999 series III connector for high-density fiber optic interconnects. These are physical-contact connections where the contact force is controlled with spring-loaded termini. These connectors support a high density of optical connections and maintain a waterproof mechanically sound connection under vibration. The redundant Low Voltage bus is distributed in the same harness, POF and copper share the connectors.



Fig. 8: Plastic fiber for high-density optical connections in harsh environments.

Plastic optical fiber is lighter than the ubiquitous CAT5 Ethernet cables used in offices and homes. As POF does not readily conduct electric current, it provides galvanic isolation between the Flight Control Units and motors and does not need to be hardened against lightning strikes. Optical fiber also reduces the susceptibility to electromagnetic interference, in particular from high-current, high-frequency silicon-carbide motor drives and motors.

Glass fiber is economical in clean and stationary environments. However, glass fiber connectors and transceivers developed for civilian or military airborne applications, which have operational environments similar to that of the energy kite, are prohibitively expensive for wind turbine design.

The main penalties for using POF over glass fiber are increased energy absorption and increased modal dispersion. Basic POF fiber attenuation typically ranges from 160 dB/km to 300 dB/km, when used with a 650 nm LED transmitter. In comparison, the loss in multimode glass fiber ranges from .3dB/km to 10 dB/km. The high attenuation in POF limits the link length to about 50m. The longest link on the kite is about 14 meters. (POF is not suitable for a link down the tether, for example). The large core in POF supports many modes of wave propagation, hence pulse dispersion limits the signalling bandwidth to Fast Ethernet speeds of 100 Mbps. The data rate (between enclosures) on the energy kite is around 30 Mbps.

V. Practical Matters

The development of the energy kite requires considerations beyond what is needed for the eventual operation of the final system. The figure below shows the communication links in use during flight testing the kite. The kite is controlled autonomously by the onboard flight controller, but during testing flight test operators can intervene and take over some aspects of the control. As the AIO network is Ethernet-based and uses IP messaging, it readily extends to communication beyond the kite.

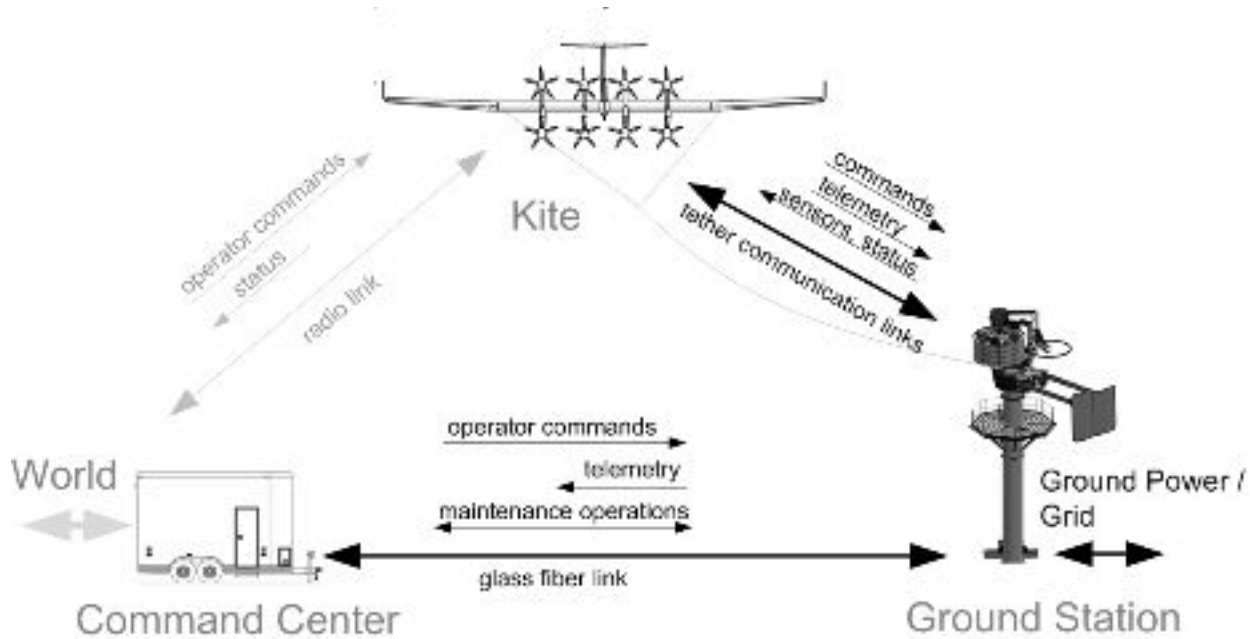


Fig. 9: Communication links for the development and flight testing of the energy kite

A. Kite-to-Ground Communications

The autonomous control of the kite resides on the kite, but there are critical interactions with the ground station that provides the perching function for the kite. The flight controller on the kite commands the winching in and out of the tether. It also uses sensors on the ground station, for wind and weather, and a GPS receiver for differential GPS measurements. It is therefore natural to have the same type of network on the ground station as on the kite. The AIO network supports a mix of star and daisy chain topologies, so kite and ground networks are readily linked by an IP link. The challenge here is to design a suitable link. The figure below shows the kite and ground stations networked by the Tether Comms. We termed the IP messaging between the kite and the ground station “Tether Comms” because some of the schemes actually used optical fiber or electrical conductors in the tether.

In many ways, the most attractive link between the kite and the ground would use glass optical fiber. GOF supports high data rates and low latencies, it is immune to EMI. The operational

environment of the tether - high temperature and sustained cyclic variations of strain - are far from ideal for glass fibers. The metal tether conductors and the carbon fiber strength members are more ductile than the glass fiber. This must be accounted for in the lay angle with which the fiber is wrapped around the tether strength member. The fiber must be protected in a buffered jacket or a gel-filled steel tube. Connectorization for reliably mating and unmating fibers in a dirty and potentially wet environment is also an expensive proposition. We did have tethers with GOF made, but we did not test them.

The tether communication most promising for a scalable product was a powerline communication scheme over a dedicated coax cable embedded in the tether. A coaxial cable ('Deep Mini RG59', engineered for subsea video applications) with a 3mm outer diameter (about the same size as the electrical conductors) gave sufficient performance to get a link speed of 15 Mbit/s (as tested with iperf) from kite to ground. A Gh.n modem was used, with a SISO 50 MHz powerline profile. The channel characteristics of the coax in the tether - most of the useful energy is between 2MHz to 28 MHz - were better suited to the Powerline profile, rather than the cable modem profile.

For flight-testing, IP radios purpose-designed for military communications were used to realize the kite-to-ground links.

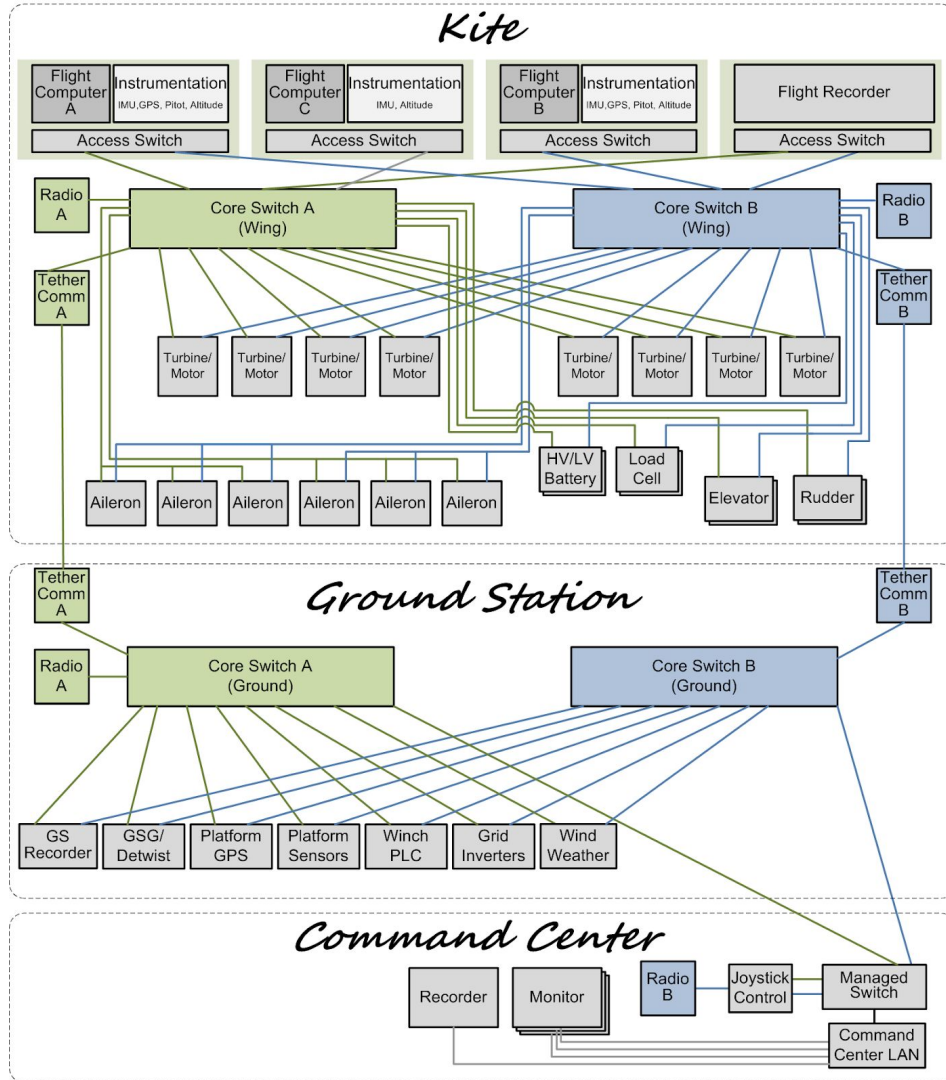


Fig. 10: The kite avionics network extends to the ground station network.

B. Unicast on the AIO Network

It is convenient to support unicast and the ARP protocol on the AIO network during development and maintenance of the system. IP addresses of end devices plugged in the network can be automatically learned and TCP/IP connections can be established. This is useful for programming microcontrollers or remotely logging into embedded computer modules attached to the network.

The most practical way to support unicast on the AIO network is to confine it to one network. A layer 2 network switch learns which MAC address destinations can be reached via each of its ports by examining the source address in packets that come in on that port. A dynamic address table is built as packets are received. Since the Access Switch receives an ARP request from a host on both the A and B network facing ports, the switch should be configured so it is only allowed to learn MAC addresses on one of the network facing ports. The ARP reply, and messages destined to

other nodes for which there are entries in the address table, will then be confined to that network. The isolation of the A and B network facing ports guarantees that ARP requests will not result in packet storms.

C. AIO Message Length

The AIO protocol is layered on top of UDP. UDP datagrams can be up to 65,507 bytes long, but datagrams longer than 1480 bytes + 20 bytes UDP overhead are transported in several Ethernet frames that are 1500 bytes long. The datagrams are then reassembled from these fragments at the destination by the network stack. If one fragment is dropped, the entire datagram is discarded. In the AIO protocol we expect datagrams to arrive in duplicate, there will be two copies of each fragment. While Ethernet protocols are somewhat robust to duplicate frames (which usually are the result of misconfigured networks), the reassembly of duplicate messages with many fragments is not always reliable. It is therefore best to limit message length to as few fragments as practical. It is preferable to transmit information with more small messages than with one long message.

D. Secure Remote Monitoring with the “Data Diode”

For the remote support of flight testing operations it was desirable to stream telemetry, over the internet, to team members that were often time zones away from the test site. To avoid the possibility of an unauthorized source putting data on the kite network, a unidirectional Ethernet link was constructed between the AIO network and the fire-walled server connecting to the internet. The link could only transmit: the fiber to receive was removed from the link. A couple of dummy transceivers were used in place of the fiber to keep the link alive. Since UDP multicast is a connectionless protocol, no handshaking is needed to receive the data.

VI. Conclusions

The AIO network is a high-availability network built on features natively supported by Layer 2 managed Ethernet switches - such as VLANs, static multicast routing, port throttling. Messages are routed messages with predictable bounds on latency, without the requirement for custom hardware processing Ethernet frames. A distinguishing feature of the network is that low-cost microcontrollers with a single media access controller can access the redundant network. We avoid the need for PCI/PCI express backplanes to add network interfaces. The cost for avoiding hardware processing in an FPGA below the L2 layer (which is how AFDX and other high-availability Ethernet protocols handle deduplication) is that the highest bandwidth to the end system is half the highest link rate (50 Mbps in our case). The tables below summarize the most important performance aspects and the fault mitigation mechanisms of the AIO protocol.

Criterion	Performance
Operating Speed	100 Mbit/sec
Network Capacity	50 Mbit/sec/link
Data Latency	< 200 μ s on LAN, 10 ms on IP radio links typ.
Maximum Bus Length	Max link length 50 m
Load Analysis	Automated profiling of network utilization
Network Expansion	Star and chain topologies
Common Cause/Mode Failure Containment	Independent networks with redundant power supplies
Availability	Zero failover time
Redundancy Management	Current Value Table in AIO protocol layer
Message Scheduling	Network Configuration File sets network topology, rate and route of messages
Electromagnetic Compatibility	Plastic Optical Fiber as physical medium is immune to HIRF and lightning. Does not emit EMI
Continued Airworthiness	Continuous monitoring of link statistics on each port. Continuous monitoring of received optical signal power on each port

1. AIO Network Performance

Failure Mode	AIO Mitigation
Loss of Power	dual independent power system
Loss of Communication	dual redundant networks
Invalid Messages	drop invalid messages based on: Invalid 16-bit AIO version number 32-bit Ethernet CRC (FCS) (detects 3-bit errors) invalid Ethernet frame formats
Non-Responsive Node	Message are sent at constant rates, defined in the network configuration file. Message rates tallied by CVT used to detect non-responsive nodes in the control application.
Babbling Idiot	Port throttling keeps any one node of consuming all network bandwidth.

2. AIO Network Failure Mode Mitigation

VII. References

- [1]. Loyd, M.L., 1980. Crosswind kite power. *Journal of Energy (AIAA)*, 4(3), 106-111, https://scholar.google.com/scholar?hl=en&as_sdt=0%2C31&q=Loyd%2C+M.L.%2C+1980.+Crosswind+kite+power.+Journal+of+Energy&btnG=
- [2]. C. M. Fuchs, "The evolution of avionics networks from ARINC 429 to AFDX", *Network Architectures and Services*, August 2012, https://scholar.google.com/scholar?hl=en&as_sdt=0%2C31&q=The+evolution+of+avionics+networks+from+ARINC+429+to+AFDX&btnG=
- [3]. A. Mifdaoui, F. Frances and C. Fraboul, "Full Duplex Switched Ethernet for Next Generation "1553B"-Based Applications," 13th IEEE Real Time and Embedded Technology and Applications Symposium (RTAS'07), Bellevue, WA, 2007, pp. 45-56, doi: 10.1109/RTAS.2007.13. https://scholar.google.com/scholar?hl=en&as_sdt=0%2C31&q=Full+Duplex+Switched+Ethernet+for+Next+Generation+%E2%80%9D1553B%E2%80%9D-based+Applications&btnG=
- [4]. R. L. Alena, J. P. Ossenfort, K. I. Laws, A. Goforth and F. Figueroa, "Communications for Integrated Modular Avionics," 2007 IEEE Aerospace Conference, Big Sky, MT, 2007, pp. 1-18, doi: 10.1109/AERO.2007.352639. https://scholar.google.com/scholar?hl=en&as_sdt=0%2C31&q=Communications+for+Integrated+Modular+Avionics&btnG=
- [5]. Aircraft Data Network Part 7 Avionics Full-Duplex Switched Ethernet (AFDX) Network, ARINC Specification 664, Part 7, Aeronautical Radio, Inc., June 27, 2005.
- [6]. Architecting ARINC 664, Part 7 (AFDX) Solutions, XAPP1130 (v1.0.1) May 22, 2009, https://www.xilinx.com/support/documentation/application_notes/xapp1130.pdf
- [7]. https://www.nts.gov/investigations/data/Documents/2015_preliminary_aviation_statistics.xls
- [8]. J. Qin, B. Huang, J. Walter, B. Bernstein and M. Talmor, Reliability analysis in the commercial aerospace industry, *The Journal of the Reliab Analysis Center, Dep. of Defense of the USA*, pp. 1-5, 2005. https://scholar.google.com/scholar?as_q=Reliability+analysis+in+the+commercial+aerospace+industry&as_occt=title&hl=en&as_sdt=0%2C31
- [9]. R. Perlman: *Interconnections: Bridges, Routers, Switches and Internetworking Protocols*, 2nd edition, Addison-Wesley, *Internetworking Protocols*, 2nd edition, Addison-Wesley Ch. 3: Bridges
- [10]. IEEE Project 802, http://www.ieee802.org/802_archive/fureq6-8.html#5.6.2

Base Station Team Final Documentation

Simon Nolet, Dean Levy, Sean Chou
January 2020

Base Station Lessons Learned	118
Challenges Facing GS02	118
BOM Cost	118
The Transform Maneuver	119
Limited Range of Motion for the GSG Termination Axis	121
PLC Requiring a Different Operating System Than the Kite	122
Management of Redundancy	123
Sensor Selection and Distribution on the Base Station	123
Testing of the Hardware	124
Expensive Auxiliary Systems	125
Potential Design Improvements to Consider	126
Impact of Detwisting the Tether	126
Slip Rings	126
Cost	127
Handling of the tether	127
Integration of all Electrical Cabinets	127
Fabrication and Assembly	128
New Architectures Considered	129
GS02.5 vs GS03, for 2023 Pilot Demo	129
GS02.x (Norway 2020, and Pilot Offshore Demo)	132
What Works Well	132
What We Would Change	133
Ways to Take Cost Out of GS02	134
GS03 (Pilot Offshore Demo Only)	135
Flight Operations	136
Drum Configuration	136
Levelwind Configuration	137
Actuated Perch Panel	138
Launch / Land, Strategies and Hardware	139
Maintenance at Sea	141
Lifting and Perching	144

Base Station Lessons Learned

Challenges Facing GS02

Main sources:

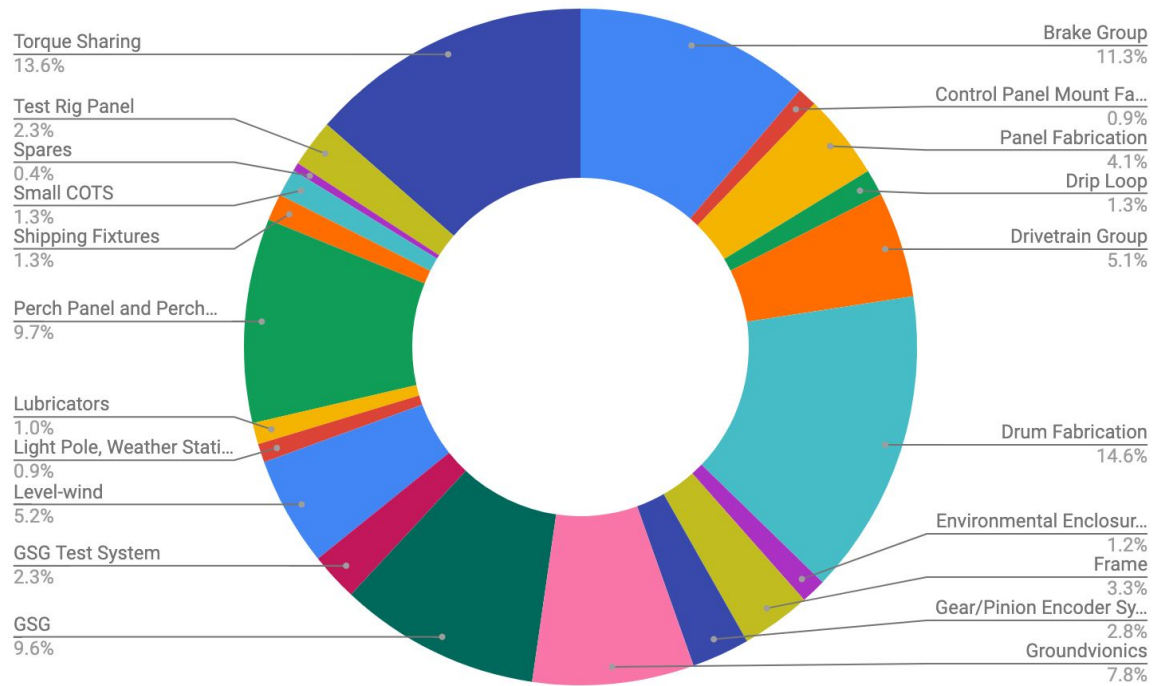
- Shell Technology Update 2020-01-27
- Base Station for Offshore Pilot: Impactful Design Changes
- GSX Review Meeting with former GS team, 2019-10-02
- GS02 vs GS03, by Dean Levy, 2019-01-15

For the last two years, the current ground station (GS02) has been used in all but a few flights. It fully met its objective to support launch, land, reeling in/out and crosswind operations. Although there were a few minor hiccups during flight, they were all fully recoverable and never forced the testing team to release a kite. Only twice were flight operations cut short because of an issue regarding the ground station (GS), the most notable one being FCW-00 in Norway because of a mis-calibration of levelwind encoders (human error). Despite limited availability for testing, repairs and upgrades, the ground station team managed to keep the system flight ready during periods of high demand for most of these two years.

However, moving forward, there are multiple challenges GS02 faces, shall we decide to mostly keep it as is but lower its production cost. Here we list the most important challenges we face to date, and what we would like to see improved in the next iteration.

BOM Cost

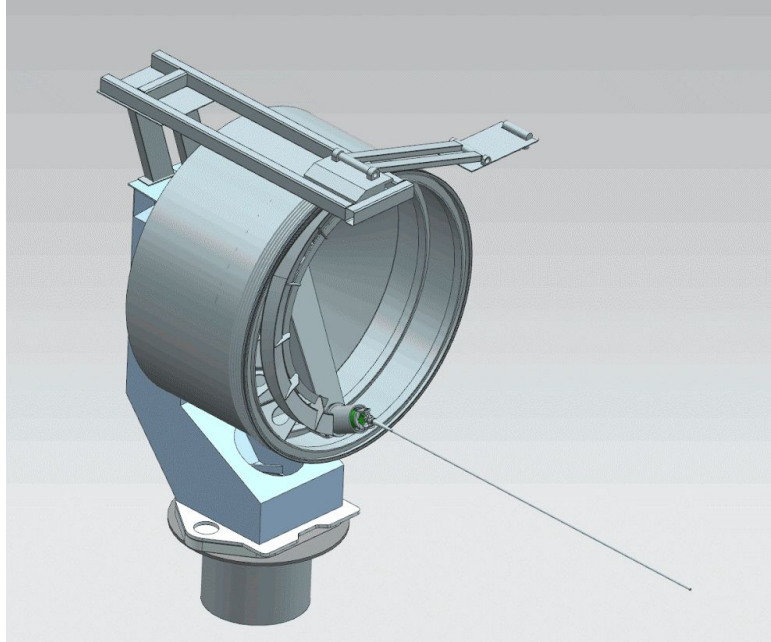
Although GS02 was originally designed to be the first base station part of the M600 kite system to go to market, it quickly became evident that its BOM cost was too high. We put together a spreadsheet [internal ref] when assembling GS02-02, the base station built for the Norway site. The distributed cost breakdown is shown in the figure below, where “Torque Sharing” represents the Azi/Winch servos and power supplies in the PLC cabinet.



The cost target per base station system for the 2023 demo has been set to 70%, based on recent estimates. Those estimates include BOM, assembly and bringup by the Makani team. But it excludes the buoy, the foundation, transportation to the site and the installation. To meet the target, the BOM cost will need to be reduced substantially, probably on the order of 40%.

The Transform Maneuver

The Transform maneuver is the dance the ground station has to accomplish to go from the reel to the crosswind configuration after paying out the tether, and back from the crosswind to the reel configuration before reeling in. It is by far the main factor driving complexity on GS02. It took over 6 months for the GS bringup team to make the Transform maneuver flight ready. By itself, the Transform maneuver does not add any value to a flight, nor does it add anything to power production or improve the performance of the kite. It rather extends the period during which the kite uses power from the grid.



The Transform maneuver as originally envisioned by the GS design team.

There are many reasons [internal ref] why the GS design team decided to proceed with an architecture requiring a Transform for GS02. The main ones were to:

1. minimize the inertia around the azimuth axis, based on the experience gained with GS01 when rotation around the azimuth axis was done in a passive way (kite pulling on the tether as opposed to an active servo drive);
2. get the perch panel out of the way in crosswind, to lower chances of interfering with the tether;
3. minimize the load to the azimuth bearings by positioning the gimbal in crosswind to:
 - a. get it as low as possible (6 o'clock), minimizing the moment arm around the rotation axis in elevation;
 - b. get the vector normal to the detwist plane intersect the azimuth rotation axis in crosswind, minimizing the moment arm around the azimuth axis.

Over the years, we realized the Transform increased the risk of having to release a kite and glide land:

1. It prevents reeling immediately after TransOut to maintain tether tautness and improve passive stability (FCW-01 RCCA, CA-09).
2. It extends the time in high hover when the kite has to carry the full weight of the tether, the riskiest part of the flight.
3. It requires all 4 axes to work and be synchronized to be successful.
4. It requires precise tether elevation control during the azimuth slew, because of the tight clearance between the tether and both the levelwind and the perch panel.
5. It requires precise azimuth control for engaging the tether in the levelwind.

In addition to these risk factors, there are other factors driving up cost:

1. It requires every axis to be precisely synchronized, which was done through the use of a PLC, which in turn drives up software complexity and cost as explained below.
2. It requires an azimuth slew rate at least an order of magnitude faster than the maximum slew rate necessary to track the wind.
3. It drives the need for redundant servo motors on every axis, since they are all critical to a successful Transform maneuver and safe landing of a kite.
4. It requires two different radio antenna configurations, one for reel and one for crosswind.

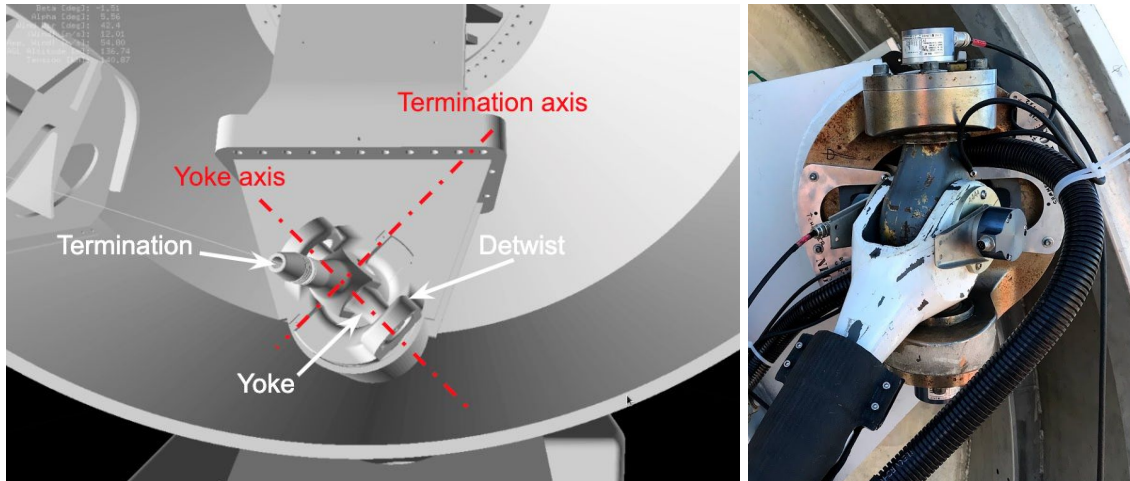
For all these reasons, the current team feels it would be important to seriously consider an architecture that does not depend on a complex Transform maneuver between reeling and crosswind.

Limited Range of Motion for the GSG Termination Axis

This limitation is due to the geometry of the ground side gimbal (GSG), as illustrated in the following figure. The GSG is composed of 3 main parts:

1. The detwist (long cylindrical part in the CAD drawing, mostly aligned with the line of sight to the center of the crosswind circle, rotating to take out the tether twist);
2. The yoke (center part in the CAD drawing);
3. The termination (attached to the tether).

The range of motion around the yoke axis is ± 90 deg, as required by the Transform maneuver. But the range of motion around the termination axis is quite limited, only ± 35 deg, less than the ± 42 deg required by the crosswind circle to track the tether, for the typical size of crosswind circle flown by the M600 kite. This imposes a requirement on the detwist control system to align the yoke axis with the tether departure vector, to prevent the termination to bind on the ears of the detwist holding the yoke, potentially breaking the tether in flight. Given an average of 20 seconds per loop, the reaction time for the operators to detect such a problem is very short, less than 5 seconds. So if the detwist would be to lose track of the tether departure vector, there is nothing much the operators could do to prevent a tether break in flight.



CAD representation of the GSG, along with a close-up picture.

The current strategy used to track the tether departure vector is well described in ECR 366 Command detwist in high hover and trans-in and ECR436 Improve detwist command in crosswind.

The GS team believes there is a way to design a gimbal that can protrude from the surface of a winch when fully reeled out, to increase the range of motion of the termination axis. The main advantage would be to completely decouple detwist from kite motion. The detwist could then be used to simply take out twists, and rotate at a constant speed roughly equivalent to the average speed of the kite around the loop. Should the detwist fail in flight, the tether would simply accumulate a few twists prior to landing, which could be taken out at the beginning of the following flight.

PLC Requiring a Different Operating System Than the Kite

Probably the biggest drawback of having to use a PLC is the need for a tailored operating system and specific software interfaces with the particular brand of PLC selected (B&R). The original code base was written by 3rd party vendors, using expensive proprietary software.

These 3rd party vendors were responsible for different aspects of the ground station code, and were not able to cross-check and cross-test each other's code prior to the delivery of the first article to Makani. Much of the software had to be heavily modified and/or simplified during the initial Makani GS commissioning program (Kalman filter removed for overload monitoring, High Tension slew controller very complex, too many state machines acting on top of each other).

On top of that, the current system requires a dedicated PLC AIO node, that runs the software interfacing the data sent to and received from the PLC.

For the next iteration, if the base station architecture is simplified and all axes decoupled, we should consider using simplified drive controllers, like the kite's servo or motor controllers, to

control the various axes. The biggest advantage would be full integration of the software with the rest of the kite, and the possibility to simulate the base station software used in flight, which currently can only be done through a GS HITL when no tether is installed on GS02.

Management of Redundancy

Because of the potential loss of a kite if any axis on the ground station fails during flight, it was decided early on to get redundant servo drives and servo motors for each axis. However, if not implemented properly, redundant systems can in fact double the chances of failures, like it was the case for most of the redundant systems on GS02 early on, until appropriate fixes were implemented (ECR404 PLC code fix to be redundant to losing drives and ECR410 Improving redundancy to servo failures on GS02 A rack).

Even with these fixes in place, we later found hardware limitations preventing redundancy to failures of the master (A) drives (bug 142504810). So to this date, the various GS02 systems are not fully redundant, like originally intended.

Redundancy can also impact how each axis is controlled. On GS02, each axis is configured in DUAL mode by default. This allows each drive to work cooperatively and share the torque load, to reduce wear and tear. However, this configuration was later found very difficult to tune. For a long time, we had the winch motors fighting each other instead of cooperating with each other (bug 68064755). The solution involved reducing some gains and implementing motor drag on the slave drive to deal with backlash. Yet this solution did not work for the oscillations around the azimuth axis, which still remain but are not blocking flight (bug 112381035).

Here is the proposed way to deal with redundancy for the next iteration, for the sake of simplicity and reducing development time and cost:

1. With all axes decoupled from each other and the possibility of being driven completely independently, determine which ones are absolutely critical to land a kite.
2. On critical axes, get two drives, but only operate them one at a time, the other one being back driven.
3. If a failure occurs in flight, a simple flag should suffice to switch from one set of drives to the redundant one, without the need to fully reconfigure the control system.

This approach is in line with the vision of a minimal viable product, rather than a complex solution intended to solve every situation.

Sensor Selection and Distribution on the Base Station

GS02 is equipped with a multitude of encoders for each axis, distributed on two different data networks (AIO and PLC). There is one redundant set on the motor side of the gearbox, directly connected to the PLC servo drives, used by the PLC controller. There is a second redundant set mechanically connected downstream of the gearbox, to be used by the ground line angle sensing (GLAS) system, which ended up never being implemented. So some of these encoders

were never used in flight (e.g. AIO drum encoders and AIO detwist encoders only used in calibration until they worn out). Although they were not used in flight, they were still brought up to meet the original design intent, which ended up taking some time and effort.

Also, the selected detwist PLC servo drives have single turn encoders, converted to multiturn via software. The big disadvantage of this selection, which was not originally foreseen, was the inability of this system to keep track of detwist motion that occur when the power to the PLC is turned off, like when having to manually reorient the detwist prior to install a tether for example. This forced a recalibration of the PLC encoders every time the detwist is moved more than 3 degrees with power off. The consequence of not doing so could lead to a boggus tether elevation estimate during Transform and crosswind, which in turn could cause the tether to bind and break in flight. The multiturn hardware version of these same servo drives, only a few \$10s more, do not suffer the same problem. A few are currently on order, meant to be installed on GS02 at the next opportunity.

Other sensors, like the tether line angle sensors on the levelwind, the load cells on azimuth and winch brakes, the flow valves on the cooling system (could be mechanical presets to equalize flow) and most temperature sensors, were simply not needed to date, and could be reconsidered for the next iteration.

It is also worthy to mention that many encoders were not rated for the environment in which they were operating, given the lack of enclosure for most of them. For example, the magnetic AIO ring encoders (perch_azi, drum and detwist) degraded faster than expected because they would attract any magnetic debris (iron particles) that would then interfere with the measurement head and eventually strip the magnetic tape from the ring (bug 134199149). The tether proximity sensors used to end the reeling process had their calibration dials quite degraded by overexposure to sunlight. Every encoder or sensor, if not rated for the environmental conditions it will operate in, has to be adequately enclosed in the next iteration.

Testing of the Hardware

For GS02, some modes of operation are very difficult to test with hardware-in-the-loop (HITL), and to tune. The brake-controlled high tension slew during crosswind is a good example that cannot be tested with a traditional GS HITL test. Because this mode of operation involves a kite pulling on the ground station with a decent amount of tension (10s of kN) generating a torque much higher than what the servo drives can do, it turned out to be quite challenging to test. For a long time, the preferred way to test included a crane (or telehandler like in the photo below), a 1+ ton concrete block, high tension rip straps, a high strength shackle and some spectra rope. Obviously such a configuration involves a decent amount of preparation, including safety, to ensure the wellbeing of the personnel involved and the hardware. To date, despite our best efforts to tune high tension slews, the performance remains marginal, mostly because of the difficulty to model the large amount of stiction in the azimuth axis (and potentially the brake), and the difficulty to pull such tests on a tight schedule.



High tension slew tests, Parker Ranch, Hawaii, May 2019.

Another aspect making testing difficult has to do with the current design of the tether terminations. On the kite end, with the tether fully reeled in, the termination sticks above the surface of the drum in such a way that it interferes with the levelwind shuttle frame, preventing the drum from rotating freely. On the GSG end, it cannot be easily disconnected to free the detwist for testing purposes. So once a tether is installed on GS02, the drum, levelwind and detwist axes all become constrained, even though there is no kite perched on the panel. Because a tether usually remains on the GS until it is deemed not usable anymore, this severely limits the opportunities for testing hardware and software upgrades to fix bugs or improve performance.

Finally, logging of data using 3rd party software is very limited and hard to augment, making it hard to record what is needed to improve things, unless the data is shared via a complex interfacing software between the PLC and the AIO networks.

For all these reasons, the next system should be designed with consideration to the ability to model, test, log data and easily tune the various control systems. Non-repeatable “passive” systems should be avoided whenever possible.

Expensive Auxiliary Systems

The various axes on GS02 are currently driven by electric servo motor which are actively cooled or heated. The azimuth and drum axes are also equipped with redundant hydraulic brakes. The combination of actively cooled electrical servos with hydraulic brakes required multiple cabinets to support every subsystem, driving up cost. Of these systems, by far the most unreliable one was the cooling system (bug 120302118, bug 131340300, bug 112503851, bug 137795790), which led to a full replacement of all cooling hoses and fittings on the Norway base station, and

the removal of all heating components in Parker Ranch. It also impacted the testing schedule during the early bringup days at Parker Ranch.

Electrical servo motors can easily be precisely synchronized with the help of a PLC, which was an enabler for the Transform maneuver. But for a configuration where the Transform maneuver is not required and each axis can be decoupled from each other, hydraulic drives become quite attractive from a cost perspective. And in the event an auxiliary system is required for a given test site, it should be integrated into the base station design as an option, rather than being required for every flight article, to reduce cost if deemed unnecessary.

Potential Design Improvements to Consider

Impact of Detwisting the Tether

The need for detwisting the tether has been a subject of debate at Makani. Although flight paths requiring detwisting (circles, ovals) are more efficient at extracting energy as opposed to figure 8's or reversing course after 10s of circles, they do increase the complexity of the base station. This section enumerates some of these factors that could be included in future tradeoffs.

Slip Rings

GS02 currently has two slip rings: one behind the drum, one behind the detwist. Of these two, the drum slip ring would be relatively easy to eliminate in the next iteration, because the drum only has to rotate a maximum of 40 turns when reeling in/out the kite. However, for as long as the flight path will be circular, the detwist slip ring will remain required.

Cost and reliability are the two main concerns with the slip rings. For reference, the BOM cost for 1 slip ring cassette assembly (MVDC, 750VDC, 120VAC) is 10% of the dentist drivetrain, about 1% of the GS cost. The reliability is still questionable, given the limited number of flight hours until now, and the mean-time-to-failure is still unknown. The design is driven by the 6" maximum diameter currently available through the GSG barrel. Although the available space is not as restricted for the drum slip ring, both assemblies share most of their design and parts. Such a small diameter for the high voltage lines precludes any off-the-shelf design, so we ended up fabricating ourselves the slip rings currently in use.

We have already had slip ring failures in the last two years that led to slips in the schedule, despite relatively limited flight time. We've had issues related to routing low voltage lines through the center of our MVDC slip ring, making repairs in the field quite difficult.

Cost

Overall, the cost of the detwist drivetrain (servo drives, encoders, slip ring), is estimated at 8% of the GS cost. As it currently stands, the detwist has its own dedicated control system that is synchronized with the drum motion during Transform. Without the need for a Transform maneuver and with a redesigned GSG, the detwist drivetrain could be greatly simplified to a non-redundant velocity-controlled drive that is only activated during crosswind.

Handling of the tether

The selection of the tether has an important impact on the design of the base station. The tether minimum bend radius based on solid core tethers and 480m length was a major design driver for GS02. The use of a stranded tether with a smaller minimum bending radius might allow for a smaller diameter drum, if deemed less expensive.

Installing a tether on GS02 in Parker Ranch (onshore) currently requires a minimum of 3 operators. The whole process takes >½ day for personnel trained to work in a man basket. The operations are not risk free. We did break a tether once during installation, when we did not synchronize properly the tether spool with the base station drum, allowed the tether to loosen up, get snagged on a protruding bolt and break. Being able to easily unmount the drum from the base station to install a tether on specialized equipment could reduce risk and time, especially on a rocking ship at sea. If not possible, at least ensuring crane access to tether termination at the GSG could simplify aerial operations.

Integration of all Electrical Cabinets

GS02 comprises many electrical cabinets, the main ones being the PLC cabinet including all components related to the servo drives, the Groundvionics cabinet including all hardware interfacing with the kite through the AIO network, and another cabinet translating optical signals to electronic for local distribution. A lot of components like DC converters, amplifiers, power supplies and other auxiliary boards are redundant between these cabinets. And because data is transmitted on two different networks, there is dedicated hardware to ensure that communication happens smoothly. Getting rid of the PLC would render a lot of that hardware obsolete, and would reduce cost.

The Norway base station also included an electrical cabinet with the same flight computers than the ones flying on a kite. It allowed closed-loop testing of the base station, without the need of a kite. It was extremely useful during the bringup of the Norway site, as we could work on both the kite and the base station at the same time.

Fabrication and Assembly

The team has identified over the years potential improvements that could speed up the fabrication and assembly of the next base station. Here is a list of the main ones.

- Make the frame and bearing/motor mount plates one part. On GS02 these are two parts. This adds time to assembly and would probably be cheaper than making two parts.
- About the use of metric bolts versus standard. We tried to standardize on metric whenever we could. But it proved to be impractical for the large bolts used on the tower, so we used standard for these. I believe NASA has a rule that all bolts bigger than M24 OR 1 time install bolts should be standard because they are way easier and cheaper to procure in the States, procurement being the key factor for us.
- Some pins inserted into welded structures have too tight of a tolerance. Mounting the panel to the boom has never been easy. This would save assembly time.
- Improved designs for lifting the GS.
 - We cannot use the spreader bar to tip the GS because the lines would interfere with the drum.
 - So far we required 2 cranes to tip the GS, and it is expensive. We should consider designing a tipping platform or other 1 time engineering cost solution, to require only 1 crane.
- The drum diameter makes transporting the GS difficult. I believe it requires specialized trailers and large width shipping containers. We should consider bringing down the diameter to fit standard shipping containers, which would facilitate transportation and lower cost.
- Wiring the GS is the most time consuming aspect of the GS assembly. And once completed, it takes a while to validate it. Reducing control complexity would also reduce electrical assembly time and testing.
- Over the years, we struggled with the lack of detailed assembly drawings for all subsystems and systems. We should have required this from the beginning. This makes it easier to handoff the fabrication and assembly to other vendors down the road.
- About contracting, to reduce cost:
 - Negotiate a good deal on procurement markup if using a 3rd party.
 - Negotiate good termination/cancellation terms if the vendor isn't working out.
 - Negotiate build and integration standards for quality control, especially electrical.
 - Make sure to include integrated testing as part of the contract, and to allow time for it if the delivery of one of the multiple 3rd party vendors slips.
 - Multiple quotes from multiple vendors with sufficient time for negotiations (~2-3 months min).

New Architectures Considered

The GS team at Makani came up during the Fall 2019 with two possible architectures for the next generation of base stations. The first one, GS02.x, is a similar architecture than GS02, meaning a Transform maneuver will be necessary to go from the reel configuration to crosswind flight, and then back to reel. The advantages of that approach are:

- to reduce the time to production by reusing a lot of the current design;
- to take advantage of all the learnings so far to improve on specific systems, and in doing so reducing uncertainty and risk.

The main inconveniences are:

- having to require a Transform maneuver, increasing flight risk in the long run;
- probably missing on opportunities to largely simplify the system and reduce cost.

GS03, on the other hand, is a completely new architecture, which will essentially be free of a Transform maneuver. There is an obvious cost and schedule risk associated with it, as the systems and configuration will need to be designed, fabricated, brought up and tested for the first time once again. But the team acquired over the years a wealth of experience and knowledge to make vast improvements on the current design. The following sections discuss the tradeoffs between the two possible scenarios.

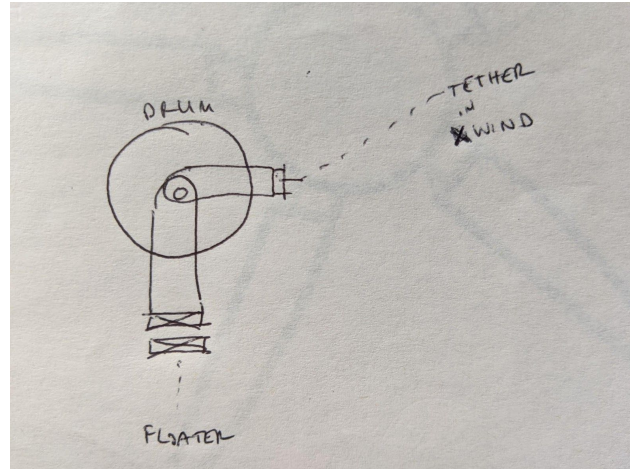
GS02.5 vs GS03, for 2023 Pilot Demo

Sources:

- GS02 vs GS03, 2019-01-15 [internal ref]
- Shell Technology Update 2020-01-27 [internal ref]

The main difference between the GS02.5 and the GS03 architectures is the need for a Transform in the GS02.5 one. All the other envisioned base stations upgrades could be implemented in the GS02.5 architecture as well.

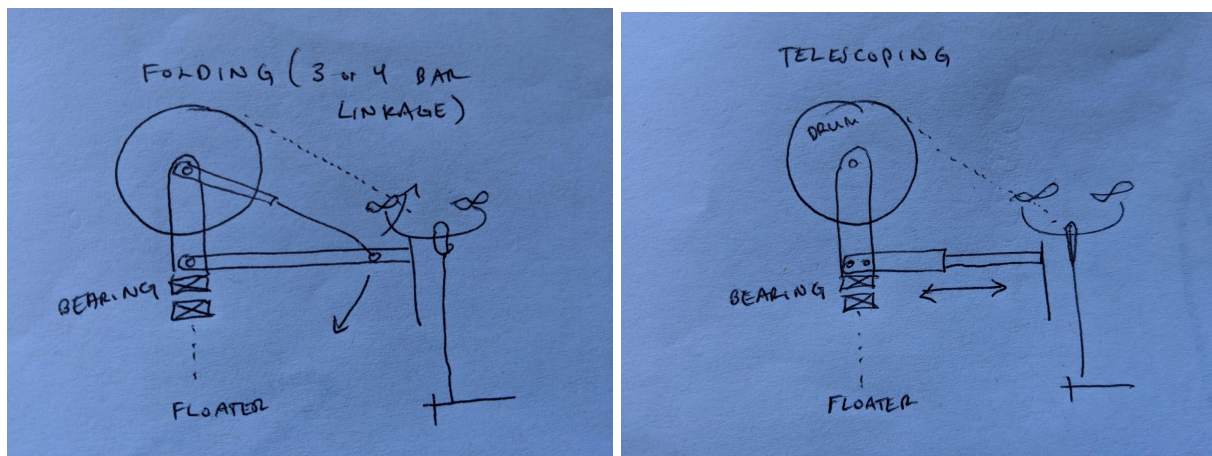
The most popular way to eliminate the Transform would be to **integrate the drum and the GSG**. The GSG would need to stand proud of the drum OD when in crosswind to have sufficient range of motion (this is a lesson we can take from GS02). I've been told this idea was explored [internal ref] and became too complex mechanically/structurally, but it seems worth pursuing again. It will likely be a significant engineering challenge, but hopefully worth it. Here are some thoughts:



- A simply supported drum has many benefits over the cantilevered drum setup
 - Reduces the winch bearing loads.
 - Reduces the levelwind structural loads.
 - Reduces loads on the perch panel and more importantly on the perch boom if the perching arms extend from both sides of the drum.
 - I believe this architecture will provide a more convenient geometry to lift and load the GS onto the floater. Ideally a lift without removing parts (like the levelwind or wind mast) would be possible, without having to install a spreader bar.
- Eliminating a Transform has many benefits.
 - Even though radios are not a long term solution, without a Transform, radio comms between the GS and kite should get easier because we won't have to accommodate two different GS orientations.
 - We could use the GS to tether tension modulate right after trans out to roll stabilize the kite.
 - Will reduce time in hover.
 - Will eliminate the scary maneuver of threading the needle between the levelwind and perch panel. It also seems very likely it'll eliminate any upper elevation limit in hover or crosswind.
 - Eliminates synchronized motion between axes.
- We should consider the following:
 - If the GSG is mounted on one side of the drum, then we will likely have significantly more mass on that side, producing asymmetric loads on the drivetrain. We might be able to balance that mass with internal structure, symmetric structure, or other methods.
 - If the drum OD is large enough (there are other reasons to keep it small) the interior could provide enough room form the additional structural support required to withstand crosswind loads without adding much inertia.
 - We should reconsider the drum OD against
 - axis inertia (I would try to match or beat our current inertia);
 - minimum tether bend radius (approx 1 meter from 3.5 m);

- space for internal structure and slip rings;
 - GSG length - the larger the drum, the longer the GSG must be to stand proud of the drum surface and therefore the larger the moment arm of tether loads;
 - loads on azimuth and winch bearing;
 - shipping requirements: too wide or too tall is problematic for shipping the drum.
- We should reconsider the clocking of the GSG in crosswind and Transform prior to the azimuth slew (top dead center to bottom dead center) - the clocking of the GSG not only determines the moment arm of the tether loads but also the elevation window between the levelwind and perch panel.
 - If the GSG is proud of the drum OD:
 - it could interfere with the levelwind;
 - we'll need a transitional surface (like the trackway on GS02) to safely lead the tether from the GSG to the drum skin;
 - we should also consider a GSG that unfolds from below the surface of the drum.
 - Without a Transform the perch panel doesn't swing out of the way in crosswind. This greatly reduces the tether elevation window in crosswind. We will need to consider swinging the panel away (separate axis) or a new position/arrangement to keep clear of the crosswind tether path. I'm going to discuss this in more detail below.

If the OctoberKite does not have a bridle, we can move the perch panel much closer to the GS. This alone may eliminate the tether elevation issue in crosswind. Otherwise, we may consider an activated perching system, something similar to a telescoping or 3 or 4-bar linkage design.



- This is essentially swapping complexity but it feels like a more readily available solution (I'm thinking boom lift or person lift) and therefore more reasonable than a Transform.

- May be convenient for working on a kite if we can lower the boom or pull the kite close to the GS.
- May be convenient geometry to dampen the perch panel and/or for buoy compensation (although this seems complex).

For both designs, whether that's GS02.5 or GS03, we should consider:

- 1 encoder and 1 motor per axis.
 - No more "redundancy" - it's complex and takes time to design, build, commission, use.
- Move to hydraulic drives.
 - This is the industrial standard.
 - It will reduce cost.
 - It may eliminate the brake system.
- Increase our GSG azi and elevation limits. We should never worry about binding a tether in crosswind.
- Increase the OD of the center hole in GSG detwist barrel to accommodate a much bigger slip ring.
- Lower the perch panel to widen the tether elevation window in hover (and crosswind for GS03).
- Levelwind redesign
 - Move the pivot point toward the drum center to increase upper elevation window.
 - For GS03, Simon had an idea of a pivoting levelwind to keep the levelwind engaged no matter the tether elevation.
 - Cam the levelwind to the drum and eliminate the levelwind drive.

GS02.x (Norway 2020, and Pilot Offshore Demo)

TODO

- Add M600 lessons learned for MX [internal ref]
- Add in diagram with naming conventions

What Works Well

- Launch and land is robust onshore with the current GS02.
- Separate load paths for hover and crosswind flight modes:
 - Allows for efficient structural choices since the two flight modes have very different load requirements.
- Transform moves perch panel out of the way in crosswind flight:
 - Reduces the acceptable minimum tether elevation, increasing the tether elevation window in flight.
- Low azimuth inertia:

- Lesson learned from GS01;
- Provides the opportunity to eliminate azimuth drives, although this seems unreasonable for offshore operations;
- Moving buoys with large inertia base stations are not well matched systems.
- Levelwind neatly spools tether on drum:
 - Protects and helps ensure the tether is not damaged during flight.
- Horizontal drum axis keeps the tether on the drum even with little or no tension:
 - Lesson learned from GS01, since a tether falling of the vertical axis drum on GS01 was a critical failure triggering a glide landing;
 - Makes installing a tether much easier.
- Low inertia GSG reduces concentrated loads on tether:
 - Lesson learned from RPX, using the Top Hat (GS01-like) GSG configuration;
 - In crosswind the tether acts to manipulate the GSG to follow the kite. Stiction in the GSG bearings and the inertia of the GSG puts stress on the tether, especially at the tether to termination interface. If that inertia or stiction is too high it will break the tether in bending.
- Active control of most axes:
 - Allows reliable control schemes;
 - Provides a tunable system. A tunable system is important to make changes easier as problems arise during flight testing, especially in the R&D stages

What We Would Change

- 1 encoder and 1 motor per axis.
 - True system redundancy is hard to accomplish. It's complex, costly, and takes time to design, build, commission, and validate.
 - Eliminate the AIO only network sensors.
- Move to hydraulic drives.
 - Cheap and reliable, very common in all sorts of heavy duty industries. Can monitor system pressure+flow to check system health. Failure mode is usually leaking which is usually a progressive failure and not sudden loss of all operation.
 - Closed loop system hydraulics can provide braking. We should be able to remove the friction brakes and reduce cost accordingly.
- Modify the GSG to increase the range of motion of our GSG yoke and termination axes.
 - Binding a tether in crosswind is a high severity incident.
- Increase the OD of the center hole in GSG detwist barrel to accommodate a much bigger slip ring.
 - This opens up possibility to use off-the-shelf (or close to) proven components.
- Lower the perch panel or make it retractable to decrease the lower elevation limit in hover.
- Consider reducing the asymmetric loading caused by GSG schnoz. This puts excessive wear on bearings and drives motor sizing.

- Redesign the levelwind:
 - Move the pivot point toward the drum center to increase upper elevation window;
 - Cam the levelwind to the drum and eliminate the levelwind drive.
- Design in lifting points such that the GS does not need to be disassembled for handling.
- Redesign the drum. The design, especially for the outer diameter (OD) and material, must consider the following:
 - BOM cost.
 - Axis inertia, which drives motor sizing.
 - Minimum tether bend radius. The current tether has a minimum bend radius of approximately 1 meter from 3.5 m in 2017.
 - Space for slip rings. There must be adequate space to install and work on electronics.
 - Loads on azimuth and winch bearings. This is determined both by the drum OD during hover and the GSG placement in crosswind.
 - Shipping requirements. Too wide or too tall is problematic for shipping the drum.
 - Could the tether be double wrapped onto the drum? This would reduce the surface area of the drum dedicated to wrapping the tether.
 - Where the GSG is placed. If using the same control scheme to realign the azimuth during high tension the GSG position determines the moment arm of the kite to realign the GS.

Ways to Take Cost Out of GS02

Reference documents: GS Cost scratchpad [internal ref], GS02 Spend Tracking [internal ref]

GS02 was built in a run of quantity 3. The cost scratchpad linked above is a line-item tally of how that unit cost could come down using a variety of quotes for a build quantity of 10 and other values.

Interesting points learned from this exercise:

1. The biggest cost savings come from replacing the servo winch and azimuth drives and their respective friction brakes with a closed loop hydraulic system capable of hydraulic lockup as a braking system.
2. We actually got a good deal on GS02 the first time. New quotes for the drum, perch panel, and GSG mount weldment all came in at nearly double their original price. The shops reported that they underestimated the complexity.
3. The table below summarizes the \$/kg cost of some of the quotes along with examples from other components we've had built. The thing to note is that we can get components built for nearly material-only cost if the design is simple enough (WLT frame, e-lot tower). The drum, perch panel, and GSG weldment are multiple times costlier than the raw material so there is immense room for improvement in cost if we can simplify the designs.

Fabrication Rates	\$USD/kg	
Shop rate for Steel WLT frame (incl. install)	6	Built in 2015
Mild steel mat'l cost	7	survey of onlinemetals.com

Shop rate for Steel Winch Frame (seems low?..)	7	Built in 2016
Shop rate for Steel e-lot tower	8	Built in 2015
Aluminum mat'l cost	17	survey of onlinemetals.com
Shop rate for Aluminum perch panel	56	quote qty 10
M+F rate for Steel GSG weldment	59	quote qty 10
Shop rate for Aluminum drum	130	quote qty 10
Shop rate for Steel GSG weldment	144	quote qty 10

The new lowered price of GS02 could be 86%. This leaves us with a cheaper GS without any major design changes.

The price can be further reduced to 59% with more ambitious design changes (but still not even an architectural change!) such as:

- Convert perch boom from fiberglass to steel w/ hydraulic damper
- Simplify design of perch panel, drum, and GSG mount weldment to achieve \$30/kg (reasonable shot in the dark)

If we start to consider major architecture changes that allow deletion of entire subsystems (i.e. levelwind, or maybe an entire axis drive) we can drive the cost even lower. This is more in line with a GS03 type of redesign.

GS03 (Pilot Offshore Demo Only)

Main sources [internal refs]:

- GS02.5 - GS03 Brainstorming Sessions
- Brainstorming photo album
- Drive folder for the brainstorm sessions
- Gen 3 (Offshore) Base Station Requirements (including pilot demo concept description)
- GS02 2020 Offshore perching requirements
- M10098 - Offshore Operations Weather and Sea State Specifications
- GS02 BOM / cost document
- GS02 Perching Strategy Brainstorm

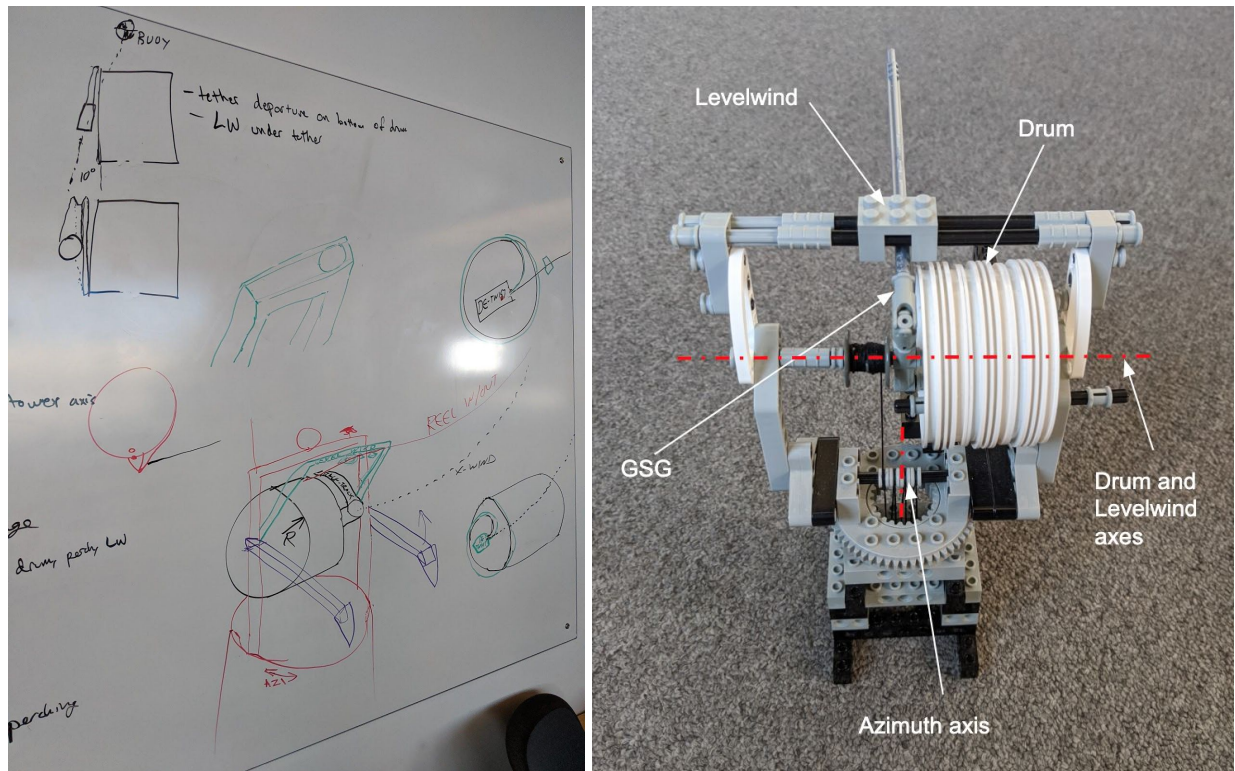
This section discusses the main ideas traded off during a series of brainstorming sessions regarding GS03 held in the Fall 2019. This new architecture, GS03, would involve a complete redesign of the base station, to implement relevant improvements based on our experience so far. The main characteristics of that new architecture are to not require a Transform maneuver between reel and crosswind operations, and to be designed for sea operations, including maintenance, lifting and perching a kite. The timeline is rather short: only 1 year would be allowed for the redesign and fabrication by a 3rd party vendor.

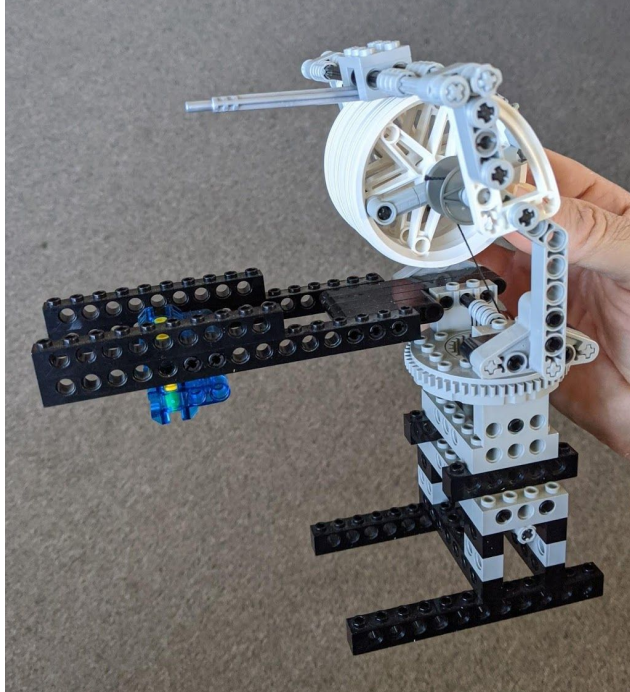
Flight Operations

The goal of this session was to find configurations that could simplify flight operations based on what they are currently for GS02. The most relevant ideas that came up proposed new configurations for the drum and the levelwind.

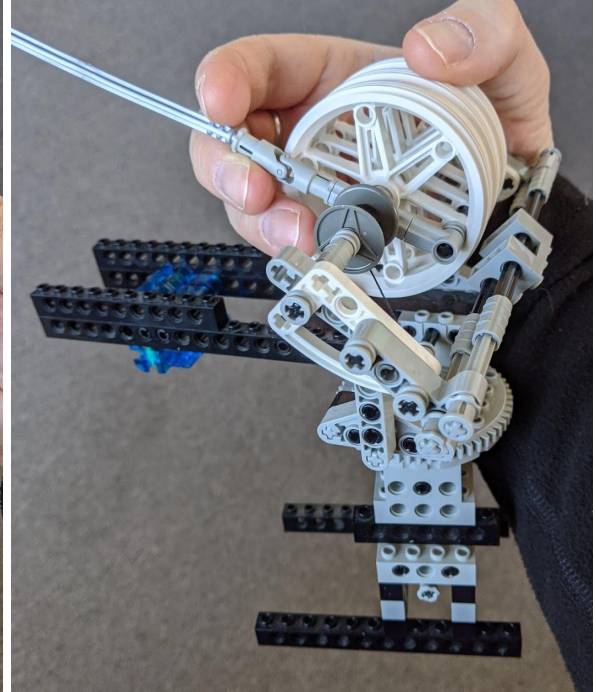
Drum Configuration

The team came up with various concepts allowing for a simply supported drum configuration, as shown in the figures below. The GSG could be positioned near the azimuth axis of rotation, to reduce the moment arm with the azimuth axis to minimize the azimuth brake load in crosswind. In the crosswind configuration, the drum would be clocked to minimize the moment arm between the corresponding reaction moment axis at the azimuth bearing and the tether force vector at the part of the loop when tension is at its highest level.





Reel configuration



Crosswind configuration

We also discussed having a GSG protruding from the surface of the drum, as opposed to being fully within the drum with a track guiding the tether to the surface of the drum. But the configuration with the GSG embedded in the drum involved the tether potentially rubbing on a surface during crosswind, which would increase wear and tears. So the preferred solution remained having a GSG protruding (or unfolding) from the surface of the drum.

Levelwind Configuration

Multiple levelwind configurations were discussed. The first one involved a fully captive levelwind with the shape of a doughnut at the end of a boom. The levelwind would be shuttled during reel-in/out, but freewheeling during crosswind. The advantage would be to always keep the tether engaged in the levelwind, but at the expense of some rubbing of the tether on the doughnut. Unless there is a way to locally reinforce the tether jacket to prevent localized wear and tear over time, a levelwind that would completely disengage in crosswind would be preferred.

A particularly interesting levelwind configuration we came up with was the *inverted levelwind*, as shown in the following picture. This levelwind has a similar shape as an inverted wing flap on the current levelwind cassette, but it is single-sided. In order to work properly, it would require an azimuth offset of a few degrees when reeling in, so that the tether would slide on its surface and be positioned on the drum. Note that the surface could consist of rollers to minimize friction.

This concept is very relevant for multiple reasons:

- it totally opens up the upper limit of the acceptable tether elevation window;

- it removes the need for the articulations in the levelwind at the shoulder and the wrist, and reduces levelwind to a 1 degree-of-freedom system (shuttle action only);
- it could be combined with a grooveless drum surface, which would drastically reduce the required position accuracy when laying down the tether on the drum surface;
- it acts similarly to a wide drum groove, and therefore is more forgiving of azimuth error.

All these factors greatly reduce complexity. It does bring other concerns though:

- We will need a different way to compute the tether elevation angle during reel-in/out, since it is currently relying on encoder measurements at the shoulder and the wrist.
- Although rollers could be added to the surface, it is likely there will be some rubbing with the tether near the interface with the drum surface. We will have to carefully design that area to minimize wear and tear on the tether.



Actuated Perch Panel

We also discussed the possibility of a hydraulically actuated perch panel, rotating around the same axis as the drum. It could be used to move the panel out of the way in crosswind and increase the tether elevation window. It could also be used for heave compensation, or to assist during kite lift.

Similarly, another hydraulic actuator could be used to quickly move the landing apparatus in azimuth by a few degrees when the kite is flying in close proximity. This could be used to compensate for side gusts, and could prevent to have to size the whole azimuth train for a quick response to these gusts.

Launch / Land, Strategies and Hardware

We had an entire brainstorm session in the Fall 2019 dedicated to launch/land for the next generation of ground stations. The top 3 known issues with launch/land that were considered:

- Approach/Retreat (kite within ~6m of the panel):
 - Vertical, tangential, or radial collision with the kite or bridles.
- Peg engaged to parked:
 - Perch peg slips off the top, side, or bottom of the panel.
 - Kite slips off the panel tangentially.
 - Tub or tail hit the panel due to kite pitch extremes.
- Tether disengages from the levelwind:
 - Combined with azi error is bad, because it might not reengage properly!

Close proximity operations are particularly tricky, because the tangential motion of the kite maps to a much larger angular motion of the base station in azimuth (up to +/- 10 degrees as shown by offshore flight data). For such large motion, phase lag is also important to consider. With a perch panel 3 m wide, and perch hooks only inches from the extremities when landed, a one degree azimuth error at perch hook contact could result in a precarious landing, similar to the one that happened in FCW-00 in Norway.

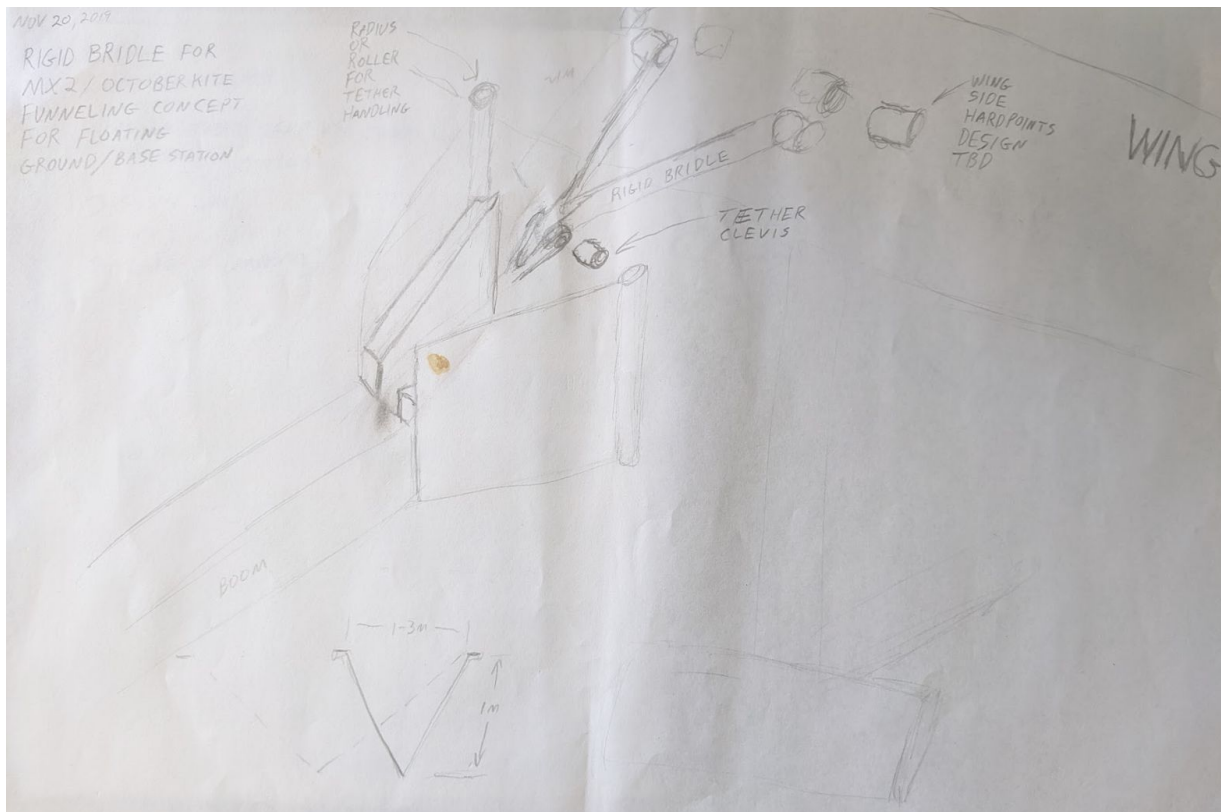
The team downselected a few concepts [internal ref] during the brainstorm session:

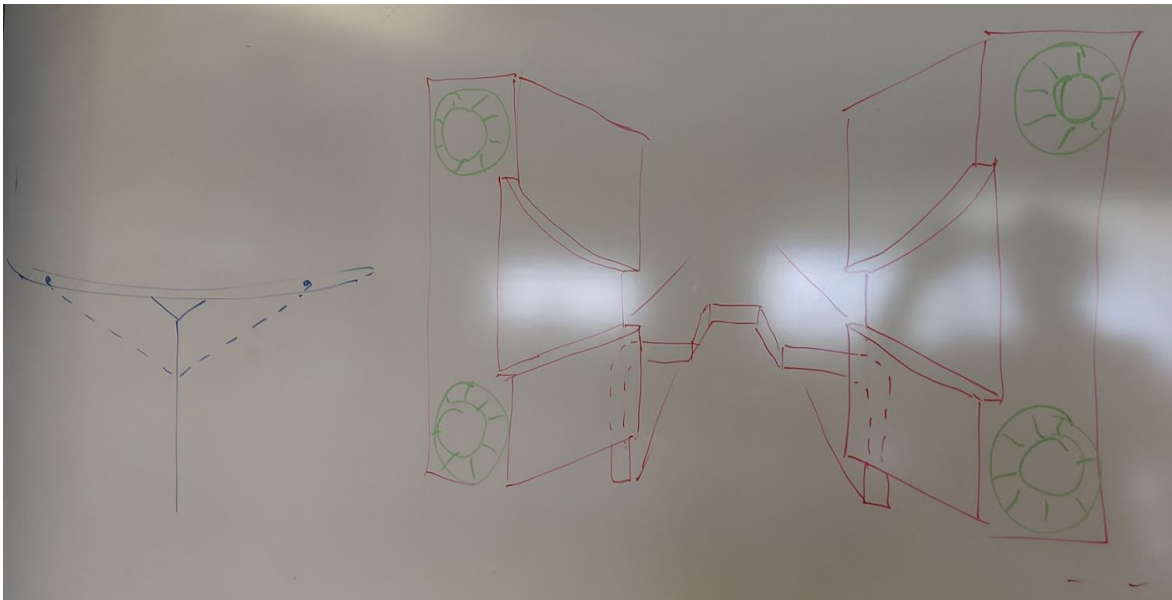
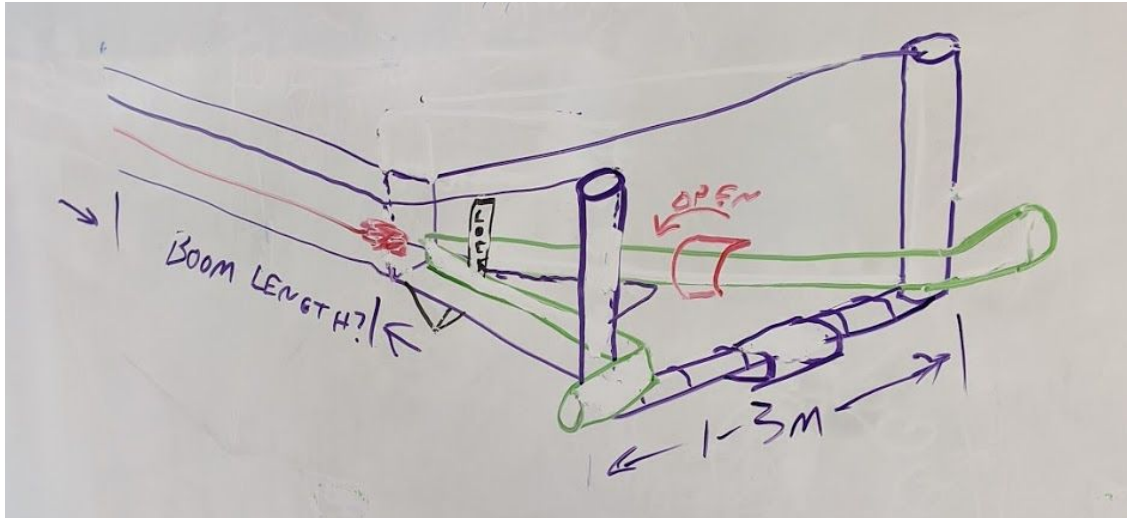
- Go and get it:
 - Actuated robotic arm grabbing and securing the kite at landing.
- Hook on a line:
 - Hooks on the kite clipping on lines spanning across the landing area on the base station.
- Funneling:
 - Mechanical funnel guiding the fuselage/wing to a constrained area when reeling in.
- Fairlead:
 - Fairleads guiding the tether/bridles to a constrained area when reeling in.

Each concept was evaluated against one another, as shown in the following evaluation matrix.

Criteria	Weight (/100)	Go and get it	Hook on line	Funneling	Fairlead	
Cost to implement and test	5	1	9	5	3	low = expensive
BOM cost	5	1	9	5	3	low = expensive
Time to bringup	5	1	3	9	5	low = long time
Ease of modeling physics for sim	5	9	1	5	3	low = hard
Airframe loading	10	1	9	3	5	low = high load
Human intervention (maintenance and operations)	13	5	1	9	3	low = lots of intervention
Component wear and tear	5	1	3	9	5	low = lots of wear and tear
Controller implementation	5	1	3	9	5	low = hard to implement
How well it deals with relative motion	14	9	3	5	5	low = low tolerance to relative motion
Kite lifting	5	9	5	9	5	low = less compatible with lifting
Junk + weight on kite	13	5	9	3	3	low = lots of load on kite
Consequence of critical failure (collision, bridle, tether)	5	1	3	9	5	low = high consequence, high probability of damage
How much experience we have (development risk)	10	1	5	9	5	low = different of our current way of doing things
Score	100	270	450	576	348	

The team agreed on funneling being the most promising approach. Further pursuing the idea, the team envisioned a landing apparatus where the kite would hang by the bridles, which might be rigid, without the need for a perch panel or a long perch boom, as shown in the figures below.





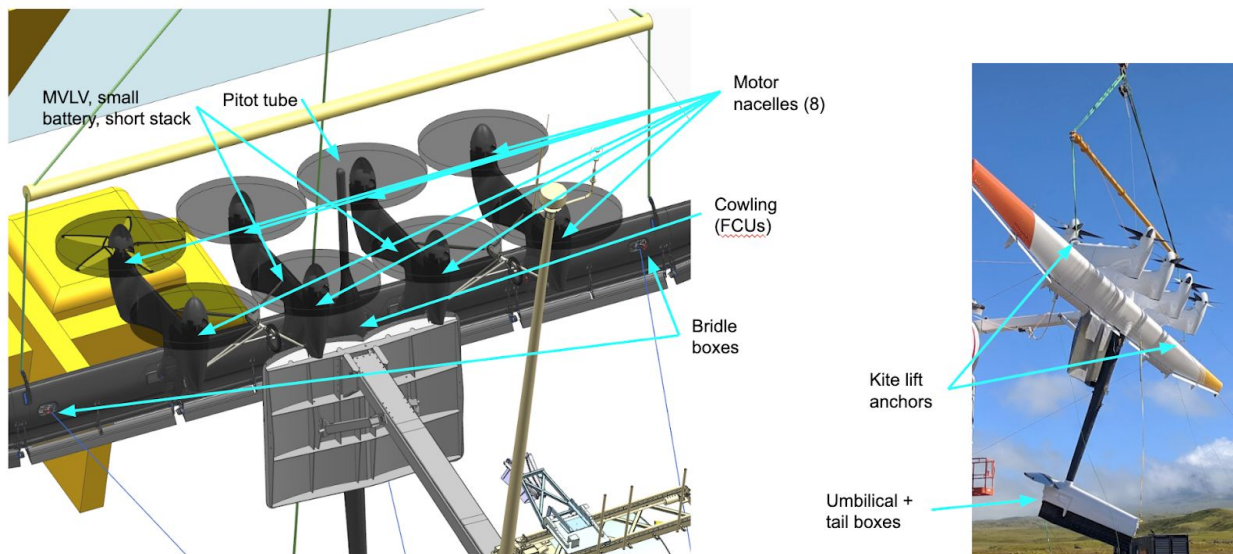
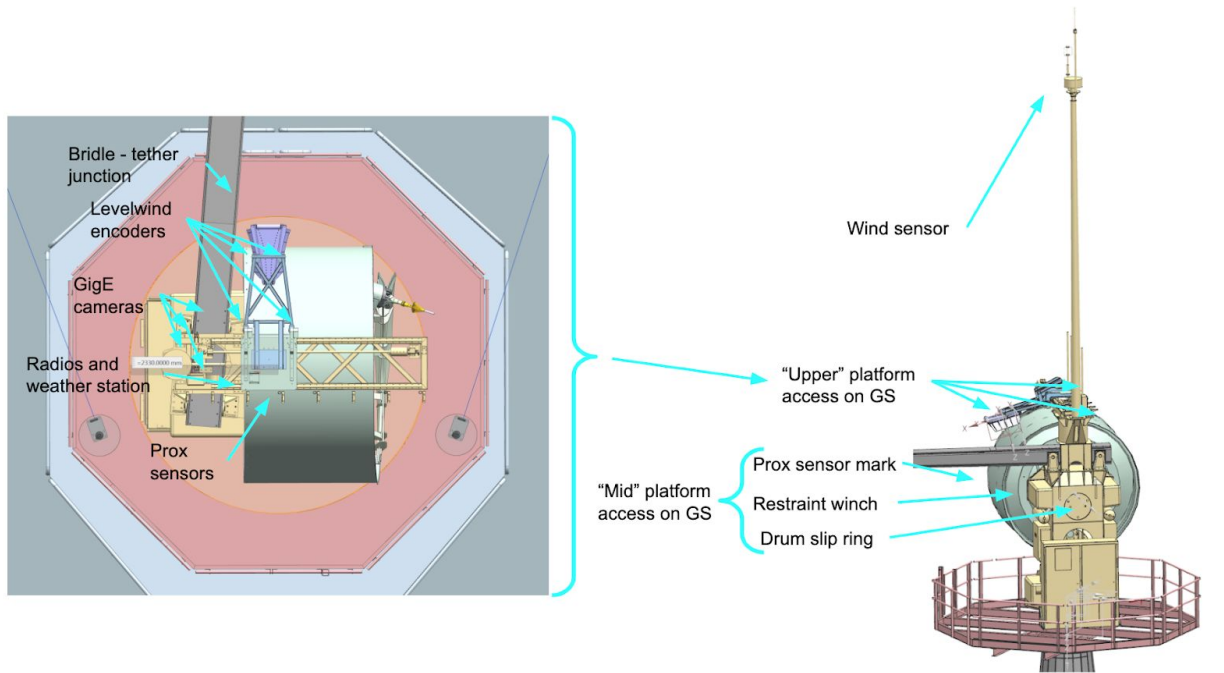
There were also other concepts considered [internal ref] for the case where it would be desired to keep the perch panel in place in the short term. But these were less relevant to GS03.

Maintenance at Sea

Over the summer in Norway, it quickly became evident that maintaining GS02 or even a kite at sea would be very difficult, without towing everything back to shore. A few components are particularly challenging given the current configuration:

- Levelwind joint bushing
- Levelwind shuttle track
- AIO ring encoders
- All AIO encoders + mounts + connectors, non-outdoor rated
- Cowling on the kite

- Everything inside the kite's nacelles
- Anything with gaffer tape
- Wind sensor on top of the mast



After review with the team, we concluded that the following components in particular will need to be accessible at sea, if they are present in the next iteration:

- Base Station:
 - All cabinets on the human platform
 - HPU cabinets
 - Both ends of the tether termination
 - Prox sensor (back of drum) + mark (front of drum)
 - Radios (levelwind shuttle on top)

- Slip rings (GSG first, drum)
- Levelwind encoders
- Shuttle frame anchor point for tether install
- Tether termination (both ends) for the purpose of installing the tether
- Kite restraint winch (GS side)
- GigE cams

- Kite:
 - Pitot tube
 - Tether termination (both ends)
 - Cowling (to access the FCUs)
 - Umbilical at tail
 - Radios + bridle boxes (loadcells, releases)
 - Tail boxes

A lot of the concepts brainstormed with the team [internal ref] focused on platform additions to GS02 to provide access to these in the short term. But the basic ideas to minimize the need for access platforms is still quite relevant to GS03:

- Group the hardware needing access to similar locations when possible (e.g. radio mast, weather station mast, prox sensor, GigE cameras should all be co-located).
- Get rid of any permit required confined space, to alleviate any constraint associated with it (like 3 people required).
- Modify the tether length to bring the schnoz at 6 o'clock when the tether is fully reeled in.
 - This gives easier access (step up from human platform) to the tether termination, the GSG encoders, the GSG slip ring cassette, and the GSG gear train.
- Potentially bring the GPS and wideband radios down to be accessible from the human platform level.

If GS03 is going to be a Transform-free base station, the tether will be departing the drum in the same direction for all phases of the flight. One could then consider building some kind of nacelle rotating in azimuth with the platform and the drum, that would protect the hardware from the elements, in addition to protect the crew that would need to access the hardware for maintenance at sea. The best analogy would be the nacelle covering the motors and pulleys in a ski lift, except that it would be rotating in azimuth.



The main advantage of such a nacelle would be to simplify environment covers by covering the whole thing at once, rather than having to design environmental covers for every component. It could also allow the use of more accessible indoor-rated industrial actuators and sensors, rather than outdoor-rated ones. And it would provide obvious human protection, especially at sea. However, it would increase the moment of inertia around the azimuth axis, which could lead to larger azimuth drives. This would have to be traded against the advantages listed above.

Lifting and Perching

The team spent another session discussing ways to lift and perch a kite at sea. So far the Makani testing team has only performed these tasks onshore using a crane and tag lines manned by a crew of 6 people [internal ref]. If the base station is to be permanently anchored at sea, similar operations will need to be performed from a ship, which might move relative to the base station, and ideally with less people.

Crane operations and motion compensation at sea are now possible. But they remain hard to access because of the highly specialized equipment required. Here is a list of possible solutions:

- Walk-to-Work Systems (information provided by Shell) [internal ref]
- Edda Fonn Offshore Vessel [internal ref]
- Minesto Project [internal ref]

There is quite a bit of work that has been done at Makani over the years to implement lifting using a strongback that could potentially be lifted by a crane or even a telehandler:

- Kite Lifting Strongback Design Documentation [internal ref]
- Telehandler Kite Lift [internal ref]

The team came up with the following criteria to compare potential solutions with each other, which could be translated into requirements:

- Lift and lower the kite between the perch and a floating vessel
 - Tolerant to off-nominal landing and damaged kite

- Safe
 - Keep people safe at all times during the lift
 - Legal in all potential jurisdictions (NO, US, EU, Asia...?)
 - Protect the hardware
- Work in specified ocean/wind conditions
 - 1–1.25 m wave expected sea state during lift and perching
 - 10 m/s wind from any direction (goal, but could reconsider)
 - stay within perching apparatus' motion/dynamic envelope
 - The larger the envelope the easier it is, TBD
- Cost / operational time
 - Low complexity
 - Easy to prepare for lift
 - Low scar drag/mass on the kite
 - Lift activity limited to 8 hours (1 shift), ideally less
 - Fewer than 10 people involved in lifting operation, ideally fewer
 - Scale to future ConOps
- Cost / availability/access to required vessels/hardware
 - Low complexity
 - Doesn't require exotic hardware/vessel we don't own or couldn't easily rent

The Various Concepts Brainstormed in Fall 2019 [internal ref] Were Grouped as Following:

- Motion compensated crane on existing ships
- Rigid coupling between spar and ship for traditional lift
- Pivots with rigid apparatus on ship / spar
- Use the GS winch itself to lift
- Ropes / ramp connection to panel
- Overhead crane lift with
 - Kite already resting on intermediate perching/lifting apparatus (so that mating pieces during the lift can be robust and handle relative motion)
 - Mating pieces have funneling geometry that allows large positional tolerance
- Simple crane + winch to mimic launch/land
 - Funneling
 - Use flight hardware
 - Could lift intermediate apparatus
- Magni on barge
 - Motion compensation
- Fly onto perch

Each of these concepts were evaluated against one another:

Criteria	Weight (/100)	Fully motion compensated crane on existing ships	Heave-only motion compensated crane on existing ships	Rigidly coupled spar+tender, with traditional crane lift	Pivots with rigid apparatus on ship / spar	Use the GS winch itself to lift	Ropes / ramp connection to panel	Overhead crane lift combined w kite+perch	Simple crane + winch to mimic launch/land	Magni on floating barge	Magni w spar/tender tidgily coupled	Fly onto perch	
Tolerance to off-nominal alignment and kite condition	20	5	5	5	9	5	1	3	3	9	9	1	low = intolerant
Feels safe ("sketchiness" factor)	25	5	3	1	3	9	3	9	5	3	5	1	low = unsafe for hardware and people
Robustness to weather (wave/wind)	20	5	3	1	1	5	5	5	5	1	3	9	low = not very robust
Cost / Op Time	20	5	3	3	3	9	1	3	5	3	5	3	low = high cost
Cost / access to required hardware	15	1	5	1	5	9	9	5	5	9	1	9	low = high cost
Score	100	440	370	220	410	740	350	520	460	470	480	420	
					1st			2nd				3rd	

The one concept that scored the highest was the overhead crane lift combining the kite and the perching/lifting apparatus, which could be used as a lifting strongback. Both would be mated onshore, transported on a ship and craned in place on the base station. The perch would then need to be designed with a focus on facilitating crane operations for the targeted sea conditions.

List of Relevant GS Documentation

- GS02 test results, PLC data [internal ref]
- ARG Running Notes (minutes from meetings) [internal ref]
- GS02 PLC FAQ [internal ref]
- Procedure: GS02 HITL [internal ref]
- GS02 Mock Controller Operation [internal ref]
- GS02 buganizer bug list [internal ref]
- DWOS buganizer bug list [internal ref]
- McLaren controller and physics repositories (Gerrit) [internal refs]
- ARG repository (GitHub) [internal ref]
- 2019-03-01 GS02 Servo Drives Redundancy Testing in PR [internal ref]
- Makani Power - M600 GS02 - Controls Requirements [internal ref]
- OUTDATED M600 GS02 Ground Station Datums and Coordinate Systems [internal ref]
- Gen 2 Ground Station Specification [internal ref]
- GS02 Perching Strategy Brainstorm [internal ref]
- GS02.5 - GS03 Brainstorming Sessions [internal ref]

Ozone Rev1 Design Document

Andrew Goessling (12/28/15)

Editorial notes:

(Geo Homsy, July 24th 2020)

- The “Ozone” is Makani’s third generation motor controller design. It is a silicon-carbide based SVPWM controller with custom firmware.
- It’s necessary to understand the stacked controller architecture to understand the following content.
 - The stacked controller architecture is a four-series, two-parallel arrangement of controllers and motor-generators.
 - This allows for a high (4500 - 4800VDC) tether voltage, while exposing the controllers to only one fourth of the tether voltage (1125 - 1200 VDC).
 - To maintain the craft in the air in case of a motor or controller failure, there is a supervisory module (the “short stack”) that can shunt any of the four series stack levels out of the stack in an emergency.
- In such a “motor out” case, we would require more power per remaining motor to stay in the air.
- More power is made available automatically *if*, rather than lowering the tether voltage in case of a failure, we maintain the tether voltage and expose the motor controllers to a *higher* voltage for a limited period of time (one third of the tether voltage: 1500 - 1600 VDC).
- To allow operation under these emergency conditions, we opted to use 1700 volt silicon carbide MOSFET modules.
- Maintaining the tether voltage in case of a motor out condition allows us in theory to connect the tether *directly* to an emergency backup battery bank, without the use of any intervening converters. This is what is meant by “direct connect” in the following discussion.
- The dynamics of the individual stack level voltages is slowed enough to enable stability and control, by introducing external “stacking capacitor banks”.
- The stack design means that the modules in each controller are at a voltage with respect to the controller case ground that is *dependent on the controller’s level in the stack*. This introduces complexities in grounding design, and also necessitates greater voltage isolation, creepage, and clearance between the power handling circuitry and the controller case.

Finally: There are several mentions of specific manufacturers and part numbers in this document. They are included as historical references only, to give an indication of our design

flow process. No suggestion about, opinion of, or endorsement of, any particular product or manufacturer is expressed, intended, or implied.

- Direct Connect Sizing
- Powertrain Risks and Mitigations
- Kt Evaluation and Recommendation
- SiC Module Sizing
 - Available Modules
 - Cooling Requirements
- DC Link Capacitor Sizing
 - Bulk Energy Buffering
 - Voltage Ripple
 - Stacking Capacitor Banks Current Isolation
- High Frequency Decoupling
- Current Sensors
- Chassis Grounding
 - CM Decoupling Capacitors
 - Impedance Grounding Considerations
- Gate Driver Design
 - Desaturation Detection
- Internal Wiring Harnesses
- Main PCB Design
 - Current Sensor Input Circuitry
 - Bus and Chassis Voltage Measurement
- Mechanical Design
 - Creepage and Clearance
 - Mechanical Design Goals
- Design Review Questions And Responses

Direct Connect Sizing

The first step to an Ozone design is understanding the implications and worst corner cases associated with direct connect battery approach. A general overview of the approach and resulting performance is given [internal ref].

It is assumed that the only allowable change (due to schedule) to the current YASA motor is change in K_t affected by a change in stator turns. Therefore, in conjunction with the above methodology, a simple procedure can be used to select a motor design:

1. Determine power requirements for various operating conditions (taken as external inputs and not addressed here).

2. Choose max allowable short-term (30s) bus voltage.
3. Choose worst Volts / Power operating condition that will be supported (possibly disallowing some fault combinations).
4. Find largest K_t where all points within the required operating region are achievable utilizing the resulting bus voltage. The operating region is defined by a required minimum torque and a required minimum power. An achievable point is defined as a point at which the motor can be operated assuming a drive capable of infinite current (i.e. motor not impedance limited).

This procedure is implemented in a script that lives [internal ref].

Powertrain Risks and Mitigations

Before we discuss potential selections for K_t it is useful to enumerate risks and mitigations related to the project as K_t and controller sizing will be difficult to change later.

- Chosen allowable max bus voltage (e.g. 1600V) during generation-motor-out (3 stack trans-out) is optimistic / not achievable.
 - Reduce generation-motor-out power requirement. 94kW -> 60kW => 1600V -> 1570V (weak effect).
 - Remove generation-motor-out on battery requirement. => 1600V -> 1560V (weak effect).
 - Remove cells from battery or run at a lower SOC. 7% reduction in cells => 1600V -> 1500V.
- Steady-state controller loss is too great (probably hover-motor-out (3 stack hover)).
 - Reduce ambient temperature requirements.
 - Reduce power / torque margin.
 - Remove cells from battery or run at a lower SOC (implies relaxing fault combination requirements).
 - Operate at elevated temperatures with reduced lifetime.
- Power not achievable with motor (K_t too high / bus voltage too low).
 - Reduce power / torque margin.
 - Relax fault combination requirements.
 - Add cells to battery if higher max bus voltage allowable.

It should be noted that almost every operating condition can be improved by lowering the battery impedance by increasing battery capacity.

K_t Evaluation and Recommendation

The K_t selection script was run in several different requirement and operating configurations. Various quantities of interest as well as initial conditions and rationale are catalogued [internal ref].

All configurations point to a K_t which is lower than the current YASA motor. The question is then how much lower of a K_t is required? The lower the K_t the higher the resulting currents in the controller. Therefore the question is a subjective tradeoff between required controller current and operational and fault combination requirements. There are three cases documented in the above sheet:

- K_t Delta = 0.95 – Trans-in on battery with 0% power margin.
- K_t Delta = 0.89 – Trans-in on battery with 5% power margin.
- K_t Delta = 0.85 – Trans-in on battery with 10% power margin.

Also listed for each K_t delta is operation given a contingency plan where 7% of the battery cells are removed in order to keep the max bus voltage during generation-motor-out to 1500V as opposed to 1600V. Only the K_t delta of 0.85 can achieve trans-in on battery under this contingency plan. The K_t delta of 0.95 also cannot achieve hover-motor-out on battery under this plan.

The K_t delta of 0.85 certainly gives the most power margin, but it also gives the least torque margin (due to increased controller currents). For this reason I believe a K_t delta of 0.95 or 0.89 is better suited for this design. The K_t delta of 0.89 has the advantage of maximum fill factor in the motor with standard wire (18T -> 16T), therefore it is probably the most desirable option from the motor's perspective. A K_t delta of 0.89 will be assumed during the rough sizing of SiC module and bus capacitors.

SiC Module Sizing

Available Modules

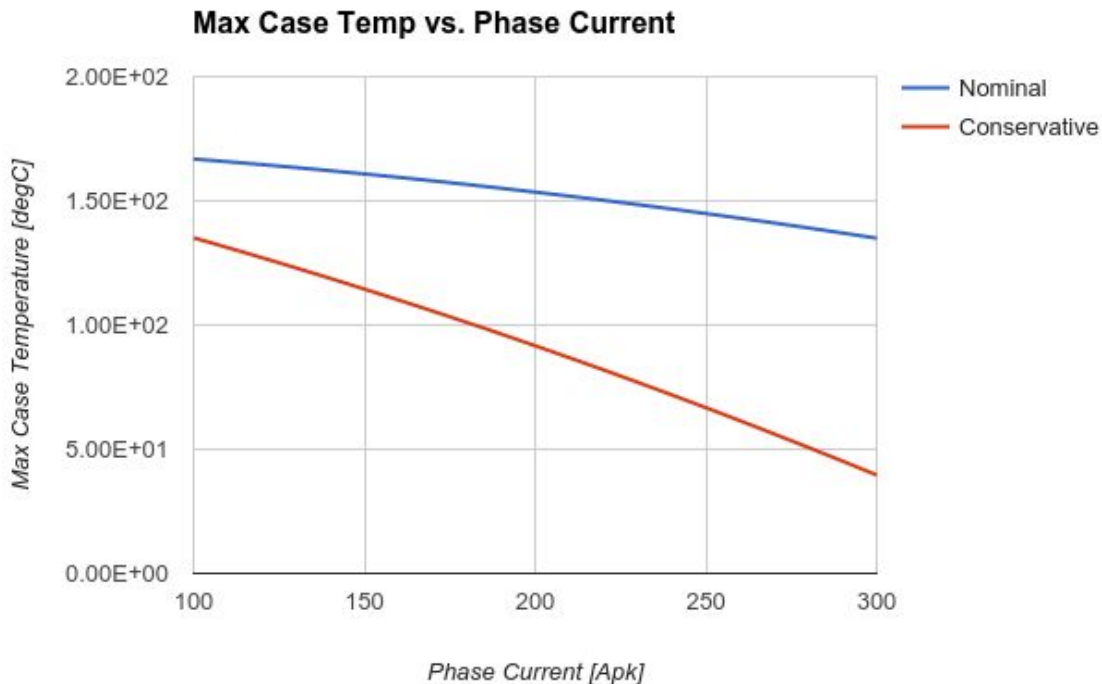
Unfortunately there are a limited number of SiC modules on the market and even fewer 1700V SiC modules. Those available for sample or purchase at this time are listed here along with known useful parameters [internal ref].

A promising module is the APEI / Wolfspeed module fitted with Wolfspeed Gen3 1700V die. APEI and Wolfspeed are currently investigating a 1700V module with 10kV baseplate isolation

(a change that would greatly simplify motor and controller chassis grounding). The above sheet has extrapolations to Gen3 HT-3000 modules with and without 10kV baseplate isolation.

Cooling Requirements

A useful way of evaluating a module's fit for an application is to calculate the temperature at which the case of the module must be held when operating in worst case conditions in order to keep the die temperature below its absolute max (175C). In this design the worst case operation is during hover-motor-out as the power requirements are elevated, the voltage is 4/3 nominal, and the operation is long enough that it is essentially steady-state. The potential module's R_{dson} is scaled from an existing module and assuming a 40% decrease in specific resistance from Gen2 to Gen3 as well as an increase in die from 5 to 8. The maximum case temperature versus controller current is calculated from nominal expected parameters, and then again from significantly conservative parameters:



The potential module's switching energy metric is estimated as a function of the industry standard Wolfspeed CAS300M17BM2 packaging. The nominal case uses a scaling factor of one, the conservative case uses a factor of two. Switching frequency is assumed to be 15x the max electrical frequency (260rad/s) for the nominal case and 30x for the conservative case. When evaluating these temperatures at the worst case operating point of 255A, I believe the HT-3000 module with Gen3 1700V die provides enough margin to warrant designing it into the Ozone controller despite the outstanding unknowns in performance.

DC Link Capacitor Sizing

Bulk Energy Buffering

The DC link capacitor bank is sized based on RMS current requirements during worst case operation. For a K_f delta of 0.89, the predicted RMS current is 93Arms. Crawling Digi-Key, some of the best film capacitors in terms of specific capacitance (uF / volume) are in the B3277X series from EPCOS. We have used capacitors from this series in the previous Gin controller and as an added benefit EPCOS provides some of the most thorough datasheets for their capacitors as well as expected lifetime data. A bank consisting of box-type PCB mount film capacitors is chosen due to its ability to achieve high volumetric efficiency in custom applications with extremely short lead-times.

All of the data from the capacitors of this series was derived from this EPCOS datasheet:

http://en.tdk.eu/inf/20/20/db/fc_2009/MKP_B32774_778.pdf

And compiled into this spreadsheet [internal ref].

Additional information regarding FIT derating values for temperature and voltage were derived from this quality document from EPCOS:

<http://en.tdk.eu/blob/541264/download/3/pdf-quality.pdf>

The aforementioned spreadsheet attempts to calculate a maximum allowable case temperature given a lifetime requirement and bank configuration. The process is as follows:

1. Calculate required number of series capacitors based on voltage rating and required bus voltage.
2. Calculate required number of parallel capacitors based on RMS current rating and required DC link RMS current. An addition of a constant (in this case two), aids in reducing RMS current heating load and increasing capacitance.
3. Calculate the required FIT rate for each individual capacitor in the bank by dividing the required DC link FIT rate (for 95% confidence in 80,000 hour life) by the number of capacitors that make up the bank.
4. Calculate the FIT derating value associated with the voltage bias on each cap compared to its rated voltage.
5. Solve for the required FIT derating value associated with the capacitor temperature by dividing required individual capacitor FIT rate by the voltage derating value as well as the individual capacitor's nominal FIT rate listed in the datasheet.

6. Lookup max allowable capacitor case temperature given by FIT derating value and allow for increased case temperature if capacitor not operated at max RMS current.

This approach is geared to yield an approximation of lifetime and comparison between different bank configurations. In particular EPCOS is very ambiguous in regards to the operating conditions associated with the FIT derating values (ambient vs. case temperature or rated RMS current vs. no current).

The various capacitor bank configurations are sorted by an artificial metric, case temperature divided by bank volume, and configurations with particularly good case temperatures and bank capacitances are highlighted for review. Availability from online distributors is also considered. This analysis points two particularly good options:

1. A 2S8P connection of B32776G0206 - 20uF 1.1kV 18Arms - with a total bank capacitance of 80uF, voltage rating of 2.2kV, and RMS current rating of 144Arms.
2. A 2S7P connection of B32776G9306 - 30uF 800V 21.5Arms - with a total bank capacitance of 100uF, voltage rating of 1.6kV, and RMS current rating of 150Arms.

Voltage Ripple

The max voltage ripple on the DC bus of a controller is related to the switching frequency, controller output current, and the specific charge of the switching pattern. The details of these calculations are given in this whitepaper [internal ref].

The result of that analysis for SVPWM is that the absolute maximum specific charge is 0.5. Therefore max peak to peak voltage ripple is:

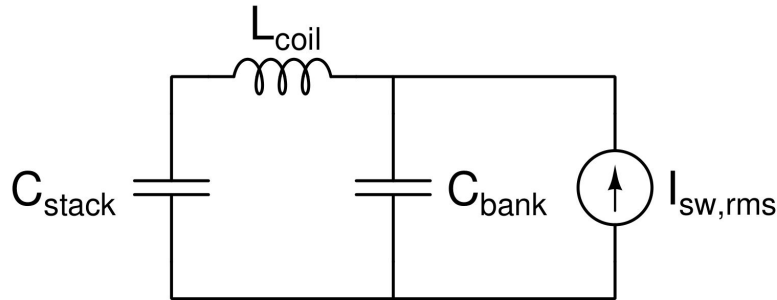
$$V_{pk-pk} = 0.5 \cdot \frac{I_{out, pk}}{2 \cdot F_{sw} \cdot C_{bank}}$$

With a peak current of 255A and a minimum switching frequency of 10kHz the three selected banks would result in 80V, 63V, and 37V of voltage ripple respectively. This represents 8.4%, 6.6%, and 3.9% of the min bus voltage of 950V.

The possible effect on voltage stacking control loop is being investigated, but initial thoughts of analog filtering voltage measurement seem promising.

Stacking Capacitor Banks Current Isolation

Currently each motor controller has 750uF of bus capacitance on the input to slow down the stacking dynamics. This is implemented as electrolytics to achieve low mass, but with the penalty of reduced lifetime and RMS current capability. Therefore it is necessary to ensure the majority of DC link RMS current flows through the bulk energy buffering bank rather than the stacking capacitance bank. To ensure this a small amount of inductance is placed between the controller and the stacking capacitor bank in the form of a coil of wire. The setup is shown in schematic form below:



With C_{stack} and order of magnitude larger than C_{bank} , and the goal of passing 90% of the switching current through C_{bank} , C_{stack} can effectively be ignored. Then we only have to ensure the impedance of L_{coil} is an order of magnitude larger than C_{bank} at the ripple frequency of 20kHz:

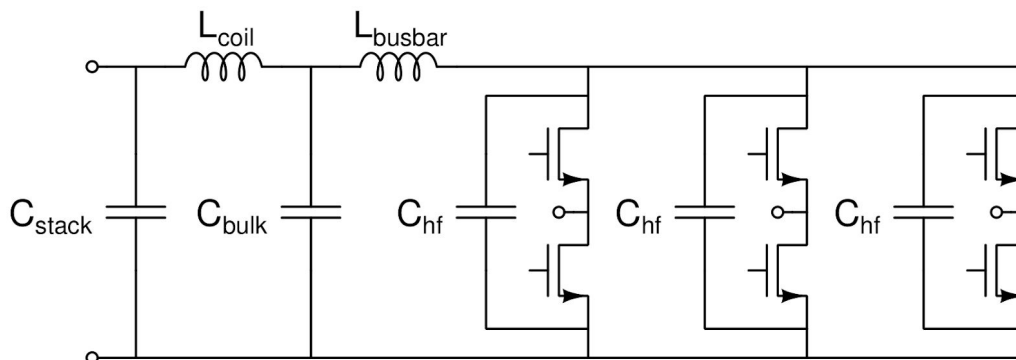
$$2\pi \cdot 20kHz \cdot L_{coil} = 20 \cdot \frac{1}{2\pi \cdot 20kHz \cdot 80\mu F}$$

$$\Rightarrow L_{coil} > 16\mu H$$

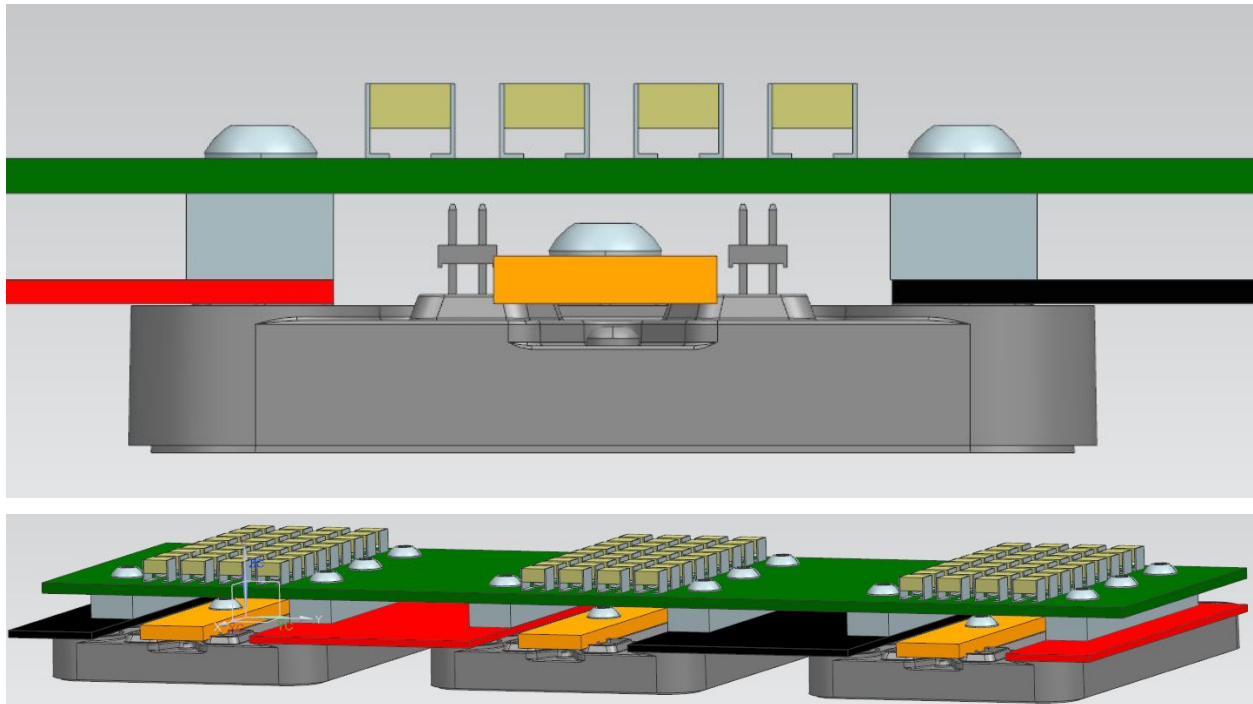
This can be achieved with six coils in air with a diameter of 20cm. Furthermore, an explicit discrete low current inductor could be placed on the stacking capacitor bank PCB.

High Frequency Decoupling

DC link capacitance is required not only for bulk energy buffering, but also for high frequency decoupling of the SiC modules during switching events. Due to their size and mass it is difficult to mechanically arrange the energy buffering capacitors in a way that minimizes inductance to the SiC modules. This increased inductance results in higher voltage overshoot during transitions and forces the use of larger gate resistors, slowing the SiC transitions down and increasing switching loss. The proposed solution to this problem is to place electrically and mechanically smaller high frequency decoupling capacitors in a tight loop with each module, thereby dividing the two DC link requirements between two separate sets of capacitors. The proposed connection is shown below:



Each of the high frequency decoupling banks will consist of a series parallel connect of SMD ceramic capacitors mounted to a PCB that is mounted directly across the terminals of the SiC module as shown below:



This achieves low inductance by minimizing the loop area from die to capacitor to die as well as increasing the loop width by connecting across the entire module tab. Potential capacitor combinations were selected from in-stock ceramic SMD capacitors on Digi-Key with a voltage rating between 200V and 2000V and with AEC-Q200 qualification. The considered capacitor combinations are here [internal ref].

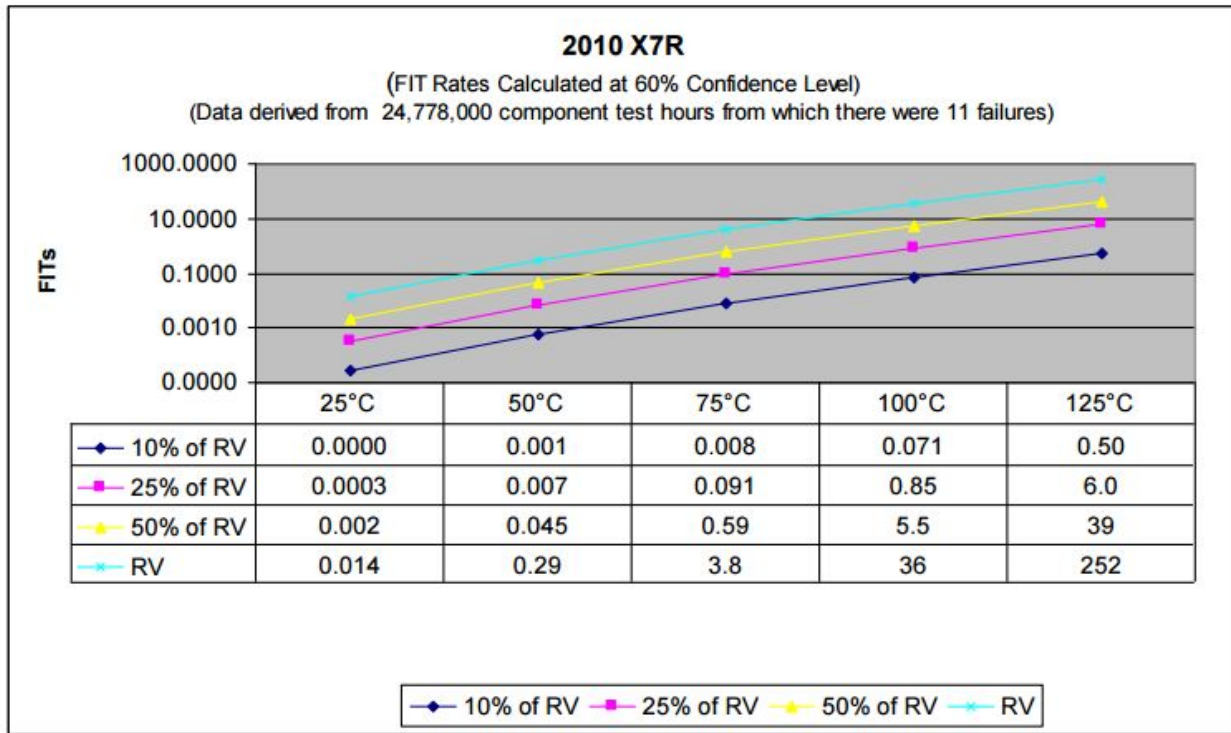
The configurations were determined by:

1. Calculating the required number of capacitors in series to achieve a 1500V rating.
2. Calculating the maximum number of capacitor strings in parallel based on the width of the capacitors and length of the module tabs.
3. Calculating and ranking based on the resulting capacitance.

This process resulted in selecting a 4S9P combination of [CKG57NX7T2W225M500JJ](#) - a 2.2uF 450V 125C capacitor in a J-lead 2220 package - resulting in a decoupling capacitance of 5uF with a voltage rating of 1800V. A rough estimate of voltage droop on the high frequency decoupling capacitors during a switching transition can be derived by calculating the amount of charge provided by the DC bus during the transition. This estimate is conservative as it assumes no charge is provided by the bulk capacitor bank. A datasheet for a similar [1700V module](#) from Cree is used to give rough approximations of quantities of interest. Total capacitive charge from 300A Ids to 900V Vds for this module is 4.7uC, which includes reverse recovering of the diode and output capacitance of the device. Another 700V Vds to 1600V at 2.5nF Coss adds another 1.75uC. Finally if we assume the transition lasts 200ns (very

conservative) and the peak output current is 255A, this adds another 51uC. A total charge of 58uC off of 5uF yields a worst case voltage droop of 11.5V. Of course this ignores inductance between the module and the high frequency decoupling capacitors, but gives some confidence around the capacitor’s ability to decouple the bus during the switching transitions.

The FIT rate of X7R ceramic capacitors (given by another manufacturer) are more than two orders of magnitude better than the film capacitors:



95% confidence in 80,000 hours of operation requires a total FIT rate lower than 462. For 3 * 4 * 9 = 108 individual capacitors this implies an individual FIT rate of 4.3. This can be achieved by operating at 66% of rated voltage just below 100C.

Current Sensors

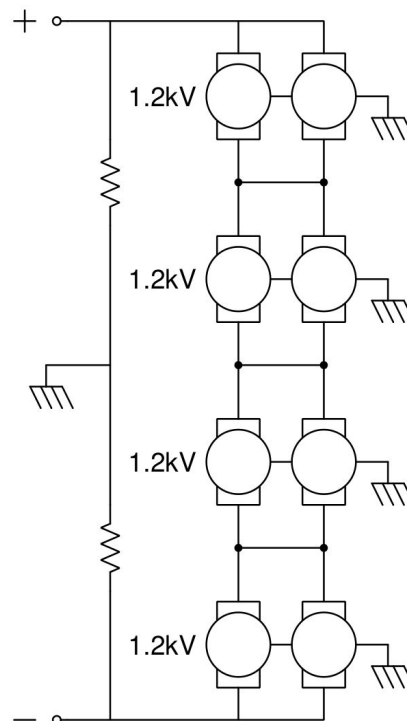
Two current sensors are required to determine the state of the current in the three phase machine. In practice, for redundancy and diagnostics, four current sensors are used: three for AC motor phases and one for the DC bus current. The controller predicted max sinusoidal output current is 255Apk, so the three AC current sensors must be rated for 180Arms and 400Apk. The controller predicted max DC bus current is 141ADC so any sensor selected for the AC measurement will be fine for use on the DC bus. Potential current sensors that meet these bare requirements were compiled here [internal ref].

A few particularly well suited sensors were highlighted on the basis of max operating temperature, bandwidth, and physical size. Of the selected sensors the lowest bandwidth is 30kHz with a response time of 10 μ s. A quick comparison of the max motor electrical frequency, $260 / (2 * \pi) * 15 = 620\text{Hz}$, and the current controller bandwidth, 1.5kHz, yields at least an order of magnitude between the frequencies of interest and the minimum sensor bandwidth. In addition, a response time of 10 μ s would yield a current rise of 160A assuming 1600V across 100 μ H, an inductance an order of magnitude below the actual YASA motor phase inductance of 1mH. This additional current would be unlikely to damage the SiC module before the fault could be detected and the module shutdown.

The exact current sensor chosen will depend on mechanical layout and packaging.

Chassis Grounding

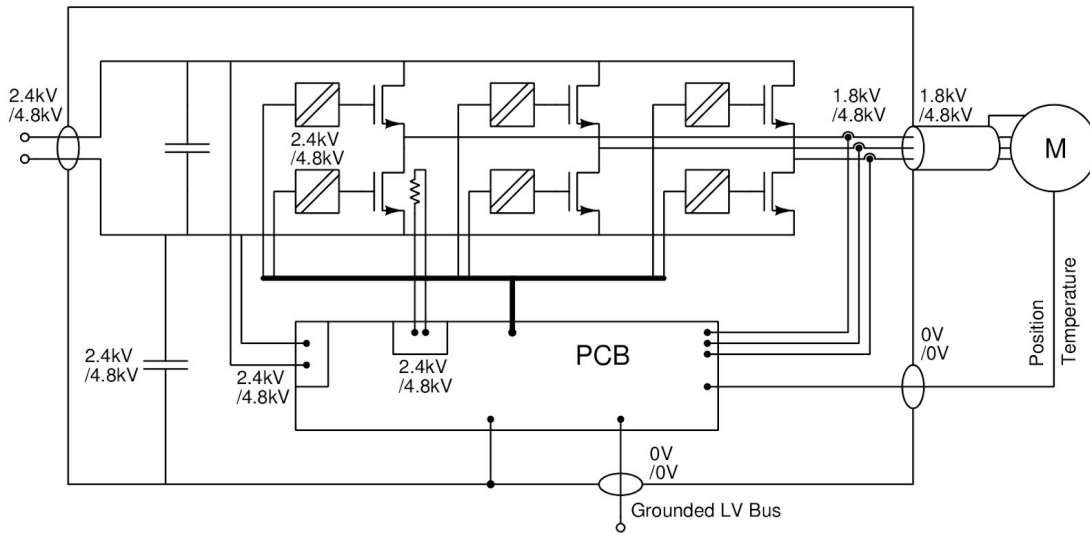
It is a goal of this design to allow the enclosure of the motor and the motor controller to be tied to the carbon ground of the wing. The schematic below illustrates the situation during max tether voltage operation (four stack generation):



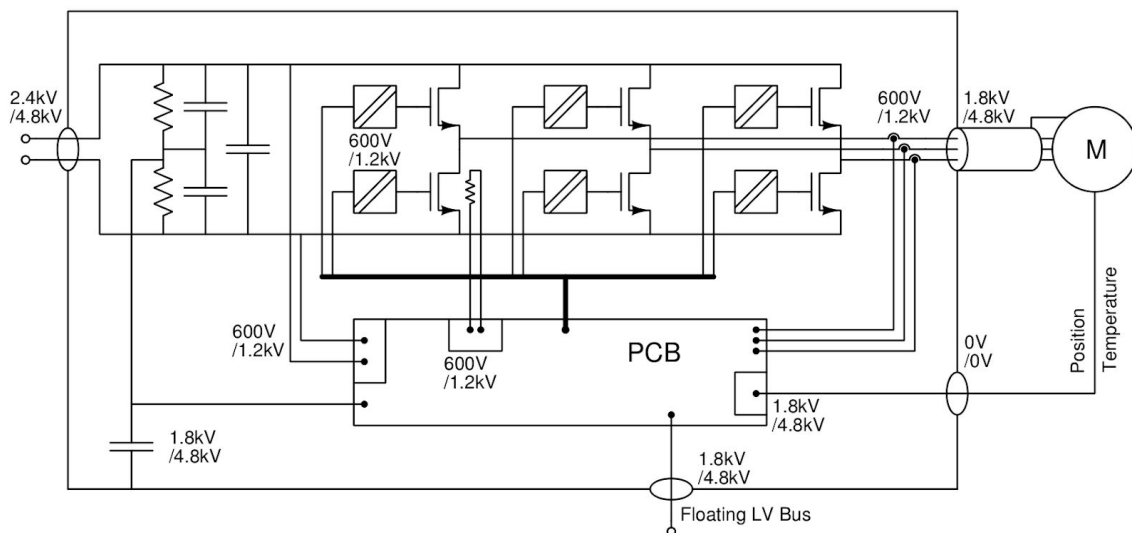
There is a decision to be made concerning to what potential the motor controller control PCB should be referenced. There are two options:

1. Referencing PCB ground to motor controller chassis, motor chassis, and carbon ground.
2. Referencing PCB ground to motor controller DC bus midpoint.

The two options are illustrated in a cartoon schematic below. Every relevant interface is annotated with two numbers (e.g. 2.4kV / 4.8kV). The first number indicates the voltage to use when designing the creepage distance. The second number indicates the voltage to use when designing the clearance distance. During normal operation the average voltage stress on the interface will be the first number, but during a wing or motor controller isolation fault the peak voltage stress could be up to the second number.



Ground Referenced PCB



DC Bus Referenced PCB

- Ground Referenced PCB
 - Advantages
 - PCB mounting simplified.
 - PCB heat-sinking simplified.

- No / Low isolation required on LV bus.
- Disadvantages
 - Gate drivers require 4x isolation (6 instances).
 - Current sensors need higher isolation.
 - RTD and DC bus circuits need higher isolation.
- DC Bus Referenced PCB
 - Advantages
 - Lower isolation gate drivers (6 instances).
 - Lower isolation current sensors.
 - Lower isolation RTD and DC bus circuits.
 - Possibly better CM noise environment.
 - Disadvantages
 - PCB mounting more difficult.
 - PCB heat-sinking more difficult.
 - High isolation required on LV bus.
 - High isolation required for motor interface.

The comparison between these two approaches is rather subjective, however it is the requirement of six instances of 2.4kV / 4.8kV gate drivers and four instances of 1.8kV / 4.8kV current sensors that stands out as a problem. As designers we have more control over the heat sinking and mounting of the PCB compared to the gate driver and current sensors where we are dependent on component availability. The issue of passing a floating (1.8kV / 4.8kV) LV bus through a grounded connector could be addressed by incorporating the isolated LV->12V converter as a “wort” on the motor controller allowing us greater control of the creepage and clearances.

CM Decoupling Capacitors

As the bulk energy storage film capacitors will be implemented as a series connection of two capacitors, a capacitively coupled midpoint to the DC bus is already present (the X capacitor bank doubles as the Y capacitors). The remaining requirement then is to capacitively couple this mid point to the chassis. In normal operation the chassis voltage relative to the chassis is maximum 1.8kV but during a fault of carbon ground to one side of the tether it could be up to 4.8kV. No reasonable capacitors exist for 4.8kV voltage rating, so a series connection will be used here as well. Selecting two 2kV series capacitors results in a short-term voltage of 1.2 times the rated voltage during a worst case fault. If we limit the search to capacitors with the same outline as the bulk energy capacitors (to aid layout) the maximum capacitance per capacitance is 750nF (MKP385475200JPP5T0). With a resulting series capacitance of 375nF. Current common-mode parasitic capacitance is around 2nF. For a worst case bus voltage of 1600V, this implies a 8.5Vpk-pk common-mode voltage swing.

Impedance Grounding Considerations

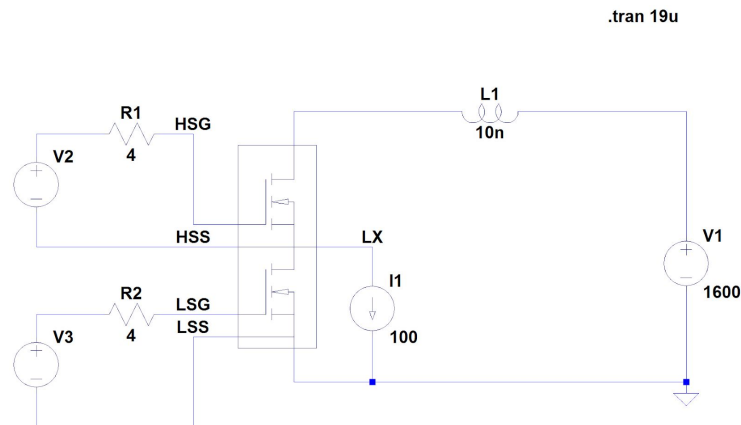
A detailed writeup explaining the implications of several different approaches of impedance grounding as well as a recommendation is contained in the following document [internal ref].

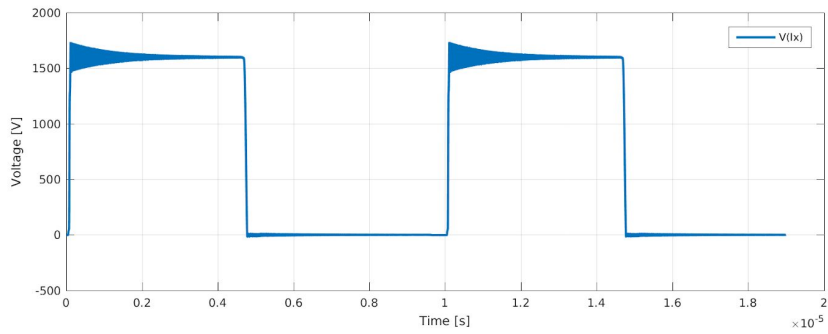
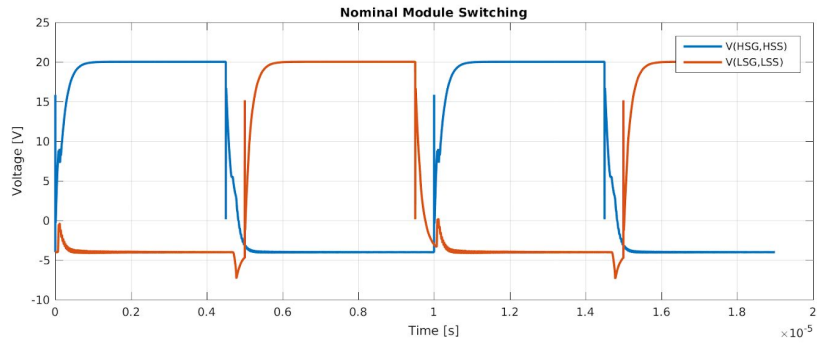
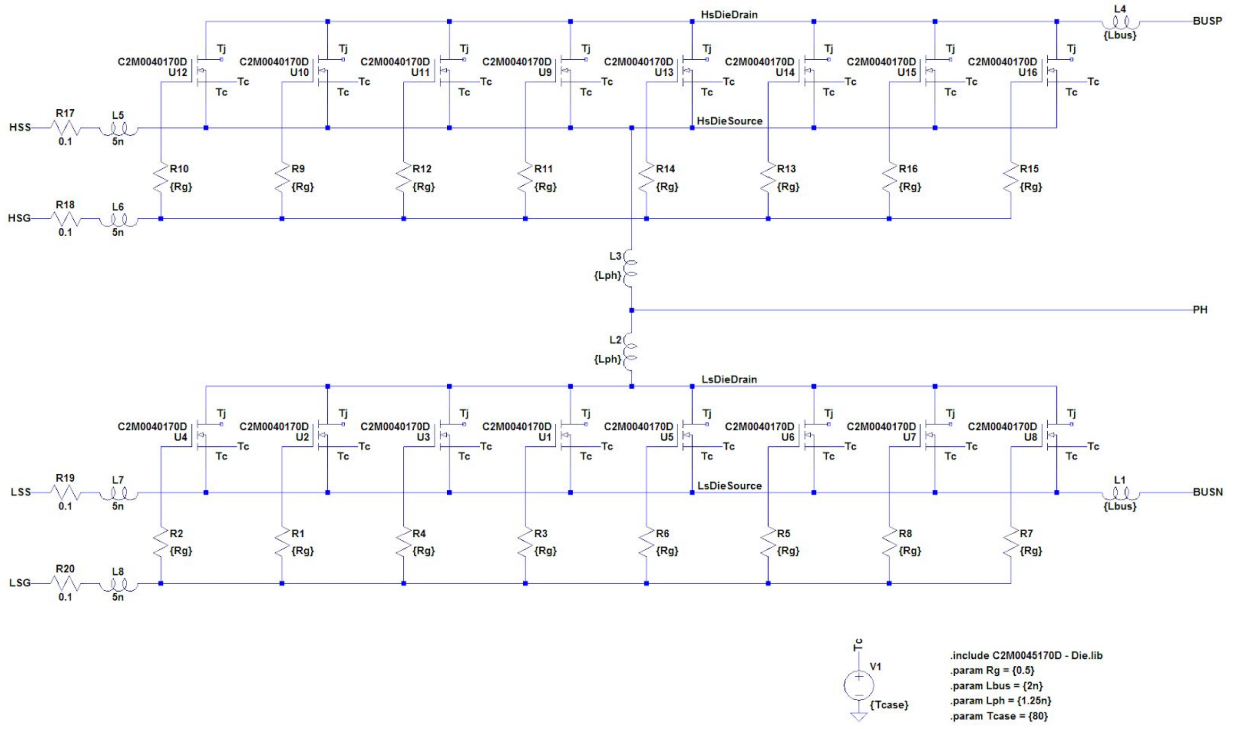
Gate Driver Design

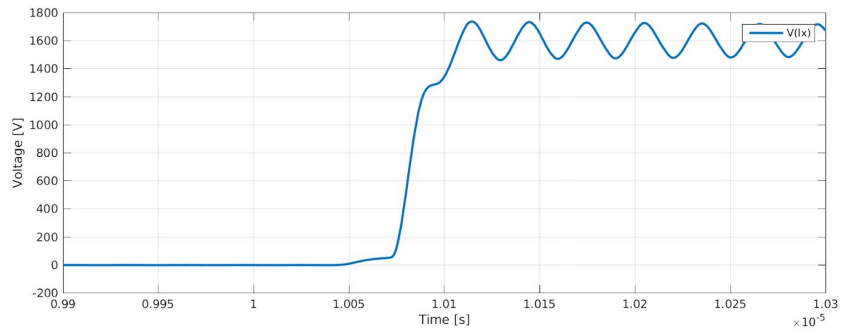
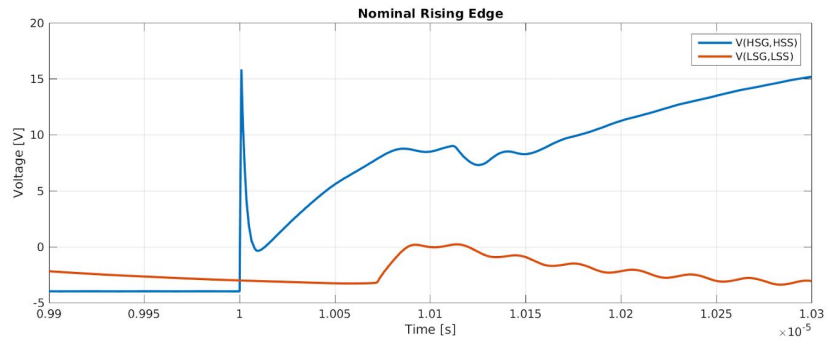
The new 1700V modules require +15/-4V drives as opposed to +20/-4V. Accordingly the UVLO is dropped from 21V to 16V. These are the only two changes to the basic gate driver design. The current isolated power supply and opto isolator will readily support the higher peak and working voltages of the Ozone controller.

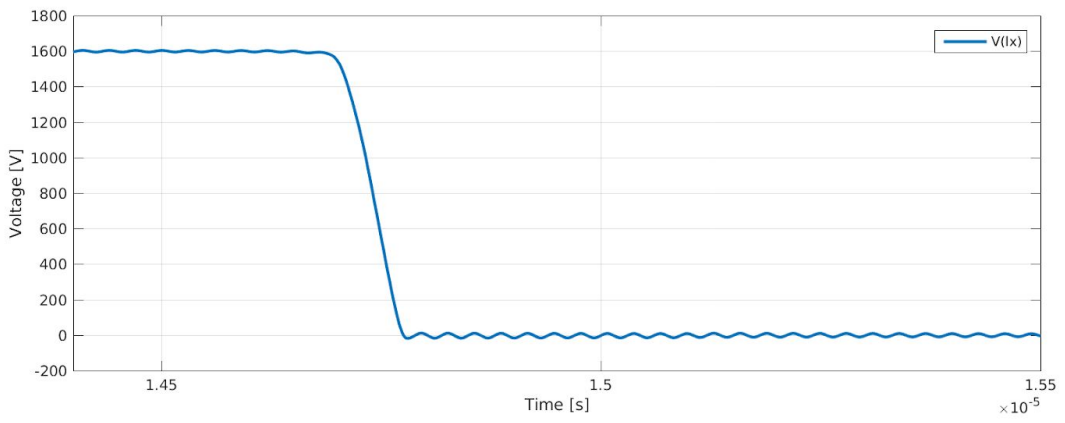
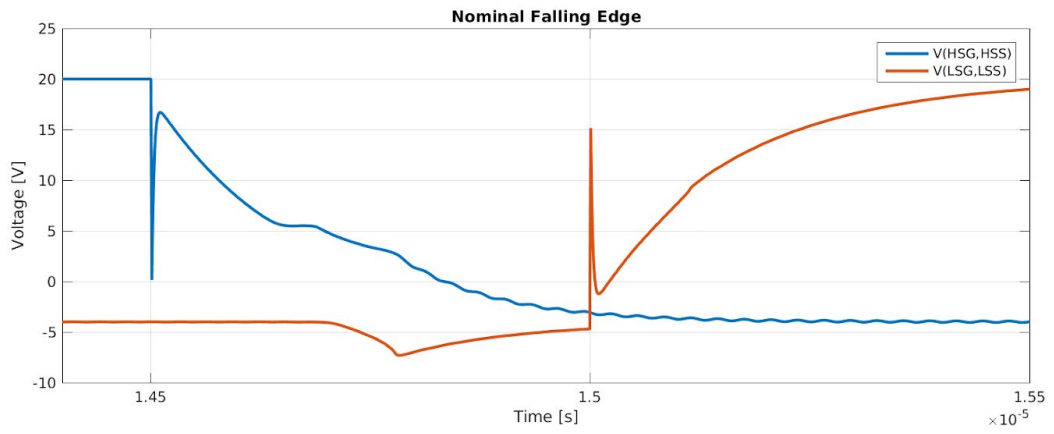
Desaturation Detection

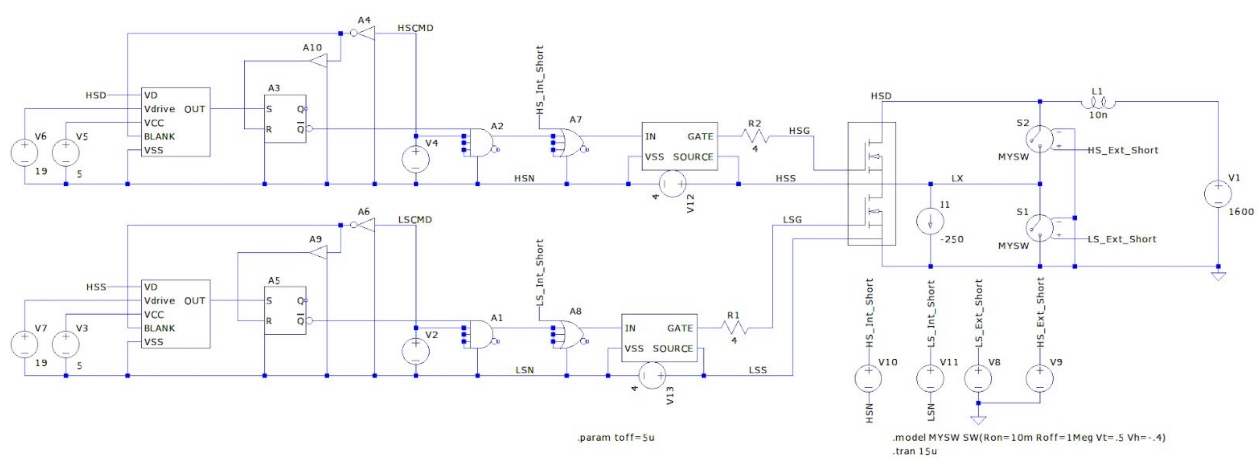
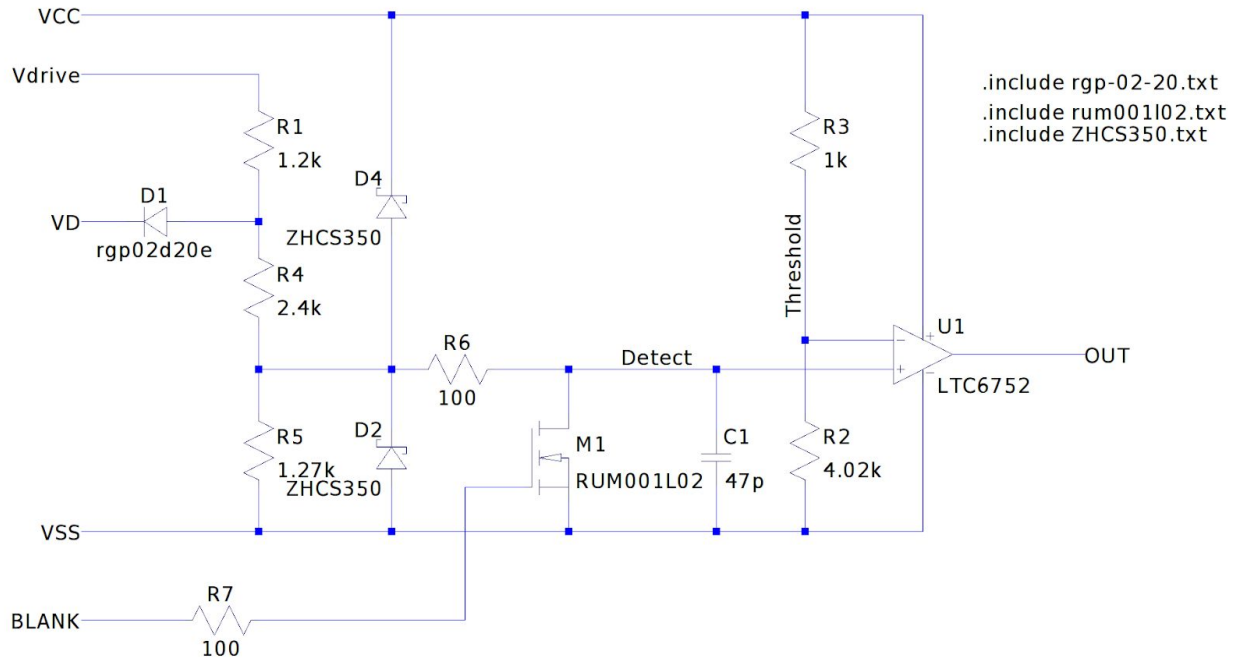
Desaturation detection is an attempt to protect the SiC modules from accidental shorts. The desaturation detection circuitry can only turn off the SiC device and can be completely disabled allowing the gate driver to function without this functionality.



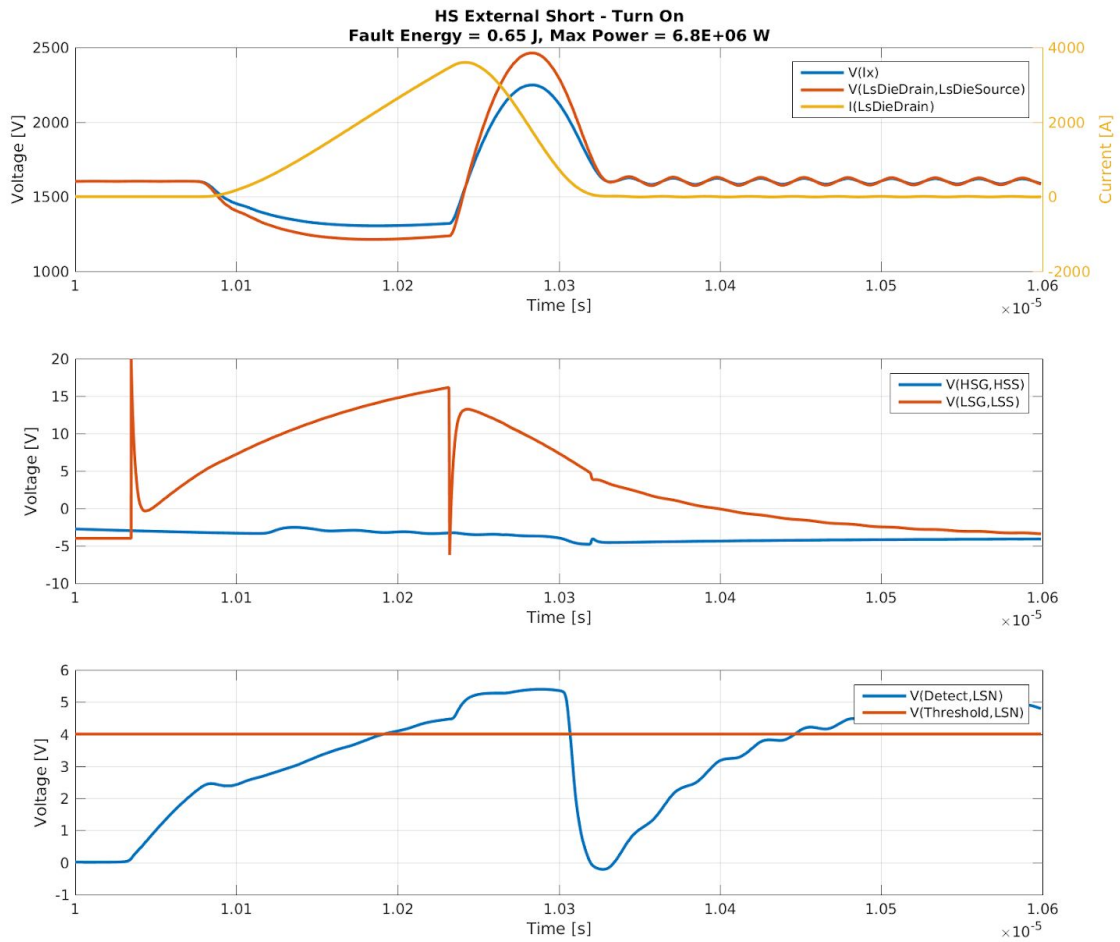


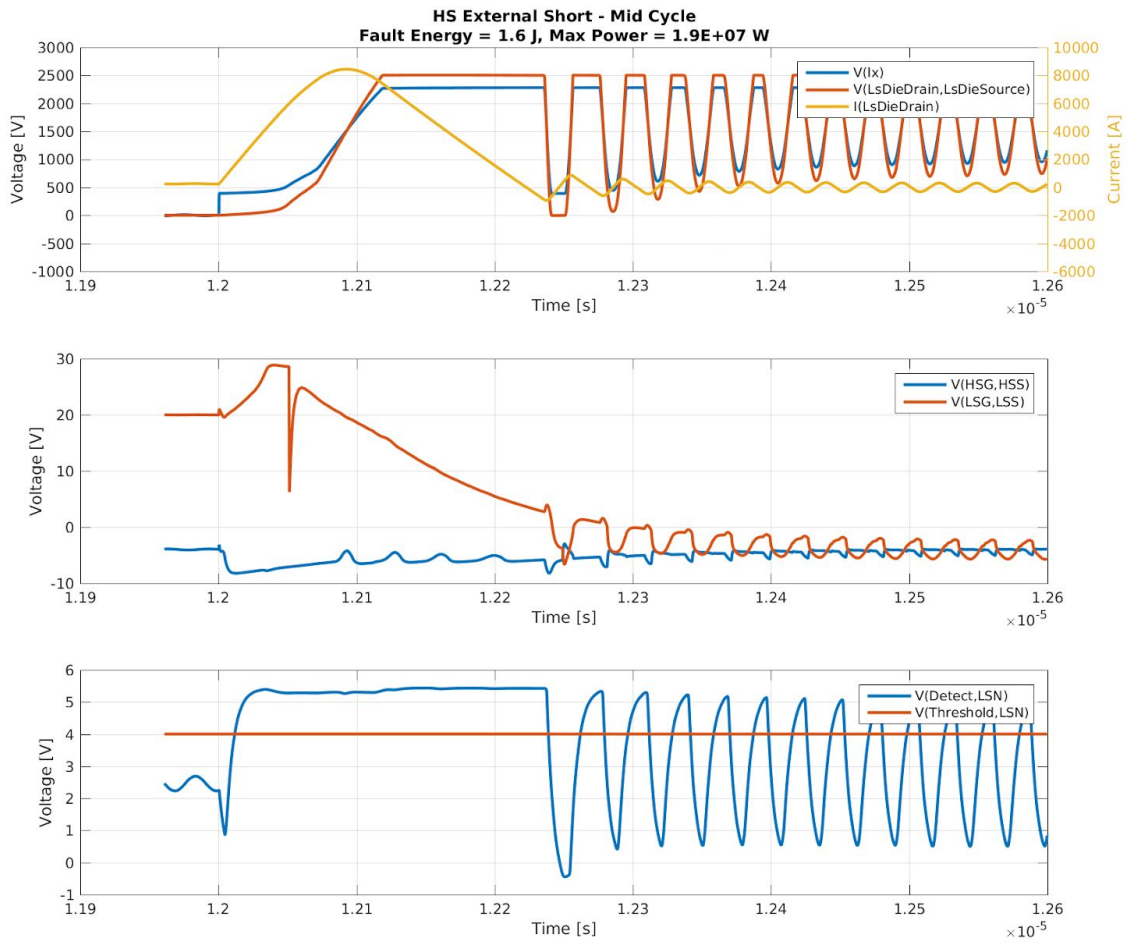


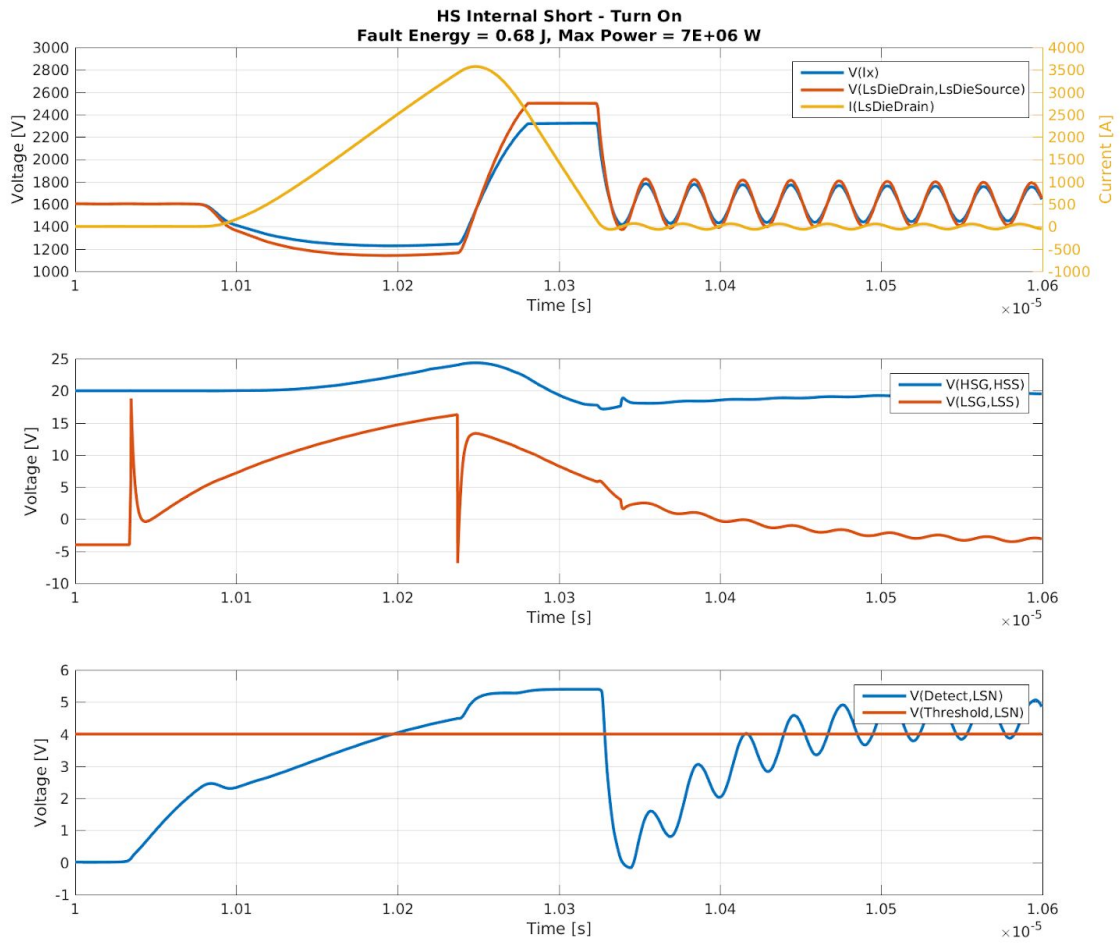


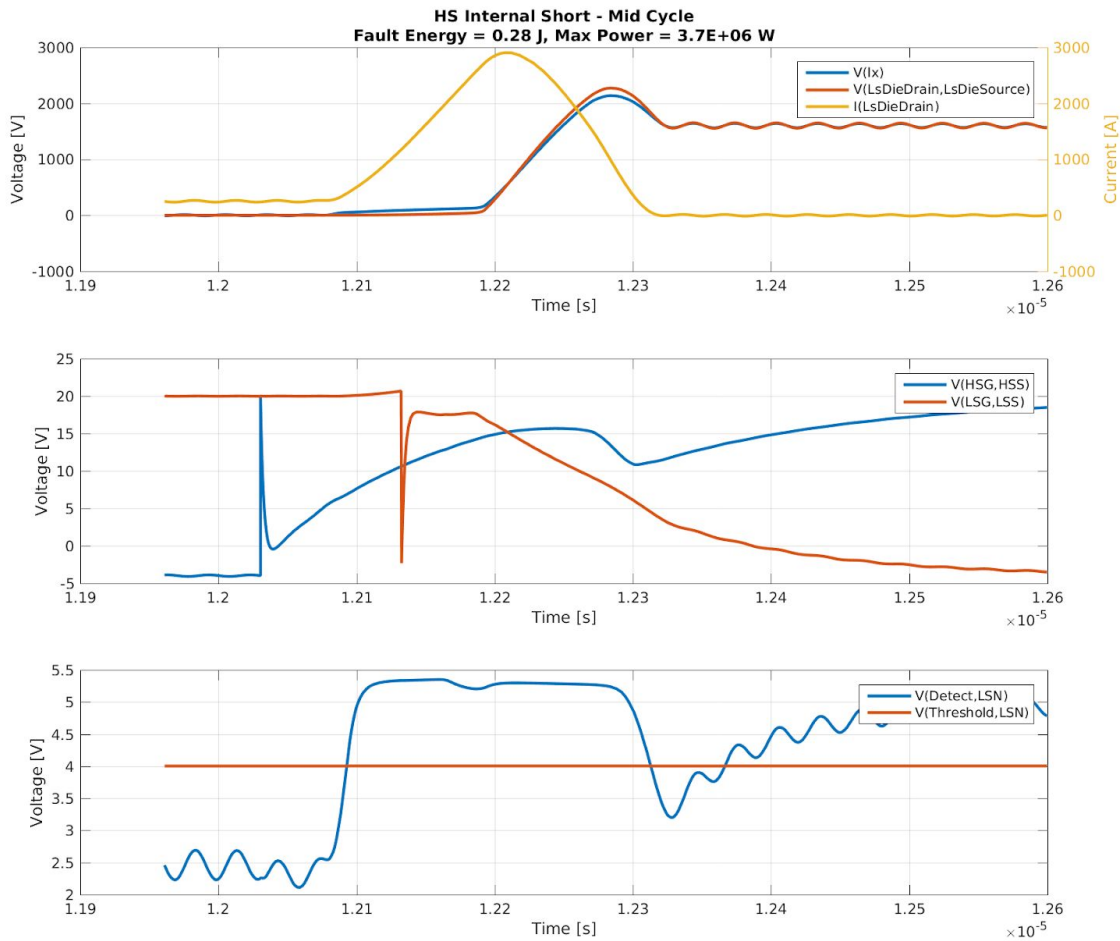


Rated pulse current of old generation 1700V die is 160A. At 8 devices in parallel that implies a 1280A rating.









Internal Wiring Harnesses

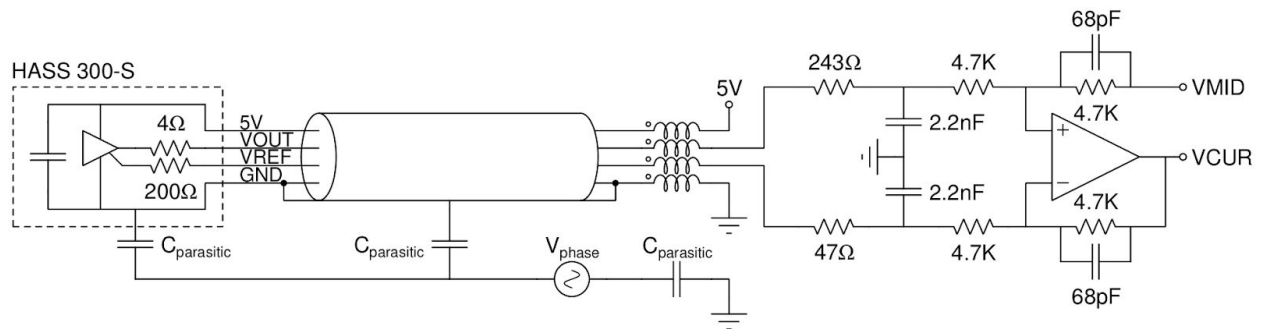
The internal wiring harness for internal and external connections is documented here [internal ref].

Main PCB Design

Current Sensor Input Circuitry

The four HASS 300-S current sensors are remotely located and a cable harness connects them to the main PCB. The sensor is supplied 5V from the main PCB and outputs two signals: VREF (nominally 2.5V) about which VOUT is centered at zero current. The main concern for this design is capacitive noise coupling from the phase node busbars (which run directly through the

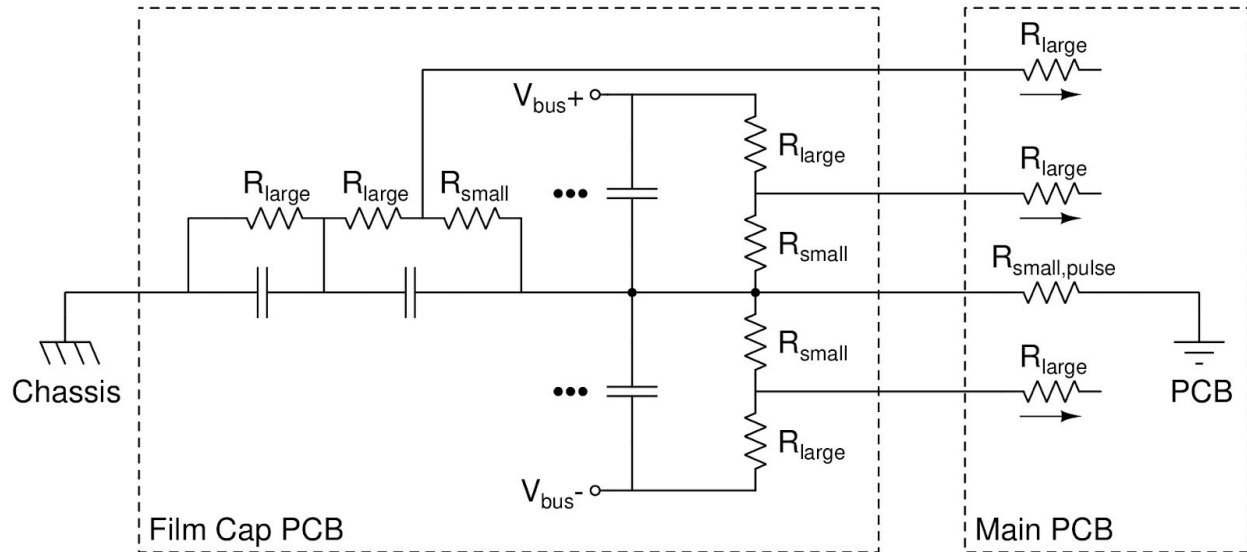
sensor) to the sensor and associated cabling. The diagram below shows the current sensor, cabling, input circuitry, and offending noise source.



A common-mode (CM) choke and capacitor are used to passively attenuate CM noise coupled from the phase node. The asymmetric input resistors are used to balance the asymmetric output impedances of the sensor. This approach is centered around collecting all noise coupling to the sensor ground so that VREF and VOUT move together. To this end, a shielded cable with drain wire has been selected. The drain wire will act as the GND conductor. The difference amplifier has been designed with a 2nd-order cutoff frequency of 250kHz and a gain slightly less than one. With a full-scale ADC reference of 3V, this circuit will provide linear current measurements +/- 750A with a resolution of 350mA / bit.

Bus and Chassis Voltage Measurement

The motor controller is interested in three voltage measurements: the DC bus differential voltage, the DC bus to chassis common-mode voltage, and the DC bus to PCB ground common-mode voltage. The DC bus differential voltage is used for motor control and stack voltage balancing, but the other two measurements are used purely to detect voltage isolation problems. The diagram below shows the basics of the approach used for voltage measurement.



The balancing resistors double as half of a voltage divider. The dividers are placed on the film capacitor PCB so that the cable connecting to the main PCB only sees low voltage (<50V). The PCB ground is not connected directly to the bus mid point but rather through a low value (<1kOhm) pulse resistor so that if the PCB shorts to the positive or negative bus, the energy in half of the bus capacitors is dissipated in a reasonable way.

Mechanical Design

Creepage and Clearance

Creepage and clearance distances are derived by the UL840 standard and are dependent of pollution degree:

9.3 Pollution degrees based on the presence of contaminants and possibility of condensation or moisture at the creepage distance are as follows:

- Pollution Degree 1 – No pollution or only dry, nonconductive pollution. The pollution has no influence.
- Pollution Degree 2 – Normally, only nonconductive pollution. However, a temporary conductivity caused by condensation may be expected.
- Pollution Degree 3 – Conductive pollution, or dry, nonconductive pollution that becomes conductive due to condensation that is expected.
- Pollution Degree 4 – Pollution that generates persistent conductivity through conductive dust or rain and snow.

This design will assume a **pollution degree 2**.

Clearance is defined as the shortest distance in air between two conductors and recommended distances are given based on equipment type:

Table 8.1
Minimum clearances for equipment^a

Phase-to-ground ^b rated system voltage (rms and dc)				Rated impulse withstand voltage peak, kV ^d	Clearance, mm ^e			
Overvoltage category ^c					Pollution degree ^f			
I	II	III	IV		1	2	3	4
50	–	–	–	0.33	0.01	0.2	0.8	1.6
100	50	–	–	0.50	0.04	0.2	0.8	1.6
150	100	50	–	0.80	0.10	0.2	0.8	1.6
300	150	100	50	1.5	0.5	0.5	0.8	1.6
600	300	150	100	2.5	1.5	1.5	1.5	1.6
1000	600	300	150	4.0	3.0	3.0	3.0	3.0
1500	1000	600	300	6.0	5.5	5.5	5.5	5.5
–	1500	1000	600	8.0	8.0	8.0	8.0	8.0
–	–	1500	1000	12.0	14.0	14.0	14.0	14.0
–	–	–	1500	16.0	19.4	19.4	19.4	19.4

^a The minimum values for pollution degrees 2, 3, and 4 are premised on the concept that pollution which may be present in these micro-environments may bridge small clearances.

^b For ungrounded systems or systems with one phase grounded, the phase-to-ground voltage is considered to be the same as the phase-to-phase voltage for the purposes of using this table.

^c Typical examples of categories for products are given below. Users of this standard will need to establish that rated impulse voltage values are appropriate for the expected applications of the products covered.

Category IV – Primary Supply Level. Overhead lines and cable systems including distribution and its associated overcurrent protective equipment (equipment installed at the service entrance).

Category III – Distribution Level. Fixed wiring and associated equipment (not electrical loads) connected to the primary supply level, Category IV.

Category II – Load Level. Appliances and portable equipment and the like connected to the distribution level, Category III.

Category I – Signal Level. Special equipment or parts of equipment such as low-voltage electronic logic systems, remote controls, signaling and power limited (per NEC Article 725) circuits connected to the load level, Category II.

^d Value to use based on the rating of the overvoltage protection means.

^e Linear interpolation of the values is permitted.

^f See 9.3.

It is unclear exactly in which category type this design fits, and the specification does not include the highest voltages in our system. IEC 60664-1 seems to be more clear:

Table F.7 – Clearances to withstand steady-state voltages, temporary overvoltages or recurring peak voltages

Table F.7a – Dimensioning of clearances to withstand steady-state voltages, temporary overvoltages or recurring peak voltages

Table F.7b – Additional information concerning the dimensioning of clearances to avoid partial discharge

Voltage ¹⁾ (peak value) ²⁾ kV	Minimum clearances in air up to 2 000 m above sea level		Voltage ¹⁾ (peak value) ²⁾ kV	Minimum clearances in air up to 2 000 m above sea level
	Case A Inhomogeneous field conditions (see 3.15) mm	Case B Homogeneous field conditions (see 3.14) mm		Case A Inhomogeneous field conditions (see 3.15) mm
0.04	0,001 ³⁾	0,001 ³⁾	0.04	As specified for case A in Table F.7a
0.06	0,002 ³⁾	0,002 ³⁾	0.06	
0.1	0,003 ³⁾	0,003 ³⁾	0.1	
0.12	0,004 ³⁾	0,004 ³⁾	0.12	
0.15	0,005 ³⁾	0,005 ³⁾	0.15	
0.20	0,006 ³⁾	0,006 ³⁾	0.2	
0.25	0,008 ³⁾	0,008 ³⁾	0.25	
0.33	0.01	0.01	0.33	
0.4	0.02	0.02	0.4	
0.5	0.04	0.04	0.5	
0.6	0.06	0.06	0.6	
0.8	0.13	0.1	0.8	
1.0	0.26	0.15	1.0	
1.2	0.42	0.2	1.2	
1.5	0.76	0.3	1.5	
2.0	1.27	0.45	2.0	
2.5	1.8	0.6	2.5	2.0
3.0	2.4	0.8	3.0	3.2
4.0	3.8	1.2	4.0	11
5.0	5.7	1.5	5.0	24
6.0	7.9	2	6.0	64
8.0	11.0	3	8.0	184
10	15.2	3.5	10	290
12	19	4.5	12	320
15	25	5.5	15	3)
20	34	8	20	
25	44	10	25	
30	55	12.5	30	
40	77	17	40	
50	100	22	50	
60		27	60	
80		35	80	
100		45	100	

¹⁾ The clearances for other voltages are obtained by interpolation.
²⁾ See Figure 1 for recurring peak voltage.
³⁾ These values are based on experimental data obtained at atmospheric pressure.

¹⁾ The clearances for other voltages are obtained by interpolation.
²⁾ See Figure 1 for recurring peak voltage.
³⁾ Dimensioning without partial discharge is not possible under inhomogeneous field conditions.

This design will require hold-off of several different potentials. They are listed below along with the required clearance distance.

Voltage [Vpk]	Clearance [mm]	Note
1600	5	Maximum Bus Voltage
4800	12	Worst-Case Chassis to Bus
4107	10	Worst-Case Chassis to PCB
1452	4	Worst-Case PCB to Bus

Creepage is defined as the path along any surface between two conductors. UL lists distances based on pollution degree and material type. Almost any material you encounter is type IIIa or IIIb.

Table 9.1
Minimum acceptable creepage distances^w

Operating voltage, volts ac rms or dc ^z	Creepage distances for equipment subject to long-term stress, mm										
	Pollution degree 1	Pollution degree 2			Pollution degree 3				Pollution degree 4		
		All material groups	Material group ^x			Material group ^x				Material group ^x	
	I		II	IIIa,b	I	II	IIIa	IIIb	I	II	IIIa
10	0.08	0.4	0.4	0.4	1.0	1.0	1.0	1.0	1.6	1.6	1.6
12.5	0.09	0.42	0.42	0.42	1.05	1.05	1.05	1.05	1.6	1.6	1.6
16	0.1	0.45	0.45	0.45	1.1	1.1	1.1	1.1	1.6	1.6	1.6
20	0.11	0.48	0.48	0.48	1.2	1.2	1.2	1.2	1.6	1.6	1.6
25	0.125	0.5	0.5	0.5	1.25	1.25	1.25	1.25	1.7	1.7	1.7
32	0.14	0.53	0.53	0.53	1.3	1.3	1.3	1.3	1.8	1.8	1.8
40	0.16	0.56	0.8	1.1	1.4	1.6	1.8	1.8	1.9	2.4	3.0
50	0.18	0.6	0.85	1.2	1.5	1.7	1.9	1.9	2.0	2.5	3.2
63	0.2	0.63	0.9	1.25	1.6	1.8	2.0	2.0	2.1	2.6	3.4
80	0.22	0.67	0.95	1.3	1.7	1.9	2.1	2.1	2.2	2.8	3.6
100	0.25	0.71	1.0	1.4	1.8	2.0	2.2	2.2	2.4	3.0	3.8
125	0.28	0.75	1.05	1.5	1.9	2.1	2.4	2.4	2.5	3.2	4.0
160	0.32	0.8	1.1	1.6	2.0	2.2	2.5	2.5	3.2	4.0	5.0
200	0.42	1.0	1.4	2.0	2.5	2.8	3.2	3.2	4.0	5.0	6.3
250	0.56	1.25	1.8	2.5	3.2	3.6	4.0	4.0	5.0	6.3	8.0
320	0.75	1.6	2.2	3.2	4.0	4.5	5.0	5.0	6.3	8.0	10.0
400	1.0	2.0	2.8	4.0	5.0	5.6	6.3	6.3	8.0	10.0	12.5
500	1.3	2.5	3.6	5.0	6.3	7.1	8.0	8.0	10.0	12.5	16.0
630	1.8	3.2	4.5	6.3	8.0	9.0	10.0	10.0	12.5	16.0	20.0
800	2.4	4.0	5.6	8.0	10.0	11.0	12.5	y	16.0	20.0	25.0
1000	3.2	5.0	7.1	10.0	12.5	14.0	16.0	y	20.0	25.0	32.0
1250	4.2	6.3	9.0	12.5	16.0	18.0	20.0	y	25.0	32.0	40.0
1600	5.6	8.0	11.0	16.0	20.0	22.0	25.0	y	32.0	40.0	50.0
2000	7.5	10.0	14.0	20.0	25.0	28.0	32.0	y	40.0	50.0	63.0
2500	10.0	12.5	18.0	25.0	32.0	36.0	40.0	y	50.0	63.0	80.0
3200	12.5	16.0	22.0	32.0	40.0	45.0	30.0	y	63.0	80.0	100.0
4000	16.0	20.0	28.0	40.0	50.0	56.0	63.0	y	80.0	100.0	125.0
5000	20.0	25.0	36.0	50.0	63.0	71.0	80.0	y	100.0	125.0	160.0
6300	25.0	32.0	45.0	63.0	80.0	90.0	100.0	y	125.0	160.0	200.0
8000	32.0	40.0	56.0	80.0	100.0	110.0	125.0	y	160.0	200.0	250.0
10000	40.0	50.0	71.0	100.0	125.0	140.0	160.0	y	200.0	250.0	320.0

^w Linear interpolation of the values is permitted.
^x See 9.2.

Special creepage distances are given for PCBs:

Table 9.2
Minimum acceptable creepage distances on printed wiring boards^{a,d}

Operating voltage, volts ac rms or dc	Minimum creepage, mm	
	Pollution degree	
	1 ^b	2 ^c
10 – 50	0.025	0.04
63	0.04	0.063
80	0.063	0.1
100	0.1	0.16
125	0.16	0.25
160	0.25	0.4
200	0.4	0.63
250	0.56	1.0
320	0.75	1.6
400	1.0	2.0
500	1.3	2.5
630	1.8	3.2
800	2.4	4.0
1000	3.2	5.0

^a Use Table 9.1 for pollution degrees 3 and 4.
^b Material Groups I, II, IIIa, IIIb.
^c Material Groups I, II, IIIa. For Material Group IIIb use Table 9.1.
^d Linear interpolation of the values is permitted.

Some creepage voltages and distances relevant to this design are listed below:

Voltage [Vpk]	Creepage [mm]	Note
1200	6 (PCB), 12	Working Voltage DC bus
1800	18	Working Voltage phase to chassis
2400	24	Working Voltage DC bus to chassis
640	3.5 (PCB), 6.5	Working Voltage DC Bus to PCB
1760	18	Working Voltage PCB to chassis

Mechanical Design Goals

Reflecting from the current design there are several aspects that this design will address and focus on:

- Sound mechanical constraint of components in high vibration and G environment.
 - Minimize mass attached to SiC module tabs.
 - Decouple mechanical and electrical connections.
 - Gate drive to module.
 - Gate drive to main PCB.
- Heat sink temperature sensitive / heat generating components.
 - Keep components cool by sinking to chassis rather than box air.
 - Keep air cool by rejecting more heat directly out of the chassis.
 - Components to cool:
 - Bulk decoupling film capacitors.
 - Main PCB.
 - Gate driver isolated supply.
 - Current sensor (if closed loop)
- Easy and quick assembly with manufacturable components.
- Easy connect and disconnect from HV cables.
 - Shielded AC cables.
 - Un-shielded DC cables.

There are many individual components that must be successfully integrated into the packaging for this design. Below is an overview of the necessary components:

- SiC modules 3x
- Current sensors 4x
- AC busbars and termination w/shield 3x
- DC busbars and termination 2x
- High frequency decoupling capacitors 3x
- Bulk decoupling capacitors 1x
- Chassis decoupling capacitors 1x
- Gate drivers 3x
- Main PCB 1x
- Motor interface connector and harness 1x
- Wing interface connector and harness 1x
- 80V -> 12V converter 1x

Design Review Questions And Responses

- What does an IGBT solution look like compared to SiC?
 - Comparing a recently released [300A 1700V IGBT Infineon](#) module in the same package as a [Cree 300A 1700V SiC](#) module.
 - IGBT Esw = 193mJ, SiC Esw = 23mJ => 8.4x decrease.
 - IGBT Vce,sat = 2.45V, SiC Vds = 5V => 2x increase.
 - Without utilizing increased temperature operation => ~4x decrease in loss.
 - This also assumes you could use a 1700V IGBT at 1600V Vbus - probably not => even worse losses for 2.5kV IGBT.
- Check on the difference of X7T vs. X7R capacitors.
 - X7T has a capacitance tolerance over temperature of +22%/-33% vs. +/-15% for X7R.
 - The TDK tech document mentions that despite the slightly greater variation in capacitance over temperature, X7T still retains the high reliability characteristics of X7R.
 - 67% of 5uF is 3.35uF and would imply a 16V droop vs. 11V droop at 5uF.
- Do AEC-Q200 (automotive) rated capacitors undergo mechanical vibration testing?
 - [AEC-Q200 revD](#) specifies vibration and mechanical shock testing.
 - Mechanical Shock - [MIL-STD-202](#) Method 213 - Table 1 of Method 213 SMD - Condition F (1500g peak) LEADED: Condition C (100g peak)
 - Vibration - [MIL-STD-202](#) Method 204 - 5g's for 20 min., 12 cycles each of 3 orientations Note: Use 8"X5" PCB .031" thick 7 secure points on one long side and 2 secure points at corners of opposite sides. Parts mounted within 2" from any secure point. Test from 10-2000 Hz.
- Can we place the bus current sensor between high frequency capacitors and bulk energy storage capacitors to detect shoot-through conditions and protect SiC Module?
 - The abs. max pulse current rating of this [Cree 300A 1700V SiC](#) is 900A. The fastest current sensors have a 3us response time. With a 1200V bus voltage this would require $1200 / 900 * 3e-6 = 4\mu\text{H}$ of inductance between the module and capacitor bank.
 - Another way to think about this is to assume a very poor inductance between the module and capacitance bank of 200nH. This implies a pulse current of $1200 / 200e-9 * 3e-6 = 18\text{kA}$.
 - I believe detecting shoot through via a current sensor before module damage will prove difficult.

Makani Telemetry Users' Guide

The Makani Simulator and Flight Controller produce telemetry which can be interpreted in real-time using the visualizer and flight monitors, and stored for later analysis in log files in the hdf5 format. The telemetry log files are the primary vehicle for analyzing and debugging the system. While most signals of interest are already available in the telemetry, adding new signals is easy to do if required. The flight controller logs produced in simulation and in real flight operation are identical in format.

This document serves as a quick introduction and reference to some of the more commonly used telemetry signals. After running a simulation, this guide will help you quickly locate and plot signals of interest.

Sources of Code and Data

After the shutdown of Makani, we have released a final snapshot of the complete software repository and a representative collection of flight data log files. These may be obtained from the following URLs.

Makani public software release	https://github.com/google/makani
Makani public flight data release	https://console.cloud.google.com/marketplace/details/makani-flight-logs

Introduction to the Telemetry Structure

All of the avionics nodes in the system send asynchronous messages in the AIO format over the network.¹ Makani log files are constructed by first simply recording the network traffic using tcpdump forming a packet capture (pcap) file. This pcap file is then converted to the format hdf5, which presents an interface with aspects both of a hierarchical tree and of a time series. These data files can be easily inspected with MATLAB, Python, or in other environments. In Python the log file data presents a dictionary-like interface; in MATLAB, a struct. The use of tab-completion for exploring the structures is all-but-necessary.²

When running a simulation, the simulator and the flight controller also communicate using AIO messages. In a simulation, messages of type SimSensorsMessage contain ersatz sensor data sent from the simulator to the flight controller. The simulator also broadcasts the true values of

¹ The avionics network and message format is described in "A Low-Cost Fiber Optic Avionics Network for Control of an Energy Kite" by Kurt Hallamasek *et al*, also included in this volume.

² See `lib/python/ipython_completer.py` for tab-completion of HDF5 fields in Python. This add-on is a must-have.

the simulator state in the message `SimulatorTelemetry`. The flight controller sends its diagnostics in a message called `ControlTelemetry`, which is identical in format whether a flight is real or simulated.

For the purposes of flight analysis, most telemetry of interest is found in the `ControlTelemetry` sent by the flight controller, running on node `ControllerA`. This guide will focus on this control telemetry.

The ultimate source of truth regarding these data structures is the code itself. Indeed, I'm writing this document by referencing the source code; the intent is for the code to be self-documenting. Instructions for obtaining the code are included at the end of this document.

One small caution: when loaded in MATLAB, array structures in the log files tend to be transposed as compared to how they are loaded in Python, or how the data structures are represented in C. The major user-visible consequence of this is that all matrices loaded in MATLAB from the h5 file will be transposed.

<i>message type</i>	<i>file containing definition(s)</i>
Control Telemetry	control/control_telemetry.h
Simulator Telemetry	sim/sim_telemetry.h
Avionics messages (approximately 134 types)	avionics/common/avionics_messages.h

Structure of the Log Files

The log files are structured as a tree. Here we dive down into the tree to get the control telemetry, and in the process describe the general structure of the log file.

1. At the top level you'll find three fields:

- **bad_packets**. Data that could not be parsed.
- **messages**. The actual telemetry messages.
- **parameters**. All configured parameters, such as the wing mass, tether length, etc.

2. To get the telemetry, select **messages**. At the second level you will now find a list of nodes on the wing, such as **kAioNodeMotorPbi** (the port-bottom-inner motor controller, known as "PBI"), **kAioNodeServoE1** (one of the two servos driving the elevator), and **kAioNodeControllerA** (the primary flight controller).

3. Now select one of these nodes. Here we'll select **kAioNodeControllerA**, which runs the flight controller. Now, at the third level, you will now see a list of all the message types sent by the flight controller:

```
kMessageTypeControlSlowTelemetry kMessageTypeControllerCommand
kMessageTypeControlTelemetry kMessageTypeQ7SlowStatus
kMessageTypeControlDebug
```

Of these, **kMessageTypeControlTelemetry** and **kMessageTypeControlDebug** represent the control telemetry, at 10 Hz and at 100 Hz, respectively. If you're examining flight data, the higher rate data is only available from the wing recorder log, as the high-rate data is not sent over the radio link from kite to ground during a flight. These two message types are identical except for the rate at which they are sent. Select one of them.

4. Now at the fourth level, there are three fields:

- **capture header.** Contains the message timestamps in seconds plus microseconds since some epoch a long time ago (Jan 1, 1970 UTC), and the destination and source IP addresses. An array of: tv_sec, tv_usec, source_address, destination_address. This timestamp is made by the computer logging the data (a laptop running Debian Stretch Linux). The latency from transmission to logging should be sub-100ms and the absolute timestamp is probably good to better than 1s.
- **aio_header.** Makani's AIO ("avionics I/O") message header. An array of: version, source, type, sequence, timestamp.
- **message.** This is the actual telemetry message. A structured array.

5. Finally, select "**message**". Now you have the actual control telemetry messages, whose structure is described below.

Structure of the Control Telemetry

The Control Telemetry (once again, defined in control/control_telemetry.h, which should be your go-to reference) contains several things:

1. **control_input** All input values used by the controller, converted to real units and useful coordinate systems. This includes the air data (pitot-static), rotor speeds, flap positions, wind, ground station encoder values, etc.
2. **control output:** All output values from the controller. Rotor speed commands and commanded flap positions.
3. **state_est:** The estimated state of the wing, including position, attitude, velocity, angle of attack, sideslip, etc.
4. **flight_mode.** The current flight mode. (See table of values below.)

5. Telemetry from the various flight controllers (hover, trans-in, crosswind, off-tether), and from the inner workings of the estimator.

Coordinate Systems, Units, and Naming Conventions

The two main coordinate systems you will encounter are (described here **for reference only**, see the link to repo below for canonical source):

- **Body coordinates**, indicated with a `_b` suffix on telemetry field names. X is forward, Y is towards starboard, and Z is down.
- **Ground coordinates**, indicated with a `_g` suffix, where for RPX flights at China Lake, X points approximately west (269°) and Z is down. Here the minus x axis is aligned with the GS-to-kite radial. The origin is on the tower axis of symmetry, "at the base of the slewing bearing." For the Parker Ranch (Hawaii) and Offshore test sites, the ground coordinate system is NED.

Further details of these coordinate systems and others in use are documented in the file `control/coordinate_systems.md`.

Units

All angles are in radians. All quantities in the controller telemetry are in SI units (meters, meters/second, Pascals, radians, radians/sec, etc).

Filtered Values

Low-pass-filtered values are indicated with an `_f` suffix.

State Estimate

The estimated state of the system is stored in the `state_est` structure, which is of type `StateEstimate`, defined in `control/estimator/estimator_types.h`.

Some fields of interest are:

<i>field</i>	<i>units</i>	<i>description</i>
Xg	vector of meters	Wing position , in ground coordinates.
Vg	vector of m/s	Wing velocity , in ground coordinates, i.e. an estimate of the time derivative of Xg.
Vb	vector of m/s	Wing velocity, in body coordinates, i.e. $dcm_g2b \cdot Vg$.

Vb_f	vector of m/s	Wing velocity, in body coordinates, low-pass-filtered. The filter is defined in config/m600/control/estimator.py (see Vb_filter_a and Vb_filter_b) and currently consists of a 2nd order butterworth low-pass at 8.3 Hz.
Ag	vector of m/s ²	Wing acceleration , in ground coordinates
Ab_f	vector of m/s ²	Wing acceleration, in body coordinates, low-pass-filtered.
dcm_g2b	3×3 matrix	Attitude , expressed as the 3×3 rotation matrix that rotates ground coordinates into body coordinates. Use the Matlab function " dcm2angle " (from the Aerospace Toolbox) to convert this to roll/pitch/yaw Euler angles if desired. Remember that matrices will be transposed when loaded from h5 into MATLAB.
pqr	array of rad/s	Angular rates. P, q, and r are the rotation rates around the body x, y, and z axes (respectively), in rad/s, using the right-hand-rule.
tether_force_b	structure	Estimated force of the tether on the wing, in body coordinates. This structure has these fields: tension [N] - the total tension roll [radians] pitch [radians]
apparent_wind	structure	Structure containing the apparent wind estimate, both as a velocity vector in the body frame [m/s], and also in spherical coordinates (airspeed, alpha, and beta). The pitot probe dynamic pressure measurements are converted to airspeed using a hard-coded value of the mean density at this particular test site. Thus it is something between indicated airspeed and true airspeed. The intent is that apparent_wind be treated as a true airspeed directly comparable to the velocity measurements obtained from GPS and the inertial navigation system.
stacking_state		Indicates whether a motor has faulted and been taken out of the "stack."
acc_norm_f		Magnitude of the wing acceleration, low-pass filtered.
joystick		Joystick stick and switch positions.
perch_azi	rad	Direction the perch is pointed.

winch	structure	State of the winch
wind_g	structure	Vector, speed, and direction of wind, in ground coordinates, observed at the wind sensor on the ground station.
vessel	structure	State of the buoy (offshore only), including its position, velocity, attitude, and angular velocity. These states define the relationship of the vessel frame with respect to the ground frame.

Note on Loop Angle:

0 degrees = 9 o'clock = where we trans-in
 90 degrees = 6 o'clock = bottom of the loop
 → Loop angle decreases as we fly forward.

Control Input

The minimally-processed (but not completely raw) input to the controller is reported in the control_input field (of type ControlInput, defined in control/control_types.h).

<i>field</i>	<i>type or units</i>	<i>description</i>
imus	structure	Inertial measurement unit data, in body coordinates. There are three independent IMUs. The fields of this structure are: acc: acceleration vector (m/s ² , body coords) gyro: angular velocities mag: magnetic field measurement (Gauss)
pitots	structure of Pascals	Air data system. There is only one air data probe (aka Pitot tube), but the ports are plumbed to two separate sets of sensors: one high-sensitivity, low-range; the other lower sensitivity but higher range. All values are in Pascals. NOTE. In 2017, three auxiliary Pitot tubes were installed (on each wingtip, and on the horizontal stabilizer). Data from these sensors is not present here. These sensors are completely ignored by the controller.
flaps	array of radians	Current flap positions. The order is [A1, A2, A4, A5, A7,

		A8, Elevator, Rudder], where A1 is the port wingtip aileron, and A8 is the starboard wingtip aileron. A3 and A6 are not reported as their positions are fixed. Positive numbers indicate trailing edge down (ailerons and elevator) or to port (rudder). The gear reduction in the rudder <i>is</i> accounted for here; this is the position of the control surface .
rotors	array of radians/sec	Measured rotor speeds. Not used by the controller but useful for offline analysis. The order of motors is: [SBO, SBI, PBI, PBO, PTO, PTI, STI, STO], where the nomenclature denotes Starboard/Port, Inner/Outer, Top/Bottom.
wind_ws	vector of meters/sec	Wind velocity vector measured by the weather station, in its own coordinate system. See state_est.wind_g for the wind as converted to ground coordinates.
loadcells	array of Newtons	Raw forces seen by the various loadcell axes at the bridle points. See state_est.tether_force_b to get the total tether force and direction.
gsg	structure	Azimuth and elevation (in radians) of the ground-side-gimbal (GSG). Azimuth increases when rotated with the right-hand-rule about the down (+z) axis and has an arbitrary zero position; elevation increases when moved upwards and is zero when horizontal.
wing_gps	structure	Solution information from the two GPS receivers onboard the wing (position [m] in ECEF, velocity [m/s, ECEF], sigmas, and solution type). If you're interested in the wing position, however, you should use state_est.Xg [m, ground frame].
gs_gps	vector	Ground station GPS location [m] ECEF.
tether_released	bool	True when the tether has been released.
joystick	structure	Positions of joystick sticks and switches.
perch	structure	Perch data. The only value here currently relevant is perch_azi, giving the values of the perch azimuth encoders. Other fields pertain to GSGv1 hardware: perch heading (if there's a perch compass), proximity flag, winch position, and levelwind elevation.

sync		
------	--	--

Control Output

The ControlOutput structure contains the controller's output commanding the various actuators (servos, motors, winch, and detwist drive). For the measured positions and speeds of these actuators see control_input; the corresponding structures may be compared to check command following of the motors, servos, winch, etc.

<i>field</i>	<i>units</i>	<i>description</i>
flaps	radians	Array of commanded positions for all the flaps. Order is the same as in control_input.
rotors	radians/sec	Array of commanded motor speeds. Order is same as in control_input. Sign convention is:
winch_vel_cmd		Commanded winch velocity. Not used with tophat.
detwist_cmd	radians	Commanded tether detwist angle.
run_actuators	bool	
tether_release	bool	Whether to command tether release.
light	bool	Whether to turn on the FAA visibility light. Not used.
sync		Not used?

Crosswind telemetry

ele_tuner		Not used
airspeed_target		
path_type		
path_center_g		
mean_airspeed_cmd	m/s	
loop_angle	radians	
eulers_cw		
target_pos_cw		
current_pos_cw		
k_geom_cmd		
k_aero_cmd		
k_geom_curr		
k_aero_curr		
pqr_cmd	radians/sec	
alpha_cmd	radians	
beta_cmd	radians	
tether_roll_cmd	radians	
airspeed_cmd	m/s	
thrust_ff	Newtons	
thrust_fb	Newtons	
int_elevator		
int_rudder		
int_aileron		

int_thrust		
deltas		

RPX-04 Experimental Test Configurations

For RPX-04 and forward, we implemented a system allowing us to choose "experimental test configurations" from an enumerated set of possibilities. Each test configuration changes the nominal angle-of-attack (alpha) and/or airspeed commands. **Without access to previous revisions of the Makani code repository, it is generally impossible to decode these test cases, as they changed from flight-to-flight.**

How to find out what test configuration was staged

Look at ControlTelemetry → state_est → experimental_crosswind_config [#]. This is a number indicating which configuration number was staged.

How to find out whether it was active

Look at ControlTelemetry → state_est -> joystick -> pitch_f < -0.5

In MATLAB to get active test configuration index:

```
int32(control_debug.message.state_est.experimental_crosswind_config) .* ...  
    int32(control_debug.message.state_est.joystick.pitch_f < -0.5)
```

See Also

Take a look at the RPX-04 Flight Controls Test Plan.

Table of Flight Modes

Unfortunately, enumerations are not stored in the h5 log files; you generally have to reference the source code to figure out what servo index corresponds to which servo, or which number corresponds to which flight mode. This is a long-standing issue that was never addressed. In particular, because the mapping between integer values and their logical interpretations changed from time to time, one must check out the particular version of code used for a particular flight in order to be sure of the meaning.

Here's a table of the current mapping of flight modes, but this may change in the future. The definitive source of truth is FlightMode in control/control_types.h.

<i>flight_mode</i>	<i>description</i>
0	Pilot Hover
1	Perched
2	Hover Ascend
3	Hover PayOut
4	Hover Full Length
5	Hover Accel
6	Trans-In
7	Crosswind Normal
8	Crosswind Prep-Trans-Out
9	Hover Trans-Out
10	Hover Reel-In
11	Hover Descend
12	Off Tether
13	Hover Transform Gs Up
14	Hover Transform Gs Down
15	Hover Prep Transform Gs Up
16	Hover Prep Transform Gs Down

Parameters

Parameters are also recorded in the log file. Arturo asks:

Hey Tobin,

Are kite inertias, mass, CG location, etc part of the data stream, or are they just internal constants in the code? Either way, how can I find them?

thanks!

These numbers are set in the configuration system (in the "config/" subdirectory) and recorded in the "parameters" structure of the log.

Take a look at config/m600/wing.py to see the configured values. You'll find:

```
# The wing_mass and center_of_mass_pos estimates are based on the mass
# tracker [internal ref] on 2016-11-14. The configuration does not include
# any mass balance but includes the landing gear.
```

```
# Wing mass [kg] includes both the rigid wing (1579.8 kg) and
# tether release and bridle (50.4 kg).
wing_mass = 1579.8 + 50.4
```

```
# Center-of-mass [m] for the low-tail configuration.
center_of_mass_pos = [-0.154, 0.009, 0.092]
```

```
# These values are from 016-09-11 and use the
# ASWING model M600_r09-7_xwind.asw
reference_wing_mass = 1560.7
I = np.array([[30140.0, 5.0, 28.3],
              [5.0, 9044.0, 27.1],
              [28.3, 27.1, 36510.0]]) * wing_mass / reference_wing_mass
```

These values are also recorded in the log file:

```
In [1]: import h5py
```

```
In [2]: log = h5py.File('20161121-142912-flight01_crosswind.h5', 'r')
```

```
In [4]: log['parameters']['system_params']['wing']['l']['d']
Out[4]:
array([[[ 3.14821734e+04, 5.22265650e+00, 2.95602358e+01],
        [ 5.22265650e+00, 9.44674108e+03, 2.83067982e+01],
        [ 2.95602358e+01, 2.83067982e+01, 3.81358378e+04]])])

In [5]: log['parameters']['system_params']['wing']['center_of_mass_pos']
Out[5]:
array([(-0.154, 0.009, 0.092)],
      dtype=[('x', '<f8'), ('y', '<f8'), ('z', '<f8')])
```

Practicalities

How to Look at a Log File Using ...

Python

Here's a small example showing how to load an h5 log file in Python and plot a variable (in this case, the kite's altitude). Accessing the log files is made much less painful by enabling tab-completion of telemetry fields; instructions are in `lib/python/ipython_completer.py`.

```
import h5py
import pylab

log = h5py.File('20161121-142912-flight01_crosswind.h5', 'r')
C = (log['messages']['kAioNodeControllerA']
     ['kMessageTypeControlTelemetry']['message'])
pylab.plot(C['time'], -C['state_est']['Xg']['z'])
pylab.show()
```

Additionally, by starting Python with "`bazel-bin/lib/bazel/pyembed ipython`", you will be able to access some Makani library functions (like `DcmToAngle`) directly from Python. Ask in the controls/avionics offices for more info.

You can also explore the field names using `.items()` or `.keys()` and `.dtype` as appropriate:

```
log.keys() # Shows [u'bad_packets', u'messages', u'parameters']
log['messages'].keys() # Shows [u'kAioNodeBattA', ...]
```



```
# The number of messages of this type in the h5 file:
log['messages/kAioNodeBattA/kMessageTypeSlowStatus'].len()

# The first message:
log['messages/kAioNodeBattA/kMessageTypeSlowStatus']][0]

# The nested field names:
log['messages/kAioNodeBattA/kMessageTypeSlowStatus']][0].dtype
```

MATLAB

Here's a small example showing 3 ways to load an h5 log file in MATLAB and plot a variable (in this case, the kite's altitude).

Method 1 (quick to load a specific telemetry dataset to workspace with MATLAB built in function):

```
C = h5read('20161121-142912-flight01_crosswind.h5',
'/messages/kAioNodeControllerA/kMessageTypeControlTelemetry');
time = C.message.time;
altitude = -C.message.state_est.Xg.z;
figure;
plot(time, altitude)
```

Method 2 (takes long to load the data to workspace but *all* telemetry data is accessible on load):

- NOTE: Only works in MATLAB 2016a and earlier. Find out your MATLAB version by running "ver" on the console. See bug 31990348 if you have spare cycles to help fix this.
- You need the makani repository loaded to your computer (see 'How to get the code' section below).
- Open MATLAB and navigate to the following directory on the console:
 - \$MAKANI_HOME/analysis
- Run the following script in the MATLAB console to set all relevant paths:
 - SetMatlab
- Now you can run the following code on console to access telemetry data:

```
log = h5load('20161121-142912-flight01_crosswind.h5');
C = log('/messages/kAioNodeControllerA/kMessageTypeControlTelemetry');
Time = C.message.time;
Altitude = -C.message.state_est.Xg.z;
figure;
plot(Time, Altitude)
```

Method 3 (the best of both worlds! Lazily loads *all* datasets *quickly*):

- You need the makani repository loaded to your computer (see 'How to get the code' section below).
- Open MATLAB and navigate to the following directory on the console:
 - \$MAKANI_HOME/analysis
- Run the following script in the MATLAB console to set all relevant paths:
 - SetMatlab
- Now open the H5Plotter (a GUI interface for opening and plotting H5 log data) by running the following in the MATLAB console:
 - H5Plotter
- Load a H5 log file using the 'Choose' button in the top right corner.
- Once the file is loaded, datasets appear in 'AIO Nodes' panel box. Click on one or more of these nodes to access the corresponding datasets in the 'AIO Messages' panel box. Only datasets common to all selected AIO nodes are shown.
- Once you have selected data to plot in the 'AIO Messages' panel box, use the 'plot' button at the bottom right corner to visualize the data. Holding ctrl or shift allows multiple fields to be selected and selecting a node in the tree will plot all data contained beneath that node. Data can also be exported by right clicking.
- NOTE: You can plot multiple datasets simultaneously on the same time axes. How many datasets you can plot at the same time is only limited by your machine's RAM; be judicious about this.

Matlab Example: Plot roll, pitch, and yaw.

Here's a small example that converts the dcm_g2b matrix into Euler angles.

```
% Read the log file.
filename = '20161121-142912-flight01_crosswind.h5';
C = h5read(filename, ...
    '/messages/kAioNodeControllerA/kMessageTypeControlTelemetry');

% Fetch the dcm_g2b matrix
dcm_g2b = C.message.state_est.dcm_g2b.d;

% Transpose the dcm_g2b matrix.
dcm_g2b = permute(dcm_g2b, [2 1 3]);

% Compute Euler angles.
[yaw, pitch, roll] = dcm2angle(dcm_g2b, 'ZYX');

% Plot the results.
plot(C.message.time, roll * 180/pi, 'l', ...
    C.message.time, pitch * 180/pi, 'l',...
    C.message.time, yaw * 180/pi, 'l')
```

```
legend('roll', 'pitch', 'yaw')  
  
ylim([-180 180]);  
set(gca, 'YTick', -180:30:180);  
grid on;  
xlabel('controller time [s]');  
ylabel('angle [degrees]');  
title(['flight attitude (' filename ')'], 'interpreter', 'none');
```

Auxiliary Sensors

After rpx-02 but prior to rpx-03, three additional sensor groups were attached to the wing: one on each wing tip and one on the horizontal stabilizer (elevator?). These were removed before CW-01. These sensors include:

Port wingtip	5-port air data probe, hover orientation GPS IMU and magnetometer
Starboard wingtip	5-port air data probe, crosswind orientation GPS IMU and magnetometer
Tail	5-port air data probe (* some channels not plumbed)

Other Documentation

ECR 170	Engineering change request for installation of wingtip pitots + other stuff.
ECR 177	Engineering change request for installation of elevator pitot + other stuff.

Example Uses of These Sensors

- Determine the actual wind speed at the kite during hover.
- Additional airspeed measurement during crosswind less affected by props/main wing?
- Use wingtip GPS's to partially determine kite attitude.

Where to Find the Data

Data from these auxiliary sensors is currently ignored by the flight controller (including the state estimator); you have to look at the raw avionics telemetry from the relevant nodes. These sensors were implemented by piggybacking on the kite wingtip and tail lighting nodes. The node names are **LightPort**, **LightStbd**, and **LightTail**. The structure of the messages is similar to those from the main flight computers (FcA, FcB, FcC) which host the main GPS receivers, IMUs, and nose cone air data system.

Known Issues

rpx-03	[bug 35893018] Wingtip GPS solution quality is poor due to self-jamming by the avionics. [bug 37252007] Plumbing issue in the tail pitot tube?

Sensor Metadata

Starboard pitot tube (front-facing):

Position: (302, 12801, -393)

Orientation: Pitched 3 degrees down from kite +x axis (same as pitot on massbalance tube)

Port pitot tube (down/hover-facing):

Position: (108, -12802, -221)

Orientation: Pitched 3 degrees backwards from kite +z axis (90 deg from starboard pitot)

GPSs:

Positions: (0, +/-12809, -555)

Orientation: Parallel to -z axis

Starboard IMU

Position: (-95, 12805, -447)

Orientation: I don't know which way is front/back/left/right of the IMU. But relative to the PCB sitting on a table, it is rolled 94.5 degrees to the left (as in port wingtip down, starboard wingtip up).

Port IMU

Position: (-95, -12805, -447)

Orientation: Relative to the PCB sitting on a table, it is rolled 94.5 degrees to the right (as in port wingtip up, starboard wingtip down).

Timebases

For analysis of rpx-01 data, many groups have used different timebases for presenting flight data. We should standardize the timebase for analysis for rpx-02. Some options:

Method 1: Time since start of log file

This is what the web log viewer uses, and consequently became the de facto standard for rpx-01 analysis.

Pros: Easy.

Cons: Inconsistent across multiple log sources (command center, wing, platform recorder); arbitrary; depends on which messages you're looking at.

Method 2: Actual wall-clock time as determined by recorder computer.

Every logger timestamps every packet with the capture time, as determined by that particular logger computer. This depends on both the actual time the packet was received at that logger, and the local clock on that logger machine.

How to: The `capture_header` structure associated with each message includes two integer values giving the capture timestamp: `tv_sec` and `tv_usec`, which together give the time in seconds and microseconds since the Unix epoch, January 1st 1970. Combine them using $t = tv_sec + 1e-6 * tv_usec$ to get a timestamp in seconds and fractional seconds since that epoch.

Pros: Reasonably accurate and syncable to other sources.

Cons: Can be offset by several seconds depending on accuracy of local clock.

Method 3: Actual wall-clock time as determined by GPS

The timestamps from Method 2 can be cross-checked with GPS timing information included in the log file.

Method 4: Controller Time

End of document.



Effect of design parameters on the M600 stability in crosswind

Jerome Sicard
May 29th, 2018

Content

Scope of the analysis

Comparison of the longitudinal/lateral models
to the full model

Tether action

Effect of the CG, BHP and AC positions

Effect of a variation of the tail volume
coefficient

Next steps ?

Summary

Summary

Summary

Summary



Scope of the analysis

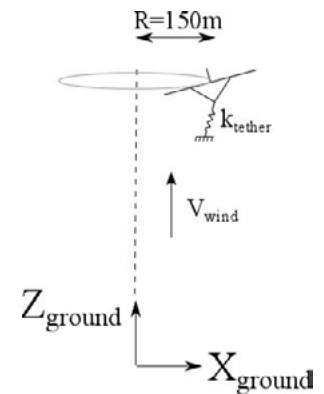
The results presented in this slidedeck were obtained using the linearized models created by `//analysis/control/crosswind.py`. These models are used at Makani to derive the inner loop control laws.

- In these models, the crosswind loop is perpendicular to the wind vector and the gravity vector.
⇒ **gravity effects are ignored.**
- The tether is modeled as a massless linear spring without damping.
 - **Tether catenary and tether drag are ignored** ⇒ the trim tether angles are approximate.
 - **Dynamics proper to the tether are ignored.**
- The longitudinal and lateral dynamics are assumed to be **uncoupled** (the validity of this assumption is discussed in [slide 8 “full system”](#)).

A sample trim state is shown on the right.

Note: at airspeeds of 45 and 60 m/s, the trim operation results in a kite that is banked out of the loop. In flight tests, we observe that the kite roll angle in the crosswind frame varies between positive and negative values.

The present investigation is focused on the open-loop plant of the M600. It aims at better understanding the intrinsic properties of the M600, and understand how it will behave if a control axis is saturated.



Example trim state at $V_{rel}=45$ m/s

```

Wing pos. g [m]: [0.0, 150.0, -404.4]
Wing vel. g [m/s]: [45.0, 0.0, 0.0]
Roll [deg]: 6.058
Pitch [deg]: -5.424
Yaw [deg]: 0.000
P, Q, R [rad/s]: [0.0, 0.0, 0.3]
Thrust [N]: -5702.5
A1, A2 [deg]: -8.814
A4, A5 [deg]: 0.000
A7, A8 [deg]: -2.645
Ele. [deg]: 3.636
Rud. [deg]: -2.363
Vrel [m/s]: 45.621
Alpha [deg]: 4.016
Beta [deg]: 0.42
Tether Force xg [N]: -2511.797
Tether Force yg [N]: -29917.132
Tether Force zg [N]: 79810.317
A_g [m/s^2]: [0.0, -13.5, 0.0]

```

Comparison of the longitudinal/lateral models to the full model

1. In this section, we introduce the full linearized model, the longitudinal model and the lateral model for the M600.
2. We compare the state matrix of the full model to that of the longitudinal and lateral models.
3. We also compare the eigenvalues and the eigenvectors of both models.
4. We present the results obtained by Systems Technology Inc.
5. In conclusion, we indicate the domain of validity of each model and their limitations.



From full system model to longitudinal/lateral systems

- In the full system model, longitudinal and lateral dynamics are not decoupled.
- The 12 states of the full model are:
 - Roll rate, pitch rate, yaw rate (p, q, r)
 - Roll, pitch, yaw (ϕ, θ, ψ)
 - Ground X, Y, Z velocities (V_x, V_y, V_z)
 - Ground X, Y, Z positions (X, Y, Z)
- The longitudinal/lateral systems replace pitch (θ), roll (ϕ), and y-velocity (V_y) with aoa (α), tether roll (ϕ_t), and aos (β), respectively. They are defined by the transformation matrix below:

	δp	δq	δr	$\delta \phi$	$\delta \theta$	$\delta \psi$	δV_x	δV_y	δV_z	δX	δY	δZ
$\delta \phi_t$	0.00	0.00	0.00	-1.01	0.00	-0.03	0.00	0.00	0.00	0.00	0.00	0.00
$\delta \beta$	0.00	0.00	0.00	0.07	0.07	-0.98	0.00	0.02	0.00	0.00	0.00	0.00
$\delta \alpha$	0.00	0.00	0.00	-0.01	1.00	0.07	0.00	0.00	0.02	0.00	0.00	0.00

- Then, some integral states are added and some states are dropped.
 - **Longitudinal system**
 - Keep states: Z, V_z, α, q
 - Add one integral state: i_α
 - Drop V_x, X states
 - **Lateral system**
 - Keep states: ϕ_t, β, p, r
 - Add two integral states: i_{ϕ_t}, i_β
 - Drop ψ, Y states



From full system model to longitudinal/lateral systems

Important notes:

- In the longitudinal/lateral models, any coupling between longitudinal and lateral states is lost.
- Ignoring the 3 integral states that were added, we transformed a 12-state model into two 4-state models.
 - ⇒ We lose the dynamics along the X-axis.
 - ⇒ We also lose all the stiffness terms (stabilizing or destabilizing) that are function of the heading angle. In particular, we show in [slide 9, "matrices"](#) how we lose the tether destabilizing effect on the yaw axis.

In the next slides, we compare:

1. The state matrix (A) of the open-loop longitudinal/lateral models, to that of the full model.
2. The poles of the open-loop longitudinal and lateral models, to the poles of the full model.



Full model (12 DOF) state (A) matrix

- Tether stiffness: 50 kN/m
- Apparent wind speed: 45 m/s
- Force/moment balance equations | Kinematic equations

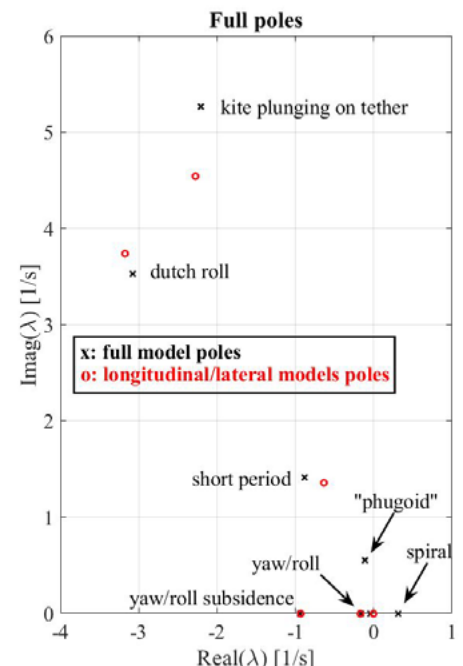
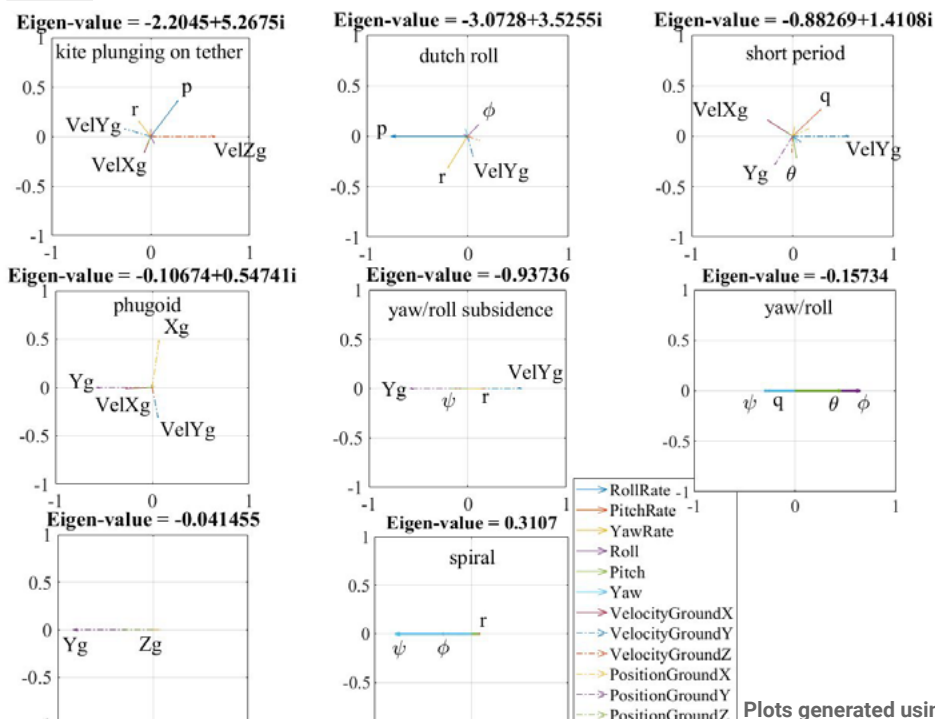
	\dot{p}	\dot{q}	\dot{r}	$\dot{\phi}$	$\dot{\theta}$	$\dot{\psi}$	\dot{V}_x	\dot{V}_y	\dot{V}_z	\dot{X}	\dot{Y}	\dot{Z}
$d(p) / dt$	-5.57	0.24	4.29	-11.87	-2.04	0.24	-0.05	-0.01	-0.05	0.00	0.46	-1.17
$d(q) / dt$	-0.15	-1.63	0.02	0.01	-2.34	-0.11	0.01	0.00	-0.05	0.00	0.01	-0.02
$d(r) / dt$	-1.86	0.00	-0.52	0.66	0.96	0.61	0.01	0.00	-0.01	0.00	-0.03	0.09
$d(\phi) / dt$	1.00	-0.01	-0.09	0.00	-0.30	0.00	0.00	0.00	0.00	0.00	0.00	0.00
$d(\theta) / dt$	0.00	1.00	-0.07	0.30	0.00	0.00	0.00	0.00	0.00	0.00	0.00	0.00
$d(\psi) / dt$	0.00	0.07	1.00	0.02	0.03	0.00	0.00	0.00	0.00	0.00	0.00	0.00
$d(V_x) / dt$	0.33	0.26	-0.02	-0.35	9.71	1.36	-0.09	-0.06	1.32	-0.10	0.00	-0.01
$d(V_y) / dt$	-1.32	0.29	1.87	55.86	9.35	31.53	0.04	-0.69	0.18	0.00	-3.49	9.12
$d(V_z) / dt$	-1.06	-2.92	0.75	-20.67	-154.23	-15.21	-1.61	0.30	-3.60	-0.01	9.23	-24.87
$d(X) / dt$	0.00	0.00	0.00	0.00	0.00	0.00	1.00	0.00	0.00	0.00	0.00	0.00
$d(Y) / dt$	0.00	0.00	0.00	0.00	0.00	0.00	0.00	1.00	0.00	0.00	0.00	0.00
$d(Z) / dt$	0.00	0.00	0.00	0.00	0.00	0.00	0.00	0.00	1.00	0.00	0.00	0.00

"CL_α"

Tether stiffness



Full system ($V_{app} = 45 \text{ m/s}$, $k_{tether} = 50 \text{ kN/m}$)



Plots generated using the script m600_eigen_analysis.m

Longitudinal/lateral state matrices

	Z	Vz	alpha	q	phi_t	beta	p	r	X	Vx	Y	psi
d(Z)/dt	0.00	1.00	0.00	0.00	0.00	0.00	0.00	0.00	0.00	0.00	0.00	0.00
d(Vz) / dt	-24.91	-0.28	-154.69	-2.92	21.42	1.80	-1.06	0.75	-0.01	-2.17	9.18	-1.40
d(alpha) / dt	-0.55	-0.01	-3.39	0.94	0.26	0.10	-0.03	0.01	0.00	-0.05	0.20	-0.03
d(q) / dt	-0.02	0.00	-2.34	-1.63	-0.01	-0.14	-0.15	0.02	0.00	0.00	0.01	-0.08
d(phi_t) / dt	0.00	-0.01	0.28	0.00	-0.03	0.09	-1.01	0.06	0.00	0.00	0.00	0.09
d(beta) / dt	0.12	0.00	-0.30	0.00	-1.18	-0.63	0.04	-0.95	0.00	-0.01	-0.04	0.00
d(p) / dt	-1.18	-0.01	-1.93	0.24	11.72	-0.81	-5.57	4.29	0.00	-0.06	0.44	-0.01
d(r) / dt	0.09	-0.03	0.95	0.00	-0.66	0.06	-1.86	-0.52	0.00	0.01	-0.03	0.58
d(X) / dt	0.00	0.00	0.00	0.00	0.00	0.00	0.00	0.00	0.00	1.00	0.00	0.00
d(Vx) / dt	-0.01	1.11	9.90	0.26	0.14	-2.17	0.33	-0.02	-0.10	-0.06	0.00	-1.48
d(Y) / dt	-0.01	-0.07	-3.37	0.00	3.18	45.65	0.00	-0.00	0.00	0.01	-0.01	45.02
d(psi) / dt	0.00	0.00	0.03	0.07	-0.02	0.00	0.00	1.00	0.00	0.00	0.00	0.00

What terms of the state matrix are we losing (highlighted in yellow)?

- We lose all the dynamics along the X-axis.
 - X-DOFs normally belong to the longitudinal system.
 - They mostly participate in the phugoid mode.
- **We lose a large destabilizing heading stiffness on the yaw axis, due to the tether. This term is 10 times greater than $Cn\beta$!**
- We ignore the change in tension force due to Y-displacement.
 - This is reasonable.
- We ignore the change in tension force due to tether roll on the Z-axis.
 - The sensibility of z-force to tether roll is one order-of-magnitude smaller than the sensitivity to angle-of-attack.
 - This is reasonable.
- We ignore the sum of forces along Y.

Comparison: Full vs. longitudinal/lateral models

Tether/kite mass-spring-damper plunge mode at $-2.205 + 5.268i$

- The frequency of the kite/tether plunging mode is slightly under-estimated in the longitudinal model compared to the full model, by approximately 1 rad/s (0.15 Hz). The corresponding difference in tether stiffness is small (around 10 kN/m).

Dutch roll mode ($-3.073 + 3.526i$) and short period mode ($-0.883 + 1.411i$)

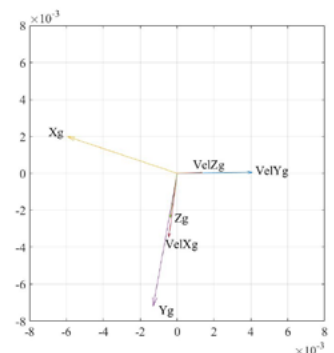
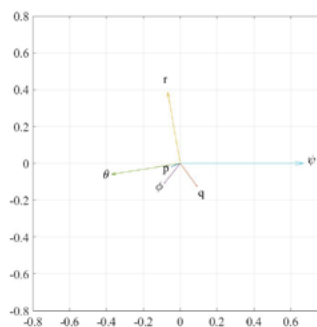
- The decoupled longitudinal and lateral models predict quite well the frequency and the mode shapes of the short period and dutch roll modes.

Phugoid mode in the full model at $-0.107 + 0.547i$

- We take another look at the mode shapes, this time scaling down the displacements and plotting them separately from the angles.
 - This mode involves mostly yaw rate and yaw angle, with non-negligible pitch and pitch rate contributions.

There is a lateral dynamic mode with some pitching motion, that gets omitted when breaking apart the lateral model from the full model.

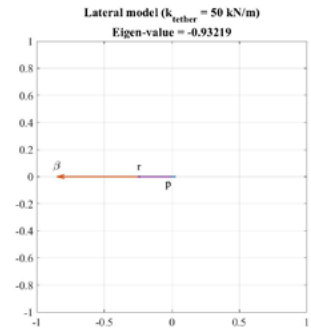
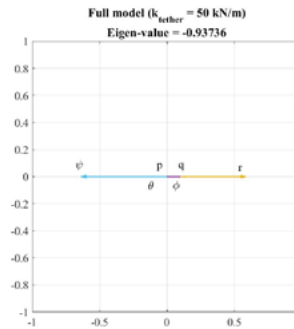
Eigen-value = $-0.10674 + 0.54741i$



Comparison: Full vs. longitudinal/lateral models

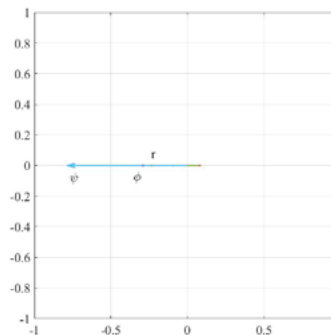
Yaw/roll subsidence (-0.937)

- At reasonable tether stiffness ($k \sim 5e4$ N/m), the frequency and mode shape of the yaw subsidence mode predicted by the full model and the lateral model are similar. Both have an eigen-value at -0.93 and their mode shapes show mostly yaw rate and sideslip.



Unstable non-oscillatory mode at +0.311

- This spiral-like mode, of mode shape shown to the right, is only present in the full model.
- It disappears from the lateral model because the heading state (ψ) is truncated.
- Time for the spiral amplitude to double: $\sim 2s$. From MIL-F-8785 C (*Flying qualities of piloted airplanes*): "The time do double should not be less than 12s for clearly adequate operation nor less than 4s for minimum acceptable operation."



Mode is absent in the lateral model.

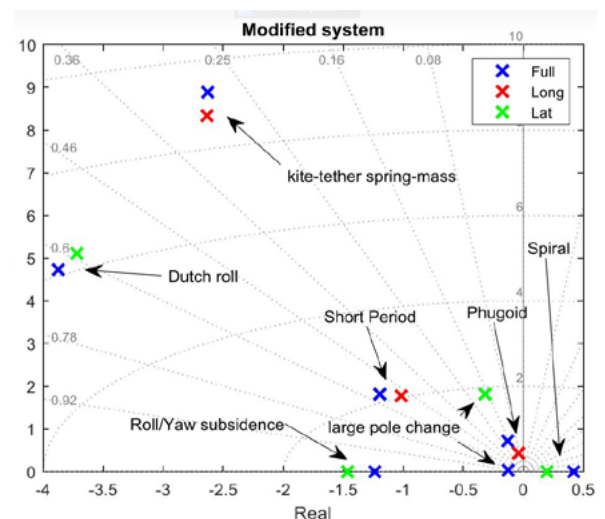


Results from Systems Technology Inc (STI) investigation

In parallel STI also investigated the crosswind linear models.

Summary (based on WP-2729-1-PreliminaryCrosswindLQRAnalysis_v6)

- STI compared the dynamics of the full 12 state model to the dynamics of a 6 state longitudinal model and a 6 state lateral model (i.e. he decoupled the models like us but he *did not drop any state*).
 - 2 notable differences:**
 - All sub-system poles have a full system pole nearby. The pole that moves the most is a lateral pole at $[0.173, 1.85$ rad/s] which has a lower frequency at $[0.958, 0.132$ rad/s] in the full system.
 - The spiral mode exists in the separated (but not truncated) lateral-directional system. It is unstable in both models.
- Comparing the bode plots of the full system to that of the decoupled systems, STI found that there is a good high frequency match. At lower frequencies, the decoupled longitudinal model matches the full model better than the truncated lateral-directional model does, though the correlation is decent in both cases.



Results from STI's investigation

- The good correlation of the bode plots indicates that short period, phugoid, spiral, dutch roll and roll dynamics are captured decently well by the decoupled models.

NOTE: From STI's results, it seems like decoupling the longitudinal states from the lateral states may be OK for a control synthesis model, as long as we don't remove any state from both models.

- The r and β responses from δ_a are similar in magnitude to the responses from δ_r , suggesting that ailerons can control β and r as well as the rudder can.
- The rudder can control ϕ and ϕ_t as well as the ailerons.

STI tried synthesizing new controllers, using the full model, tracking rates, etc... (see appendix B of his report).

- **When comparing the newly synthesized controllers to the existing controllers in close loop with the full model, the existing controllers compare mostly favorably.**

STI made some suggestions to improve the performance of the controller (see full list in section 5 of his report).

- Consider modal-based LQR weighting.
- Analyze the effect of feedforward comprehensively. Use feedforward in the lateral system.
- Consider gain scheduling in another dimension with another parameter: e.g., alpha.
- Consider H2 or H-infty to allow frequency domain loop-shaping
- Look at alternative command system: ϕ_t and r , instead of beta. With beta outer loop. Or use beta feed-forward to achieve same thing.



Summary

What is well captured by the current longitudinal/lateral models?

- The tether extension mode, short period and dutch roll modes.
- The tether roll stiffening, which modifies the classical roll subsidence of free flying airplanes.

⇒ For pitch dynamics, the current longitudinal model is appropriate.

What we are losing?

- The X-dynamics, which coupled with pitch and yaw motion, gives rise to a "phugoid-like" mode. This mode disappears when the full model is decoupled into longitudinal and lateral.
- The full model also shows an **extra fast, unstable and non-oscillatory mode: a spiral mode**. This mode is not in the decoupled lateral model because the tether destabilizing action on the yaw axis is dropped.

⇒ For the evaluation of lateral stability, the lateral model is inadequate.

Proposed path forward?

- Use a decoupled 6 state (V_x , X , V_z , Z , q , α) longitudinal model by moving the airspeed loop (ControlAirspeed in crosswind_inner.c) inside of the alpha loop (ControlAlpha in crosswind_inner.c). I believe this change would also enable Tobin's wish to have the propulsive lift be a part of the airspeed controller.
- Use a decoupled 5 state (p , ϕ_t , r , β , ψ) lateral model. Adding Y-position is harder (current crosstrack controller is nonlinear).



Action of the tether on the dynamic equations

1. First, we investigate the action of the tether on the open-loop plant of the M600. For that, we compare the Jacobian matrix of the tether force and moment to the terms in the M600 state matrix (A matrix).
2. Then, we compute the tether force and moment sensitivities for a range of pitch and roll angle, and we highlight the operating region during RPX-09, particularly at the time when we departed the tether sphere.
3. Finally, we explore the effect of decreasing the tether stiffness on the M600 dynamics.



Longitudinal/lateral state matrices

Recall the full model state matrix transformed into longitudinal/lateral states, shown earlier in [slide 9](#), and pasted below. This matrix is the result of aerodynamic effects, inertial effects and tether effects acting on our kite.

We can move forward and backward between this slide and the next one to observe the tether effects.

	Z	Vz	alpha	q	phi_t	beta	p	r	X	Vx	Y	psi
d(Z)/dt	0.00	1.00	0.00	0.00	0.00	0.00	0.00	0.00	0.00	0.00	0.00	0.00
d(Vz) / dt	-24.91	-0.28	-154.69	-2.92	21.42	1.80	-1.06	0.75	-0.01	-2.17	9.18	-1.40
d(alpha) / dt	-0.55	-0.01	-3.39	0.94	0.26	0.10	-0.03	0.01	0.00	-0.05	0.20	-0.03
d(q) / dt	-0.02	0.00	-2.34	-1.63	-0.01	-0.14	-0.15	0.02	0.00	0.00	0.01	-0.08
d(phi_t) / dt	0.00	-0.01	0.28	0.00	-0.03	0.09	-1.01	0.06	0.00	0.00	0.00	0.09
d(beta) / dt	0.12	0.00	-0.30	0.00	-1.18	-0.63	0.04	-0.95	0.00	-0.01	-0.04	0.00
d(p) / dt	-1.18	-0.01	-1.93	0.24	11.72	-0.81	-5.57	4.29	0.00	-0.06	0.44	-0.01
d(r) / dt	0.09	-0.03	0.95	0.00	-0.66	0.06	-1.86	-0.52	0.00	0.01	-0.03	0.58
d(X) / dt	0.00	0.00	0.00	0.00	0.00	0.00	0.00	0.00	0.00	1.00	0.00	0.00
d(Vx) / dt	-0.01	1.11	9.90	0.26	0.14	-2.17	0.33	-0.02	-0.10	-0.06	0.00	-1.48
d(Y) / dt	-0.01	-0.07	-3.37	0.00	3.18	45.65	0.00	0.00	0.00	0.01	-0.01	45.02
d(psi) / dt	0.00	0.00	0.03	0.07	-0.02	0.00	0.00	1.00	0.00	0.00	0.00	0.00

"Cm_α"

"Cn_β"

"Cn_ψ"



Tether force/moment Jacobian vs. longitudinal/lateral states

The script used to compute the Jacobian is on gerrit: [go/makani/cl/38420](https://gerrit.makani.com/r/gitweb/?p=makani;v=38420). In this script, the tether Jacobian is rearranged to show the contribution to the A matrix.

- Tether stiffness: 50 kN/m
- Moment computed about the kite CG

Trim states

- ω_b : [0., 0., -0.3] rad/s
- $euler_g$: [4.3, -5.4, 0.] deg.
- $wing_vel_g$: [45., 0., 0.] m/s
- $wing_pos_g$: [0., 150., -405.3] m

	Z	Vz	alpha	q	phi_t	beta	p	r	X	Vx	Y	psi
d(Z)/dt	0.00	0.00	0.00	0.00	0.00	0.00	0.00	0.00	0.00	0.00	0.00	0.00
d(Vz) / dt	-24.90	0.06	-3.99	0.00	22.21	-0.95	0.00	0.00	-0.01	-0.02	9.18	-1.45
d(alpha) / dt	-0.55	0.00	-0.09	0.00	0.49	-0.02	0.00	0.00	0.00	0.00	0.20	-0.03
d(q) / dt	-0.02	0.00	-0.21	0.00	-0.01	-0.02	0.00	0.00	0.00	0.00	0.01	-0.08
d(phi_t) / dt	0.00	0.00	0.00	0.00	0.00	0.00	0.00	0.00	0.00	0.00	0.00	0.00
d(beta) / dt	0.12	0.00	0.02	0.00	-0.12	-0.02	0.00	0.00	0.00	0.00	-0.05	-0.02
d(p) / dt	-1.18	0.00	-0.09	0.00	11.63	-0.02	0.00	0.00	0.00	0.00	0.44	-0.03
d(r) / dt	0.09	-0.03	1.56	0.00	-0.65	0.11	0.00	0.00	0.00	0.01	-0.03	0.58
d(X) / dt	0.00	0.00	0.00	0.00	0.00	0.00	0.00	0.00	0.00	0.00	0.00	0.00
d(Vx) / dt	-0.01	0.00	-0.02	0.00	0.01	0.00	0.00	0.00	0.00	-0.10	-0.06	0.09
d(Y) / dt	0.00	0.00	0.00	0.00	0.00	0.00	0.00	0.00	0.00	0.00	0.00	0.00
d(psi) / dt	0.00	0.00	0.00	0.00	0.00	0.00	0.00	0.00	0.00	0.00	0.00	0.00

Important coefficients

Important coefficients that are dropped when separating longitudinal and lateral models



Observations

Roll axis (d(p)/dt equation)

- The tether roll stiffening ($\partial M_x / \partial \phi = 11.63$) is clearly present in the full plant.
- There is no other major contribution from the tether on the roll axis.

Pitch axis (d(q)/dt equation)

- The tether has a very small stabilizing effect on the total Cm_α derivative (-0.21) which is dominated by the aerodynamic contribution (-2.34). This effect is small *because the bridle hardpoints (BHP), the Aerodynamic Center (AC) and the CG are coincident*. In [slide 28](#), we find that moving the bridle hardpoints away from the AC changes the pitch dynamics very significantly.

Yaw axis (d(r)/dt equation)

- Most importantly, the tether in the present trim conditions applies a large destabilizing yaw moment at non-zero yaw angles ($Cn_\psi = 0.58$), which is much larger than $Cn_\beta = 0.06$.
 \Rightarrow **This effect is lost when we drop the heading state (ψ) from the lateral model. This is likely why the unstable spiral mode that was present in the full 12 state model disappeared in the lateral model.**
- We also observe the pitch coupling from the tether on the yaw axis (1.56).
 \Rightarrow *This effect is lost when the full plant is broken into longitudinal and lateral plants.*
- Cn_ϕ (-0.65) due to the tether is also unstable in the current trim condition.
 \Rightarrow *This effect is captured in the lateral model.*

Is the tether always destabilizing on the yaw axis? No, it depends on the pitch and roll angles, as seen in the next slide.

Stability derivative: tether yaw moment w.r.t. heading angle ($C_n\psi$)

We computed the tether derivative $C_n\psi$ for a range of kite euler pitch and roll angles, and about $\psi=0$.

- Pitch is positive when the tether is towards the tail of the kite.
- Roll is positive when the kite is banked out of the loop (i.e. starboard wing down)

		Euler pitch angle (deg)									
		-60	-50	-40	-30	-20	-10	0	10	20	30
Euler roll angle (deg)	-60	-5.97	-7.33	-8.33	-8.07	-3.69	18.37	59.39	13.54	-5.04	-8.62
	-50	-5.10	-5.62	-5.21	-2.65	4.15	16.18	23.43	14.41	2.67	-3.51
	-40	-3.69	-3.40	-2.11	0.70	5.15	9.92	11.87	9.21	4.20	-0.12
	-30	-2.15	-1.45	-0.15	1.77	4.00	5.84	6.45	5.48	3.43	1.16
	-20	-0.84	-0.17	0.71	1.73	2.68	3.35	3.52	3.15	2.33	1.31
	-10	0.07	0.48	0.91	1.31	1.64	1.83	1.85	1.71	1.43	1.05
	0	0.58	0.70	0.78	0.84	0.87	0.88	0.87	0.83	0.78	0.71
	10	0.82	0.69	0.54	0.41	0.31	0.25	0.23	0.25	0.31	0.39
	20	0.93	0.62	0.32	0.05	-0.15	-0.27	-0.30	-0.22	-0.07	0.14
	30	1.05	0.62	0.18	-0.26	-0.63	-0.87	-0.91	-0.76	-0.45	-0.06
	40	1.28	0.79	0.18	-0.53	-1.22	-1.71	-1.82	-1.53	-0.93	-0.21
	50	1.73	1.23	0.41	-0.75	-2.01	-2.99	-3.27	-2.72	-1.57	-0.28
60	2.46	2.03	0.97	-0.81	-3.05	-4.97	-5.61	-4.57	-2.42	-0.17	

→ Where in this table were we during RPX-09? At the angles highlighted in yellow (see next slide).

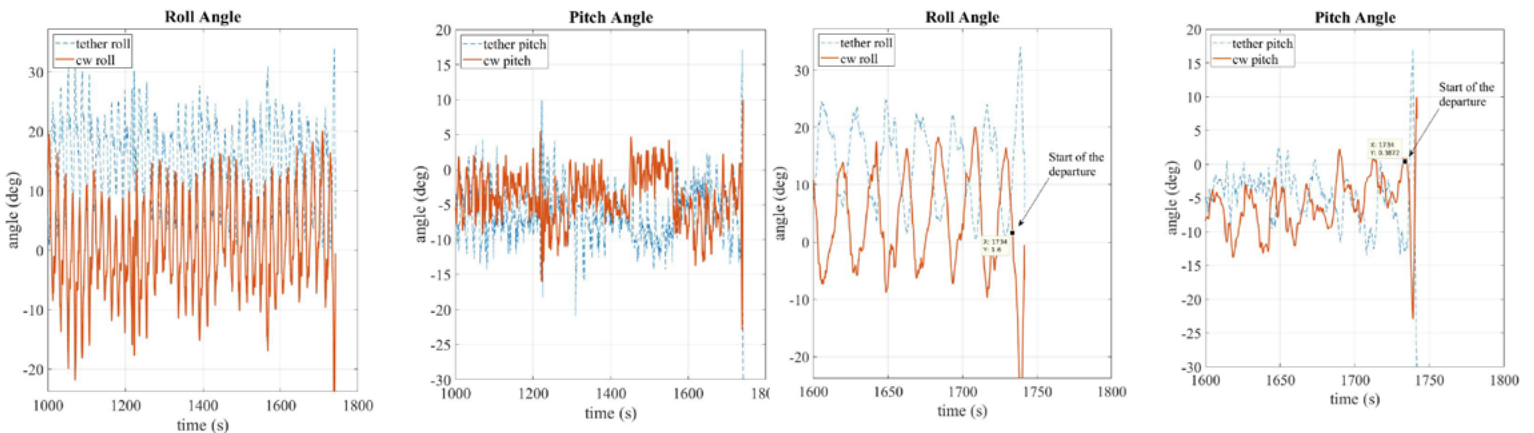
→ In which direction did we depart during RPX-09? In the direction shown by the arrow.



Kite roll and pitch angles during RPX-09

Ideally, it would be better to look at $C_n\psi$ in terms of tether pitch and roll angles.

In the linear analysis, we assume that the crosswind loop is parallel to the ground. Thus, we can compare the Euler roll and pitch angles from the linear models, to the “crosswind” Euler roll and pitch angles available in the Control Telemetry. These Euler angles are the angles between the kite body frame and the crosswind plane.



Investigation on varying the tether stiffness

In order to reduce the tether effects and tend towards free-flight dynamics, we must do 2 things:

1. Decrease the tether stiffness
2. Decrease the distance between the bridle knot and the center of gravity.

In the next slides, we investigate the effect of item #1 only on the longitudinal axis, where item #2 is automatically enforced by having the bridle hardpoint (BHP) be almost coincident with the CG.

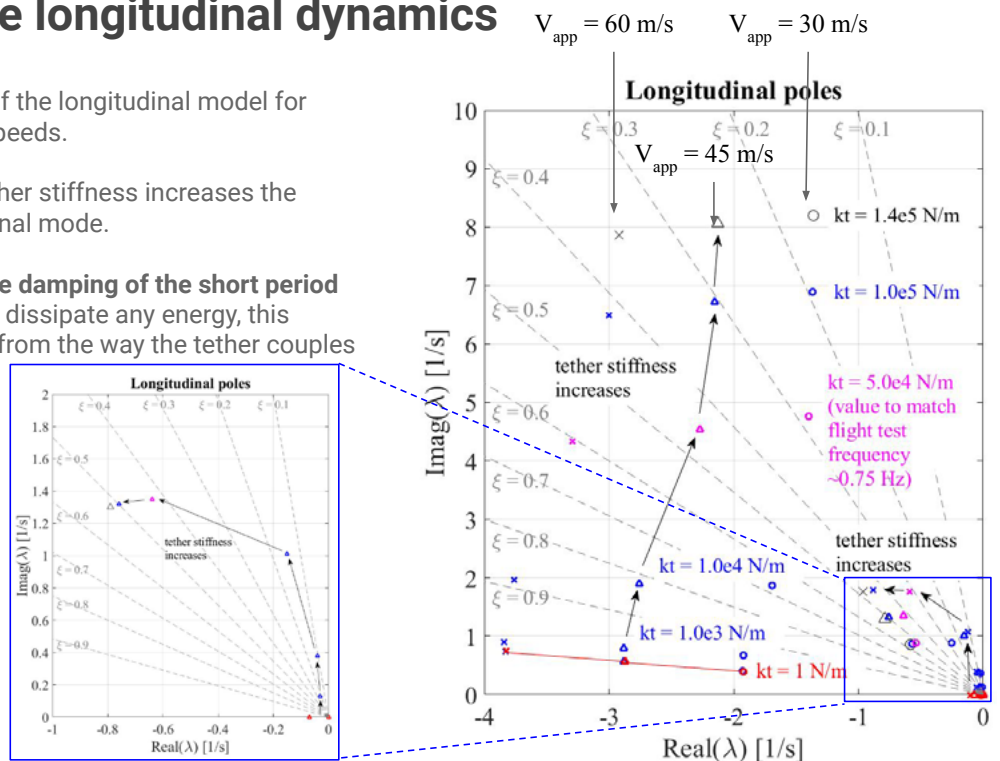


Tether stiffness on the longitudinal dynamics

The plot on the right shows the poles of the longitudinal model for varying tether stiffnesses and kite airspeeds.

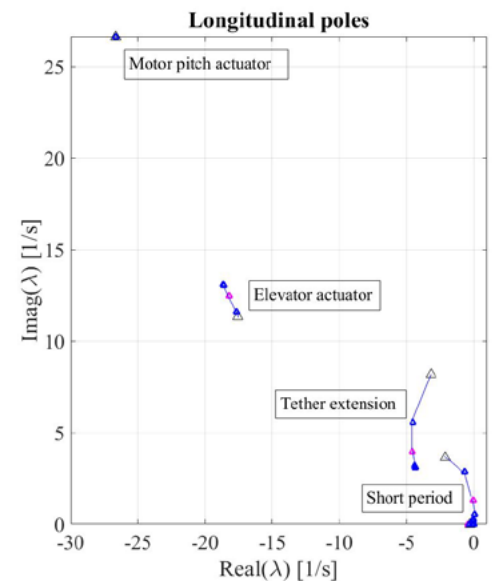
- As we expect, increasing the tether stiffness increases the frequency of the tether extensional mode.
- **It also stiffens and increases the damping of the short period mode.** Since the tether does not dissipate any energy, this additional damping must come from the way the tether couples vertical and pitching motions.

⇒ We found here that the tether augmented the longitudinal dynamics stability of the M600, at least for its current configuration (CG, AC, BHP locations).



Tether interaction with the closed-loop system

- When the stiffness of the tether becomes < 7.5 kN/m in this model, **the closed-loop short period mode (actuator dynamics included) becomes unstable.**
This instability occurs at a tether stiffness close to the value needed to match the tether extensional frequency measured in flight tests (pink marker in the root locus plots)
→ Could this be the reason why Paul S. observed instabilities when he tried to tighten up the inner loop?



Summary

- By not including the heading angle as a state in the lateral model, we omitted a very destabilizing tether effect. In turns, we removed an unstable spiral mode from the lateral dynamics.
⇒ **Let's add the heading angle back into the lateral model.**
- By decoupling longitudinal and lateral dynamics, we ignore a non-negligible tether yaw moment due to tether pitch. This tether effect is why we found in [slide 10, "Comparison,"](#) that our "phugoid" mode showed some yaw motion.
This omission is likely not as bad as the previous one. But let's discuss.
- In the present M600 configuration (i.e. for the present CG, BHP and AC positions), the tether augmented the stability of the longitudinal dynamics.
- Stability criteria that don't involve heading and pitch angle derivatives are inadequate.



Effect of the CG, BHP and AC positions

CG = center of gravity of the kite
 BHP = bridle hardpoint
 AC = aerodynamic center

In this section, we vary the positions of these three points and we investigate the consequence on the kite longitudinal stability.

For this analysis, the reduced longitudinal model is valid.



Baseline + 3 configurations

0	Baseline	
1	Shift the CG of the kite +/- 20 cm forward and aft of baseline	
2	Shift the bridle hardpoints +/- 20 cm forward and aft of baseline	
3	Shift the CG and the bridle hardpoints together	

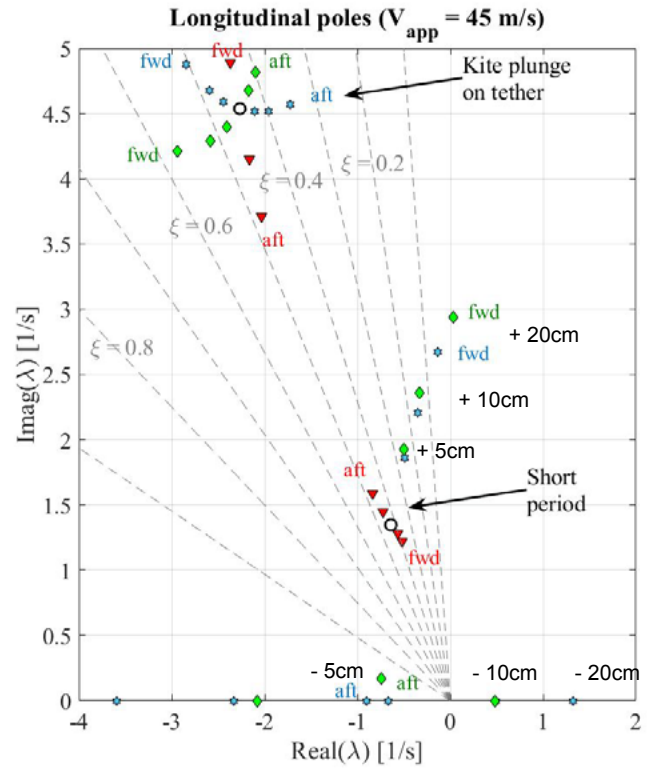


Longitudinal dynamics

Shifting the CG, the BHP, or both has a much larger effect on the short period mode than on the kite/tether plunge mode.

For the short period mode:

- **Shifting the CG alone** has a pretty small effect.
- **Shifting the BHP alone**, or the **BHP + the CG** have very similar effects:
 - When shifted aft by 5 cm or more, a divergence occurs. The oscillatory short period mode gives rise to two real poles, one of which is unstable.



Note: a 5% error on the longitudinal static margin is equivalent to a 6 cm error on the position of the aerodynamic center.

Longitudinal dynamics

- **Shifting the BHP alone**, or the **BHP + the CG** (continued)
 - Shifting the BHP (or the BHP + the CG) forward allows to increase the margin from where the divergence occurs.

But when the BHP is shifted forward more than 10 cm, then the damping of the short period mode decreases significantly. For a shift of 20 cm, it becomes unstable.

This can be explained by looking at the analytical expression for the damping ratio of the short period mode:

$$\zeta_{sp} = -\frac{M_q + M_{\dot{a}} + Z_a/u_0}{2 \omega_{n\ sp}}$$

From the second equation:

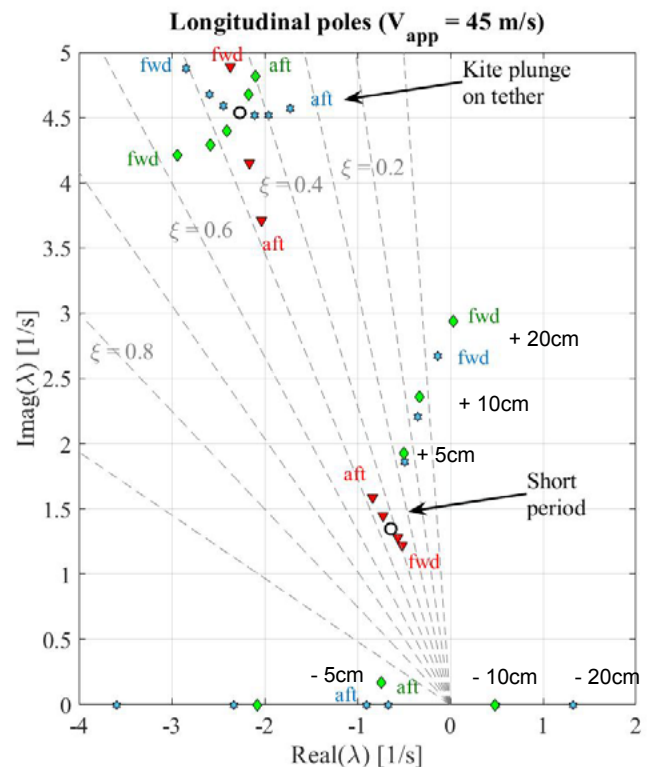
$$\omega_{n\ sp} = \sqrt{\frac{Z_a M_q}{u_0} - M_a}$$

BHP shifts forward $\rightarrow C_{m\alpha}$ decreases $\rightarrow \omega_n$ increases.

From the first equation:

BHP shifts forward $\rightarrow \omega_n$ increases, M_q becomes more negative (because the distance to the elevator is increased) $\rightarrow \zeta$ decreases.

- At higher airspeed, both effects are amplified: the short period mode becomes unstable more quickly.



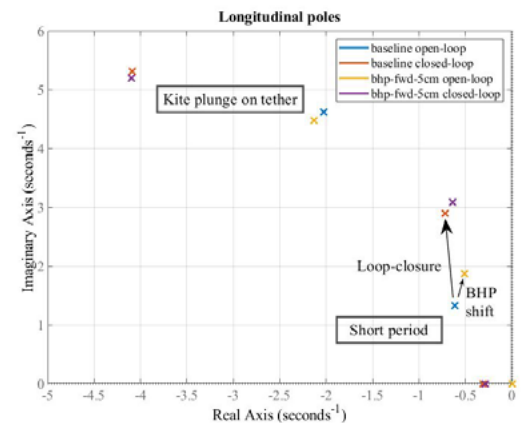
Longitudinal dynamics

⇒ To maximize the open-loop longitudinal stability:

- Never place the BHP aft of the AC.
- Increase the margin from static divergence by placing the BHP reasonably forward of the AC (BHP must be placed 19 cm forward of the AC for a 15% static margin).
- Placing the BHP too far forward of the AC leads to an unstable short period mode.

The distance along the x-axis from the bridles to the aerodynamic center dictates the stability of the short period mode.

Note that the closed-loop system is much less sensitive to the position of the BHP, given the stability augmentation offered by the control system (see plot to the right)... until an actuator is saturated.



Effect of a variation of the tail volume coefficient

In this section, we investigate the impact of an increase of the tail volume coefficient on the dynamic stability and on the flight quality (via Monte Carlo batch sims).

- The tail volume coefficient is increased by increasing the length of the fuselage by 0.5 meter, 1.0 meter and 2.0 meters.
- The impact on the stability derivatives is investigated.
- Then, the aero coefficients are overridden in the sim and the poles of the new full system are calculated (evaluating the existing lateral model would be inaccurate because of the missing spiral mode).
- Finally, we run Monte Carlo batch sim for each new configurations.



Variation in fuselage length

We investigated the effect of an increase in tail volume coefficient (via an increase of the fuselage length) on the dynamic stability of the M600 and on the scoring functions.

First, we analyzed how the stability and control derivatives, and the center of mass vary with the fuselage length (see this study [internal ref] and the summary below).

Config	vtail x-position	htail x-position	Cn_beta	Cm_alpha	Cn_r	Cm_q	Cn_dr	Cm_de	X-cg (m)
baseline	6.569	6.3079	0.0245	-2.392	-0.107	-29.942	-0.00146	-0.0453	-0.147
	Scale factor	Scale factor							
vtail & htail shifted aft by 0.5 meter	1.08	1.08	0.031	-2.569	-0.117	-34.366	-0.002	-0.049	-0.201
vtail & htail shifted aft by 1 meter	1.15	1.16	0.038	-2.745	-0.1282	-39.098	-0.00166	-0.0521	-0.254
vtail & htail shifted aft by 2 meters	1.30	1.32	0.0516	-3.097	-0.1521	-49.489	-0.00186	-0.0588	-0.361

From this study, we found that:

- Cm_α , Cm_{de} and Cn_{dr} scale linearly with the fuselage length.
- Cn_r scales linearly with $1.1 * \text{fuselage_length}$.
- Cm_q scales linearly with $1.2 * \text{fuselage_length}$.
- Cn_\square scales linearly with $1.4 * \text{fuselage_length}$.
- All the other stability and control derivatives remain constant.



Configuration overrides

How to apply the scaling factors in the Sim?

- In config/m600/sim/aero_sim.py, there are factors available to scale the total moment coefficients, their rate derivatives and their flap derivatives. There are also factors to offset Cm_α and Cn_\square .
- Since $Cn(\alpha = 0) \neq 0$, we cannot apply a linear scaling factor on $Cntot$ to model a linear change in Cn_\square . Instead, we apply an offset on Cn_\square , which for the baseline (un-modified configuration) is equal to $0.0572 / \text{rad}$.
- $Cm(\alpha = 0) = 0$, hence we can directly apply a scaling factor on $Cmtot$.

The table below shows the four configurations of interest, and the list of overrides.

	moment_coeff_b_scale_factors			coeff_offsets			wing_params
	coeff	rate_derivatives	flap_derivatives	dCLdbeta	dCMdalpha	dCNdbeta	center_of_mass_pos
baseline	[1.0, 1.0, 1.0]	'p': [1.0, 1.0, 1.0], 'q': [1.0, 1.0, 1.0], 'r': [1.0, 1.0, 1.0]	de: [1.0, 1.0, 1.0], 'dr': [1.0, 1.0, 1.0]	0.0	0.0	0.0	-0.147
vtail & htail shifted aft by 0.5 meter	[1.0, 1.08, 1.0]	'p': [1.0, 1.0, 1.0], 'q': [1.0, 1.30, 1.0], 'r': [1.0, 1.0, 1.19]	de: [1.0, 1.08, 1.0], 'dr': [1.0, 1.0, 1.08]	0.0	0.0	0.0293	-0.201
vtail & htail shifted aft by 1 meter	[1.0, 1.15, 1.0]	'p': [1.0, 1.0, 1.0], 'q': [1.0, 1.38, 1.0], 'r': [1.0, 1.0, 1.27]	de: [1.0, 1.15, 1.0], 'dr': [1.0, 1.0, 1.15]	0.0	0.0	0.0349	-0.254
vtail & htail shifted aft by 2 meters	[1.0, 1.31, 1.0]	'p': [1.0, 1.0, 1.0], 'q': [1.0, 1.57, 1.0], 'r': [1.0, 1.0, 1.44]	de: [1.0, 1.31, 1.0], 'dr': [1.0, 1.0, 1.31]	0.0	0.0	0.0477	-0.361

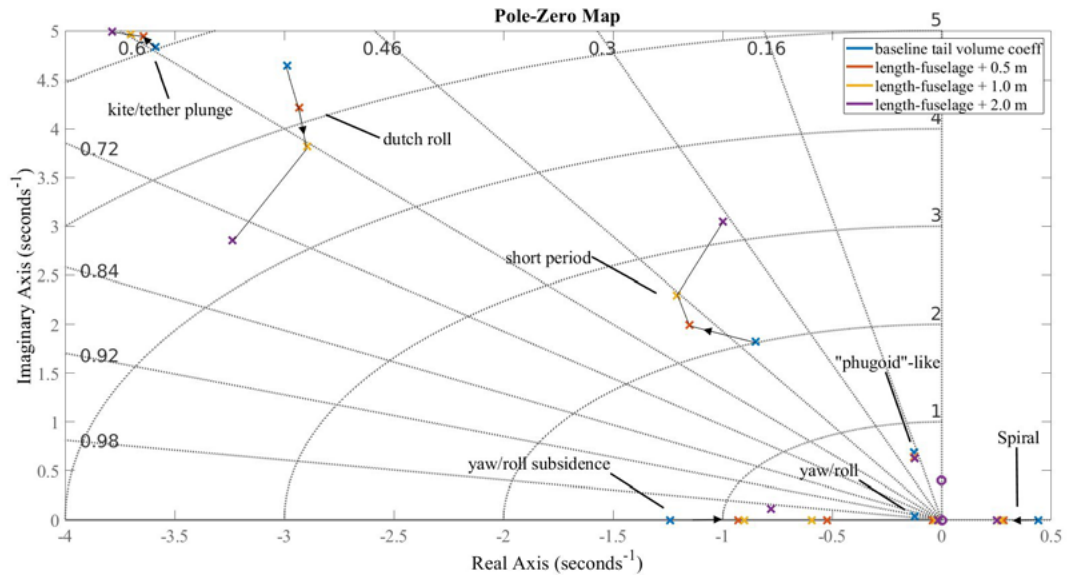
Stability analysis

The map on the right shows how each mode varies as the length of the fuselage increases (see direction of the arrows).

3 modes are mostly impacted:

Short period

- As the fuselage length increases, the Aerodynamic Center of the kite moves aft (of the BHP), and the damping of the short period mode increases.
- Past a 1.0 meter increase, the damping reduces again. We observed the same result when we shifted the BHP forward (see [slide 28, "Longitudinal dynamics."](#)).
- The reduction in damping for large increase in fuselage length may not be a result of a shift in CG. Instead it seems to be due to having the AC too far aft of the BHP.



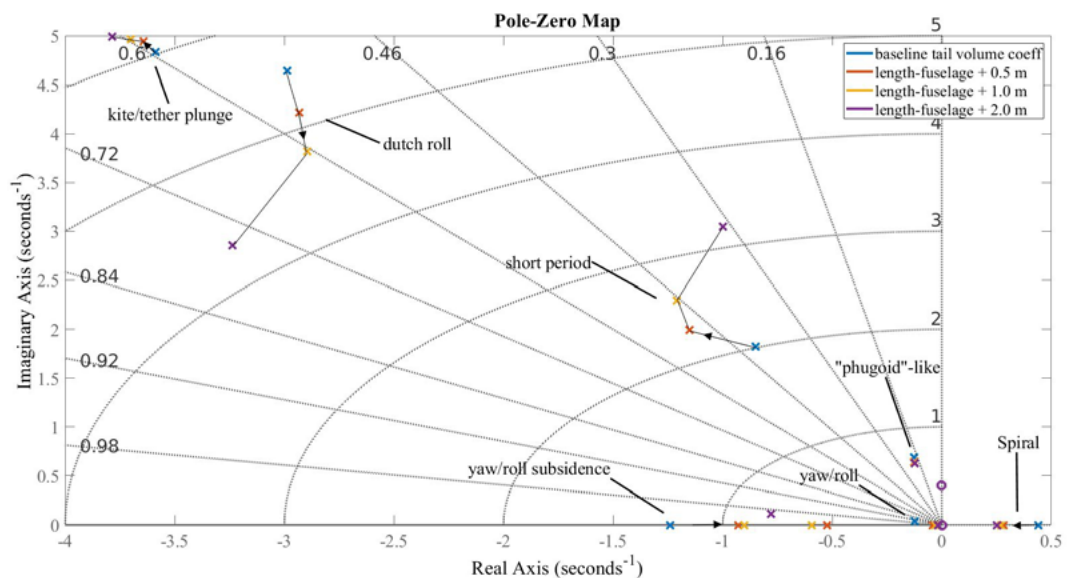
Stability analysis

Spiral

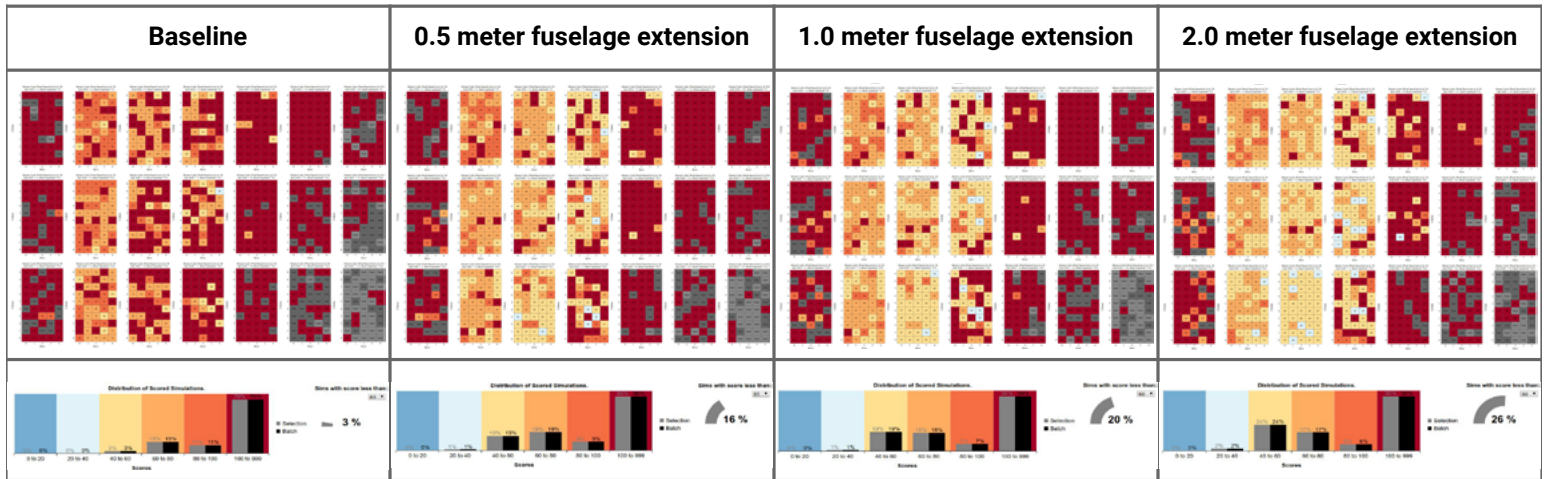
- The 0.5 meter increase in fuselage length has a non-negligible stabilizing effect on the spiral mode.
- Further increase in fuselage length (+1.0, +2.0 meters) shows no more improvement.

Yaw/roll subsidence

- For free-flying airplanes, increasing the tail volume coefficient has no effect on the roll subsidence mode.
- Because of the tether, this mode for our kite includes some yaw motion.
- The increase in fuselage length decreases the damping of this mode.
- But the damping of this mode is so large that it is likely not an issue.



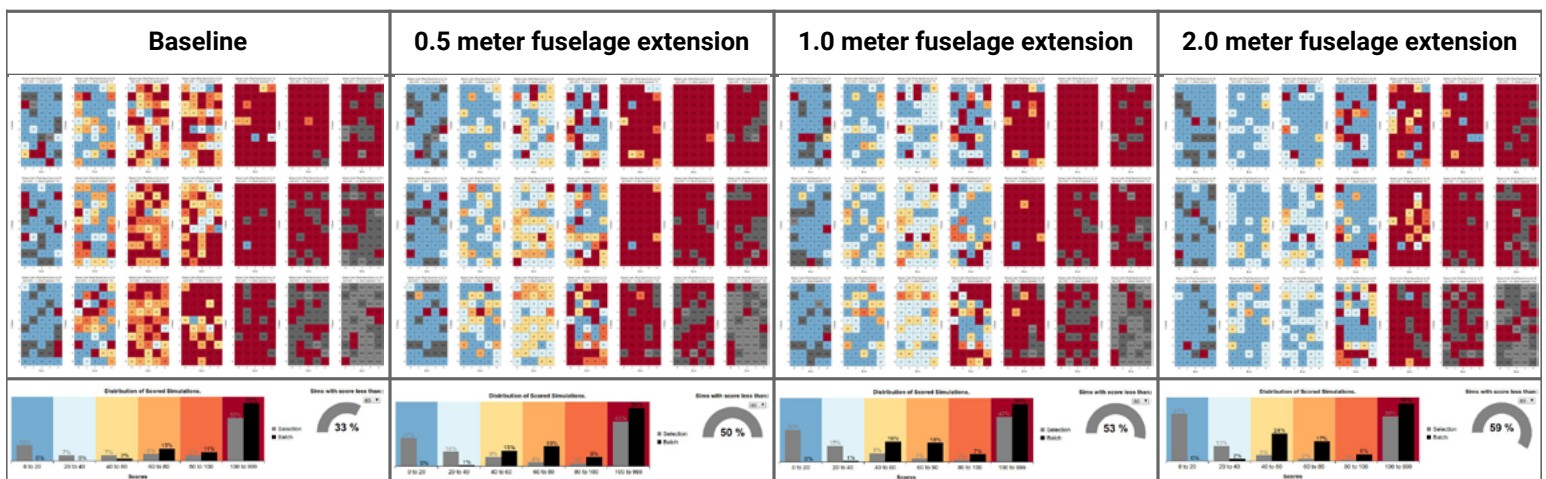
Batch simulations - Big picture



- Overall, when all the scoring functions are selected, the effect of increasing the fuselage length strictly improves all the simulations.
- **The number of simulations with a score less than 60 quintuples when the fuselage length is increased by 0.5 meter.**
- The simulations continue to improve but at a slower rate for the 1.0 and 2.0 meter fuselage extension cases. This is also what we observed in the stability analysis.



Batch simulations - Crash scoring functions



- The observations made in the previous slide are very clear when looking at the crash scores only: **the 0.5 meter increase in fuselage length almost doubles the number of crash scores which are less than 60.** A further increase in the fuselage length offers less improvements.
- The main scoring function that gets improved and that drives the aggregated crash scores is **PrepTransOut Tether Roll**. The improvement is only seen for wind speeds less than 9 m/s because aggregated crash scores at higher wind speeds are driven by the **PrepTransOut Tether Pitch**.



Summary

Aerodynamic effects

Recall the results from the free-flight static stability analysis:

- **Longitudinal stability**
 - Adding the slats increased the destabilizing effect of the wing (Cm_{α}) by a factor 2.
 - The rotors are destabilizing.
 - This effect is not accounted for in the C-Sim or in the linear stability analysis.
 - Rotors in generation decrease the tail efficiency.
 - This effect is accounted for in the C-Sim but not in the linear stability analysis.
 - The free-flight longitudinal static margin is marginal (between -1 and 1%)
- **Directional stability**
 - The value used for Cn_{β} in the controller design is conservative for moderate aero angles.
 - The free-flight directional static margin is somewhere between 2% and 5%.
- **Roll stability**
 - The sign of the derivative Cl_{β} used in the C-Sim was wrong.

How do these results change in a dynamic analysis of the tethered M600?

- Shifting the AC aft of the BHP by increasing the tail volume coefficient improves the longitudinal stability. This result is true only up to an increase of fuselage length between 0.5 and 1.0 meter. Past this value, increasing the fuselage length degrades the longitudinal stability.
- Increasing the fuselage length by 0.5 meter also improves the lateral stability.



Next steps?

In order of priority:

1. Have the results reviewed.
2. Add the heading (yaw) angle to the lateral model.
 - STI has taken on this task and is prototyping it in MATLAB.
 - If successful, this step will lead to an augmented lateral gain matrix, which would require a way to feed-back the heading angle (or more likely the heading angle in crosswind frame: `crosswind_eulers.z`).
3. Explore stability envelope
4. Add the forward motion states (X, V_x) to the longitudinal model.
 - If successful, this step will result in having the airspeed loop and the longitudinal loop merged into the longitudinal loop.
5. Run batch-simulations for the configurations with increased tail volume coefficients highlighted in this slide deck. Assess the flight quality.



Appendix

- Eigenvalues and eigenvectors of the longitudinal and lateral models.
- Tether force/moment Jacobian as a function of the original 12 CrosswindStates.



Longitudinal model

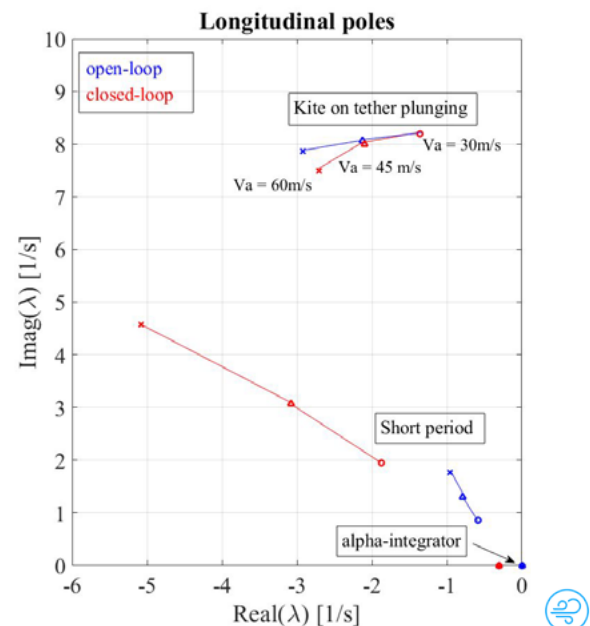
Longitudinal dynamics

5 states: Zg-position, Zg-velocity, Alpha, Pitch rate, Alpha-integral

- 2 oscillatory modes
 - Short period (a rapid pitch mode)
 - Plunging kite on tether (= tether extensional mode)
- 1 alpha-integrator (open-loop), which becomes a real pole in the closed-loop longitudinal system.

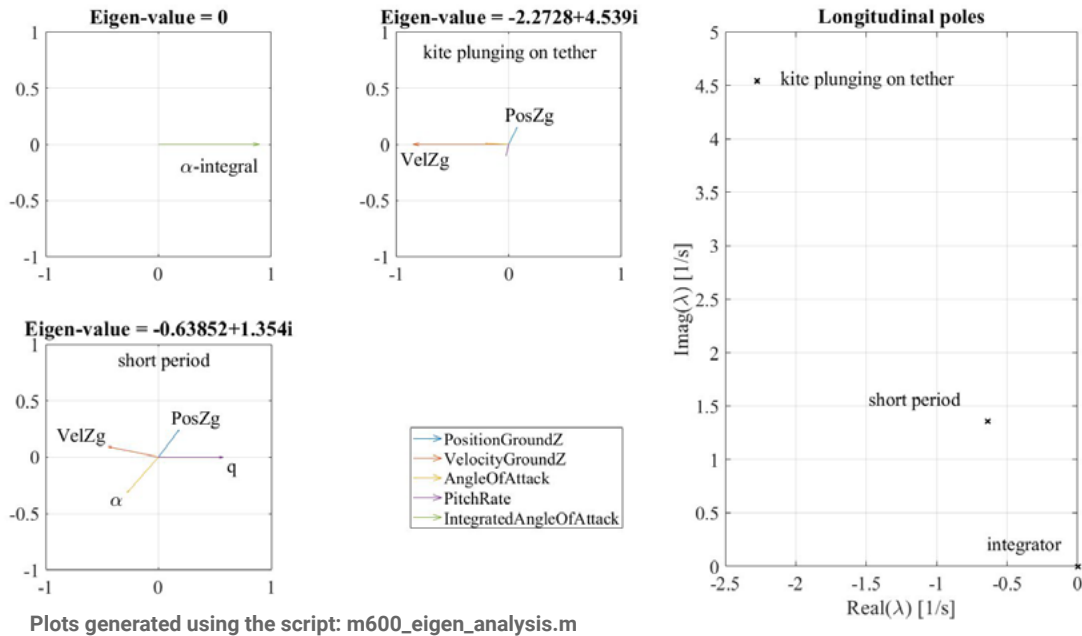
At the time when this slide was edited, the tether stiffness in the linear models ($k = 1.4e5$ N/m) was too high, as shown by the frequency of the tether extension mode (~ 8 rad/s, 1.27 Hz) vs. the frequency measured in flight tests (0.75 Hz). We corrected this stiffness (see bug 79927035). **In the rest of this slidedeck, the tether stiffness is corrected.**

Open-loop and closed-loop poles for 3 different airspeeds



Longitudinal model

Eigen-vectors for $V_{app} = 45 \text{ m/s}$ and $k_{tether} = 50 \text{ kN/m}$



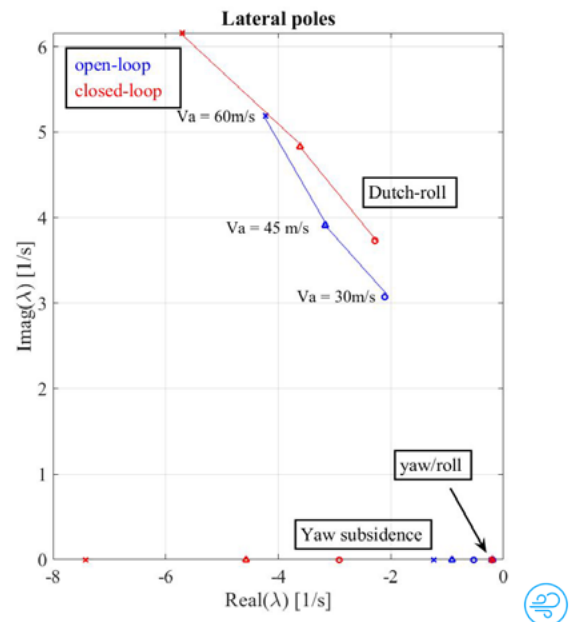
Lateral model

Lateral dynamics

6 states: Tether-roll, Sideslip, Roll rate, Yaw rate, tether-roll-integral, sideslip-integral

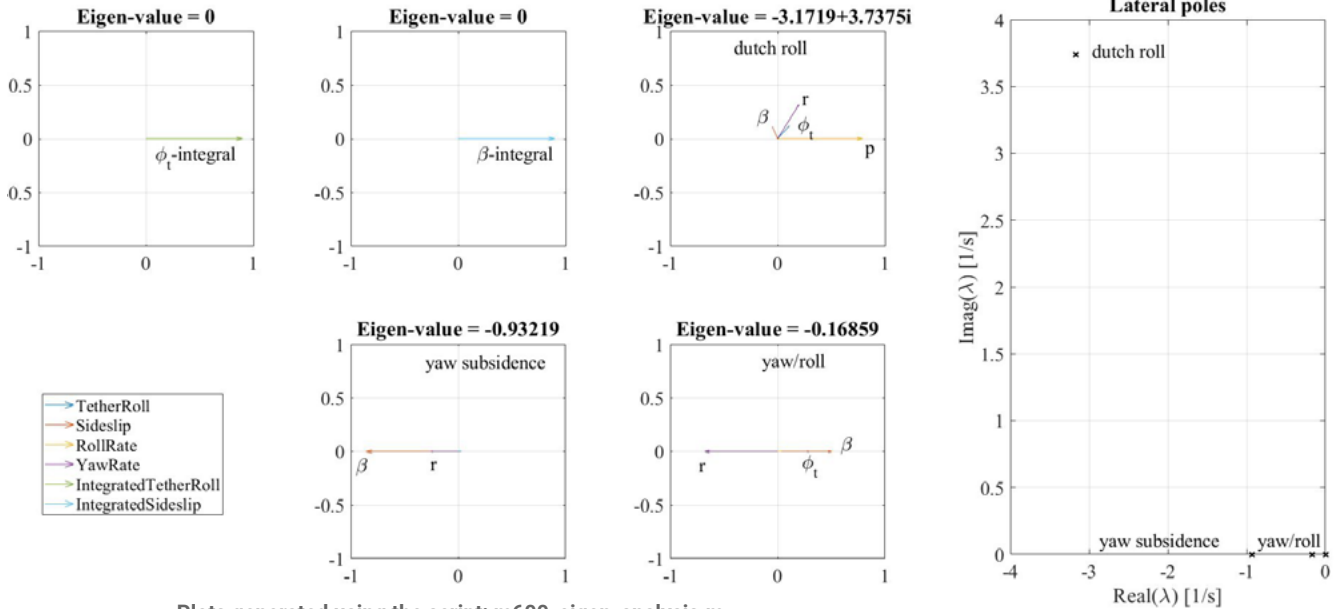
- 1 oscillatory mode
 - Dutch-roll (a combined roll and yaw motion)
- 2 non-oscillatory modes
 - Yaw/roll subsidence (the most stable of the two real poles)
 - Varies with airspeed
 - Varies with Cl_{β}
 - Another stable mode: yaw/roll
- 2 integrators (tether-roll, beta) - not shown in the root locus
- No clear spiral mode.

Open-loop and closed-loop poles for 3 different airspeeds



Lateral model

Eigen-vectors for $V_{app} = 45 \text{ m/s}$ and $k_{tether} = 50 \text{ kN/m}$



Full (12 DOF) state matrix

Recall the M600 full state space matrix shown earlier in slide 7. This matrix is the result of aerodynamic effects, inertial effects and tether effects acting on our kite. By moving forward and back between this slide and the next one, we can observe the terms in the state matrix that are due to the tether.

	p	q	r	ϕ	θ	ψ	V_x	V_y	V_z	X	Y	Z
$d(p) / dt$	-5.57	0.24	4.29	-11.87	-2.04	0.24	-0.05	-0.01	-0.05	0.00	0.46	-1.17
$d(q) / dt$	-0.15	-1.63	0.02	0.01	-2.34	-0.11	0.01	0.00	-0.05	0.00	0.01	-0.02
$d(r) / dt$	-1.86	0.00	-0.52	0.66	0.96	0.61	0.01	0.00	-0.01	0.00	-0.03	0.09
$d(\phi) / dt$	1.00	-0.01	-0.09	0.00	-0.30	0.00	0.00	0.00	0.00	0.00	0.00	0.00
$d(\theta) / dt$	0.00	1.00	-0.07	0.30	0.00	0.00	0.00	0.00	0.00	0.00	0.00	0.00
$d(\psi) / dt$	0.00	0.07	1.00	0.02	0.03	0.00	0.00	0.00	0.00	0.00	0.00	0.00
$d(V_x) / dt$	0.33	0.26	-0.02	-0.35	9.71	1.36	-0.09	-0.06	1.32	-0.10	0.00	-0.01
$d(V_y) / dt$	-1.32	0.29	1.87	55.86	9.35	31.53	0.04	-0.69	0.18	0.00	-3.49	9.12
$d(V_z) / dt$	-1.06	-2.92	0.75	-20.67	-154.23	-15.21	-1.61	0.30	-3.60	-0.01	9.23	-24.87
$d(X) / dt$	0.00	0.00	0.00	0.00	0.00	0.00	1.00	0.00	0.00	0.00	0.00	0.00
$d(Y) / dt$	0.00	0.00	0.00	0.00	0.00	0.00	0.00	1.00	0.00	0.00	0.00	0.00
$d(Z) / dt$	0.00	0.00	0.00	0.00	0.00	0.00	0.00	0.00	1.00	0.00	0.00	0.00

"CL_α"

Tether stiffness

Tether force/moment jacobian w.r.t. 12 crosswind states

- Tether stiffness: 50 kN/m
- Moment computed about the kite CG

The script used to compute the Jacobian is on gerrit: [go/makani/38420](https://gerrit.makani.com/r/gitweb/?p=makani;v=38420). In this script, the tether Jacobian is rearranged to show the contribution to the A matrix.

Comparing against the previous state matrix, the highlighted cells show where the tether impacts the kite dynamics.

	p	q	r	phi	theta	psi	Vx	Vy	Vz	X	Y	Z
$d(p) / dt$	0.00	0.00	0.00	-11.74	-0.14	-0.42	0.00	0.01	0.00	0.00	0.46	-1.17
$d(q) / dt$	0.00	0.00	0.00	0.01	-0.21	-0.08	0.00	0.00	0.00	0.00	0.01	-0.02
$d(r) / dt$	0.00	0.00	0.00	0.65	1.56	0.60	0.00	0.00	0.00	0.00	-0.03	0.09
$d(phi) / dt$	0.00	0.00	0.00	0.00	0.00	0.00	0.00	0.00	0.00	0.00	0.00	0.00
$d(theta) / dt$	0.00	0.00	0.00	0.00	0.00	0.00	0.00	0.00	0.00	0.00	0.00	0.00
$d(psi) / dt$	0.00	0.00	0.00	0.00	0.00	0.00	0.00	0.00	0.00	0.00	0.00	0.00
$d(Vx) / dt$	0.00	0.00	0.00	-0.01	-0.02	0.09	-0.06	0.00	0.00	-0.10	0.00	-0.01
$d(Vy) / dt$	0.00	0.00	0.00	8.88	1.54	0.61	0.00	-0.03	0.00	0.00	-3.54	9.22
$d(Vz) / dt$	0.00	0.00	0.00	-22.45	-4.14	-1.57	0.00	0.00	-0.03	-0.01	9.22	-24.87
$d(X) / dt$	0.00	0.00	0.00	0.00	0.00	0.00	0.00	0.00	0.00	0.00	0.00	0.00
$d(Y) / dt$	0.00	0.00	0.00	0.00	0.00	0.00	0.00	0.00	0.00	0.00	0.00	0.00
$d(Z) / dt$	0.00	0.00	0.00	0.00	0.00	0.00	0.00	0.00	0.00	0.00	0.00	0.00



Kite stability in crosswind flight

Edited 2020-07-25

Authors: Jerome Sicard, Geo Homsy, Michael Abraham

Contents

- [Introduction](#)
- [Reference frames](#)
- [State variables](#)
- [Equations of motion](#)
- [Small perturbation equations](#)
- [Aerodynamic force and moment](#)
 - [Longitudinal derivatives](#)
 - [Lateral derivatives](#)
- [Tether force and moment](#)
 - [Force and moment vectors in the b-frame](#)
 - [Perturbations of the tether force](#)
 - [Perturbations of the tether moment](#)
- [Kinematics](#)
 - [Perturbed velocities: \$\Delta \dot{x}, \Delta \dot{y}, \Delta \dot{z}\$](#)
 - [Perturbed Euler rates: \$\Delta \dot{\phi}, \Delta \dot{\theta}, \Delta \dot{\psi}\$](#)
- [State-space equations of motion](#)
- [Numerical implementation](#)
- [Validation](#)
 - [Free flight](#)
 - [Tethered flight](#)
- [Eigenvalues of the M600](#)

Introduction

This document presents a derivation of the equations of motion of a kite in crosswind flight. The scope of this derivation is centered around the dynamic stability of the kite. To that end, the effects of the ambient wind and gravity are ignored.

In the following analysis, we assume that the kite is flying circles at constant speed and constant attitude with respect to the flight plane. We assume we know

- the kite velocity, v_k
- the kite attitude with respect to the flight circle
- the diameter of the flight circle or the angular rate of flight around the circle
- the tether departure direction from the airframe, \mathbf{t}
- the tether tension, T
- the wind speed, v_w (assumed to be in the "up" direction)
- the "power drag" applied by the props, D_p , assumed to be along the body $-\hat{x}$ direction

Reference frames

- g -frame centered at the ground origin O and inertial.
- b -frame centered at the kite center-of-gravity CG and rotating with the kite.

State variables

- x, y, z : the b -frame components of $\mathbf{r}_{CG/O}$

- u, v, w : the b-frame components of $\mathbf{V}_{CG/O}$
- ϕ, θ, ψ : the Euler angles used in the 3-2-1 coordinate transformation from the g-frame to the b-frame (defined, equivalently, as the DCM $_{GtoB}$ matrix Ψ_0)
- p, q, r : the b-frame components of $\omega_{b/g}$

Notice that we choose to express the position vector in body-frame coordinates, whereas the equations of motion of an aircraft are typically derived using the position vector expressed in ground-frame. This choice greatly simplifies the analytical derivation of the components of the tether force and moment vectors in body-frame.

Equations of motion

Defining \mathbf{A} and \mathbf{T} as the aerodynamic and tether force vectors acting on the kite, \mathbf{M}_A and \mathbf{M}_T as their respective moment about the kite center-of-mass, the equilibrium equations are:

$$\mathbf{A} + \mathbf{T} = m \mathbf{a}_{CG} \tag{1}$$

$$\mathbf{M}_A + \mathbf{M}_T = \dot{H}_{CG} \tag{2}$$

Assuming symmetry of the aircraft with respect to the (xz) plane, the inertia tensor is:

$$I_G^b = \begin{bmatrix} I_x & 0 & -I_{xz} \\ 0 & I_y & 0 \\ -I_{xz} & 0 & I_z \end{bmatrix} \tag{3}$$

Once projected in the b-frame, the equations of motion become:

$$D_P + X + T_x = m (\dot{u} + qw - rv) \tag{4}$$

$$Y + T_y = m (\dot{v} + ru - pw) \tag{5}$$

$$Z + T_z = m (\dot{w} + pv - qu) \tag{6}$$

$$L + M_{Tx} = I_x \dot{p} - I_{xz} \dot{r} + qr(I_z - I_y) - I_{xz}pq \tag{7}$$

$$M + M_{Ty} = I_y \dot{q} + rp(I_x - I_z) + I_{xz}(p^2 - r^2) \tag{8}$$

$$N + M_{Tz} = -I_{xz} \dot{p} + I_z \dot{r} + pq(I_y - I_x) + I_{xz}qr \tag{9}$$

Note that the right-hand side of these equations is a classical results of rigid-body dynamics, presented for instance in page 101 of Ref.¹.

Small perturbation equations

Following the small-disturbance theory, we apply small perturbations to the equations of motion. All the state variables are replaced by a reference value plus a variation, e.g. $x = x_0 + \Delta x$. From symmetry and assuming a constant motion, the reference (trim) conditions are defined as:

$$\Psi_0 = \text{DCM}_{321}(\phi_0, \theta_0, \psi_0) = \begin{bmatrix} c_{\theta_0} c_{\psi_0} & c_{\theta_0} s_{\psi_0} & -s_{\theta_0} \\ -c_{\phi_0} s_{\psi_0} + s_{\phi_0} s_{\theta_0} c_{\psi_0} & c_{\phi_0} c_{\psi_0} + s_{\phi_0} s_{\theta_0} s_{\psi_0} & s_{\phi_0} c_{\theta_0} \\ s_{\phi_0} s_{\psi_0} + c_{\phi_0} s_{\theta_0} c_{\psi_0} & -s_{\phi_0} c_{\psi_0} + c_{\phi_0} s_{\theta_0} s_{\psi_0} & c_{\phi_0} c_{\theta_0} \end{bmatrix} \tag{10}$$

$$\begin{bmatrix} u_0 \\ v_0 \\ w_0 \end{bmatrix} = \Psi_0 \begin{bmatrix} -R_0 \Omega_0 \\ 0 \\ 0 \end{bmatrix} \tag{11}$$

$$\begin{bmatrix} p_0 \\ q_0 \\ r_0 \end{bmatrix} = \Psi_0 \begin{bmatrix} 0 \\ 0 \\ \Omega_0 \end{bmatrix} \tag{12}$$

Note that for a "left turning" kite, Ω_0 is understood to be negative.

In this document, the subscript $()_0$ refers to the variable being evaluated at trim.

Expanding the equations of motion as indicated above and evaluating all the functions about the trim state, the trim forces and moments cancel out and the perturbed equations of motion can be reduced to:

Ⓜ TODO: add some model of power drag as a function of airspeed

$$\Delta D_P + \Delta X + \Delta T_x = m (\Delta \dot{u} + q_0 \Delta w + w_0 \Delta q - r_0 \Delta v - v_0 \Delta r) \quad (13)$$

$$\Delta Y + \Delta T_y = m (\Delta \dot{v} + r_0 \Delta u + u_0 \Delta r - p_0 \Delta w - w_0 \Delta p) \quad (14)$$

$$\Delta Z + \Delta T_z = m (\Delta \dot{w} + p_0 \Delta v + v_0 \Delta p - q_0 \Delta u - u_0 \Delta q) \quad (15)$$

$$\Delta L + \Delta M_{T_x} = I_x \Delta \dot{p} - I_{xz} \Delta \dot{r} + (I_z - I_y)(q_0 \Delta r + r_0 \Delta q) - I_{xz}(p_0 \Delta q + q_0 \Delta p) \quad (16)$$

$$\Delta M + \Delta M_{T_y} = I_y \Delta \dot{q} + (I_x - I_z)(r_0 \Delta p + p_0 \Delta r) + 2I_{xz}(p_0 \Delta p - r_0 \Delta r) \quad (17)$$

$$\Delta N + \Delta M_{T_z} = -I_{xz} \Delta \dot{p} + I_z \Delta \dot{r} + (I_y - I_x)(p_0 \Delta q + q_0 \Delta p) + I_{xz}(q_0 \Delta r + r_0 \Delta q) \quad (18)$$

We can expand each variation as the sum of partial derivatives with respect to the state variables that they depend on, evaluated at the reference flight conditions. In the following sections, the variations of the aerodynamic and tether force and moments are derived.

Aerodynamic force and moment

The partial derivatives of the aerodynamic forces and moments are also called *stability derivatives*. For each component of the aerodynamic forces and moments, only a subset of the partial derivatives are known to be significant for the aircraft motion. These significant derivatives are listed in page 107 of Ref.¹, and summarized below.

$$\Delta X = \frac{\partial X}{\partial u} \Delta u + \frac{\partial X}{\partial w} \Delta w \quad (19)$$

$$\Delta Y = \frac{\partial Y}{\partial v} \Delta v + \frac{\partial Y}{\partial p} \Delta p + \frac{\partial Y}{\partial r} \Delta r \quad (20)$$

$$\Delta Z = \frac{\partial Z}{\partial u} \Delta u + \frac{\partial Z}{\partial w} \Delta w + \frac{\partial Z}{\partial \dot{w}} \Delta \dot{w} + \frac{\partial Z}{\partial q} \Delta q \quad (21)$$

$$\Delta L = \frac{\partial L}{\partial v} \Delta v + \frac{\partial L}{\partial p} \Delta p + \frac{\partial L}{\partial r} \Delta r \quad (22)$$

$$\Delta M = \frac{\partial M}{\partial u} \Delta u + \frac{\partial M}{\partial w} \Delta w + \frac{\partial M}{\partial \dot{w}} \Delta \dot{w} + \frac{\partial M}{\partial q} \Delta q \quad (23)$$

$$\Delta N = \frac{\partial N}{\partial v} \Delta v + \frac{\partial N}{\partial p} \Delta p + \frac{\partial N}{\partial r} \Delta r \quad (24)$$

Longitudinal derivatives

ⓘ TODO: $\langle u_0, v_0, w_0 \rangle$ is the *inertial* velocity. Adjust these for the *aerodynamic* velocity in the presence of wind.

$$X_u = \frac{-(C_{D_u} + 2C_{D_0})qS}{u_0} \quad X_w = \frac{-(C_{D_\alpha} - 2C_{L_0})qS}{u_0}$$

$$Z_u = \frac{-(C_{L_u} + 2C_{L_0})qS}{u_0} \quad Z_w = \frac{-(C_{L_\alpha} + C_{D_0})qS}{u_0} \quad Z_{\dot{w}} = C_{z_{\dot{w}}} \frac{cqS}{2u_0^2}$$

$$Z_\alpha = u_0 Z_w \quad Z_{\dot{\alpha}} = u_0 Z_{\dot{w}} \quad Z_q = C_{z_q} \frac{cqS}{2u_0}$$

$$M_u = C_{m_u} \frac{QSc}{u_0} \quad M_w = C_{m_w} \frac{qSc}{u_0} \quad M_{\dot{w}} = C_{m_{\dot{w}}} \frac{qSc^2}{2u_0^2}$$

$$M_\alpha = u_0 M_w \quad M_{\dot{\alpha}} = u_0 M_{\dot{w}} \quad M_q = C_{m_q} \frac{qSc^2}{2u_0}$$

Lateral derivatives

ⓘ TODO: $\langle u_0, v_0, w_0 \rangle$ is the *inertial* velocity. Adjust these for the *aerodynamic* velocity in the presence of wind.

$$Y_\beta = qSC_{y_\beta} \quad Y_p = \frac{qSbC_{y_p}}{2u_0} \quad Y_r = \frac{qSbC_{y_r}}{2u_0}$$

$$N_\beta = qSbC_{n_\beta} \quad N_p = \frac{qSb^2C_{n_p}}{2u_0} \quad N_r = \frac{qSb^2C_{n_r}}{2u_0}$$

$$L_\beta = qSbC_{l_\beta} \quad L_p = \frac{qSb^2C_{l_p}}{2u_0} \quad L_r = \frac{qSb^2C_{l_r}}{2u_0}$$

$$Y_v = \frac{Y_\beta}{u_0} \quad N_v = \frac{N_\beta}{u_0} \quad L_v = \frac{L_\beta}{u_0}$$

Tether force and moment

Force and moment vectors in the b-frame

Ⓜ TODO: This is Jerome's original straight-line tether derivation. Eventually, we should adjust this to a pure differential form, in which ΔT is proportional to ΔL , along the tether departure vector \mathbf{t} : $\Delta \mathbf{T} = -k\Delta L\mathbf{t}$. In this way, we can incorporate tether catenary effects (the kite doesn't actually care where the ground station is; it just cares about the tether departure direction at trim). The math is also a lot simpler.

The tether force vector can be written as:

$$\mathbf{T} = -k(L - L_n)\mathbf{t} \tag{25}$$

where:

- $L = \|\mathbf{r}_{K/O}\|$ is the norm of the position vector from the ground frame origin to the bridle knot K.
- L_n is the unstretched tether length.
- $k = EA/L_n$ is the elastic spring constant of the tether (a 75% knockdown can be applied in order to account for catenary effects).
- $\mathbf{t} = \mathbf{r}_{K/O}/L$ is a unit vector oriented in the same direction as a straight-line tether.

If (x_K, y_K, z_K) are the b-frame coordinates of the bridle knot K, then the distance L is:

$$L = \sqrt{(x + x_K)^2 + (y + y_K)^2 + (z + z_K)^2} \tag{26}$$

And the components of \mathbf{T} in the b-frame become:

$$\mathbf{T}^b = -EA \left(\frac{1}{L_n} - \frac{1}{L} \right) \begin{pmatrix} x + x_K \\ y + y_K \\ z + z_K \end{pmatrix} \tag{27}$$

In order to compute the tether torque about the center of mass of the kite, we introduce one additional point and three unit vectors:

- Point B, called the bridle pivot, is the perpendicular projection of the bridle knot on the bridle hinge line. Its b-frame coordinates are (x_B, y_B, z_B)
- \mathbf{h} is a unit vector colinear with the bridle hinge axis.
- \mathbf{b} is a unit vector in the direction from B to K.
- \mathbf{n} is defined as: $\mathbf{n} = \mathbf{b} \times \mathbf{h}$.
- The distance from B to K is typically called the bridle radius, noted in this document as b_r .

The tether torque about CG is:

$$\mathbf{M}_{\mathbf{T}/CG} = (\mathbf{r}_{B/CG} + \mathbf{r}_{K/B}) \times \mathbf{T} \tag{28}$$

Since the tether force is always in the plane defined by the two bridles, we can decompose its vector into two components aligned with the unit vectors \mathbf{h} and \mathbf{b} :

$$\mathbf{T} = \mathbf{T}_h + \mathbf{T}_b \tag{29}$$

Hence, the tether torque becomes:

$$\mathbf{M}_{\mathbf{T}/CG} = \mathbf{r}_{B/CG} \times \mathbf{T} + \mathbf{r}_{K/B} \times \mathbf{T}_h \tag{30}$$

Moreover, since $\mathbf{r}_{K/B}$ and \mathbf{T}_h are perpendicular to each other, their cross-product simplifies as:

$$\mathbf{M}_{\mathbf{T}/CG} = \mathbf{r}_{B/CG} \times \mathbf{T} + b_r \|\mathbf{T}_h\| \mathbf{n} \quad (31)$$

$$= \mathbf{r}_{B/CG} \times \mathbf{T} + b_r (\mathbf{T} \cdot \mathbf{h}) \frac{\mathbf{b} \times \mathbf{h}}{\|\mathbf{b} \times \mathbf{h}\|} \quad (32)$$

Noting that $\frac{\mathbf{b} \times \mathbf{h}}{\|\mathbf{b} \times \mathbf{h}\|} = \frac{\mathbf{T} \times \mathbf{h}}{\|\mathbf{T} \times \mathbf{h}\|}$ and assuming that $\mathbf{h} = \mathbf{y}$, the b-frame components of the tether moment vector are:

$$\mathbf{M}_{\mathbf{T}/CG} = \begin{pmatrix} y_B T_z - z_B T_y \\ z_B T_x - x_B T_z \\ x_B T_y - y_B T_x \end{pmatrix} + b_r \frac{T_y}{\sqrt{T_x^2 + T_z^2}} \begin{pmatrix} -T_z \\ 0 \\ T_x \end{pmatrix} \quad (33)$$

Perturbations of the tether force

The total differential of the x-component of the tether force is expanded below (other components follow a similar derivation).

$$\Delta T_x = \frac{\partial T_x}{\partial x} \Delta x + \frac{\partial T_x}{\partial y} \Delta y + \frac{\partial T_x}{\partial z} \Delta z + \frac{\partial T_x}{\partial \phi} \Delta \phi + \frac{\partial T_x}{\partial \theta} \Delta \theta + \frac{\partial T_x}{\partial \psi} \Delta \psi \quad (34)$$

$$= \frac{\partial T_x}{\partial \mathbf{r}} \Delta \mathbf{r} + \frac{\partial T_x}{\partial \Theta} \Delta \Theta \quad (35)$$

where $\mathbf{r} = [x, y, z]^T$ and $\Theta = [\phi, \theta, \psi]^T$. The first three terms are straight-forward to compute because the tether force components are readily expressed as functions of x , y and z . To compute the last three terms, we use the chain rule:

$$\frac{\partial T_x}{\partial \Theta} = \frac{\partial T_x}{\partial \mathbf{r}} \frac{\partial \mathbf{r}}{\partial \Theta} \quad (36)$$

which gives:

$$\Delta T_x = \frac{\partial T_x}{\partial \mathbf{r}} \left(\Delta \mathbf{r} + \frac{\partial \mathbf{r}}{\partial \Theta} \Delta \Theta \right) \quad (37)$$

The components of \mathbf{r} are related to the Euler angles via the direction-cosine matrix transforming the g-frame into the b-frame:

$$\mathbf{r}_{CG/g} = \begin{Bmatrix} x \\ y \\ z \end{Bmatrix}_b = \text{DCM}_{GtoB} \begin{Bmatrix} 0 \\ R_0 \\ Z_0 \end{Bmatrix}_g \quad (38)$$

where R_0 is the crosswind path radius and Z_0 is the (negative) height below ground. From the above equations, one can expand $\mathbf{r}_{CG/g}$ and compute its Jacobian with respect to $\Theta = \{\phi, \theta, \psi\}^T$ to obtain the following:

$$\frac{\partial \mathbf{r}_{CG/g}}{\partial \Theta} = \left[\frac{\partial r_i}{\partial \theta_j} \right] = \begin{bmatrix} 0 & -R_0 \sin \theta_0 \sin \psi_0 - Z_0 \cos \theta_0 & R_0 \cos \theta_0 \cos \psi_0 \\ -R_0 \sin \phi_0 \cos \psi_0 + R_0 \cos \phi_0 \sin \theta_0 \sin \psi_0 + Z_0 \cos \phi_0 \cos \theta_0 & R_0 \sin \phi_0 \cos \theta_0 \sin \psi_0 - Z_0 \sin \phi_0 \sin \theta_0 & -R_0 \cos \phi_0 \sin \psi_0 + R_0 \sin \phi_0 \sin \theta_0 \cos \psi_0 \\ -R_0 \cos \phi_0 \cos \psi_0 - R_0 \sin \phi_0 \sin \theta_0 \sin \psi_0 - Z_0 \sin \phi_0 \cos \theta_0 & R_0 \cos \phi_0 \cos \theta_0 \sin \psi_0 - Z_0 \cos \phi_0 \sin \theta_0 & R_0 \sin \phi_0 \sin \psi_0 + R_0 \cos \phi_0 \sin \theta_0 \cos \psi_0 \end{bmatrix} \quad (39)$$

Finally, the gradient of T_x with respect to $\mathbf{r}_{CG/O} = \{x, y, z\}^T$ is:

$$\frac{\partial T_x}{\partial \mathbf{r}} = \left[-\frac{EA}{L_0} \left(\frac{L_0}{L_n} - 1 + \frac{(x_0 + x_K)^2}{L_0^2} \right) \quad -\frac{EA}{L_0} \frac{(x_0 + x_K)(y_0 + y_K)}{L_0^2} \quad -\frac{EA}{L_0} \frac{(x_0 + x_K)(z_0 + z_K)}{L_0^2} \right] \quad (40)$$

Similar derivations can be repeated for T_y and T_z . Using the substitutions $\bar{x} = x_0 + x_K$, $\bar{y} = y_0 + y_K$ and $\bar{z} = z_0 + z_K$, the full Jacobian of the tether force vector is:

$$\frac{\partial \mathbf{T}}{\partial (\mathbf{r}, \Theta)} = \begin{bmatrix} \frac{\partial T_i}{\partial r_j} & \mathbf{0} \\ \mathbf{0} & \frac{\partial T_i}{\partial \theta_j} \end{bmatrix} \quad (41)$$

where:

$$\begin{bmatrix} \frac{\partial T_i}{\partial r_j} \end{bmatrix} = -\frac{EA}{L_0} \begin{bmatrix} \frac{L_0}{L_n} - 1 + \frac{\bar{x}^2}{L_0^2} & \frac{\bar{x}\bar{y}}{L_0^2} & \frac{\bar{x}\bar{z}}{L_0^2} \\ \frac{\bar{x}\bar{y}}{L_0^2} & \frac{L_0}{L_n} - 1 + \frac{\bar{y}^2}{L_0^2} & \frac{\bar{z}\bar{y}}{L_0^2} \\ \frac{\bar{x}\bar{z}}{L_0^2} & \frac{\bar{z}\bar{y}}{L_0^2} & \frac{L_0}{L_n} - 1 + \frac{\bar{z}^2}{L_0^2} \end{bmatrix} \quad (42)$$

and

$$\begin{bmatrix} \frac{\partial T_i}{\partial \theta_j} \end{bmatrix} = \begin{bmatrix} \frac{\partial T_i}{\partial r_j} \end{bmatrix} \begin{bmatrix} \frac{\partial r_i}{\partial \theta_j} \end{bmatrix} \quad (43)$$

Perturbations of the tether moment

The derivation of the tether moment Jacobian is very similar to the one above, except that one must carry many more terms.

$$\frac{\partial \mathbf{M}_T}{\partial(\mathbf{r}, \boldsymbol{\Theta})} = \begin{bmatrix} \frac{\partial M_{T_i}}{\partial r_j} & \mathbf{0} \\ \mathbf{0} & \frac{\partial M_{T_i}}{\partial \theta_j} \end{bmatrix} = \begin{bmatrix} \frac{\partial M_{T_i}}{\partial T_k} \frac{\partial T_k}{\partial r_j} & \mathbf{0} \\ \mathbf{0} & \frac{\partial M_{T_i}}{\partial T_k} \frac{\partial T_k}{\partial \theta_j} \end{bmatrix} \quad (44)$$

where:

$$\begin{bmatrix} \frac{\partial M_{T_i}}{\partial T_j} \end{bmatrix} = \begin{bmatrix} b_r \frac{T_x T_y T_z}{T_{xz}^3} & -z_B - b_r \frac{T_z}{T_{xz}} & y_B - b_r \frac{T_x^2 T_y}{T_{xz}^3} \\ z_B & 0 & -x_B \\ -y_B + b_r \frac{T_y T_z^2}{T_{xz}^3} & x_B + b_r \frac{T_x}{T_{xz}} & -b_r \frac{T_x T_y T_z}{T_{xz}^3} \end{bmatrix} \quad (45)$$

using the notation: $T_{xz} = \sqrt{T_x^2 + T_z^2}$.

Kinematics

In addition to the equations of motion, we must derive the kinematic relationships between $\Delta \dot{\mathbf{r}}_{G/O}^b$, $\Delta \dot{\boldsymbol{\phi}}$, $\Delta \dot{\boldsymbol{\theta}}$ and $\Delta \dot{\boldsymbol{\psi}}$, and the perturbed state variables.

Perturbed velocities: $\Delta \dot{x}$, $\Delta \dot{y}$, $\Delta \dot{z}$

From the transport theorem:

$$\frac{{}^g d}{dt} \mathbf{r}_{CG/O} = \frac{{}^b d}{dt} \mathbf{r}_{CG/O} + \boldsymbol{\omega}_{b/g} \times \mathbf{r}_{CG/O} \quad (46)$$

$$\begin{Bmatrix} u \\ v \\ w \end{Bmatrix}_b = \begin{Bmatrix} \dot{x} \\ \dot{y} \\ \dot{z} \end{Bmatrix}_b + \begin{Bmatrix} p \\ q \\ r \end{Bmatrix}_b \times \begin{Bmatrix} x \\ y \\ z \end{Bmatrix}_b \quad (47)$$

By expanding the cross-product and re-arranging the terms in the equation, we get:

$$\dot{x} = u - (qz - ry) \quad (48)$$

$$\dot{y} = v - (rx - pz) \quad (49)$$

$$\dot{z} = w - (py - qx) \quad (50)$$

Whence, the perturbed velocities are:

$$\Delta \dot{x} = \Delta u - q_0 \Delta z - z_0 \Delta q + r_0 \Delta y + y_0 \Delta r \quad (51)$$

$$\Delta \dot{y} = \Delta v - r_0 \Delta x - x_0 \Delta r + p_0 \Delta z + z_0 \Delta p \quad (52)$$

$$\Delta \dot{z} = \Delta w - p_0 \Delta y - y_0 \Delta p + q_0 \Delta x + x_0 \Delta q \quad (53)$$

$$\text{Where } \begin{bmatrix} p_0 \\ q_0 \\ r_0 \end{bmatrix} = \boldsymbol{\Psi}_0 \begin{bmatrix} 0 \\ 0 \\ -\Omega_0 \end{bmatrix}$$

Perturbed Euler rates: $\Delta \dot{\boldsymbol{\phi}}$, $\Delta \dot{\boldsymbol{\theta}}$, $\Delta \dot{\boldsymbol{\psi}}$

The Euler rates can be expressed in terms of the body angular velocities as follows (see derivation in page 103 of Ref.¹)

$$\dot{\phi} = p + q \sin \phi \tan \theta + r \cos \phi \tan \theta \quad (54)$$

$$\dot{\theta} = q \cos \phi - r \sin \phi \quad (55)$$

$$\dot{\psi} = q \sin \phi \sec \theta + r \cos \phi \sec \theta \quad (56)$$

Differentiating and linearizing about the trim state, the perturbed Euler velocities are:

$$\Delta \dot{\phi} = \Delta p + \Delta q \sin \phi_0 \tan \theta_0 + q_0 \cos \phi_0 \Delta \phi \tan \theta_0 + q_0 \sin \phi_0 \sec^2 \theta_0 \Delta \theta \quad (57)$$

$$+ \Delta r \cos \phi_0 \tan \theta_0 - r_0 \sin \phi_0 \Delta \phi \tan \theta_0 + r_0 \cos \phi_0 \sec^2 \theta_0 \Delta \theta \quad (58)$$

$$\Delta \dot{\theta} = \Delta q \cos \phi_0 - q_0 \sin \phi_0 \Delta \phi - \Delta r \sin \phi_0 - r_0 \cos \phi_0 \Delta \phi \quad (59)$$

$$\Delta \dot{\psi} = \Delta q \sin \phi_0 \sec \theta_0 + q_0 \cos \phi_0 \Delta \phi \sec \theta_0 + q_0 \sin \phi_0 \sec \theta_0 \tan \theta_0 \Delta \theta \quad (60)$$

$$+ \Delta r \cos \phi_0 \sec \theta_0 - r_0 \sin \phi_0 \Delta \phi \sec \theta_0 + r_0 \cos \phi_0 \sec \theta_0 \tan \theta_0 \Delta \theta \quad (61)$$

State-space equations of motion

The general form of the state-space equations of motion is:

$$\mathbf{M} \Delta \dot{\mathbf{s}} = \mathbf{A} \Delta \mathbf{s} \quad (62)$$

where $\Delta \mathbf{s}$ is the state vector:

$$\Delta \mathbf{s}^T = [\Delta x \quad \Delta y \quad \Delta z \quad \Delta u \quad \Delta v \quad \Delta w \quad \Delta \phi \quad \Delta \theta \quad \Delta \psi \quad \Delta p \quad \Delta q \quad \Delta r] \quad (63)$$

\mathbf{M} is the mass matrix:

$$\mathbf{M} = \begin{bmatrix} 1 & 0 & 0 & 0 & 0 & 0 & 0 & 0 & 0 & 0 & 0 & 0 \\ 0 & 1 & 0 & 0 & 0 & 0 & 0 & 0 & 0 & 0 & 0 & 0 \\ 0 & 0 & 1 & 0 & 0 & 0 & 0 & 0 & 0 & 0 & 0 & 0 \\ 0 & 0 & 0 & m & 0 & 0 & 0 & 0 & 0 & 0 & 0 & 0 \\ 0 & 0 & 0 & 0 & m & 0 & 0 & 0 & 0 & 0 & 0 & 0 \\ 0 & 0 & 0 & 0 & 0 & m - Z_{\dot{w}} & 0 & 0 & 0 & 0 & 0 & 0 \\ 0 & 0 & 0 & 0 & 0 & 0 & 1 & 0 & 0 & 0 & 0 & 0 \\ 0 & 0 & 0 & 0 & 0 & 0 & 0 & 1 & 0 & 0 & 0 & 0 \\ 0 & 0 & 0 & 0 & 0 & 0 & 0 & 0 & 1 & 0 & 0 & 0 \\ 0 & 0 & 0 & 0 & 0 & 0 & 0 & 0 & 0 & I_x & 0 & -I_{xz} \\ 0 & 0 & 0 & 0 & 0 & -M_{\dot{w}} & 0 & 0 & 0 & 0 & I_y & 0 \\ 0 & 0 & 0 & 0 & 0 & 0 & 0 & 0 & 0 & -I_{xz} & 0 & I_z \end{bmatrix} \quad (64)$$

and \mathbf{A} is the state matrix:

$$\mathbf{A} = \begin{bmatrix} 0 & r_0 & -q_0 & 1 & 0 & 0 & 0 & 0 & 0 & 0 & 0 & -z_0 & y_0 \\ -r_0 & 0 & p_0 & 0 & 1 & 0 & 0 & 0 & 0 & 0 & z_0 & 0 & -x_0 \\ q_0 & -p_0 & 0 & 0 & 0 & 1 & 0 & 0 & 0 & 0 & -y_0 & x_0 & 0 \\ T_{xv} & T_{xw} & T_{xz} & X_u & m r_0 & X_w - m q_0 & T_{xv} & T_{xw} & T_{xz} & 0 & -m u_0 & m v_0 & m w_0 \\ T_{yv} & T_{yw} & T_{yz} & -m r_0 & Y_v & m p_0 & T_{yv} & T_{yw} & T_{yz} & Y_p + m u_0 & 0 & Y_r - m u_0 & 0 \\ T_{zv} & T_{zw} & T_{zz} & Z_u + m q_0 & -m p_0 & Z_w & T_{zv} & T_{zw} & T_{zz} & -m v_0 & Z_q + m u_0 & 0 & 0 \\ 0 & 0 & 0 & 0 & 0 & 0 & q_0 \cos \phi_0 \tan \theta_0 - r_0 \sin \phi_0 \tan \theta_0 & q_0 \sin \phi_0 \sec^2 \theta_0 + r_0 \cos \phi_0 \sec^2 \theta_0 & 0 & 0 & 1 & \sin \phi_0 \tan \theta_0 & \cos \phi_0 \tan \theta_0 \\ 0 & 0 & 0 & 0 & 0 & 0 & -q_0 \sin \phi_0 - r_0 \cos \phi_0 & 0 & 0 & 0 & 0 & \cos \phi_0 & -\sin \phi_0 \\ 0 & 0 & 0 & 0 & 0 & 0 & q_0 \cos \phi_0 \sec \theta_0 - r_0 \sin \phi_0 \sec \theta_0 & q_0 \sin \phi_0 \sec \theta_0 \tan \theta_0 + r_0 \cos \phi_0 \sec \theta_0 \tan \theta_0 & 0 & 0 & 0 & \sin \phi_0 \sec \theta_0 & \cos \phi_0 \sec \theta_0 \\ M_{Txx} & M_{Txy} & M_{Txz} & 0 & L_v & 0 & M_{Txx} & M_{Txy} & M_{Txz} & M_{Txx} & L_p + I_{zz} q_0 & I_{zz} p_0 - (I_x - I_y) r_0 & L_r - (I_x - I_y) q_0 \\ M_{Tyy} & M_{Tyy} & M_{Tyz} & M_u & 0 & M_w & M_{Tyy} & M_{Tyy} & M_{Tyz} & M_{Tyy} & -(I_x - I_z) r_0 - 2I_{xz} p_0 & M_q & -(I_x - I_z) p_0 + 2I_{xz} r_0 \\ M_{Tzz} & M_{Tzy} & M_{Tzz} & 0 & N_v & 0 & M_{Tzz} & M_{Tzy} & M_{Tzz} & M_{Tzz} & N_p - (I_y - I_z) q_0 & -I_{xz} r_0 - (I_y - I_z) p_0 & N_r - I_{zz} q_0 \end{bmatrix}$$

Numerical implementation

The state-space equations of motion were implemented in a [Colab notebook](#). The eigenvalues were computed and analyzed to determine the stability of the kite design.

Validation

Free flight

The present analysis and its implementation in Colab were validated against two textbook problems presented in Ref.¹ (problem 4.3 on page 155 and problem 5.3 on page 198). The longitudinal and lateral eigen-values of the general aviation airplane *Navion* were computed and compared to the values

presented in the textbook. Note that the state-space equations of motion derived in the textbook included a gravity force acting at the center of mass of the airplane and directed downward. For comparison, this gravity force was also temporarily added in the present analysis.

Longitudinal model

With gravity terms added to the analysis, the longitudinal eigenvalues were found to match the values presented in the textbook:

$$\lambda_{1,2} = -0.017 \pm 0.213 i \text{ (phugoid)} \quad (66)$$

$$\lambda_{3,4} = -2.511 \pm 2.592 i \text{ (short period)} \quad (67)$$

It is interesting to note that when gravity is ignored, the longitudinal eigenvalues become:

$$\lambda_1 = 0.0 \text{ (rigid-body pitch)} \quad (68)$$

$$\lambda_1 = -0.047 \text{ (heave)} \quad (69)$$

$$\lambda_{3,4} = -2.511 \pm 2.592 i \text{ (short period)} \quad (70)$$

Note that the oscillatory phugoid mode has been replaced by a rigid-body pitch mode and a damped, non-oscillatory heave mode. The short period mode, which is a pure pitching mode, is unchanged which is expected since gravity does not create any pitching moment about the center of gravity of the aircraft.

Lateral model

The lateral eigenvalues, when gravity is included, are:

$$\lambda_1 = -0.00820 \text{ (spiral)} \quad (71)$$

$$\lambda_2 = -8.435 \text{ (roll subsidence)} \quad (72)$$

$$\lambda_{3,4} = -0.487 \pm 2.347 i \text{ (dutch roll)} \quad (73)$$

Omitting gravity, these eigenvalues become:

$$\lambda_1 = 0.0 \text{ (rigid-body roll mode)} \quad (74)$$

$$\lambda_2 = -8.393 \text{ (roll subsidence)} \quad (75)$$

$$\lambda_{3,4} = -0.512 \pm 2.276 i \text{ (dutch roll)} \quad (76)$$

Notice that gravity has a negligible impact on the roll subsidence and dutch roll modes of the aircraft. But the absence of gravity suppresses the spiral mode.

Full model

The eigenvalues of the full model (coupled longitudinal and lateral, 12 state model) were computed as:

$$\lambda_{1,2,3,4} = 0.0 \quad (77)$$

$$\lambda_5 = -8.435 \text{ (roll subsidence)} \quad (78)$$

$$\lambda_6 = -0.487 \pm 2.347 i \text{ (dutch roll)} \quad (79)$$

$$\lambda_7 = -0.00820 \text{ (spiral)} \quad (80)$$

$$\lambda_{3,4} = -2.511 \pm 2.592 i \text{ (short period)} \quad (81)$$

$$\lambda_{1,2} = -0.017 \pm 0.213 i \text{ (phugoid)} \quad (82)$$

We can verify that for the free-flying aircraft, the assumption that longitudinal and lateral modes are decoupled is accurate, as the eigenvalues are unchanged as a result of this assumption.

Tethered flight

Next, we introduced the tether and removed gravity. For this validation case, the tether attachment point was collocated with the center of gravity of the airplane.

The full-system, longitudinal and lateral eigenvalues were computed as follows.

Full model

We started with the full model, in order to verify the later assumption that longitudinal and lateral models can be decoupled.

$$\begin{aligned}\lambda_{1,2,3} &= 0.0 & (83) \\ \lambda_{4,5} &= -0.576 \pm 2.306 i \text{ (short period)} & (84) \\ \lambda_{6,7} &= -1.647 \pm 5.029 i \text{ (tether extension)} & (85) \\ \lambda_{8,9} &= 1.481 \pm 6.978 i \text{ (dutch roll)} & (86) \\ \lambda_{10} &= -12.169 \text{ (roll damping)} & (87) \\ \lambda_{11} &= -0.670 \text{ (forward damping)} & (88) \\ \lambda_{12} &= -0.150 \text{ (spiral)} & (89)\end{aligned}$$

Longitudinal model

We added the position state z to the list of longitudinal states to capture the tether mode. The longitudinal eigenvalues are:

$$\begin{aligned}\lambda_1 &= 0.0 & (90) \\ \lambda_{2,3} &= -0.844 \pm 1.151 i \text{ (short period)} & (91) \\ \lambda_{4,5} &= -1.683 \pm 5.038 i \text{ (tether extension)} & (92)\end{aligned}$$

We can verify that the frequency of the tether extension mode is approximately as we expect:

$$\omega_{4,5} = \sqrt{\frac{k}{m}} = \sqrt{\frac{EA}{mL}} = \sqrt{\frac{(0.75)(40.4e5 \text{ lb})}{(85.4 \text{ slug})(1397.0 \text{ ft})}} = 5.040 \text{ rad/s} \quad (93)$$

In addition, we can see that the tether has a significant effect on the short period mode. Comparing the eigenvalue in Eq. (91) to the one in Eq. (70), we notice that both the frequency and the damping of this mode has changed.

Finally, we can see that the present selection of longitudinal states does not allow to fully recover the short period mode as it is in the full model.

Lateral model

$$\begin{aligned}\lambda_1 &= -0.117 \text{ (spiral)} & (94) \\ \lambda_2 &= -10.810 \text{ (roll damping)} & (95) \\ \lambda_{3,4} &= 0.755 \pm 5.357 i \text{ (dutch roll)} & (96)\end{aligned}$$

We can see that the lateral states do a decent job at capturing the spiral, roll damping and dutch roll modes, although the damping of the unstable dutch roll mode is overestimated.

Eigenvalues of the M600

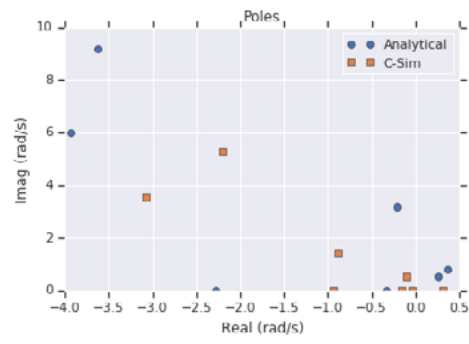
The poles of the M600 were computed by linearizing the C-Sim model (see [Effect of design parameters on the M600 stability in crosswind](#)):

$$\begin{aligned}\lambda_{1,2} &= -2.2045 \pm 5.268 i \text{ (Tether extension)} & (97) \\ \lambda_{3,4} &= -3.0728 \pm 3.525 i \text{ (Dutch roll)} & (98) \\ \lambda_{5,6} &= -0.883 \pm 1.411 i \text{ (Short period)} & (99) \\ \lambda_{7,8} &= -0.10674 \pm 0.547 i \text{ (Phugoid)} & (100) \\ \lambda_9 &= -0.937 \text{ (Roll damping)} & (101) \\ \lambda_{10} &= -0.157 \text{ (Yaw/roll damping)} & (102) \\ \lambda_{11} &= -0.041 & (103) \\ \lambda_{12} &= 0.311 \text{ (Spiral)} & (104)\end{aligned}$$

The root locus plot below also shows the poles computed using the present analytical model.

Note that the poles do *not* agree well. We believe this is because the analytically computed poles correspond to a trivial reference attitude ($\phi_0 = \theta_0 = \psi_0 = 0$), while the numerically computed poles correspond to an actual trim state. A few minutes of experimentation with different reference attitudes with the generalized python code was enough to convince us that the poles vary radically if the reference state deviates from trim.

Unfortunately, the Makani project was shut down before we had a chance to return to this work, so the model must still be considered unverified. We propose, though, that the work accomplished here is nonetheless valuable and presents a sound basis for a derivation of a set of canonical stability criteria for tethered flight.



1. Nelson, R., C., *"Flight Stability and Automatic Control"*, 2nd edition, McGraw-Hill. ↵

Tether Attachment and Bridle Knot Trim Considerations for Energy Kites

Nulling aerodynamic moments by strategic positioning of the tether attachment point and bridle knot

Geo Homsy, Trevor S. Orr, Nicholas Tucker
2019.09.27

Introduction

For a tethered kite, both the tether tension and the aerodynamic forces can be many times greater than the weight of the aircraft. The tension force, by definition, balances the aerodynamic, gravitational, and inertial forces. But what of the *moment* due to the tether? Since the forces are so large, the moments are also, and it would be nice if when the forces were balanced, the moments were as well.

We have design degrees of freedom available with which to affect the tether moment: Where we choose to attach the tether. This paper addresses strategies on how to make that choice.

The first approach is analytical. It assumes we have a craft with a specified trim state, and asks, how should we position the tether attachment so as to minimize control effort to maintain trim? The hope is that choosing the tether attachment to balance the aero and tether moments will ultimately allow greater power output.

The second approach is numerical, and uses the FBL optimizer to optimize total power output of the system, as a function of tether attachment position. This is arguably the most authoritative analysis, so it is best to think of the analytical treatment as an initial thought experiment, to gain insight into the problem.

Analytical Treatment

The situation is shown in the figure below:

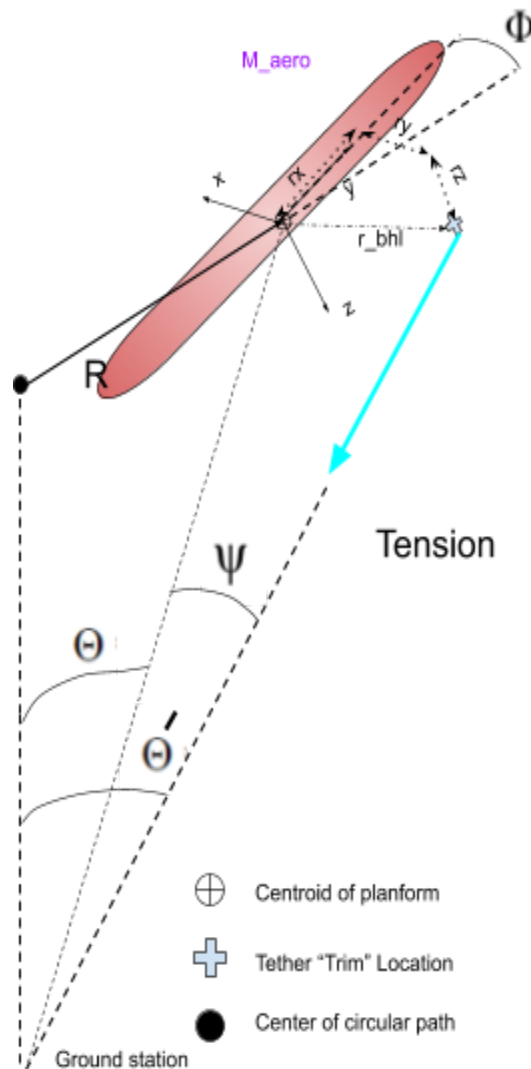


Figure - Sketch of the tether tension acting on a bridle hardpoint location (BHL) an arbitrary distance away from the c.g. of the wing.¹

Positioning the tether attachment point such that the tether moment balances the aerodynamic moment:

Consider a kite in an aerodynamic trim state s . It has some aero force and moment acting on it:

¹ By taking the moments about the c.g. of the kite, the orientation of the kite crosswind path relative to its inclination angle is irrelevant. The equations are all taken about the center of gravity (c.g.) which eliminates the orientation of the gravity vector from the problem.

$$F_a(s), M_a(s)$$

These are typically expressed in the body frame by the mappings:

$$F_a : \langle u, v, w, p, q, r \rangle \rightarrow \langle X, Y, Z \rangle$$

$$M_a : \langle u, v, w, p, q, r \rangle \rightarrow \langle L, M, N \rangle$$

A trim state is by definition a steady state. This requires:

$$F_a + F_t = 0 \tag{1}$$

$$M_a + M_t = 0 \tag{2}$$

Where F_t is the tether tension and M_t is the moment due to tether tension.

M_t is, in turn, given by $M_t = F_t \times r_t$, where r_t is the attachment point of the tether, in body coordinates.

PROBLEM (how to position the tether attachment point to achieve trim): We seek r_t such that (2) is solved: $F_t \times r_t = -M_a$, or

$$F_a \times r_t = M_a \tag{3}$$

We may express this as a matrix multiplication problem using the “ \otimes ” tensor:

$$[F_a \otimes] r_t = M_a \tag{4}$$

Now, the “ \otimes ” operator always, of course, produces a singular matrix, since the solution to (3) is not unique. We may find one solution (the minimum norm solution, in fact), by use of the Moore-Penrose pseudoinverse:

$$A^+ = A(AA^T)^{-1} \tag{5}$$

The minimum norm solution for r_t is:

$$r_0 = [F_a \otimes]^+ M_a \tag{6}$$

And the class of *all* solutions is given by:

$$r_k = r_0 + kF_a = [F_a \otimes]^+ M_a + kF_a \tag{7}$$

This describes a straight-line set of possible tether attachment points, collinear with the tether force vector (makes sense, huh?).

Using the additional degrees of freedom to choose a bridle geometry that maintains trim under perturbations of the trim state

Note that the aerodynamic forces and moments will change as the kite departs from its trim state – their derivatives are, in general, nonzero. Interestingly, a two-point bridle (for instance, in the style of the M600) results in an “effective” tether attachment point (the point around which the tether moment is zero) that changes in response to perturbations in attitude relative to the tether. This effect can help or hinder flight stability, as discussed in “Effect of design parameters on the M600 stability in crosswind”, and in “Kite stability in crosswind flight” [both in this volume].

Substituting a two-point bridle for a single-point tether attachment introduces three additional degrees of freedom into the choice of attachment points.² It is intriguing to entertain the idea of using the entire complement of six degrees of freedom to adjust some or all of the stability coefficients of the craft.

One approach is to perturb the trim attitude (which in general perturbs r_0), and try to solve for the additional bridle degrees of freedom such that the aero moments and the tether moments remain in balance.

PERTURBATION OF ATTITUDE

Let’s say now that we rotate the body through a small rotation. Let the modified aerodynamic state be called s' . The aero forces and moments change slightly:

$$F_a(s'), M_a(s')$$

Let’s compute the differences in F_a and M_a in the body frame:

$$\begin{aligned}\Delta F_a &= F_a(s') - F_a(s) \\ \Delta M_a &= M_a(s') - M_a(s)\end{aligned}\tag{8}$$

If we have the matrix of stability coefficients in terms of α and β , linearized about the trim state, then we can linearize the force and moment to find:

² There are at least two ways to see this. Choosing one extra point is three additional degrees of freedom. Alternatively, choosing a “hinge direction” and a “bridle height” is three additional degrees of freedom.

$$\begin{aligned}\Delta F_a &= C_F \Delta s \\ \Delta M_a &= C_M \Delta s\end{aligned}\tag{9}$$

Where $\Delta s = \langle \Delta\alpha, \Delta\beta \rangle$, and C_F and C_M are submatrices of the stability matrix.

Let's solve for the modified r_0' :

$$r_0' = [F_a(s') \otimes]^+ M_a(s') = [(F_a(s) + \Delta F_a) \otimes]^+ (M_a(s) + \Delta M_a)\tag{10}$$

Now, the \otimes is linear, so we may rewrite the RHS:

$$\begin{aligned}r_0' &= \{[F_a(s) \otimes + \Delta F_a \otimes]^+\} (M_a(s) + \Delta M_a) \\ &= \{[F_a(s) \otimes + (C_F \Delta s) \otimes]^+\} (M_a(s) + C_M \Delta s)\end{aligned}$$

Sadly, the pseudoinverse is not linear, so this whole thing is not linear. If we could linearize it by expanding the pseudoinverse term, we could find the optimal bridle geometry, such that the derivative of tether moment with attitude locally balances the derivative of aero moment with attitude.

But for now, we have abandoned this line of inquiry and done numerical analysis to find the best bridle location.

A Numerical Treatment

We can also perturb the tether location and bridle lengths within FBL to numerically determine an optimal trim state, as well as see sensitivities to being off optimal.

For this exercise, we have selected the 'BigM600_r04c_v04f' config from the "BigM600: Refining Preliminary Design" doc [internal ref].

Important features of this kite:

- Circular paths
 - An artificial minimum turning radius constraint of 90m is applied (unless specified otherwise)
- No yaw moment constraints
 - Enables us to explore a larger space without worrying about zero position of the rudder. We feel this centerpoint is fairly easy to retrim without much consequence, within reason.

- Drag flaps coefficients taken from the M600

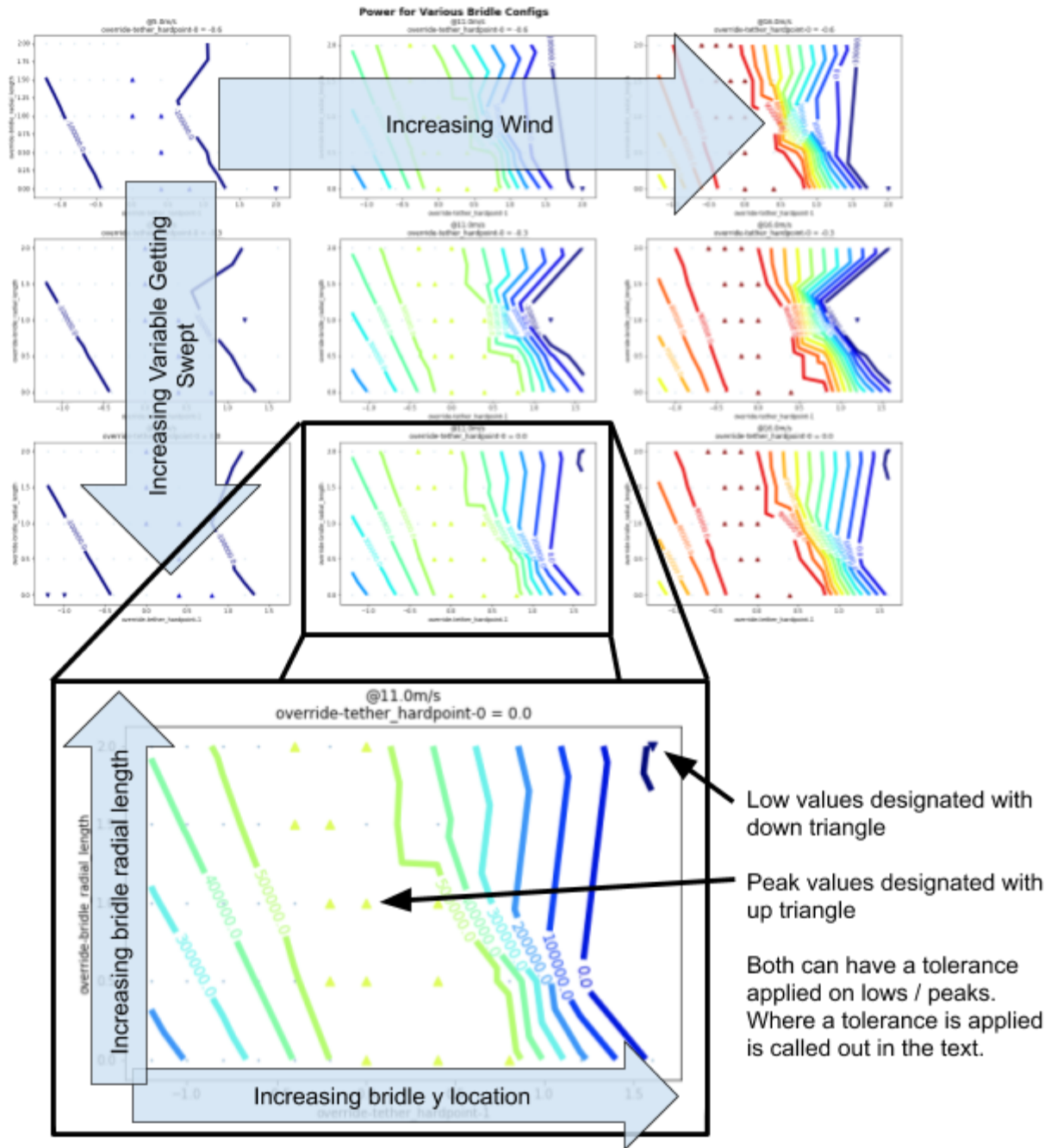
Results

All results are pulled from the following notebooks and datasets:

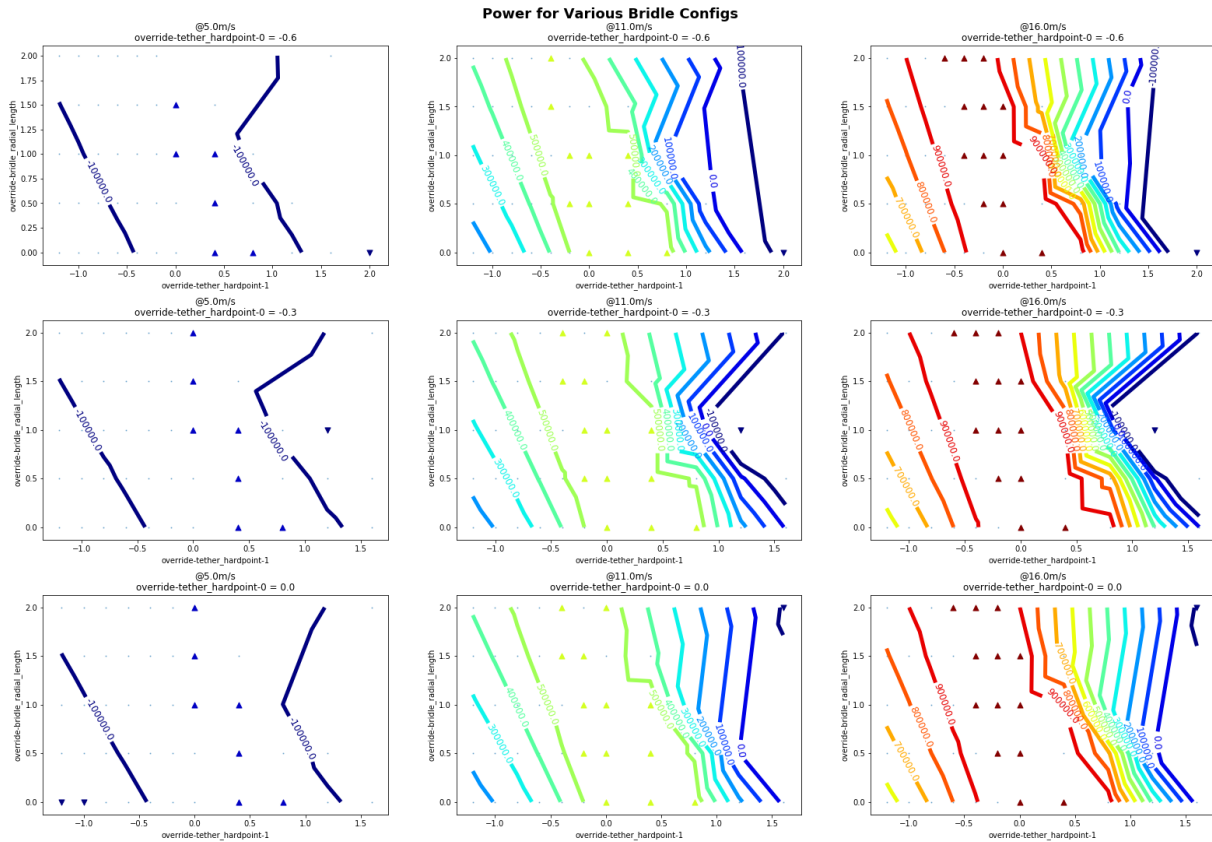
- CoLab notebook - Sensitivity Study V4
- Datasets from this folder:
 - 'BigM600_r04c_v04f_bridle_big_sweep3.json'
 - 'BigM600_r04c_v04f_bridle_sweep_large.json'

Bridle Location

How to read these plots:



Effect on Power



Four dimensions are swept—tether hardpoint x and y location, bridle radial length, and wind speed.

There is a relatively narrow line of ideal bridle knot locations in y and z.

Unsurprisingly, there is little sensitivity to tether attachment in x, at least within the narrow range tried. This is for 2 reasons:

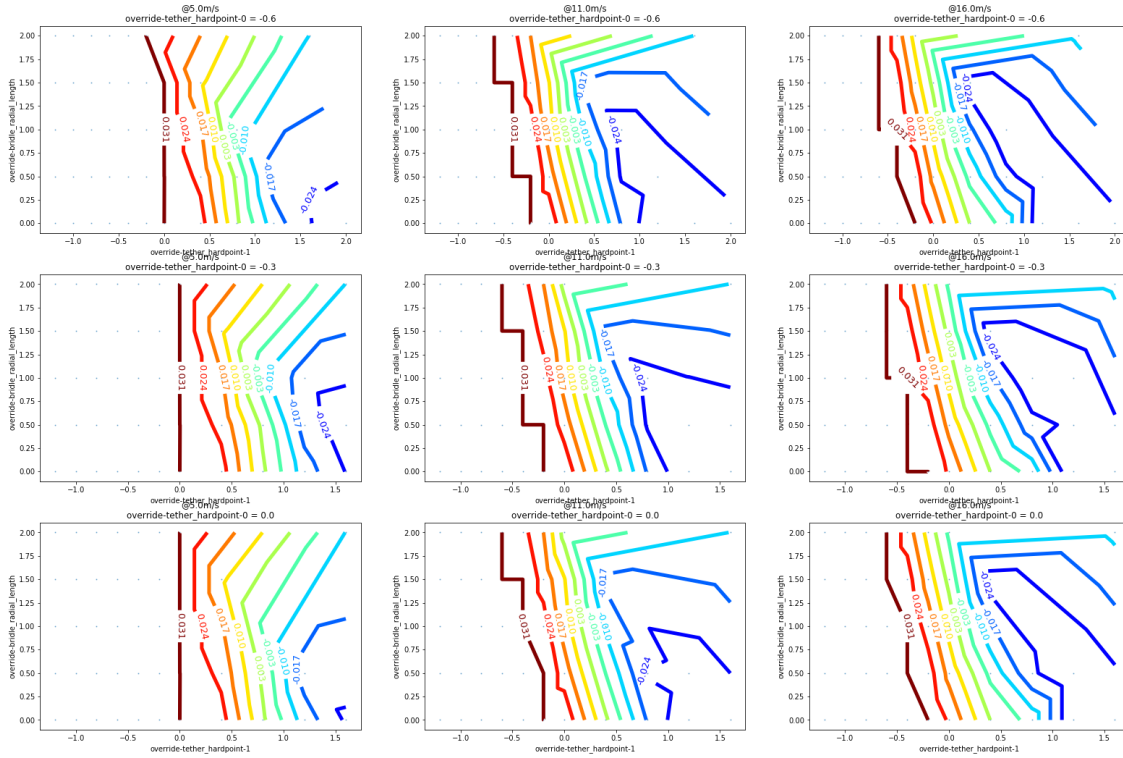
1. The bridle cannot carry moments about its axis of rotation, and the offset of this axis from CG is small, leaving pitch moments from this offset fairly small.
2. The elevator is generally underutilized and is not a limiting factor

In addition, the forces resulting from required elevator trim are ignored in the current model—if substantial downforce is required to trim the kite, this will reduce total lift and therefore power.

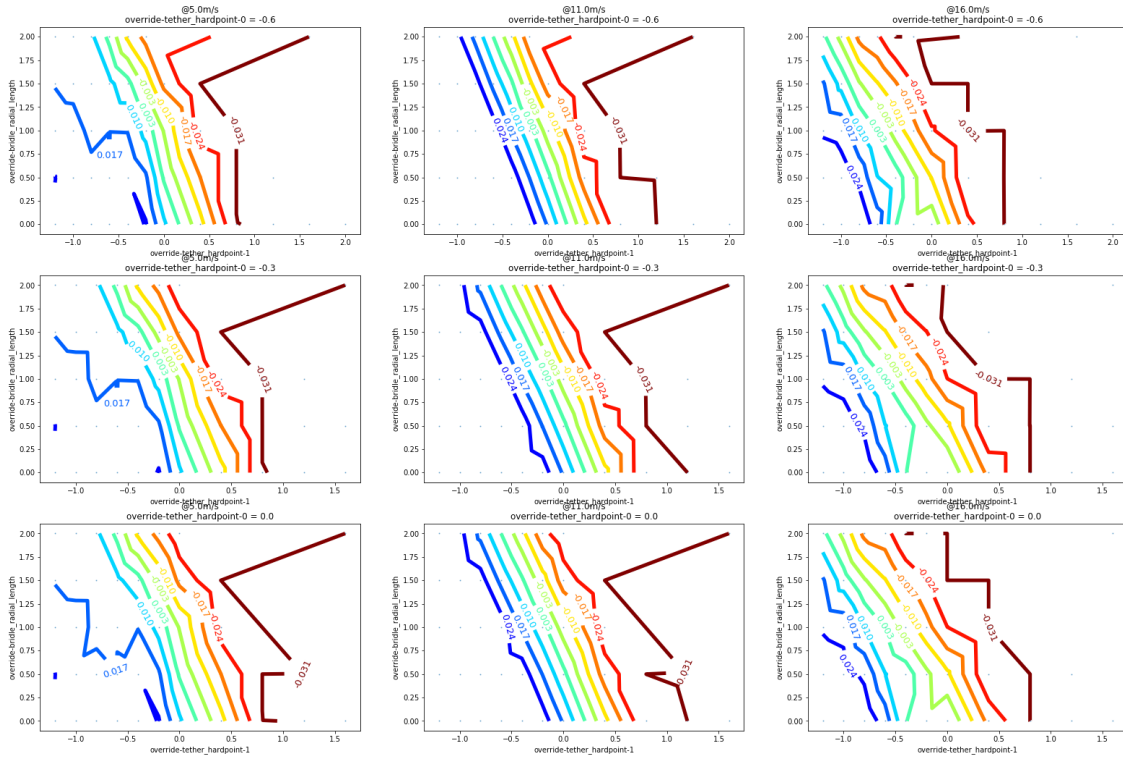
Interestingly, it appears strongly one sided for movement of the knot location in y. There appear to be control strategies that can soften the effect of the poor placement for negative y's, that are not effective for positive y's (knot locations to the right of ideal).

Effect on Roll Moments

Roll Flap Max Coeff for Various Bridle Configs



Roll Flap Min Coeff for Various Bridle Configs



Here, we place levels such that the darkest red values are the current control moment limits for min and max, respectively. The color scales are reversed for the min plot.

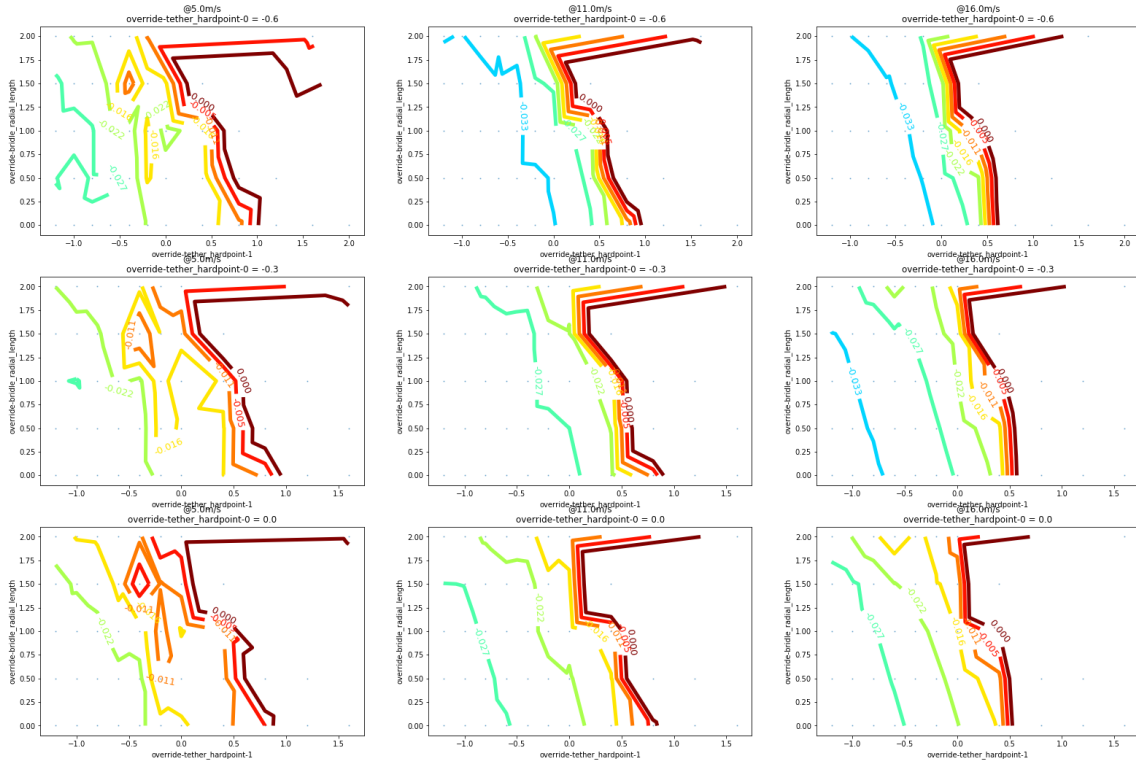
It appears we also have a fairly wide region where we aren't operating continuously against the constraint—i.e., the zone between the red line on the max plot and the red line on the min plot.

However, the model is known to be unconservative here—having additional roll authority margin over our limit will greatly aid control of the kite.

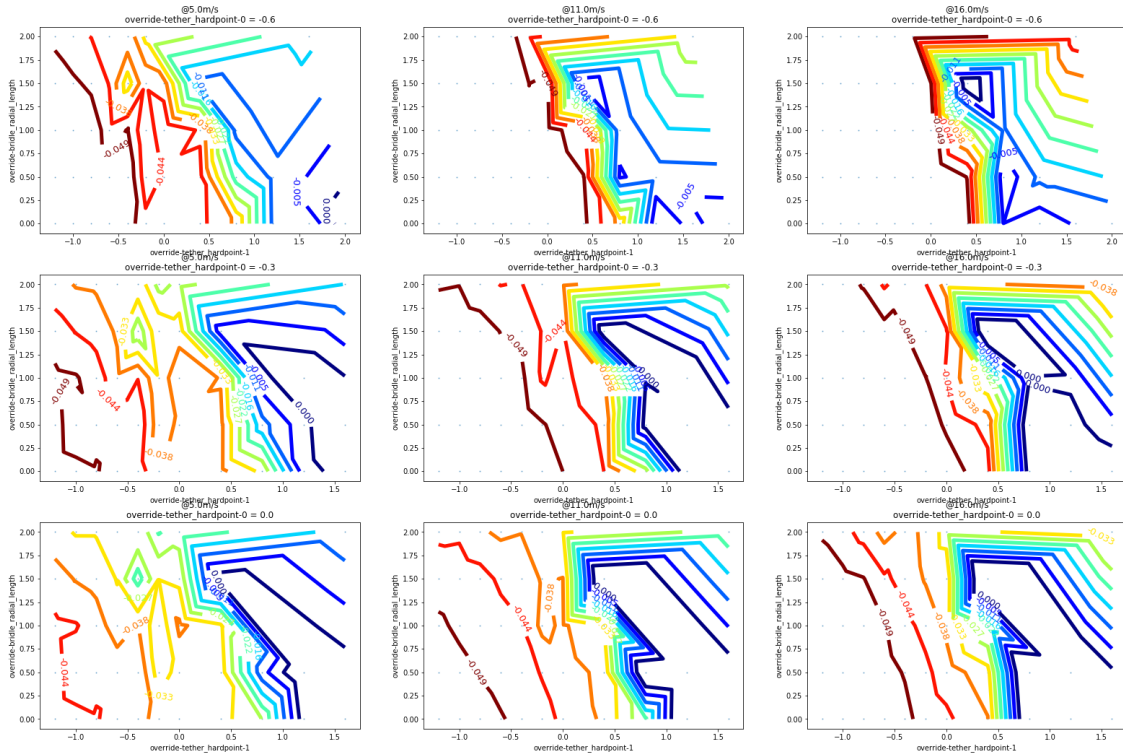
Fortunately, the ideal zone for power is right in this zone. This is not a coincidence—once a constraint is hit, it begins to impact power.

Effect on Yaw Moments

Yaw Flap Max Coeff for Various Bridle Configs



Yaw Flap Min Coeff for Various Bridle Configs



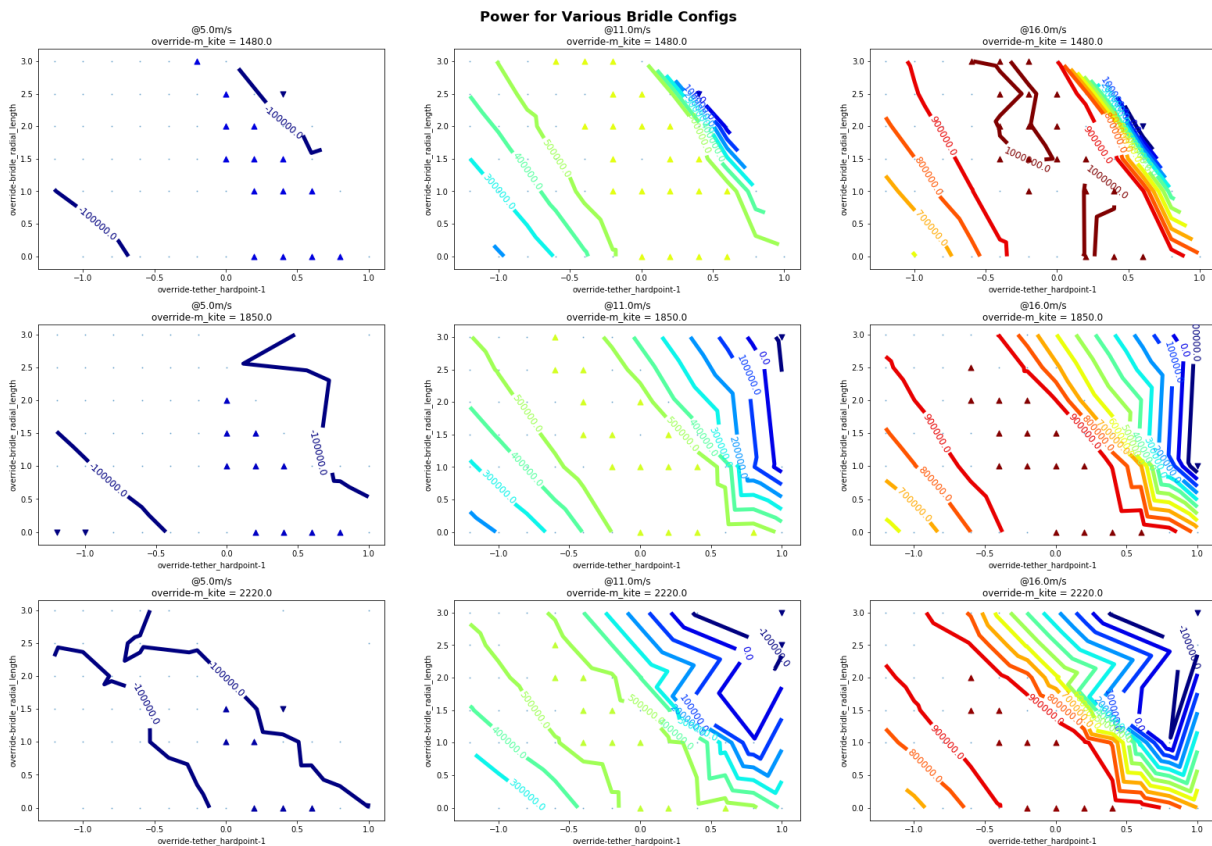
The yaw axis is more interesting, perhaps because this experiment allowed the kite to be unconstrained in this axis.

Without a constraint, levels were manually selected such that the *range* is the same as similar kites where we applied limits, but *shifted* so that the red values were centered around the best power zone.

There is substantial movement of the min coeff with changes in x location of the hardpoint, and a sharp gradient with increasing y offset.

It's unclear if these trends would stay the same once limits are in place, and this is an area for a future study.

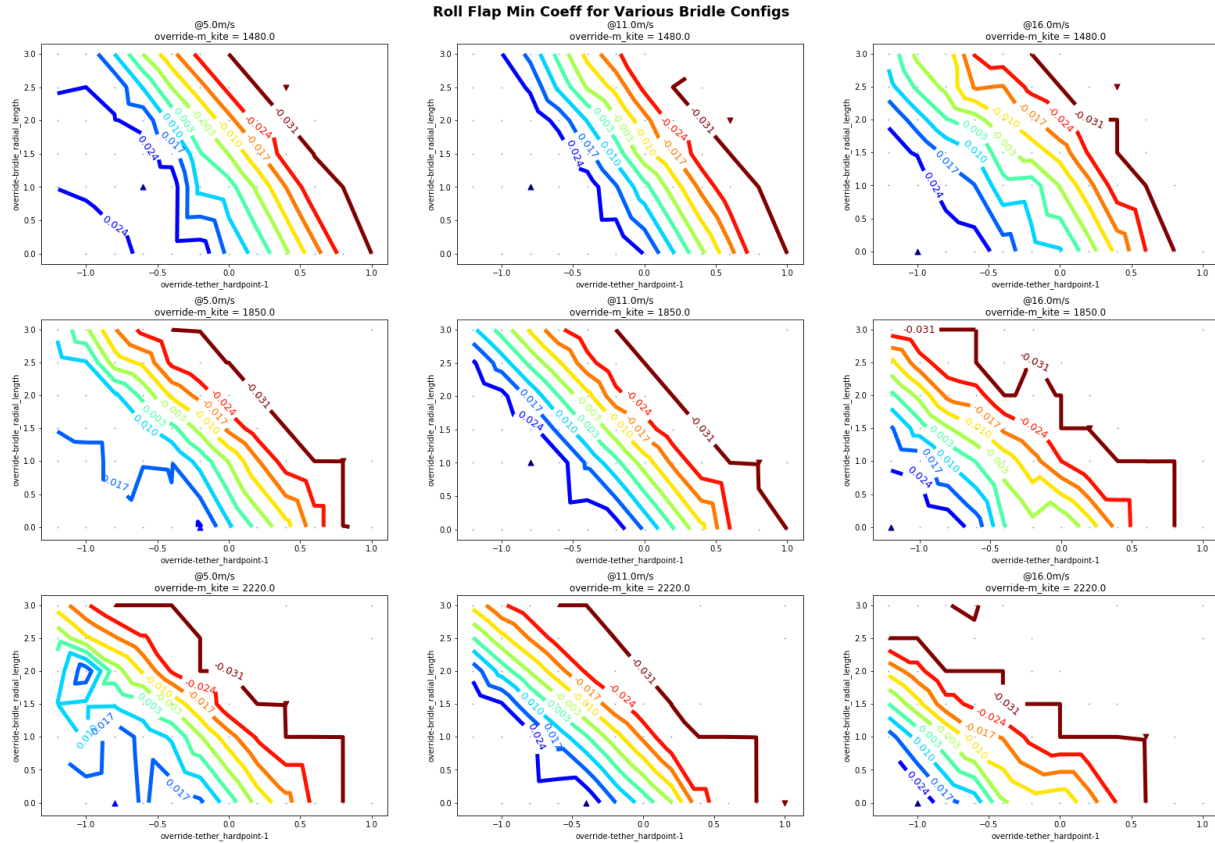
Sensitivity to Mass



The vertical subplot axis is now mass, with values of 0.85, 1.0, and 1.2 times nominal, going top to bottom.

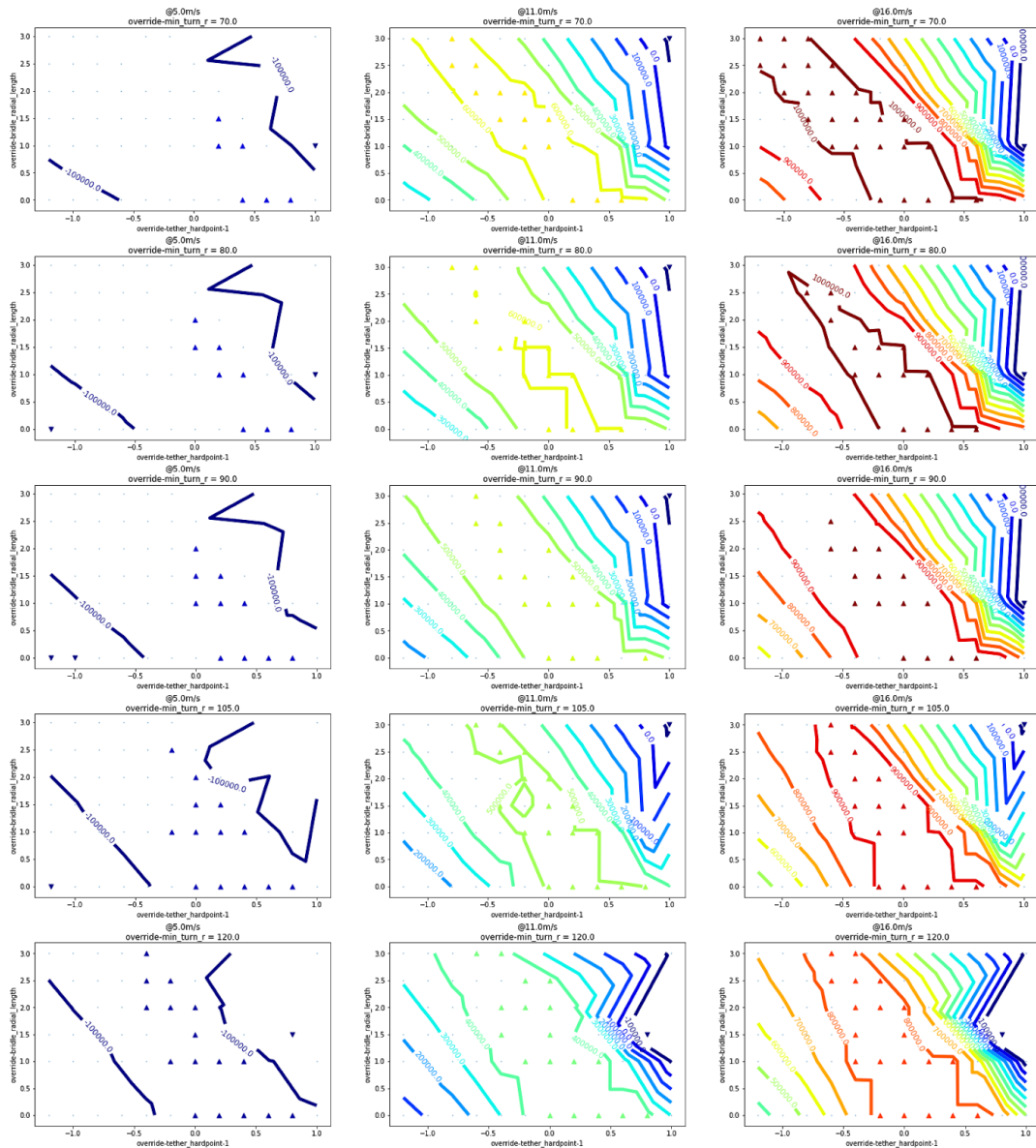
Peak and valley markers are for anything with 10kW of the max and min, respectively, for each contour plot.

Heavier kites require large roll for the same turn, and this tilts the ideal zone as kite mass grows. This requires increasing amounts of negative roll flap aero coefficients, as shown in the plot below. The min flap coefficient drifts continually left, and roughly aligns with the start of the drop off ledge in power.



Sensitivity to Loop Size

Power for Various Bridle Configs



Loop size strongly affects power, but bridle location appears to have little effect on the shape of these contours.

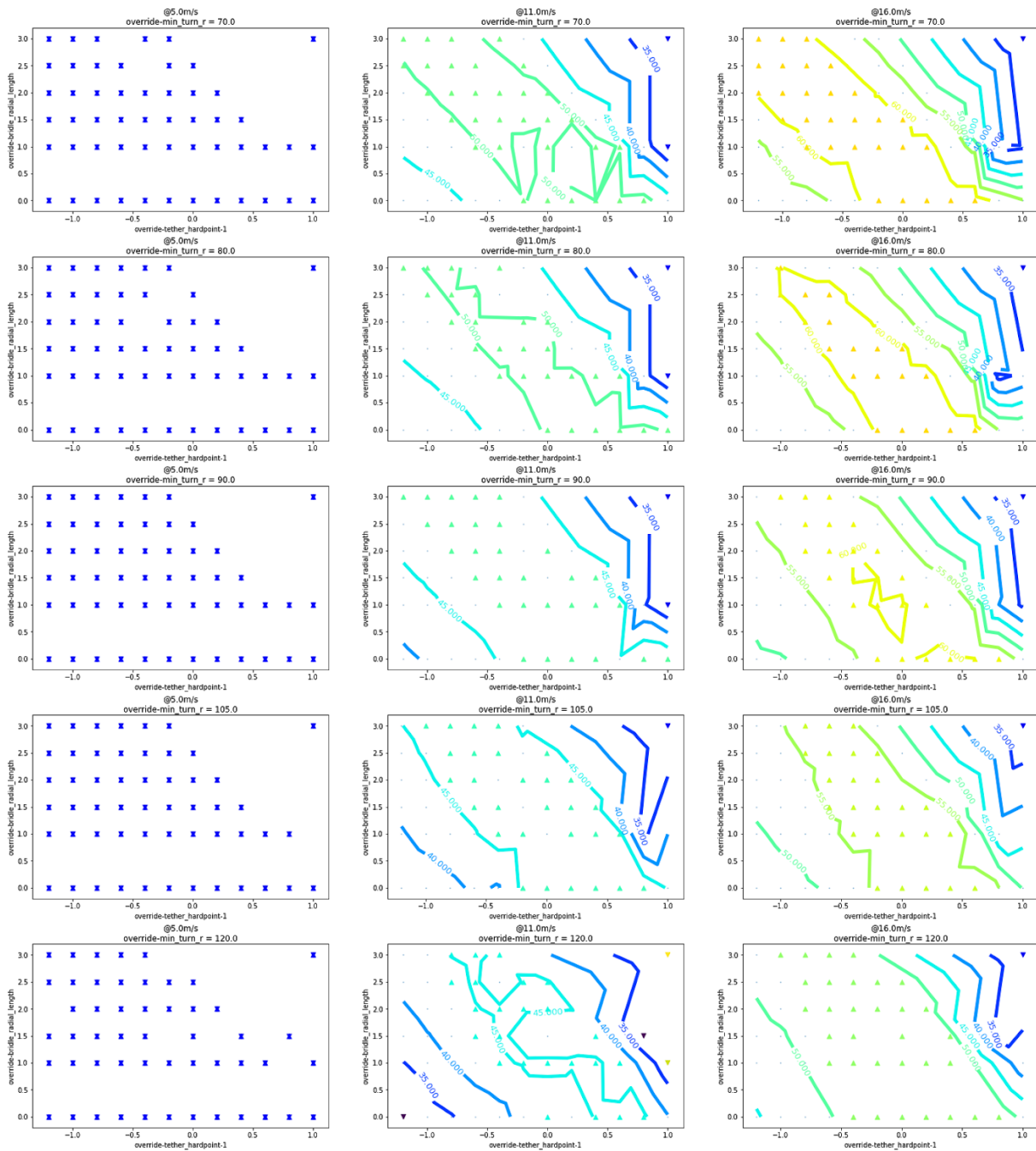
In other words, bridle changes are unable to recoup the losses associated with larger loop sizes.

This is because fundamentally, larger loop sizes hurt performance due to pushing the loop increasingly off wind as average inclination increases in order to hold the minimum height the same.

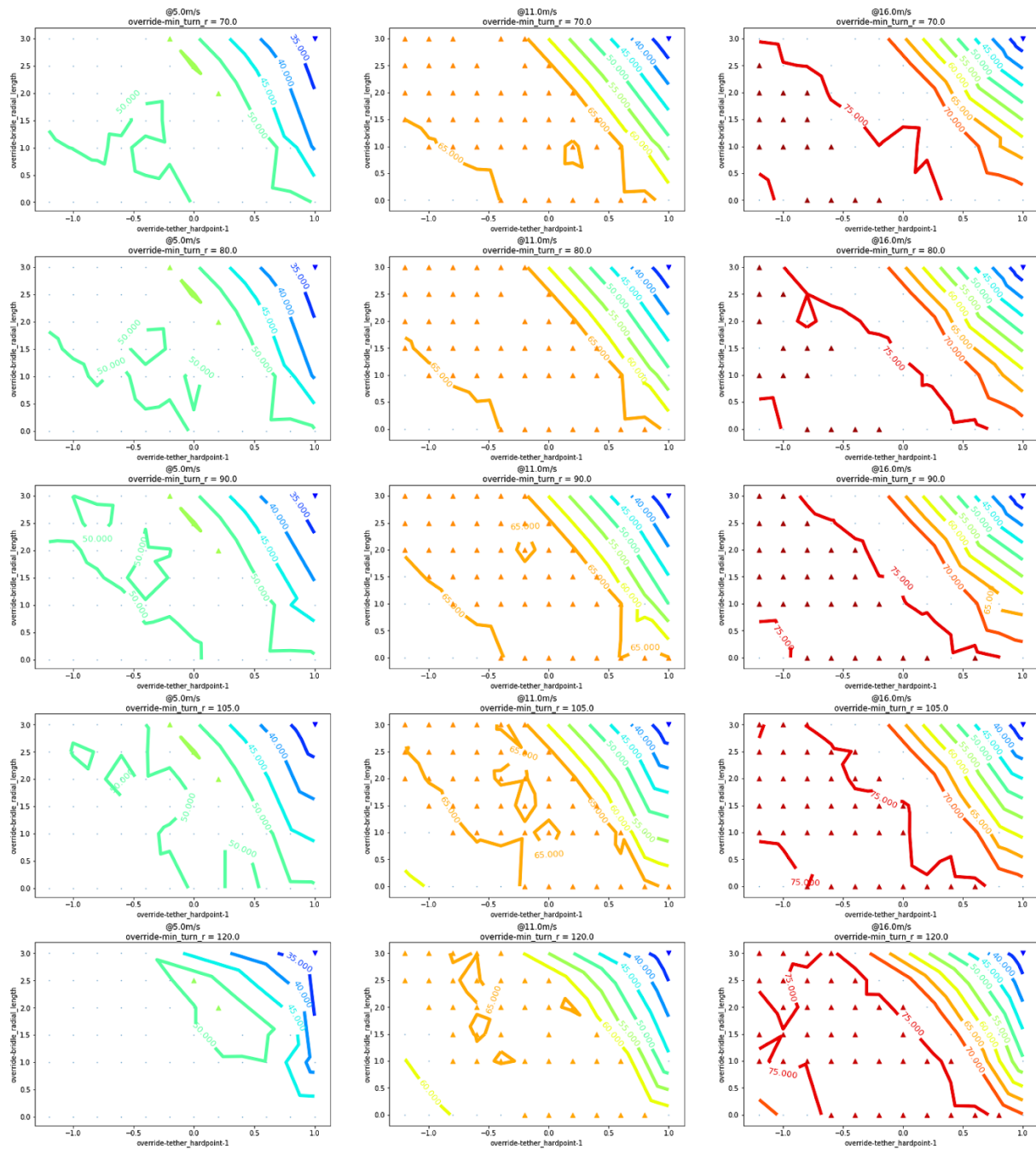
There are smaller effects from increasing loop size. For example:

- The region that isn't hitting roll limits gets slightly smaller.
 - Clearly has a small impact. If it was large, we would see a big sensitivity with power, as we saw in previous results that the power zone follows these limits.
- The airspeed range grows to store more potential energy in kite speed, but this mostly shows up as the slowest airspeed getting slower.
 - Interestingly, the fastest airspeeds don't really change much.
 - Why? Why doesn't the kite like faster?
 - The power vs speed curve is steeper on the high side. It costs more delta speed to store the same energy on the slow side of optimum, but the lost power is relatively less.
 - This is shown in the plots below
 - Peaks and lows are marked for all points within 2.5 m/s of the max and min, respectively.

V_a Min for Various Bridle Configs



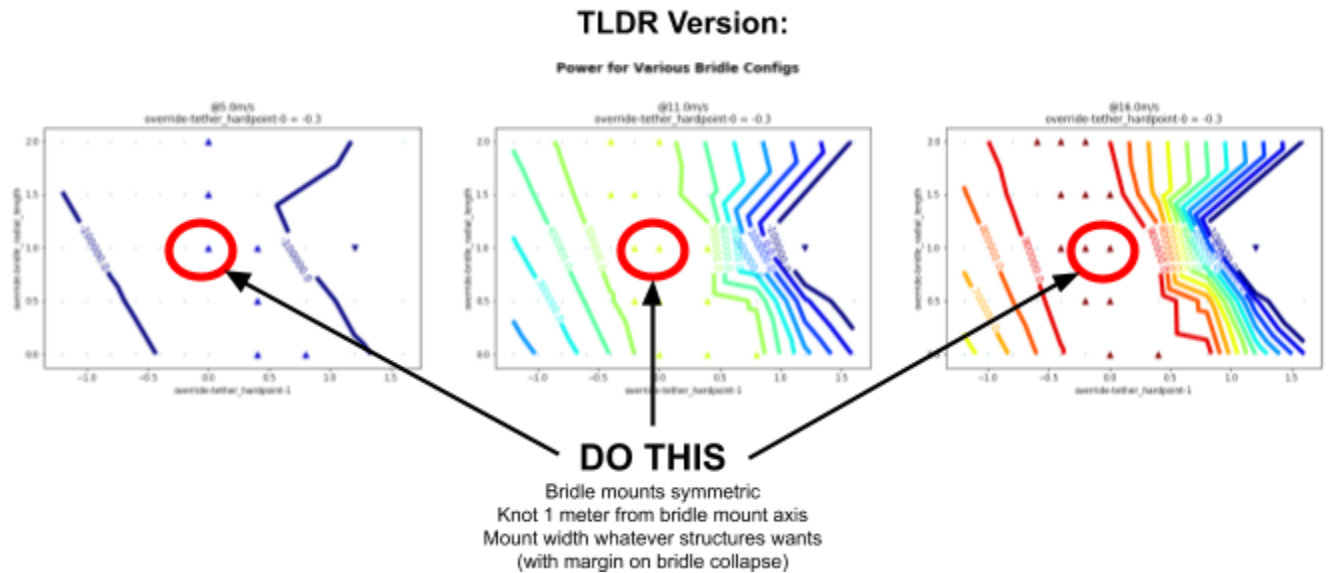
V_a Max for Various Bridle Configs



Conclusion

There appears to be a point that covers optimums for a wide range of kite mass, loop size, and wind speeds, while simultaneously supporting a symmetric tether attach config.

This is great news! We should pick that point.



Appendix: Comparison with M600

This study is based on a “degraded” M600. The intent is to be an M600 that conservatively approximates the M600 in CW01-09 config. Roll and yaw control authority is degraded by 20% from the max authority at full deflection to add conservatism. This was found in a prior study to translate well into high flight quality scores in Csim.

Source data can be found in the folder [internal ref], and the study results are in [internal ref]:
CurrM600_bridle_sweep.json

The full override can be found in the study result file, but is repeated below:

```
m600_degraded_override = {
  'name': 'M600_degraded',
  'aero_db_file': 'm600_aswing_baseline.json',
  'CG': [-0.085, 0.037, 0.108],
  # 'aero_device_name': 'm600_drag_flaps',
  'aero_thrust_p_max': 650000.0,
  'aero_thrust_p_min': -1000000.0,
  'alpha_max': 4.0,
  'alpha_min': -8.0,
  'b': 25.66,
```

```
'beta_max': 5.0,  
'beta_min': -5.0,  
'bridle_y_offset': 0.,  
'bridle_radial_length': 4.786,  
'c': 1.28,  
'cD_tether': 0.7,  
'cD_offset': 0.0901,  
'cL_offset': -0.125,  
'cl_residual_max': 0.088,  
'cl_residual_min': -0.08,  
'cm_residual_max': 0.32,  
'cm_residual_min': -0.48,  
'cn_residual_max': 0.016,  
'cn_residual_min': -0.016,  
'eta_motors': 0.94,  
'eta_motor_ctrls': 0.96,  
'eta_pad_trans': 0.975,  
'gs_position': [0.0, 0.0, 6.122],  
'h_min': 90.0,  
'incl_max': 1.1,  
'inertia': [[3.30683958e+04, 4.98113169e+01, 2.34839824e+01],  
            [4.98113169e+01, 8.66580012e+03, 2.34839824e+01],  
            [2.34839824e+01, 2.34839824e+01, 3.88217609e+04]],  
'l_tether': 439.2,  
'm_kite': 1692.2999999999997,  
'm_tether': 390.45,  
'ohms_per_m_tether': 0.0023485,  
'power_shaft_max': 900000.0,  
'rotor_mach_limit': 0.75,  
'rotor_thrust_axis': [1., 0., 0.],  
'rotor_thrust_center': [ 1.78650000e+00, -5.55111512e-17, 1.90500000e-01],  
's': 32.9,  
'rotor_pitch': 0.,  
'a_rotors': 33.238,  
'n_rotors': 8,  
't_tether': 0.0294,  
'tension_max': 240000.0,  
'tether_hardpoint': [-0.1494, -0.5091, 0.13035],  
'tether_roll_max': 0.5813529864767953,
```

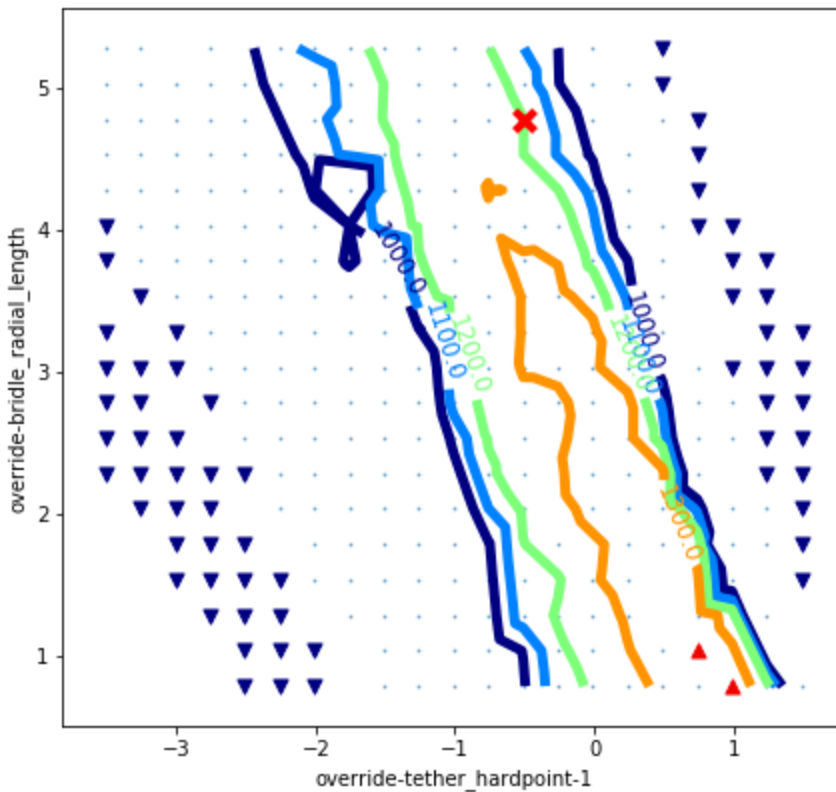
```
'tether_roll_min': -0.3786470135232046,
'torque_shaft_max': 1000.0,
'v_a_max': 70.0,
'v_a_min': 35.0,
'v_tether': 4200.}
```

Effect on Power

The bridle position pre-ECR425 is shown with the **X**. ECR425 shifted the radial position out and the knot further in -y, by 200mm and 185mm, respectively, nearly the same as moving one point up and left from the marked location. This change was only present for some of the PR test flights from CW01 - CW09. The default location was used for all RPX flights.

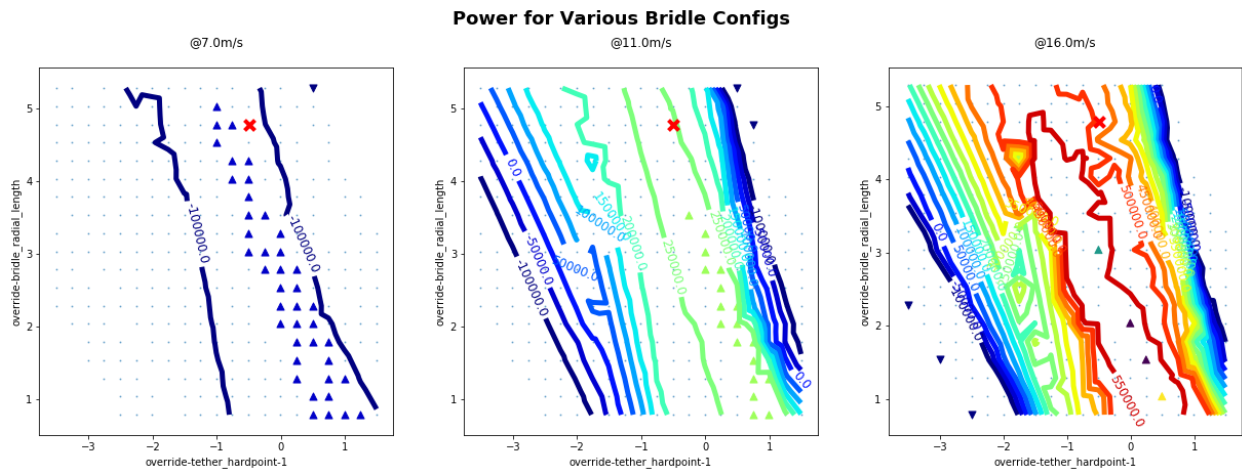
Note that these plots have a MUCH expanded range compared to the above plots. This is because the radial length of the M600 bridle is large at almost 5 meters, so I wanted to cover everything from this range down to no bridle at all.

AEP for Various Bridle Configs



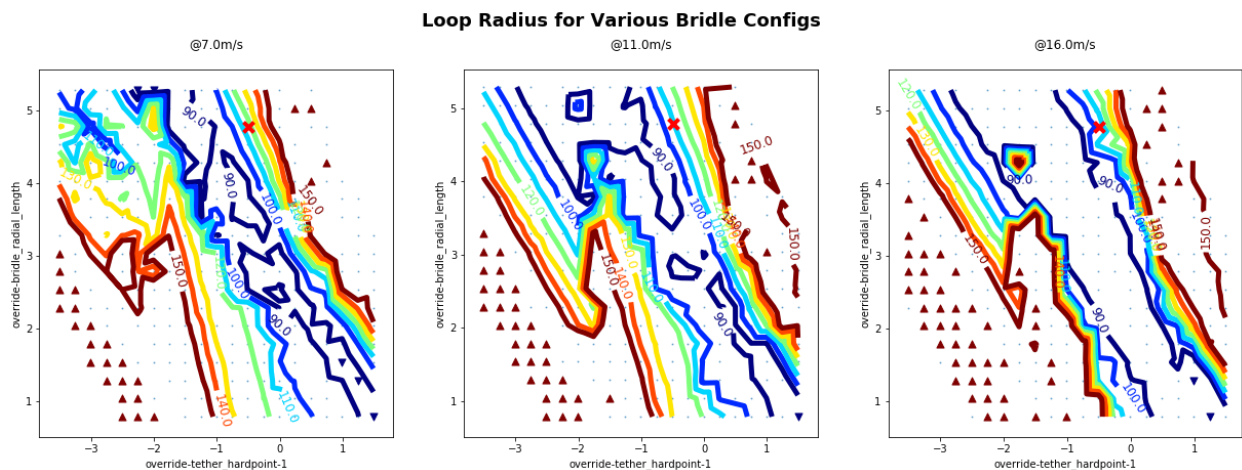
Peak / valley markers have a tolerance of 10 MWh. The M600 is surprisingly close to the plateau. Looking at the BigM600 sensitivity to mass presented above, we'd expect a lighter kite to shift the contours clockwise, and move this point further into a plateau—it may be well suited for the original design intent.

Performance continues to meaningfully increase for shorter bridles, but the peak only represents ~15% increase in AEP. For reference, AEP is gross (i.e., no losses, availability, etc), calculated for a class 1 site with an average wind speed of 9 m/s and no shear. Further details on the resource specifications are in the data file.



Looking at power, peak / valley markers have a tolerance of 10 kW. Contour lines are every 50 kW. The optimal bridling gains are larger at higher winds, but it's at such high wind speeds with low probability of occurrence it has a smaller impact on AEP.

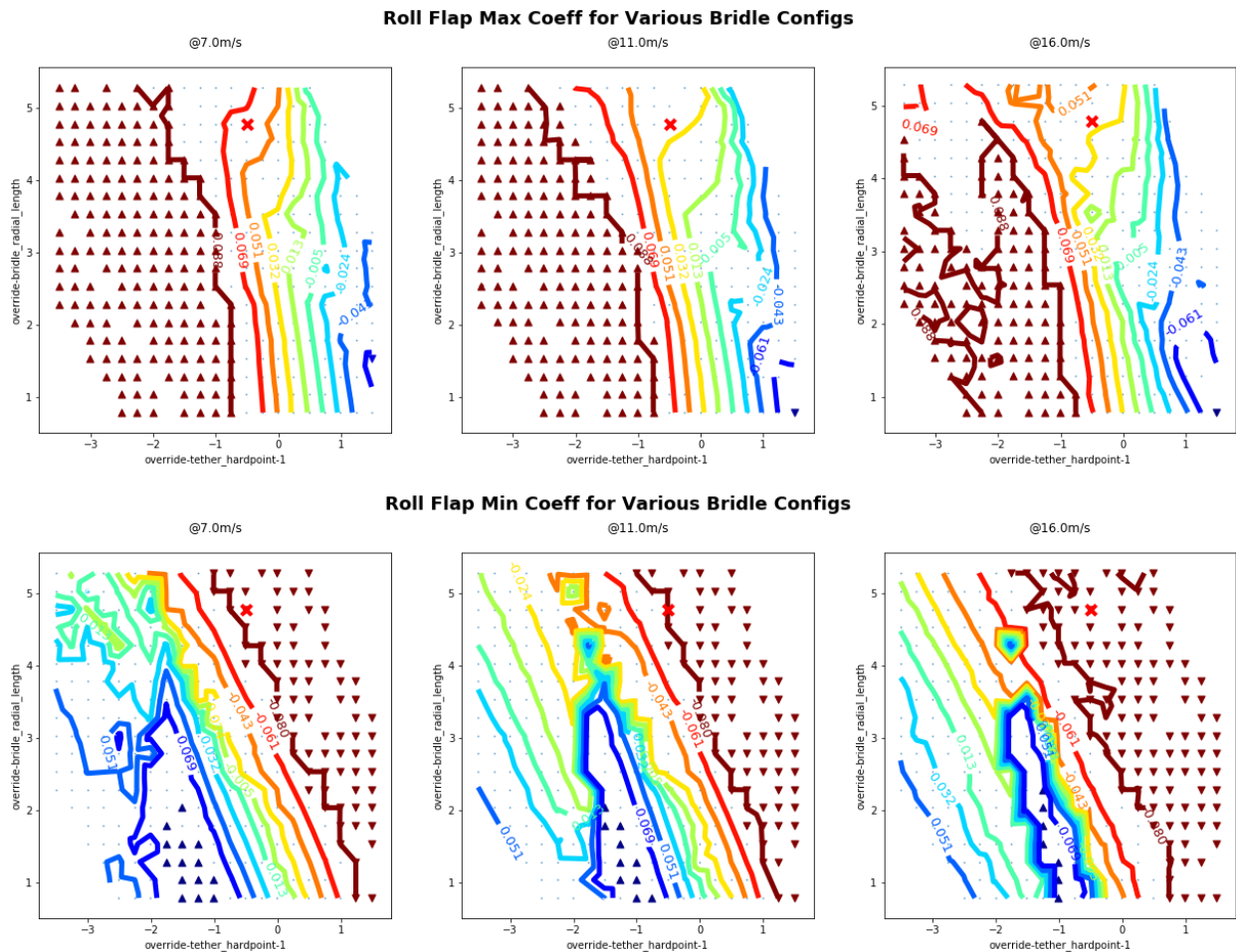
Other Effects



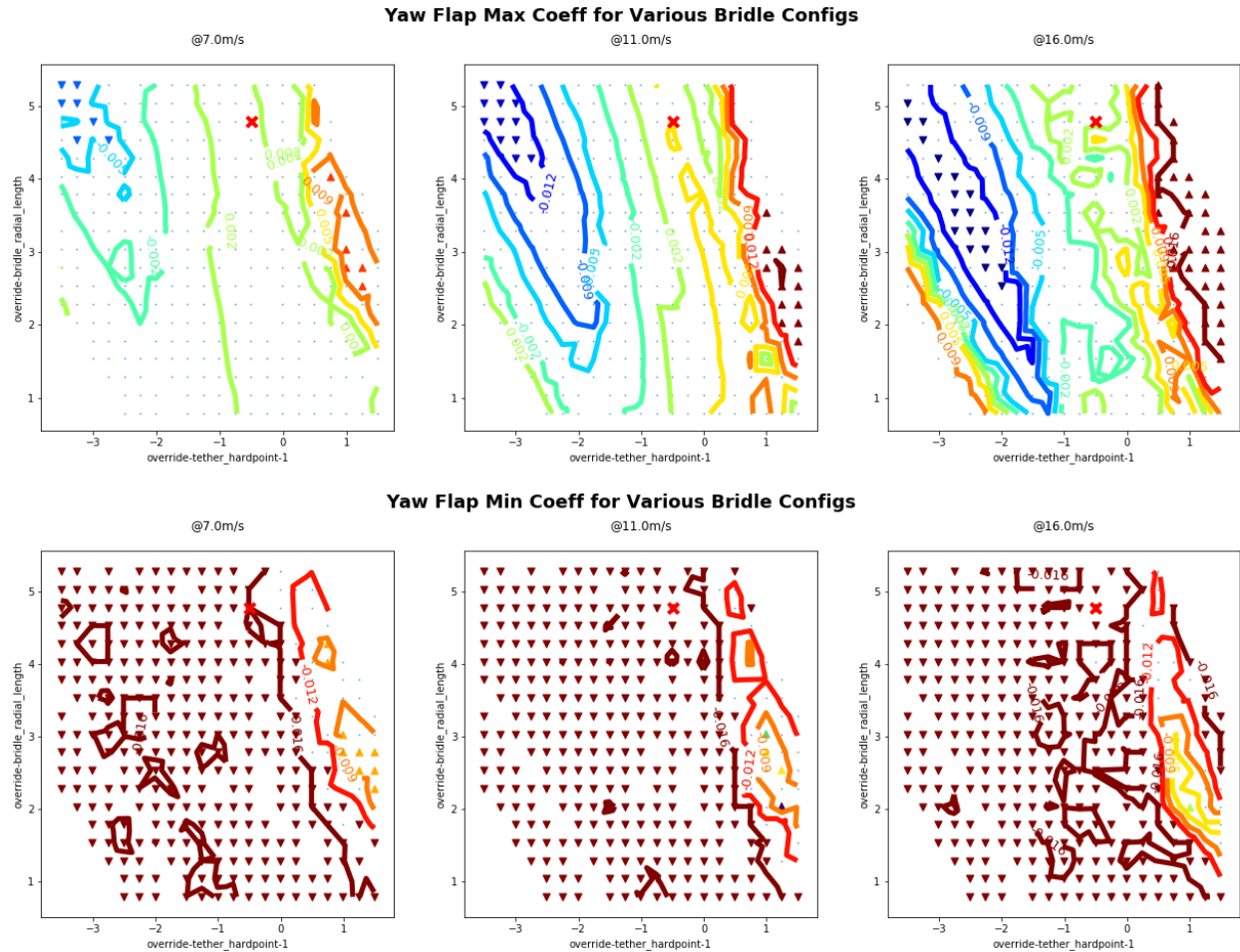
We'd expect improper bridling to have a strong influence on minimum loop size, and it does. Min loop radius was unconstrained, naturally resulting from bridling and control authority.

The M600 sits around 110 - 120 m loop radius as the minimum possible, but a relatively minor shift in bridle knot (250mm in or towards the left wing) would get another 10m of loop radius.

There appears to be some divergence in optimizer solutions for loop radius indicated by the jagged left edge of the plateau, but this has a small effect on power output.



As we saw in the October kite example above, the best power region occurs when the required roll moment is well centered within the flap limits—i.e., the kite is not constrained by its control authority on the roll axis. Peak / valley marker tolerance is +/- 0.001 in flap coefficient.

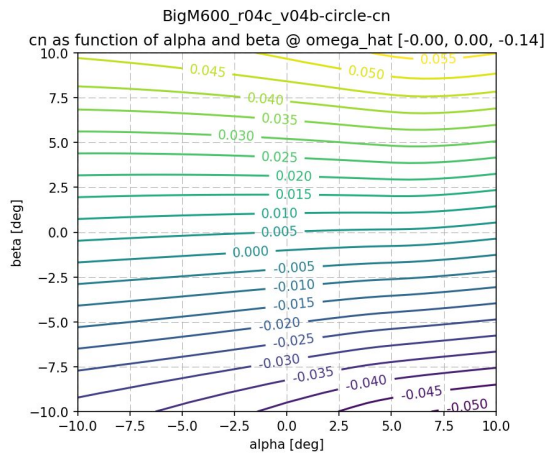
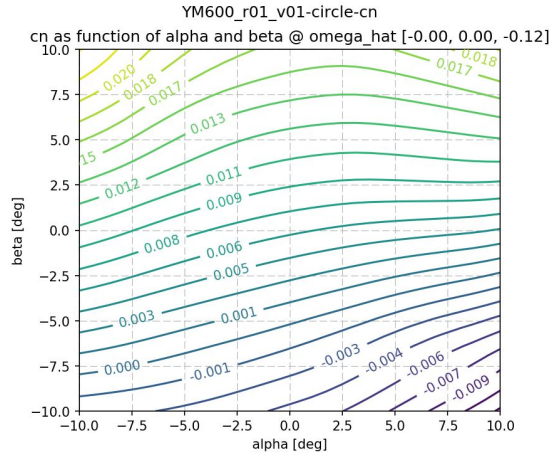


Moments on the yaw axis appear poorly centered for the M600, as it always rides the minimum flap coefficient for nearly all points.

Is this backed by flight test data? Do we usually saturate left rudder at smaller loop sizes? Given that loop sizes don't continue to meaningfully lower once bridle position is such that the kite is no longer constrained in the roll axis, I think this becomes the main limiting factor.

Important to keep in mind is that the M600 has much less yaw stability than October kite designs. This makes FBL analysis on the yaw axis much less conservative for the M600.

$C_{n_{\beta}}$ is ~ 0.0012 for the M600, and ~ 0.0048 for the BigM600, approximately 4x greater. The means the BigM600 can self correct for yaw axis moments by flying a different beta, while the M600 is much more reliant on the rudder surface.



Crosswind Kinematics

The Consequences of Outer Loop Commands

Michael Abraham

`michael.d.abraham@gmail.com`

Introduction & Motivation

The purpose of this document is to derive the complete 6-degree-of-freedom commanded kite state from the outer loop flight control commands and the wind estimate. This complete state can be used to compute the detailed kite motion consequences of proposed playbook commands and also to create feedforward commands for the inner loop flight control laws.

As of March 2019, the flight controls do only a subset of this derivation with many (frustrating) assumptions in place: only circular paths, only a subset of the 6-DOF kite state, uses numerical differentiation (not analytic), ignores the time derivatives of alpha and beta, etc. This document describes how to remove the assumptions and shows how to **analytically compute the complete kite state for paths of general shape**.

As of CW04 the outer loop commands used to compute a subset of the kite state command are:

From Playbook

- circle radius, azimuth, & elevation
- airspeed
- alpha
- beta

From the Path Controller

- tether roll angle

From the Estimator

- wind vector

The above inputs **are not sufficient** to fully specify the complete rigid body kite state. At minimum, the 1st time derivatives of alpha, beta, and tether roll are required in order to compute the complete angular velocity command. Furthermore, several of the commanded quantities are associated with the apparent wind (airspeed, alpha, beta) and so they must be combined with the wind vector to compute quantities with respect to the ground frame.

The complete 6-degree-of-freedom kite state consists of translation states and rotation states. This kite state is the purpose of this document and it is summarized below.

States

- Position of kite
- Velocity of kite with respect to ground
- Direction Cosines Matrix from ground to kite
- Angular Velocity of kite w.r.t. ground

Nomenclature

- {x, y, z} in frame g components
- {u, v, w} in frame b components
- DCM_g2b
- {p, q, r} in frame b components

This is the typical choice of states for atmospheric flight vehicles: position written in frame g but linear velocity and angular velocity both expressed in vehicle-fixed coordinates (frame b). The attitude parameterization is left as general as possible: the direction cosines matrix itself. Because DCM_g2b is an output, the velocities may be easily transformed to frame g if desired.

Nomenclature

Points

- o Origin of the Ground Frame. This is also the center of the sphere.
- k Kite. Origin of the Body Frame. Also origin of the Fly Frame.

Reference Frames

- g Ground. Centered at point o with NED unit vectors (North, East, Down)
- a Atmosphere. Same directions as frame g but with the atmosphere's translational motion
- b Body. Rigidly attached to the kite, centered at point k. (Nose, Starboard, Belly)
- f Fly. X axis along the kite's airspeed vector. Y axis tangent to sphere. Centered at point k.

Vectors

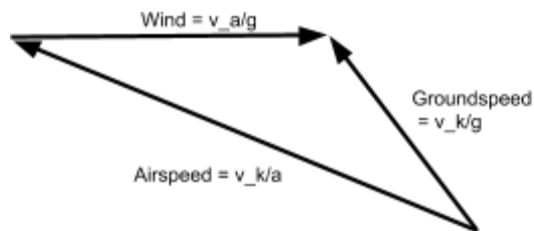
- \vec{r}_{ok} Position vector from point o to point k
- $\vec{v}_{k/g}$ Velocity vector of point k with respect to frame g
- $\vec{a}_{k/g}$ Acceleration vector of point k with respect to frame g
- $\vec{\omega}_{b/g}$ Angular velocity vector of frame b with respect to frame g
- $\hat{i}_g, \hat{j}_g, \hat{k}_g$ Unit vectors of frame g (hats for unit vectors in general)

Assumptions

1. There is wind and we have an estimate of its magnitude and direction.
 - a. Wind is held steady for this analysis.
2. There is a commanded path (position vector from point o to point k).
 - a. Tangent Vector & Curvature Vector also given at every point
3. There is a commanded airspeed and its 1st time derivative
4. There are commanded angles for alpha, beta
 - a. Their 1st time derivatives are also provided
5. The final rotational degree of freedom of the kite is specified as a roll angle about the airspeed vector, "airspeed roll". In practice this will come from the path controller.
 - a. Its 1st time derivative is provided

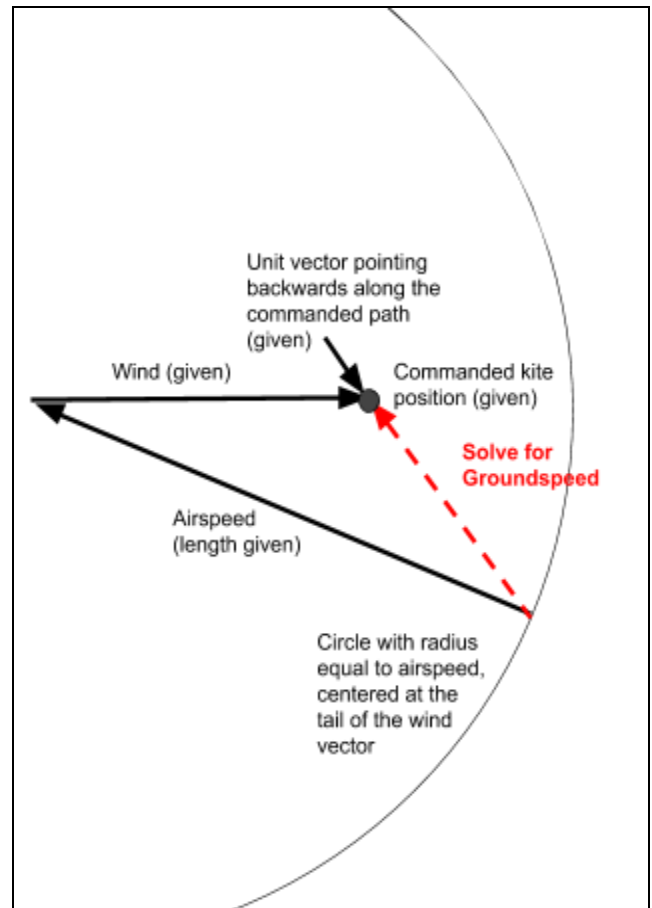
Solving The Wind Triangle

The kite groundspeed, kite airspeed, and wind vectors form a vector equation sometimes called The Wind Triangle. It says simply that the airspeed vector is the groundspeed vector minus the wind vector.



$$\vec{v}_{k/a} = \vec{v}_{k/g} - \vec{v}_{a/g}$$

Presently, playbook specifies a path to fly and an airspeed. Together with the wind vector, this is enough information to uniquely determine the kite's velocity vector with respect to the ground. The direction of the path tangent is critically important to this calculation.



Given the path tangent unit vector (the direction of the commanded kite ground speed vector), we solve for the magnitude of the groundspeed in the flight controls like this:

```
// It's useful to split up the wind vector into components that are
// parallel and perpendicular to the kite velocity. These obey the
// following scalar equation:
//
//     wind^2 = wind_par^2 + wind_perp^2
...
// Calculate the kite speed we need to achieve a given airspeed.
//
// Given wind_par and wind_perp, this becomes a purely scalar
// equation:
//
//     airspeed^2 = (kitespeed - wind_par)^2 + wind_perp^2

const double kitespeed =
    wind_par + Sqrt(Square(airspeed) - Square(wind_perp));
```

The Acceleration Vector

The acceleration of the kite with respect to the ground frame can be constructed from its components along two unit vectors defined at each point on the path: tangent and normal. The component tangent to the path is associated with changes in the kite's inertial speed. The component normal to the path is associated with the kite's local centripetal acceleration.

$$\vec{a}_{k/g} = \frac{dv_k}{dt} \hat{e}_t + \frac{v_k^2}{\rho} \hat{e}_n$$

The path tangent vector, \hat{e}_t , the path normal vector, \hat{e}_n , and the path radius of curvature, ρ , are provided as inputs. In addition, the kite's airspeed, v_a , and its first time derivative are provided as inputs. The procedure for calculating the acceleration vector from these quantities is outlined below.

The wind triangle gives the following scalar relationship among the kite airspeed, v_a , the kite groundspeed, v_k , and the components of wind which are parallel to and perpendicular to the kite groundspeed vector, $w_{||}$ and w_{\perp} .

$$v_a^2 = (v_k - w_{||})^2 + w_{\perp}^2$$

Eliminating the perpendicular wind component with substitution and then taking a time derivative gives an equation which can be solved for the scalar kite acceleration.

$$v_a^2 = (v_k - w_{||})^2 + w^2 - w_{||}^2$$

$$2v_a \frac{dv_a}{dt} = 2(v_k - w_{||}) \left(\frac{dv_k}{dt} - \frac{dw_{||}}{dt} \right) + 2w \frac{dw}{dt} - 2w_{||} \frac{dw_{||}}{dt}$$

$$\frac{dv_k}{dt} = \frac{v_a \frac{dv_a}{dt} + v_k \frac{dw_{||}}{dt}}{(v_k - w_{||})}$$

This above solution for the scalar kite acceleration depends upon the time derivative of the parallel component of the wind. Despite the assumption that the wind vector itself is constant, the kite groundspeed vector changes direction and so the component of wind along that changing derivative has a nonzero time derivative.

The parallel wind component is the dot product of the path tangent unit vector and the wind:

$$w_{||} = \hat{e}_t^T \vec{w}$$

Taking a time derivative (assuming the wind vector is constant):

$$\frac{dw_{||}}{dt} = \frac{d\hat{e}_t^T}{dt} \vec{W}$$

The time derivative of the path tangent unit vector depends upon the path's local radius of curvature, ρ , and the velocity along the path.

$$\frac{d\hat{e}_t}{dt} = \frac{v_k}{\rho} \hat{e}_n$$

$$\frac{dw_{||}}{dt} = \frac{v_k}{\rho} \hat{e}_n^T \vec{W}$$

The “Fly” Frame

This is the frame away from which the kite's rotational degrees of freedom are commanded.

In words, the Fly Frame is: “Nose at the apparent wind. Wings tangent to the sphere.” Another way to say it is: “ $\alpha = \beta = 0$ ” with the addition of a “zero roll” definition (but not zero “tether roll”).

Formal Definition of the Fly Frame

X-axis: Along the kite's commanded airspeed vector

Y-axis: Tangent to the sphere (normal to the kite position vector)

Note: This Y-axis definition is ambiguous. Choose the one which doesn't orient the kite “upside down” from what you'd expect normally.

Z-axis: X cross Y

To rotate **from** the Fly Frame **to** the kite's Body Frame, execute the following single axis Euler Angle Rotations in order:

0. Begin in the Fly Frame: X axis along the airspeed vector, Y axis tangent to sphere
1. Roll (about the airspeed vector) by angle ϕ_a , the “airspeed roll angle”
2. Yaw (about an intermediate axis) by angle $-\beta$
3. Pitch about the kite y axis by angle $+\alpha$

This is an unusual Euler Angle sequence for atmospheric flight applications. Normally, the sequence used is “3-2-1” or “yaw-pitch-roll” but this sequence is instead “1-3-2” or “roll-yaw-pitch”. The reason for this is that **alpha and beta are specified** and **these angles are defined sequentially** with the airspeed vector as the zero reference point. Therefore, the remaining degree of freedom **MUST** be along the airspeed vector and also must come first. If you instead tried to put the rotation about the airspeed vector last in the sequence, it would not be an “Euler Angle” because it would be mixing intrinsic (rotating with the frame) and extrinsic (rotating about some externally defined axis) rotations.

The Fly Frame's axes definitions depend upon (change with):

- Kite position
- Kite velocity
- Wind

This means that even with $\phi_a = \alpha = \beta = 0$, the Fly Frame has angular velocity resulting from the changing kite position and velocity. Calculating the contribution of this frame's motion to the commanded kite angular velocity vector is nontrivial.

An animation of the Fly Frame is provided [internal ref]. In this animation, the kite's translational motion on the sphere is a random combination of sine waves and the kite's attitude is exactly the attitude of the Fly Frame: wings tangent to the sphere, nose toward the apparent wind. Notice the Fly Frame x axis (kite's nose in this movie) points into the sphere a bit, toward the wind.

Direction Cosines for the "Fly" Frame

DCM_f2g is a matrix whose columns are frame f's unit vectors written using frame g components.

$$DCM_{f2g} = \left[\left\{ \hat{i}_f \right\}_g \quad \left\{ \hat{j}_f \right\}_g \quad \left\{ \hat{k}_f \right\}_g \right]$$

Said differently, DCM_f2g is how f's unit vectors look when viewed from frame g. The equation above expresses this relationship using curly brackets with a subscript to indicate a column of components in a certain frame.

Components of DCM_f2g are constructed from kite commands as follows.

Unit vector along airspeed	$\hat{i}_f = \frac{\vec{v}_{k/a}}{ \vec{v}_{k/a} }$
Unit vector pointing at kite (sphere normal)	$\hat{r}_{ok} = \frac{\vec{r}_{ok}}{ \vec{r}_{ok} }$
Unit vector normal to both of the above	$\hat{j}_f = \frac{\hat{i}_f \times \vec{r}_{ok}}{ \hat{i}_f \times \vec{r}_{ok} }$
Right Hand Rule	$\hat{k}_f = \hat{i}_f \times \hat{j}_f$

Each of the above vectors must be written using g frame components to create DCM_f2g. The only vectors which are required for this construction are the kite's commanded airspeed vector (found by solving the Wind Triangle) and the kite's commanded position (given).

Direction Cosines for the Kite

The “1-3-2” Euler Angle sequence to construct DCM_{f2b} can be written in terms of elemental rotation matrices, multiplying right to left:

$$[DCM_{f2b}] = [L_2(\alpha)][L_3(-\beta)][L_1(\phi_a)]$$

Details for this choice of Euler Angles and their sequence is provided in a previous section of this document, [The “Fly” Frame](#).

The complete DCM_{g2b} which describes the kite’s attitude with respect to the ground can be built from DCM_{g2f} and DCM_{f2b} , remembering that we multiply right to left:

$$[DCM_{g2b}] = [DCM_{f2b}][DCM_{g2f}]$$

The elemental rotation matrices are below. Each matrix takes an angle as an input argument. We are rotating frames, not vectors. We rotate our view of the vectors, not the vectors themselves.

$c = \cos(\text{angle})$

$s = \sin(\text{angle})$

$$L1 = \begin{bmatrix} 1 & 0 & 0 \\ 0 & c & s \\ 0 & -s & c \end{bmatrix}$$

$$L2 = \begin{bmatrix} c & 0 & -s \\ 0 & 1 & 0 \\ s & 0 & c \end{bmatrix}$$

$$L3 = \begin{bmatrix} c & s & 0 \\ -s & c & 0 \\ 0 & 0 & 1 \end{bmatrix}$$

The Angular Velocity of the Kite w.r.t. The Ground

The angular velocity of the kite is built up from two pieces:

1. The angular velocity of the Body Frame with respect to the Fly Frame
2. The angular velocity of the Fly Frame with respect to the Ground Frame

$$\vec{\omega}_{b/g} = \vec{\omega}_{b/f} + \vec{\omega}_{f/g}$$

The above is a vector equation, of course. Each vector must be written using components in the same frame before they can be added together. This can be easily done with the DCMs described in previous sections.

The Angular Velocity of the Kite w.r.t. The Fly Frame

The angular velocity of the kite with respect to the Fly Frame is built up from time derivatives of the Euler Angles which define DCM_f2b. This is the usual procedure for deriving an angular velocity vector from Euler Angle rates with the exception that the Euler sequence is an atypical one for atmospheric flight vehicles: “1-3-2” instead of the usual “3-2-1”. For any Euler Angle sequence, you can construct the resulting angular velocity vector by summing contributions from individual angular rate, taking care to correctly apply each rate to the axis on which it occurs:

$$\vec{\omega}_{b/f} = \dot{\phi}_a \hat{i}_f - \dot{\beta} \hat{k}_{intermediate} + \dot{\alpha} \hat{j}_b$$

Notice that the above equation (a vector equation) emphasizes that the “airspeed roll rate” contribution is along the Fly Frame’s x axis but the “alpha rate” contribution is along the body’s y axis. The “beta rate” contribution occurs about an intermediate z axis which is neither in frame f nor in frame b. The minus sign is due to the aerospace conventions for sideslip and yaw rate.

Recall that the “1-3-2” Euler Angle sequence to construct DCM_f2b can be written in terms of elemental rotation matrices, multiplying right to left:

$$[DCM_{f2b}] = [L_2(\alpha)][L_3(-\beta)][L_1(\phi_a)]$$

To write the vector $\vec{\omega}_{b/f}$ using frame b components requires transforming both \hat{i}_f and $\hat{k}_{intermediate}$ to the b frame. Noting that elemental rotations leave components along their rotation axis unchanged, we can write the b frame components of the angular velocity vector in a simplified form as follows:

$$\left\{ \vec{\omega}_{b/f} \right\}_b = [L_2(\alpha)][L_3(-\beta)] \{ \dot{\phi}_a, 0, 0 \}^T + [L_2(\alpha)] \{ 0, 0, -\dot{\beta} \}^T + \{ 0, \dot{\alpha}, 0 \}^T$$

Aside: The above equation looks very much like the implicit version of the strapdown equation which deals with the angular velocity of a flight vehicle with respect to the inertial frame: relating pqr to euler angle rates.

The Angular Velocity of The Fly Frame w.r.t. The Ground

The angular velocity of the Fly Frame with respect to the Ground Frame is constructed from an analytical time derivative of DCM_{f2g} . The time derivative of a DCM gives rise to [Thomas Kane's](#) definition of the angular velocity vector, shown below with frames f and g.

$$\left[DCM_{f2g} \dot{\quad} \right] = \left[DCM_{f2g} \right] \left[\left\{ \vec{\omega}_{f/g} \right\}_f \times \right]$$

Here $\left[\left\{ \vec{\omega}_{f/g} \right\}_f \times \right]$ is a skew-symmetric cross product matrix built from the f frame components of the angular velocity vector of f with respect to g. A definition of this matrix constructed from general vector components xyz is given below.

Skew-Symmetric Cross Product Matrix

$$\begin{bmatrix} 0 & -z & y \\ z & 0 & -x \\ -y & x & 0 \end{bmatrix}$$

The components of the angular velocity vector are extracted from the lower left corner of this skew-symmetric matrix after analytically constructing the time derivative of DCM_{f2g} :

$$\left[\left\{ \vec{\omega}_{f/g} \right\}_f \times \right] = \left[DCM_{g2f} \right] \left[DCM_{f2g} \dot{\quad} \right]$$

Analytical Time Derivatives of Fly Frame Unit Vectors

Unit vectors are fixed length: they only rotate. Therefore, a time derivative of a matrix constructed from unit vectors (the DCM) should involve only angular velocity components. Indeed the time derivative of a unit vector IS a cross product with the angular velocity vector of the frame where the time derivative is being taken:

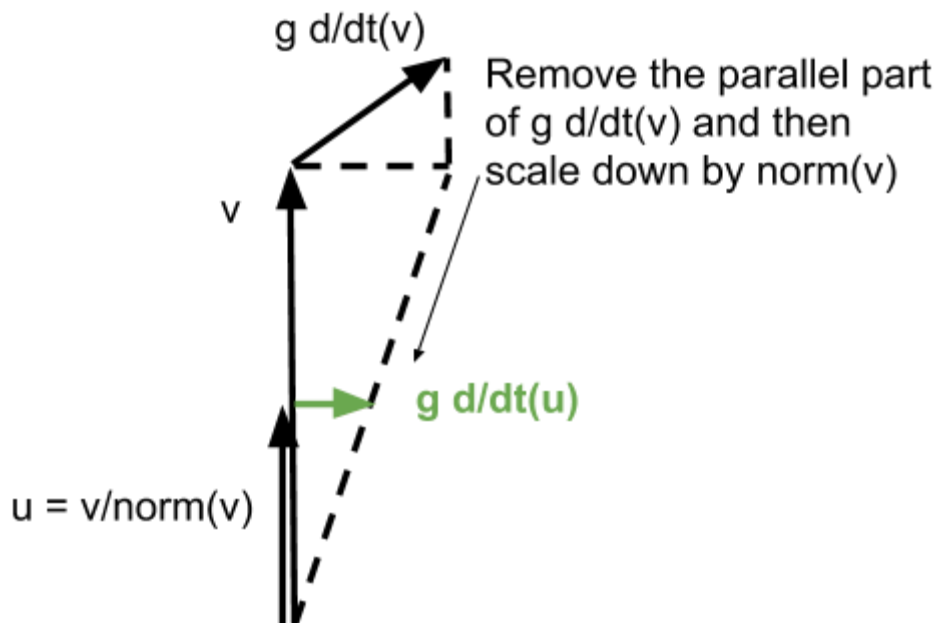
$${}^g \frac{d}{dt} \hat{i}_f = \vec{\omega}_{f/g} \times \hat{i}_f \quad {}^g \frac{d}{dt} \hat{j}_f = \vec{\omega}_{f/g} \times \hat{j}_f \quad {}^g \frac{d}{dt} \hat{k}_f = \vec{\omega}_{f/g} \times \hat{k}_f$$

It is useful to remember this property of unit vectors when trying to construct their analytical time derivatives from given quantities.

Constructing the Time Derivative of a Unit Vector In Practice

Unit vectors are often defined as some vector divided by its own length. In the diagram below, u represents a unit vector based upon the vector v . Also shown is the g frame time derivative of the vector v . To construct the g frame time derivative of u :

1. Remove the part of ${}^g d/dt(v)$ which is parallel to v
2. Scale down the resulting vector by $1/\text{norm}(v)$



Analytical g-Frame Time Derivative of Fly Frame X axis

Recall that the x axis of the Fly Frame is defined to be along the kite's airspeed vector.

$$\hat{i}_f = \frac{\vec{v}_{k/a}}{|\vec{v}_{k/a}|} \quad \vec{v}_{k/a} = \vec{v}_{k/g} - \vec{v}_{a/g}$$

As described in the previous section, the time derivative of this unit vector is constructed from the time derivative of the vector on which it is based.

For the purposes of this analysis, the wind vector changes slowly enough to be ignored. Therefore, the time derivative of the airspeed is only due to the kite's acceleration.

$${}^g \frac{d}{dt} \vec{v}_{k/a} = {}^g \frac{d}{dt} \vec{v}_{k/g} = \vec{a}_{k/g}$$

The construction described in the previous section applied to the kite acceleration vector yields an expression for the g-frame time derivative of the Fly Frame X axis:

$${}^g \frac{d}{dt} \hat{i}_f = \frac{\vec{a}_{k/g} - \hat{i}_f \hat{i}_f^T \vec{a}_{k/g}}{|\vec{v}_{k/a}|}$$

Remember that the above equation is a vector equation. We want the components of the above vectors in the g frame in order to construct the time derivative of DCM_f2g.

Analytical g-Frame Time Derivative of Fly Frame Y axis

Recall the definition of the Fly Frame's Y axis: tangent to the sphere and normal to the airspeed vector. It is defined using a normalized crossproduct:

$$\hat{j}_f = \frac{\hat{i}_f \times \hat{r}_{ok}}{|\hat{i}_f \times \hat{r}_{ok}|}$$

It will be easier to work with the "not yet normalized" version of this cross product, swapping the hat notation for a regular vector notation:

$$\vec{j}_f = \hat{i}_f \times \vec{r}_{ok}$$

The g-Frame time derivative gets distributed across the cross product:

$${}^g \frac{d\vec{j}_f}{dt} = {}^g \frac{d\hat{i}_f}{dt} \times \vec{r}_{ok} + \hat{i}_f \times {}^g \frac{d\vec{r}_{ok}}{dt}$$

The first term, ${}^g \frac{d\hat{i}_f}{dt}$, was already calculated in the previous section. The next term involves

${}^g \frac{d\vec{r}_{ok}}{dt}$ which is simply the velocity of the kite with respect to the ground frame (because point o is fixed in frame g). Introducing the kite velocity into the equation explicitly, we have:

$${}^g \frac{d\vec{j}_f}{dt} = {}^g \frac{d\hat{i}_f}{dt} \times \vec{r}_{ok} + \hat{i}_f \times \vec{v}_{k/g}$$

The nomenclature below looks awkward, but it is the same "unit vector time derivative" method as was used in the previous section, this time applied to the "not yet normalized" cross product: subtract the parallel part of the derivative and scale down by the vector norm.

$${}^g \frac{d\hat{j}_f}{dt} = \frac{{}^g \frac{d\vec{j}_f}{dt} - \hat{j}_f \hat{j}_f^T {}^g \frac{d\vec{j}_f}{dt}}{|\hat{i}_f \times \vec{r}_{ok}|}$$

Constructing The Angular Velocity Vector: Summary

The angular velocity of the kite with respect to the ground is constructed from two parts: motion of the kite with respect to the Fly Frame and the motion of the Fly Frame with respect to the ground.

$$\vec{\omega}_{b/g} = \vec{\omega}_{b/f} + \vec{\omega}_{f/g}$$

The angular velocity of the kite with respect to the Fly Frame is built from Euler Angle rates:

$$\left\{ \vec{\omega}_{b/f} \right\}_b = [L_2(\alpha)][L_3(-\beta)]\{\dot{\phi}_a, 0, 0\}^T + [L_2(\alpha)]\{0, 0, -\dot{\beta}\}^T + \{0, \dot{\alpha}, 0\}^T$$

The angular velocity of the Fly Frame with respect to the ground is constructed from Thomas Kane's definition of the angular velocity vector:

$$\left[\left\{ \vec{\omega}_{f/g} \right\}_f \times \right] = \left[DCM_{g2f} \right] \left[D\dot{C}M_{f2g} \right]$$

The DCM is constructed from unit vectors.

$$DCM_{f2g} = \left[\left\{ \hat{i}_f \right\}_g \quad \left\{ \hat{j}_f \right\}_g \quad \left\{ \hat{k}_f \right\}_g \right]$$

$$D\dot{C}M_{f2g} = \left[\begin{array}{ccc} {}^g \frac{d}{dt} \left\{ \hat{i}_f \right\}_g & {}^g \frac{d}{dt} \left\{ \hat{j}_f \right\}_g & {}^g \frac{d}{dt} \left\{ \hat{k}_f \right\}_g \end{array} \right]$$

Time derivatives of the Fly Frame unit vectors are provided analytically:

$${}^g \frac{d}{dt} \hat{i}_f = \frac{\vec{a}_{k/g} - \hat{i}_f \hat{i}_f^T \vec{a}_{k/g}}{|\vec{v}_{k/a}|}$$

$${}^g \frac{d}{dt} \hat{j}_f = \frac{{}^g \frac{d}{dt} \vec{j}_f - \hat{j}_f \hat{j}_f^T {}^g \frac{d}{dt} \vec{j}_f}{|\hat{i}_f \times \hat{r}_{ok}|}$$

Validation of the Algorithm

Matlab code is provided which implements the mathematics described in this document (`SphereKinematics.m`). The code also includes a script to test the calculated angular velocity vector of the kite with respect to the ground (`Test.m`). This is done by comparing:

- The angular velocity output by the algorithm
- The angular velocity derived from a finite-difference time derivative of the DCM output by the algorithm

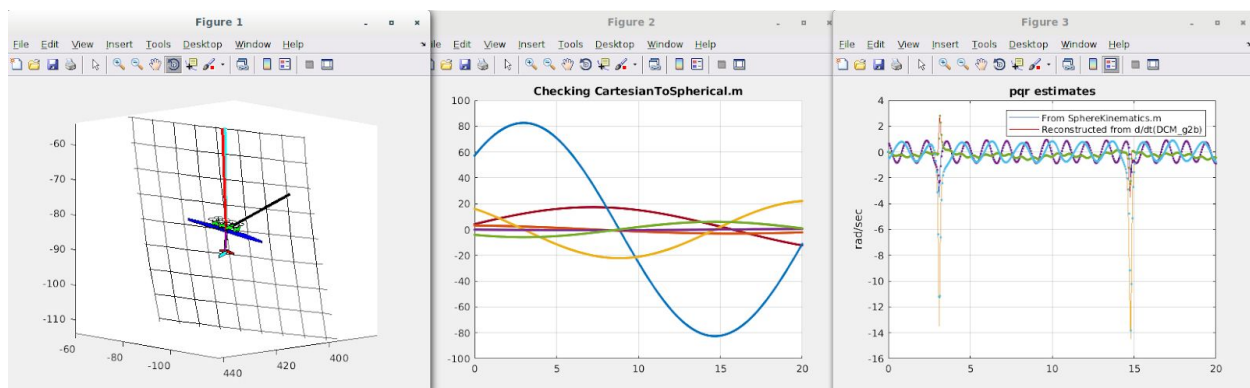
This check is for internal consistency of the kite state which is output: do the attitudes and angular rates go together?

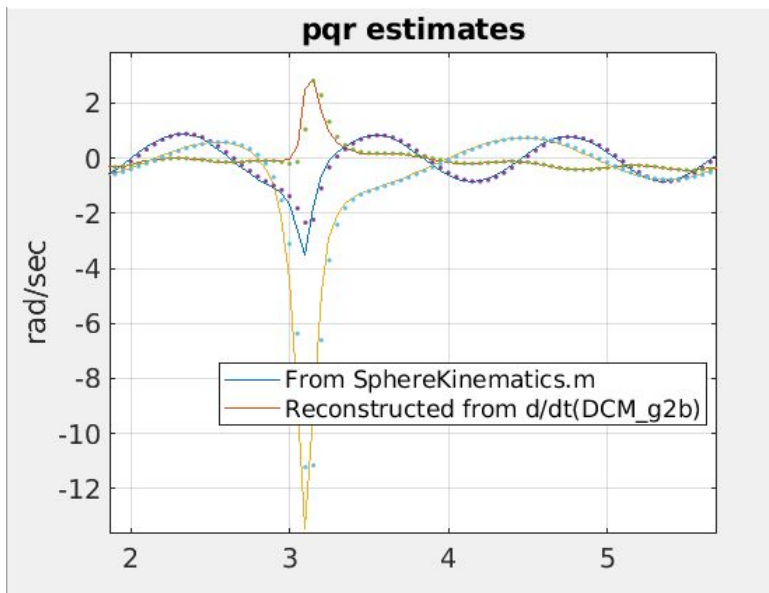
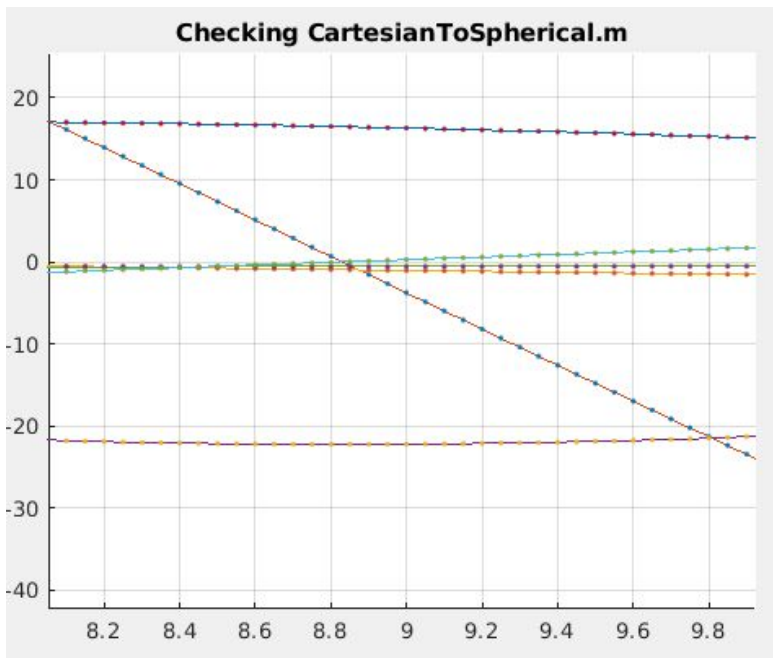
Focus is placed on the angular velocity vector because the position of the kite and linear velocity of the kite are trivial by comparison (directly provided by outer loop commands).

Running `Test.m` at the Matlab prompt will create an animation of randomly generated smooth kite motion (including randomly generated smooth motion for ϕ_a , α , and β). The animation shows the kite, the sphere, the kite's groundspeed vector (red), the kite's airspeed vector (cyan), and the wind (dark blue) plotted as a triangle with one corner at the kite.

At the end of the animation, two validation plots are produced: One checks a transformation from cartesian to spherical coordinates. The other compares angular velocity estimates as described above. See detailed comparisons on the next page.

The plots below go with this animation [internal ref]. You will see the kite pitching, rolling, and yawing about its airspeed vector. The airspeed vector direction depends upon the kite's translational motion and the wind. The motion here is not meant to be optimal or even achievable by the m600 but rather is meant only to sufficiently test the algorithms described in this document.



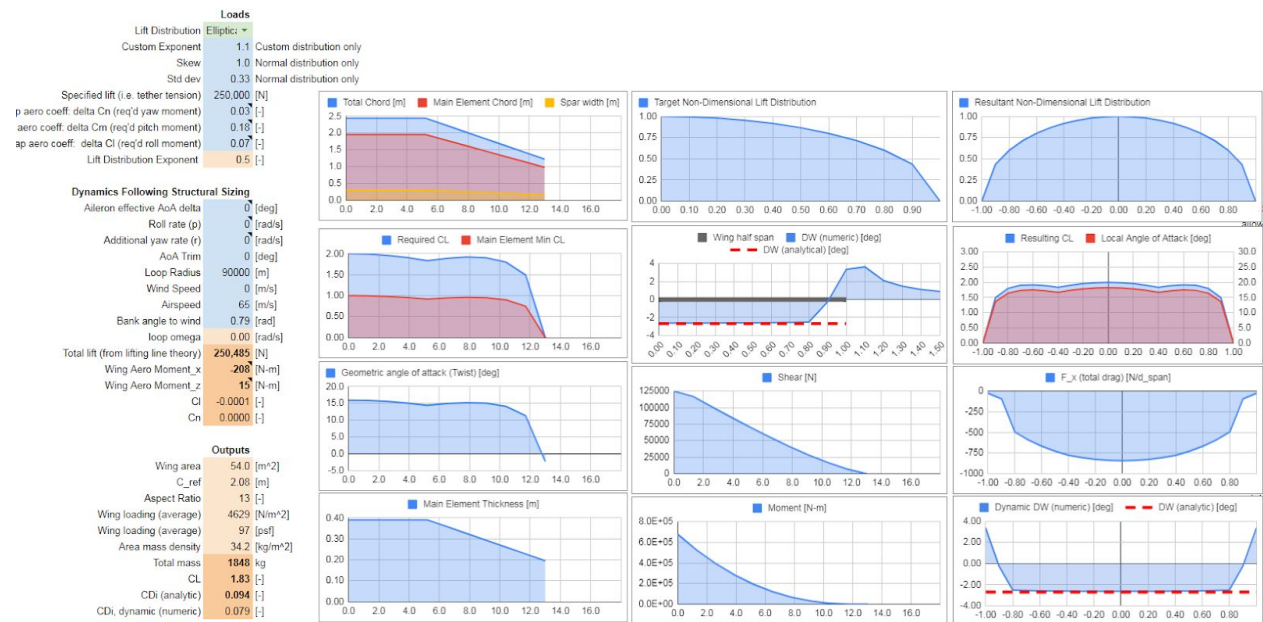


The legend in the above figure is wrong. Solid lines are directly output from SphereKinematics.m and the dots are from the finite difference time derivative of the DCM output.

The Spreadsheet Kite Structure Sizer

A guide to how the sizer works and how to use it

Florian Kapsenberg, Dec 2019



Overview

Wing Sizing

Structural Configuration

CL Requirements

Second Element Span and Chord Overrides

Accounting for Thrust Coefficient

Loads & Spar Sizing

ASWING Beam Properties

Bending Stiffness

Torsional Stiffness

High Resolution Version of Wing Sizer

Empennage & Control Surface Sizing

Loads

Mass Buildup

Maneuvering Loads & Lifting Line Theory

Overview

The sheet's primary function is to size a wing structure based on a given tether load which is assumed to be generated by aerodynamic lift of a specified distribution at a specified airspeed. Additionally, a tail is sized based on required pitch and yaw authority from the Force Balance Loop (FBL) runs, as well as stability requirements. Given the hand-calc nature of this spreadsheet tool, it is only suitable for preliminary sizing, providing planform geometry that can be achieved with a specified mass budget. Final sizing and analysis should be performed with more sophisticated tools.

There are many colors used in this sheet to help the user understand where to enter data and where to look for outputs. Here is a guide to the most common ones:

Color Meaning		
Lift Distribution	Elliptical	User choice between option (pulldown menu)
Span	26.0	User-defined value
Root Chord	1.84	Calculated value
Total mass	1636	Important calculated value
Spar width	0.30	Value copied from elsewhere in sheet
2-Element max CL	2.0	Value intended to remain fixed
Size for thrust coefficient	TRUE	True
Aileron	FALSE	False

In the case of a TRUE / FALSE cell, the conditional formatting overrides the color that would otherwise be used (i.e. TRUE / FALSE may be a user choice, or calculated).

Wing Sizing

Sizing of the wing structure is performed on a half-span (center to tip), and doubled again in the mass roll-up. To size a wing, a specific structural configuration is assumed (shown below). This configuration of spar, ribs, and skin was chosen primarily for its commonality with general aviation wings, high performance wing sails, and high performance aircraft wings. Additionally, it is straightforward to perform the structural analysis (especially in a spreadsheet) and construction of such a configuration, providing high confidence in the performance and mass estimates.

In the spreadsheet, the user usually only modifies the following in order when creating a new configuration:

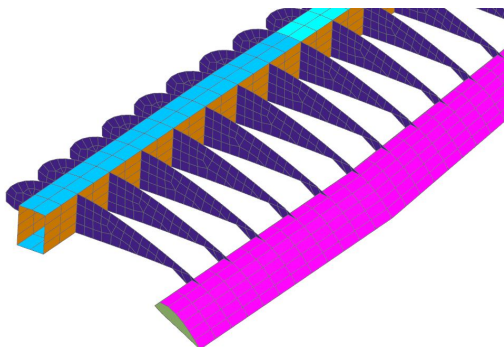
1. Loads & Aero

- Tether Tension [N]
 - Lift Distribution
 - Airspeed at which specified tension shall be achieved [m/s]
 - Air density [kg/m^3]
2. Geometry
- Wing profile (usually driven by choice of lift distribution)
 - i. Straight span fraction
 - ii. Tip chord fraction
 - Bridle hardpoint span fraction (if any)
 - Span [m] (usually made as large as possible without exceeding the maximum allowable mass for the airframe)
3. Concentrated mass elements
- Pylons (assumed 40 kg each for structure)
 - Nacelles (assumed 60 kg each including powertrain, rotors, spinners)
 - Any hardpoint masses not accounted for in primary structure sizing
 - i. Tether or bridle hardpoints
 - ii. Pylon and fuselage hardpoints
 - iii. Avionics
 - Mass balance assembly (used to tune the kite's fore-aft center of gravity location)

Other variables that are usually left alone include (but are not limited to):

- Thickness/chord ratio of airfoil
- Fraction of chord that is occupied by 2nd element
- Safety Factor
- Nonstructural mass density
- Etc

Structural Configuration



The structure consists of a box-beam spar, ribs, and a skin. A second element is attached as shown in the image above.

- Spar
The spar carries the bending load, and is assumed to be of rectangular cross section for

design and manufacturing simplicity (likely required for the fast-paced schedule required for the next kite). It features two spar caps and two shearwalls.

- **Spar caps** (blue in above image)
 - On the top and bottom, sized as if made entirely of spanwise unidirectional carbon fiber, and then an additional 20% is added to account for the interwoven twill plies that will need to carry the load to the shearwall.
- **Shearwalls** (orange in above image)
 - Sized for the larger of either
 - 1mm of carbon fiber twill @ $\pm 45^\circ$ on either side of a $\frac{1}{2}$ inch HP60 PVC foam core (4mm total for both shearwalls).
 - A thickness that will carry the shear load in the wing with a $\frac{1}{2}$ inch HP60 PVC. foam core.
- **Ribs** (purple in above image)

Assumed to be at 0.5 m spacing, and of an area equal to (total chord) * (main element thickness). Each rib consists of a 2-core-2 ($\pm 45^\circ$) sandwich panel. This of course is a rectangular shape, and not the shape of the actual rib which would be an airfoil, but some additional area needs to be added to account for flanges and adhesive mass, so rectangular seemed like it would provide a fairly realistic/conservative estimate of the total mass of the installed rib.
- Skin (not shown in image above)

The skin is assumed to be 1.9mm thick @ $\pm 45^\circ$. The top skin is cored as it experiences compression and needs some buckling mitigation. The 1.9mm number comes from scaling the skin thickness such that the total mass buildup matches the m600 mass for an m600 planform (250 kN @ 85 m/s).
- **2nd element**

Same architecture as the skin. Mounting is assumed to be covered by the ribs for fixed 2nd elements (not acting as ailerons). Additional mass is added by scaling the mass by a factor of 2.4 (this is the ratio of m600 flap weight to what the model predicts for a fixed flap). Attachment hardware for a moving 2nd element is assumed to weigh the same as for the m600 (3 brackets + servo & controller = 9.3 kg / 2.9 m)

C_L Requirements

This part of the sizer determines how much of the span requires a 2nd element, as well as sizes the root chord. The root chord is sized by solving for the chord in

$$Lift [N/m] = \frac{1}{2} \rho v^2 C_L chord$$

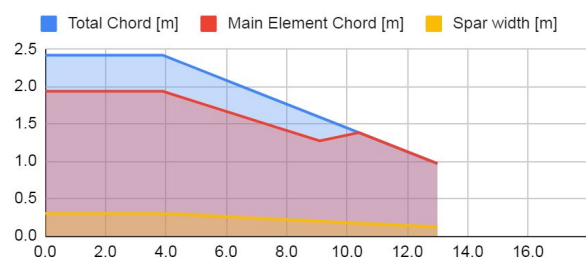
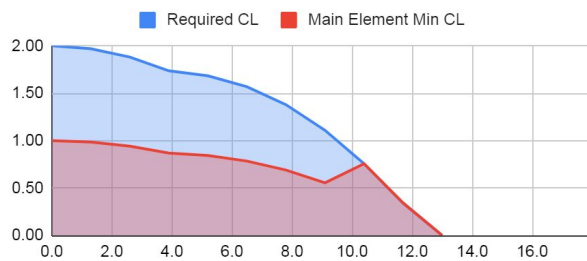
where the lift in N/m is determined by the lift distribution and specified span, and C_L is defined as the max C_L for a 2-element airfoil (assumed to be 2.0 for a turbulent airfoil with $\sim 5^\circ$ margin for stall):

2-Element max CL	2.0 [-]
------------------	---------

The wing's planform is sized based on this root chord and user-defined span, using the straight span fraction and tip chord fraction to size the chord along the span. Once the planform is sized, the required C_L for the rest of the wing is calculated by solving the same equation for C_L , as the chord is now known. This allows the user to adjust the straight span fraction and tip chord fraction to achieve a C_L as close to the max of 2.0 as possible across the entire wing, making the most efficient use of area and structure. If the required C_L is ever less than 1.0, the sizer recognizes this and does not require or size for a second element. Below is an example of how the structure can be optimized by tuning the straight span fraction and tip chord fraction to bring C_L as close to 2.0 as possible across the majority of the span, along with a visualization of the same planform geometry and associated mass estimate. Visible is both an increase in overall C_L as well a greater portion of the span using a second element to achieve the higher C_L :

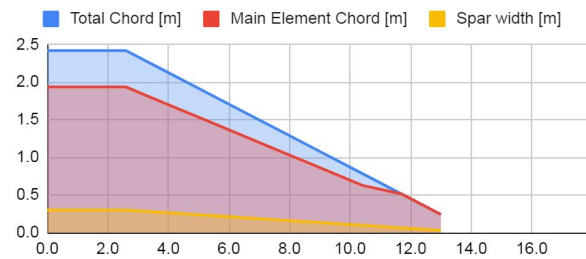
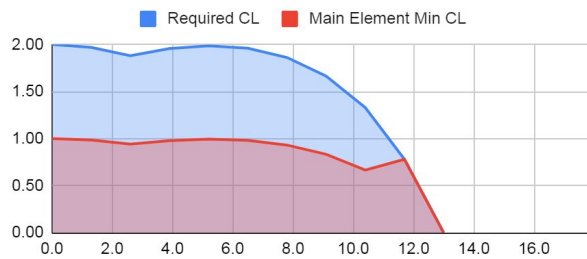
Less optimized (note mass):

Straight span fraction	0.30
Tip chord fraction	0.40
Total mass	1707 kg

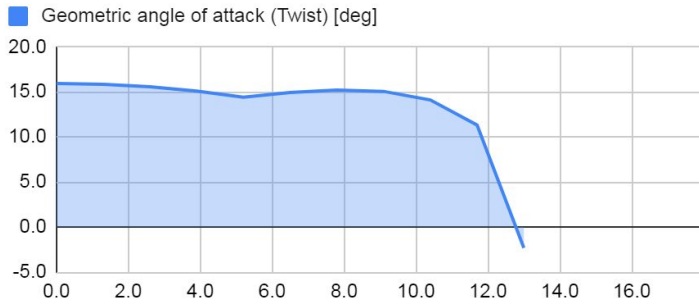


More optimized (lower mass):

Straight span fraction	0.20
Tip chord fraction	0.10
Total mass	1562 kg



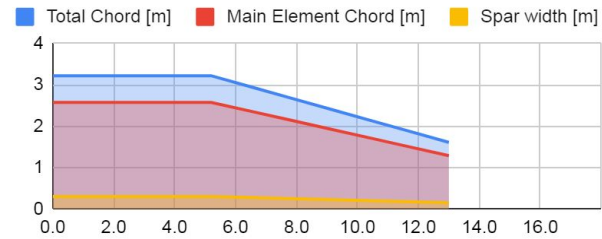
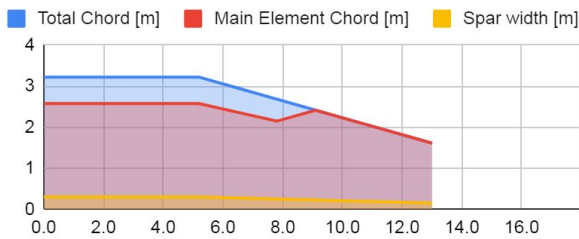
Further C_L reduction near the wing tips is achieved by means of de-twisting the airfoil to reduce the local angle of attack. The de-twist angle is computed with a 2π /rad lift curve slope assumption:



Second Element Span and Chord Overrides

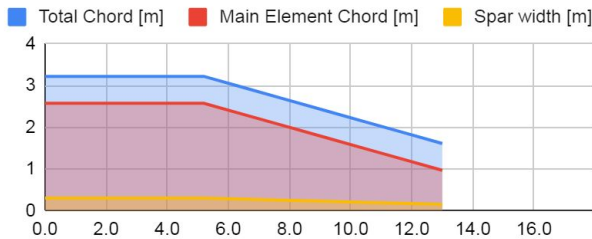
A second element may not be required for the full span to achieve the target lift distribution. However, for structural simplicity and/or control authority requirements it may be necessary to extend the second element the full span (e.g. such as for the M600). The user can override the calculated minimum span coverage of the second element to achieve this as by selecting **TRUE** below.

Second element full span override	TRUE	[-]
-----------------------------------	-------------	-----



Additionally, it may be desirable for reasons of manufacturing simplicity, to maintain a constant second element chord along the span, regardless of wing taper (e.g. such as for the M600). This is achieved by selecting **TRUE** below.

2nd element root chord fraction	0.20	[-]
Constant 2nd element chord	TRUE	



Accounting for Thrust Coefficient

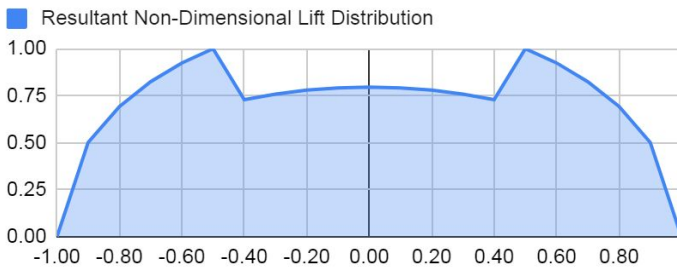
The impact of generating/thrusting rotors on the dynamic pressure over the wing can be accounted for in the sheet. The user must define the span over which this effect acts:

Rotor span coverage	12.0	[m]
---------------------	------	-----

As well as the thrust coefficient, which adjusts the dynamic pressure over the wing within the above-defined range. With a negative thrust coefficient (i.e. generating rotors) the sheet recognizes the reduction in dynamic pressure and computes a lower-than specified tether tension as a result:

Specified lift (i.e. tether tension) 250,000 [N]

Thrust coefficient @ wing -0.31 [-]

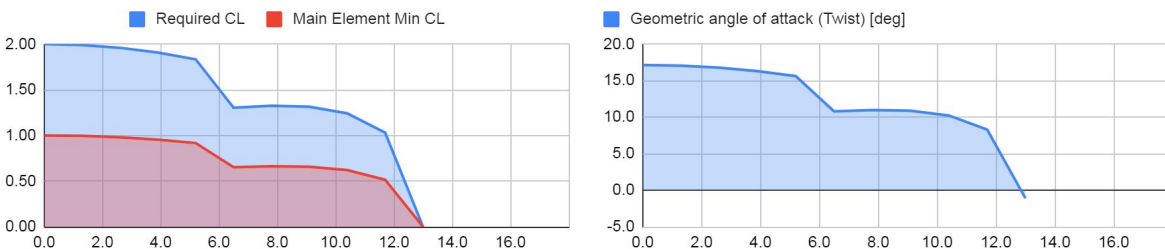


Total lift (from lifting line theory) 207,036 [N]

If the thrust coefficient is significant and known (e.g. nacelles mounted directly in front of the wing), it is wise to account for this in sizing the wing. The user has this option:

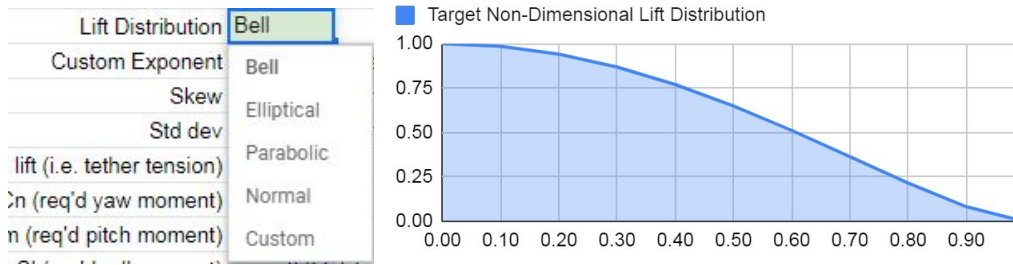
Size for thrust coefficient TRUE

Selecting **TRUE** adjusts the root chord to produce the specified lift per unit span when subject to the user-defined thrust coefficient and span coverage. The discontinuity in dynamic pressure from the zone aft of the rotors to that in clean air requires either an abrupt change in chord, or CL to ensure the lift distribution is preserved. As the sheet is configured to size a wing that has a straight and tapered section only, such an abrupt drop in chord is not possible. Instead, the discontinuity manifests itself in the C_L and subsequently the prescribed geometric angle of attack:



Loads & Spar Sizing

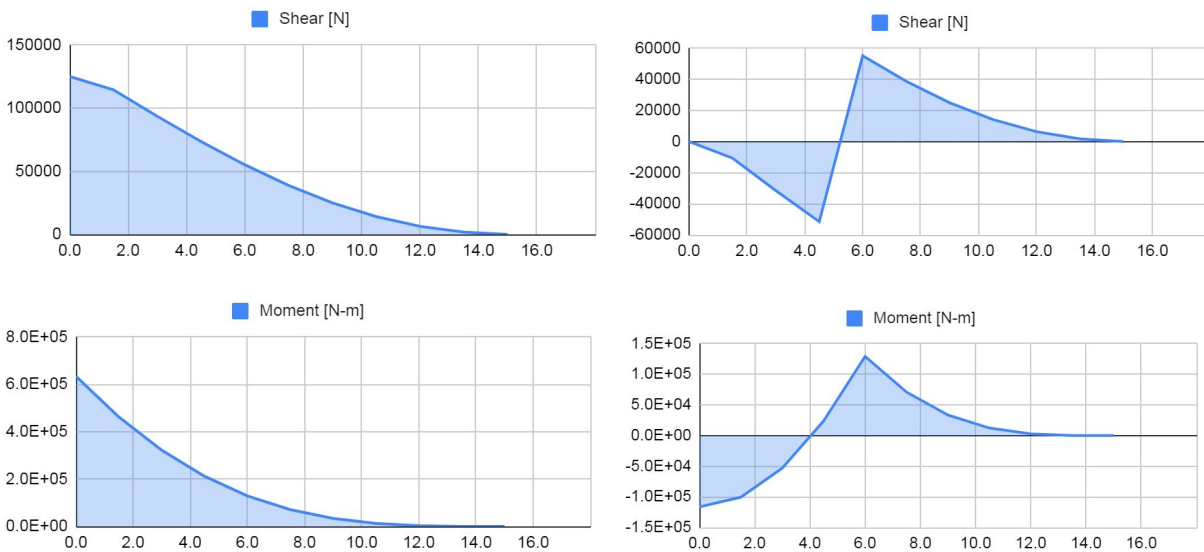
Loads are applied initially via a non-dimensional user-prescribed lift profile such as shown below.



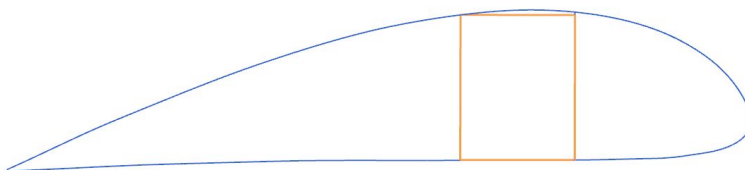
This distribution is dimensionalized such that the integrated sum matches the specified tether tension. Integrating the lift load from the tip toward the root provides the total shear due to lift. This shear load is used to size the shear wall. The bending moment at each station in the wing is determined by the sum of all moments from outboard stations (lift * distance). The user also has the option of defining a bridle spanwise hardpoint position:

Bridle hardpoint half-span fraction	0.4 [-]
-------------------------------------	---------

If non-zero, it is included in the calculation for shear force and bending moment inboard of this station. Below is an example of no bridle, and one at 40% span:



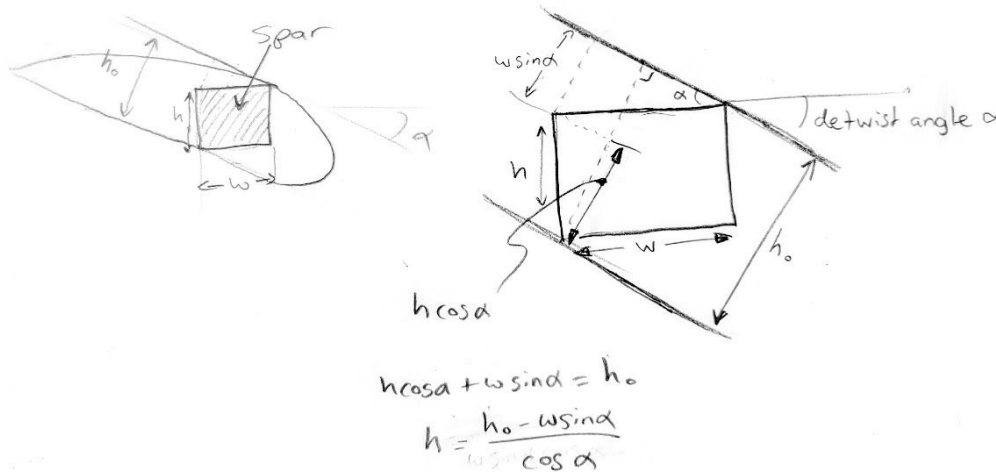
Before sizing the spar caps the height of the spar needs to be computed. This is not as simple as the airfoil thickness. A truly rectangular spar cannot be as high as the thickest part of the airfoil as the airfoil is curved.



The user must therefore define a fraction of the local airfoil thickness that the spar height is defined as:

Spar height fraction of wing thickness	0.95 [-]
--	----------

Additionally, the de-twist angle further reduces the allowable section height for a rectangular spar if not rotated with the airfoil section. Since an untwisted spar is far easier to manufacture, this reduced spar height is assumed and computed as shown below:



Once the bending moment and spar height are known, the spar cap stress for a range of spar cap thicknesses is calculated as a function of the bending moment and the spar cap and skin bending stiffnesses:

$$\sigma = \frac{My}{I}$$

$$\frac{\sigma}{Ey} = \frac{M}{EI} \quad \leftarrow \text{curvature}$$

$$\frac{\sigma_{\text{spar cap}}}{E_{\text{spar cap}} \cdot y} = \frac{M}{E_{\text{spar cap}} I_{\text{spar cap}} + E_{\text{skin}} I_{\text{skin}}}$$

$$\sigma_{\text{spar cap}} = \frac{M \cdot E_{\text{spar cap}} \cdot y}{E_{\text{spar cap}} I_{\text{spar cap}} + E_{\text{skin}} I_{\text{skin}}}$$

The minimum spar cap thickness for the user-defined material strength and safety factor is determined by tabulating all thickness options and picking the value with the lowest positive margin:

Bending moment [N-m]	6.33E+05	5.08E+05	3.86E+05	2.75E+05	1.80E+05	1.06E+05	5.32E+04	2.07E+04	4.75E+03	0.00E+00	0.00E+00
Spar height [m]	0.45	0.45	0.45	0.40	0.35	0.30	0.25	0.20	0.15	0.12	0.06
Spar cap width [m]	0.30	0.30	0.30	0.27	0.23	0.20	0.17	0.13	0.10	0.06	0.03
Minimum cap thickness [m]	0.010	0.008	0.006	0.006	0.004	0.004	0.004	0.002	0.002	0.002	0.002

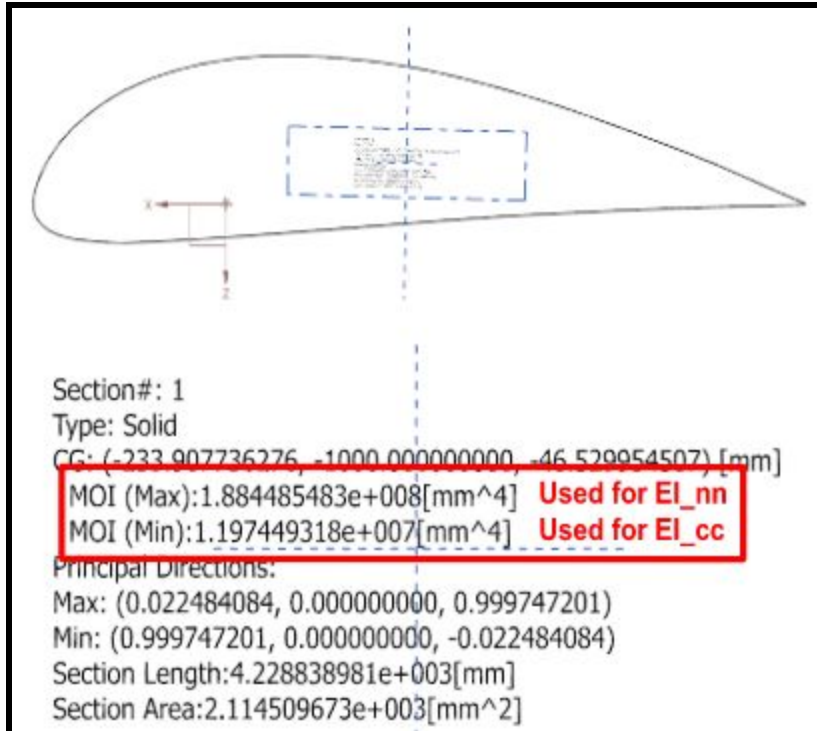
Section inertia [m^4]	2.86E-04	2.31E-04	1.75E-04	1.22E-04	5.44E-05	3.39E-05	1.93E-05	4.91E-06	2.00E-06	8.67E-07	8.70E-08	
Cap thickness [mm]	Spar Cap Stress Margin as Function of Spar Cap and Wing Skin Thickness											
0.002	-0.75	-0.69	-0.59	-0.54	-0.47	-0.34	-0.10	0.46	2.48	No Load	No Load	
0.004	-0.50	-0.38	-0.18	-0.10	0.05	0.30	0.77	1.86	5.77	No Load	No Load	
0.006	-0.26	-0.08	0.22	0.34	0.55	0.92	1.61	3.20	8.87	No Load	No Load	
0.008	-0.02	0.22	0.61	0.77	1.05	1.52	2.42	4.48	11.79	No Load	No Load	
0.010	0.21	0.51	0.99	1.19	1.53	2.11	3.21	5.71	14.54	No Load	No Load	
0.012	0.44	0.80	1.37	1.60	2.00	2.68	3.96	6.89	17.11	No Load	No Load	
0.014	0.67	1.08	1.74	2.00	2.45	3.23	4.70	8.00	19.52	No Load	No Load	
0.016	0.89	1.35	2.10	2.40	2.90	3.77	5.40	9.07	21.78	No Load	No Load	
0.018	1.11	1.62	2.45	2.78	3.34	4.29	6.08	10.09	23.87	No Load	No Load	
0.020	1.32	1.89	2.80	3.16	3.76	4.80	6.73	11.06	25.82	No Load	No Load	
0.022	1.53	2.15	3.15	3.53	4.17	5.29	7.36	11.97	27.63	No Load	No Load	

ASWING Beam Properties

Chordwise bending stiffness (EI_{cc}) and spanwise torsional stiffness (GJ) are calculated for each skin and spar separately.

Bending Stiffness

For the bending stiffness of the spar, the EI_{cc} is assumed to come solely from the spar caps, and is a relatively straightforward calculation. For the skin, a “unit 20% airfoil” was created in NX, with 1m chord, and 1mm thick skin. The section properties were extracted and are fixed in the sheet:



1m Chord x 1mm thk skin section I _{cc}	1.20E-05	[m^4]
1m Chord x 1mm thk skin section I _{nn}	1.88E-04	[m^4]

For each wing station this value is scaled to the equivalent chord length and skin thickness of that station, scaled from the 1m chord and 1mm thickness as follows:

$$I_{cc} = 1.20E - 05 (chord / 1)^3 (t_{skin} / 0.001)$$

The spanwise stiffness of the wing skin was computed from a ±45° twill laminate using NX's laminate modeler:

```
Laminate Equivalent Properties:
Stiffness Matrix A      : | 2.926e+007 2.310e+007 0.000e+000
                        : | 2.310e+007 2.926e+007 0.000e+000
                        : | 0.000e+000 0.000e+000 2.355e+007
No Bending-Extension Coupling. Laminate is symmetric.
Stiffness Matrix D      : | 2.439e+006 1.925e+006 0.000e+000
                        : | 1.925e+006 2.439e+006 0.000e+000
                        : | 0.000e+000 0.000e+000 1.962e+006
Transverse Shear Matrix (S) : | 2.873e+006 -0.000e+000
                        : | -0.000e+000 2.873e+006
Mass per unit area      : 1.564e-006 kg/mm^2
Total thickness         : 1.000e+000 mm
Mass density            : 1.564e-006 kg/mm^3
Symmetric               : YES
Balanced                : YES
Young's Modulus X      : 1.103e+007 mN/mm^2(kPa)
Young's Modulus Y      : 1.103e+007 mN/mm^2(kPa)
Young's Modulus Z      : Not defined
Bending Young's Modulus X : 1.103e+007 mN/mm^2(kPa)
Bending Young's Modulus Y : 1.103e+007 mN/mm^2(kPa)
Poisson's Ratio XY     : 7.894e-001 Unitless
Poisson's Ratio YX     : 7.894e-001 Unitless
Poisson's Ratio XZ     : Not defined
Poisson's Ratio YZ     : Not defined
Shear Modulus XY       : 2.355e+007 mN/mm^2(kPa)
Bending Shear Modulus XY : 2.355e+007 mN/mm^2(kPa)
Shear Modulus XZ       : 2.873e+006 mN/mm^2(kPa)
Shear Modulus YZ       : 2.873e+006 mN/mm^2(kPa)
```

Torsional Stiffness

For the purpose of torsion, both the spar and the wing skin are assumed to be comprised solely of ±45° carbon fiber fabric. This is expected to be true for the skin, and nearly true for the spar, as the contribution to torsional stiffness from the unidirectional fiber in the spar caps is assumed to be negligible, and the load is assumed to be carried solely in the shearwall plies extending and interleaved in the spar caps (a conservative assumption).

The thin wall tube approximation for the torsion constant is assumed for both structures:

$$J = \frac{4A^2t}{S}$$

Where **A** is the enclosed area (rectangular for the spar, airfoil-shaped for the skin), **t** is the thickness, and **S** is the perimeter length.

In addition to the above mechanical properties, the geometry (chord and angle at each spanwise location) is also extracted.

Below is a table showing the computed values of EI_{cc}, GJ, and EA (might as well, EA is easy to extract) for m600 geometry and loads, showing close agreement with the numbers extracted from the M600 FEM [internal ref]:

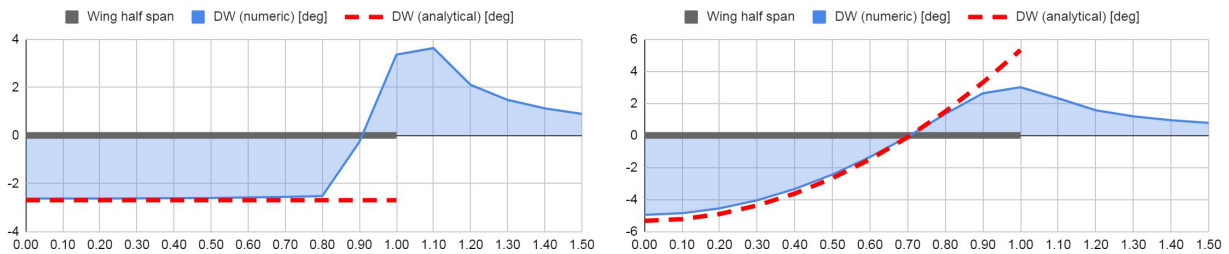
ASWING Export											
Span Fraction [-]	0.0	0.1	0.2	0.3	0.4	0.5	0.6	0.7	0.8	0.9	1.0
Span Location [m]	0.00	1.30	2.60	3.90	5.20	6.50	7.80	9.10	10.40	11.70	13.00
Total Chord [m]	1.47	1.47	1.47	1.47	1.47	1.47	1.39	1.22	1.06	0.90	0.73

Required Cl	2.50	2.49	2.45	2.38	2.29	2.17	2.12	2.14	2.08	1.78	0.00
Angle [deg]	19.82	19.71	19.36	18.77	17.92	16.77	16.33	16.56	15.96	13.28	-2.98
EA [N]	3.5E+08	3.5E+08	3.5E+08	2.1E+08	2.1E+08	4.9E+08	3.3E+08	1.7E+08	1.5E+08	1.3E+08	1.0E+08
EL_cc [N-m ² /rad]	4.2E+06	4.2E+06	4.2E+06	2.3E+06	2.3E+06	6.0E+06	3.5E+06	1.4E+06	8.8E+05	5.3E+05	2.9E+05
EL_nn [N-m ² /rad]	8.5E+06	8.5E+06	8.5E+06	7.5E+06	7.5E+06	9.6E+06	7.2E+06	4.3E+06	2.8E+06	1.7E+06	9.3E+05
GJ [N-m ² /rad]	3.3E+06	3.3E+06	3.3E+06	3.3E+06	3.3E+06	3.3E+06	2.8E+06	1.9E+06	1.3E+06	7.6E+05	4.2E+05

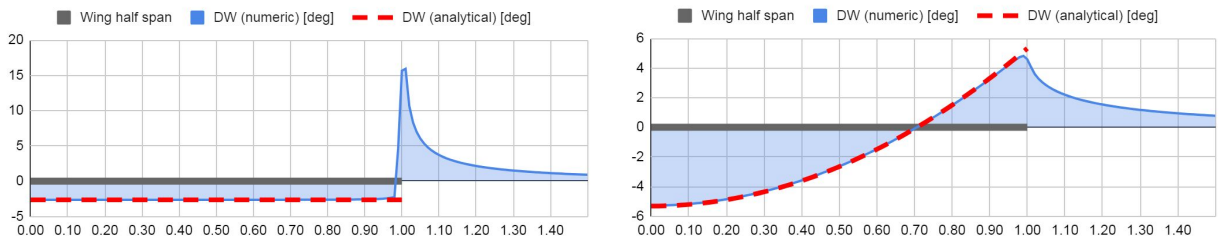
High Resolution Version of Wing Sizer

A duplicate wing sizer was created to resolve upwash/downwash effects with greater precision to help validate the implementation of lifting line theory in the lower resolution sizer (10 half-span segments). The high resolution version uses 100 segments for the half span. Shown below is the downwash profile for elliptical and bell shaped lift distributions respectively for both low and high resolution versions of the sizer. It is clear that as the resolution increases, the numeric solution approaches the analytic solution.

Low res:



High res:

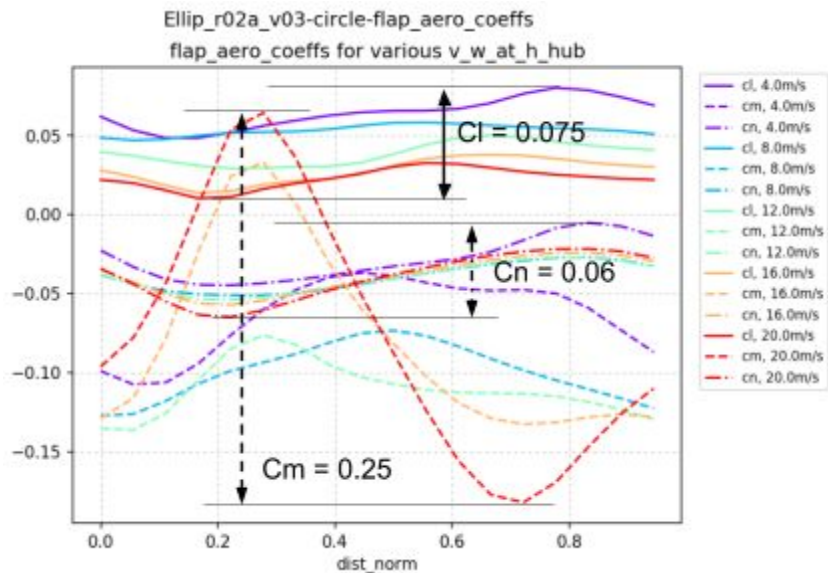


Empennage & Control Surface Sizing

The empennage and fuselage structure is sized following a Force Balance Loop (FBL) run of the wing planform which generates a set of required roll/pitch/yaw moments that are necessary to fly the loop.

Loads

Non-dimensional tail moment coefficients (Cl, Cn, Cm) are extracted manually from the FBL model's outputs as shown below



...and entered in the loads section of the sheet:

	Loads	
Flap aero coeff: delta Cn (req'd yaw moment)	0.03	[-]
Flap aero coeff: delta Cm (req'd pitch moment)	0.18	[-]
Flap aero coeff: delta Cl (req'd roll moment)	0.07	[-]

The values are dimensionalized in the following equation to determine the magnitude of the roll/pitch/yaw moments:

$$M_{roll} = C_l q S_{ref} b_{ref}$$

$$M_{pitch} = C_m q S_{ref} c_{ref}$$

$$M_{yaw} = C_n q S_{ref} b_{ref}$$

To determine the size of the aileron, elevator and vertical tail/rudder respectively the C_L range of these control surfaces must be known. These values are hard coded in the control requirements section:

Control Requirements		
Vertical tail volume	25.8	m ³

Horizontal tail volume	10.8	m ³
efficiency factor	0.690	[-]
dCL v-tail	1.820	[-]
dCL h-tail	2.460	[-]
dCL aileron	0.450	[-]
control safety factor	1.300	[-]

A detailed explanation of the empennage and control surface sizing is available in the white paper “[Dimensionalizing and Sizing of Control Surfaces for Stability and Authority](#),” also included in this volume.

Mass Buildup

Densities for the various structural elements are set here:

Mass Properties		
Composite Structure Density	1600	[kg/m ³]
Skin Core Density	60	[kg/m ³]
2nd element Core Density	31	[kg/m ³]
Nonstructural mass (areal)	1.0	[kg/m ²]
Nonstructural mass (linear)	1.0	[kg/m]

Mass is summed for each structural element at each spanwise station (see below). The blue region is for manual user input of known masses. Areal and linear mass densities reference wing area and span respectively, this nonstructural mass is summed in the “wire, glue, paint” row. The totals are summed, then doubled (to account for both halves of the symmetric kite) to provide a total mass of the fully integrated kite.

Mass													Full span	
Spar cap mass [kg]	5.99	14.98	11.98	8.99	5.99	5.49	2.50	2.25	2.00	1.75	0.75		125	kg
Main Element Skin mass [kg]	9.22	18.43	18.43	18.43	18.43	16.51	14.59	12.67	10.75	8.83	3.46		300	kg
Trailing Edge strap mass [kg]	0.21	0.42	0.42	0.42	0.42	0.37	0.33	0.29	0.24	0.20	0.08		7	kg
2nd Element mass [kg]	1.73	3.45	3.45	3.45	3.45	3.45	3.45	8.29	8.29	8.29	4.15		103	kg
Aileron hardware [kg]								4.17	4.17	4.17	2.08		29	kg
Shearwall mass [kg]	2.15	4.29	4.27	4.24	4.20	3.79	3.36	2.91	2.43	1.90	0.56		68	kg
Rib mass [kg]	3.09	6.18	6.18	6.18	6.18	5.07	4.08	3.19	2.40	1.73	0.58		90	kg
wire, glue, paint [kg]	2.24	4.48	4.48	4.48	4.48	4.21	3.95	3.68	3.42	3.15	1.44		80	kg
Pylon assembly [kg]		40.0		40.0									160	kg
Nacelles + Powertrain + Booms [kg]		120.0		120.0									480	kg

Fuselage assembly [kg]	25.2												50	kg
Empennage assembly [kg]	114.4												229	kg
Hardpoints [kg]	12.5	8.0		8.0									57	kg
Wing Tip Thruster [kg]											7.0		14	kg
Avionics [kg]	13.0												26	kg
Mass Balance Assembly [kg]	18.0												36	kg
												Total	1854	kg

Intertials are determined about the origin (kite’s center of mass is assumed to be located at the origin which corresponds to the kite ¼ chord). Each station contributes some inertia about each axis. For the roll and yaw axis (x and z) it is assumed that these are point masses and don’t carry their own inertia (i.e. only the $I = M \cdot R^2$ parallel axis theorem is applied). Intertias about the y(pitch)-axis assume symmetric and linearly distributed masses ($I = 1/12 \cdot M \cdot L^2$) for the pylons and wing stations (chord as length), cantilevered linearly distributed mass ($I = 1/3 \cdot M \cdot L^2$) for the fuselage, and point masses for the empennage. These values are tabulated, summed, then doubled (to account for both halves of the symmetric kite) in the table below.

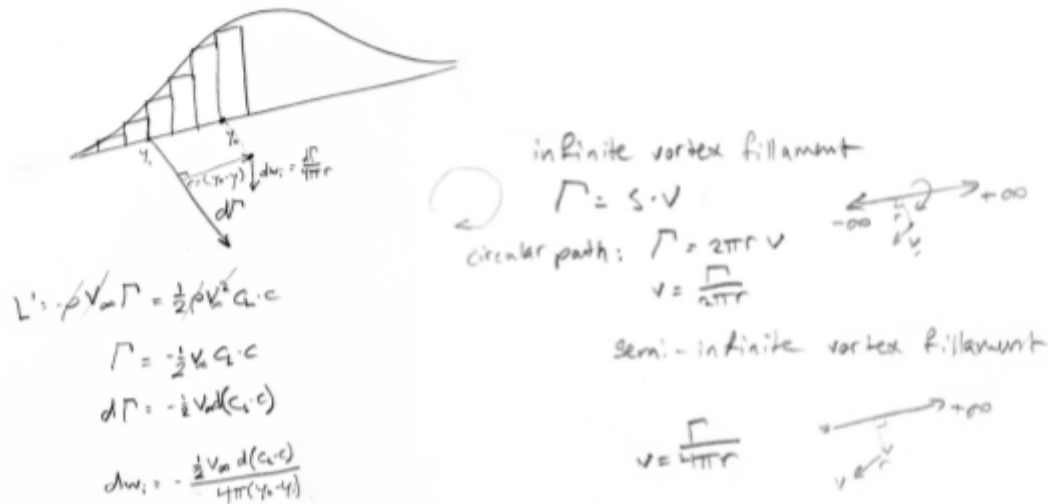
													Total
Mass [kg]	208	220	49	214	43	39	32	37	34	30	20		1854
lxx [kg-m ²]	22	372	333	3258	1167	1644	1962	3101	3645	4109	3229		4.57E+04
lyy [kg-m ²]	6416	356	24	353	21	16	11	10	7	5	2		1.44E+04
lzz [kg-m ²]	22	372	333	3258	1167	1644	1962	3101	3645	4109	3229		4.57E+04
lyy_wing [kg-m ²]	12	26	24	23	21	16	11	10	7	5	2		
lyy_pylons [kg-m ²]	0	30	0	30	0	0	0	0	0	0	0		
lyy_nacelles [kg-m ²]	0	300	0	300	0	0	0	0	0	0	0		
lyy_fuselage [kg-m ²]	438	0	0	0	0	0	0	0	0	0	0		
lyy_empennage [kg-m ²]	5966	0	0	0	0	0	0	0	0	0	0		

Maneuvering Loads & Lifting Line Theory

Perhaps you’ve noticed that the structure is sized for “straight and level flight” conditions. This is correct, and of course not accurate for a kite that flies in loops. For a given tether tension however, an increase in load on one side would necessarily be balanced by a decrease in load on the other, so the net effect is not anticipated to have a significant impact on the final mass (nor structure) of the airframe. As stated in the overview section, this tool is only suitable for preliminary sizing.

The impact of maneuvering (roll and yaw rates only in this tool) is determined using [lifting line theory](#). It is not easy to summarize without a bunch of math, but I’ll attempt it nonetheless. The

lift on the wing is proportional to a circulation Gamma (Γ) around the span of the wing that varies in proportion to the spanwise lift distribution. In order to decrease lift (and thereby circulation) when moving outward from the center of the wing, some of the circulation ($d\Gamma$) must be shed downstream (see [Helmholtz's theorems](#)). It is precisely this line of shed vortices that each contribute some upward/downward velocity to each spanwise location (dw_i), resulting in a net upward or downward flow:



This flow is known as the “downwash” as the net wake of an airplane is downward in straight and level flight. Additionally, this downwash is what is responsible for a wing’s induced drag, the portion of lift (which is defined as being perpendicular to the incident airflow at each spanwise station, the angle of which is determined by the horizontal and downwash components) that is pointed opposite the direction of travel.

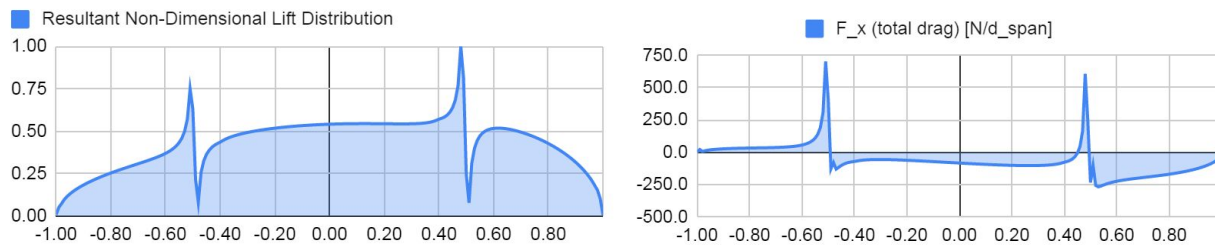
What is particularly useful about the lifting line theory, is that you can specify any dynamic pressure distribution (airspeed and yaw rates) and C_L *chord distribution and compute the resulting lift and downwash, and therefore the drag and lift at each spanwise station, which in turn can be used to calculate any of the following:

- Roll and Yaw moments due to roll rate
- Roll and Yaw moments due to yaw rate
- Roll and Yaw moments due to aileron deflection

Dynamics Following Structural Sizing	
Aileron effective AoA delta	5.5 [deg]
Roll rate (p)	-0.5 [rad/s]
Additional yaw rate (r)	0 [rad/s]
AoA Trim	0 [deg]
Loop Radius	90 [m]
Wind Speed	0 [m/s]

Airspeed	65 [m/s]
Bank angle to wind	0.79 [rad]
loop omega	-0.72 [rad/s]
Total lift (from lifting line theory)	256,490 [N]
Wing Aero Moment_x	-237,949 [N-m]
Wing Aero Moment_z	100,777 [N-m]

Below are the lift and drag distributions used to determine the above moments. The sharp discontinuity is due to the sharp discontinuity in CL due to aileron deflection.



In reality the areas just on either side of the discontinuity would be partially stalled due to the large \pm local C_L requirements. This effect is not accounted for, and as such not captured in the calculated wing aero moments.

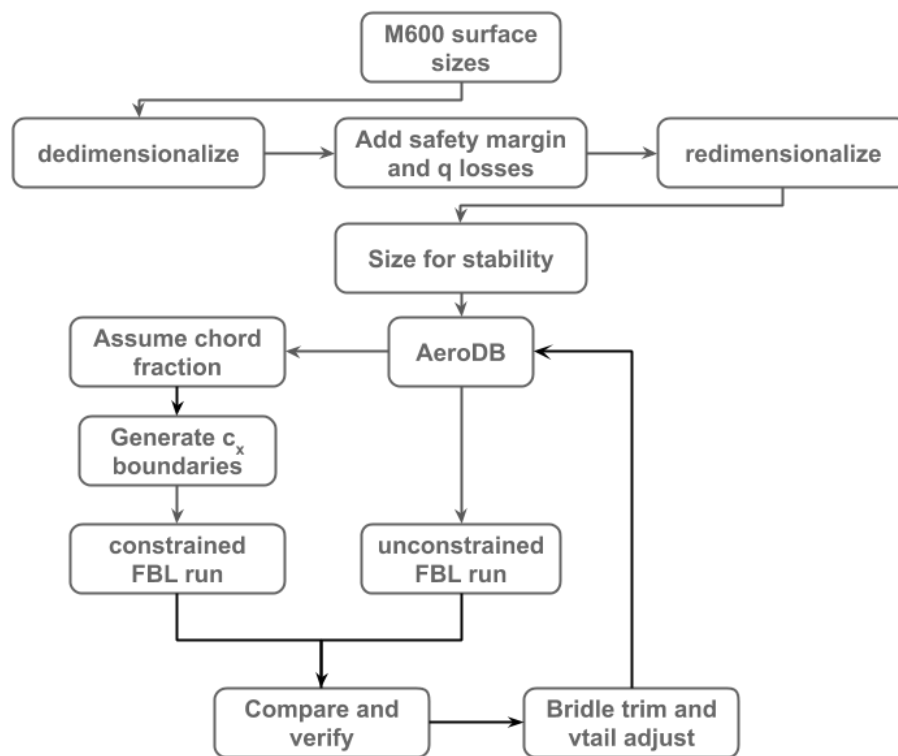
Dimensionalizing and Sizing of Control Surfaces for Stability and Authority

By the Makani “Oktoberkite” Team

09/18/2019

Introduction

This white paper summarizes the tail surface sizing workflow used during the “Oktoberkite” phase of the MX2 preliminary design. It consists of two main stages: sizing for stability, and sizing for control. These stages are discussed separately in the following subsections. A summary of the overall workflow is shown in the figure below.



Sizing for Stability

Preliminary stability sizing for future planforms follows a scaled approach from the M600 while attempting to compensate for the loss in dynamic pressure due to the rotor wake. This works to resolve the M600 lateral stability issue.

First we define our references for (non)dimensionalizing:

$$S_{ref} \text{ (m600)} = 32.9 \text{ m}^2$$

$$B_{ref} \text{ (m600)} = 25.5 \text{ m}$$

$$C_{ref} \text{ (m600)} = 1.28 \text{ m}$$

$$X_v \text{ (m600)} = 8.00 \text{ m}^1$$

$$X_h \text{ (m600)} = 8.00 \text{ m}$$

We calculate the tail volume coefficient of the M600 by taking the sum of all the vertical surface volumes.

$$\bar{V}_{VS} = \frac{\sum_i^N A_{VS_i} \cdot x_{VS_i}}{B_{ref} S_{ref}}$$

For the M600 this value would be (ref: m600 aero database sn4_r04):

$$\bar{V}_{VS_{M600}} = \frac{4.908 \text{ m}^2 \cdot 8.0 \text{ m} - 4 \cdot (4.08 \text{ m}^2 \cdot 1 \text{ m})}{26.0 \text{ m} \cdot 32.9 \text{ m}^2} = 0.0276$$

Note that if we exclude the pylon area in this calculation the tail volume coefficient appears to be much larger than actuality. The following is an INCORRECT calculation of the M600 tail volume coefficient.

$$\bar{V}_{VS_{M600}} = \frac{4.908 \text{ m}^2 \cdot 8.0 \text{ m}}{26.0 \text{ m} \cdot 32.9 \text{ m}^2} = 0.046$$

So it is important to account for ALL surfaces in the sizing calculation. We will use the V_{vs} of 0.0276.

Now, we must also account for the loss in dynamic pressure on these surfaces that is due to energy extraction during generation. We do this recognizing that when these surfaces are lifting/dragging and applying moments about the reference location, the lift and drag forces will be degraded by the loss in dynamic pressure.

So we calculate q^*/q as the modified dynamic pressure due to rotor effects and find that $q^*/q = (1+CT)$; where $CT_{min} = -0.31$ for the current M600 rotors and powertrain

¹ The X_v and X_h distances are from the aerodynamic center of the corresponding surface to the reference location, about which all forces and moments are calculated. It could be arbitrary, it could be the tether attachment point or the center of gravity for example.

$$q^*/q = 1 + C_T = 0.69$$

Note that this value changes depending on velocity and thrust from the rotors, but the given value is a conservative (minimum) value.

We then use q^*/q to scale the current M600 tail volume coefficient.

Let the geometric tail volume be:

$$\bar{V}_{geom} = \frac{\sum_i^N A_{VS_i} \cdot x_{VS_i}}{B_{ref} S_{ref}}$$

The adjusted effectiveness is then

$$\bar{V}_{aero} = \frac{q^*}{q} \frac{\sum_i^N A_{VS_i} \cdot x_{VS_i}}{B_{ref} S_{ref}} = \frac{q^*}{q} \cdot \bar{V}_{geom}$$

And our requirement for the time being is:

$$\bar{V}_{aero} \geq \bar{V}_{VS_{M600}} = 0.0276$$

Which means

$$\bar{V}_{geom} = \bar{V}_{VS_{New}} = \bar{V}_{VS_{M600}} \cdot \frac{q}{q^*} = \bar{V}_{VS_{M600}} / (1 + C_T) = 0.0276 / 0.690 = 0.0400$$

If we follow this method to recalculate the vertical tail surface area for the M600 we would have

$$\bar{V}_{VS_{New}} = \frac{A_{NewVT} \cdot 8.0 \text{ m} - 4 \cdot (4.08 \text{ m}^2 \cdot 1 \text{ m})}{26 \text{ m} \cdot 32.9 \text{ m}^2} = 0.0400$$

Substitute and rearrange to solve for the recalculated vertical tail area² we have

$$A_{VT_{New}} = \frac{\bar{V}_{VS_{New}} \cdot 26 \text{ m} \cdot 32.9 \text{ m}^2 + 4 \cdot (4.08 \text{ m}^2 \cdot 1 \text{ m})}{8.0 \text{ m}} = 6.22 \text{ m}^2$$

² Note this is the vertical tail area the M600 *should have had* to meet our design requirements. This is not to be confused with the vertical tail area of the new craft.

Sizing of the horizontal tail surface would follow the same logic, substituting vertical areas for horizontal and using the correct offsets for determining the resultant volume.

For sizing of the horizontal tail surface first we determine the current horizontal tail volume coefficient

$$\bar{V}_{HS_{M600}} = \frac{3.54 \text{ m}^2 \cdot 8.0 \text{ m}}{1.28 \text{ m} \cdot 32.9 \text{ m}^2} = 0.673$$

And our new requirement is then:

$$\bar{V}_{HS_{New}} = \frac{q}{q^*} \cdot \bar{V}_{HS_{M600}} = .975$$

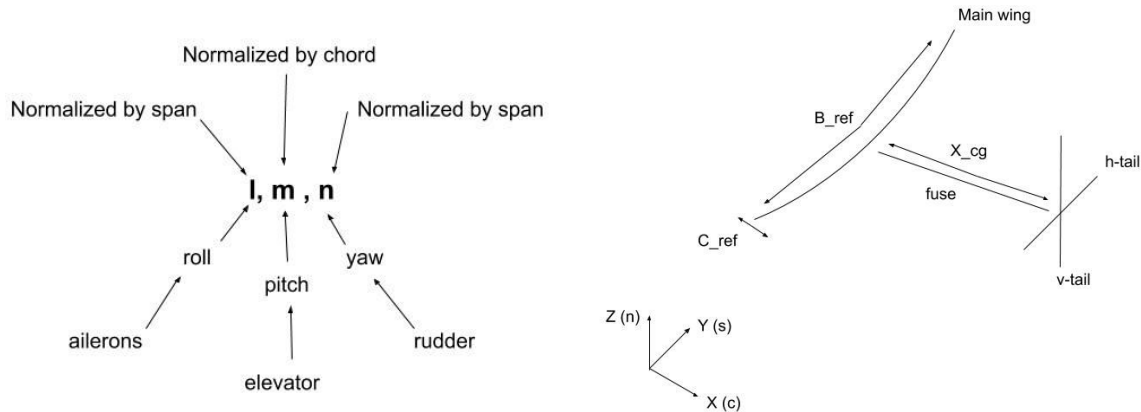
Sizing for Control

For control authority sizing we run the FBL with *no* moment constraints, but with the moment regularization term applied. This encourages the optimizer to use the minimal surface deflection possible. One can then pick out $C_{m,max}$, $C_{m,min}$, and $C_{m,avg}$ from the FBL outputs and evaluate the following:

- $\Delta C_m = C_{m,max} - C_{m,min}$
- If $C_{m,avg}$ is far from zero (say, if $C_{m,avg} > 0.2 \cdot \Delta C_m$, for instance), then the airframe is not well trimmed. Adjust trim surface positions and repeat regularized FBL run.
- If $C_{m,avg}$ is near zero ($C_{m,avg} < 0.2 \cdot \Delta C_m$), then the airframe is adequately trimmed. In this case, proceed to surface sizing using the computed ΔC_m

A similar workflow, of course, applies to C_l and C_n .

Having our necessary range of control authority in hand, we then take the 'flap aero coeff' array from FBL and dimensionalize each term, Cl, Cm, Cn as follows using the indicated reference axis:



Assumptions and definitions:

Definition: δC_L : range of total surface C_L as a function of the range of flap deflection in degrees (limited to +/- 10 degrees for all surfaces)

- Assumption: $\delta C_{L,htail} = 0.123/deg \cdot 20deg = 2.46$
- Assumption: $\delta C_{L,vtail} = 0.091/deg \cdot 20deg = 1.82$
- Assumption: $\delta C_{L,aileron} = 0.045/deg \cdot 20deg = 0.9$

Assumption: $\eta = q^*/q = 1 + C_T \approx 0.69$ (based on loss of q from rotor wash during gen, see [internal ref]: moment coefficient limits equations)

Definition: $q = \frac{1}{2}\rho v^2$ (at nominal operating point)

Computation of control surface sizes:

We apply a safety factor (SF = 1.3) to the required tail surface volumes, to ensure we don't run out of control authority.

We compute as follows:

$$\Delta C_m = C_{m,max} - C_{m,min}$$

$$\Delta M_{y,req} = \Delta C_m S_{ref} C_{ref} q = q^* \cdot \delta C_{L,htail} \cdot S_{htail} X_h = q^* \cdot \delta C_{L,htail} \cdot V_{htail,geom}$$

$$V_{htail,geom} = SF \cdot \Delta C_m S_{ref} C_{ref} / (\eta \cdot \delta C_{L,htail})$$

$$S_{htail} = V_{htail} / X_h$$

$$\Delta C_n = C_{n,max} - C_{n,min}$$

$$M_{z,req} = \Delta C_n S_{ref} B_{ref} q = q^* \cdot \delta C_{L,vtail} \cdot S_{vtail} X_v = q^* \cdot \delta C_{L,vtail} \cdot V_{vtail,geom}$$

$$V_{vtail,geom} = SF \cdot \Delta C_n S_{ref} C_{ref} / (\eta \cdot \delta C_{L,vtail})$$

$$S_{vtail} = V_{vtail} / X_v$$

Final Sizing

Now we can take the larger of the two areas, the one required for stability or the one required for control at our desired flight configuration as determined by FBL. This provides our final tail surface areas and can be used for calculating the aero-database in ASWING. Since FBL does not use the aero-db for control authority limitations, the full sized surfaces can be included when generating the db since we will want them in there for other uses. The control moments will be adjusted for FBL next.

Verification Step

Then finally we recalculate the realized control limits (Cl,Cm,Cn) based on the resultant sizing for use in FBL to check FBL results with hard control limits imposed. Since we do not want FBL to make use of the additional area resultant from the imposed safety factor, for this area is meant to on-reserve for unknown perturbations, we divide back out the safety factor when providing control moment constraints to the FBL. We do the same for the q deficit since FBL does not simulate the pressure drop across the tail from the rotors during gen. These equations are shown below.

$$\Delta C_n = \frac{V_{vtail} \cdot (1+C_T) \cdot \delta C_{L,vtail}}{S_{ref} \cdot b_{ref} \cdot SF} \quad \Delta C_m = \frac{V_{htail} \cdot (1+C_T) \cdot \delta C_{L,htail}}{S_{ref} \cdot c_{ref} \cdot SF}$$

$$V_{vtail} = \frac{\Delta C_n \cdot S_{ref} \cdot b_{ref}}{(1+C_T) \cdot \delta C_{L,vtail}} \quad V_{htail} = \frac{\Delta C_m \cdot S_{ref} \cdot c_{ref}}{(1+C_T) \cdot \delta C_{L,htail}}$$

$$A_s = \frac{V_s}{X_s}$$



BigM600 Tail Sizing White Paper

Report: TLG-MAK-004

For: Florian Kapsenberg, Makani Technologies, LLC
Trevor Orr, Makani Technologies, LLC
Geo Homsy, Makani Technologies, LLC

Revision: IR

Current Release Date: 01/30/2020

REPORT: TLG-MAK-004		REVISION: IR	PAGE i
AIRCRAFT: BigM600		REV DATE: 01/30/2020	PROPRIETARY
TITLE: BigM600 Tail Sizing White Paper		CUSTOMER: Makani Technologies, LLC	

Table of Contents

Table of Contents..... i

List of Figures ii

List of Tables iii

References iv

Revision Page v

1.0 Introduction 1-1

2.0 Tail Sizing Theory..... 2-1

 2.1 Deformation of the Fuselage Boom 2-1

 2.2 Lift & Side Force at the Tail 2-2

 2.3 Horizontal Tail Sizing for Stability..... 2-3

 2.4 Horizontal Tail Sizing for Trim 2-4

 2.5 Vertical Tail Sizing for Trim..... 2-5

3.0 Tail Sizing Results 3-1

 3.1 FBL Data..... 3-1

 3.2 Sizing for Max Allowable Normal Force 3-1

 3.3 Sizing for Stability 3-2

 3.4 Sizing for Trim..... 3-6

 3.5 Summary 3-9

4.0 Lateral-Directional Static Stability..... 4-1

 4.1 Governing Equations 4-1

 4.2 Validation using FBL aero 4-2

 4.4 Aerodynamic Models for Configuration Options 4-6

REPORT: TLG-MAK-004		REVISION: IR	PAGE ii
AIRCRAFT: BigM600		REV DATE: 01/30/2020	PROPRIETARY
TITLE: BigM600 Tail Sizing White Paper		CUSTOMER: Makani Technologies, LLC	

List of Figures

Figure 1 Minimum horizontal and vertical tail areas as a function of tail arm.....	3-2
Figure 2 The impact of the propeller planform lifting effect on the horizontal tail area, sizing for stability.....	3-3
Figure 3 The impact of desired static margin on the horizontal tail area, sizing for stability	3-3
Figure 4 The impact of the fuselage boom stiffness on the horizontal tail area, sizing for stability (S.M. = 10%)	3-5
Figure 5 The impact of the fuselage boom stiffness on the horizontal tail area, sizing for stability (S.M. = 12%)	3-5
Figure 6 The impact of the elevator chord fraction on the horizontal tail area, sizing for trim.....	3-6
Figure 7 The impact of the fuselage boom stiffness on the horizontal tail area, sizing for trim.....	3-7
Figure 8 The impact of the rudder chord fraction on the vertical tail area, sizing for trim	3-8
Figure 9 The impact of the fuselage boom stiffness on the vertical tail area, sizing for trim	3-8
Figure 10 CAD layout of the “V” tail configuration.....	3-11
Figure 11 CAD layout of the inverted-“V” tail configuration.....	3-11
Figure 12 CAD layout of the cruciform tail configuration.....	3-12
Figure 13 CAD layout of the dual-boom configuration.....	3-12
Figure 14 Comparison of lateral-directional trim points against FBL. Here, beta was fixed to the FBL result.....	4-4
Figure 15 Comparison of lateral-directional trim points against FBL. Here, beta was free to be set by the linear system.	4-4
Figure 16 Comparison of lateral-directional trim points against FBL. Here, control surfaces could produce control forces and cross moments.	4-5
Figure 17 Example of the vortex lattice model used to calculate linear aerodynamics. Example shows the “V” tail configuration.....	4-7
Figure 18 Summary of the dihedral effect for the 4 empennage configurations examined.....	4-10

REPORT: TLG-MAK-004		REVISION: IR	PAGE iii
AIRCRAFT: BigM600		REV DATE: 01/30/2020	PROPRIETARY
TITLE: BigM600 Tail Sizing White Paper		CUSTOMER: Makani Technologies, LLC	

List of Tables

Table 1 Stiffness of the M600 fuselage boom, results from Reference [3] 3-4

Table 2 Summary of outputs from the tail sizing calculations 3-9

Table 3 Tail planforms configurations which meet the tail sizing requirements 3-10

Table 4 Linearized aerodynamics from database used for FBL tail-sizing exercise 4-3

Table 5 Linearized aerodynamics calculated from VLM, "V" tail configuration 4-8

Table 6 Linearized aerodynamics calculated from VLM, inverted-"V" tail configuration 4-8

Table 7 Linearized aerodynamics calculated from VLM, dual-boom tail configuration 4-9

Table 8 Linearized aerodynamics calculated from VLM, cruciform tail configuration 4-9

REPORT: TLG-MAK-004		REVISION: IR	PAGE iv
AIRCRAFT: BigM600		REV DATE: 01/30/2020	PROPRIETARY
TITLE: BigM600 Tail Sizing White Paper		CUSTOMER: Makani Technologies, LLC	

References

- 1 Makani Technologies, LLC. "Dimensionalizing and Sizing of Control Surfaces for Stability and Authority", September 2019.
- 2 E. Patten, "M10091: Tether Moment Coupling", February 2019.
- 3 F. Kapsenberg, "M600 Fuselage FEM Validation Report", May 2017.
- 4 F. Kapsenberg, "Appendix A – Specification for Makani Airframe Design by TLG Aerospace", Rev 07, January 2020

REPORT: TLG-MAK-004		REVISION: IR	PAGE v
AIRCRAFT: BigM600		REV DATE: 01/30/2020	PROPRIETARY
TITLE: BigM600 Tail Sizing White Paper		CUSTOMER: Makani Technologies, LLC	

Revision Page

<u>Revision</u>	<u>Date</u>	<u>Description</u>	<u>Approval</u>
IR	01/30/2020	Initial Release	See Cover Page

REPORT: TLG-MAK-004		REVISION: IR	PAGE 1-1
AIRCRAFT: BigM600		REV DATE: 01/30/2020	PROPRIETARY
TITLE: BigM600 Tail Sizing White Paper		CUSTOMER: Makani Technologies, LLC	

1.0 Introduction

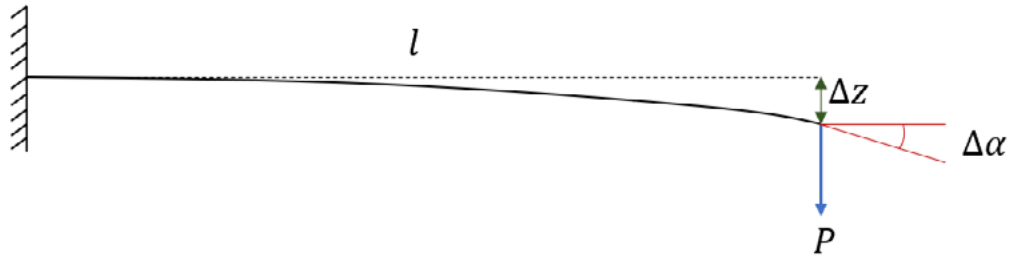
This document details the sizing of tail surfaces for the BigM600 Energy Kite which has been undertaken by TLG Aerospace, LLC. Tail sizing has been undertaken for both stability and trimability while accounting for the elastic effects of a deformable fuselage boom. The initial tail sizing is done independent of the final tail planform and thus determines tail areas given a prescribed free-air lift-curve slope of the tail. Put another way, the initial tail sizing determines free air values for the derivatives $C_{L,\alpha}$ and $C_{Y,\beta}$ that must be met by the final planform. A subsequent step looks holistically at the entire kite to determine the interplay between the tail configuration and the rest of the vehicle. In this way, we can try to understand the impact of issues such as dihedral effect, adverse/proverse rudder roll and adverse yaw on the static stability of the aircraft in order to further evaluate tail sizing and find further efficiencies.

REPORT: TLG-MAK-004		REVISION: IR	PAGE 2-1
AIRCRAFT: BigM600		REV DATE: 01/30/2020	PROPRIETARY
TITLE: BigM600 Tail Sizing White Paper		CUSTOMER: Makani Technologies, LLC	

2.0 Tail Sizing Theory

2.1 Deformation of the Fuselage Boom

To model the elastic relief of the fuselage due to tail load, we use a beam model with a point load. The theoretical deflection and change in angle-of-attack are shown below.



$$\Delta z = \frac{-Pl^3}{3EI}$$

$$\Delta\alpha = \frac{Pl^2}{2EI}$$

We can re-write the load P in terms of aerodynamic quantities of the tail and convert the angle to degrees.

$$\Delta\alpha_e = \frac{-(C_{Lh}q_hS_h)l_h^2}{2EI_y} \left(\frac{180}{\pi}\right)$$

Here, we have used C_{Lh} as the lift coefficient of the tail normalized by the dynamic pressure at the tail and the area of the tail. The same process can be done for the vertical tail, using the appropriate parameters for normalization.

$$\Delta\beta_e = \frac{-(C_{Yv}q_vS_v)l_v^2}{2EI_z} \left(\frac{180}{\pi}\right)$$

Lastly, we can create a new grouping to simplify derivations that follow. This simple grouping will allow for the change in angle at the tail to be written in terms of the tail area and tail arm ratios.

$$\Omega_y = \frac{q_i S_w C_{ref}^2}{2EI_y} \left(\frac{180}{\pi}\right)$$

$$\Omega_z = \frac{q_i S_w b_{ref}^2}{2EI_z} \left(\frac{180}{\pi}\right)$$

REPORT: TLG-MAK-004		REVISION: IR	PAGE 2-2
AIRCRAFT: BigM600		REV DATE: 01/30/2020	PROPRIETARY
TITLE: BigM600 Tail Sizing White Paper		CUSTOMER: Makani Technologies, LLC	

2.2 Lift & Side Force at the Tail

The lift at the tail is determined by the effective angle-of-attach at the tail.

$$\alpha_h = \alpha + i_h - \epsilon + \tau_e \delta_e + \Delta\alpha_e$$

The downwash can be modelled as a linear function of alpha.

$$\epsilon = \epsilon_0 + \frac{\partial \epsilon}{\partial \alpha} \alpha$$

We can explicitly solve for the tail lift coefficient by substituting in the expression for the elastic relief of the tail.

$$C_{Lhe} = C_{N,ih} \alpha_h$$

$$C_{Lhe} = \frac{C_{N,ih} \left(\alpha + i_h - \epsilon_0 - \frac{\partial \epsilon}{\partial \alpha} \alpha + \tau_e \delta_e \right)}{1 + C_{N,ih} \frac{q_h S_h}{q_i S_w} \left(\frac{l_h}{C_{ref}} \right)^2 \Omega_y}$$

A similar process can be done for the vertical tail.

$$\beta_v = \beta + i_v + \sigma + \tau_r \delta_r + \Delta\beta_e + \Delta\beta_r$$

Here, we have replaced downwash (ϵ) with sidewash (σ) and also added a term for the yaw-rate induced sideslip.

Including the yaw-rate term is important since a crosswind kite is always flying with significant yaw rates.

$$\Delta\beta_r = \tan^{-1} \left(\frac{-r \frac{l_v}{b_{ref}} b_{ref}}{V} \right) \left(\frac{180}{\pi} \right) = \tan^{-1} \left(-2\hat{r} \frac{l_v}{b_{ref}} \right) \left(\frac{180}{\pi} \right)$$

We can use the Makani tops-down estimate of the tail arm length to get an initial idea of the size of the induced sideslip angle. This estimate also assumes flying crosswind circles with a diameter of 90.0 m.

$$\hat{r} = \frac{rb}{2V} = \frac{(-V/R)b}{2V} = \frac{-b}{2R} = \frac{-26 \text{ m}}{2 * 90 \text{ m}} = -0.144$$

$$\Delta\beta_r = \tan^{-1} \left(-2(-0.144) \frac{8.5 \text{ m}}{26 \text{ m}} \right) \left(\frac{180}{\pi} \right) = 5.4 \text{ deg}$$

Returning to the side force coefficient, we can find the close-form solution with elastic effects by substituting in the expression for the elastic relief of the tail.

REPORT: TLG-MAK-004		REVISION: IR	PAGE 2-3
AIRCRAFT: BigM600		REV DATE: 01/30/2020	PROPRIETARY
TITLE: BigM600 Tail Sizing White Paper		CUSTOMER: Makani Technologies, LLC	

$$C_{Yve} = -C_{N,iv}\beta_v$$

$$C_{Yve} = \frac{-C_{N,iv} \left(\beta + i_v + \sigma_0 + \frac{\partial \sigma}{\partial \beta} \beta + \tau_r \delta_r + \Delta \beta_f \right)}{1 + C_{N,iv} \frac{q_v S_v}{q_i S_w} \left(\frac{l_v}{b_{ref}} \right)^2 \Omega_z}$$

Lastly, we have used the subscript “N” to denote normal force in order for the horizontal and vertical tail sizing expressions to retain a similar appearance.

2.3 Horizontal Tail Sizing for Stability

We start by defining the static margin of the kite.

$$S.M. = \frac{C_{m,\alpha}}{C_{L,\alpha}}$$

We can expand the lift-curve slope and longitudinal static stiffness in terms of a wing-body component and a tail component.

$$C_L = C_{Lwb} + C_{Lh} \frac{q_h S_h}{q_i S_w}$$

$$C_{L,\alpha} = C_{Lwb,\alpha} + \frac{C_{N,ih} \left(1 - \frac{\partial \epsilon}{\partial \alpha} \right) \frac{q_h S_h}{q_i S_w}}{1 + C_{N,ih} \frac{q_h S_h}{q_i S_w} \left(\frac{l_h}{C_{ref}} \right)^2 \Omega_y}$$

$$C_m = C_{mwb} - C_{Lh} \frac{q_h S_h}{q_i S_w} \frac{l_h}{C_{ref}}$$

$$C_{m,\alpha} = C_{mwb,\alpha} - \frac{C_{N,ih} \left(1 - \frac{\partial \epsilon}{\partial \alpha} \right) \frac{q_h S_h}{q_i S_w} \frac{l_h}{C_{ref}}}{1 + C_{N,ih} \frac{q_h S_h}{q_i S_w} \left(\frac{l_h}{C_{ref}} \right)^2 \Omega_y}$$

We can then substitute these expressions back into the definition of the static margin and solve for the area ratio S_h/S_w .

$$\frac{S_h}{S_w} = \frac{C_{mwb,\alpha} - C_{Lwb,\alpha}(S.M.)}{C_{N,ih} \frac{q_h}{q_i} \left(\left(1 - \frac{\partial \epsilon}{\partial \alpha} \right) \left(S.M. + \frac{l_h}{C_{ref}} \right) - \left(C_{mwb,\alpha} - C_{Lwb,\alpha}(S.M.) \right) \left(\frac{l_h}{C_{ref}} \right)^2 \Omega_y \right)}$$

REPORT: TLG-MAK-004		REVISION: IR	PAGE 2-4
AIRCRAFT: BigM600		REV DATE: 01/30/2020	PROPRIETARY
TITLE: BigM600 Tail Sizing White Paper		CUSTOMER: Makani Technologies, LLC	

As noted in the introduction, the resulting tail area ratio uses an assumed value of the free-air lift-curve slope of the tail $C_{N,ih}$. The product of these two values represents the free-air lift-curve slope that needs to be achieved by any final tail planform and will be normalized by the wing reference area.

Additionally, the planform lifting effect of the propellers can be considered by modifying the values of $C_{Lwb,\alpha}$ and $C_{mwb,\alpha}$ to include propeller effects. The basic idea of this correction is that when viewed in planform, the propeller blades have a non-zero area. This planform area then acts as a lifting surface and creates a force in response to changes in angle of attack. A 1st order approximation to this effect is to set the propeller lift-curve slope to be the value from thin airfoil theory, $C_{L,\alpha} = 2\pi/radian$. We can then modify the body lift-curve slope and longitudinal static stiffness as follows.

$$C_{Lwbr,\alpha} = C_{Lwb,\alpha} + \left(2\pi \frac{\pi}{180}\right) \left(\frac{N_r S_r}{S_w}\right)$$

$$C_{mwbr,\alpha} = C_{mwb,\alpha} + \left(2\pi \frac{\pi}{180}\right) \left(\frac{N_r S_r}{S_w}\right) \left(\frac{l_r}{C_{ref}}\right)$$

Here, S_r is the projected *planform* area of a single rotor, N_r is the number of rotors and l_r is the longitudinal distance from the moment reference point to the center of the rotors.

2.4 Horizontal Tail Sizing for Trim

We can size the horizontal tail for trimability by sizing the tail such that the elevator deflection does not exceed a certain range. We start with the definition of equilibrium in the pitching moment.

$$C_m = 0$$

$$C_{mwb} - \frac{C_{N,ih} \left(\alpha + i_h - \epsilon_0 - \frac{\partial \epsilon}{\partial \alpha} \alpha + \tau_e \delta_e \right) \frac{q_h S_h l_h}{q_i S_w C_{ref}}}{1 + C_{N,ih} \frac{q_h S_h}{q_i S_w} \left(\frac{l_h}{C_{ref}} \right)^2 \Omega_y} = 0$$

$$\frac{S_h}{S_w} = \frac{C_{mwb}}{C_{N,ih} \frac{q_h l_h}{q_i C_{ref}} \left(\alpha + i_h - \epsilon_0 - \frac{\partial \epsilon}{\partial \alpha} \alpha + \tau_e \delta_e - C_{mwb} \frac{l_h}{C_{ref}} \Omega_y \right)}$$

However, the last equation has the unknown elevator deflections included in the denominator. Since our constraint on the tail area problem in trim is to limit the usable range of elevator deflections, it is useful to re-arrange this equation.

REPORT: TLG-MAK-004		REVISION: IR	PAGE 2-5
AIRCRAFT: BigM600		REV DATE: 01/30/2020	PROPRIETARY
TITLE: BigM600 Tail Sizing White Paper		CUSTOMER: Makani Technologies, LLC	

$$i_h + \tau_e \delta_e = \frac{C_{mwb}}{C_{N,ih} \frac{q_h S_h l_h}{q_i S_w C_{ref}}} - \left(\alpha - \epsilon_0 - \frac{\partial \epsilon}{\partial \alpha} \alpha - C_{mwb} \frac{l_h}{C_{ref}} \Omega_y \right)$$

This equation can now be solved by iteratively to find the minimum tail area ratio which meets the requirements for the elevator deflection range, for a given stiffness and tail arm ratio. The tail incidence can be used to center the elevator deflections, up to some limit, which should help reduce the magnitude of the deflections at the extremes.

Additionally, we can add a constraint that the tail surface should never separate by setting an upper limit for the allowable lift coefficient which is conservative for the tail airfoils & planform.

$$C_m = 0 = C_{mwb} - C_{Lh} \frac{q_h S_h l_h}{q_i S_w C_{ref}}$$

$$\frac{S_h}{S_w} \geq \frac{C_{mwb}}{\max(C_{Lh}) \frac{q_h l_h}{q_i C_{ref}}}$$

Note that this constraint does not depend on the elasticity of the tail, since it concerns the net balancing tail lift and not the local angle of attack at which it occurs.

2.5 Vertical Tail Sizing for Trim

This section follows the same steps as used in the previous one for sizing the horizontal tail. We start with the definition of equilibrium in the yawing moment.

$$C_n = 0$$

$$C_{nwb} + \frac{C_{N,iv} \left(\beta + i_v + \sigma_0 + \frac{\partial \sigma}{\partial \beta} \beta + \tau_r \delta_r + \Delta \beta_{\hat{r}} \right) \frac{q_v S_v l_v}{q_i S_w b_{ref}}}{1 + C_{N,iv} \frac{q_v S_v}{q_i S_w} \left(\frac{l_v}{b_{ref}} \right)^2 \Omega_z} = 0$$

$$\frac{S_v}{S_w} = \frac{-C_{nwb}}{C_{N,iv} \frac{q_v l_v}{q_i b_{ref}} \left(\beta + i_v + \sigma_0 + \frac{\partial \sigma}{\partial \beta} \beta + \tau_r \delta_r + \Delta \beta_{\hat{r}} + C_{nwb} \frac{l_v}{b_{ref}} \Omega_z \right)}$$

However, the last equation has the unknown rudder deflections included in the denominator. Since our constraint on the tail area problem in trim is to limit the usable range of rudder deflections, it is useful to re-arrange this equation.

REPORT: TLG-MAK-004		REVISION: IR	PAGE 2-6
AIRCRAFT: BigM600		REV DATE: 01/30/2020	PROPRIETARY
TITLE: BigM600 Tail Sizing White Paper		CUSTOMER: Makani Technologies, LLC	

$$i_v + \tau_r \delta_r = \frac{-C_{nwb}}{C_{N,iv} \frac{q_v S_v l_v}{q_i S_w b_{ref}}} - \left(\beta + \sigma_0 + \frac{\partial \sigma}{\partial \beta} \beta + \Delta \beta_{\dot{r}} + C_{nwb} \frac{l_v}{b_{ref}} \Omega_z \right)$$

This equation can now be solved by iteratively to find the minimum tail area ratio which meets the requirements for the rudder deflection range, for a given stiffness and tail arm ratio. For a symmetric kite, the vertical tail incidence would be set to 0.

Additionally, we can add a constraint that the tail surface should never separate by setting an upper limit for the allowable lift coefficient which is conservative for the tail airfoils & planform.

$$C_n = 0 = C_{nwb} - C_{Yv} \frac{q_v S_v l_v}{q_i S_w b_{ref}}$$

$$\frac{S_v}{S_w} \geq \frac{C_{nwb}}{\max(C_{Yv}) \frac{q_v l_v}{q_i b_{ref}}}$$

Note that this constraint does not depend on the elasticity of the tail, since it concerns the net balancing tail side-force and not the local angle of sideslip at which it occurs.

REPORT: TLG-MAK-004		REVISION: IR	PAGE 3-1
AIRCRAFT: BigM600		REV DATE: 01/30/2020	PROPRIETARY
TITLE: BigM600 Tail Sizing White Paper		CUSTOMER: Makani Technologies, LLC	

3.0 Tail Sizing Results

The following sections detail the tail sizing results from trim and stability separately as a function of tail arm and tail boom stiffness. Results are also presented for an idealized, rigid tail which can be found by setting $\Omega_y = 0$ or $\Omega_z = 0$ in the equations from section 2.0. Additionally, all results presented are compared against the results of a Makani tops-down estimate on tail sizing which included insight from lessons learned on the M600 (Ref. [1]). The comparison of the Makani tops-down estimate against the TLG bottoms-up estimate allows for more confidence in the final selected values for the tail size.

3.1 FBL Data

Makani used their FBL tool to provide the tail-off aerodynamic forces and moments which are needed to perform the tail sizing exercise. The process was to first compute each set of poses using an aerodynamic database which had tail-on contributions. The second step was to re-run the analysis with a new aerodynamic database that was built without any tail contributions. This second run was also forced to have exactly the same poses as the initial tail-on run. In this way, we would be able to extract the balancing forces and moments required of the tail. This process was run for a range of wind speeds from 4.0 – 20.0 m/s. FBL includes not just forces from the aerodynamics of the kite, but also from the tether, the rotors, gravity and inertia.

3.2 Sizing for Max Allowable Normal Force

A useful starting point for tail sizing is to determine the minimum area required such that the tail surfaces do not exceed a maximum normal force coefficient. This constraint ensures that the tail surface is always flying, i.e. – never separated. Figure 1 shows the results of this analysis for both the horizontal and vertical tail surfaces. For both surfaces, we set the maximum normal force coefficient at 0.7 which is a typical, if conservative, value used for general aviation aircraft. The results are consistent with Makani flight-test experience which has been conveyed to TLG, namely that the pitching moment requirements from the tail are small but the yawing moment requirements are large. The Makani tops-down estimate of the tail size used a tail arm of 8.5m, which shows that the estimated tail areas are both above the minimum area constraint. However, below a tail arm of 8.0m there is a risk that this constraint would be violated. Lastly, it should be noted that FBL data was used to extract the pitching & yawing moment coefficients, as well as the rotor thrust coefficients used to calculate the dynamic pressure ratio at the tail.

REPORT: TLG-MAK-004		REVISION: IR	PAGE 3-2
AIRCRAFT: BigM600		REV DATE: 01/30/2020	PROPRIETARY
TITLE: BigM600 Tail Sizing White Paper		CUSTOMER: Makani Technologies, LLC	

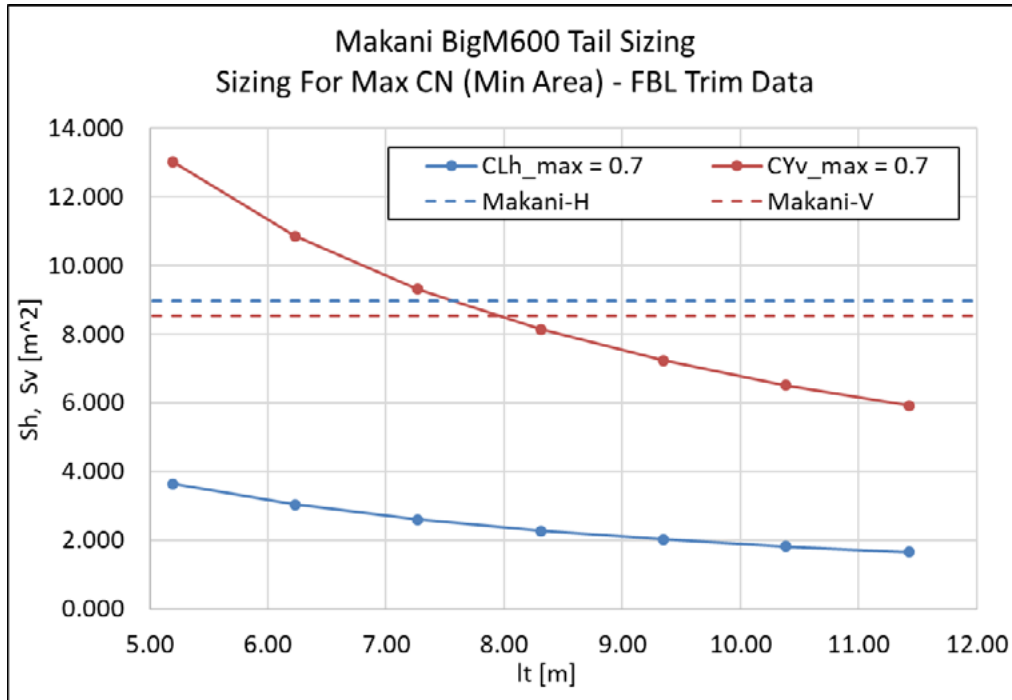


Figure 1 Minimum horizontal and vertical tail areas as a function of tail arm

3.3 Sizing for Stability

It is useful to first look at the tail sizing results for static margin using the assumption of a rigid boom. This allows for examination of the impact the propeller planform lifting affect as well as varying values of the static margin itself. First, it is useful to look at the relationship between tail area ratio and tail arm ratio for a rigid fuselage boom.

$$\frac{S_h}{S_w} = \frac{C_{mwb,\alpha} - C_{Lwb,\alpha}(S.M.)}{C_{N,ih} \frac{q_h}{q_i} \left(\left(1 - \frac{\partial \epsilon}{\partial \alpha} \right) \left(S.M. + \frac{l_h}{C_{ref}} \right) \right)}$$

$$\frac{l_h}{C_{ref}} \gg S.M. \rightarrow \frac{S_h}{S_w} \frac{l_h}{C_{ref}} \approx \frac{C_{mwb,\alpha} - C_{Lwb,\alpha}(S.M.)}{C_{N,ih} \frac{q_h}{q_i} \left(1 - \frac{\partial \epsilon}{\partial \alpha} \right)}$$

The equations above show that a decent approximation for a rigid boom is that the tail area and tail arm ratios are inversely proportional to one another. In addition to assuming that the tail arm ratio is much larger than the static margin, this assumption assumes that the downwash gradient is a weak function of tail arm length.

REPORT: TLG-MAK-004		REVISION: IR	PAGE 3-3
AIRCRAFT: BigM600		REV DATE: 01/30/2020	PROPRIETARY
TITLE: BigM600 Tail Sizing White Paper		CUSTOMER: Makani Technologies, LLC	

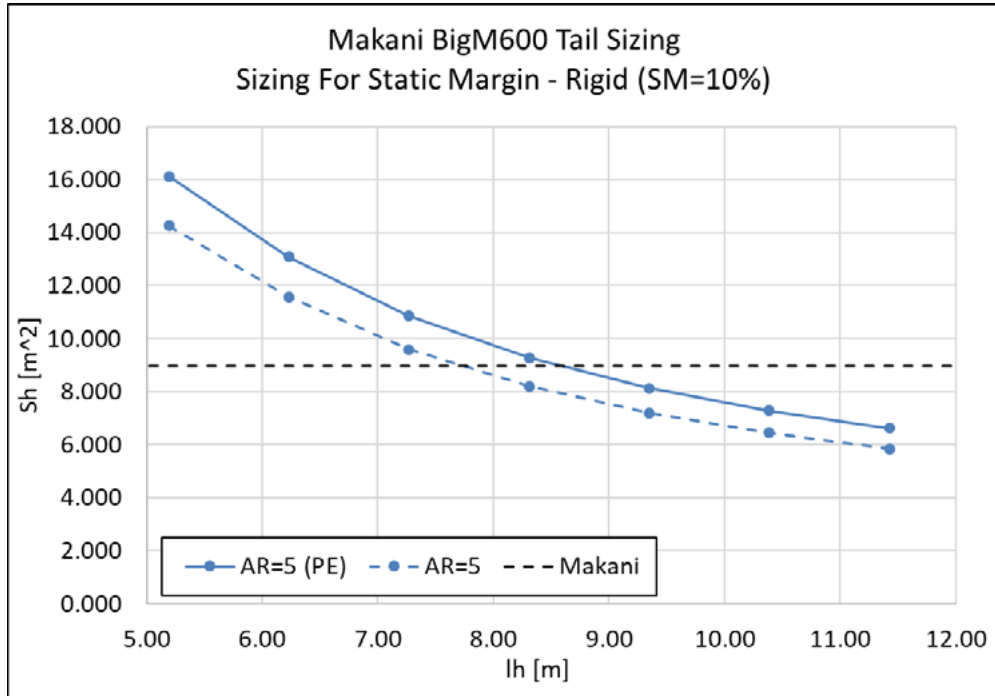


Figure 2 The impact of the propeller planform lifting effect on the horizontal tail area, sizing for stability

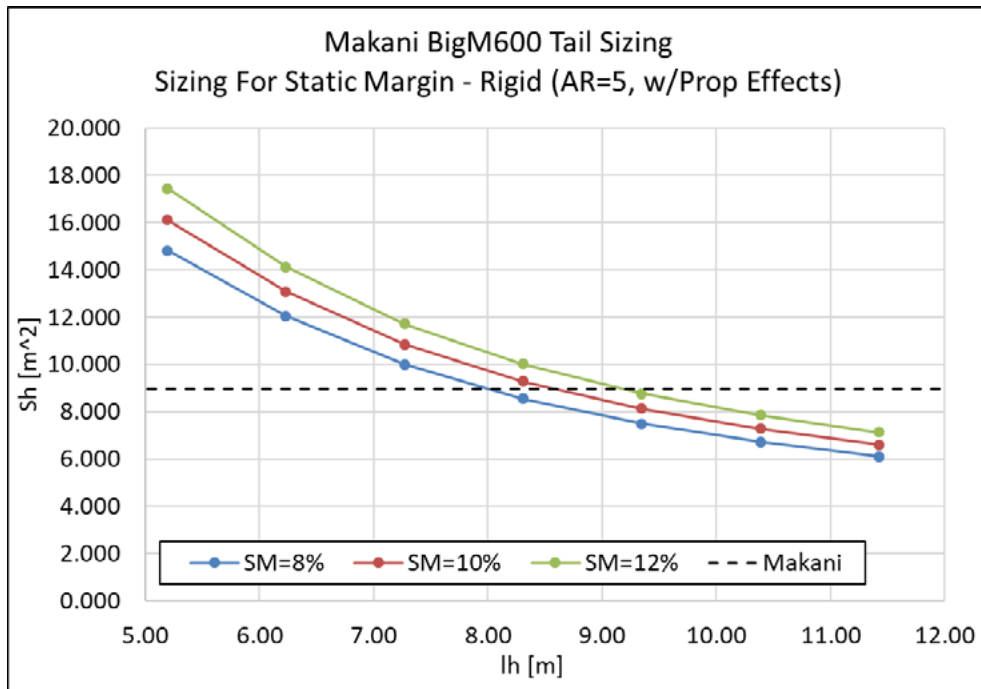


Figure 3 The impact of desired static margin on the horizontal tail area, sizing for stability

REPORT: TLG-MAK-004		REVISION: IR	PAGE 3-4
AIRCRAFT: BigM600		REV DATE: 01/30/2020	PROPRIETARY
TITLE: BigM600 Tail Sizing White Paper		CUSTOMER: Makani Technologies, LLC	

Figure 2 and Figure 3 show the results of sizing the horizontal tail area for stability with a rigid fuselage boom. In both of these figures a tail aspect ratio (AR) of 5.0 was assumed in order to estimate $C_{N,ih}$ for the tail from finite wing theory.

$$C_{N,ih} = \frac{C_{L,\alpha}^{2D}}{1 + \frac{C_{L,\alpha}^{2D}}{\pi AR}}$$

It should be noted that when designing the actual tail planform, any changes to the planform which decrease the lift-curve slope will need to be countered by increasing the tail area.

Figure 2 shows the large impact that including the propeller planform lifting effect has on the results. At a tail arm of 8.5m, which is the value from the Makani tops-down estimate, the difference is almost 1.0 m² of area or about a 13% larger tail area. Likewise, Figure 3 shows how a variation from ±2% in the desired static margin can have an impact of roughly ±0.7 m² (±7.5%) in tail area. Lastly, the Makani tops-down estimate of a horizontal tail area of 8.97 m² for a tail arm of 8.5 m is very close to the value obtained from Figure 3 for a static margin of 10% and the same tail arm. However, this does not account for any differences in tail planform or fuselage boom elasticity.

Figure 4 and Figure 5 show the tail area size for a flexible boom. The equivalent stiffness, EI, is on the x-axis while the different curves represent different tail arm lengths. In general, the two plots show similar results with the only difference being that Figure 4 is for a desired static margin of 10% while Figure 5 is for 12%. The key point to take away from these charts is the point of diminishing returns for an increasingly stiff boom or where the curves start to level off. This point occurs for stiffness values roughly between 1.0E+07 and 2.0E+07 N-m². To compare these stiffness values against the M600, reference [3] provides validation data which suggest the EI values are within this range.

$$EI = \left(\frac{P}{d}\right) \left(\frac{l^3}{3}\right) = k \left(\frac{l^3}{3}\right)$$

Table 1 Stiffness of the M600 fuselage boom, results from Reference [3]

Test	k_y [N/mm]	EI [N-m ²]
HALB	87.5	0.965E+07
LALB	103.5	1.142E+07

REPORT: TLG-MAK-004		REVISION: IR	PAGE 3-5
AIRCRAFT: BigM600		REV DATE: 01/30/2020	PROPRIETARY
TITLE: BigM600 Tail Sizing White Paper		CUSTOMER: Makani Technologies, LLC	

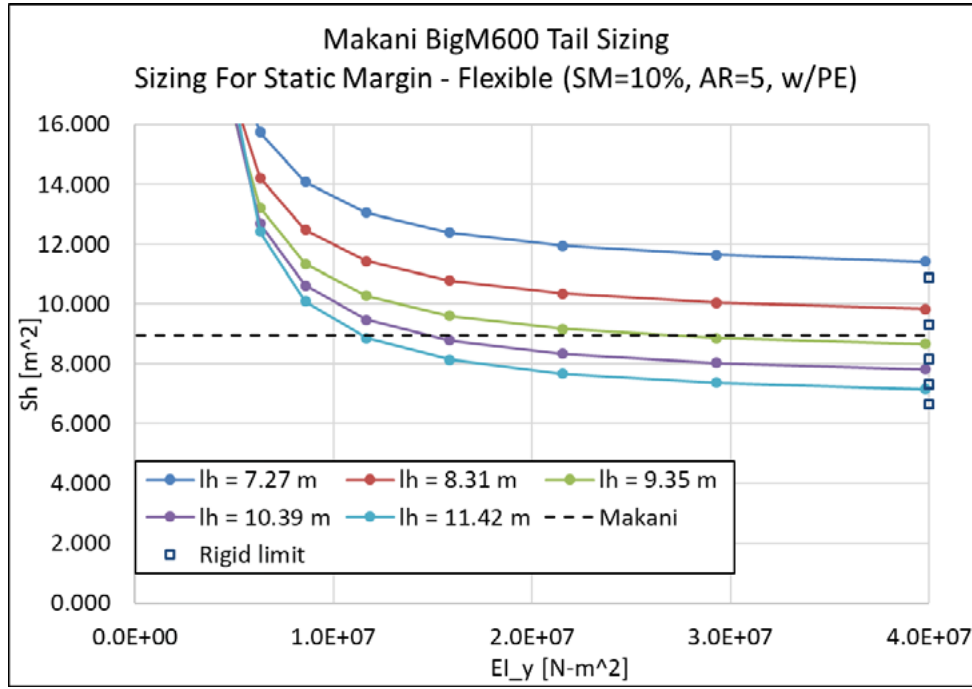


Figure 4 The impact of the fuselage boom stiffness on the horizontal tail area, sizing for stability (S.M. = 10%)

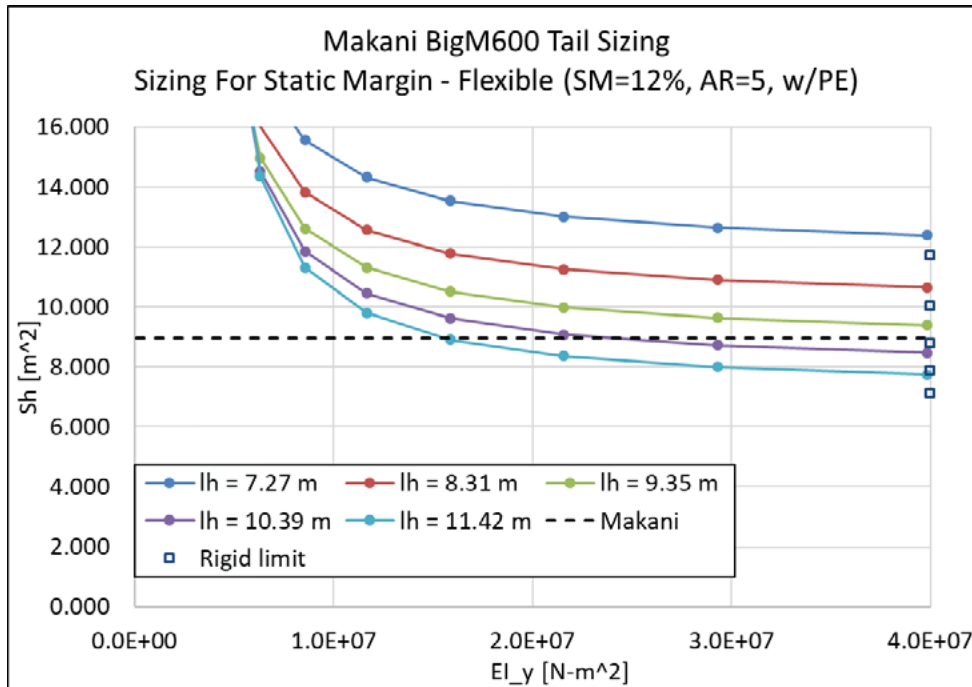


Figure 5 The impact of the fuselage boom stiffness on the horizontal tail area, sizing for stability (S.M. = 12%)

REPORT: TLG-MAK-004		REVISION: IR	PAGE 3-6
AIRCRAFT: BigM600		REV DATE: 01/30/2020	PROPRIETARY
TITLE: BigM600 Tail Sizing White Paper		CUSTOMER: Makani Technologies, LLC	

Looking at Figure 4 and Figure 5 for a fixed stiffness value, one can also see the inversely proportional relationship between tail area and tail arm that could be seen in the rigid results. Put another way, there are diminishing returns in area for increasingly long tail arms. This, of course, says nothing of the added difficulty of maintaining stiffness for longer fuselage boom lengths.

3.4 Sizing for Trim

The horizontal tail and vertical tail have very different trim requirements on the M600 kite. According to discussions with Makani engineers and recordings of flight test data, the elevator is not very active in flight while the rudder is often varying between maximum deflections in either direction. The sizing routine and FBL data for the BigM600 kite also exhibits this same behavior.

Figure 6 shows the rigid boom results for 3 different values of the elevator chord fraction. Figure 7 shows results for a flexible boom with an elevator chord fraction of 25%, which was chosen to result in the largest tail areas. For these results, the maximum elevator deflection was enforced at $\pm 10^\circ$. As the results show, the trim requirements are much smaller than the stability requirements for the horizontal tail.

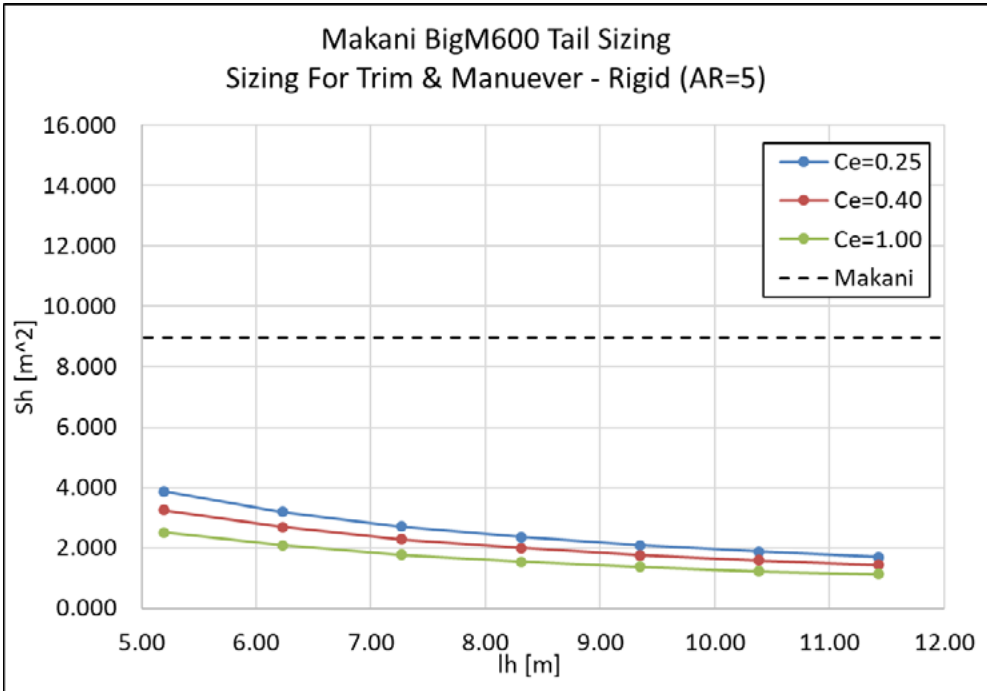


Figure 6 The impact of the elevator chord fraction on the horizontal tail area, sizing for trim

REPORT: TLG-MAK-004		REVISION: IR	PAGE 3-7
AIRCRAFT: BigM600		REV DATE: 01/30/2020	PROPRIETARY
TITLE: BigM600 Tail Sizing White Paper		CUSTOMER: Makani Technologies, LLC	

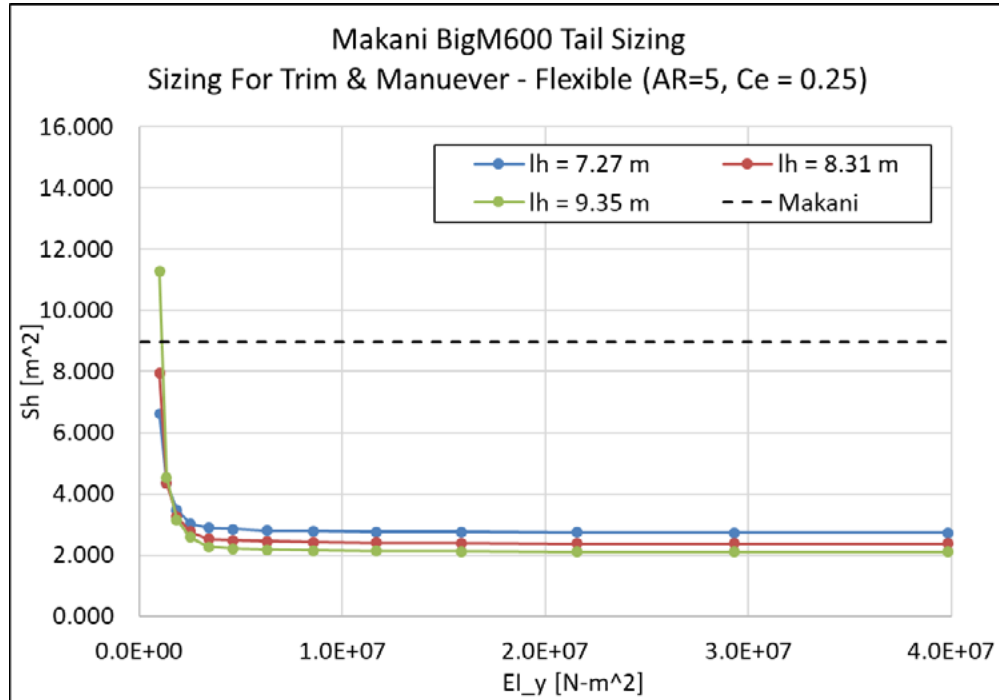


Figure 7 The impact of the fuselage boom stiffness on the horizontal tail area, sizing for trim

For the vertical tail, the story is very different. One of the contributors to the large directional trim requirements of the vertical tail is that a crosswind energy kite is constantly flying at significant yaw rates. Flying at significant yaw rates induces additional sideslip at the tail as described in section 2.2. Importantly, this additional sideslip will be roughly a linear function of the tail arm length for the range of yaw rates shown in the data. The challenge this poses is that it requires the rudder to fight against this additional sideslip at the tail, in addition to meeting the trim requirements. Further, if the choice is made to retain kite symmetry then you cannot set an incidence angle for the vertical tail in attempt to offset this issue, unless one chooses to use an all-moving vertical tail surface.

Figure 8 shows the tail sizing requirements due to trim for the vertical tail for 3 different rudder chord fractions. Additionally, the gray-dashed line indicates the minimum tail area necessary to meet the maximum side force coefficient constraint. This constraint line was added to show that even if a certain rudder size could meet the trim requirements with a smaller area, it would still need to be sized up to keep the side force coefficient below the threshold. The effect of the yaw-rate induced sideslip at the tail can be seen in how the curves start to flatten out, and even turn upwards, at the largest tail lengths. We note that the rudder deflection limits were set to $\pm 20^\circ$ for these results. A typical value for this range is $\pm 15^\circ$, but it was expanded by 5° to prevent over-sizing the vertical tail surface.

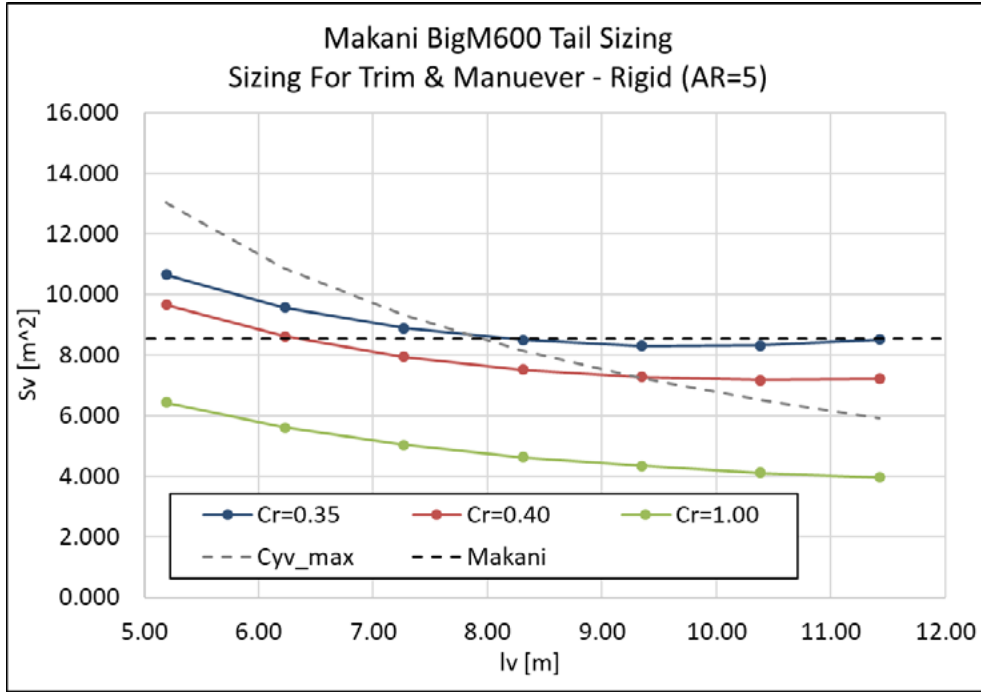


Figure 8 The impact of the rudder chord fraction on the vertical tail area, sizing for trim

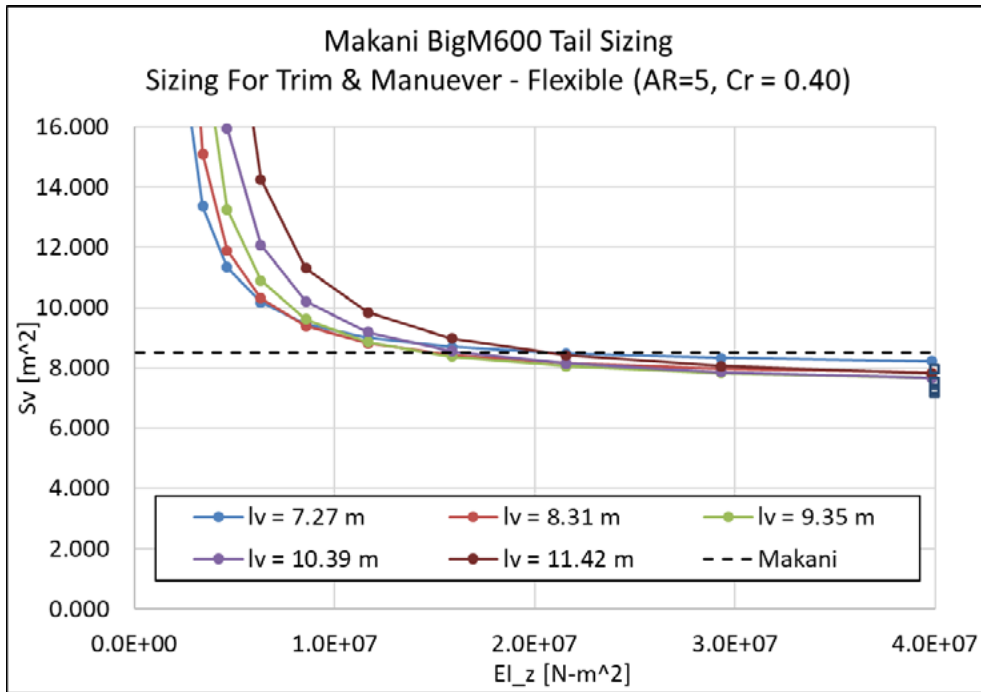


Figure 9 The impact of the fuselage boom stiffness on the vertical tail area, sizing for trim

REPORT: TLG-MAK-004		REVISION: IR	PAGE 3-9
AIRCRAFT: BigM600		REV DATE: 01/30/2020	PROPRIETARY
TITLE: BigM600 Tail Sizing White Paper		CUSTOMER: Makani Technologies, LLC	

Figure 9 shows the vertical tail area as a function of tail stiffness for a 40% rudder chord fraction. Similar to the rigid results, the tail arm length is not a big driver of the final tail area due to the yaw-rate of the kite. However, the stiffness does play an important role, especially for larger tail arms. Similar to the static margin sizing results for the horizontal tail, Figure 4, the point of diminishing returns for stiffness is roughly between 1.0E+07 and 2.0E+07 N-m².

3.5 Summary

The final output from the initial tail sizing calculations are the charts themselves, which should be used together with a weight and cost model to find an optimal tail size across all disciplines. That said, we have selected a baseline tail size to serve as a starting point and have listed the details in Table 2. The key charts for sizing the horizontal tail are Figure 4 and Figure 5, which summarize the sizing necessary for a desired static margin with an elastic boom. A tail arm of 9.5 m shows balances the benefits of a longer tail arm before seeing the diminishing returns of a longer arm. This is slightly longer than the Makani tops-down estimate. Additionally, we choose a target stiffness of EI = 2.0E+07 N-m² to get the most benefit of stiffening the tail before the area curves plateau. Lastly, we selected a horizontal tail area of 10.0 m² based on the 12% static margin chart. This provides some buffer in the tail sizing beyond the target 10% static margin stated in the kite specification (Ref [4]). To re-iterate, any final decisions on tail arm length, stiffness and tail area would require, at the least, a detailed weights model to allow for study of the multi-disciplinary trade-offs. Lastly, we can convert the preliminary sizing of the horizontal tail into a target $C_{L,\alpha}^h$ which must be achieved by a resulting planform, when normalized by the wing area. This value is listed in the last column of Table 2.

$$C_{L,\alpha}^h = C_{N,ih}(S_h/S_w) = 0.078 (10.0 \text{ m}^2 / 54.0 \text{ m}^2) = 0.0145$$

Table 2 Summary of outputs from the tail sizing calculations

	$C_{N,ih}, C_{N,iv}$	S_i/S_w	l_h/C_{ref}	l_v/b_{ref}	EI [N-m ²]	i_h [deg]	$C_{L,\alpha}^h, C_{Y,\beta}^v$
Horizontal	0.078	0.185	4.574	N/A	2.0E+07	5.0	0.0145
Vertical	0.078	0.157	N/A	0.365	2.0E+07	N/A	-0.0123

REPORT: TLG-MAK-004		REVISION: IR	PAGE 3-10
AIRCRAFT: BigM600		REV DATE: 01/30/2020	PROPRIETARY
TITLE: BigM600 Tail Sizing White Paper		CUSTOMER: Makani Technologies, LLC	

Likewise, a similar baseline value was created for the vertical tail using the result in Figure 9. The tail arm and fuselage boom stiffness values are carried over from the horizontal tail and so an area of 8.5 m² is selected from the chart. This value is almost identical to the Makani tops-down estimate and based on the charts provides some margin, which should be useful given some of the uncertainties around the vertical tail. The resulting target $C_{Y,\beta}^v$ value is calculated below.

$$C_{Y,\beta}^v = -C_{N,iv}(S_v/S_w) = -0.078 (8.5 \text{ m}^2/54.0 \text{ m}^2) = -0.0123$$

To go along with the tail sizing charts and baseline sizes, 3 different tail planforms were created to support 4 possible empennage configurations. The planform for the “V” tail and the inverted-“V” tail are the same, hence the difference between the number of planforms and the number of tail configurations. Additionally, a traditional low-T tail configuration has been tracked for use with the Makani CSim tool. For all of the planforms, the decision was made to use a low aspect ratio in order to minimize bending moments while also providing the most structural depth to react the moments. While low-aspect ratio surfaces will result in reduced lift-curve slopes, past TLG projects on general aviation aircraft has provided data which shows that tail planforms with lower aspect ratios, within the range of 2.5-5.0, tend to weigh less. For the 3 configurations with a “V”-shaped tail, the aspect ratio is a per-side, or geometric, aspect ratio and hence why the values tend to be the smallest. For the cruciform, the aspect ratio has its traditional definition and the aspect ratio is slightly larger since the size of the moment arm is only the semi-span. To reiterate, it should be expected that some iteration on these configurations would be required once a full weight and cost model have been developed.

Table 3 Tail planforms configurations which meet the tail sizing requirements

	Area [m ²]	Aspect Ratio, AR	Taper Ratio, λ	i_h [deg]	Dihedral [deg]
“V” (each side)	13.20	2.5	0.6	5.0	50.0
Dual-boom (each side)	13.50	3.0	1.0	5.0	45.0
Cruciform (each surface)	12.60	3.5	0.6	5.0	N/A
“Low-T” (stab)	12.60	3.5	0.6	5.0	N/A
“Low-T” (fin)	10.25	2.5	0.6	N/A	N/A

Pictures of all of the possible configurations are shown below.

REPORT: TLG-MAK-004		REVISION: IR	PAGE 3-11
AIRCRAFT: BigM600		REV DATE: 01/30/2020	PROPRIETARY
TITLE: BigM600 Tail Sizing White Paper		CUSTOMER: Makani Technologies, LLC	

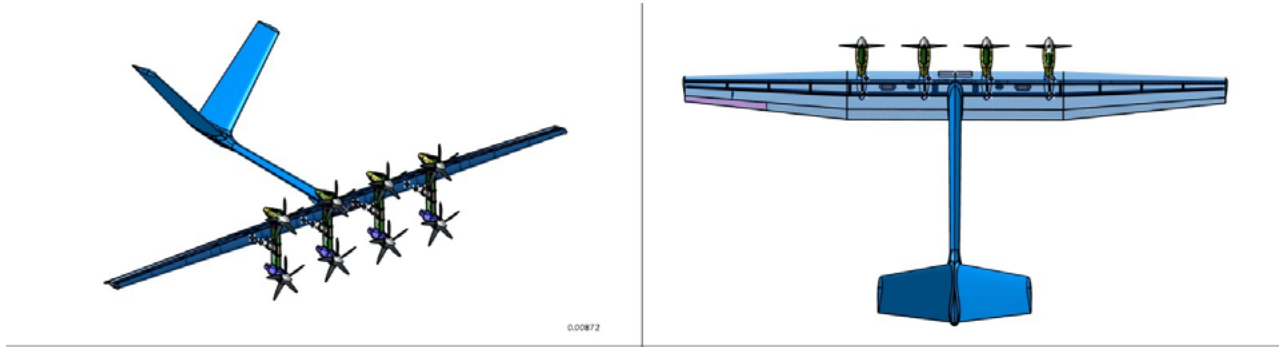


Figure 10 CAD layout of the “V” tail configuration

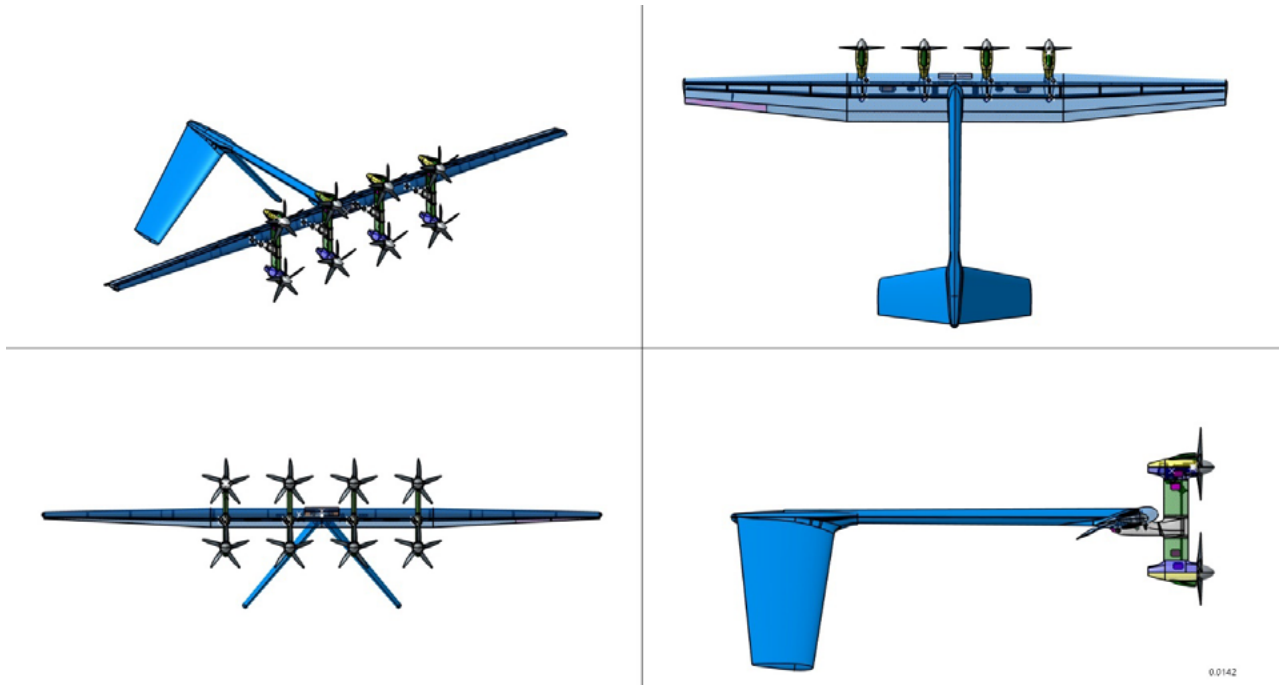


Figure 11 CAD layout of the inverted-“V” tail configuration

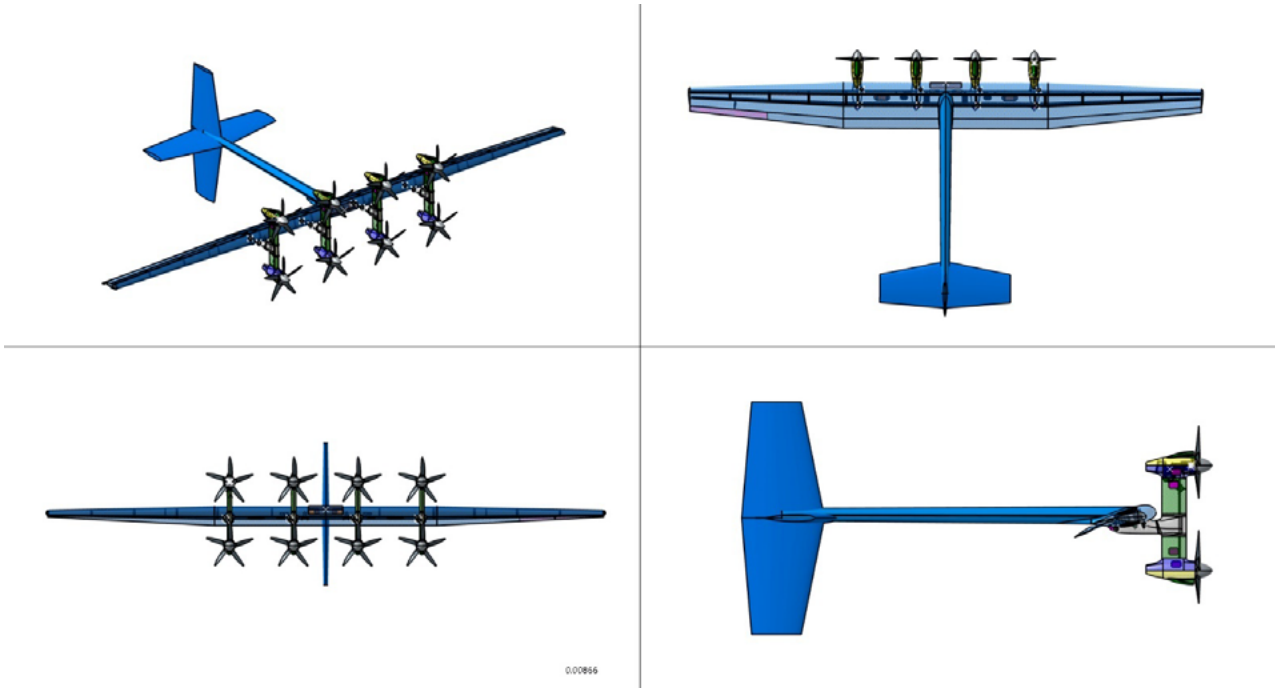


Figure 12 CAD layout of the cruciform tail configuration

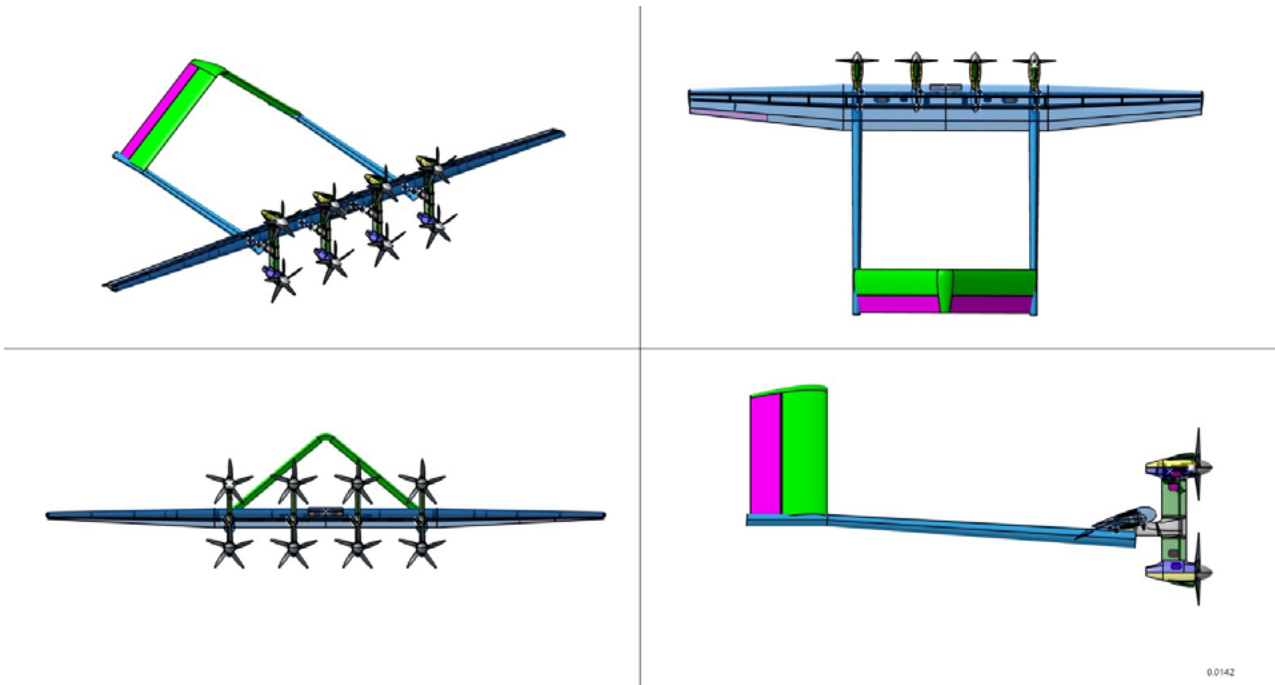


Figure 13 CAD layout of the dual-boom configuration

REPORT: TLG-MAK-004		REVISION: IR	PAGE 4-1
AIRCRAFT: BigM600		REV DATE: 01/30/2020	PROPRIETARY
TITLE: BigM600 Tail Sizing White Paper		CUSTOMER: Makani Technologies, LLC	

4.0 Lateral-Directional Static Stability

The initial tail sizing exercise determined the tail areas and tail arms necessary for static margin and trimability of the kite. This section examines the static stability of the kite for different empennage and wing configurations. Specifically, this analysis is used to determine the interplay between terms such as rudder roll and adverse yaw as well as understanding the natural and apparent dihedral effect for different configurations. The stability and control impact of different configurations would then need to be weighed against measures of both weight and cost to determine a final configuration.

4.1 Governing Equations

For our governing equations, we will adopt a similar grouping for forces and moments as the FBL tool, as well as using the same aircraft reference point. This allows us to directly extract the non-aero forces and moments from FBL to use on the right-hand-side of our force and moment balance equations. The key groupings for the lateral-directional static stability equations are tether, inertial and gravity forces. The aero forces will be provided by a linearized aero model, with data generated from vortex-lattice models of the different configurations. An example of the force balance is shown below for the side force coefficient C_Y .

$$C_Y^{aero} + C_Y^{tether} + C_Y^{inertia} + C_Y^{gravity} = 0$$

$$C_Y^{aero} = C_{Y0} + C_{Y,\beta}\beta + C_{Y,\delta_R}\delta_R + C_{Y,\delta_A}\delta_A + C_{Y,\hat{p}}\Delta\hat{p} + C_{Y,\hat{q}}\Delta\hat{q} + C_{Y,\hat{r}}\Delta\hat{r}$$

$$C_{Y,\beta}\beta + C_{Y,\delta_R}\delta_R + C_{Y,\delta_A}\delta_A = -C_Y^{tether} - C_Y^{inertia} - C_Y^{gravity} - C_{Y0} - C_{Y,\hat{p}}\Delta\hat{p} - C_{Y,\hat{q}}\Delta\hat{q} - C_{Y,\hat{r}}\Delta\hat{r}$$

Combining the side force balance with the yaw and roll moment balance equations gives the following system of equations.

$$\begin{bmatrix} C_{Y,\beta} & C_{Y,\delta_R} & C_{Y,\delta_A} \\ C_{n,\beta} & C_{n,\delta_R} & C_{n,\delta_A} \\ C_{l,\beta} & C_{l,\delta_R} & C_{l,\delta_A} \end{bmatrix} \begin{bmatrix} \beta \\ \delta_R \\ \delta_A \end{bmatrix} =$$

$$- \begin{bmatrix} C_Y \\ C_n \\ C_l \end{bmatrix}^{tether} - \begin{bmatrix} C_Y \\ C_n \\ C_l \end{bmatrix}^{inertia} - \begin{bmatrix} C_Y \\ C_n \\ C_l \end{bmatrix}^{gravity} - \begin{bmatrix} C_{Y0} \\ C_{n0} \\ C_{l0} \end{bmatrix} - \begin{bmatrix} C_{Y,\hat{p}} \\ C_{n,\hat{p}} \\ C_{l,\hat{p}} \end{bmatrix} \Delta\hat{p} - \begin{bmatrix} C_{Y,\hat{q}} \\ C_{n,\hat{q}} \\ C_{l,\hat{q}} \end{bmatrix} \Delta\hat{q} - \begin{bmatrix} C_{Y,\hat{r}} \\ C_{n,\hat{r}} \\ C_{l,\hat{r}} \end{bmatrix} \Delta\hat{r}$$

REPORT: TLG-MAK-004		REVISION: IR	PAGE 4-2
AIRCRAFT: BigM600		REV DATE: 01/30/2020	PROPRIETARY
TITLE: BigM600 Tail Sizing White Paper		CUSTOMER: Makani Technologies, LLC	

We note here that the FBL tool assumes that control surfaces produce no control forces and no cross moments. This assumption would reduce the LHS to be a lower diagonal matrix.

$$\begin{bmatrix} C_{Y,\beta} & 0 & 0 \\ C_{n,\beta} & C_{n,\delta_R} & 0 \\ C_{l,\beta} & 0 & C_{l,\delta_A} \end{bmatrix} \begin{bmatrix} \beta \\ \delta_R \\ \delta_A \end{bmatrix}$$

At this point, the model above does not include stiffness terms for the tether forces & moments due to perturbations in the kite yaw angle. However, even without those terms the equations should be useful for comparisons between configurations due to the presence of control forces and cross moments, as will be shown in section 4.2. Returning to the tether stiffness terms, according to reference [2] the tether forces can be expressed in body coordinates by using the kite-to-tether Euler angles. This transformation is uniquely defined by 2 angles, tether pitch and tether roll. A third angle is unnecessary since rotating the tether about its own axis leaves the tether force vector unchanged. The effect of a perturbation in the kite yaw angle would be a change in the tether pitch and roll angles, as well as a change in the moment arm to the tether knot. The moment arm is a function of two fixed vectors, kite origin to bridle hard point and kite origin to center of gravity, as well as a vector depending on kite attitude, bridle hard point to bridle knot. The latter is a function of the tether pitch angle only. An assumption of using this method would be that the tether tension vector remains constant in a fixed ground frame. Further, a perturbation in the kite yaw angle would also result in changes to the components of the gravity and inertial forces/moments in the new kite stability axis. At the current moment, the inclusion of tether stiffness terms has not been validated for use in analysis and thus these notes are added for posterity.

4.2 Validation using FBL aero

Before we use this model, we performed some basic validations against the FBL data set. The validations allow us to perform basic checks, such as that we have included all of the relevant terms in our aerodynamic model as well as that there are no sign errors in the equations. The first step was to extract linearized aerodynamics from the database which was used as input to FBL (namely “Big_M600_r07c_aero_w_flaps_zero_alpha_beta_Re5e6.json”). The database lists that it was linearized about the rotation rate vector $[\hat{p}, \hat{q}, \hat{r}] = [0.0, 0.0018, -0.14267]$. The results are shown below in Table 4 and are linearized about $[\alpha, \beta] = [0.0, 0.0]$.

REPORT: TLG-MAK-004		REVISION: IR	PAGE 4-3
AIRCRAFT: BigM600		REV DATE: 01/30/2020	PROPRIETARY
TITLE: BigM600 Tail Sizing White Paper		CUSTOMER: Makani Technologies, LLC	

Table 4 Linearized aerodynamics from database used for FBL tail-sizing exercise

	CX	CY	CZ	Cl	Cm	Cn
CAMBER	-0.1182	-0.0125	-1.8105	-0.0555	-0.2908	0.0033
BETA	0.0007	-0.0208	0.0007	0.0013	0.0004	0.0029
RUDDER	-0.0007	0.0084	0.0000	0.0002	0.0003	-0.0028
AILERON	0.0005	-0.0005	0.0041	0.0066	0.0009	-0.0007
PB/2V	0.0263	-0.0110	-0.1664	-0.5878	-0.0028	-0.1388
QC/2V	-0.9228	0.0046	-11.3834	-0.1040	-22.8005	0.0102
RB/2V	-0.0240	0.3739	0.1001	0.4029	0.0308	-0.1591

Once the aerodynamics were known, different validation tests can be run. The first test restricts the control surfaces to the FBL assumption of no control forces or cross moments, as well as fixing beta to be the value from the FBL data. The results from this test are shown in Figure 14. Note that we have converted the FBL field “flap_aero_coeffs” into flap deflections via scaling by the appropriate derivatives. Overall, the results agree well, and the slight discrepancies could be attributed to the linearization of the aero data. Figure 15 shows a similar comparison but one which no longer fixes the value of beta. This variation proves that the C_y equation is well-posed as well as providing another check of the overall formulation. As in the first validation, there are some slight differences but overall the agreement is good.

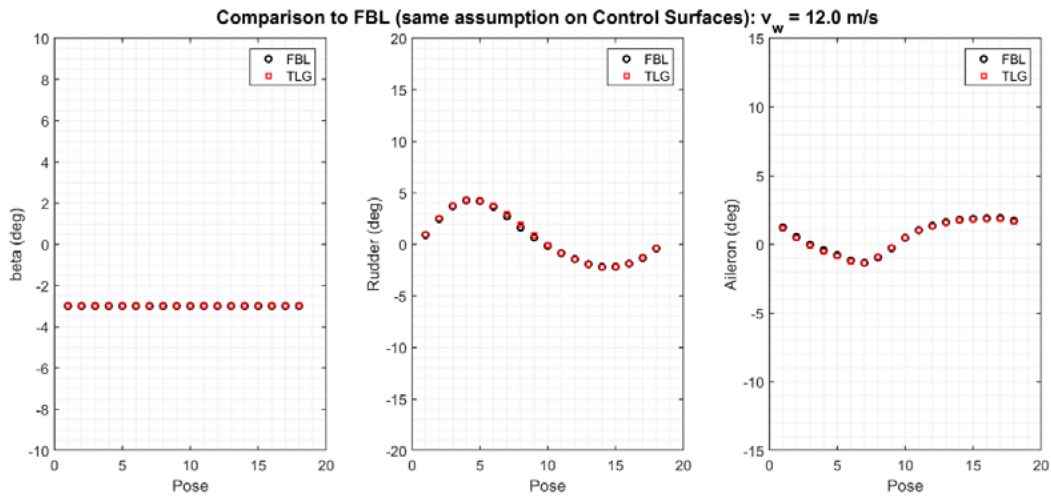


Figure 14 Comparison of lateral-directional trim points against FBL. Here, beta was fixed to the FBL result.

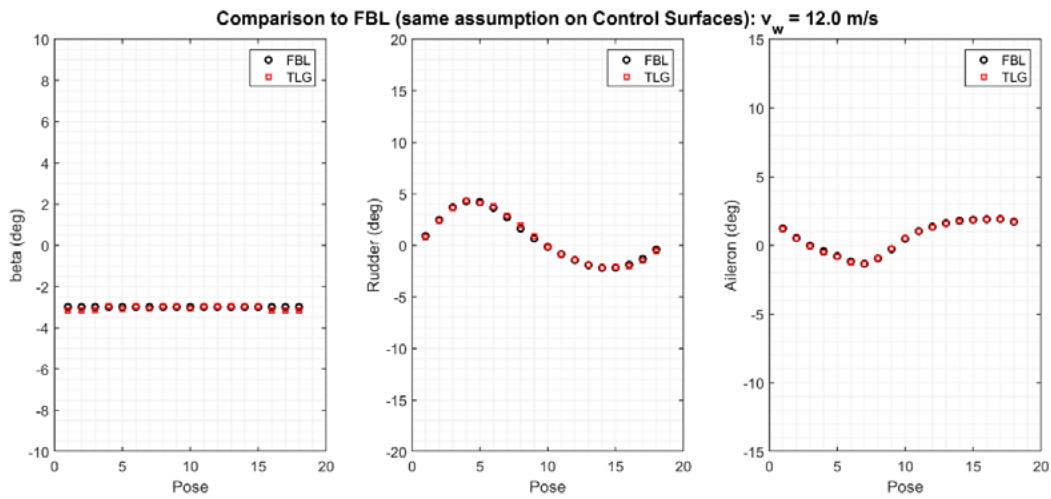


Figure 15 Comparison of lateral-directional trim points against FBL. Here, beta was free to be set by the linear system.

REPORT: TLG-MAK-004		REVISION: IR	PAGE 4-5
AIRCRAFT: BigM600		REV DATE: 01/30/2020	PROPRIETARY
TITLE: BigM600 Tail Sizing White Paper		CUSTOMER: Makani Technologies, LLC	

A next comparison is less of a validation than a study of the effect of including the control forces and cross moments generated by the control surfaces. Figure 16 shows these results and it is particularly interesting to note the coupling between beta and the rudder, which is caused by the inclusion of the C_{Y,δ_R} term. A conclusion from this test is the need for a more detailed review of the control surface deflections after the initial tail sizing, particularly due to the cross-coupling of terms that was not captured initially.

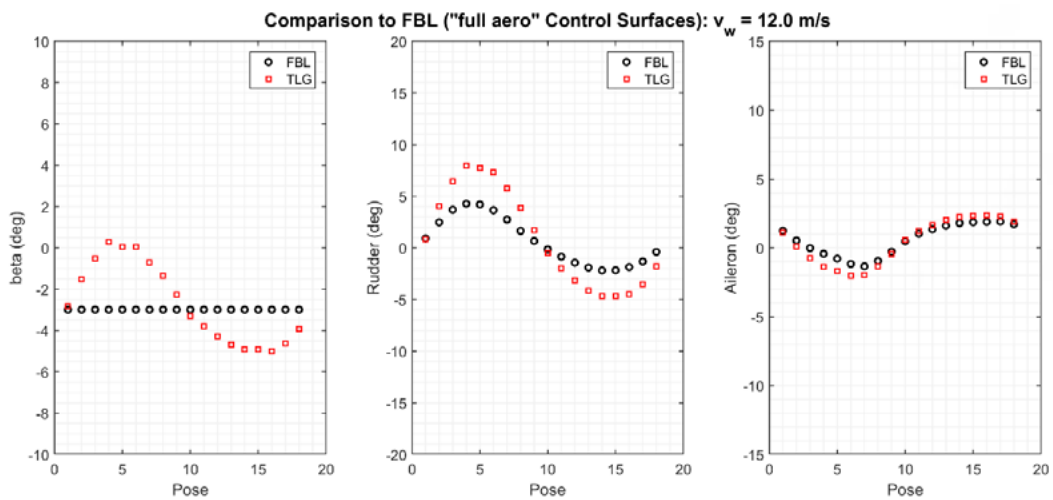


Figure 16 Comparison of lateral-directional trim points against FBL. Here, control surfaces could produce control forces and cross moments.

REPORT: TLG-MAK-004		REVISION: IR	PAGE 4-6
AIRCRAFT: BigM600		REV DATE: 01/30/2020	PROPRIETARY
TITLE: BigM600 Tail Sizing White Paper		CUSTOMER: Makani Technologies, LLC	

4.4 Aerodynamic Models for Configuration Options

A vortex lattice method was developed for each of the configuration options that TLG was exploring. These included empennage configuration options, changes in the wing sweep axis and a single model with aeroelastic wing deflection. The goal of changing the wing sweep axis was to understand any changes to adverse yaw, while including the aeroelastic wing deformation allowed estimation of the dihedral effect. The empennage configuration options are listed below.

- “V” tail
- Inverted-“V” tail
- Dual-boom “V” tail
- Cruciform tail

All of the vortex lattice models shared a number of calibration factors meant to produce more accurate results. These calibrations are listed below.

- Wing lift-curve slope modified from ideal based on MSES results of OctoberKite v1.1 airfoil
- Aileron flap effectiveness modified from ideal based on MSES results for flap deflection of the OctoberKite v1.1 airfoil
- Pylon airfoil lift-curve slope reduced from ideal based on MSES results for a naca0030 airfoil, which is used as a proxy for an eventual aero-strut profile
- Empennage control surfaces corrected for viscous effects based on the flap-chord ratio and data presented in Abbott and von Doenhoff
- Variable dynamic pressure distribution across the wing to approximate what is seen by a crosswind kite

An example of the vortex lattice model used can be seen in Figure 17 below, which shows the “V”-tail configuration. It should be noted that the fuselage boom was not included in any of the vortex lattice models.

REPORT: TLG-MAK-004		REVISION: IR	PAGE 4-7
AIRCRAFT: BigM600		REV DATE: 01/30/2020	PROPRIETARY
TITLE: BigM600 Tail Sizing White Paper		CUSTOMER: Makani Technologies, LLC	

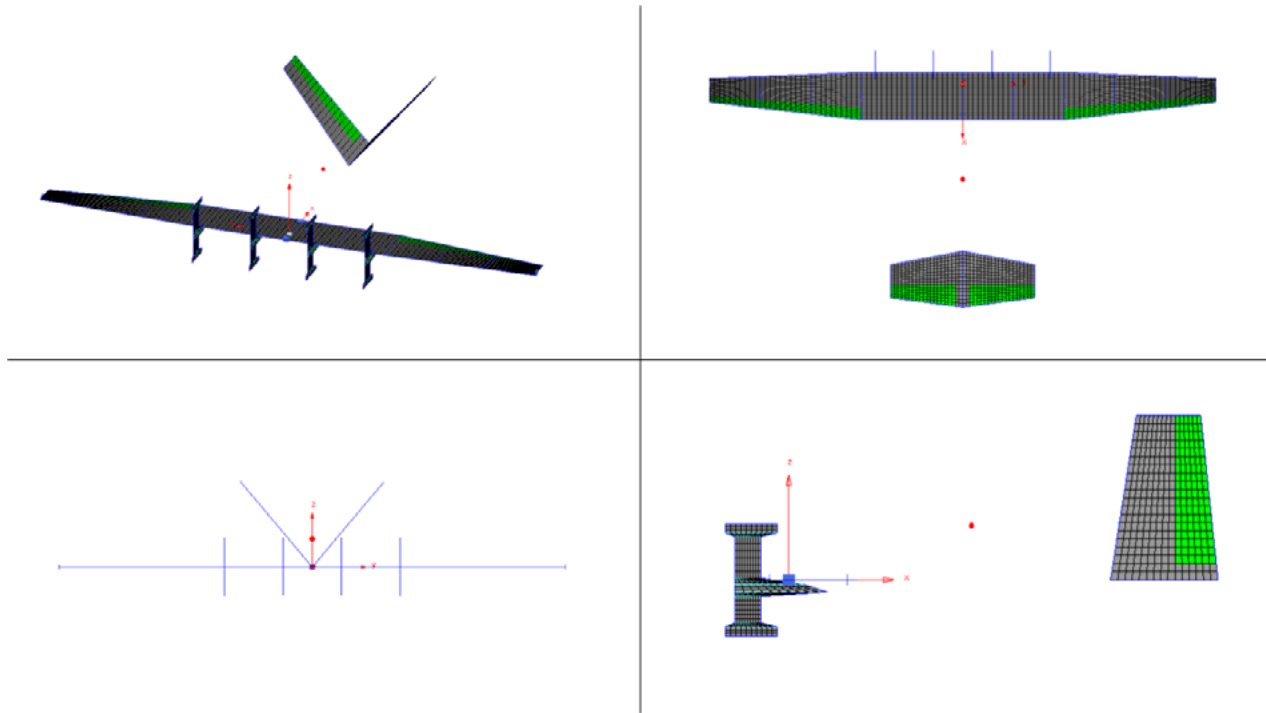


Figure 17 Example of the vortex lattice model used to calculate linear aerodynamics. Example shows the “V” tail configuration.

Each of the configurations listed in Table 3, except the Low-T, have been evaluated using VLM to calculate their stability derivatives. The derivatives were linearized around the point $[\alpha, \beta, \hat{p}, \hat{q}, \hat{r}] = [0.0, 0.0, 0.0, 0.002, -0.143]$ in order to make a more direct comparison to the Makani database used as input to FBL. The results are shown below in Table 5 through Table 8. In the tables, all capital letters are used to distinguish the different coefficients in stability axes and thus “CR” represents the roll coefficient (or C “little-L”) to avoid confusion with “CL” the lift coefficient (or C “big-L”).

REPORT: TLG-MAK-004		REVISION: IR	PAGE 4-8
AIRCRAFT: BigM600		REV DATE: 01/30/2020	PROPRIETARY
TITLE: BigM600 Tail Sizing White Paper		CUSTOMER: Makani Technologies, LLC	

Table 5 Linearized aerodynamics calculated from VLM, "V" tail configuration

	CD	CY	CL	CR	CM	CN
CAMBER	0.0921	-0.0790	1.8674	-0.0128	-0.3169	0.0325
BETA	-0.0005	-0.0196	0.0001	-0.0019	-0.0004	0.0041
RUDDER	-0.0010	0.0112	0.0000	0.0017	-0.0012	-0.0046
AILERON	-0.0005	-0.0011	-0.0056	0.0081	0.0012	-0.0006
PB/2V	0.0616	-0.0739	0.4289	-0.6557	0.0166	0.1088
QC/2V	1.9075	0.0448	16.0683	-0.1567	-44.2221	0.0541
RB/2V	-0.0513	0.5527	0.0086	0.0879	-0.0513	-0.2274

Table 6 Linearized aerodynamics calculated from VLM, inverted-"V" tail configuration

	CD	CY	CL	CR	CM	CN
CAMBER	0.0921	-0.0791	1.8672	0.0120	-0.3318	0.0283
BETA	-0.0005	-0.0196	0.0001	0.0018	0.0004	0.0037
RUDDER	-0.0010	0.0112	0.0000	-0.0017	0.0011	-0.0040
AILERON	-0.0005	0.0011	-0.0057	0.0081	0.0013	-0.0014
PB/2V	0.0162	0.0651	0.4322	-0.6559	0.0058	0.0572
QC/2V	1.9056	-0.0471	16.0696	-0.1570	-45.9115	-0.0135
RB/2V	-0.0508	0.5526	0.0152	-0.0852	0.0442	-0.1977

REPORT: TLG-MAK-004		REVISION: IR	PAGE 4-9
AIRCRAFT: BigM600		REV DATE: 01/30/2020	PROPRIETARY
TITLE: BigM600 Tail Sizing White Paper		CUSTOMER: Makani Technologies, LLC	

Table 7 Linearized aerodynamics calculated from VLM, dual-boom tail configuration

	CD	CY	CL	CR	CM	CN
CAMBER	0.0891	-0.0785	1.8411	0.0007	-0.2048	0.0318
BETA	-0.0005	-0.0192	0.0000	0.0000	-0.0004	0.0040
RUDDER	-0.0010	0.0115	0.0000	-0.0001	-0.0011	-0.0045
AILERON	-0.0006	-0.0016	-0.0059	0.0084	0.0026	-0.0004
PB/2V	0.0451	0.0747	0.4331	-0.6481	-0.0773	0.0482
QC/2V	1.2833	0.0140	18.0053	-0.1637	-52.7126	-0.0351
RB/2V	-0.0484	0.5490	-0.0014	-0.0066	-0.0489	-0.2222

Table 8 Linearized aerodynamics calculated from VLM, cruciform tail configuration

	CD	CY	CL	CR	CM	CN
CAMBER	0.0780	-0.0934	1.7864	-0.0004	0.0266	0.0357
BETA	-0.0008	-0.0204	0.0000	-0.0001	-0.0002	0.0042
RUDDER	-0.0008	0.0103	0.0000	0.0000	0.0000	-0.0039
AILERON	-0.0004	0.0000	-0.0058	0.0083	0.0024	-0.0011
PB/2V	0.0316	0.0012	0.4636	-0.6494	-0.1547	0.0718
QC/2V	-5.3030	-0.0011	14.4235	-0.1640	-37.6251	0.0163
RB/2V	-0.0483	0.6564	0.0034	0.0003	-0.0157	-0.2503

REPORT: TLG-MAK-004		REVISION: IR	PAGE 4-10
AIRCRAFT: BigM600		REV DATE: 01/30/2020	PROPRIETARY
TITLE: BigM600 Tail Sizing White Paper		CUSTOMER: Makani Technologies, LLC	

We can use the stability derivatives to look at the natural and apparent dihedral effect. The apparent dihedral is defined below and considers the adverse (or proverse) roll from the rudder as well as how much rudder is needed for a given sideslip angle.

$$(C_{l,\beta})_{app} = (C_{l,\beta})_{nat} - C_{l,\delta_R} \left(\frac{\partial \delta_R}{\partial \beta} \right) = (C_{l,\beta})_{nat} - C_{l,\delta_R} \left(\frac{C_{n,\beta}}{C_{n,\delta_R}} \right)$$

The results for the 4 configurations are summarized below in Figure 18. The figure shows that the upward “V” tail has the most natural dihedral effect, while the inverted-“V” tail has almost equal and opposite anhedral effect. Surprisingly, the dual-boom configuration, which also features an inverted “V” arrangement, is essentially neutral in terms of dihedral effect. The difference with the inverted-“V” is likely the different vertical positions of the two orientations. The apparent dihedral maintains the same trends but reduces the magnitude when compared against the natural dihedral. This is because the adverse roll of the upward “V”-tail counteracts a portion of the natural dihedral of the arrangement. Likewise, the proverse roll of the inverted-“V” helps to reduce the strong anhedral effect, but not enough to remove the anhedral effect entirely. The finding that the inverted-“V” has natural anhedral effect is a strong factor for removing it from future consideration. Lastly, a VLM model which includes the wing deflections under 250 kN of tether tension was used to calculate the deflected wing contribution to the dihedral effect. This contribution is added to the apparent dihedral and is plotted as the far right grouping below.

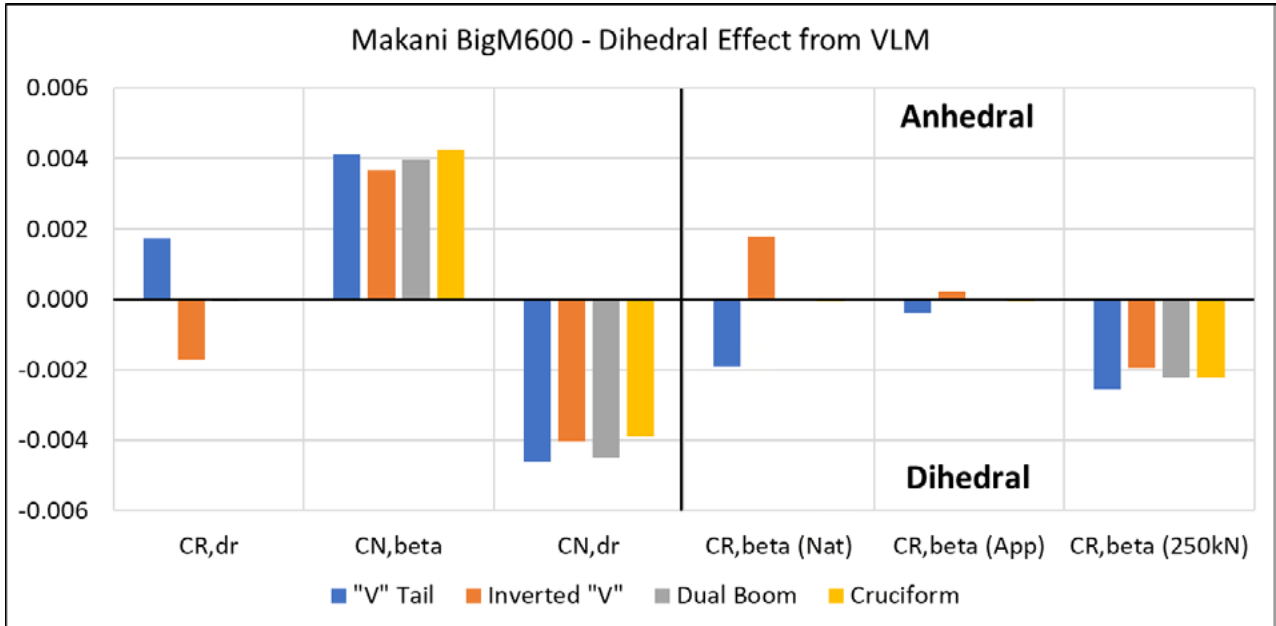


Figure 18 Summary of the dihedral effect for the 4 empennage configurations examined

REPORT: TLG-MAK-004		REVISION: IR	PAGE 4-11
AIRCRAFT: BigM600		REV DATE: 01/30/2020	PROPRIETARY
TITLE: BigM600 Tail Sizing White Paper		CUSTOMER: Makani Technologies, LLC	

Future work would use the framework from section 4.1 to evaluate the configuration options against one another. Additionally, the framework would allow for what-if analysis whereby the input linearized aerodynamics is varied in order to better understand the sensitivity of control surface deflections to the different stability derivatives, specifically as it pertains to crosswind kites.



Airfoil Design for the October Kite - Feasibility Studies

Report: TLG-MAK-003

For: Trevor Orr, Makani Technologies, LLC

Revision: 01

Current Release Date: 11/18/2019

REPORT: TLG-MAK-003		REVISION: 01	PAGE i
AIRCRAFT: October Kite		REV DATE: 11/18/2019	PROPRIETARY
TITLE: Airfoil Design for the October Kite – Feasibility Studies		CUSTOMER: Makani Technologies, LLC	

Table of Contents

Table of Contents..... i

List of Figures ii

List of Tables iv

References v

Revision Page vi

1.0 Introduction 1-1

2.0 Analysis Methods 2-1

 2.1 2D Multi-element Airfoil Analysis - MSES 2-1

3.0 Airfoil design 3-1

 3.1 Planform Twist Distribution 3-3

 3.2 Leading-Edge Design 3-5

 3.3 Flap Design 3-10

 3.3.1 Nominal Flap Deflection Study 3-13

 3.4 Section Performance 3-18

4.0 Summary 4-1

REPORT: TLG-MAK-003		REVISION: 01	PAGE ii
AIRCRAFT: October Kite		REV DATE: 11/18/2019	PROPRIETARY
TITLE: Airfoil Design for the October Kite – Feasibility Studies		CUSTOMER: Makani Technologies, LLC	

List of Figures

Figure 1 Upper and lower bounds of the design section lift coefficients for the October Kite planform.....	3-2
Figure 2 Makani nomenclature used for the 2D lift curve.....	3-3
Figure 3 VLM solution for $\alpha = 0$ deg showing pressure difference across planform – steady level flight.....	3-4
Figure 4 Comparison of the bounding range of spanwise lift coefficients to the results of the VLM model which neglects the yaw-rate term.....	3-5
Figure 5 Leading-edge design process - seed and modified airfoils.....	3-7
Figure 6 Leading-edge design process – seed and modified pressure coefficient profiles.....	3-7
Figure 7 Integration of spar box constraint into leading-edge design.....	3-8
Figure 8 Skin friction coefficient on the suction surface – 008613 section from M600.....	3-9
Figure 9 Skin friction coefficient on the suction surface – new design section.....	3-9
Figure 10 M600 energy kite data used to inform the choice of flap chord ratio to achieve the actuated section lift metric.....	3-11
Figure 11 Symmetric flap unit airfoil (blue) with naca0018 (dashed black) shown for reference.....	3-12
Figure 12 Sections used for the nominal flap deflection study plotted with chord line along the x-axis.....	3-13
Figure 13 2D section raw endurance parameter from nominal flap deflection study – Free transition.....	3-15
Figure 14 2D section trimmed endurance parameter from nominal flap deflection study – Free transition.....	3-16
Figure 15 2D section raw endurance parameter including fixed tether drag from nominal flap deflection study – Free transition.....	3-16
Figure 16 2D section raw endurance parameter from nominal flap deflection study –5% fixed transition.....	3-17
Figure 17 2D section trimmed endurance parameter from nominal flap deflection study – 5% fixed transition.....	3-17
Figure 18 2D section raw endurance parameter including fixed tether drag from nominal flap deflection study – 5% fixed transition.....	3-18
Figure 19 Geometry for OctKite v1.1 airfoil.....	3-19
Figure 20 Comparison of pressure profiles for the OctKite v1.1 section and the center section of the Guppy (008613) – $C_l = 2.0$	3-19
Figure 21 OctKite v1.1 section with free and 5% fixed transition – C_l vs α	3-20
Figure 22 OctKite v1.1 section with free and 5% fixed transition – C_l vs C_d	3-21
Figure 23 OctKite v1.1 section with free and 5% fixed transition – C_m vs α	3-21
Figure 24 OctKite v1.1 section with free and 5% fixed transition – C_l vs C_l/C_d	3-22
Figure 25 OctKite v1.1 section with free and 5% fixed transition – C_l vs $C_l^{(1.5)}/C_d$	3-22

REPORT: TLG-MAK-003		REVISION: 01	PAGE iii
AIRCRAFT: October Kite		REV DATE: 11/18/2019	PROPRIETARY
TITLE: Airfoil Design for the October Kite – Feasibility Studies		CUSTOMER: Makani Technologies, LLC	

Figure 26 OctKite v1.1 section with free transition only – C_l vs transition location 3-23

Figure 27 OctKite v1.1 section flap effectiveness for 5% fixed transition – C_l vs alpha 3-24

Figure 28 OctKite v1.1 section flap effectiveness for free transition – C_l vs alpha 3-24

Figure 29 OctKite v1.1 section flap effectiveness for 5% fixed transition – $\Delta C_l/\delta$ vs alpha 3-25

Figure 30 OctKite v1.1 section flap effectiveness for free transition – $\Delta C_l/\delta$ vs alpha 3-25

Figure 31 CAD model of the OctKite v1.1 wing with key design features highlighted 4-1

REPORT: TLG-MAK-003		REVISION: 01	PAGE iv
AIRCRAFT: October Kite		REV DATE: 11/18/2019	PROPRIETARY
TITLE: Airfoil Design for the October Kite – Feasibility Studies		CUSTOMER: Makani Technologies, LLC	

List of Tables

Table 1 October Kite planform	3-1
Table 2 Operating conditions for the airfoil sections	3-2
Table 3 Key 2D design points for the center section based on 3D kite operating conditions.....	3-3
Table 4 Values of gap and overlap from M600 sections	3-12

REPORT: TLG-MAK-003		REVISION: 01	PAGE v
AIRCRAFT: October Kite		REV DATE: 11/18/2019	PROPRIETARY
TITLE: Airfoil Design for the October Kite – Feasibility Studies		CUSTOMER: Makani Technologies, LLC	

References

- 1 T. Orr, “October Kite Airfoil Design: Stage 1 Data”, Revision 4, October 2019
- 2 M. Drela, “A User’s Guide to MSES 3.05”, MIT Department of Aeronautics and Astronautics, July 2007
- 3 P. Burns and A. McComas, “Aerodynamic Design for Increased Roll Authority on the M600 Energy Kite,” TLG-MAK-002, Revision 02, September 2019

REPORT: TLG-MAK-003		REVISION: 01	PAGE vi
AIRCRAFT: October Kite		REV DATE: 11/18/2019	PROPRIETARY
TITLE: Airfoil Design for the October Kite – Feasibility Studies		CUSTOMER: Makani Technologies, LLC	

Revision Page

<u>Revision</u>	<u>Date</u>	<u>Description</u>	<u>Approval</u>
IR	10/31/2019	Initial Release	On file at TLG
01	11/18/2019	Updated based on feedback from T. Orr	See Cover Page

REPORT: TLG-MAK-003		REVISION: 01	PAGE 1-1
AIRCRAFT: October Kite		REV DATE: 11/18/2019	PROPRIETARY
TITLE: Airfoil Design for the October Kite – Feasibility Studies		CUSTOMER: Makani Technologies, LLC	

1.0 Introduction

A preliminary airfoil design effort has been performed by TLG Aerospace, LLC (TLG) to help understand the feasibility and roll control of the Makani Technologies, LLC (Makani) October Kite. The airfoil sections are required to meet a number of performance objectives and constraints as outlined by Makani; however, it should be noted that one of the primary drivers of the section design is a surface contamination constraint. This constraint states that all performance metrics must be achievable when forcing the laminar-turbulent transition at 5% of the normalized x-coordinate, $x/c = 0.05$. A full list of performance objectives and constraints is provided in Reference [1], with some of the key drivers for preliminary design copied below.

- For the center section, the linear regime of lift curve must extend from $C_{l,design-min} \leq 0.9$ to $C_{l,design-max} \geq 2.0$.
- An additional 5 degrees of alpha for gust margin must exist before stall on both ends of the curve.
- The drag performance of the section must exceed $C_l/C_d \geq 75$, quantified using a forced transition model
- To ensure adequate roll power, a minimum change in lift with flap deflection of $\partial(C_l)/\partial(\delta) \geq 0.045$ must be achieved over the range $-10^\circ \leq \delta \leq 10^\circ$
- The section must be thick enough to accommodate a spar box centered on the quarter-chord with 2D dimensions of $(\Delta x/c, \Delta y/c) = (0.15, 0.19)$

TLG also imposed the design constraint of no laminar separation bubble formation. This is to minimize the risk of laminar separation from the leading-edge under contaminated conditions. Formation of a laminar separation bubble is predictable with analysis; however, the effect of laminar separation at the leading edge is not readily predicted. This constraint minimizes the risk of an unexpected degradation in performance during service. However, to fully exhaust this risk will require wind tunnel testing at simulated full-scale Reynolds numbers.

The airfoil sections are composed of two elements with a slotted flap for high lift performance. The flap element has a nominal deflection in the deployed position and rotates about a fixed hinge location to provide lateral control. Preliminary design focused on the leading-edge design of the main element as well as the nominal deflection, shape, and position of the flap element. The design of the main element leading-edge was driven by $C_{l,max}$ performance, laminar run robustness and spar constraints while the nominal flap deflection, or aft-camber, was used to optimize performance at the design C_l .

REPORT: TLG-MAK-003		REVISION: 01	PAGE 2-1
AIRCRAFT: October Kite		REV DATE: 11/18/2019	PROPRIETARY
TITLE: Airfoil Design for the October Kite – Feasibility Studies		CUSTOMER: Makani Technologies, LLC	

2.0 Analysis Methods

2.1 2D Multi-element Airfoil Analysis - MSES

A large portion of this work considers the development of 2D sectional aerodynamic coefficients, pressure distributions, and boundary layer properties. The generation of sectional data is performed using the multielement design and analysis tool MSES which is the industry standard for generation of 2D multielement data and is developed by Prof Mark Drela of MIT.

MSES uses a hybrid solution technique which couples an inviscid “outer” solution to a viscous “inner” solution. The outer solution solves Euler’s equations on a 2D grid using either a momentum- or entropy-conserving formulation. For subsonic flows, it is more important to use the entropy-conserving formulation, also called the Full Potential solver, since it conserves total pressure in the inviscid region. The inner solution solves the integral boundary layer equations coupled to either a laminar or turbulent closure. Transition is predicted using the e^n method, which is based on the Orr-Sommerfeld equation. The two solutions are coupled together using the displacement thickness of the boundary layer which is used to displace the surface streamline of the outer solution normal to the airfoil surface. The coupled equations are then solved using a Newton-type solver. A full overview of the MSES program can be found in the MSES User Guide [2].

In addition to overall section lift, drag and pitching moment coefficients, MSES can provide detailed surface profiles for a number of quantities, including pressure and skin friction coefficients.

It is also important to note that MSES uses a coordinate system convention which differs from the convention typically used in Makani CAD files. The MSES convention is to have the positive x-direction point from the leading edge to the trailing edge of the airfoil and the positive y-direction point from the lower to the upper surface. Additionally, though not strictly required, it is best practice to try to place the airfoil leading edge near the origin of the coordinate system and this practice has been followed in this work. Lastly, the airfoil coordinates are scaled by a reference chord length, which is then used as the relevant length scale in the normalization of the force/moment coefficients which are output by MSES.

Since this work concerns first developing section airfoils and then using these to build a CAD representation, the transformation from MSES coordinates to CAD coordinates is provided below. The transformation places the quarter-chord location at $x = 0$ in the CAD coordinate system. Also, please note the MSES convention of using “y” for the vertical coordinate in 2D, while the CAD convention used “y” as the spanwise coordinate and “z” as the vertical coordinate.

REPORT: TLG-MAK-003		REVISION: 01	PAGE 2-2
AIRCRAFT: October Kite		REV DATE: 11/18/2019	PROPRIETARY
TITLE: Airfoil Design for the October Kite – Feasibility Studies		CUSTOMER: Makani Technologies, LLC	

$$x^{CAD} = \left(\left(\frac{x}{c} \right)^{MSES} - 0.25 \right) c_{ref}$$

$$z^{CAD} = \left(\frac{y}{c} \right)^{MSES} c_{ref}$$

All moment coefficients are presented about the point (0.25, 0.00), as per MSES convention. The chord line is defined using the Makani convention, which defines the chord line using the furthest forward x-coordinate of the main element and the mean trailing-edge point of the flap.

REPORT: TLG-MAK-003		REVISION: 01	PAGE 3-1
AIRCRAFT: October Kite		REV DATE: 11/18/2019	PROPRIETARY
TITLE: Airfoil Design for the October Kite – Feasibility Studies		CUSTOMER: Makani Technologies, LLC	

3.0 Airfoil design

The goal of the airfoil design process is to understand the feasibility of the Makani provided planform, given the objectives and constraints placed on the performance of the section airfoils. As such, it makes sense to first review the planform before discussing the airfoil section design. Table 1 shows the chord distribution over the planform, which has a root chord of 2.44 m and a taper ratio of 0.5 starting from 40% of the semi-span.

Table 1 October Kite planform

Spanwise location (m)	Chord (m)
0.0	2.44
5.2	2.44
13.0	1.22

Makani also provided a preliminary wing incidence and twist distribution; however, it is not listed here because the planform has been re-twisted as part of the design. This process was undertaken in order to optimize the performance trade-offs between camber and alpha for a given section. The full details of this process are discussed below in sections 3.1 and 3.3.1.

The reference area of the new planform is 54.0 m², which is a 64% increase of that of the M600 Energy Kite. Additionally, the mean aerodynamic chord has increased 62% up to 2.077 m. As a result of these increases, the overall kite will be operating at a lower C_L value and the sections themselves will also operate at lower section C_l values. Figure 1 shows the upper and lower bounds on the design section lift coefficients for the planform, as well as bounds for the additional 5 degrees of gust margin.

Details of the operating conditions for the sectional analysis are shown in Table 2. The Mach number was chosen based on an airspeed of 60.0 m/s and standard sea-level (SSL) conditions. The resulting Mach number of 0.176 is firmly in the subsonic regime and TLG does not expect significant variation of airfoil characteristics with Mach number up to the DNE speed of 100.0 m/s.

REPORT: TLG-MAK-003		REVISION: 01	PAGE 3-2
AIRCRAFT: October Kite		REV DATE: 11/18/2019	PROPRIETARY
TITLE: Airfoil Design for the October Kite – Feasibility Studies		CUSTOMER: Makani Technologies, LLC	

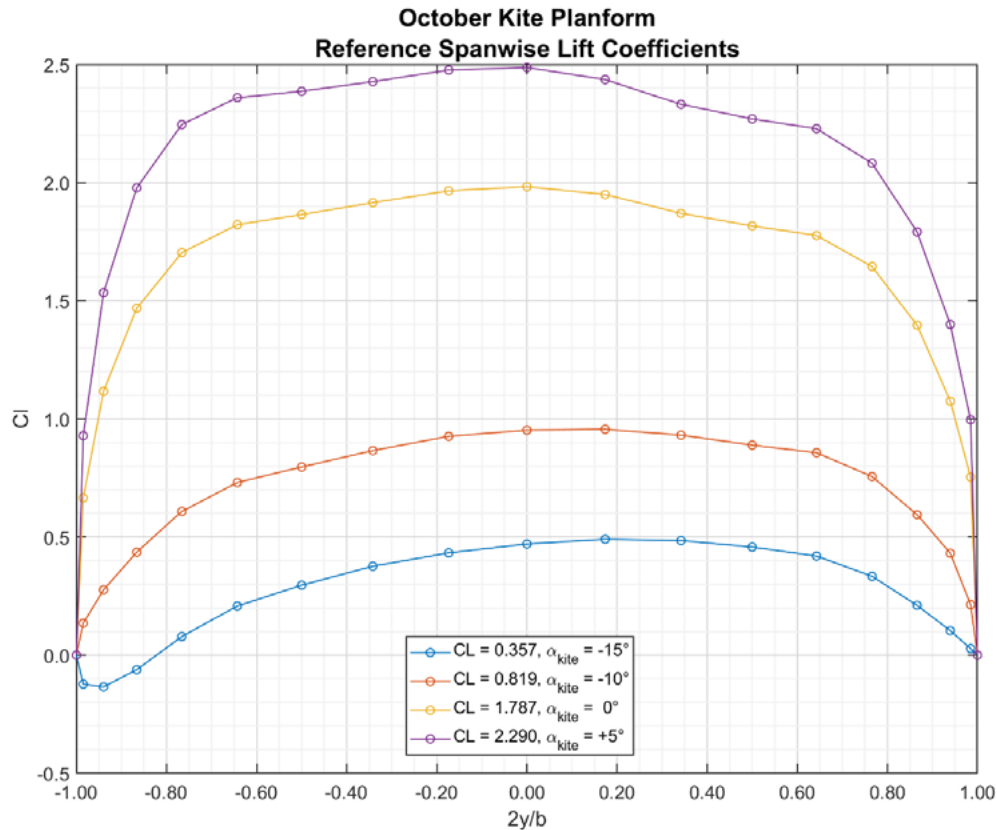


Figure 1 Upper and lower bounds of the design section lift coefficients for the October Kite platform

Table 2 Operating conditions for the airfoil sections

U_∞ (m/s)	q_∞ (Pa)	Ma	Re ($/10^6$)
60.0	2205.0	0.176	9.2

Before transitioning from 3D spanwise lift coefficients into 2D sectional design points, Figure 2 defines the Makani nomenclature used for the 2D lift curve with the key (C_l, α) pairs defined. The “design” C_l points should occur within the linear region of the lift curve. Table 3 extracts the relevant sectional C_l values from the 3D spanwise lift coefficients for the center section. Out of these four values, conversations with Makani have indicated that the most important point for optimization is $C_{l,design,max}$, since this will be the most important for maximizing power extraction from the kite.

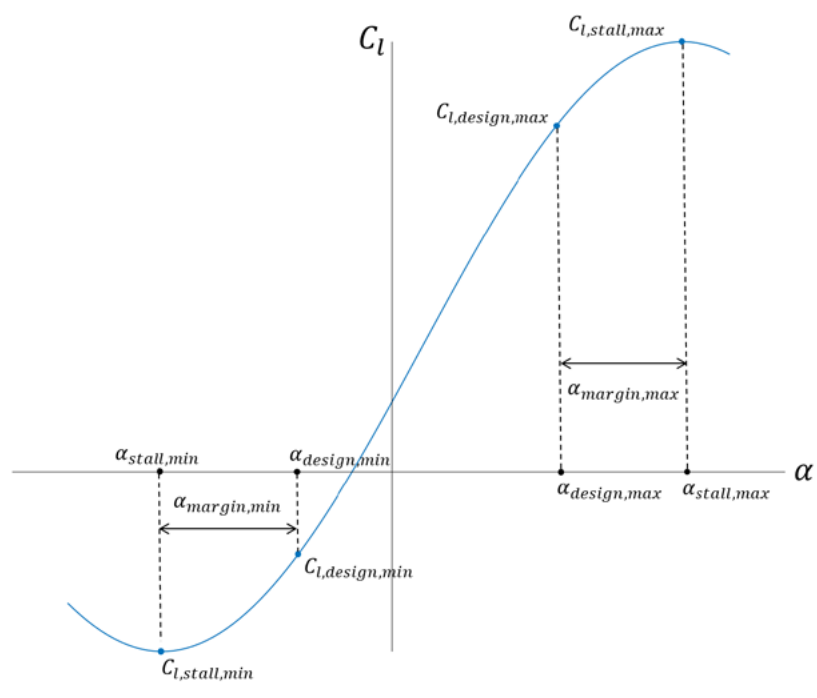


Figure 2 Makani nomenclature used for the 2D lift curve

Table 3 Key 2D design points for the center section based on 3D kite operating conditions

	C_l (center section)	CL_{kite}	α_{kite}
$C_{l,design,max}$	1.98	1.787	0°
$C_{l,design,min}$	0.95	0.819	-10°
$C_{l,stall,max}$	>2.49	2.290	+5°
$C_{l,stall,min}$	<0.47	0.357	-15°

3.1 Planform Twist Distribution

A Vortex Lattice Method (VLM) model of the planform was created in order to calculate the total fixed angle, θ , at each section. Knowing the total fixed angle allows for a trade-off study between incidence, i_w , twist, τ , and camber, C , at each section in order to maximize the local performance.

REPORT: TLG-MAK-003		REVISION: 01	PAGE 3-4
AIRCRAFT: October Kite		REV DATE: 11/18/2019	PROPRIETARY
TITLE: Airfoil Design for the October Kite – Feasibility Studies		CUSTOMER: Makani Technologies, LLC	

$$\theta(y) = i_w + \tau(y) + C(y)$$

In the equation above, i_w refers to the wing incidence and the center section twist is assumed to be 0. The target spanwise lift coefficients were taken to be the average of the left- and right-side lift coefficients from the data provided in Reference [1]. The left and right lift distributions differ by the yaw-rate induced dynamic pressure change across the span.

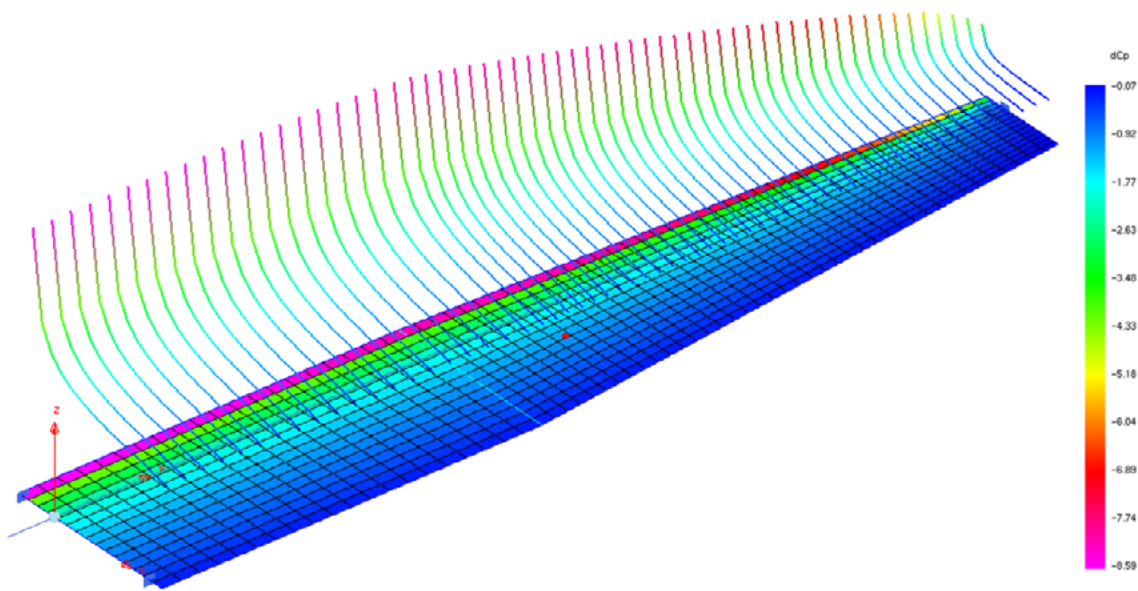


Figure 3 VLM solution for $\alpha = 0$ deg showing pressure difference across platform – steady level flight

Figure 3 shows the VLM pressure difference across the VLM panels at $\alpha = 0$. Figure 4 shows a comparison of the spanwise section lift coefficients at 4 key design points for the kite. The solid lines show the bounding range of the yaw-rate solution from the Makani data, the square symbols show the mean of the bounding range and the dashed line shows the VLM solution. A key feature of the plots is the good match against the induced-lift effects of the data. This is achieved with a total fixed angle of 20.5° at the centerline which is held constant up to the taper break before washing out to 12.5° at the wingtip. The ability to maintain constant twist from the centerline to the taper break is a feature that was not present in the original specification provided by Makani and should provide additional structural/manufacturing benefit. An untwisted section should provide opportunity for a simpler spar layout and the possibility of simpler system interfaces. The 8° of washout from the centerline to the tip matches the preliminary twist data that was provided by Makani.

REPORT: TLG-MAK-003		REVISION: 01	PAGE 3-5
AIRCRAFT: October Kite		REV DATE: 11/18/2019	PROPRIETARY
TITLE: Airfoil Design for the October Kite – Feasibility Studies		CUSTOMER: Makani Technologies, LLC	

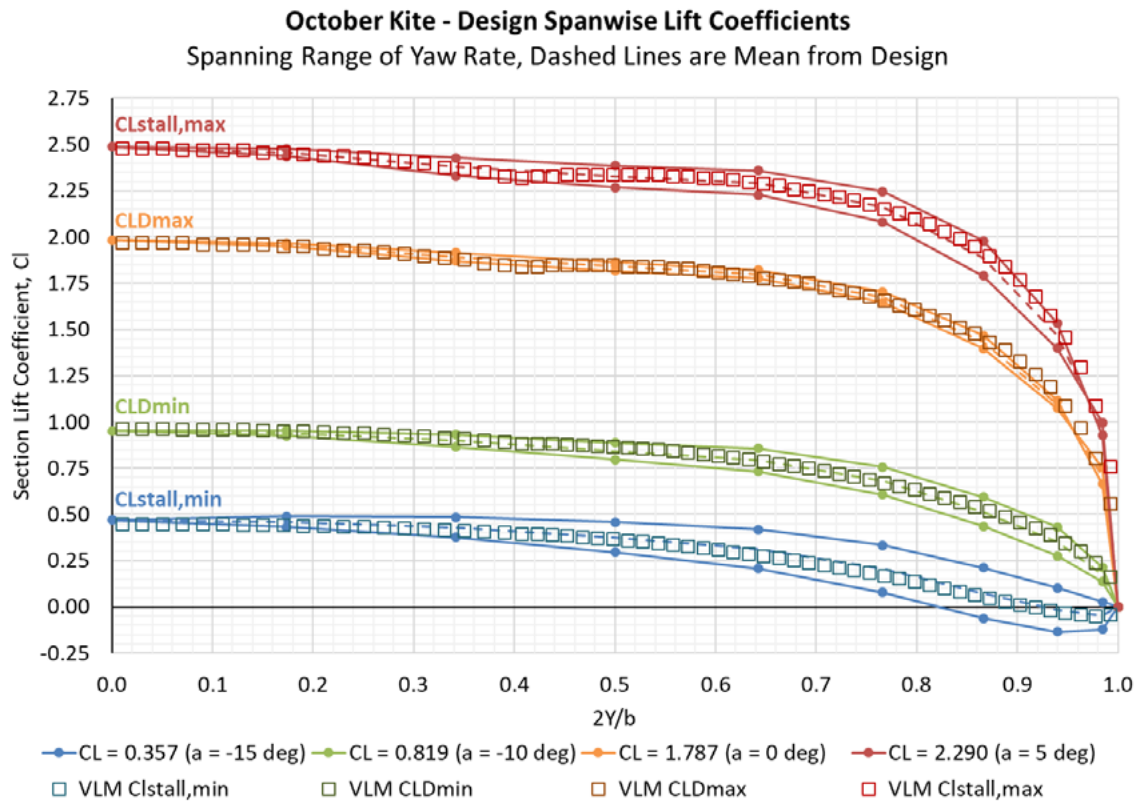


Figure 4 Comparison of the bounding range of spanwise lift coefficients to the results of the VLM model which neglects the yaw-rate term

3.2 Leading-Edge Design

The design of the leading-edge is the main driver for both $C_{l,max}$ performance and the extent of laminar flow over the section, both in terms of length and robustness. The laminar flow properties are particularly interesting due to performance requirements which must be met with a contaminated leading edge. Leading edge contamination was simulated by fixing transition at 5% chord for this preliminary design iteration. As part of this effort, it was identified that 5% may not be forward enough to simulate real-world contamination conditions. This is due to the large leading-edge radius and large laminar run, even at 5% chord. Further forward transition locations will be explored in subsequent design iterations; however, the minimum performance targets should still be achievable with fully turbulent flow. Additionally, the leading-edge must be able to accommodate the spar box as dictated by the constraints laid out in sections 1.3.2 & 1.6 of Reference [1].

REPORT: TLG-MAK-003		REVISION: 01	PAGE 3-6
AIRCRAFT: October Kite		REV DATE: 11/18/2019	PROPRIETARY
TITLE: Airfoil Design for the October Kite – Feasibility Studies		CUSTOMER: Makani Technologies, LLC	

Before delving into the details of the design process, it is useful to review the 2 main sources of drag for a low-speed airfoil; pressure drag and skin friction drag. The pressure drag is largely determined by the frontal area, or thickness, of the section and the re-distribution of the vertical pressure distribution due to viscous effects. The pressure drag is largely dictated by the spar box constraint, which will effectively set the airfoil thickness. In terms of skin friction, the magnitude of this source of drag will largely be driven by the length of laminar flow that the airfoil is able to achieve. Focusing first on an idealized surface, one approach would be to develop a laminar flow airfoil which would maximize the extent of laminar flow at the design point. Even with an idealized surface, a possible issue with a traditional natural laminar flow airfoil is their lack of high-lift performance, which can compromise the necessary gust margin. The bigger issue with a traditional laminar flow airfoil is that the surface is not always ideally smooth, and real-world contamination can lead to a substantial performance penalty. An alternative approach, which considers the operating conditions of the kite, would be to design for a very robust run of laminar flow at the main operating point. Such a design would have a strong favorable gradient up to the desired transition location, which should provide a strong forcing for the flow to re-laminarize if a disturbance trips the flow earlier.

To design the leading-edge shape, TLG utilized inverse-design methods which allow for desired changes in the pressure profile to be transformed into changes in the local curvature of the airfoil. This method requires a baseline shape, or seed airfoil. Multiple different starting airfoils could be considered, though in general they should have a thickness comparable to the spar box constraint, which is $t/c = 0.20$. The reason for starting with a 20% thick airfoil is that inverse methods are suited to subtle changes in section curvature but not to large scale modification of airfoil properties. While airfoils from the M600 Energy Kite could be used as seed airfoils, the decision was made not to use these in order not to bias the design of the sections. It should be noted that the leading-edge design was performed using a single element. The properties of the leading-edge should transfer to a two-element design as long as the total circulation being driven about the leading-edge is constant.

Figure 5 shows both the seed and modified airfoils for the candidate leading-edge design. The accompanying pressure profiles are shown in Figure 6. The leading-edge radius has been increased to reduce the peak suction pressure. These changes have been accomplished by increasing the leading-edge slope of the mean camber line by roughly 5° and shifting the mean camber line highpoint to occur at $x/c \approx 0.14$. Similarly, the thickness highpoint has been moved forward to $x/c \approx 0.24$, from a previous value of $x/c \approx 0.40$. Lastly, the upper surface of the airfoil has been modified to support a more Stratford-like pressure recovery, which should minimize stress on the upper surface boundary layer. A small region of trailing-edge separation can be seen in the modified pressure profile of Figure 6, which will not be present at the design C_l in the two-element design.

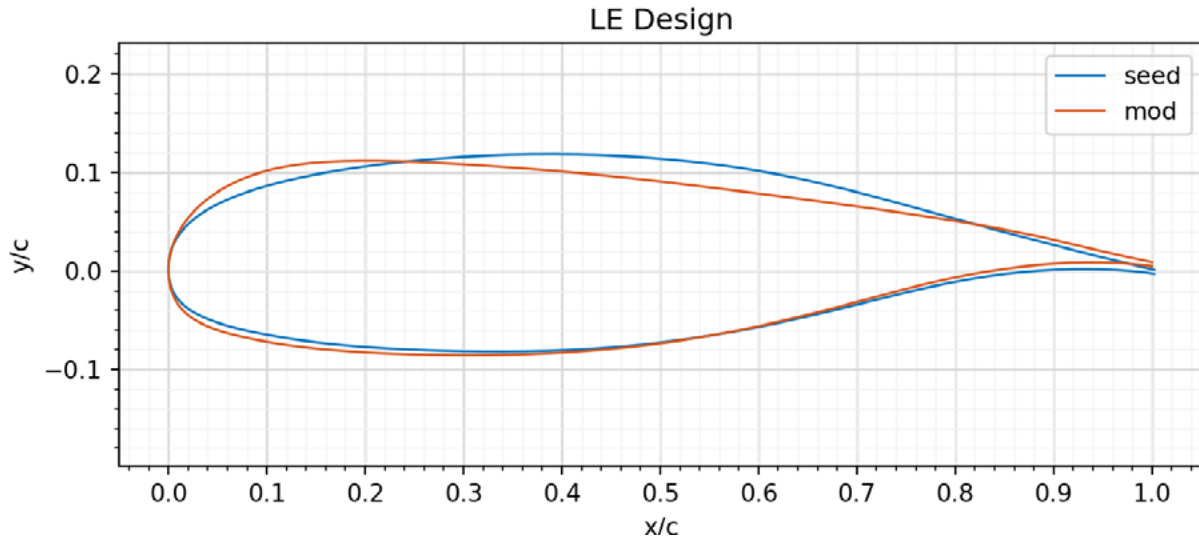


Figure 5 Leading-edge design process - seed and modified airfoils

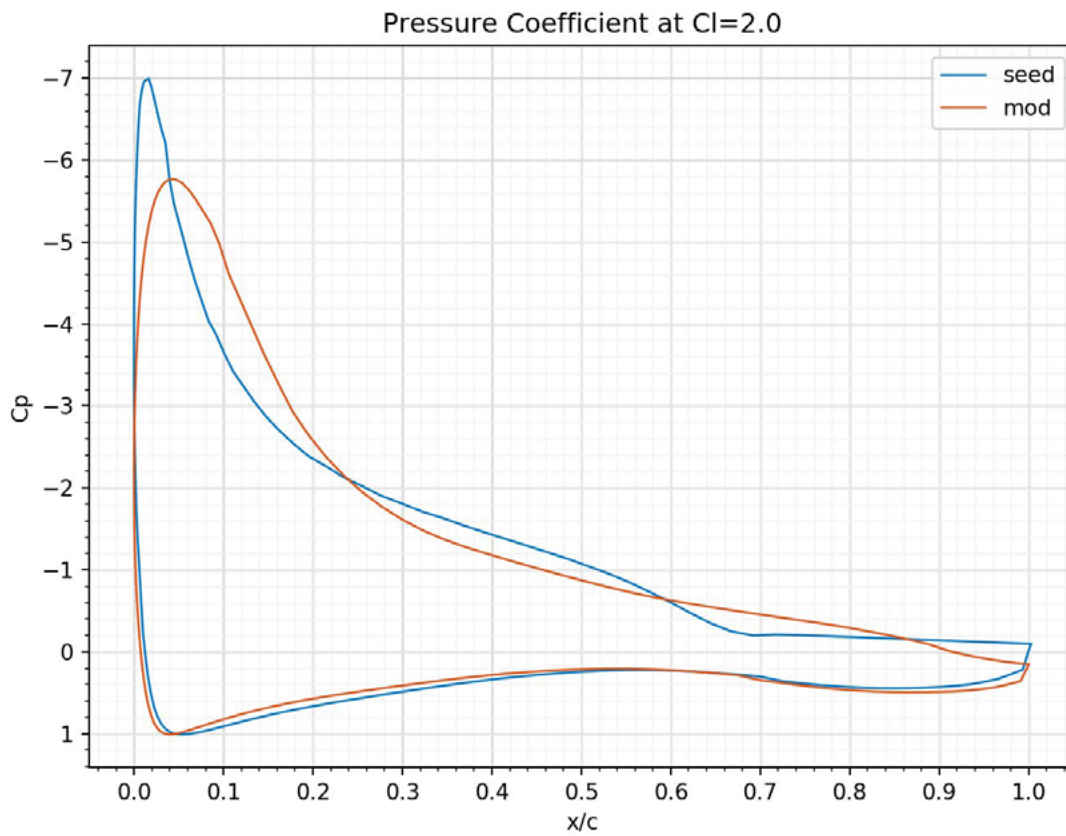


Figure 6 Leading-edge design process – seed and modified pressure coefficient profiles

REPORT: TLG-MAK-003		REVISION: 01	PAGE 3-8
AIRCRAFT: October Kite		REV DATE: 11/18/2019	PROPRIETARY
TITLE: Airfoil Design for the October Kite – Feasibility Studies		CUSTOMER: Makani Technologies, LLC	

Figure 7 illustrates modifications made to the airfoil to integrate the spar box and flap, which will be discussed in more detail in section 3.3 below. The blue curve in Figure 7 is the modified single element airfoil from above (mod) added for reference to better visualize the further modifications made for the spar box and flap. Focusing on the leading-edge, an adjustment was made to the airfoil lower surface in order to better integrate with the spar constraint. After the spar box, the airfoil was contoured to create room for the flap and slot flow, while maintaining a convex lower surface. The convex lower surface was a request included in Reference [1], which allows for the use of a stressed skin construction which may or may not provide manufacturing options. Whether this convex topology can be retained in the final design iteration is TBD.

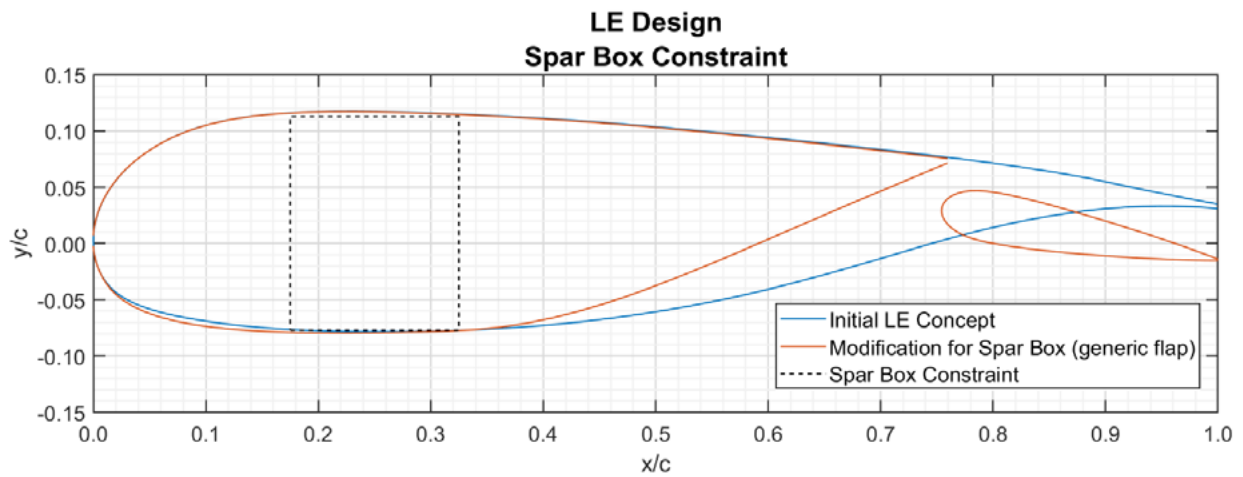


Figure 7 Integration of spar box constraint into leading-edge design

As mentioned earlier, a key driver in the design of the new section is to minimize performance impacts due to the effects of contamination. As such, one of the main design goals was to reduce the presence of any laminar separation bubbles. A laminar separation bubble would indicate that an airfoil is more susceptible to a violent, leading-edge laminar separation event. Figure 8 and Figure 9 present the upper surface skin friction coefficient for the 008613 section from the M600 Energy Kite and from the new airfoil, both run at the Reynolds number for the higher section chord. The skin friction data is plotted against the normalized arc-length s/c , with the stagnation point set to $s/c = 0$ for all cases. A laminar separation bubble is indicated by a negative value of the skin friction coefficient, i.e. – a change in flow direction due to recirculation in the bubble. In interpreting these plots, keep in mind that the minimum skin friction is hard to predict exactly and instead the trend of the curves on either side of the minimum should be used to inform whether a bubble is present. Put another way, even coming close to crossing the x-axis is likely an indication of a bubble. The first plot shows that the 008613 section likely has a bubble at low-

REPORT: TLG-MAK-003		REVISION: 01	PAGE 3-9
AIRCRAFT: October Kite		REV DATE: 11/18/2019	PROPRIETARY
TITLE: Airfoil Design for the October Kite – Feasibility Studies		CUSTOMER: Makani Technologies, LLC	

to-moderate angles-of-attack. In contrast, the new airfoil has a much higher minimum skin friction, considering the trend, and thus should be less likely to have a bubble.

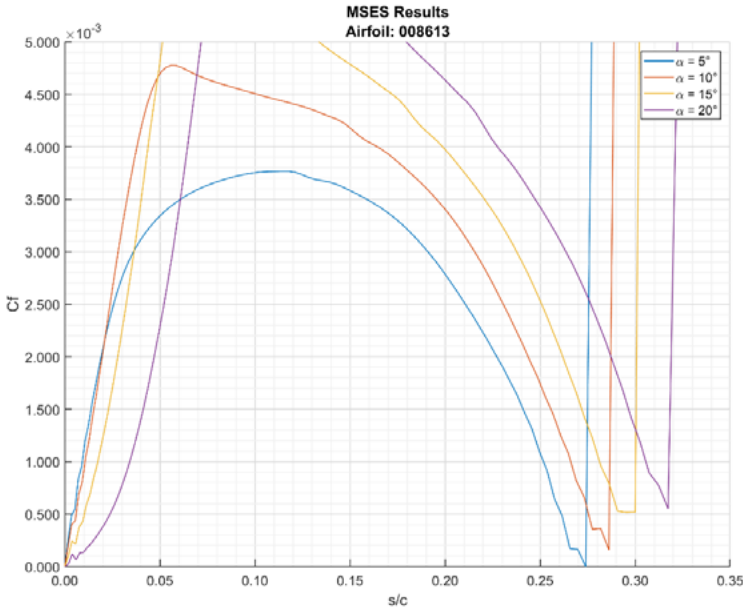


Figure 8 Skin friction coefficient on the suction surface – 008613 section from M600

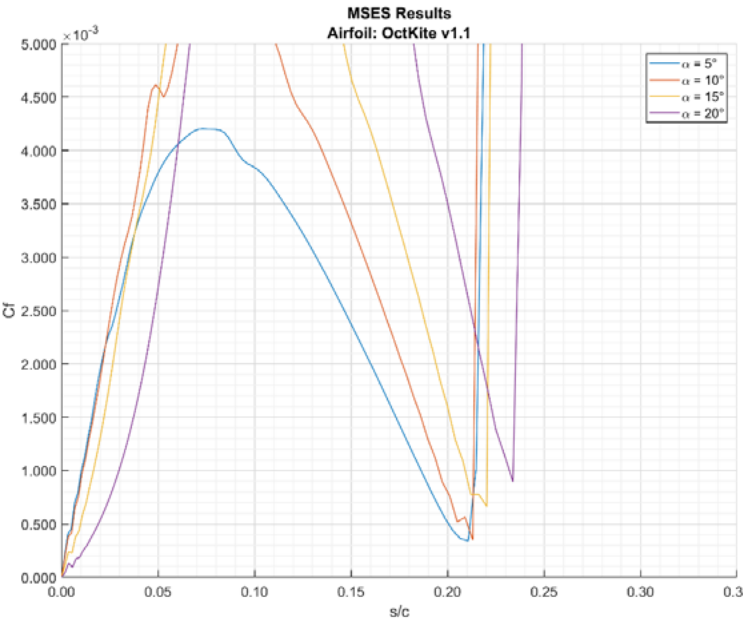


Figure 9 Skin friction coefficient on the suction surface – new design section

REPORT: TLG-MAK-003		REVISION: 01	PAGE 3-10
AIRCRAFT: October Kite		REV DATE: 11/18/2019	PROPRIETARY
TITLE: Airfoil Design for the October Kite – Feasibility Studies		CUSTOMER: Makani Technologies, LLC	

3.3 Flap Design

Flap design is a very important aspect of the October Kite due to the way the kite operates. The kite needs to operate at high lift coefficient values to maximize the C_L^3/C_D^2 parameter while also maintaining the ability to produce high rolling moments. These two requirements mean that the flap element is a crucial component driving the performance and controllability of the kite. The flap needs to be both powerful and efficient in the nominal position while maintaining high effectiveness across a large flap deflection range. To achieve these goals, the preliminary design of the flap was composed of four main decisions; the flap-chord ratio, the flap gap (slot throat dimension), the flap overlap (flap fore/aft position), and the flap section shape. The first three decisions were informed based on a combination of TLG experience and data available from the analysis of the M600 airfoil sections. Further optimization of these parameters may be possible in future design iterations.

The M600 provides a valuable source of data on the impact of flap chord ratio due to using a constant chord flap with a tapered main wing element. Further, the effort to increase roll authority of the M600 (Reference [3]) studied the impact of extending the flap chord of each section. Thus, data is available for 6 values of the flap chord fraction which can be used to inform choices on the October Kite design. The driver in choosing a flap chord ratio is to make sure that we are able to exceed the actuated section lift metric, section 1.2.4 of Reference [1], which states $\partial(C_L)/\partial(\delta) \geq 0.045$ for $-10^\circ \leq \delta \leq 10^\circ$.

Figure 10 plots the actuated section lift metric data for all 6 flap chord ratios studied from the M600 planform. The blue lines represent the derivative for -10° flap deflection (trailing-edge up), while the orange lines represent $+10^\circ$ flap deflection (trailing-edge down). The solid lines are taken from an angle-of-attack of $\alpha=0^\circ$, while the dashed lines are taken from a higher angle-of-attack of $\alpha=15^\circ$. The motivation of including two separate angles of attack for each flap deflection is that the M600 flaps (and most flaps) show a loss of effectiveness as they approached C_{Lmax} . Another feature of the M600 flap, as is typical of most flaps, was that negative deflections were more effective than positive deflections. This fact was actually more significant beyond $+10^\circ$ of flap deflection shown below. This could have been a result of the different nominal flap deflection setting, though likely other factors such as gap and overlap played a role as well. One concern that Makani raised in conversations with TLG is that the slot flow was being choked with increasing positive flap deflections, i.e. – the gap was getting too small. This issue will be addressed below in the discussions around the nominal gap and overlap setting. Based on the data presented in Figure 10, we have chosen a flap chord ratio of 0.25 as a starting point.

REPORT: TLG-MAK-003		REVISION: 01	PAGE 3-11
AIRCRAFT: October Kite		REV DATE: 11/18/2019	PROPRIETARY
TITLE: Airfoil Design for the October Kite – Feasibility Studies		CUSTOMER: Makani Technologies, LLC	

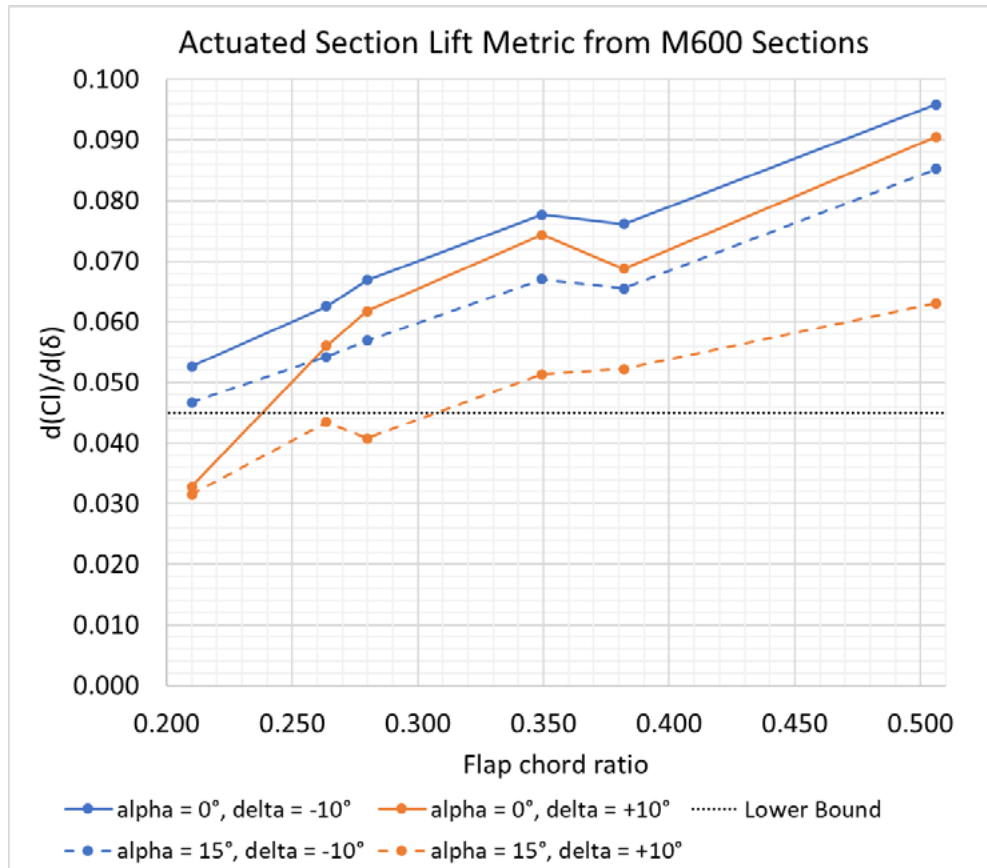


Figure 10 M600 energy kite data used to inform the choice of flap chord ratio to achieve the actuated section lift metric

The next step was to choose initial values for the gap and overlap. A primary concern when selecting the gap and overlap values was that both positive and negative flap deflections must perform well. This is because the flap may be at the extremes of the deflection range during the power extraction phase of the energy cycle. Based on M600 data, this meant that positive flap deflections were critical. With this in mind, initial values of gap and overlap would bias towards a larger gap, to prevent choking or throttling of the slot flow, and a more protected (positive) overlap to mitigate the possibility of abrupt performance loss that can occur at large values of unprotected (negative) overlap. Data from the M600 sections is used to inform this decision and is presented in Table 4. The section closest to the selected flap chord ratio of 0.25 is 008570 with a flap chord of 0.264. To mitigate against potential choking of the slot flow, TLG chose to use an increased gap setting of 12%, similar to that of the 008613 section. The preliminary value of gap and overlap used for the nominal flap deflection trade-study are 2% and 12%, respectively.

REPORT: TLG-MAK-003		REVISION: 01	PAGE 3-12
AIRCRAFT: October Kite		REV DATE: 11/18/2019	PROPRIETARY
TITLE: Airfoil Design for the October Kite – Feasibility Studies		CUSTOMER: Makani Technologies, LLC	

Table 4 Values of gap and overlap from M600 sections

Section	Flap chord ratio	Gap (% flap chord)	Overlap (% flap chord)
008613	0.210	12.0	-1.5
008570	0.264	9.8	2.0
008586	0.382	7.2	6.1

Next, a flap section profile needs to be selected. A symmetric profile was chosen to reduce manufacturing costs as this would eliminate tooling handedness for the outboard flap, where the flap tapers with the wing. This choice is made possible by the fact that the Energy Kite does not have a flaps-retracted detent. A symmetric flap section would generally not be possible on a flap designed for aviation applications. A relatively thick section was desired in order to have a large leading-edge radius which would facilitate the flow to stay attached across a large local alpha range, especially in the absence of camber in the section itself. As a starting point, a naca0018 section was used with the point of maximum thickness modified to occur at 20% chord. Additional consideration will be given to the flap shape in subsequent design iterations. Figure 11 shows the unit airfoil used for the flap shape.

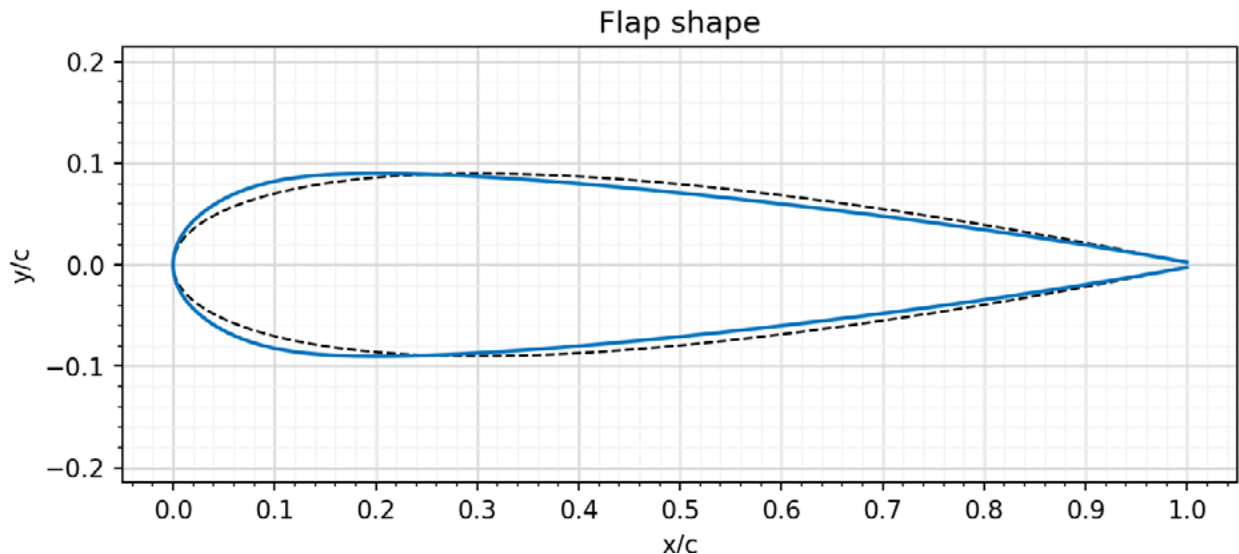


Figure 11 Symmetric flap unit airfoil (blue) with naca0018 (dashed black) shown for reference

REPORT: TLG-MAK-003		REVISION: 01	PAGE 3-13
AIRCRAFT: October Kite		REV DATE: 11/18/2019	PROPRIETARY
TITLE: Airfoil Design for the October Kite – Feasibility Studies		CUSTOMER: Makani Technologies, LLC	

3.3.1 Nominal Flap Deflection Study

With the initial flap section designed, a trade-study was performed in order to optimize overall section performance at the nominal flap deflection. This study is a follow-on to the work done in section 3.1 in that it quantifies the trade-offs between twist (alpha) and aft-camber (nominal flap angle) to achieve the total fixed angle required to match the target spanwise lift coefficients. Since the October kite will always have a deployed flap, aft-camber is synonymous with the nominal flap deflection angle. Five different flap angles were investigated and they are identified by the angle the flap chord line makes with the x-axis, as shown in Figure 12.

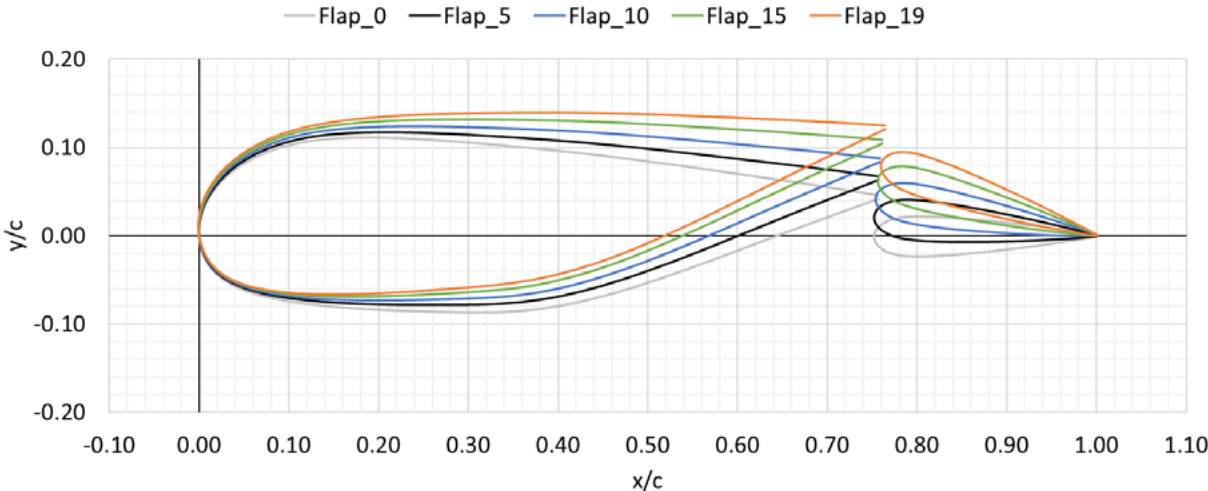


Figure 12 Sections used for the nominal flap deflection study plotted with chord line along the x-axis

The section performance will be judged on both the raw section performance and a “trim-corrected” performance metric. The trim-correction is a proxy which enables a contribution from the pitching moment effect on trim drag to be included in the assessment of the airfoil section. Without this proxy metric, section design would bias towards large negative pitching moments and corresponding large stabilizing surface sizes and trim drag. This 2D sectional trim correction is computed by analogy to the additional induced drag created by the balancing tail lift required to put a 3D wing or aircraft in trim.

$$C_{l,h} = \frac{C_m}{(L_h/MAC)} \left(\frac{S}{S_h} \right)$$

REPORT: TLG-MAK-003		REVISION: 01	PAGE 3-14
AIRCRAFT: October Kite		REV DATE: 11/18/2019	PROPRIETARY
TITLE: Airfoil Design for the October Kite – Feasibility Studies		CUSTOMER: Makani Technologies, LLC	

$$C_{d,h} = \frac{C_{l,h}^2}{\pi e_h AR_h}$$

$$C_{l,t} = C_l + C_{l,h} \left(\frac{S_h}{S} \right)$$

$$C_{d,t} = C_d + C_{d,h} \left(\frac{S_h}{S} \right)$$

In the equations above L_h is the tail-arm, MAC is the mean-aerodynamic chord of the wing, S is the wing reference area, S_h is the tail reference area, $C_{l,h}$ & $C_{d,h}$ are the tail lift- and drag-coefficients normalized by the tail area, e_h is Oswald’s efficiency factor for the tail and AR_h is the tail aspect ratio.

Figure 13 through Figure 18 presents multiple forms of the 2D endurance parameter for the different sections used in the nominal flap deflection investigation. The endurance parameter is presented using the raw data, using the trim-correction proxy and using the addition of a constant, 2D equivalent tether drag term. Figure 13 through Figure 15 show results for a free transition model while Figure 16 through Figure 18 shows results with transition fixed at 5%, on both sides of both elements. In these charts, particular attention should be paid to the values at $C_l = 2.0$, which is $C_{l,design-max}$, since this is the point where we want to extract the maximum performance.

A general observation that holds for all of the figures is that reducing the aft camber tends to shift the peak of the endurance parameter to lower C_l values. However, the goal is to have the value be as large as possible, not that the peak of the endurance parameter be located exactly at $C_l = 2.0$. In that vein, less aft camber also tends to reduce the peak value of the endurance parameter. Too much nominal flap deflection has a similar deleterious effect, even before taking the trim correction into account.

Another interesting feature is the impact of the trim correction on the ordering of the peak endurance parameter values, as can be seen by comparing Figure 13 and Figure 14. In Figure 13, the sections “Flap_10” and “Flap_15” are roughly equivalent in terms of maximum endurance parameter value, slightly beating out “Flap_5”. However, Figure 14 shows that the trim correction caused by the larger pitching moment of the “Flap_15” setting results in a lower maximum endurance parameter than “Flap_5”. There is a similar switch between “Flap_5” and “Flap_10” when looking at the endurance parameter value when $C_l = 2.0$.

With the addition of forced transition, the performance of “Flap_15” gets closer to the maximum value when evaluated at $C_l = 2.0$, even beating out “Flap_5” in the results without a trim correction. However, the section which is best performing across the entire range of transition conditions and performance metrics is the “Flaps_10” section and thus it will be used as the centerline section.

Recalling the results from section 3.1, knowing that our planform has 8° of washout at the tip station means that the relevant C_l value for the tip section is $C_l \approx 1.1$. An interesting feature of the endurance parameter plots is the degree to which sections with different nominal flap deflection all collapse onto a single curve, at least below a certain threshold. For free transition, “Flap_15” & “Flap_19” are both noticeably lower performing in the range $0.5 \leq C_l \leq 1.5$. For fixed transition, the “Flap_15” results are closer to the sections with less aft camber. At this lower C_l , the two best performing sections seem to be “Flap_5” and “Flap_10”, though the difference between the sections seems to be minimal. Thus, the “Flap_10” section will also be used for the tip section.

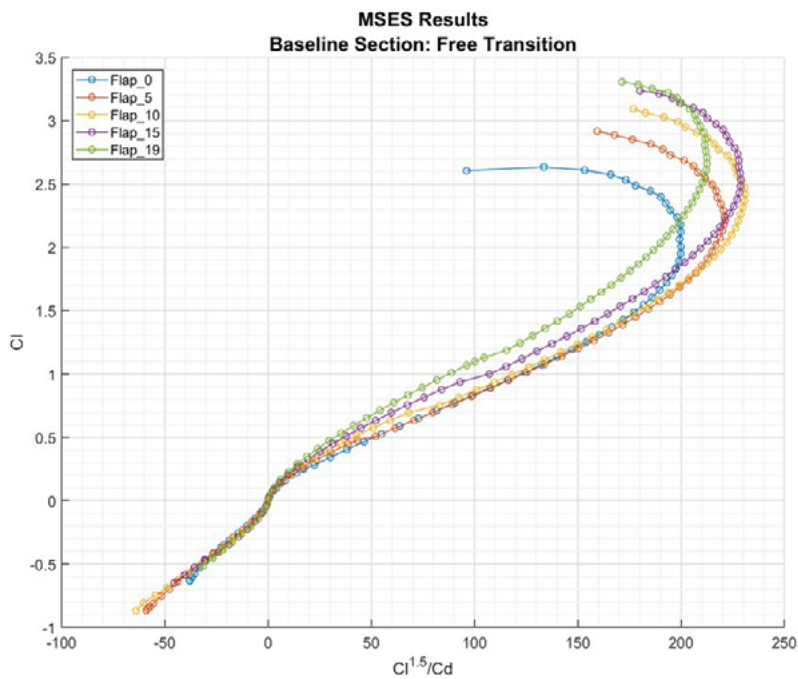


Figure 13 2D section raw endurance parameter from nominal flap deflection study – Free transition

REPORT: TLG-MAK-003		REVISION: 01	PAGE 3-16
AIRCRAFT: October Kite		REV DATE: 11/18/2019	PROPRIETARY
TITLE: Airfoil Design for the October Kite – Feasibility Studies		CUSTOMER: Makani Technologies, LLC	

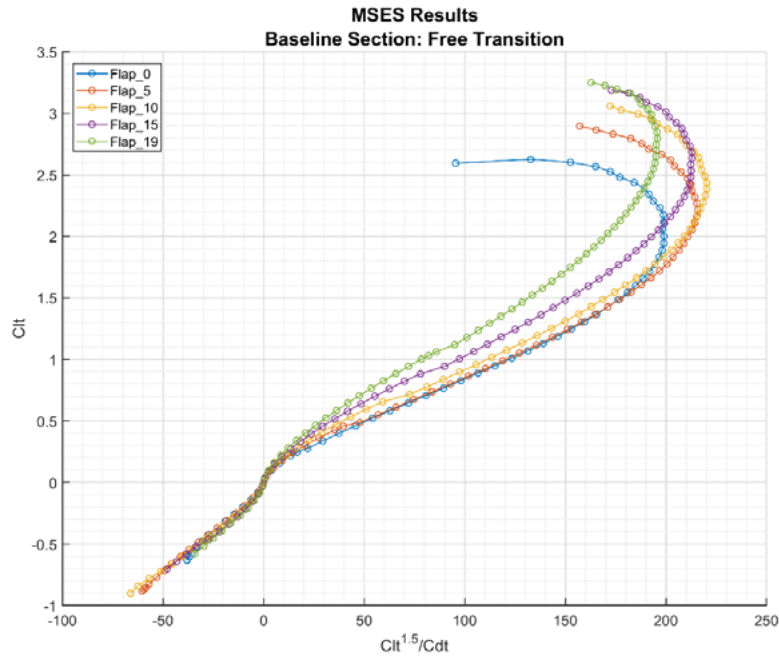


Figure 14 2D section trimmed endurance parameter from nominal flap deflection study – Free transition

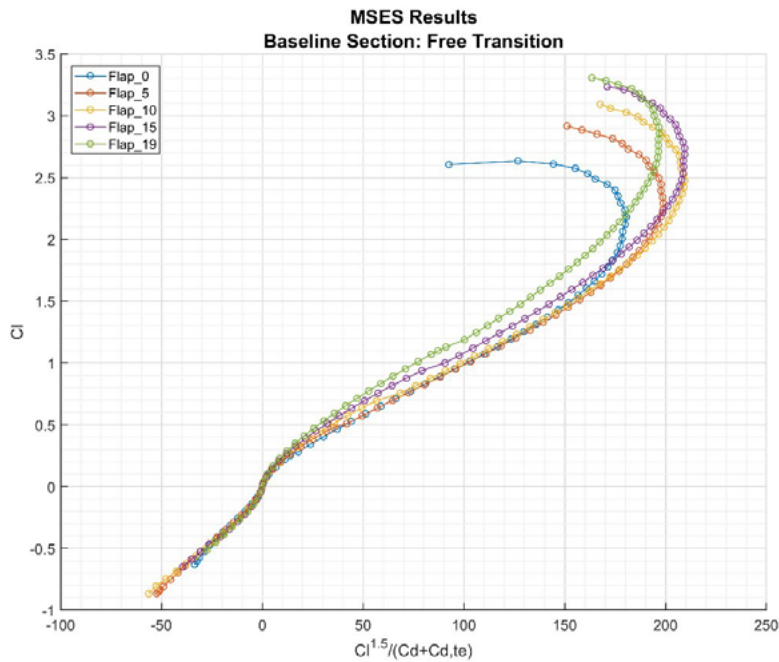


Figure 15 2D section raw endurance parameter including fixed tether drag from nominal flap deflection study – Free transition

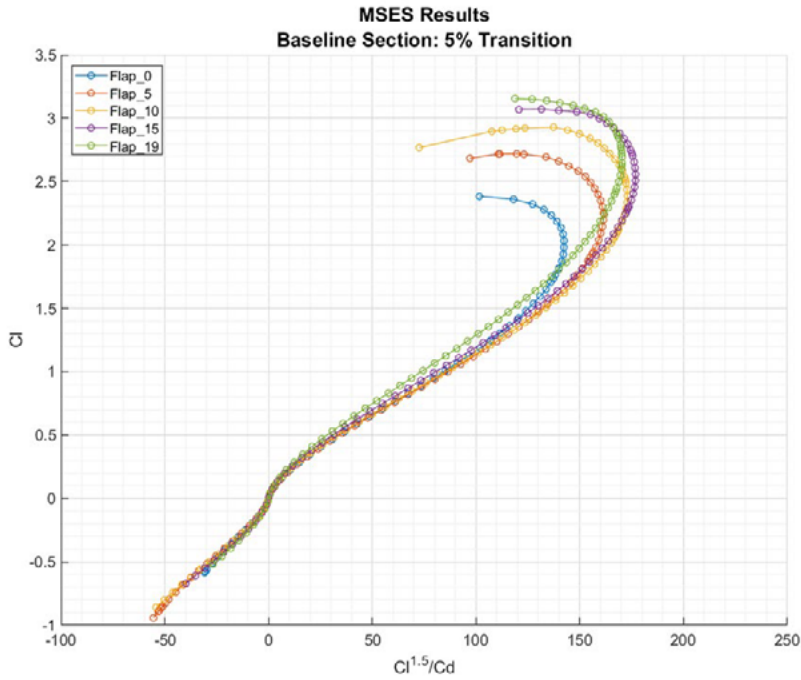


Figure 16 2D section raw endurance parameter from nominal flap deflection study –5% fixed transition

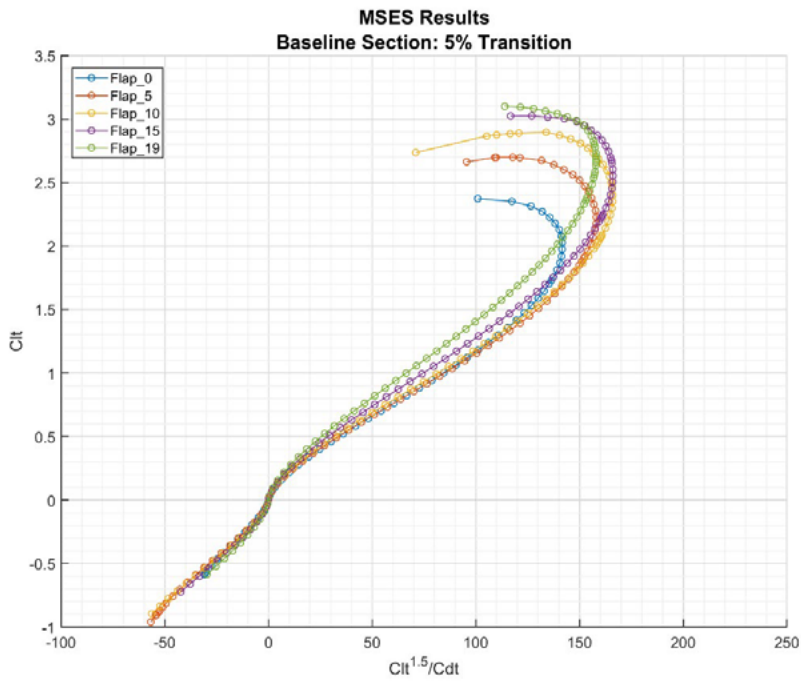


Figure 17 2D section trimmed endurance parameter from nominal flap deflection study – 5% fixed transition

REPORT: TLG-MAK-003		REVISION: 01	PAGE 3-18
AIRCRAFT: October Kite		REV DATE: 11/18/2019	PROPRIETARY
TITLE: Airfoil Design for the October Kite – Feasibility Studies		CUSTOMER: Makani Technologies, LLC	

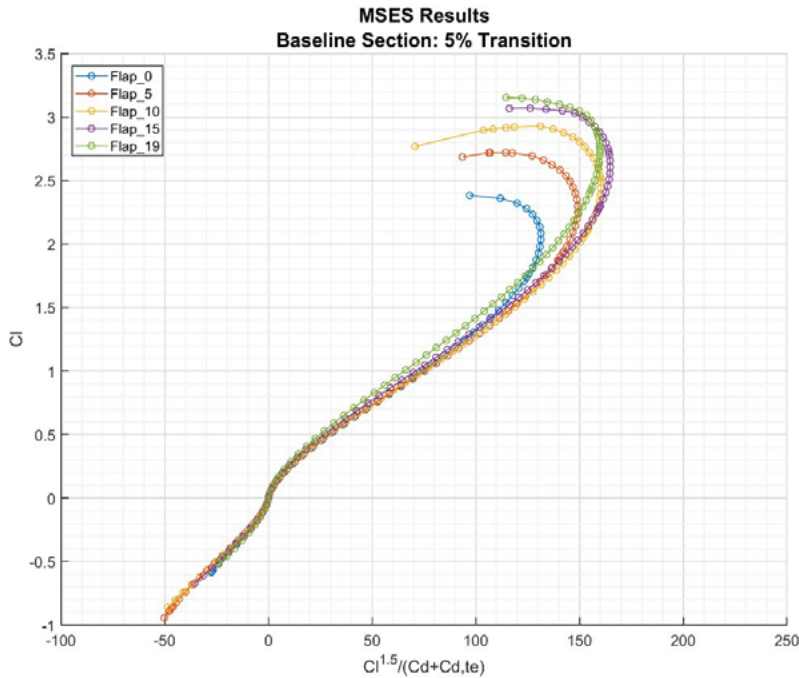


Figure 18 2D section raw endurance parameter including fixed tether drag from nominal flap deflection study – 5% fixed transition

3.4 Section Performance

The airfoil detailed in sections 3.2 and 3.3 is named OctKite v1.1, for Stage 1 - Iteration 1 of the October Kite project. The airfoil geometry is shown in Figure 19 below. Before presenting performance data for the new section, it is insightful to make a comparison to the center section (008613) of the M600 Energy Kite. Figure 20 compares the pressure profiles for the two sections at $C_l = 2.0$. One of the key differences is the location and magnitude of the peak suction-side pressure. The new design has moved the peak to align with the 5% fixed transition location in order to ensure as robust a run of laminar flow as possible, which is supported by the stronger favorable pressure gradient up to this point. A secondary effect of this choice is that the airfoil is carrying much more of its load close to the leading edge, which means that it will have a lower pitching moment coefficient than the 008613 section. A compromise of this decision will be more structural load being carried by the leading-edge structure forward of the spar.

REPORT: TLG-MAK-003		REVISION: 01	PAGE 3-19
AIRCRAFT: October Kite		REV DATE: 11/18/2019	PROPRIETARY
TITLE: Airfoil Design for the October Kite – Feasibility Studies		CUSTOMER: Makani Technologies, LLC	

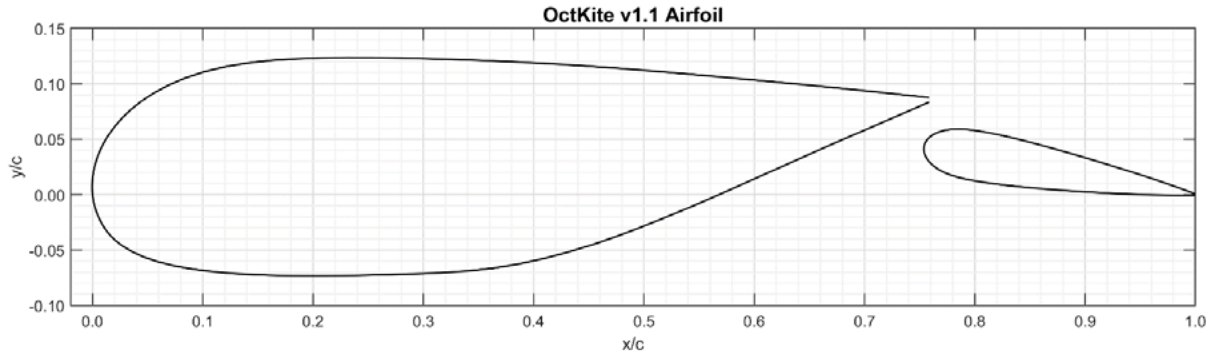


Figure 19 Geometry for OctKite v1.1 airfoil

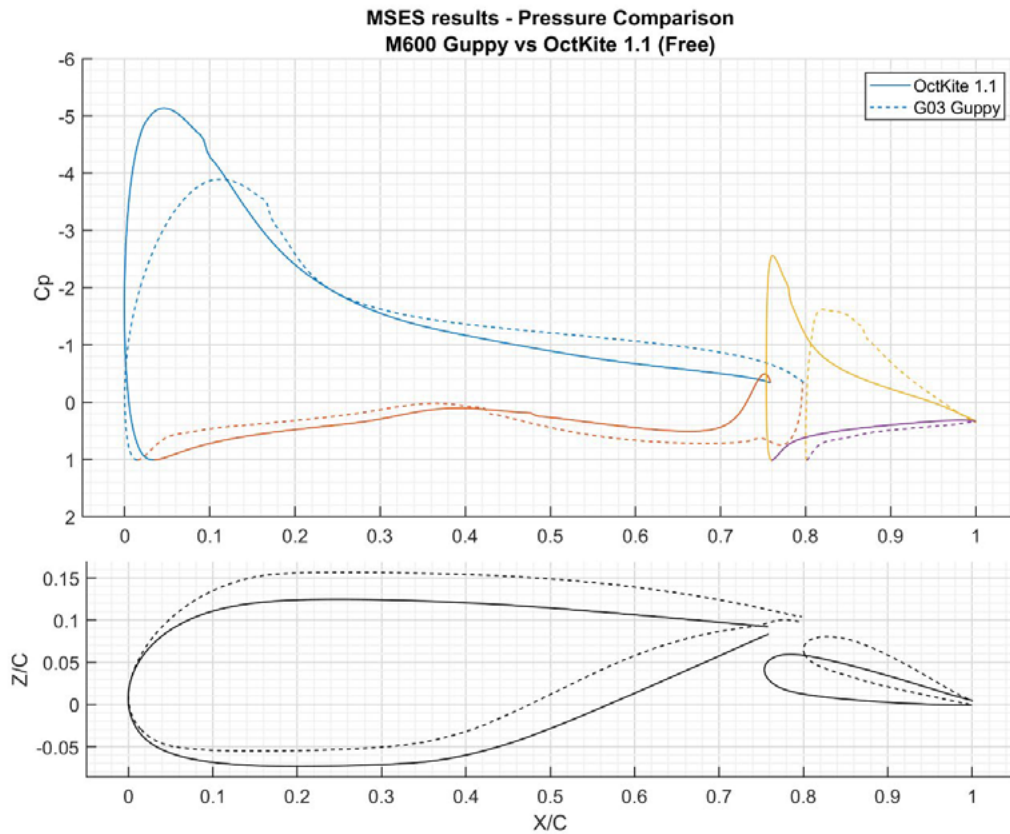


Figure 20 Comparison of pressure profiles for the OctKite v1.1 section and the center section of the Guppy (008613) – $C_l = 2.0$

The performance of the section, with the flap in the nominal position, is shown below in Figure 21-Figure 26. Small differences in the lift-curve due to transition can be seen in Figure 21. From the figure, the value of $C_{l, stall, max}$ for the 5% fixed transition case is roughly 2.9, though TLG internal best practice is to apply an uncertainty knockdown of 0.2

REPORT: TLG-MAK-003		REVISION: 01	PAGE 3-20
AIRCRAFT: October Kite		REV DATE: 11/18/2019	PROPRIETARY
TITLE: Airfoil Design for the October Kite – Feasibility Studies		CUSTOMER: Makani Technologies, LLC	

to MSES $C_{l,max}$ results, giving a value of 2.7. The gust margin can then be evaluated between $C_{l,design,max} = 2.0$ and $C_{l,stall,max} = 2.7$, which gives $\Delta\alpha_{margin,max} = 7^\circ$ and exceeds the specification of 5° . At the opposite end of the spectrum, the tip section needs to achieve a value of $C_{l,stall,min} = -0.5$, which is easily achievable given that the tip will have 8° of washout relative to the center section. Figure 24 shows that the section achieves the drag performance metric with values of 207% and 155% as compared to the minimum standard of $C_l/C_d = 75$, respectively.

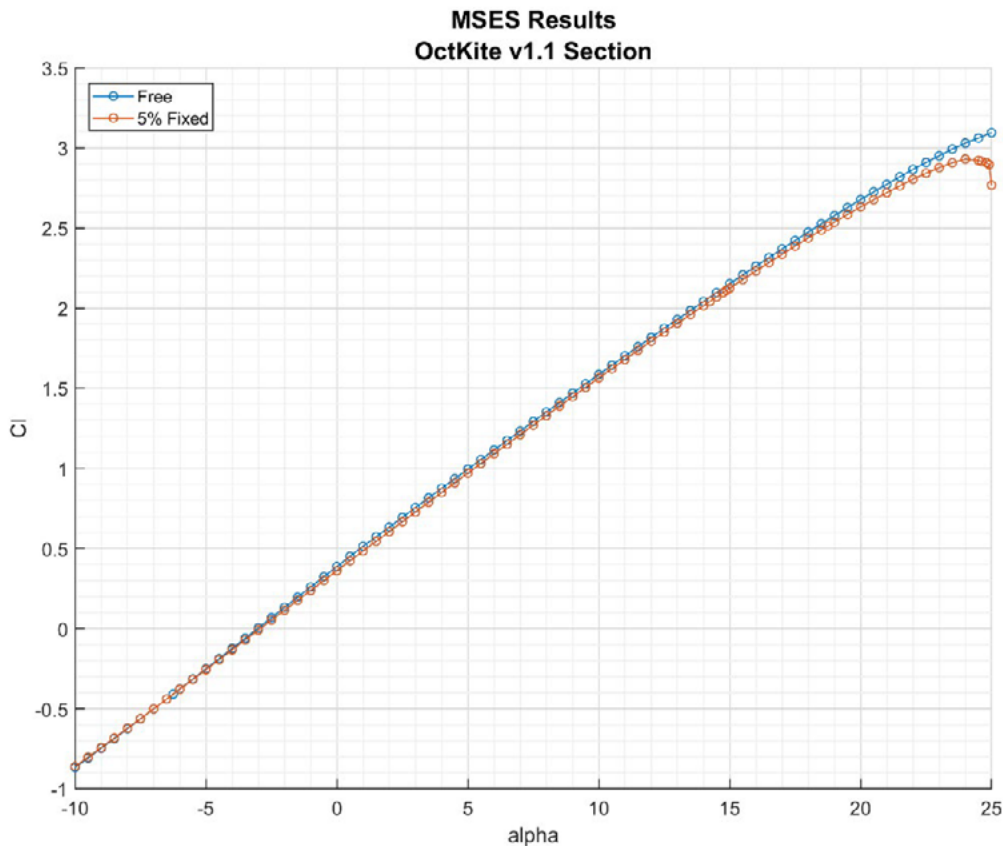


Figure 21 OctKite v1.1 section with free and 5% fixed transition – Cl vs alpha

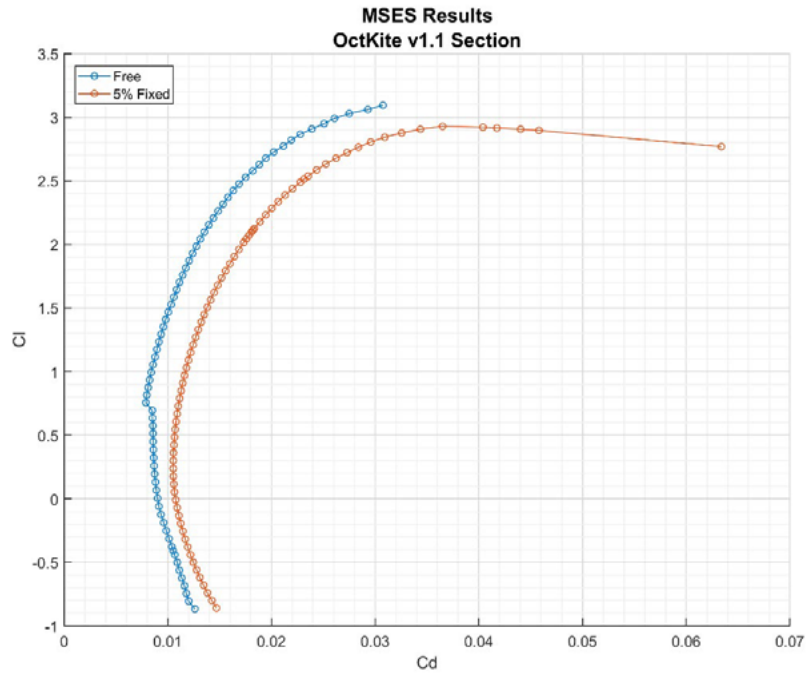


Figure 22 OctKite v1.1 section with free and 5% fixed transition – C_l vs C_d

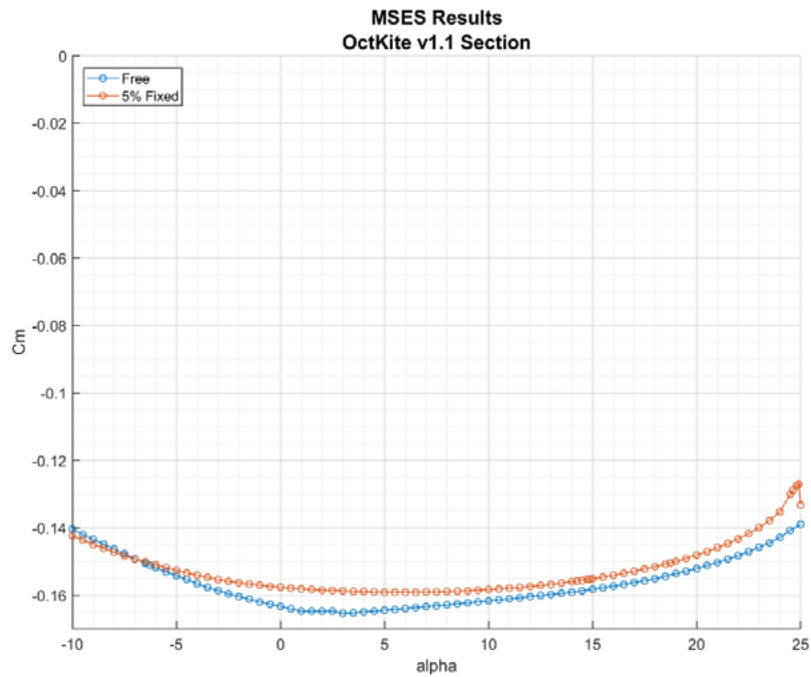


Figure 23 OctKite v1.1 section with free and 5% fixed transition – C_m vs α

REPORT: TLG-MAK-003		REVISION: 01	PAGE 3-22
AIRCRAFT: October Kite		REV DATE: 11/18/2019	PROPRIETARY
TITLE: Airfoil Design for the October Kite – Feasibility Studies		CUSTOMER: Makani Technologies, LLC	

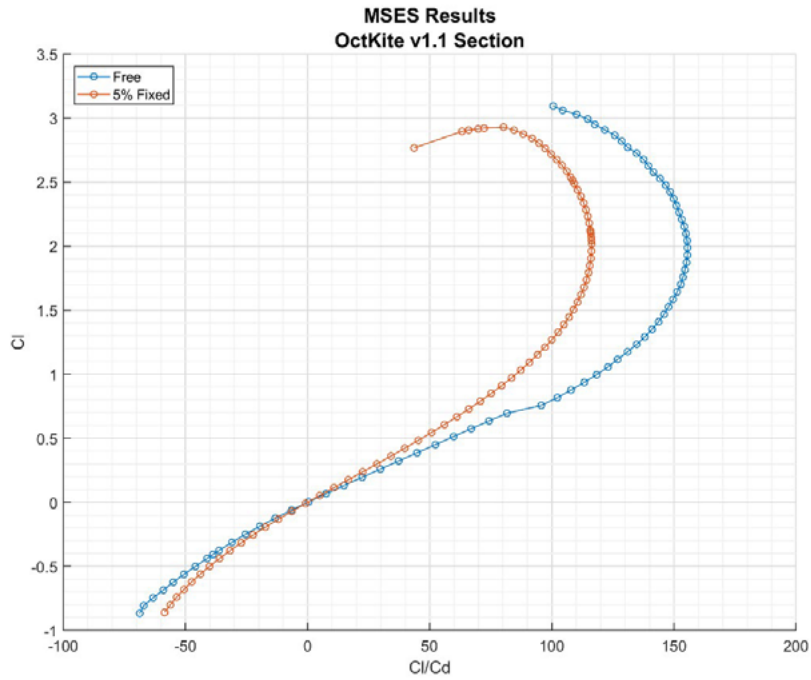


Figure 24 OctKite v1.1 section with free and 5% fixed transition – CI vs CI/Cd

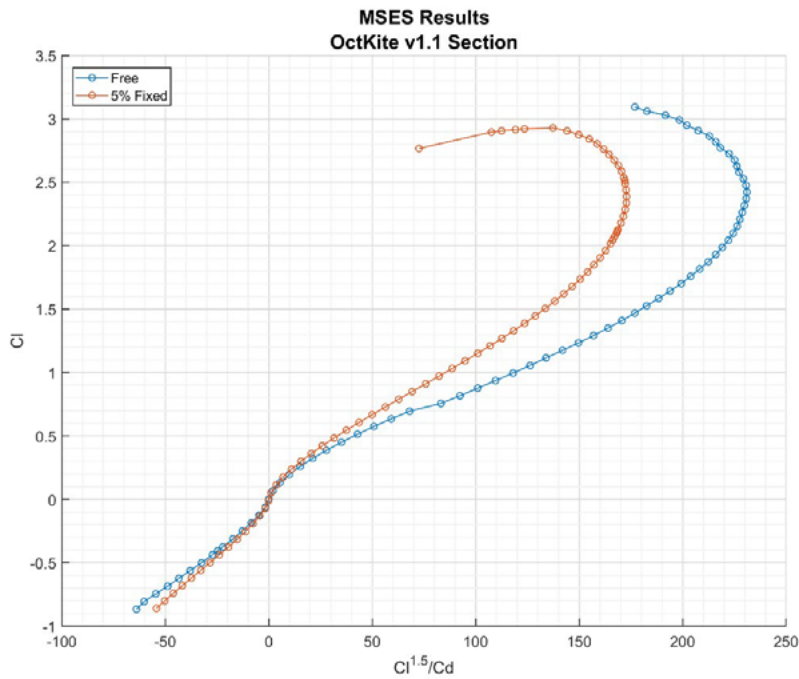


Figure 25 OctKite v1.1 section with free and 5% fixed transition – CI vs CI^{1.5}/Cd

REPORT: TLG-MAK-003		REVISION: 01	PAGE 3-23
AIRCRAFT: October Kite		REV DATE: 11/18/2019	PROPRIETARY
TITLE: Airfoil Design for the October Kite – Feasibility Studies		CUSTOMER: Makani Technologies, LLC	

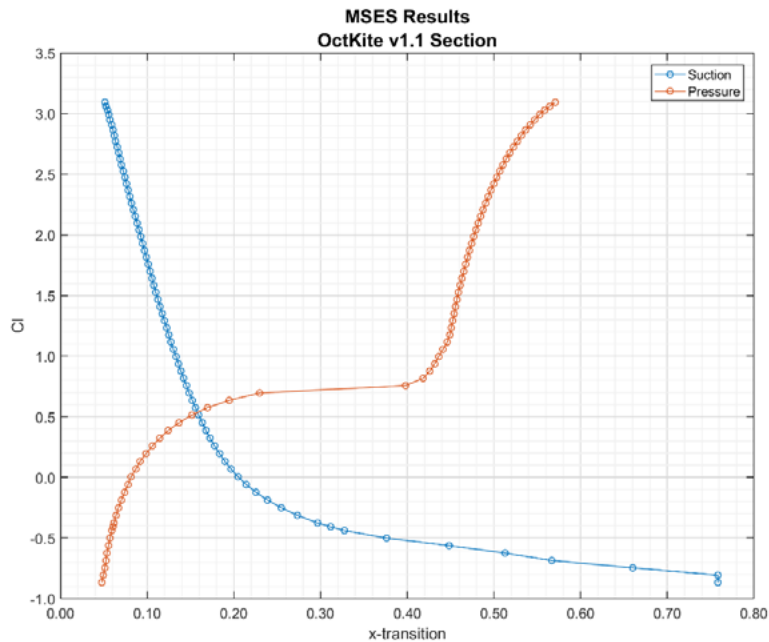


Figure 26 OctKite v1.1 section with free transition only – Cl vs transition location

Lift curves for flap deflections ranging from -20° to $+20^\circ$ are shown in Figure 27 and Figure 28. Those plots show that the flap performs well across the entire range of deflections, with the exception of the -20° deflection case at small angles-of-attack. The root cause of the poor performance is premature separation off of the lower surface which is caused by a less than ideal curvature distribution aft of the spar box, likely the result of trying to also maintain a convex shape. It is TLG's belief that this separation can be fixed in subsequent iterations by improving the lower surface contour, though it remains to be seen how this might affect the convex surface requirement. Figure 29 and Figure 30 show the actuated section lift metric, i.e. $-\Delta C_l / \delta$ with δ as the flap deflection angle and ΔC_l taken relative to the nominal ($\delta = 0$) position. The lines for $\pm 10^\circ$ of deflection remain above the specification of 0.045 for the entire operating range of the section. Additionally, the $\pm 20^\circ$ deflections also stay above this limit for a large portion of the operating range. Lastly, the lower surface separation for negative deflections is illustrated by the performance decline at low alpha values, though TLG anticipates eliminating these performance drops with further iterations.

REPORT: TLG-MAK-003		REVISION: 01	PAGE 3-24
AIRCRAFT: October Kite		REV DATE: 11/18/2019	PROPRIETARY
TITLE: Airfoil Design for the October Kite – Feasibility Studies		CUSTOMER: Makani Technologies, LLC	

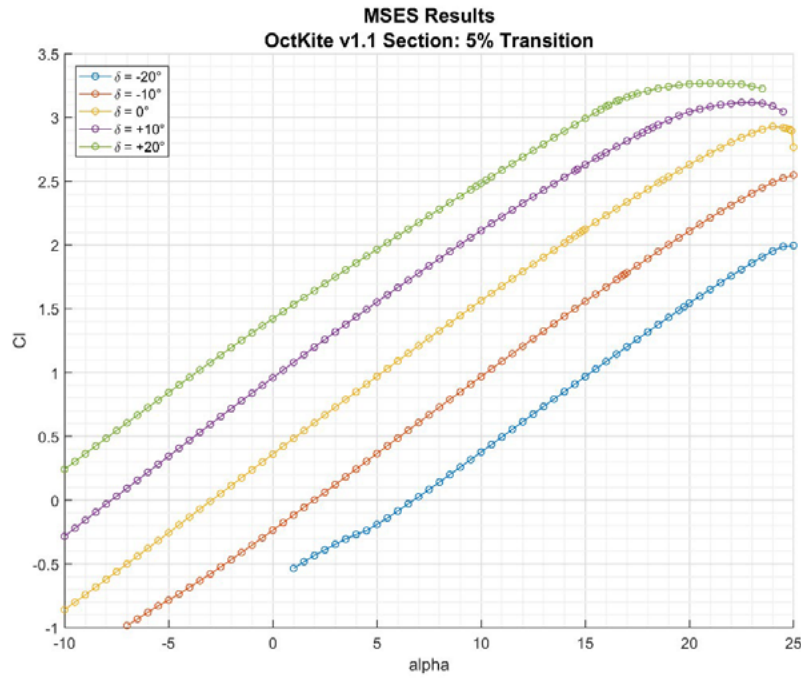


Figure 27 OctKite v1.1 section flap effectiveness for 5% fixed transition – C_l vs alpha

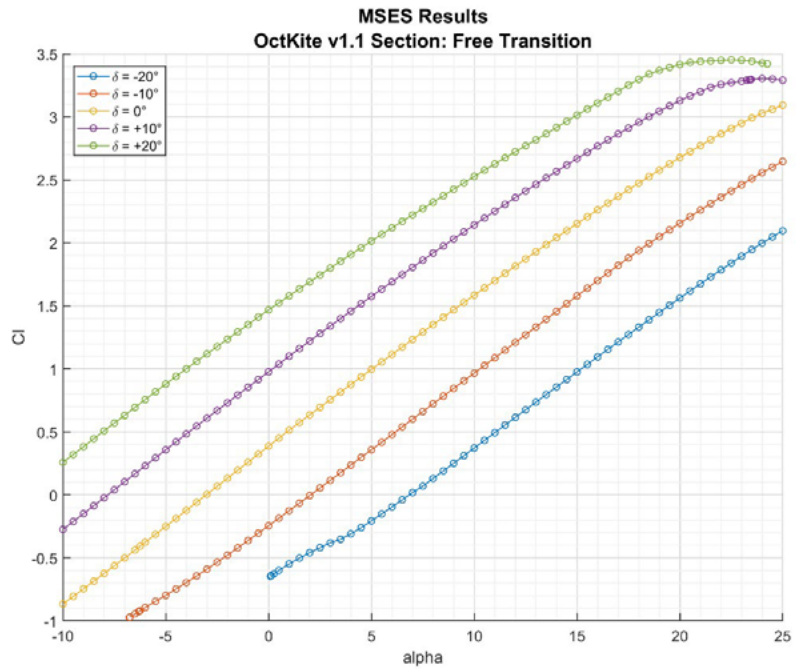


Figure 28 OctKite v1.1 section flap effectiveness for free transition – C_l vs alpha

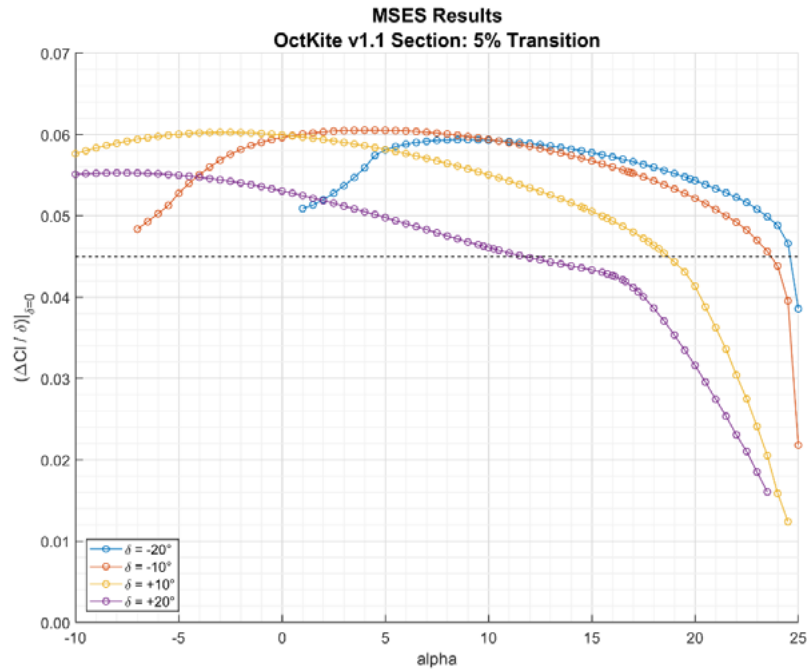


Figure 29 OctKite v1.1 section flap effectiveness for 5% fixed transition – $\Delta Cl/\delta$ vs alpha

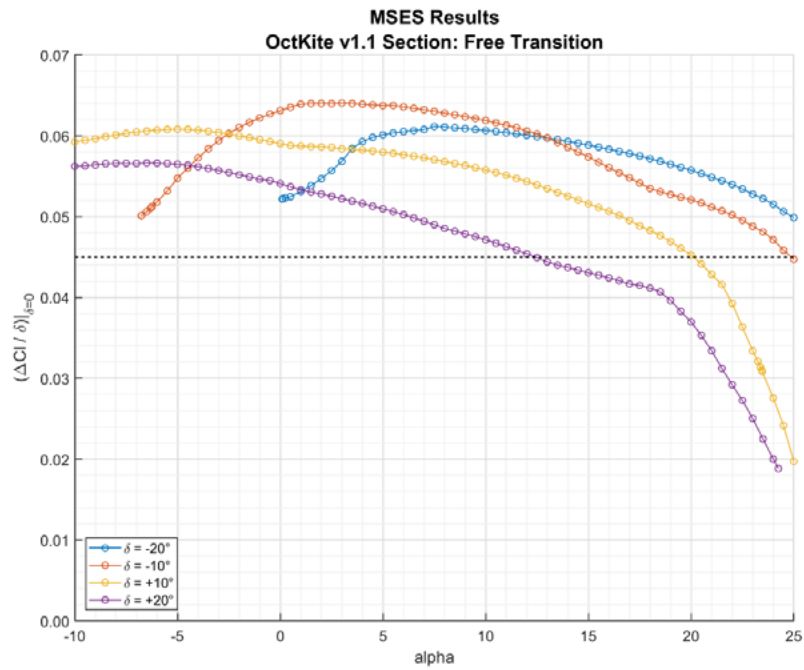


Figure 30 OctKite v1.1 section flap effectiveness for free transition – $\Delta Cl/\delta$ vs alpha

REPORT: TLG-MAK-003		REVISION: 01	PAGE 4-1
AIRCRAFT: October Kite		REV DATE: 11/18/2019	PROPRIETARY
TITLE: Airfoil Design for the October Kite – Feasibility Studies		CUSTOMER: Makani Technologies, LLC	

4.0 Summary

A preliminary section airfoil has been designed which confirms the feasibility of the October Kite planform designed by Makani. Figure 31 presents a CAD model of the full wing using the OctKite v1.1 section, along with an annotation of the key design features. The section was able to meet all of the performance objectives and constraints outlined by Makani in Reference [1]. In fact, the “contaminated” airfoil, i.e. – transition forced at 5% of chord, was able to achieve $C_l/C_d = 116$, which is 155% of the specified minimum performance value. However, as was mentioned in sections 1.0 and 3.2, more work is needed during subsequent iterations in order to more fully quantify contamination performance and any associated risks. Additionally, the current performance should be understood in the context of Stage 1 of the design process, which means that further performance improvements should be possible. Furthermore, one of the main drivers for the airfoil shape is the spar box constraint. Relaxing this constraint, for example through a more coupled aero-structures design process, could lead to a more dramatically different airfoil shape with the potential for greater performance gains.

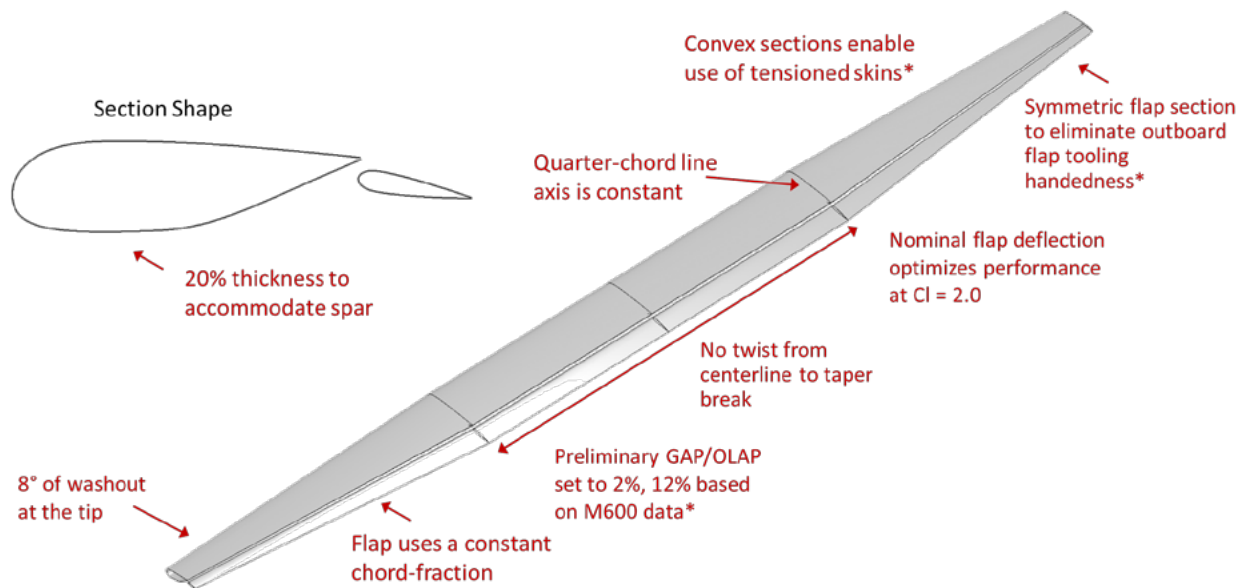


Figure 31 CAD model of the OctKite v1.1 wing with key design features highlighted

An interesting result of the nominal flap deflection investigation was that a single airfoil shape performs at an optimal or near-optimal level across the entire span. It was initially discussed that preliminary design would result in two distinct sections being designed; one for the center-section to the taper break and then another at the tip. However, the results demonstrated that the tip airfoil, which operates at a lower $C_{l,design,max}$ value due to washout, needed a

REPORT: TLG-MAK-003		REVISION: 01	PAGE 4-2
AIRCRAFT: October Kite		REV DATE: 11/18/2019	PROPRIETARY
TITLE: Airfoil Design for the October Kite – Feasibility Studies		CUSTOMER: Makani Technologies, LLC	

similar amount of nominal flap deflection as the root airfoil. This result is likely influenced by the contamination restriction, since this eliminated the possibility of designing a longer laminar flow run which might perform well for a perfectly smooth surface.

Another interesting feature is the relative similarity of the 008613 airfoil from the M600 Energy Kite and the new OctKite v1.1 airfoil designed in this effort. To some extent, the shape of the airfoil is driven by the constraints imposed on the design process and so it is not surprising to see similarities. It should be noted that the new airfoil was completely independent of the previous airfoil during the design process, i.e. – it was not used as a “seed” airfoil during design. Two of the noticeable differences, the leading-edge droop and the location of the suction peak, are likely different due to the contamination criteria. The new design purposefully chose to move the suction peak forward in order to add robustness to a 5% transition location, contributing to the less gradual, more “blunt”, upper surface curvature transition. Further iterations would likely refine the leading-edge design and explore other approaches to adding robustness to contamination while achieving a high performing airfoil.

Another extension of this work that TLG has identified is the need to continue improving the lower surface curvature transition aft of the spar box in order to eliminate the separation which is present at negative flap deflections. The integration of the aero and structures design process would also be very important to this aspect of the design by opening up the design space. This lower surface optimization should also include the cove and flap leading-edge integration. The M600 Energy Kite identified the potential for poor flap performance for moderate flap deflection which impacted the roll power of the kite. Continued improvement of this aspect of the design will be critical to achieving, and exceeding, the roll power requirements necessary for optimal performance of the kite. An additional aspect of optimization in this area would include integrating section performance with deflected flaps into the overall section performance evaluation. This would require a detailed understanding of the in-flight operation of the kite, including the fraction of time spent at different flap deflections and roll rates.

Lastly, the potential for further improvements only further reinforces the feasibility of the October Kite planform. This preliminary design effort has helped to better understand the potential performance of this planform, as well as key areas of the design to focus on in order to maximize overall performance. TLG looks forward to the opportunity to continue working with Makani on this project in order to produce the best overall product possible.